A Petrographic Investigation into the Durability of Common Replacement Sandstones to the Crystallisation of De-icing Salts

Callum James Graham
BSc. (Hons) University of Glasgow

Submitted in fulfilment of the requirements for the Degree of Doctor of Philosophy

School of Geographical and Earth Science
College of Science and Engineering
University of Glasgow

May 2016

Abstract

Scottish sandstone buildings are now suffering the long-term effects of salt-crystallisation damage, owing in part to the repeated deposition of de-icing salts during winter months. The use of de-icing salts is necessary in order to maintain safe road and pavement conditions during cold weather, but their use comes at a price. Sodium chloride (NaCl), which is used as the primary de-icing salt throughout the country, is a salt known to be damaging to sandstone masonry. However, there remains a range of alternative, commercially available de-icing salts. It is unknown however, what effect these salts have on porous building materials, such as sandstone. In order to protect our built heritage against salt-induced decay, it is vital to understand the effects of these different salts on the range of sandstone types that we see within the historic buildings of Scotland.

Eleven common types of sandstone were characterised using a suite of methods in order to understand their mineralogy, pore structure and their response to moisture movement, which are vital properties that govern a stone's response to weathering and decay. Sandstones were then placed through a range of durability tests designed to measure their resistance to various weathering processes. Three salt crystallisation tests were undertaken on the sandstones over a range of 16 to 50 cycles, which tested their durability to NaCl, $CaCl_2$, $MgCl_2$ and a chloride blend salt. Samples were primarily analysed by measuring their dry weight loss after each cycle, visually after each cycle and by other complimentary methods in order to understand their changing response to moisture uptake after salt treatment.

Salt crystallisation was identified as the primary mechanism of decay across each salt, with the extent of damage in each sandstone influenced by environmental conditions and pore-grain properties of the stone. Damage recorded in salt crystallisation tests was ultimately caused by the generation of high crystallisation pressures within the confined pore networks of each stone.

Stone and test-specific parameters controlled the location and magnitude of damage, with the amount of micro-pores, their spatial distribution, the water absorption coefficient and the drying efficiency of each stone being identified as the most important stone-specific properties influencing salt-induced decay.

Strong correlations were found between the dry weight loss of NaCl treated samples and the proportion of pores <1μm in diameter. Crystallisation pressures are known to scale inversely with pore size, while the spatial distribution of these micro-pores is thought to influence the rate, overall extent and type of decay within the stone by concentrating crystallisation pressures in specific regions of the stone.

The water absorption determines the total amount of moisture entering into the stone, which represents the total amount of void space for salt crystallisation. The drying parameters on the other hand, ultimately control the distribution of salt crystallisation. Those stones that were characterised by a combination of a high proportion of micro-pores, high water absorption values and slow drying kinetics were shown to be most vulnerable to NaCl-induced decay.

$CaCl_2$ and $MgCl_2$ are shown to have similar crystallisation behaviour, forming thin crystalline sheets under low relative humidity and/or high temperature conditions. Distinct differences in their behaviour that are influenced by test specific criteria were identified. The location of $MgCl_2$ crystallisation close to the stone surface, as influenced by prolonged drying under moderate temperature drying conditions, was identified as the main factor that caused substantial dry weight loss in specific stone types. $CaCl_2$ solutions remained unaffected under these conditions and only crystallised under high temperatures. Homogeneous crystallisation of $CaCl_2$ throughout the stone produced greater internal change, with little dry weight loss recorded.

NaCl formed distinctive isometric hopper crystals that caused damage through the non-equilibrium growth of salts in trapped regions of the stone.

Damage was sustained as granular decay and contour scaling across most stone types.

The pore network and hydric properties of the stones continually evolve in response to salt crystallisation, creating a dynamic system whereby the initial, known properties of clean quarried stone will not continually govern the processes of salt crystallisation, nor indeed can they continually predict the behaviour of stone to salt-induced decay.

Table of contents

List of tables

List of figures

List of equations

Acknowledgement

Acknowledgments . . . where does one start?

It goes without saying, that without the help, assistance and patience of so many wonderful people this project would never have been the success that it is. I know there are people I will have missed and for that, I sincerely apologise.

First of all, I would like to thank Historic Scotland (now Historic Environment Scotland) for fully funding this PhD project.

Also to the School of Geographical and Earth Sciences who have now had to deal with seeing my face every day for the last 8 years! More importantly, the department has supported my work, provided me with a fantastic working environment and helped fund numerous conferences and meetings. Furthermore, without the excellent grounding in the subject from my undergraduate degree, and without the great opportunity to undertake my undergraduate level 4 project, which was to be the pre-cursor for this PhD, I would never have had this exciting opportunity. It will be sad to finally say goodbye to something that has been a part of my life for so long.

Thank you to my amazing supervisors Martin Lee, Vernon Phoenix, Maureen Young, Alick Leslie, and formerly Craig Kennedy. Without their continued support, dedication, expertise and belief, not only would this project not have been as successful, it would never have made it off the ground. A special individual mention must be given to Martin. Throughout this PhD, he has allowed me the freedom to really design and plan the project myself. He always encouraged and supported my decisions throughout the project, while providing sound advice and expertise. Martin has allowed me to become my own independent researcher, which has been a fantastic and eye-opening experience.

Out-with my official supervisor team, I would like to extend special thanks to various individuals that have all helped me in different ways. I would like to say thanks to Ewan Hyslop and Clare Torney from Historic Environment

Scotland for consistently taking a keen interest in my work and for their constant willingness to help. From The University of Glasgow, I would like to extend thanks to Neil Owen, Hugh Flowers, John Davidson and Derek Fabel for assistance with the construction of equipment, ion chromatography, strength testing and atomic absorption spectroscopy analysis, respectively. Also to Alison Wright, who was always willing to help with my research and always took a keen interest in all the work that I did. And along with Clare, was great company on the conference trip to New York.

From the BGS, Luis provided expertise in my initial stone choice, while Fiona Sillars, from Strathclyde University, Colin Taylor and Natalie Farrell, from Aberdeen University, Robert Atwood, Nghia Vo, and Kate Dobson from Diamond Light source, all provided expertise in undertaking various experiments throughout the project.

Special thanks are also paid to the fantastic team of technical support staff in the school. Particular thanks are given to Robert McDonald for being able to turn his hand to anything I needed support with, John Gilleece for continued support in thin section and sample preparation and for hours of friendly chat and banter, and to Gary Tait for his IT support. Thanks also to Peter Chung for his expertise in SEM training, and to Kenny Roberts for his priceless support and patience in countless experiments (also for allowing me to take over his lab on countless occasions!), and again for their friendly chat. Lastly, thank you to Margaret Jackson, Jacqueline McKie and Dawn Bradshaw for being the unsung heroes behind the scene!

I'm sure that without the amazing atmosphere in the post-grad office, none of us would have enjoyed our PhD experience quite as much as we all have. Thank you to everyone in the office for being amazing friends and for sharing such an amazing time with me. For the fantastic cakes baked by Rebecca, Heather and Kasia (among others) to the hilarious conversations with Jill and Eric; football with Mark; help with experiments from Emma, Caroline and Jessica and the general support and friendliness from everyone else. I have made friends for life. Thank you.

A huge thanks to my family who have all supported me from day one, while always putting up with my geeky rants about my work . . . and for not being too jealous of my various trips to places like New York and Portugal!

Finally to Jen, the person who has always been there for me. Through thick and thin, through the highs and lows, the good times and bad, she was always there for me, supporting my decisions and being the person I could always turn to. You have been my rock throughout the last few years. Your family have also treated me as one of their own during some testing times over the last few years. All I can say is thank you for absolutely everything, and I can't wait to make many more happy memories together.

Declaration

The material presented in this thesis is the result of four years of independent research undertaken at the School of Geographical and Earth Sciences at The University of Glasgow. The research was supervised by Prof Martin Lee, Dr Vernon Phoenix, Dr Maureen Young and Dr Alick Leslie. This thesis represents my own research and any published or unpublished work by other authors has been given full acknowledgment in the text.

Definitions/abbreviation

SEM Scanning electron microscope

ESEM Environmental scanning electron microscope

BSE Backscatter electron

SE Secondary electron

PSD Pore size distribution

MIP Mercury intrusion porosimetry

μCT Micro computed tomography

DWL Dry weight loss

MWL Maximum weight loss

BGS British Geological Survey

BRE Building Research Establishment

XRD X-ray diffraction

XRF X-ray fluorescence

RH Relative humidity

IC Ion chromatography

AAS Atomic absorption spectroscopy

CMC Critical moisture content

EDX Energy-dispersive X-ray spectroscopy

CEC Cation exchange capacity

DIA Digital image analysis

USV Ultrasonic velocity

FT Freeze-thaw

Linac Linear accelerator

1 Introduction

The aim of this study is to understand the most important micro-structural properties of sandstone that control its sensitivity to the crystallisation of three different de-icing salts and to understand the salt-specific mechanisms controlling the observed changes in the stone. In order to accomplish this task, a detailed review of the literature must be undertaken. Particular goals are to assess the current state of the art, to identify the most important weathering processes associated with salt-induced decay, and the characteristics of the stone that promote increased salt decay. In addition, the current issues surrounding stone decay in Scotland are reviewed, including the importance of Scottish built heritage and current stone-decay research in Scotland. Finally, it is important to understand current de-icing practices within Scotland, including recent developments in policy, the de-icing salts available to the transport authorities and the associated environmental issues surrounding de-icing salt use. Each topic is discussed in turn in this chapter.

1.1 Historical Importance: Building stones in Scotland

Every built structure has been constructed from natural resources found on or within the Earth.

"The link between architecture and geology is inescapable" (Maxwell, 2010)

Scotland has a rich and complex geological history, and its traditional buildings showcase the varied and unique rock types from which they were built; this property gives the towns and cities of Scotland their distinctive character. During the mid-late 19th Century, Scotland had in excess of 700 working quarries (Hunt, 1859 in McMillan and Hyslop, 2008) satisfying local, national, and international demands for stone. Through increased trade-links with North America, Scottish building stone was frequently exported as ballast on returning merchant ships. This commerce ultimately led to Scottish stone being used as high quality building material internationally, with Caithness flagstone being employed as a paving stone throughout Europe, India and North America, and Locharbriggs and Cove sandstones being used to construct the base of the Statue of Liberty (Blockstone Ltd website, 2013). Today however, Scotland has roughly 20 operating quarries, 12 of which supply sandstone (McMillan et al., 2006). This loss of local stone sources has increased the severity of the long standing problem of sourcing suitable stone for replacement masonry. Many of these remaining quarries cannot provide building materials of sufficient quality, which has led to Scotland, formally a great stone nation to import many of its building stones. Through extensive investigation we have a good understanding of how the traditional stones decay (Smith et al., 2002), but long-term weathering responses between newly emplaced stones and the original stone within historic building façades is often unknown, thus further exacerbating current problems faced by the heritage industry.

There are two approaches to understanding the long-term weathering behaviour of replacement, "foreign" sandstone in historic buildings, namely: (i) Finding better replacement stones by: re-opening historic quarries, finding new and more suitable matching stone, re-using sound stone from demolished buildings; and (ii) Protecting historic masonry by better understanding the

decay mechanisms, using safe and suitable maintenance techniques and taking steps to limit future stone breakdown, for example, by carefully selecting suitable salts for de-icing. This thesis considers the second approach, and specifically looks to better understand the process of salt crystallisation within sandstone. The results will ultimately help Historic Environment Scotland to inform the owners of vulnerable buildings in their care of the most suitable de-icing salts to be used around them, and will also allow Historic Environment Scotland to make recommendations on the best types of replacement stone to use in the lower courses of buildings (bottom 1 to 2 metres) for future salt resilience.

1.1.1 Building stone in Scotland

The use of building materials in central Scotland can be divided historically into three phases (Lawson, 1981); each is characterised by differences in the cost and ease of transportation and extraction. The first phase dates to the early 1800's, when only locally sourced material was used in any substantial quantity. Construction was therefore constrained and determined by local geology. During this time appearance was not a crucial consideration for building stone; durability, ease of extraction and accessibility were the most important factors. A second phase dates to the 19th century. The dawn of the industrial revolution and subsequent railway transportation significantly influenced the cost and ease of building stone transportation and production. As a consequence, the local character of the buildings within many towns and cities across the country was changing owing to the use of more durable 'imported' stone. This innovation sparked a great resurgence in the construction industry with the expansion of many towns and cities. The second phase buildings have perhaps influenced the distinct character of towns and cities to a greater extent than any other period in history. As the cost of labour increased during the 20th century, quarrying became un-economical and the direction of the construction industry switched once again. Today, most buildings are constructed from steel and concrete, with the use of natural stone typically confined to cladding.

The 18th century saw the start of substantial growth in both Glasgow and Edinburgh. In 1736 plans for Edinburgh's New Town were drawn up that were

to have a lasting legacy on the city and prompt further expansion of the city throughout the 19th century. The best quality local stone was used during these initial constructions including the famous Craigleith sandstone that was also used extensively throughout the old town of Edinburgh. The history of use of Craigleith sandstone is covered in depth in the 'Building Stones of Edinburgh' (McMillan et al., 1999). The cultural, historical and architectural importance and beauty of the old and new towns of Edinburgh were acknowledged in 1995 by their inclusion as a UNESCO World Heritage Site.

In Glasgow, rapid expansion took place towards the end of the 18th century, and throughout the 19th and into the 20th centuries. The city is characterised by some of the finest examples of Victorian architecture in the UK (McMillan and Hyslop, 2008). Local blonde sandstone, quarried at sites across Glasgow and Lanarkshire, was the stone of choice used throughout the city. Following the expansion of the railway network in the mid 1800's, red sandstone (Locharbriggs, Cove etc), quarried in Dumfries and Galloway and Ayrshire, was in greater demand. This combination of sandstones is clearly evident throughout parts of the city, with Kelvingrove Museum uniting these contrasting stones within its construction, as is illustrated in Figure 1-1. Other notable sandstones used throughout both Glasgow and Edinburgh and across the world include the flagstones of Angus and Caithness. Due to their high strength and regular bedding, they provide durable internal and external paving stones. Quarrying continued within Glasgow until the early 20th century, where the flooding of quarries and a rising cost of stone extraction ended this once lucrative industry.

Elsewhere in Scotland, other building stones are used more extensively than sandstone. Granite is the most prominent construction material within Aberdeen and the surrounding areas (Peterhead etc), and is also used extensively throughout the rest of Scotland for the lower courses of buildings. Additional notable sources of granite were in Galloway and the Scottish highlands (e.g. Ross of Mull). Other igneous rocks have been used sparingly across Scotland as building stone, with examples of dolerite used throughout Edinburgh (McMillan et al., 1999). Metamorphic rocks also provide important construction materials, with marble used as decorative and ornamental pillars within buildings, while slate is used as traditional roofing material,

quarried extensively in Ballachulish and the southern Hebridean islands of Luing, Seil and Easdale. Throughout the UK, stone from the whole geological column (Precambrian – Quaternary) has been used at some point (Jefferson, 1993; Lott, 2013) with towns and cities traditionally characterised by the underlying geology of the area.

Figure 1-1: Exterior and interior of Kelvingrove Museum.

Kelvingrove museum marries two of the distinctive Glasgow stone types into the one building. Giffnock sandstone is used as the interior stone and Dumfriesshire red sandstone used as for the exterior façade.

1.1.2 Protecting Scotland's built heritage

Scottish built heritage is subject to varying forms of decay processes that pose considerable current and future threats to its conservation and preservation. In addition, recent figures show that 83% of tourists come primarily to visit Scotland's historic sites, with research findings showing that Scotland's historic environment supports more than 60,000 jobs and contributes in excess of £2.3 billion to Scotland's GVA (Gross Value Added) (Historic Scotland, 2009; Historic Scotland, 2012). Thus, safeguarding the built heritage of Scotland remains unquestionably important and this starts with our understanding of stone decay mechanisms and the implementation of protocols for the conservation and protection of historic buildings and stone resources.

Throughout this thesis, the term "historic buildings" is used extensively but its definition can vary with individual perception. According to Historic Environment Scotland, a building is classified as being "historic" or "traditional" if it was built before 1919 and uses load-bearing mass masonry walls, with pitched roofs covered in slate or other natural roofing materials. Furthermore, there are approximately 47,600 listed buildings within Scotland;

this equates to ~1% of Scotland's total building stock (Historic Scotland, 2011; Historic Scotland, 2013). A listed building is recognised as being of special interest (Historic Scotland, 2013). Historic Scotland is charged with maintaining this list under the Scottish Historic Environment Policy, 2011. Buildings are selected in accordance to: (i) age and rarity, (ii) architectural or historic interest and (iii) close historical association (with nationally important people or events). There are three categories of listing and are arranged according to their importance to the above criteria. A listing serves to protect the building from further development in order to preserve its character and ensure its preservation. Not all listed buildings are "historic", but are no less important to Scotland's rich heritage. In order to protect these buildings, it is vitally important to understand the changing behaviour of the stones used in their construction.

1.1.3 Building Stone Resources in the UK

There has been considerable recent work published within the UK highlighting the increased awareness and practical need for a substantial, sustainable and nationally collective UK database and archive of indigenous stone types and sources in response to the closure of many historic quarries and the reduction of indigenous stone from the UK marketplace (Lott, 2013). These closures present a significant problem for those working in the heritage and conservation industry as many of the remaining indigenous stones are incompatible with historic stone types, while the compatibility of other replacement stones over substantial time-scales is unknown. Furthermore, there has been an increased awareness of the importance of the local character and architectural and historic identity of our towns and cities on tourism to the Scottish and UK economy (McMillan et al., 2006).

Lott (2013) presents a comprehensive overview of the stratigraphic distribution of building stones in the UK, covering limestone, sandstone, igneous and metamorphic stone sources and their importance as regional building stones in the UK. Lott recommends the use of an indigenous stone database for the UK, citing one specific initiative led by English Heritage, whereby the localities of closed quarries are identified along with the number

of remaining buildings constructed from each identified quarry. It is thought that this initiative will help to ascertain where lucrative markets for the indigenous stone remain. Subsequent industry interest and economic potential must then be generated for operators to consider re-opening abandoned quarries.

Thomas and Cooper (2014) propose a novel approach to safeguarding heritage building stone resources in England and Wales. They propose a hierarchical system of protecting building stone resources in a similar manner as those implemented for the protection of mineral resources in the UK. Its development would rely on a score system dependent on: (i) known geological features of the quarry/lithological unit, (ii) the historical and cultural importance of buildings built from its stone, (iii) the former scale of production and reasons for its closure, (iv) technical parameters of block size, physical properties and wastage associated with workings, cuttings and block sizes, (v) anticipated market trends of colour, size, proximity and competition, (vi) accessibility and (vii) legislative limitations and access to capital.

Hyslop et al., (2010) gives an overview of the resources offered by the British Geological Survey (BGS) for the repair and conservation of historic buildings. An essential procedure when selecting suitable replacement stone is through petrographic analysis of thin sections and porosity and permeability measurements of representative samples of the original stone. The BGS currently retains the BRITPITS database on UK mines and quarries, holding over 2300 entries on currently active mine workings. There are currently over 400 active and a further 17000 inactive quarries archived by BRITPITS. In addition, the BGS holds a comprehensive petrographic database on historic stones, and are responsible for maintaining the Scottish building stone quarries database containing over 16000 records of mines and quarries, with additional information relating to the use of these building stones.

McMillan and Hyslop (2008) give an overview of the building stone geology and its use in Edinburgh. The current policies and strategies as used in The World Heritage Site Management Plan for the conservation and protection of the Edinburgh World Heritage Site are summarised.

Results of the Glasgow Built Heritage Project are given by Hyslop and Albornoz-Parra (2009). The aim of this project was to address the issues of poorly maintained buildings, poor availability of replacement sandstone and stone decay within Glasgow. It was commissioned by Scottish Enterprise Glasgow and the Scottish Stone Liaison Group, with results from the original report summarised by Hyslop et al. (2006). They undertook condition surveys of 234 building façades and petrographic analyses of a representative range of the stone types used in both listed and non-listed buildings. Choices of analysed buildings were made in relation to their age, geographic distribution throughout the city, architecture style and façade orientation. They characterised the blonde and red sandstones of Glasgow and categorised them into ten distinct sub-groups, (B1 – B6) and (R1-R4) based on their mineralogy and using comparisons to archived thin sections of historic sandstones (Figure 1-2).

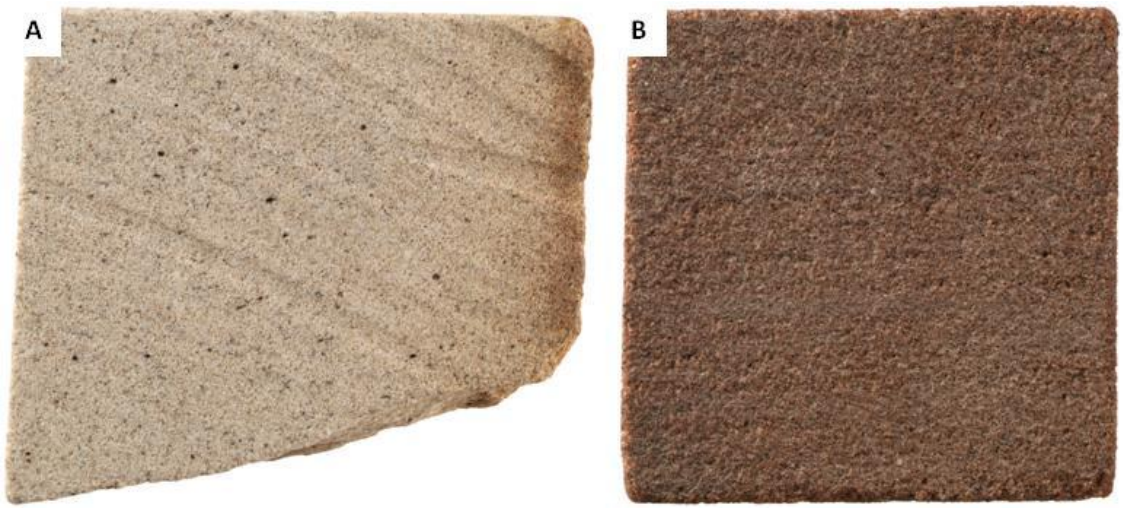

Figure 1-2: Examples of sandstone commonly used throughout Glasgow.

Examples of the common blonde and red stone types used within Glasgow. (A) Giffnock sandstone; an example of stone type B2a taken from the University of Glasgow. (B) Locharbriggs sandstone; an example of stone type R3 acquired from Locharbriggs Quarry. These are the same stone types used in Kelvingrove Museum: Giffnock was used in the interior and Locharbriggs was used in the exterior.

Hyslop and Albornoz-Parra (2006) concluded that a likely cause for decay across many of the studied buildings in Glasgow was from past air pollution and subsequent inappropriate repairs. A legacy of poor stone cleaning methods has also caused significant discolouration and has weakened the outer zones of the stones. Scaling decay and case-hardening was shown to be a major phenomenon affecting blonde sandstone due their higher carbonate,

Fe oxide and clay contents. Red sandstones experience granular disaggregation owing to a more open pore structure and higher volume of quartz cement. It is estimated that repairs to blonde sandstone would require 60% more stone and 45% more total masons time in comparison to red sandstone within the city (Hyslop and Albornoz-Parra, 2006). This difference is linked to the complex mineralogy and weathering systems within blonde sandstone and their older age when compared to red sandstones. 91,000 tonnes of red and 294,000 tonnes of blonde sandstone are estimated to be needed for repairs over the next 15-20 years from 2006.

An important issue relevant to Scottish building stones as identified in the literature is the legacy of past cleaning. Young et al. (2003) presents a review of cleaning techniques used within Scotland on a range building stone types. They highlighted that bleaching is an important and irreversible consequence of chemical cleaning on granites and is caused by the washing out of strongly coloured minerals. Granites are, however, less vulnerable to negative impacts of cleaning and, in some cases, stone cleaning was shown to be beneficial for their long-term durability. Sandstones are generally more vulnerable to post-cleaning decay, specifically immature sandstones containing high clay and carbonate contents, such as the blonde sandstones of the Glasgow region. Abrasive stone cleaning methods may open up pores close to the surface and enlarge micro-cracks in sandstones, changing the intensity of wetting-drying cycles and increasing the vulnerability of the surface to penetration by other decay agents. Chemical cleaning may enhance salt related decay in the form of granular disintegration and increase the susceptibility of stone to biological growth (Young et al., 2003).

In light of several contradictory reports of the effects of stone cleaning on the long-term susceptibility of stone to decay, Zurakowska and Hughes (2013) conducted a field-based façade survey on sandstone buildings in Paisley, West Scotland, using a method similar to Warke et al (2003). They chose sections of both cleaned and non-cleaned building façades that suffered decay entirely related to cleaning practices using a simple decision making process that is highlighted in Figure 1-3. This procedure was designed in order to exclude the influence from other decay factors on the individual blocks, such as enhanced water ingress through capillary rise and leaking from damaged

parapets. They found that in the 49 investigated buildings, previous stone cleaning was not an important contributor to decay, with the majority of cleaned buildings found in a better condition than non-cleaned ones due to the continued maintenance of rainwater goods. The authors conclude that while stone cleaning was expected to have a lasting impact on stone behaviour, other factors had a greater influence across the studied buildings. The most important factors influencing decay were associated with moisture ingress linked to building design and poor maintenance.

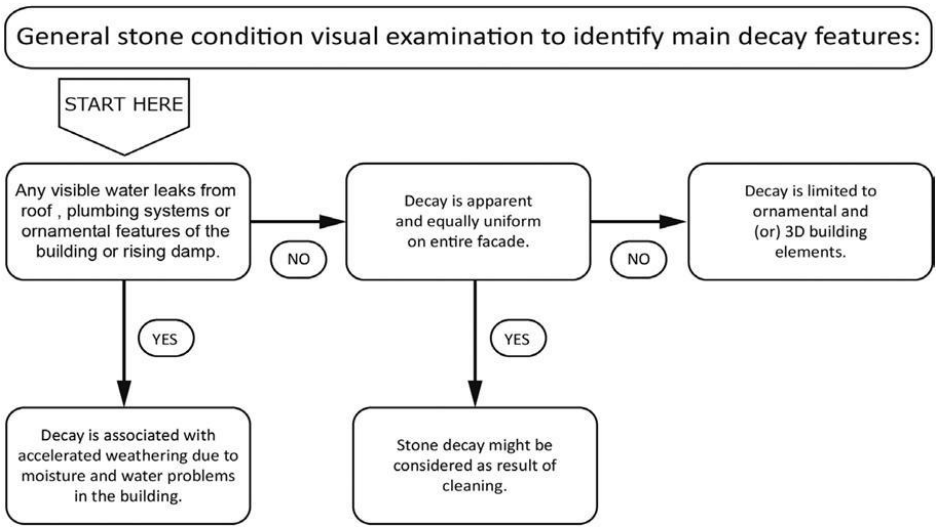

Figure 1-3: Decision making process used by Zurakowska and Hughes (2013).

1.2 Stone Decay

Most masonry decay processes are natural phenomena, driven by environmental forces and influenced by inherent properties of the stone. The understanding of natural weathering processes can be invaluable in the prediction and mitigation of various forms of decay (Siedel and Siegesmund, 2011). The classification of stone decay has been debated for many years, with much of the terminology being criticised for a lack of coherence (Siedel and Siegesmund, 2011). In 2008 the International Council on Monuments and Sites (ICOMOS) International Scientific Committee for Stone (ISCS) released a definitive glossary including all recorded definitions of stone decay, which is now regarded as a standard for its categorisation (Cartwright et al., 2008).

The glossary recognises six main areas of decay: (i) general terms, (ii) crack and deformation, (iii) detachment, (iv) features induced by material loss, (v) discolouration and (vi) deposits and biological colonisation. Accepted

terminology refers to either physical or mechanical processes such as “impact damage” and “scratch marks” and feature oriented observations including “honeycomb weathering” and “peeling”.

Decay, deterioration, degradation and other general terms are commonly misused and poorly referenced. Decay is defined as the actual chemical or physical *modification* of the stone properties that may lead to a loss of aesthetic value or mechanical functionality. Stone weathering on the other hand, which is regularly used interchangeably with decay (Pope et al., 2002), refers to the chemical or mechanical *process* that causes the chemical/physical modification to the stone, consequently leading to a change in stone character and deterioration. The reason for this extensive list of sometimes equivalent terms stems from the various disciplines in which they originate. Not all perceived “alteration” of masonry is necessarily detrimental to the mechanical integrity of stones, as the definition entails. What might be perceived as a loss of aesthetic value may not be indicative of actual degraded masonry. Conversely, what might appear to be superficial and initially insignificant may well be symptomatic of an underlying and more severe problem. Smith and Přikryl (2007) suggest a medical analogy for understanding stone decay, whereby decay is compared to the effects of an illness. What is evident however is that in time, stones will naturally degrade and change in response to the changing environment even when devoid of serious underlying problems (Smith and Přikryl, 2007). Durability is therefore not a continuous property of the stone that can be determined by a single test, nor can it be used indefinitely to determine the life-span of a building stone. When trying to understanding durability, a substantial number of tests must be carried out, together with an understanding of the use of the stone and the environmental conditions that it has been exposed to. It is essential for the classification of stone decay that we recognise and understand observable damage and associated processes.

The weathering and decay of building stone is a natural response of the stone to reach equilibrium within the environment due to the differences between its conditions of formation within the earth’s crust and the environment to which it is exposed on a building façade. Weathering and decay of building stone is a response to four main weathering parameters: physical, chemical,

biological and anthropogenic. Physical weathering involves the decay associated with freezing and thawing of water and saline solutions, and the crystallisation of salts within the pore spaces of the rock. Chemical weathering entails dissolution, precipitation and hydration de-hydration reactions, while biological weathering involves the growth and habitation of micro organisms and plant species within the stone (Miller et al., 2012). Anthropogenic parameters involve the damage of stone through forceful impact, vandalism and quarrying processes. The protection and conservation of building materials is therefore a multi-disciplinary field, relying on the integration of research from a number of fields including geology, physics, biology, chemistry, engineering and architecture.

1.2.1 Freeze-thaw Weathering

Freeze-thaw is an important weathering mechanism affecting both the built environment and helping to shape our natural world. Freeze-thaw weathering occurs due to recurrent freezing and thawing events affecting water and saline solutions within porous materials. The actual freezing of solution that is under pressure within stone occurs in a very similar way to non-pressurised water, forming common hexagonal crystals when below the solution freezing point ($0^{o}C$ for pure water). Freeze-thaw weathering is therefore intimately linked to climatic conditions. A recent study by Grossi et al. (2007) considered the long-term importance of freeze-thaw cycling as a major weathering process affecting the built heritage of Europe by using climate model predictions. They concluded that the number of freeze-thaw cycles experienced by several important cities around Europe will fall, while archaeological sites in Northern Europe may become more susceptible to freeze-thaw decay as protective permafrost layers will diminish. Freeze-thaw weathering can be traced as an important and widely accepted geomorphic process in cold regions (Matsuoka and Murton, 2008). However, as Hall and Thorn (2011) report, there are many contentious issues surrounding the regularly cited terminology and scales of damage associated with freeze-thaw as a geomorphic weathering agent. Some of the most prominent issues raised by the authors include the conflation of the freeze-thaw “process” and “product” and in particular, the process and product descriptive terms macrogélivation and microgélivation.

The characteristics of water freezing in stone may be the same as free water; however, the behaviour of the liquid-ice system is different when placed under increased pore pressure, as explained by thermodynamics. Ice formation in stone is governed by temperature and pressure; the latter influenced by the curvature of the ice-solution interface and pore size. Ice will initiate and grow within the largest pores, with subsequent growth into smaller pores taking place with decreasing temperature. Therefore ice and water will exist in equilibrium at the same temperature when experiencing an increase in pressure. The thermodynamics associated with ice growth in porous materials are identical to the approach used to understand salt crystallisation (Scherer, 1999) and as explained later, certain salt crystallisation models have been adapted from original freeze-thaw models (Everett, 1961).

There have been three main mechanisms proposed by which freeze-thaw cycling of pure water can cause damage to porous materials (Ingham, 2005). The first mechanism concerns the 9% increase in volume of water upon freezing (Figure 1-4). Pressure is exerted by the expansion of ice through a thin water film separating the ice from the solid pore walls. By maintaining this film, which is essential for growth, by continued fluid replenishment, high pressures are exerted on the rock through this ice-solution-solid film (Tharp, 1987). The freezing pressure due to a volume increase was considered an important process by Hirschwald (1908) when he suggested the use of a saturation coefficient to determine the susceptibility of stone to freeze-thaw weathering. The saturation coefficient is the ratio between the pore space capacity of natural stone saturated under atmospheric conditions and the capacity of pores when saturated under vacuum (Přikryl, 2013). Hirschwald observed that stones with a saturation coefficient of 0.8 (80% saturation) were most susceptible to freeze-thaw damage (Ingham, 2005), with samples giving values of 0.7-0.85 categorised as unsafe and values <0.7 categorised as resistant to freeze-thaw weathering (Přikryl, 2013). In theory, any stone with a saturation coefficient of > 0.91 will experience damage associated with the 9% volume expansion of ice. However, such conditions that force water into pores as to allow for complete saturation of stone by water to take place are extremely unlikely within a building façade. Other

mechanisms have therefore been proposed to explain the phenomenon of freeze-thaw damage.

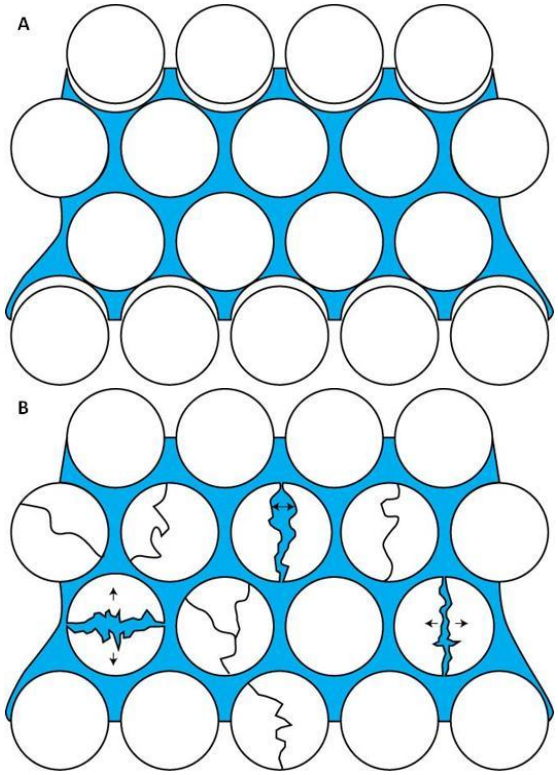

Figure 1-4: Schematic diagram showing freeze-thaw damage through the volume expansion theory.
(A): water is occupying most of the available pore space within the stone. (B): Upon freezing, there is a 9% volume increase owing to the water-ice phase change. If the stone has a high saturation coefficient, then high pressures will develop within the stone.

A second proposal is linked to the volume expansion of ice as discussed above, but relies on the expulsion of free, un-frozen water from pores as ice forms within them. It is thought that if water is expelled from these pores at a high enough rate then subsequent damage could take place caused by an increased hydraulic pressure in the water (Powers, 1945). A similar mechanism was proposed by Chatterji and Cristensen (1979), who suggested that if the outer surface of the stone was sealed with ice, then any accumulation of hydrostatic pressure caused by ice formation within the stone cannot be relieved by water expulsion to the surface and so high pressures may develop. As highlighted by Ross et al. (1991), damage associated with an increase in hydraulic pressure requires an improbably high freezing rate, while the first proposal does not (Ingham, 2005).

A third mechanism is related to the formation of an ice lens that develops within the largest pores of the stone. Water available within the small pores

connected to the growing crystal continues this growth by diffusion. A pressure will develop in the smaller pores allowing ice growth to initiate once the large pores are filled. If water remains in the small pores, continued growth will take place there (Ingham, 2005).

Pressure plays an important role in reducing the freezing point of water and therefore influencing freeze-thaw processes. Pressure experienced by the pore water is influenced by the material properties of the stone; several important parameters are known, which include the pore size distribution (Chen et al., 2004; Al-Omari et al., 2015), however, saturation is accepted as the most important parameter used to assess freeze-thaw susceptibility (Ingham, 2005).

Other important parameters that have been measured to help predict and evaluate freeze-thaw damage include the change in properties such as capillary coefficient (Thomachot and Jeannette, 2002), compressive strength (Martinez-Martinez et al., 2013), tensile strength (Jamshidi et al., 2013), pore size distributions as determined by mercury intrusion porosimetry (Mallidi, 1996) and ultrasonic velocity testing (Thomachot and Jeannette, 2002). Martinez-Martinez et al., (2013) highlight that the effective porosity is an important parameter correlating with the eventual breakdown of carbonate rock types after freeze-thaw tests. They find that the decay pattern of rocks under freeze-thaw weathering is non-linear, with rapid decay eventually taking place after micro cracks and micro fractures within the rock are exploited. Martinez-Martinez et al., (2013) recommend the use of ultrasonic velocity testing in understanding and predicting catastrophic decay from freeze-thaw processes.

Nicholson and Nicholson (2000) show that the presence of pre-existing rock flaws does not directly affect the amount of decay but can influence the locality of further decay. They found in laboratory tests that crystalline rocks tend to fracture across linear planes of weakness such as veins and stylolites, while decay to sandstone specimens was influenced by textural characteristics. In weak stones such as chalk, decay was completely random.

Several decay function models have been proposed for understanding the freeze-thaw process of building stone types (Yavuz et al., 2006; Bayram, 2012). Mutlutürk et al. (2004) suggested a mathematical model using a decay constant and disintegration rate to explain how rocks behave under freeze-thaw weathering. They indicate that the disintegration rate is related to the changing rock integrity, as measured by the shore hardness test at the start of each freeze-thaw cycle. By using this model, the amount of freeze-thaw cycles needed to predict durability can be dramatically reduced. This model was successfully evaluated by Jamshidi et al. (2013) and Khanlari et al. (2014) when using the Brazilian tensile strength and point load tests and uniaxial compressive strength tests, respectively to measure changing stone integrity. The model accurately predicted stone durability in both studies. The above cited mechanisms only consider pure, uncontaminated water and do not consider the range of thermal properties of stone that will also contribute to mechanical stresses experienced by the stone.

1.2.1.1 *Freeze-thaw Weathering with Salts*

Standard freeze-thaw tests assume that pure water is the only freezing liquid present. In natural conditions however, pore waters within building stones usually contain a number of dissolved chemicals, most notably dissolved salts (McCabe et al., 2013). Freeze-thaw tests using pure water may then seem like a simplification, and it is; however, within the freezing process, only pure water within the solution will freeze and salt ions are expelled from the ice forming process. It stands as fact though, that laboratory studies have shown that the addition of salt solution alters the behaviour of the sample within the freeze-thaw test. Unfortunately, freeze-thaw weathering in the presence of salts is poorly understood, although there have been attempts from the fields of concrete and natural stone research to explain the phenomenon, and certainly it must be considered as a weathering process when associated with understanding the effects of de-icing salts on natural stone.

One of the most commonly cited decay mechanisms caused by the freeze-thaw of salt solution on cement is through salt scaling (Pigeon and Pleau, 1995; Şahmaran and Li, 2007; Valenza II and Scherer, 2007 a, b). Salt scaling

is superficial damage in itself, caused when saline solution freezes on the surface of concrete. During the freezing process, flakes of the cement paste break from the surface leaving the internal body of the cement vulnerable to further decay (Valenza II and Scherer, 2007b). This process is discussed further in both papers by Valenza II and Scherer (2007 a, b).

One of the first studies of freeze-thaw weathering of natural stone by salt solution was by Williams and Robinson (1981), who built on previous results by Goudie (1974). They reported preliminary results of freeze-thaw tests on Ardingly sandstone from southeast England using de-ionised water, saturated NaCl and saturated Na_2SO_4 solutions. Their results showed that in less than 20 freeze-thaw cycles vacuum saturated NaCl, vacuum saturated Na_2SO_4 and partial saturated NaCl samples completely disintegrated, while de-ionised water saturated samples remained unaltered. These results correlate well with those reported by Goudie 7 years earlier, highlighting the potential of salt solutions to increase the destructiveness of freeze-thaw cycling.

In reply to the works of Williams and Robinson (1981) and Goudie (1974), McGreevy (1982) published contradictory results from salt freeze-thaw tests on limestone samples. In his work, water saturated samples produced more damage than either salt solutions, however agreement was found with Williams and Robinson (1981) showing that NaCl was more destructive than Na_2SO_4. As discussed by McGreevy, all three studies cannot be accurately compared due to differences in salt concentrations, freezing rates, freezing intensities, solution uptake mechanisms and lithologies used.

It has been postulated that lower concentrations of salts cause more damage than higher concentrations (0.25, 0.5 and 1M concentrations were used in McGreevy's (1982) work), with the freezing of water to form ice being the dominant mechanism causing damage. Partial saturation allows accommodation space for ice growth within the sample and even with salt crystallisation, stress levels within the stone will not be enough to damage the stone. McGreevy (1982) concludes that the higher levels of damage found in previous studies is likely caused by the use of saturated salt solutions. With saturated solution, ice growth will quickly lead to the supersaturation of the remaining solution and high levels of salt crystallisation will take place.

Combined with ice expansion, high pressures will develop, thus causing considerable damage. At lower salt concentrations, supersaturation of the solution will take much longer to attain, if it is met at all, while at the same time, the addition of salt lowers the freezing point and therefore less ice crystallisation takes place, hindering the onset of damaging pressures. Therefore it is considered that salt concentration thresholds must be met before: (i) salt significantly depresses ice growth at low concentrations, and (ii) salt crystallisation becomes dominant, causing greater damage. These thresholds can be compared to the "pessimum" salt concentrations as discussed in concrete salt scaling research (Valenza II and Scherer, 2007b).

In a follow-up paper to their 1981 work, Williams and Robinson (2001) undertook salt freeze-thaw tests using mixed salt solutions. NaCl is shown again to be the most damaging salt; however an acknowledgement of the importance of McGreevy's suggestion of salt concentration thresholds is made.

From this literature review on salt freeze-thaw weathering it can be concluded that this is an area of research that is in need of continued development. It is thought that at high salt concentrations and low temperatures, salt crystallisation will operate alongside ice growth to cause increased damage. At lower salt concentrations however, a threshold is met whereby the addition of salt will depress the freezing point and lower the amount of ice growth. While not meeting supersaturation, salt crystallisation does not take place, inhibiting freeze-thaw weathering. Figure 1-5 highlights the relationships between the salt concentration and damage vulnerability of building stones.

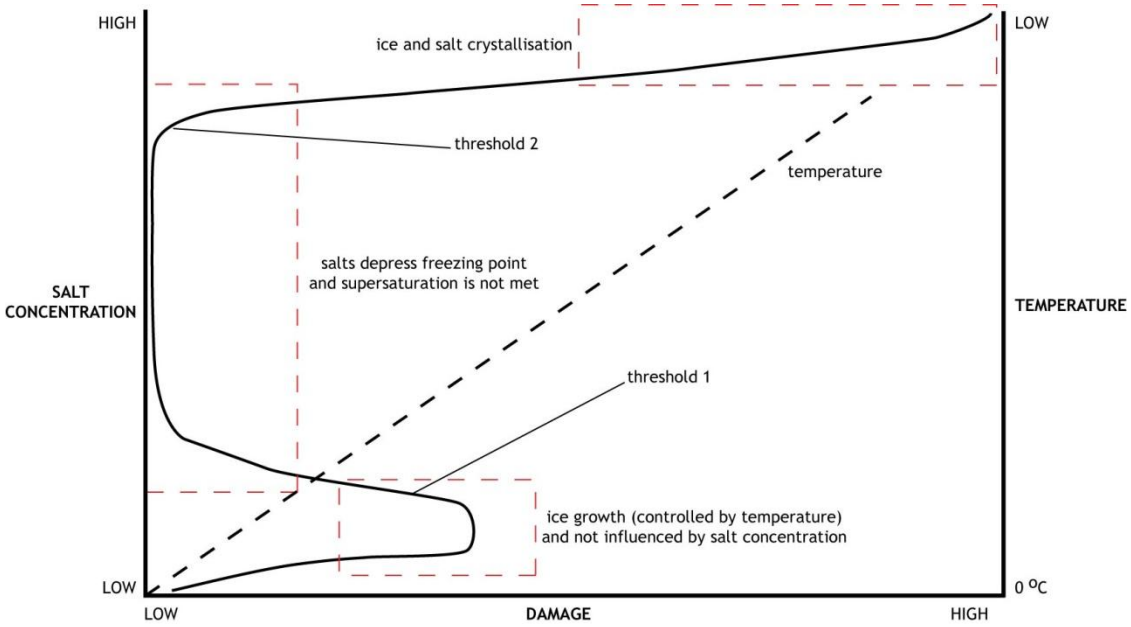

Figure 1-5: Schematic graph highlighting the relationships between salt concentration, temperature and damage potential on building stones.

At low salt concentrations and low temperatures, there is a low damage potential within building materials. At low salt concentrations, ice will grow if the temperature is low enough, with little influence from the salt concentration. Damage from ice growth will depend on the temperature (as shown by the dashed line), the freezing rate, saturation and strength of the stone. A threshold is met at a specific salt concentration, whereby salts will depress the freezing point and no damage is expected. At a higher salt concentrations, a second threshold will be met (that is quasi-dependent on temperature), whereby supersaturation of the salt solution is met and salt crystallisation will initiate. At low temperatures above the salt concentration threshold, salt and ice will grow together and high damage is expected.

1.2.2 Chemical Weathering

Chemical weathering is a broad term incorporating chemical reactions that alter mineral components, and the bulk chemistry of constituents within the stone, leading, in some cases, to eventual breakdown via other processes after the rock has been weakened. Generally, chemical weathering concerns dissolution, carbonation and hydration reactions involving water, minerals and oxygen within the stone. It is an important geomorphic weathering process (Dixon and Thorn, 2005; Turkington et al., 2005; Gabet et al., 2010), but unlike physical and biological weathering, most chemical weathering reactions take place over geological time-scales and so are less important for the life-span of a building façade.

An important geomorphic weathering process is the dissolution of minerals under highly acidic/alkaline conditions. It has long been acknowledged that dissolution rates of carbonate lithologies are far greater than siliciclastic

rocks. The former consensus that siliciclastic rocks such as sandstones are mainly inert and highly resistant to chemical weathering has only recently been challenged. Wray (1997) presents a global review of chemical solution weathering on quartz arenite sandstones. Evidence is presented of chemical weathering of highly siliciclastic landforms that show near-identical morphologies to those seen in karst environments. Certainly, silicate minerals show a range of dissolution rates (Table 1-1) far exceeding the rates of quartz, such as muscovite, biotite and alkali feldspar (Lasaga 1998; Simão et al., 2006). It is the dissolution of these other minerals that influence the overall karst-esque environments as highlighted by Wray (1997). Lee et al. (1998) show, using SEM observations, that different intragranular microtextures of alkali feldspars significantly influence the weathering behaviour of the mineral.

Mineral	Lifespan	Dissolution rate (log moles $m^{-2}s^{-1}$)
Quartz	34,000,000 years	-13.4
Kaolinite	6,000,000 years	-13.3
Muscovite	2,600,000 years	-13.1
K-Feldspar	921,000 years	-12.5
Dolomite	36 days	-5.5

Table 1-1: Expected lifespan of 1mm sized crystals at pH 5 and 25^{o}C. From Lasaga (1998)

Young (1987) suggests that the cavernous weathering forms found in Western Australia and New South Wales, Australia, were influenced by the dissolution of quartz grains by NaCl-rich pore waters. By assuming that the weathered surfaces of quartz grains behave and react similarly to amorphous silica, and that increased chloride ion concentrations increase the solubility of amorphous silica, it was hypothesised that dissolution of quartz grains further creating pores within the sandstone was the primary mechanism promoting cavernous weathering in these regions. Turkington et al. (2002), Smith (2009) and McCabe et al. (2013) give further credence to the argument that quartz and specifically amorphous silica dissolution at high alkaline pH conditions might be an important weathering agent, in conjunction with physical salt crystallisation affecting sandstone buildings.

One of the most important and best understood chemical decay processes is sulphate weathering through the crystallisation of gypsum crusts on building façades. Gypsum is one of the most common minerals within the outer crusts of building stones, and is particularly common within sandstone and limestone façades. Gypsum formation is hypothesised to occur through two main processes; by direct precipitation on the stone surface through solution droplets (Turkington et al., 2003) and from sulphuric acid-mineral reactions within the stone (Török, 2003; Ruiz-Agudo et al., 2015). Particulate matter enters the stone surface via two main pathways; dry deposition and wet deposition (Charola and Ware, 2002). Dry deposition is the transfer of pollutants and gases from the atmosphere to the stone without the assistance of rainwater, and is controlled by molecular diffusion of gasses onto the stone. Wet deposition on the other hand is the transfer of pollutants within rainwater onto the stone surface. Also termed “acid rain”, it is thought that this is a secondary process to dry deposition, concerning the incorporation of pollutants from far distance sources. Wet deposition will only affect exposed stone surfaces, while dry deposition is likely to affect all stone surfaces in a building (Charola and Ware, 2002).

In agreement with Viles (2002), Duthie (2011) concludes that with increased temperatures predicted for Glasgow, Scotland, over the next 60-70 years, there will be an increase in chemical weathering by mineral dissolution. Dissolution rates of ankerite and feldspar are predicted to rise, while changes to the dissolution process of muscovite, kaolinite and Fe-oxides are also expected to take place. Duthie (2011) found that the weathered exterior of blonde Glasgow sandstones was formed by the oxidation of iron liberated from carbonates in the stone by their dissolution.

1.3 Salt-mediated Decay

Salt decay is a highly complex system, and so the mechanisms of salt decay will be discussed in 3 parts: (i) solution transport phenomena within porous stone; (ii) the physical properties of the stone and their influence on solution transport and salt crystallisation; (iii) salt crystallisation mechanisms.

1.3.1 Solution Transport Phenomena

Water is a key factor in natural building stone decay, influencing a range of chemical reactions. It is also a major transport medium for several agents of decay, specifically salt ions (sulphate, chloride and nitrate) and biology onto the surface and outer few mm of the stone (Charola, 2000; Ingham, 2005; Mauricio et al., 2005). Water can also be damaging itself through freeze-thaw cycles (McGreevy, 1982; Chen et al., 2004; Martinez-Martinez et al., 2013) and by substantially lowering the tensile and compressive strength of the stone (Török and Vasarhelyi, 2010; Rossana and Paola, 2012). Water, in various forms such as liquid, ice, and vapour is introduced into a stone block by capillarity through groundwater and road spray/run-off, infiltration from surrounding stone and mortars, and by condensation on the stone surface from sea spray and precipitation (Franzen and Mirwald, 2004).

Under dry conditions, condensation takes place with the accumulation of layers of water molecules on the stone surface. At this point vapour dominated transport is the only mechanism of moisture ingress into the stone. As moisture accumulates on the surface through condensation, surface flow begins as a prominent and efficient transport mechanism, infilling the smallest pores first; this is known as capillary condensation (Camuffo, 1998; Carmeliet et al., 1999). Hygroscopicity is a secondary vapour absorption process whereby materials, especially salts, can readily absorb moisture from the air into their crystalline structure. The addition of salts within building stone can therefore increase their water content as an effect of enhanced hygroscopicity. Salts are capable of moisture absorption only when the RH of air surrounding the salt is greater than the salt's equilibrium humidity. Salts including NaCl, $CaCl_2$, $MgCl_2$ and NaOH are known as desiccant salts, and will undergo a process of deliquescence, whereby they form a saturated solution through vapour moisture absorption (Charola, 2003; Goncalves et al., 2007). This process can allow the re-distribution and transportation of salts throughout stone and can actively influence crystallisation processes and cycles. It must be noted however that this increased moisture content is not free water as it is incorporated into the crystal structure or within a salt solution. Once moisture is present within the stone, one of the main transport processes is through capillarity.

A second important solution transport mechanism within near-saturated porous materials containing salt solutions is through salt diffusion. Recent studies present projections of climate change that are expected to increase the degree and length of saturation within building stone. Smith et al. (2010) considered the response of stone decay dynamics to future climate change, using Belfast, Northern Ireland as an example. From UKCP09 climate projections for forty years (2010 – 2039) it is expected that the seasonality of precipitation is set to increase and dominate the climate of Northern Britain. If accurate, the projected changes are expected to have profound implications for stone decay dynamics. It is thought that this shift towards a wetter climate could cause building stones to experience an increase in deep-seated wetness, termed 'deep wetting' (McCabe et al., 2013), involving a greater depth of moisture penetration and thus changing the wetting and drying cycles experienced by the stone. Conceptual models propose a shift to larger amplitude seasonal cycles of wetting and drying, but with regular cycles experienced on the outer zones of the stone. This process could lead to a greater concentration of salt at depth and therefore greater damage potential over a sustained period of time.

With increased values of stone saturation suggested for many areas in the UK, the importance of salt diffusion on a large scale is expected to increase. Chloride diffusion is known as a major transport pathway of chloride salts into cement based structures (Zhang and Zhang, 2014) leading to increased corrosion of steel reinforcement bars and increased alkali-carbonate and alkali-silica reactions taking place at depth (Shi et al., 2010). Within natural stone, diffusion plays an important role in salt crystallisation in two ways: (i) by lowering the saturation values during drying and preventing the crystallisation of salts on lower parts of walls, and (ii) as a mechanism by which solution reaches equilibrium within a stone, as small crystals dissolve and diffuse to larger crystals in neighbouring pores (Scherer, 2004; Pel and Saidov, 2012).

The research team from Queen's University, Belfast built on this concept of increased "deep wetting" in northern UK with a paper in 2013 considering the implications of a wetter climate to salt transportation and salt weathering in sandstone (McCabe et al., 2013). This study presents results from an ion

diffusion experiment on three common masonry sandstones. The experiment is based on earlier work by Poupeller et al. (2003), with the belief that "deep wetness" as described by Smith et al. (2010) will lead to increased ion diffusion of salts into the stone interior over time. This increased period of wetness and greater diffusion of salt ions will signify a change in the salt weathering process; one from a physical dominated regime through which crystallisation pressure damage is prevalent, to a chemical weathering process with the potential of silica dissolution and silica mobilisation under alkaline pore waters, as caused by increased salt content. They show that the main parameters controlling ion diffusion in sandstone are: (i) stone specific parameters of: pore connectivity, tortuosity and mineralogy as these influence grain surface-salt solution interactions and (ii) salt specific properties such as salt type and salt concentration as it affects the concentration gradient.

1.3.1.1 *Capillarity*

There is a consensus that unsaturated flow is dominant within porous building structures (Hall and Hoff, 2007) but it cannot be completely understood without knowledge of the basics of saturated flow. Saturated flow can be explained by Darcy's law, whereby the rate of flow is controlled by the length and cross-sectional area of the material and by the hydrostatic pressure difference across it. In this situation, external forces such as the differences in hydrostatic pressures and gravity would ultimately control fluid flow. By considering saturated flow within a complex porous material, such as sandstone or limestone that contains numerous pore channels, Darcy's Law must be expanded to take into account the changing pore structure. The Blake-Kozeny equation takes into account the complexities imposed by the irregular pore networks found within natural building materials. It considers the particle size of the grains, porosity, viscosity of the fluid and the tortuosity of the material (Al-Farris and Pinder, 1987).

Unsaturated flow is an inherently different phenomenon to the basic model of saturated fluid flow and is controlled almost entirely by capillary forces. Capillarity itself is influenced by a multitude of parameters such as the volume of liquid, viscosity, surface tension and the petrographic properties of

the stone (Lago and Araujo, 2001). Capillarity controls the uptake of moisture into the stone and the transfer and redistribution of moisture within it. It is possible to expand Darcy's law for unsaturated flow by considering the volume fraction saturation and capillary diffusivity amongst other parameters (Hall and Hoff, 2002), and by considering the parameters used within the Blake-Kozeny equation.

In general, capillarity is mainly influenced by the surface tension of the liquid, the contact angle between the liquid and pore wall and the diameter of the pore throat (Taylor et al., 2000). The pressure that drives capillary action can be described y the Laplace equation:

$$P_C = \gamma(1/r_1 + 1/r_2)$$

Equation 1-1: Laplace Equation.

where γ= the surface tension and r_1 and r_2 are the radii of the menisci as determined by the pore radius (Hammecker and Jeanette, 1994; Peruzzi et al., 2003). All liquids have a surface tension; these are the cohesive forces that keep the water molecules together in the one body. On the surface of a body of water, the water molecules are not completely surrounded by other water molecules and therefore a greater attraction exists between the water molecules that are in contact with each other. This greater attraction to the water molecules directly below the surface and on the surface provides a weak surface tension, holding the surface together. The contact angle between the liquid and stone is a function of the material and acts against the cohesive forces of the liquid surface. Adhesive forces between the water molecules and the material are in opposition to the cohesive forces creating the surface film. Adhesive forces are generally greater than these cohesive forces and create a distinctive concave meniscus, whereby the leading edges of the meniscus promote the movement of solution into the pores (Taylor et al., 2000). Ballester and González, 2001 highlight the importance of contact angle for fluid ingress into a porous material. By comparing different water repellent treatments on different types of limestone, they use a minimum contact angle value of 90^o to determine whether the material is water repellent. A decreasing water contact angle will therefore increase the rate

of capillary rise within the material. This phenomenon is highlighted in Figure 1-6.

Figure 1-6: Simplified schematic diagram explaining capillary rise dynamics and surface tension phenomena.

(A): Capillary pressure is directly related to pore size, with greater capillary absorption taking place within smaller capillaries. (B): A meniscus is formed from the surface tension on the water surface. The adhesive forces between the water and the grain surfaces are greater than the cohesive forces between the water molecules as indicated by the size difference of the arrows. This creates a concave meniscus and subsequent capillary rise. (C): Water molecules are evenly attracted to each other within a body of water. At the water surface there is a greater attraction between the top layer molecules and those below them, creating a surface tension. This will change depending on other present ions and their concentration within the fluid.

As water infiltrates the stone, air within the pores can easily escape when connected to external air on the surface of the stone. In some instances air can become trapped within the stone. The pressure experienced in the pore is influenced by the curvature of the meniscus. Over time, the meniscus will change shape in order to reach equilibrium with the trapped air, and according to Henry's law, the solubility of gas increases with increasing pressure and therefore over time the trapped air within the pores will diffuse to other trapped pockets of air and eventually to the surface, with the invading meniscus ultimately filling the pores in this process.

As shown by Equation 1-1, capillary pressure is also influenced by pore sizes within the stone. The capillary pressure is greater in smaller pores, with the overall capillary uptake a function of the mean pore size (Beck et al., 2003). Capillary rise continues until equilibrium is attained between adhesive forces of the fluid-material interface and gravitational forces caused by the mass of liquid within the pores. The theoretical mechanics of capillarity can be traced to Washburn (1921), where he proposed a simple model comprising identically sized parallel tubes representing the porous medium. This model has since been shown to be inaccurate for complex porous materials such as sandstone and limestone (Dullien et al., 1977; Hammecker and Jeanette, 1994; Grattoni et al., 1995). Benavente et al., (2002) highlight the importance of introducing significant petrographic parameters into theoretical capillarity models. By modifying the original Washburn equation with the introduction of tortuosity and experimentally measured pore shape parameters, the prediction of capillary imbibition kinetics are significantly

improved. It must also be noted that the addition of dissolved salts into solution can also significantly influence the capillary transport properties within the stone through increased surface tension and viscosity (Steiger et al., 2008).

1.3.1.2 *Stone Drying and Environmental Factors*

Evaporation of water in stone is an extremely complex process and is controlled by numerous factors including: (i) the total available surface area exposed to drying; (ii) the vapour pressure gradient above the stone surface; (iii) the ambient temperature experienced by the stone; (iv) the petrographic properties of the stone; (v) salt type, if present; (vi) the movement of air throughout the stone (Hall et al., 1984; Benavente et al., 2003; Espinosa-Marzal and Scherer, 2010). Evaporation is characterised by the invasion and replacement of liquid within pores by gas, with the drying front defined by the interface separating the liquid-filled and gas-filled zones (Lehmann et al., 2008). Evaporation, as defined in the literature, relates to “typical” porous materials such as sands and soils and is therefore applicable to the evaporation from porous stone; particularly porous sandstone. Figure 1-7 is a schematic representation of the drying stages experienced by stone.

The two stage drying regime that was first discussed by the workers such as Cooling (1930) and Sherwood (1930) is well established and understood in the literature. Stage one is defined as the “constant rate period” and has been discussed at length (Van Brakel, 1980). This first stage is characterised by an initial high evaporation rate maintained by a hydraulic connection between the drying front in the matrix (e.g. stone) and the evaporative surface (Lehmann et al., 2008). There has been increasing evidence that this rate is equal to the evaporation rate of a free water surface under the same environment conditions (Van Brakel, 1980). Stage one drying is therefore unlikely to be influenced by the material properties (Hall et al., 1984) and is consequently related to the evaporating liquid properties such as; the saturated vapour pressure, surface tension and viscosity, and the environmental conditions: temperature, air flow and RH (Hall et al., 1984). However, the duration of stage one and the subsequent onset of stage two is likely to be partly controlled by the material properties.

The advancement into stage two starts when the hydraulic connectivity between the drying front and evaporative surface is interrupted. This second stage is therefore limited by vapour-diffusion and unsaturated flow within the porous material (Hall et al., 1984, Lehmann et al., 2008). At the onset of stage two, the distribution of liquid is not uniform and so presents a complex process in space and time. A third drying stage was proposed by Fisher (1923) for the drying of soils, characterised by a deep drying front and diffusive vapour transport (Fisher, 1923 in Nachshon, 2011). The theory of drying is discussed further in informative papers by Scherer (1990) and Lehmann et al., (2008).

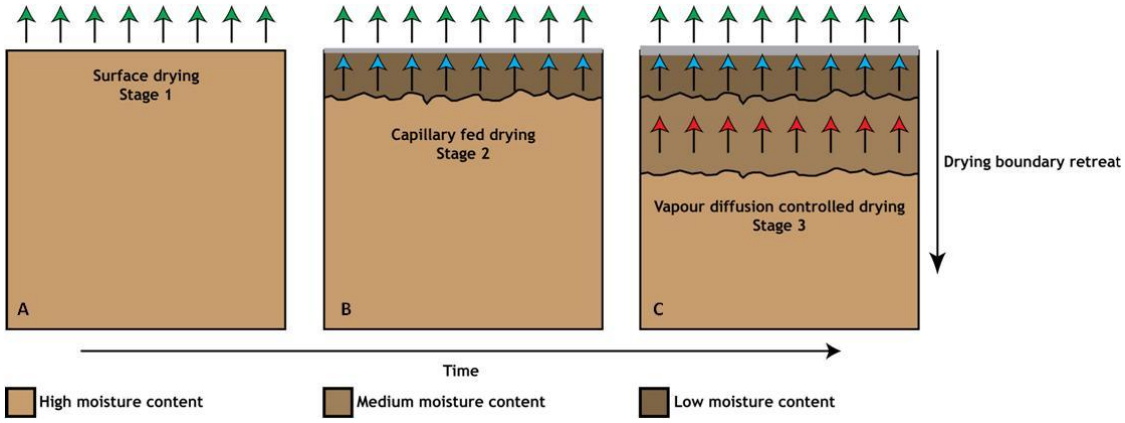

Figure 1-7: Schematic diagram showing the drying stages within sandstone. (A): Stage 1 drying with all drying taking place on the stone surface. (B): Stage 2 drying - the drying boundary retreats, with drying taking place from the surface through capillary connection to depth within the stone and vapour diffusion controlled drying from the new drying boundary. (C): Stage 3 drying – drying is now entirely controlled by vapour diffusion at depth within the stone. Moisture content is now greatly reduced near the surface but there remains a high moisture content at depth. Green arrows: fast drying, Blue arrows: moderate drying rate, Red arrows: slow drying rate.

The presence of salts; both in solution and crystalline form, will have a marked effect on the drying rate of porous material. Water provides the ionic pathway allowing salts to reach the stone, enhancing and controlling crystallisation and dissolution cycles within the material (Mauricio et al., 2005). During initial stages of drying, air penetrates into the larger pores. A continuous movement of solution from large to small pores ensures that small pores are kept connected with a solution film linking filled pores to the stone surface allowing evaporation to continue (Espinosa-Marzal and Scherer, 2010). The addition of dissolved salts into solution decreases the water activity that controls the vapour pressure above the solution. This lowers the vapour pressure gradient between the solution and surrounding air and in

turn, lowers the evaporation and drying rate (Goncalves et al., 2007; Espinosa-Marzal and Scherer, 2010).

Research by Benavente et al. (2003), and later by other authors including Cnudde et al. (2013) showed that under laboratory conditions, the drying rate and loss of moisture of various stone samples was markedly influenced by the addition of dissolved NaCl and de-icing salts, respectively. As moisture content in the stone is gradually reduced, solution transfer between pores may be impeded by the increase in solution viscosity (by an increase in solution concentration) and by crystals blocking pores (Espinosa-Marzal and Scherer, 2010). This process will interrupt solution flow to the surface and hinder evaporation. Crystallisation within the pores (subflorescence) may then occur as the evaporation boundary retreats into the stone interior (Goncalves et al., 2007). A reduction in moisture content provides the onset of a second, slower drying stage (Hall et al., 1984; Benavente et al., 2003). Pore blocking by subflorescence and a reduction in salt mobilisation will decrease the effective porosity within the stone. Consequently, moisture infiltration and deep penetration of salt solution will decrease, leading to recurrent evaporation cycles and salt enrichment in shallow, near-surface levels (Smith et al., 2002). This scenario can then provide conditions favourable for granular disintegration and sanding decay. Rodriquez-Navarro and Doehne (1999) concluded that low RH conditions were favourable for salt crystallisation. A large vapour pressure gradient enhances the evaporation rate and therefore the onset of supersaturation, and would lead to subflorescence and the potential of greater pressures developing within the stone.

A simple model was developed by Scherer's work in 2004 showing the interaction between capillary rise of salt solution and evaporation within a wall structure. Figure 1-8 is a re-drawn schematic taken from Scherer (2004).

A study by Angeli et al., (2007) highlighted the importance of stone dimension on drying rate. The easier a stone can be dried, the quicker will be the onset of crystallisation. The smallest dimension of a stone sample will significantly influence the drying regime, allowing a greater drying rate at

depth. Drying rate is heavily influenced by salt type, environmental conditions (temperature and RH) and the petrographic properties of stone.

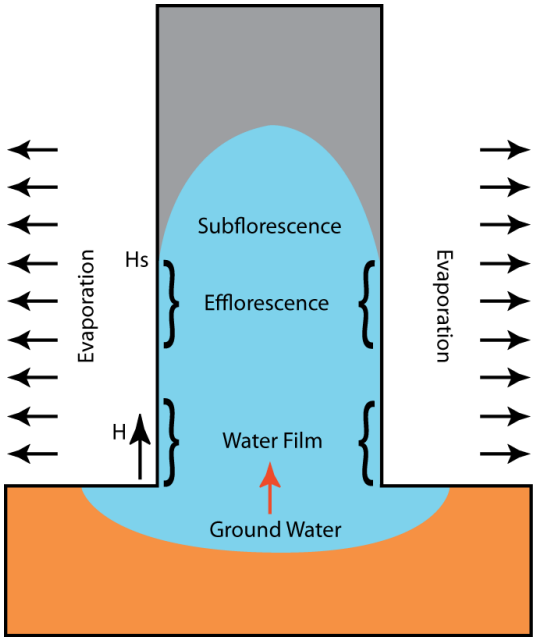

Figure 1-8: Capillary rise and evaporation schematic diagram as redrawn from Scherer (2004).
At ground level, moisture is absorbed by capillary action. The rate of capillary rise is proportional to height (H) (decreasing with increasing height). Evaporation takes place on the stone surface and at a near constant rate under un-changed conditions. Near the bottom, capillary rise exceeds evaporation and consequently this section remains constantly wet. With increasing height, evaporation rates begin to exceed rates of capillary rise, allowing supersaturation to be met and efflorescence to form. Generally, it can be expected that when migration rates of solution to the surface ≥ evaporation (at a given height, Hs) efflorescence will take place and when migration rates ≤ evaporation (above Hs) subflorescence will take place. A sustained lower drying rate over time may lead to a continued enrichment of salts within the stone. If efflorescence allows diffusion of vapour at the surface then evaporation at depth can continue, leading to the onset of subflorescence.

Environmental factors significantly influence the drying regime experienced by the stone and consequently affect whether salts crystallise as subflorescence or efflorescence. Smith et al. (2011) analysed heating profiles at depth within stone. They found that a large temperature gradient existed within the upper 10mm of the sample, with complex temperature fluctuations and reversals taking place below this depth. This research expanded on previous work by Gomez-Heras and Fort (2007) who revealed that the heating regime experienced by stone can influence the type of crystallisation that takes place. In this study it was shown that radiative heating promotes faster drying and the onset of subflorescence, with slower conductive heating promoting efflorescence. These processes were shown to take place on a limestone containing a significant proportion of micro-pores.

1.3.1.3 *Efflorescence*

Numerous studies have researched the process of drying within porous media, with many of them considering the effect of salt efflorescence on the evaporation process. Recent work by Eloukabi et al. (2013) highlights the significance of efflorescence on the drying regime experienced by a porous medium. The study presents findings from a range of repeat experiments that consider the drying of a porous medium consisting of different sized beads and a range of concentrations of NaCl solution. The study reveals the operation of two distinct drying regimes that correspond to the formation of two types of efflorescence. Under the same environmental conditions, different types of efflorescence growth are observed that relate to the mean bead size. The efflorescence pattern can significantly alter the drying dynamics of the porous medium, with “patchy” efflorescence creating a faster regime and “crusty” efflorescence blocking pores and significantly reducing the drying rate. Over time the occurrence of “crusty” efflorescence could lead to the formation of subflorescence, and highlights the interplay between mean pore size, the drying rate and the effect of efflorescence on the salt crystallisation process.

A similar study was undertaken by Veran-Tissoires et al. (2012). They set out to understand the spatial crystallisation behaviour of discrete efflorescence structures in porous media. They found that the initial nucleation sites of efflorescence are controlled by a velocity field in the porous medium, itself a function of liquid density, flow rate and evaporation rate. Salt ions are then directed to certain areas on the surface by advection. This process causes a salt peak to develop and ultimately crystallisation to take place. A concentration gradient can then develop, and competition will arise between advection to the surface and diffusion back into the pores. Between areas of efflorescence growth screening occurs where the evaporation flux is negligible and the liquid flow rate between the underlying matrix and efflorescence remains high.

These studies build on related work carried out by Sghaier and Prat (2009), also looking at drying dynamics in the presence of salt. Their surprising results showed that the formation of efflorescence contributes to an initial

increase in the evaporation rate which is explained by the capillary pumping effect associated with the wet, porous structure of the efflorescence; this process was later confirmed by Veran-Tissoires et al. (2012). Sghaier and Prat (2009) found that evaporation occurs on top of the efflorescence, with the drying rate becoming significantly reduced as the efflorescence dries out. A schematic model explaining this phenomenon is shown in Figure 1-9. These findings were challenged by Nachshon et al. (2011b) who discovered, by using different sand columns and constant hydraulic head conditions, that evaporation takes place below the efflorescence surface, experiencing the three stages of drying outlined previously by Nachshon et al. (2011a). Closely following the well established drying stages as mentioned earlier, these new stages of drying differ in the mechanisms controlling the transitions between each stage and are only relevant to the drying of saline solutions. The first stage exhibits a declining evaporation rate caused by an increasing osmotic potential of the solution and a resistance to vapour flow. The second stage is characterised by a progressive decrease in the evaporation rate due to salt crust formation and pore blocking, and the third stage features a constant low evaporation rate. It was found that the onset of stages two and three took place even with hydraulic connectivity between the drying front and evaporation surface; seen usually as classic stage one drying (Nachshon et al. 2011).

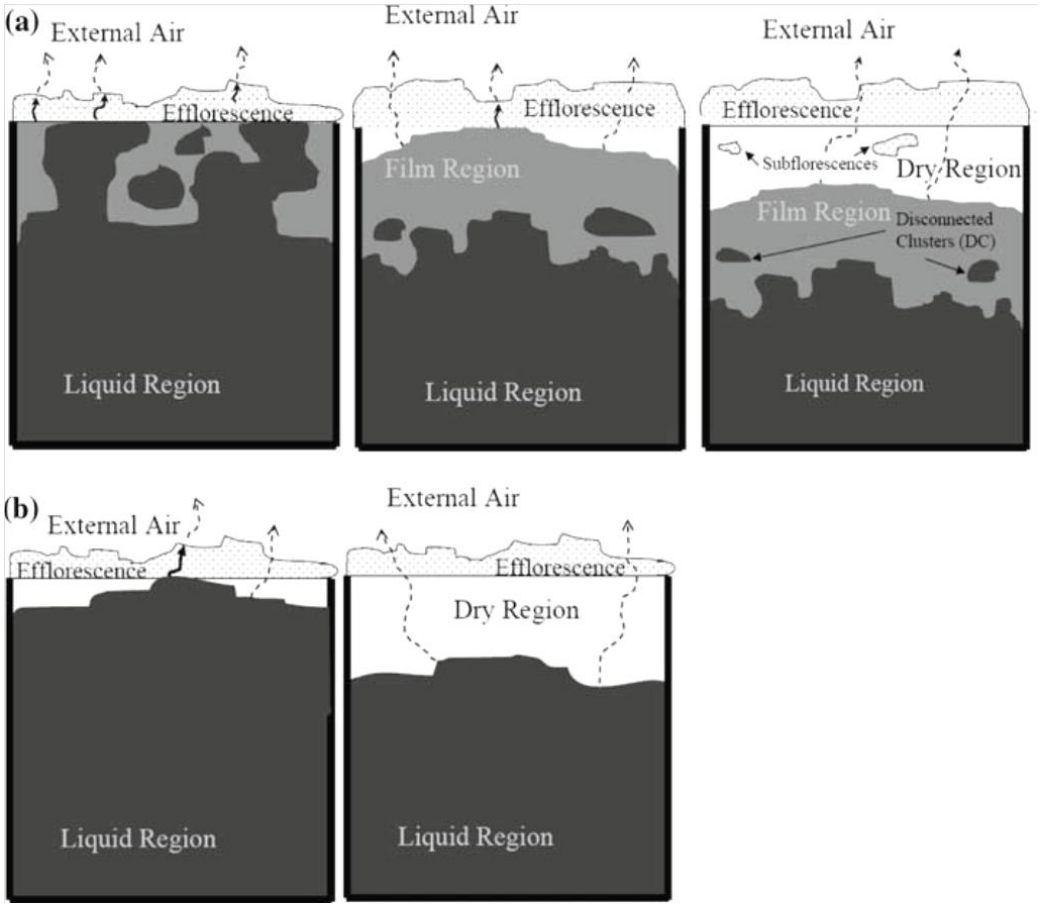

Figure 1-9: Schematic model of drying in the presence of salt efflorescence.

(a) Schematic diagram of the efflorescence capillary pumping effect. Solid arrows indicate capillary pumping from the liquid region through efflorescence. Drying takes place on the external edges of the efflorescence, contributing to continued salt growth. (b) The effect of salt efflorescence as a porous barrier to vapour diffusion, causing the drying boundary to retreat into the material interior and subflorescence to form (Sghaler and Prat, 2009).

Gupta et al. (2014) obtained similar results to Sghaier and Prat (2009), whereby the formation of a thick and friable efflorescence permits hydraulic flow, maintaining a similar drying rate and a delayed receding drying front. Interestingly, they show a paradoxical situation whereby an extremely low RH drying regime, known to be fast drying conditions for water-wet materials, significantly slows the drying rate of salt-saturated brick when compared to the same experiment under higher RH conditions. This phenomenon is explained by the formation of two distinct types of efflorescence on the brick surface. Under extremely low RH conditions a thin, impermeable salt crust is formed that blocks surface pores and reduces evaporation by preventing hydraulically connected drying. The drying front does not penetrate into the sample as prominently as with water. This process is in contrast to the efflorescence structure that forms at higher RH. Under these conditions, efflorescence formation is prolonged, creating a thick layer that is poorly

attached to the brick surface. Although the receding drying front is suppressed and the second drying stage delayed, this efflorescence maintains hydraulic flow between the stone surface and interior, creating a faster drying rate than that experienced under the extremely low RH conditions.

This section has shown that evaporation and drying within porous media is an extremely complex process that is significantly influenced by a host of factors. Drying is ultimately controlled by: (i) solution properties such as viscosity, surface tension, vapour diffusivity, osmotic potential when in salt solutions and salt type; (ii) petrographic properties of stone, including pore size distributions; (iii) environmental conditions experienced by the stone, including temperature, conductive or radiative heating, RH and air flow. The drying regime can then be significantly altered by efflorescence on the stone surface.

1.3.2 Petrographic Properties

The transfer, absorption and loss of moisture from natural stone is influenced not only by the solution properties of viscosity and surface tension, but also by petrographic properties of the stone. The rate and quantity of moisture ingress is effectively controlled by the pore structure and this is why the Washburn equation, as discussed in section 1.3.1.1, is not directly applicable to complex porous and permeable bodies such as sedimentary rocks. Numerous studies have highlighted the significance of pore structure on the durability of stone in response to various decay mechanisms (e.g. Benavente et al., 2006; Benavente et al., 2008; Cultrone et al., 2008; Anania et al., 2012; Vázquez et al., 2013), with several papers considering the relationship between salt crystallisation mechanisms and the pore structure of porous materials. These papers include Cultrone et al. (2012), who researched sodium sulphate crystallisation within selected sandstone and calcarenite stones from Spain.

The most important petrographic properties of the stone that influence salt crystallisation have been shown to include: (i) effective porosity; (ii) permeability; (iii) pore size distribution; (iv) pore connectivity; (v) pore geometries; (vi) pore throat dimensions; (vii) tortuosity (Perrett et al., 1999;

Benavente et al., 2004; Coussy, 2006; McKinley and Warke, 2007; Buj and Gisbert, 2010; Yu and Oguchi, 2010). These properties primarily control the uptake of solution by means of capillary processes and the movement of liquid within the stone. The stone fabric significantly influences both petrophysical characteristics, and the stone's mechanical strength. Stone mineralogy and grain properties including roundness, sorting and grain contacts will influence the porosity, permeability and tortuosity. The type, extent and origin of clays are all factors of importance in blocking of pores and lowering of porosity, while the extent of cementation and nature of cement crystals will influence the mechanical strength of the stone. These are features resulting from the stone's geological provenance, and its formation by sedimentation, diagenesis and subsequent modification by natural weathering processes.

Early workers believed that stones containing a greater proportion of micro-pores were more susceptible to salt induced decay (Russell, 1927). Many laboratory and theoretical studies have since confirmed this hypothesis (Ordonez et al., 1997; Theoulakis and Moropoulou, 1997; Rodriguez-Navarro and Doehne, 1999; Flatt, 2002; Angeli et al., 2008). A number of explanations have been proposed to explain the why the presence of smaller pores makes salt crystallisation more damaging. Micro-pores increase the effective surface area for solution evaporation, and by slowing the rate of transportation throughout the pore network, supersaturation ratios are more easily met (Rodriguez-Navarro and Doehne, 1999). Smaller pores absorb water more frequently through increased capillary suction, retain it for longer and experience more recurrent condensation cycles than larger pores (Theoulakis and Moropoulou, 1997). During the drying of stone with a wide range of pore sizes and containing salt solution, evaporation will preferentially take place in the larger pores. This process causes them to empty as solution migrates to the smaller surrounding pores through increased capillary suction. Assuming that the initial salt solution concentration was dilute, a great deal of evaporation must take place before supersaturation with respect to salts can be reached. At this point, when crystallisation can take place, solution will have migrated into smaller pores where damaging pressures may develop (Scherer, 2006).

Yu and Oguchi (2010) established a correlation between the total connected porosity of various Japanese building stones and salt solution ingress during salt crystallisation tests. They concluded that the total connected porosity was a factor controlling the amount of observed damage. A strong correlation was found between the proportion of micro-pores smaller than 0.05μm and 0.1 μm diameter and measured dry weight loss to the samples.

Pore size distribution is a major damage estimator, promoting favourable conditions for high salt crystallisation pressures when large pores are either connected to, or separated by considerably smaller micro-pores and pore throats (Theoulakis and Moropoulou, 1997; Iglesia et al., 1997; Yu and Oguchi, 2010). This finding was confirmed in work by Buj and Gilbert (2010), who showed that stones characterised by high porosity, low pore connectivity and a tortuous pore network, were more susceptible to salt decay. Pore size distribution and pore throats primarily control properties relevant to fluid transport: (i) water saturation of the stone; (ii) water desorption; (iii) capillary water absorption; (iv) saturation; (v) critical water content (Buj and Gilbert, 2010).

Přikryl (2013) produced an insightful overview of pore nomenclature and the subsequent influence that each pore size class has on water behaviour. Figure 1-10 shows that macropores extend from 7.5μm – 0.05μm, mesopores between 0.05μm – 0.002μm and micro-pores are those pores < 0.002μm in diameter. Generally, macropores and mesopores control capillary processes within the stone, with capillary pores occupying the range between 0.05μm – 0.01μm. Within these pores, fluid movement is governed by diffusion processes, multilayer adsorption and surface tension forces of the fluid. Bulk water movement through free water occurs in pores > 7.5-10μm, and is thought to be of less direct importance for durability behaviour in relation to salt-induced decay (Rossi-Manaresi and Tucci, 1991, Benavente et al., 2004); however these pores will significantly influence the overall porosity values of the stone.

Several durability estimators have been used to predict the rate and susceptibility of different lithologies to salt-induced decay. These estimators use a range of petrographic properties in order to deduce: (i) the actual loss

of material (Richardson, 1991; Bell, 1993); (ii) the test cycle when first visible damage occurs (Angeli et al., 2007); (iii) the general susceptibility of stone to decay. However, many of these estimators neglect to include important salt solution and salt crystallisation properties. As highlighted in Figure 1-10 (Přikryl, 2013), macropores, mesopores and micro-pores encompass a range of pore sizes > 7.5μm, and numerous sub-classes within the macro-micropore range have been shown by different authors to be the most important for influencing salt crystallisation damage.

Furthermore, different hydric properties have been used as the basis for other estimations of stone durability. Figure 1-10 summarises some of the most important durability estimators that have been described to date. Durability estimators allow indirect prediction of stone response to different decay mechanisms using common and easily measured properties of the rock, thus reducing the need for time-consuming durability tests. Unfortunately, many of these durability estimators have relied on correlations between durability tests and measured petrographic properties of specific lithologies, and therefore may not necessarily be attributable to other rock types. Papers by Benavente et al., (2004), Yu and Oguchi (2010) and Přikryl (2013) successfully summarise most of these durability estimators.

All areas of petrography must be understood, considered and quantified before any accurate predictions concerning stone durability can be made. The petrographic properties of the stone must also be considered in conjunction with other factors including salt type and environmental conditions.

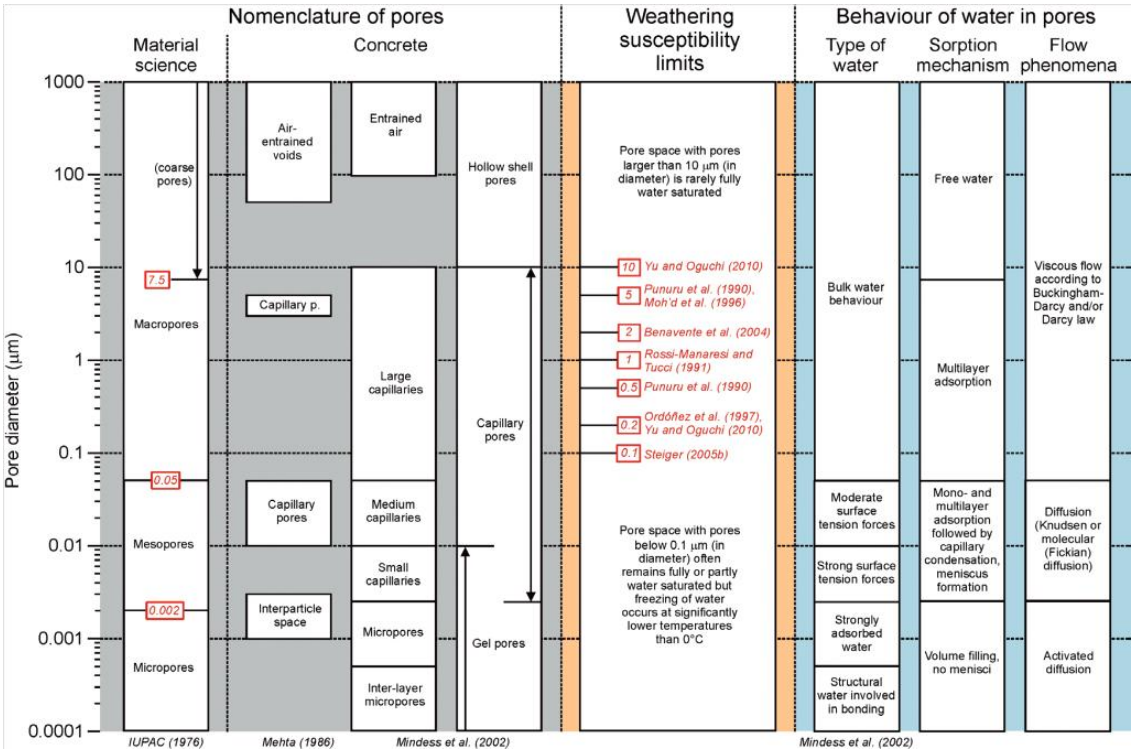

Figure 1-10: Přikryl (2013) overview of pore nomenclature.

Literature overview of pore nomenclature, weathering susceptibility limits of each pore range and water behaviour within pores.

1.3.3 Salt-Induced Decay

Salt crystallisation is one of the most important processes affecting the structural and aesthetic integrity of our built heritage (Theoulakis and Moropoulou, 1999; Rodriguez-Navarro et al., 2000; Doehne, 2002 and references therein; Lopez-Arce et al., 2009; Buj and Gisbert, 2010). Experimental studies undertaken over 150 years ago by Lavalle (1853) provide evidence of the ability of salts to exert pressure during crystal growth, with the first salt crystallisation tests dated to 1828 (Rodriguez-Navarro and Doehne, 1999). There has since been extensive research within the field concerning: (i) salt damage mechanisms (Mortensen, 1933; Wellman and Wilson, 1965); (ii) salt crystallisation mechanisms (Scherer, 1999); (iii) salt phase transitions (Hamilton et al., 2008); (iv) environmental salt monitoring (Zehnder and Schoch, 2009); (v) salt treatments (Pel et al., 2010); (vi) stone durability to salt decay (e.g. Cultrone et al., 2008; Anania et al., 2012). Research focussed on material durability to salt decay has also been extremely comprehensive. This degree of coverage is due, in part, to the prevalence of salts within almost all environments. Papers have studied the effects of salts on sedimentary (Warke et al., 2006; Cardell et al., 2008;

McCabe et al., 2011), metamorphic (Chabas et al., 2000; Yavuz and Topal, 2007) and igneous building stones (Zedef et al., 2007; Ulusoy, 2007; López-Arce et al., 2010), mortars (Costa et al., 2009), paintings (Sawdy and Heritage, 2007) and plaster (Lubelli and Rooij, 2009). Only recently have the factors and mechanisms influencing salt crystallisation been identified and understood. Recent studies show a generally accepted consensus regarding the fundamental principles of salt crystal growth within porous materials (Coussy, 2006).

Important studies of salt-induced weathering include the excellent and highly informative papers by Charola (2000), Doehne (2002) and Rodriguez-Navarro and Doehne (1999) and books by Amoroso and Fassina (1983) and Goudie and Viles (1997).

Salts are introduced into masonry by a number of pathways, including: (i) the alteration of inherent materials that contain salt, such as the mobilisation of salt ions within stone mortars (Perry and Duffy, 1996; Vallet et al., 2006; Ruedrich and Siegesmund, 2007); (ii) capillary rise of ions derived from de-icing salts and fertilised soils saturated into groundwater (Charola, 2000; Lopez-Arce et al., 2009); (iii) vapour diffusion and infiltration from air pollution, rainwater and sea spray (Cardell et al., 2003; Lubelli et al., 2004; Vallet et al., 2006, Viles and Goudie, 2007, Heinrichs, 2008; Silva and Simão, 2009); (iv) inappropriate cleaning methods (Young et al., 2003). Despite a wealth of observational studies, there continues to be a lack of understanding in several fields of stone decay and salt crystallisation research (Doehne, 2002; McCabe et al., 2013), including the need for further research on ion diffusion within building stone and on understanding the complexity of interactions between salt, stone and mortar. This lack of understanding is due to the complexity of the thermodynamic-pore system, involving interactions between salt mixtures (Franzen and Mirwald, 2009; Linnow et al., 2013; Gupta et al., 2015), climate (and its current and future trends) and the petrophysical properties of natural (heterogeneous) stone. A further problem arises from the difficulty in accurately measuring the vital chemical reactions taking place within micro and nanometer-scale pores and solution films present within porous materials. Only recently, with the development of sophisticated analytical techniques, have scientists been able to study salt

crystallisation on the micrometer – nanometre length scales. In the past, salt decay was studied via *in-situ* observations and salt-crystallisation laboratory experiments; both are still used extensively today (Beck and Al-Mukhtar, 2010; Alves et al., 2011). The development of several methods have been invaluable in aiding recent research by providing extra dimensions of measurement (Doehne, 2002): (i) Scanning Electron Microscopy (SEM) (Theoulakis and Moropoulou, 1999; Rogen et al., 2001; Cardell et al., 2002); (ii) Environmental Scanning Electron Microscopy (ESEM) (Rodriguez-Navarro and Doehne, 1999; Doehne, 2006); (iii) Nuclear Magnetic Resonance (NMR) (Rijniers et al., 2005; Gupta et al., 2014); (iv) X-Ray Computed Tomography scanning (CT scanning) (Louis et al., 2007; Long et al., 2009; Ruiz de Argandoňa et al., 2009; Peng et al., 2012); (v) Neutron Tomography Scanning (Dewanckele et al., 2014; Mongy, 2014).

A range of salts have been found to be major destructive agents, including sodium sulphate (Rodriguez-Navarro et al., 2000; Ruedrich and Siegesmund, 2007; Espinosa et al., 2008; Espinosa-Marzal and Scherer, 2010), magnesium sulphate (Lopez-Arce et al., 2009; Balboni et al., 2011), gypsum (Lubelli et al., 2004; Ruffolo et al., 2015) and sodium chloride (Ruedrich et al., 2007; Lopez-Arce et al., 2009). The increased availability and exposure of many other salts within the environment creates a complex and dynamic system that is capable of substantially altering the properties of sandstone. Numerous mechanisms for damage to building materials have been proposed from theoretical and empirical studies and include the thermal expansion of salts (Al-Naddaf, 2009; Cnudde et al., 2013), hydration pressures, (Mortensen, 1933; Goudie, 1977), chemical weathering by dissolution of silica minerals (Smith, 2009) and crystallisation pressures (Wellman and Wilson, 1965; Theoulakis and Moropoulou, 1999; Doehne, 2002).

Stone decay through chemical, physical and biological processes can take the form of several patterns. These decay patterns are influenced by environmental conditions (RH, temperature, wind velocity and direction), the structural and petrographic properties of the stone and the decay type. Salt weathering has a set of several typical decay patterns, with some receiving considerably more attention than others. Smith et al. (2010) highlight the most common salt weathering decay patterns affecting limestones, with

alveolar and cavernous hollowing highlighted as the most common ones associated with coarse grained rocks. Similarly, there are three main convergent decay morphologies associated to salt-decay (also caused by other processes) affecting sandstones: (i) granular disintegration, involving the loss of individual grains from the stone; (ii) contour scaling, whereby scales in the order of cm's are lost due to positive feedback mechanisms during repeated drying cycles; (iii) multiple flaking, in which smaller flakes (mm in thickness) are lost from the stone surface. To help explain the weathering patterns affecting quartz sandstones, Smith et al. (2010) produced a decay model integrating common decay mechanisms expected from a polluted environment (Figure 1-11).

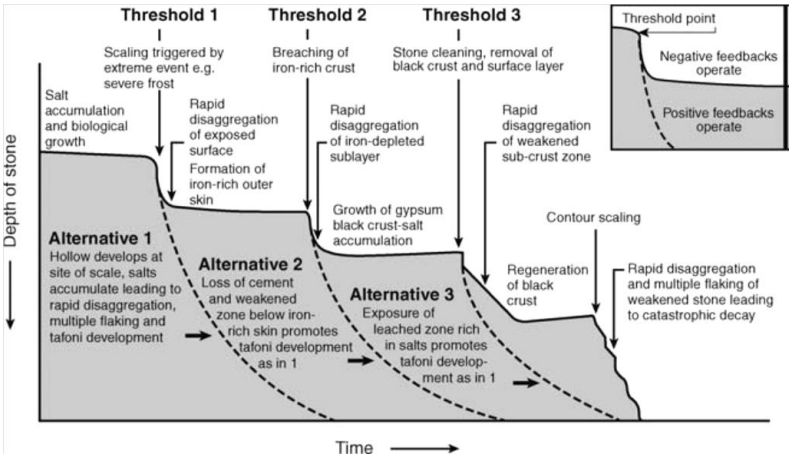

Figure 1-11: Model illustrating hypothetical decay pathways within quartz sandstone.

Substantial decay episodes are expected to take place once certain thresholds are met. Re-stabilisation and quasi-equilibrium then takes place before another decay mechanism is triggered. Salts are continually absorbed and contained within the stone throughout this process. A decay sequence may be triggered by the breaching of a salt threshold within the stone, leading to contour scaling and granular decay. From Smith et al. (2010).

1.3.3.1 *Salt Crystallisation Mechanisms*

Crystal growth within a porous material involves the interplay between several processes, which include: (i) surface reactions of adsorption; (ii) ion exchange; (iii) surface nucleation; (iv) ion diffusion (Theoulakis and Moropoulou, 1999). Diffusion controlled crystal growth is driven by the concentration gradient between the bulk solution and the crystal surface. Growth takes place by the accumulation and attachment of ions onto the crystal surface only when the crystal is in contact with a saturated or supersaturated solution. Supersaturation is a measure of the difference

between actual solution concentration and the solubility concentration at a certain temperature. Supersaturation is achieved by evaporation and is a function of temperature, RH, initial solution concentration and salt type (Ruedrich and Siegesmund, 2007). Gibbs' theory suggests that supersaturation is thermodynamically essential for salt nucleation and growth (Espinosa-Marzal and Scherer, 2010), with Sunagawa (1981) showing that the rate of supersaturation is a determinant of the habit of growing salt crystals.

High energy barriers must be overcome before a critical salt nucleus can form. The formation of a critical nucleus is a function of the relationship between the supersaturation level and the number of molecules needed at this level to form. Initially, low supersaturation levels will encourage the growth of larger crystals as the growth rate exceeds nucleation rate. At higher levels of supersaturation, crystal nucleation is favoured over crystal growth, which results in the initial nucleation of many small crystals. For magnesium and sodium sulphate salts, the number of molecules needed to form a critical nucleus is much larger at each supersaturation level than for NaCl. Thus, greater supersaturation (energy) levels are generated before the onset of crystallisation. Higher supersaturation levels can significantly influence the damage potential for each salt as crystallisation pressures subsequently rise (Espinosa-Marzal and Scherer, 2010). Other important parameters include the dynamic interaction between the initial nucleation phase, the growth kinetics of individual crystals and ion transport throughout the pore system, and how this may affect certain types of salts. These processes must then be acknowledged for a crystal growing in a confined pore space.

Pressure can only be applied by a growing crystal when it is in contact with a thin film of supersaturated solution present between the crystal and the pore wall (Theoulakis and Moropoulou, 1999; Scherer, 2004; Steiger, 2005; Espinosa-Marzal and Scherer, 2010). Without this film, growth would discontinue and pressure would not be exerted. Crystallisation pressure is therefore a function of the degree of local supersaturation (Theoulakis and Moropoulou, 1999; Steiger, 2005). The existence of this film arises from adsorption forces and the interfacial tensions between: (1) the salt and solution; (2) the salt and pore wall; (3) the pore wall and solution (Rodriguez-

Navarro and Doehne, 1999). Growth, ultimately leading to damage, can only continue if the salt-pore tension (2) exceeds (1) + (3). The film will continue to exist until a substantial energy threshold is exceeded by the growing crystal (Flatt, 2002). The law of thermodynamics dictates that crystallisation pressure must be exerted to maintain equilibrium between the growing crystal and the supersaturated solution (seen now as saturated for the crystal under pressure) (Espinosa-Marzal and Scherer, 2010). As a result, the addition of an unconfined crystal would lower the supersaturation level and grow at the expense of the confined crystal (Figure 1-12). Equilibrium is maintained by the lowering of any increase in the supersaturation ratio by ion diffusion onto the crystal. If this is a long process, sufficient pressures may develop that could damage the pore network.

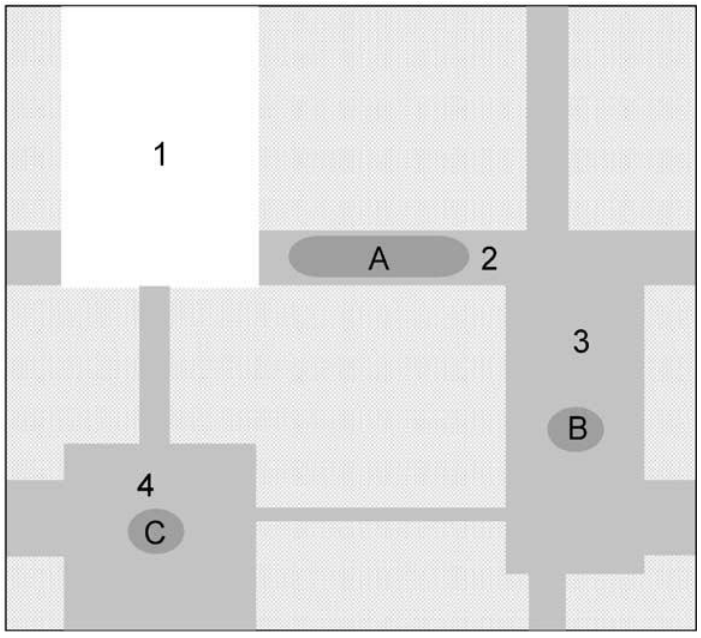

Figure 1-12: Schematic model of crystal growth within an idealised pore network. Pore 1 has been emptied by evaporation at the material surface and subsequent crystal nucleation has taken place at sites 2, 3 and 4. The growth of crystal A is quickly constrained by the pore walls, while crystals B and C continue to grow. Crystals B and C will continue to grow at the expense of crystal A, lowering the supersaturation experienced by A and bringing the system into equilibrium (Flatt, 2002).

In small pores, crystal growth is quickly constrained as the crystal reaches the pore wall and equilibrium in that pore is met. A small crystal has a larger chemical potential than a bigger crystal, owing to greater curvature and its higher surface energy; thus both crystals cannot reach equilibrium when in the same solution. With unconstrained crystals, the larger crystal will be supersaturated in respect to the smaller crystal and grow at its expense

(Scherer, 2002). As the smaller crystal dissolves, the solute will move through the pore network by diffusion. During this time, non-equilibrium growth may take place as random crystals nucleate through pores of a range of sizes. The rate of non-equilibrium growth and duration of transient stress/crystallisation pressure throughout the stone is dependent on: (i) the rate and supply of solute; (ii) the growth rate of crystals; (iii) the rate of diffusion of solute to mesopores. The diffusion of solute therefore influences the transient stress experience by the stone during non-equilibrium growth and is dependent on the pore size distribution, the tortuosity of the pore network, and the proximity between loaded and unloaded crystals (Scherer, 2002). Fluctuations in temperature can cause the onset of supersaturation and non-equilibrium growth by lowering the solubility and by causing evaporation (Scherer, 2002; Coussy, 2006).

High stress values are also possible in non-equilibrium systems lacking smaller pores only when supersaturation ratios are sufficiently high (Figure 1-13) (Scherer, 2004; Espinosa-Marzal and Scherer, 2010). High supersaturation ratios result from rapid drying as the evaporation barrier moves into the interior of the stone. This rapid drying raises the concentration of the remaining solution until it becomes discontinuous throughout the pore network and between the crystal and the pore wall (Scherer, 2004). Supersaturation can now only be relieved by growth towards the pore wall, leading to high pressures.

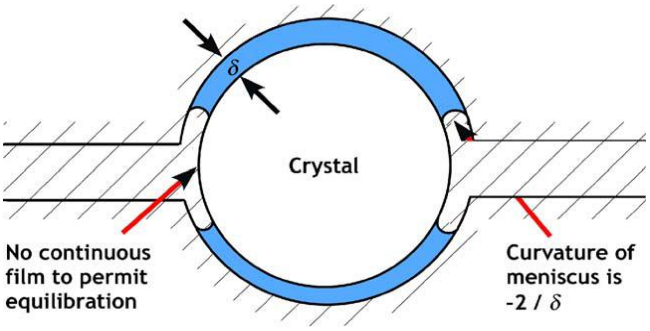

Figure 1-13: Non-equilibrium growth of a crystal within a pore. Supersaturation ratios cannot be relieved once the remaining solution becomes discontinuous as ion diffusion cannot reach the unconfined ends of the crystal. *δ* is the thickness of the liquid film between the crystal and the pore wall (Scherer, 2004).

1.3.3.2 *Common masonry salts*

The three most important salts affecting building stone are undoubtedly NaCl, Na_2SO_4 and $CaSO_4.2H_2O$ due to their extremely high abundance and availability within the built environment. NaCl is a relatively stable salt, with one simple solution-solid phase transition at 75% RH and room temperature. Conversely Na_2SO_4 undergoes a significantly more complex set of phase transitions. At room temperature Na_2SO_4 has two stable phases: anhydrous thenardite (Na_2SO_4) and hydrous mirabilite ($Na_2SO_4.10H_2O$), and a metastable phase heptahydrate ($Na_2SO_4.7H_2O$). Na_2SO_4 has an important dependence on both temperature and RH. Unlike NaCl, the Na_sSO_4 RH deliquescence point has a greater dependency on temperature. Mirabilite will crystallise at a temperature below 32.4°C and at a RH above ~62% RH. Thenardite will therefore exist at higher temperatures and lower values of RH, while hepahydrate is likely to crystallise upon cooling more easily than mirabilite (Denecker et al., 2012).

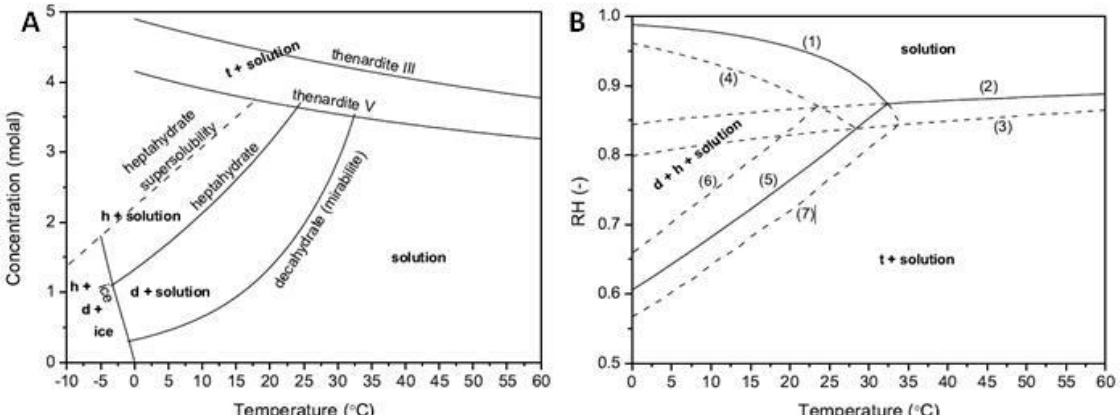

Figure 1-14: Solubility and phase diagrams of Na_2SO_4 (Derluyn, 2012).

(A) Solubility diagram for Na_2SO_4 hydrate system. (t): thenardite, (h): heptahydrate, (d): decahydrate. (B) Phase diagram for Na_2SO_4 hydrate system. (1): $Na_2SO_4.10H_2O$, (2): Na_2SO_4 (V), (3): Na_2SO_4 (III), (4): $Na_2SO_4.7H_2O$, (5): Na_2SO_4 (V) - $Na_2SO_4.10H_2O$, (6): Na_2SO_4 (V) – $Na_2SO_4.7H_2O$, (7): Na_2SO_4 (III) – $Na_2SO_4.10H_2O$.

There has been considerable recent research on the stability and accurate phase transition modelling of heptahydrate (Hall and Hamilton, 2008; Derluyn et al., 2011) with important consequences for understanding the salt weathering of porous stone (Saidov et al., 2012). Figure 1-14 shows solubility and phase diagrams for the Na_2SO_4 – H_2O system. The various stable and meta-stable phases are shown, with solid lines representing the stable equilibria lines and the dashed lines representing the meta-stable equilibria lines between heptahydrate and thenardite III. Under conditions of high

temperature and low RH, thenardite will form crystals. At higher RH and lower temperature, mirabilite will be crystalline, with a marker at ~ 32°C and 86% RH showing the thenardite-mirabilite-solution interface. Meta-stable phases occur in close proximity to these equilibria boundaries.

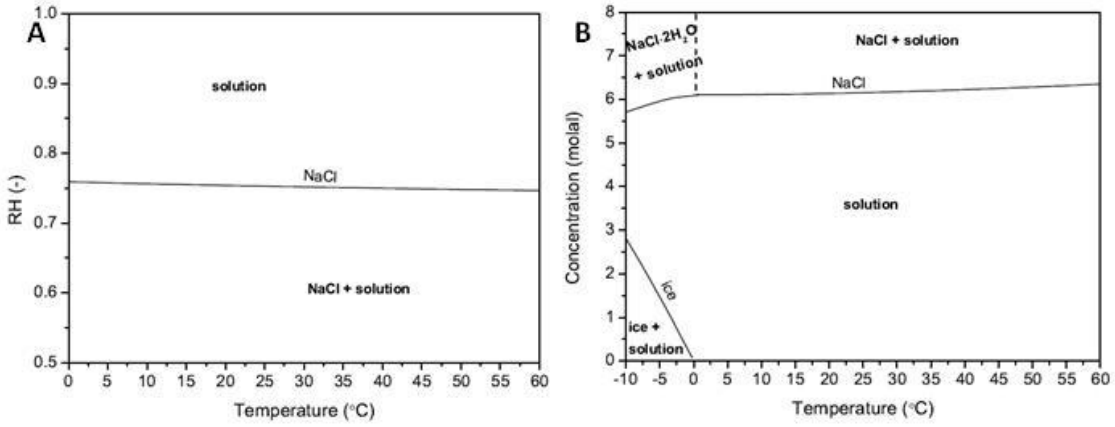

Figure 1-15: Solubility and phase diagrams of NaCl (Derluyn, 2012).

One of the most intense discussions within the field of salt weathering has been that of the thenardite – mirabilite phase transition. Although the chemistry behind the transition was quickly understood (Steiger and Asmussen, 2008), the hydration of thenardite to mirabilite and the reasons behind the damage potential have been highly contested. Mortensen (1933) originally suggested that the damaging potential of Na_2SO_4 originated from the development of a hydration pressure through a volume increase associated with the addition of water molecules into the crystal lattice during the solid crystal phase.

This original theory of Na_2SO_4 crystallisation was accepted by the early workers (Goudie, 1977; Cooke, 1981) but was eventually found to be inaccurate. Further research showed that the thenardite-mirabilite reaction takes places through initial thenardite dissolution before the crystallisation of mirabilite (Rodriguez-Navarro and Doehne, 1999). Although this process is related to a volume increase, the mechanism of this reaction was shown to be incorrect. As thenardite is dissolved in solution through contact with liquid water or at high RH values, it becomes supersaturated in regards to mirabilite and high crystallisation pressures develop against the pore walls associated with the volume increase (Rodriguez-Navarro et al., 2000; Steiger and Asmussen, 2008). Importantly, Na_2SO_4 preferentially crystallises within

solution, increasing the chance of subflorescence forming in the pores, while NaCl tends to crystallise at the solution-air interface, creating less harmful efflorescence (Rodriguez-Navarro and Doehne, 1999). Figure 1-15 shows the solubility and phase diagrams for NaCl. Above 0°C, only one NaCl phase exists, with NaCl crystallising below 75% RH. The solubility diagram shows that a second hydrated phase, $NaCl.2H_2O$, is possible, although only at very high concentrations and temperatures below 0°C.

The number of molecules needed to form a critical nucleus and therefore start crystallisation is much lower with NaCl than with each Na_2SO_4 phase (Espinosa-Marzal and Scherer, 2010). Experimental data confirms that NaCl tends to grow isometric, hopper crystals at low supersaturations during slow drying conditions (Rodriguez-Navarro and Doehne, 1999). Chatterji (2005) found that the formation of NaCl hopper crystals was due to a raised temperature above the centre of the crystal as heat is released during crystallisation. Heat is dissipated at a greater rate from the corners and edges of a crystal and therefore the centre of the crystal remains warmer. Due to the increased temperature, the centre of the crystal has a higher solubility and therefore a higher relative supersaturation ratio exists at the edges, leading to increased growth from these areas. Other studies have shown that NaCl is efficient at clogging pores (Rodriguez-Navarro and Doehne, 1999) and is shown to crystallise within small micro-pores (Rodriguez-Navarro and Doehne, 1999) due to NaCl crystals growing under low supersaturation levels.

Gypsum crystallisation on stone surfaces is commonly characterised by black crusts, formed by the dry deposition of pollutants incorporated with gypsum. Simão et al. (2006) studied the effects of particulate matter derived from gasoline and diesel vehicle exhaust emissions on silicate stone surfaces. The authors reveal through laboratory experiments that stones subject to diesel particulate matter accumulated large quantities of gypsum crystals, while exposure to gasoline particulate matter produced much smaller quantities. This difference is in response to the diesel matter containing high amounts of C^- and Fe-rich particles that are responsible for increased catalytic oxidation of SO_2 and the formation of H_2SO_4 that causes stone sulfation on silicate

stones. C and Pb-rich particles found in gasoline particulate matter do not play a significant role in the process of silicate sulfation.

Several authors have successfully used isotope analysis of various elements to identify the sources of pollutants within black gypsum crusts (Aberg et al., 1999; Vallet et al., 2006; Kloppmann et al., 2011; Rivas and Paz, 2014). Common sulphur sources include construction materials such as mortars, plaster and carbonate stone, seawater and combustion products.

1.3.3.3 *Salt Crystallisation Models*

Crystallisation is accepted as the main mechanism by which salts cause damage to most porous materials. It is through salt crystallisation that high pressures develop as crystals grow within confined pore spaces.

Since salt was first identified as a major agent of stone decay, numerous empirical and theoretical models have been proposed to explain this phenomenon. Correns (1949) was the first to recognise that observed salt damage to porous materials could have been caused by the crystallisation pressure exerted by growing salt crystals. Correns recognised the need for a supersaturated solution to allow sufficient pressures to develop between the growing crystal and pore wall, and developed an equation for crystallisation pressure as a function of the supersaturation ratio:

$$P = (RT/Vs)\ ln\ (c/c_s)$$

Equation 1-2: Correns Equation.

where P = the crystallisation pressure of a growing crystal, R = gas constant (cm^3 atm K^{-1} g-mol^{-1}), T = temperature in Kelvin (k), V*s* = molar volume of the crystal substance (cm^3 mol^{-1}) and (c/c_s) = superstation ratio. This work by Correns has since been recognised as "a milestone in the field of durability of porous materials" (Flatt et al., 2007), with several alternative models proposed, expanding on Correns' original expression (Weyl, 1959; Neugebauer, 1973; Xie and Beaudoin, 1992; from Rodriguez-Navarro and Doehne, 1999; Steiger, 2005). As discussed by Flatt et al. (2007) in their excellent translation of Correns and Steinborn's 1939 paper, the work

accredited to Correns in 1949 had actually been proposed previously by Correns and Steinborn (1939). It is suggested that Correns' famous equation was in reply to criticisms received from his earlier 1926 paper over a lack of experimental data (Flatt et al., 2007). Regardless of when this equation was first produced, it remains an extremely important milestone in our subsequent understanding of salt crystallisation.

Correns' model has been subject to much criticism however due to the assumptions of unrealistically high supersaturation ratios (Lewin, 1974; Snethlage, 1997; in Theoulakis and Moropoulou, 1997; Steiger, 2005). It has since been shown that the model is only valid for low supersaturation ratios (Charola, 2000) and for monomolecular crystals (Flatt et al., 2007). Subsequent models have followed, building on the idea by Everett (1961) that pressure is influenced by known, measurable pore dimensions as opposed to assumed supersaturation ratios. It was Wellman and Wilson (1965) who proposed the use of an equation adapted from Everett's model of ice crystallisation in porous materials. The first adaptation concerns the curved interfaces of the crystal and solution as measurements of the crystal shape and size:

$$P=\gamma_{cl}\, dA/dV$$

Equation 1-3: First adaption of Everett's Equation.

where γ_{cl}= interfacial free energy, A= surface of the crystal and V= volume of the crystal. Another way to consider the maximum crystal size and shape within porous materials is through measurable pore sizes. It is therefore applicable to substitute the surface and volume of the crystal for pore sizes in Equation 1-4. A second adaption therefore gives the following equation:

$$P=2\,\gamma_{cl}(1/r_1 - 1/r_2)$$

Equation 1-4: Second adaption of Everett's Equation.

Where r_1 = the radius of the large pore and r_2 = radius of the small adjacent pore. As later observed by Zehnder and Arnold (1989), crystal growth preferentially takes place in larger pores, with the greatest pressures and damage expected in areas where large pores are connected to small pores

(Charola, 2000). As larger pores are filled by a growing crystal, the curvature of this crystal must change as it moves towards the smaller pore, owing to higher crystallisation pressures at this point (Steiger, 2005). In his extremely informative paper, Scherer (2004) explains that pore shape is a very important parameter influencing the preferential growth of crystals in certain directions leading to the potential onset of damaging pressures within the pore as crystals move into smaller pores. Equation 1-4 also predicts that pressures will increase with diminishing pore sizes, with results from Fitzner and Snethlage (1982) supporting this claim. Rossi-Manaresi and Tucci (1991) successfully employed this equation using previously calculated interfacial energies for NaCl and measured pore size distributions to calculate theoretical crystallisation pressures within a range of stone types.

In order to fully understand the salt weathering process, it is essential to combine the various influential factors, including stone petrographic properties, salt solution movement and salt crystallisation. Lewin (1982) successfully proposed a comprehensive model of the full salt weathering process affecting porous materials (Cardell et al., 2008). In his model, capillary rise is the dominant mechanism influencing solution transport into and throughout the porous material. The location where salts crystallise is determined by the capillary rise-evaporation flux; this is the balance between capillary supply and evaporation and relates to the model by Scherer (2004) (Figure 1-11). As previously discussed, evaporation is controlled mainly by temperature and RH, while capillary transfer is influenced by pore size distributions, viscosity and the surface tension of the solution. The capillary flux is determined by:

$$Jc = 2\gamma\cos\theta/h\ k_s/\eta(1/r_{mS} - 1/r_L)$$

Equation 1-5: Capillary flux equation.

where γ = surface tension, θ = liquid-solid contact angle, k_S = permeability of the partially saturated pore network, h = distance to the evaporative boundary, η = viscosity, r_{mS} = small pore radius and r_L = large pore radius. Therefore it is shown that capillary flux decreases with distance from the point of moisture ingress, leading to a point of change between the formation of efflorescence and subflorescence within the stone at a specific height

(Scherer, 2004; Cardell et al., 2008). When evaporation rate exceeds capillary flux, subflorescence takes place within the stone. Cardell et al., (2008) found that viscosity of the solution within their experiments had the greatest influence on capillary rate.

It is now recognised that crystallisation pressure is the major mechanism of salt-induced damage within building stone, and is influenced by both the supersaturation ratios and pore network properties. Many other mechanisms have been suggested including hydration pressures and thermal expansion. Work by Steiger (2005 I and II) and Theoulakis and Moropoulou (1997) successfully summarise the many proposed theories and models in considerable detail.

1.4 De-icing Salts

De-icing salts and snow ploughing provide some of the most successful and cost effective snow and ice clearance methods available. The use of de-icing salts, specifically NaCl, have been relied upon for well over 50 years (Ramakrishna and Viraraghavan, 2005; Houska, 2007), and there has been increased interest since the early 1970's on the effects of de-icing salts on the local environment and ecosystems (Ramakrishna and Viraraghavan, 2005).

An early, but incorrect assumption was that the influence of de-icing salts on the environment was limited to areas immediately adjoining heavily "salted" areas, such as footpaths and roads (Houska, 2007). Research has since identified de-icing salt accumulations out-with localised spreading areas (Ramakrishna and Viraraghavan, 2005). This widespread exposure and mobilisation of salts into the environment can significantly increase their environmental impact and increase the number of buildings at risk of salt decay. The effect of de-icing salts on the environment, masonry structures and on transport infrastructure is a worldwide problem with known impacts linked to the corrosion of metals (vehicles, bridges and buildings) (Menzies, 1992), damage to concrete (Valenza and Scherer, 2007) and to environmental contamination (Ramakrishna and Viraraghavan, 2005).

De-icing salts can be categorised into three separate product types: chlorides (NaCl, $CaCl_2$ and $MgCl_2$), acetates (calcium, magnesium and potassium acetate) and organic de-icers (such as urea, methanol and glycols) (Houska, 2007; Jenks et al., 2007). De-icing salts are used to initially depress the freezing point of water and to break the bonds between ice and its substrate. This goal is achieved by applying the salt as brine. The time of application and the concentration of brine are key variables influencing how fast and how effectively the salt will act. As the brine begins to melt the ice, dilution will take place, hindering its effectiveness and causing the freezing point of water to subsequently rise, leading to the need for further, repeat applications (Salt Institute, 2011). Other important constraints include: the thickness of snow/ice, atmospheric and substrate temperature and salt particle size as this influences the rates of salt penetration and undercutting within the ice.

Several studies have revealed the deleterious effects of NaCl, $CaCl_2$ and $MgCl_2$ on hardened concrete and metals (Koenig and Rupp, 1999; Jenks et al., 2007; Shi et al., 2009; Environment Agency, 2010). An investigation by the Michigan Technology Transportation Institute (2008) revealed the effects of all chloride de-icers on concrete mortars and pastes. Their study concluded that the prolonged exposure of concrete to $CaCl_2$ and $MgCl_2$ results in a significant chemical interaction, with associated stress caused by expansion, cracking and a loss of compressive strength.

Similar results were presented by Lee et al. (2000), who showed that magnesium in any form (acetate or chloride) is extremely damaging to pavement concrete, causing breakdown through the replacement of calcium silicate hydrate by non-cementitious magnesium silicate hydrate. Darwin et al. (2007) also confirm the increased damage potential of $CaCl_2$ and specifically $MgCl_2$ to concrete under wetting and drying tests. They concluded that NaCl had a negligible effect on the concrete at both low and high concentrations, while $CaCl_2$ was most damaging at higher concentrations. $MgCl_2$ on the other hand was extremely damaging at both low and high concentrations, with damage likely caused by chemical changes in the cement paste and crystallisation taking place within pores and cracks. Wang et al. (2006) show that $CaCl_2$ had a greater penetration into concrete than

NaCl, with $CaCl_2$ causing the leaching of calcium hydroxide and other chemicals into the concrete.

$CaCl_2$ and $MgCl_2$ are known to deteriorate concrete than contains reactive dolomite aggregates as they accelerate the alkali-carbonate reaction, while NaCl can enhance the alkali-silica reaction. Shi et al. (2010) provide contrasting reports from freeze-thaw tests on Portland cement concrete, whereby weight loss values and SEM analysis showed that NaCl was the most damaging de-icer when compared to a wide range of alternatives including $CaCl_2$ and $MgCl_2$. Each de-icer (at 3% concentration) chemically reacted with the cement hydrates, forming new products in the pores and cracks. Şahin et al. (2010) agreed that the commonly used 3% preparation is the most damaging concentration for NaCl solution in freeze-thaw tests on cement.

Padilla et al. (2013) present results from a range of experiments considering the combined effects of de-icing salts and sulphur on the corrosion of galvanized steel under high sulphate soil conditions. Using electrochemical testing methods they showed that sulphate contaminated soils significantly increase the corrosion vulnerability of galvanized steel and identified the need to understand the effects of de-icing salts under these corrosive conditions. Under normal soil conditions, potassium acetate has the lowest impact on corrosion rates, while NaCl has the greatest impact. Conversely, the damaging effect of $MgCl_2$ and $CaCl_2$ was significantly reduced under sulphate conditions as the corrosion layer caused by sulphate had a higher protective effect with regards to both of these salts. NaCl was shown to be damaging under all investigated soil conditions, with all de-icing salts shown to produce similar corrosion effects but at different rates.

Recently, there has been a raised awareness of the impacts of increased salinity on the environment through the use of de-icing salts. An extensive review on the environmental impacts of various chemical de-icers was produced by Ramakrishna and Viraraghavan (2005). Long and short term studies following the influx of de-icing salts into the environment were reviewed. Several studies were examined, with data confirming that, as a result of increased de-icing applications, a significant increase in Na^+ and Cl^- ions was evident within surface waters and soils. This increase in salt ions was

found to induce lake stratification, stimulate algal growth and lead to a reduction in the mixing of dissolved salts entering lakes. An increase in NaCl within soils rendered them less permeable, reduced soil aeration and consequently increased overland flow, surface runoff and erosion as high concentrations Na replaced lower, naturally occurring Ca^{2+} and Mg^{2+} cations within the stone. These findings were attributed to the dispersal of salt by wind, soil percolation, direct deposition and surface run-off.

$CaCl_2$ and $MgCl_2$ react differently to NaCl on soil properties. Both salts contain positively charged cations that readily bind to negatively charged surfaces within soils. Although Cl^- has a negligible effect on soil, both Ca^{2+} and Mg^{2+} have a high absorption affinity and are likely to bind with certain soil particles, creating larger, aggregated particle sizes through flocculation. The presence of soil aggregates can create macropores within soils, increasing permeability, aeration and drainage. The exposure of cations such as Ca^{2+} and Mg^{2+} can thus be seen to a degree as being beneficial for soil properties (Bohn, McNeal and O'Conner, 1985 within Jenks et al., 2007).

Sanzo and Hecnar (2006) exposed wood frog tadpoles to a range of NaCl salt concentrations measured from 59 wetlands in Ontario, Canada. 96 hour lethal concentration 50 values of 2636 mg/l and 5109 mg/l were measured, with surviving tadpoles experiencing reduced activity, reduced weight and physical abnormalities. Frog larvae experienced increased stress, mortality and altered development when exposed to acute and chronic salt concentrations. Negative correlations were found between chloride concentration, distance from the road and amphibian richness, leading to the conclusion that increased salinity was caused by de-icing salt use.

An analogous study by Collins and Russell (2009) revealed similar results, showing that both wood frogs and spotted salamanders were extremely sensitive to increased salinity levels. Field studies from Nova Scotia showed that wood frogs and spotted salamanders did not occupy high salinity pools, while American toads had no preference to salinity. The application and transport of de-icing salts into the road side vegetation and ecosystems influenced community structure by excluding salt intolerant species.

Cañedo-Argüelles et al. (2013) reviewed the ecological impacts of river salinisation. Secondary salinisation affects the environment at a range of ecosystem levels leading to a reduction in aquatic biodiversity; as highlighted by Collins and Russell (2009). Management of secondary salinisation should be monitored, while suggestions of using ionic composition as a better indicator of secondary salinisation are proposed.

Studies by Cekstere et al. (2008) and Munck et al. (2010) highlight the long term impact of de-icing salt levels on the health of trees and road side greenery in Latvia and North America respectively. Most damage was found to take place within 10m of roads, with damage limited to 30m distance, while fir trees showed a greater tolerance to increased salinity than pines (Munck et al., 2010). Cekstere et al. (2008) estimate the critical ion concentrations for visual leaf necrosis of *tilia x vulgaris* leaves at 0.14% Na and 0.66% Cl.

Howard and Maier (2007) consider the issues surrounding the continued use of de-icing salts as an obstruction of further urban growth within the Greater Toronto Area, Canada. Citing that with few alternatives to conventional NaCl, the continued contamination of shallow aquifers could lead to difficulty in future growth as an expanding population in the Greater Toronto Area would continually rely on shallow aquifer use. They suggest that future planning needs to consider the protection and management of aquifers, specifically in relation to increased Cl^- levels.

1.4.1 De-icing Strategies

Due to the extensive variety of de-icing materials currently available to the public and highway authorities, there must be careful consideration of the suitability of each de-icing compound. For sensible de-icing strategies, it is vital to gauge each situation in accordance with a number of factors, including: (i) the severity of underfoot and road conditions (Figure 1-16) and weather forecasts; (ii) site specific factors (including priority of routes); (iii) the ice melting performance of available de-icers; (iv) the adverse effects (if any) on the environment; (v) the relevant cost of implementation.

Figure 1-16: Ice covered pavements in Glasgow, February, 2015.
(A): large section of untreated pavement covered by ice. (B): Close-up image of the pavement, showing small cleared patches after treatment with de-icing salt. (C): Hard-packed ice on an untreated pavement.

Scotland's national road maintenance authority, Transport Scotland, have made significant changes to their winter maintenance schedule that were initiated by the extreme challenges that the country faced in the winter of 2010-11 when large sections of the road network became impassable and extremely dangerous for extended periods of time. Transport Scotland is tasked with the maintenance of trunk roads in Scotland to ensure the safety of vehicles and pedestrians at all times. Four main operating companies look after the different regions of Scotland (North West, North East, South West and South East). Each company works to their own operating plan running 24 hours a day from October – May. These plans can be directly accessed from the Transport Scotland website. 195 gritters are shared between each region, ensuring on average of 1 gritter/18km of trunk road.

Operations are divided between precautionary treatments and post ice/snow treatments. Figure 1-17 shows the priority A and B class routes, with Figure

1-18 showing the live updated routes as accessed from the Transport Scotland website. A range of methods are currently employed to predict and maintain de-icing throughout the winter period. Live meteorological data are collected from 156 weather stations throughout Scotland, with live information transferred between weather stations and gritting vehicles when on patrol. Each vehicle is equipped with road temperature sensors and “airwave” technology that allows the continued contact with emergency services.

Salt is spread at a ratio of 70% dry NaCl/30% NaCl brine at a combined concentration of 23%. This recipe has been implemented since 2007-08. Alternatives have been subsequently explored for use at lower temperatures. The addition of brine to dry salt helps to increase the melting rate and reduce the lag time between the application and effective penetration into the ice. Stored salt levels are managed and maintained by the Scottish Salt Group which is assembled from representatives from all local authorities. Over the past 4 years there has been in excess of 1.5million tonnes of de-icing salt deposited on pavements and roads, with 645,000 tonnes applied across Scotland in 2010-11, 691,000 tonnes in 2012-13 and 334,603 tonnes in 2013-14 (Transport Scotland, 2014). Local council authorities are responsible for the maintenance of all local roads and footpaths. For the aims of this thesis, it is thought that any changes to de-icing strategies for the protection of historic buildings should be focussed at the local council level as it is through council run de-icing services and personal de-icing that the majority of salt-mediated damage to buildings will occur.

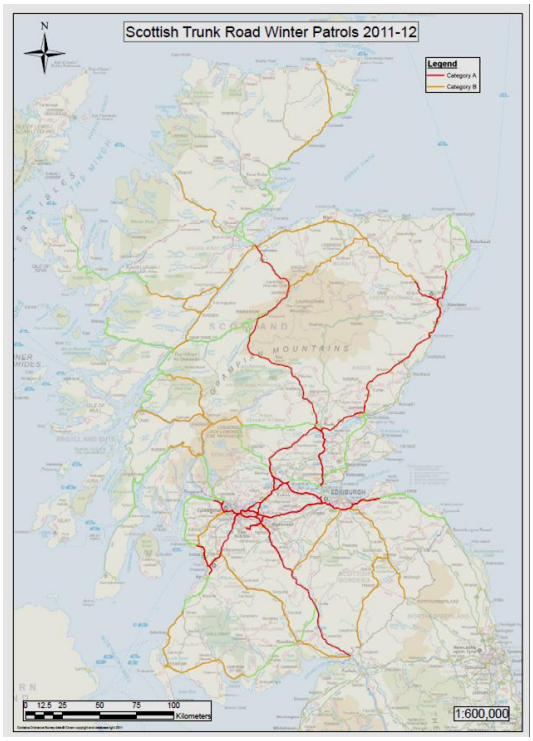

Figure 1-17: Scottish trunk road winter patrol map, (Transport Scotland, 2014). Priority A and B category roads as used by Transport Scotland for priority de-icing.

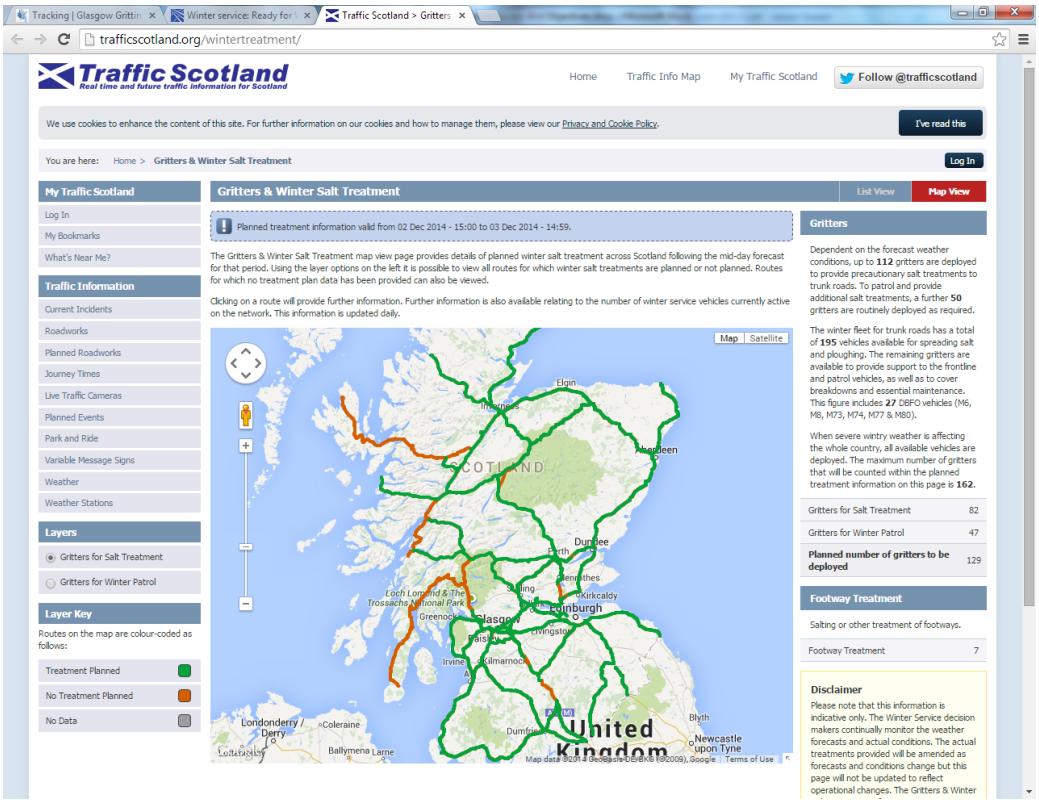

Figure 1-18: Live-updated planned de-icing treatment map.

Live updated planned treatment map for Scotland for 02 December, 2014 highlighting the planned routes and the number of gritting vehicles needed for forecast gritting (Traffic Scotland, 2014).

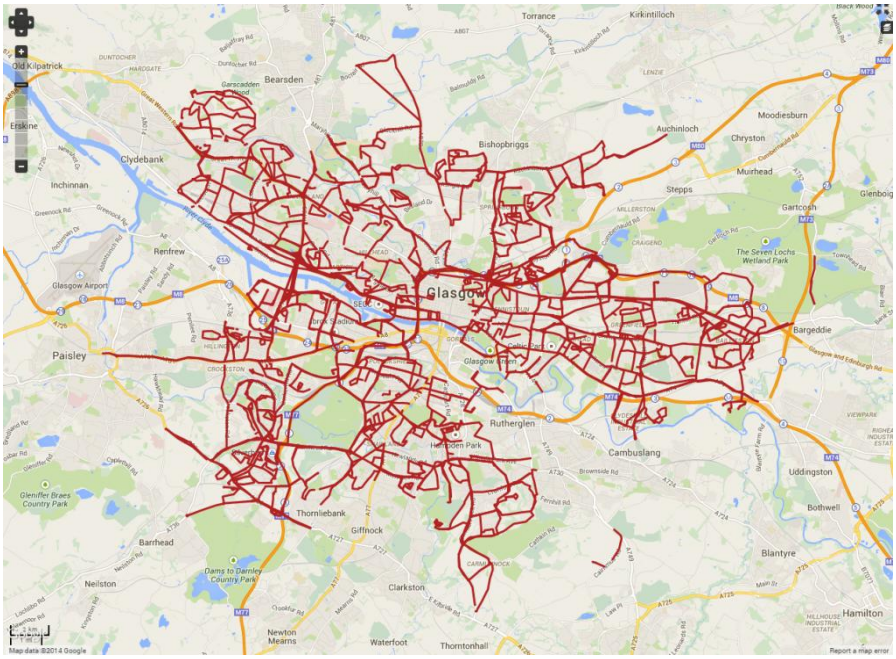

Figure 1-19: Live-updated recently gritted treatment map for Glasgow.
Live updated map showing the recently gritted streets in Glasgow for 02 December, 2014 (Glasgow City Council, 2014).

Glasgow City Council operates a winter maintenance schedule that works through a priority system of roads and pathways. Priority one routes include A and B class roads, bus routes, roads to park and ride car parks, hills steeper than a 1 in 10 gradient and entrances to emergency vehicle centres including police stations, hospitals and bus garages. Priority 2 and 3 routes include local shopping areas, health centres, places of worship and routes onto A and B class roads. Similar classifications exist for footpaths, with city centre footpaths that contain high pedestrian traffic prioritised. Within Glasgow there are 1242 salt bins located strategically throughout the city, with 23,000 tonnes of salts and 4000 tonnes of grit salt held in storage. Several more salt bins are provided by institutes and companies within the city (Figure 1-20). NaCl with the addition of the “safecote” additive (sugar, starch, cereal carbohydrate processing by-products) is used extensively throughout the city, with spreading rates determined by environmental conditions as highlighted in Table 1-2 and Table 1-3. Figure 1-19 shows the free access content available on the Glasgow City Council website, highlighting a map of recently gritted roads within Glasgow. Access to the winter maintenance scheduled used by Glasgow City Council can be accessed directly from their website.

Figure 1-20: Salt bin located outside the entrance to the Gregory Building, The University of Glasgow.

Weather Conditions	Rocksalt Spread Rates (g/m^2)	Safecote Spread Rates (g/m^2)
Frost	10	10
Ice and/or light snow	20	10
Freezing conditions expected after rain	30	20
Continuous snow expected	40	30
Priority footways – all conditions	60	N/A

Table 1-2: Precautionary treatment salt spreading rates used in Glasgow (2014-2015), (Glasgow City Council, 2014).

Road Surface Conditions	Air Temperature (°C)	Rocksalt Spread Rates (g/m^2)	Safecote Spread Rates (g/m^2)
Ice formed	Above -5	40	20
Hard packed snow/ice	Below -5	40	30
Snow cover exceeding 30mm	Above -5	40	30
Snow accumulation – prolonged falls	Above -5 Stable	40	30

Table 1-3: Ice and snow clearance – salt spreading rates used in Glasgow (2014-2015), (Glasgow City Council, 2014).

In response to the extreme conditions experienced over the 2010-11 winter period, Transport Scotland has obtained and trialled a range of alternative de-icing compounds. Transport Scotland commissioned the Transport

Research Laboratory (TRL) to develop guidance for the use of these alternative de-icers (Evans et al., 2011).

The range of alternative de-icing compounds considered by Transport Scotland included: (i) magnesium chloride brine; (ii) sodium chloride brine with safecote additive (agricultural by-products/sodium chloride mix); (iii) sodium chloride and calcium chloride brine with safecote additive; (iv) Eco-thaw liquid de-icer (agricultural by-products and magnesium chloride).

Similar ratios to current guidelines for NaCl (30% brine – 70% dry salt) are recommended for each alternative de-icer, with the composition of each de-icer listed in the appendix. The TRL report lists important equipment and pre/post salting method implications for each de-icer, highlighting the importance of ice penetration and ice undercutting rates for each compound. A trial use of Ecothaw was undertaken by Transport Scotland in Aberdeen during 2011. The concentrated Eco-thaw product was spread in a lined pattern on top of compact snow with a surface temperature of between -6 to -8^{o}C. The trial showed that concentrated Eco-thaw was effective at penetrating hard packed snow, especially when concentrated in lines during spreading with little subsequent traffic. This lack of traffic allowed fast penetration and undercutting rates, which would be lowered with increased traffic as extra dispersal on the snow surface would take place.

It is the long-term aim of research outlined in this thesis to categorise and implement heritage friendly de-icing strategies for environmentally vulnerable zones. These strategies will consider the most suitable choice of de-icing materials to be used in areas of increased sensitivity to salt deposition, taking into account the frequency, timing and rate of applications. Areas of higher vulnerability and cultural importance will therefore be subject to strategies of increased sensitivity.

1.5 "Testable hypotheses" and objectives of the study.

The main purpose of this study is to understand the effects of de-icing salts on the durability of various sandstone types, specifically in relation to the stone's petrographic and petrophysical properties and notably their hygric properties; that is the transfer of moisture (as water and vapour) through the pore system. Following recent hard winters, national agencies such as Historic Scotland have become very concerned that damage to the structural and aesthetic integrity of properties in their care is accelerating owing to the widespread use of de-icing salts on pavements and roads.

In response to these concerns a range of experimental methodologies were devised to help answer the question: "What are the effects of different de-icing salts on sandstone masonry structures?" In order to answer this question, two separate approaches must be considered: one investigating the properties of the building materials and the second investigating the properties of de-icing compounds. It is also extremely important to combine both threads of enquiry into single experiments, such as salt crystallisation tests; however, to accurately understand the processes taking place within the stone, the two components, salt and stone, must also be thoroughly examined individually. A range of complimentary experimental methods have therefore been devised. These will focus on different aspects of the topic and will be compared to help optimise the understanding of the individual results. For example, complimentary methods of calculating porosity are made including the calculation of total, open and effective porosities using mercury intrusion porosimetry (MIP), micro computed tomography scanning (μCT), helium porosimetry and vacuum saturation methods to determine the porosity values at different pore size thresholds and to critique each method to help optimise porosity measurements.

In order to answer the initial question: *"What are the effects of de-icing salts on sandstone masonry structures in Scotland?"* certain objectives must be met, which are outlined in this next section.

(1) Understand the petrographic and mineralogical properties of different sandstones in the study.

Twelve different sandstones were examined. They were chosen in accordance to: (i) their petrographic variation; (ii) their historical importance as replacement building stones in Scotland. A range of techniques have been used to meet this objective, including optical microscopy, SEM analysis and μCT scanning.

(2) Understand the decay mechanisms of different weathering agents (salt crystallisation, freeze-thaw).

Recognising the behaviour of salt and water within porous stone and the mechanisms of phase changes and moisture movement significantly aid our understanding of the processes of deterioration and decay.

In order to meet this objective, samples of each stone will be put through crystallisation and freeze-thaw tests, with mechanisms of decay studied by SEM, ESEM, optical microscopy and several other techniques.

It is hypothesised that the mechanisms of each decay process are constant but the durability/susceptibility to weathering will be controlled by the stone type; not all the stones will react in the same way.

(3) Understand the crystallisation of each individual salt on the damage mechanisms.

It is known that salt can be extremely damaging to stone, however certain phase changes may be transient and each salt will react differently under changing environmental conditions. Not all salt minerals will exert damaging crystallisation pressures. This aspect will be investigated by droplet and in-situ ESEM analysis of de-icing salt crystallisation.

It is hypothesised that each salt has a different crystallisation mechanism.

It is hypothesised that subsequent decay varies with the salt type, and the damage characteristics are controlled by the different salt types.

It is hypothesised that the degree of decay is controlled by the stone type.

(4) To understand the reactions that take place within the stone between de-icing salts and other, possibly intrinsic salts?

It is extremely unlikely in the natural environment that only one salt is present in masonry at any time. Rather, studies have shown that a complex mixture of ions exist within stone (Larsen, 2007). The crystallisation behaviour of mixed salt solutions is far more complex than that of a single solution. The crystallisation pathways for single salts are well documented (Godts et al., 2012). Under changing environmental conditions and in the presence of a mixed ion solution however, the prediction of phase changes and crystallisation becomes extremely difficult. It is therefore of fundamental importance that we understand the complexities of mixed salt solutions.

The crystallisation of mixed salt systems is investigated using the chemical equilibrium model ECOS-RUNSALT® using measured ion concentrations and theoretical "increased" de-icing salt ion levels to predict the salt phase transitions that may be expected in stones situated susceptible to high rates of de-icing salt accumulation.

It is hypothesised that reactions between salts are expected to take place because there are sufficient quantities of de-icing salts entering into the stone and favourable environmental conditions (RH and temp) exist.

(5) Identify the petrophysical properties of the stone that are the most responsible for the decay of each individual salt.

Even within a sedimentary rock such as sandstone, the petrophysical properties of individual rock types can be extremely diverse. Different strength parameters and pore structure properties may significantly influence the durability of a stone to the crystallisation of salts (Benavente et al., 2004). The recognition of these vital parameters is crucial to understanding the overall decay process.

A plethora of complimentary stone testing methods are used to investigate particular properties of the pore network and the structural integrity of each

stone. Moreover, these properties are investigated as potential durability estimators for sandstone.

It is hypothesised that any one property is the most important for stone durability.

It is hypothesised that there are a range of properties that are important and not solely one.

It is hypothesised that the above is true across each stone type.

It is hypothesised that this is true across each salt type.

(6) Find the most adequate methodology/best practice for durability estimation of sandstones: a critique of the methods used.

It is important to critique previously used methodologies in an attempt to optimise future research in this field. Results from the stone characterisation and salt crystallisation tests will be analysed against one another to establish a relationship between pore structure, moisture transport properties and durability. Since each method investigates a different property of the pore network, those methods with a stronger correlation can be seen as a better durability estimator.

It is hypothesised that specific tests are more important.

It is hypothesised that they are all equally important.

(7) Find a salt resilient replacement sandstone to be used on areas of high salt susceptibility.

This is one of two practical outcomes of this study and will allow Historic Scotland to recommend the most suitable replacement sandstones to be used in areas of high salt susceptibility. Recommendations will be limited however to the actively quarried stones used within the study. The recognition of the most important petrophysical properties of stone that are the most

responsible for salt decay will also be vital when choosing a suitable replacement stone.

It is hypothesised that a certain type of sandstone will be better/a stone showing certain petrographic properties will be most suitable.

It is hypothesised that a different type of lithology be used, such as using a lower course of granite.

It is hypothesised that a combination of stone and suitable mortar be used.

(8) Recommend de-icing strategies that will be least damaging to our built heritage.

Following on from objective 7, this is the second practical outcome of the study. This will inform Historic Scotland and local councils as to the most "stone friendly" salts.

It is hypothesised that no change of salt is needed.

It is hypothesised that a change of actual spreading practice is needed.

It is hypothesised that a change of both salt type, type of spreading and salt particle size is needed.

1.6 Thesis structure

The materials and experimental methods used within the thesis are presented in chapter two. The properties, geological and historic importance of each sandstone, and the ice-melting performance of each de-icing salt are presented in chapter three. The results from durability tests (salt crystallisation and freeze-thaw tests) are presented in chapter four. Chapter five presents results from a case study that looks at the future salt crystallisation cycles at The University of Glasgow with theoretically increased de-icing salt levels and measured temperature and RH conditions from sites across the university campus. Chapter six and seven discuss the changes to the stone properties from durability tests and the main stone

properties that control durability to salt-induced decay respectively. Chapter eight presents a short critique of the methodologies used with the study and offers recommendations on best practice for stone durability assessment. Chapter nine presents avenues of future work from this research and discusses some of the future key advancements within the scientific field. The final summary and conclusions of the thesis are presented in chapter ten. Figure 1-21 summarises the thesis structure and highlights the links between each chapter.

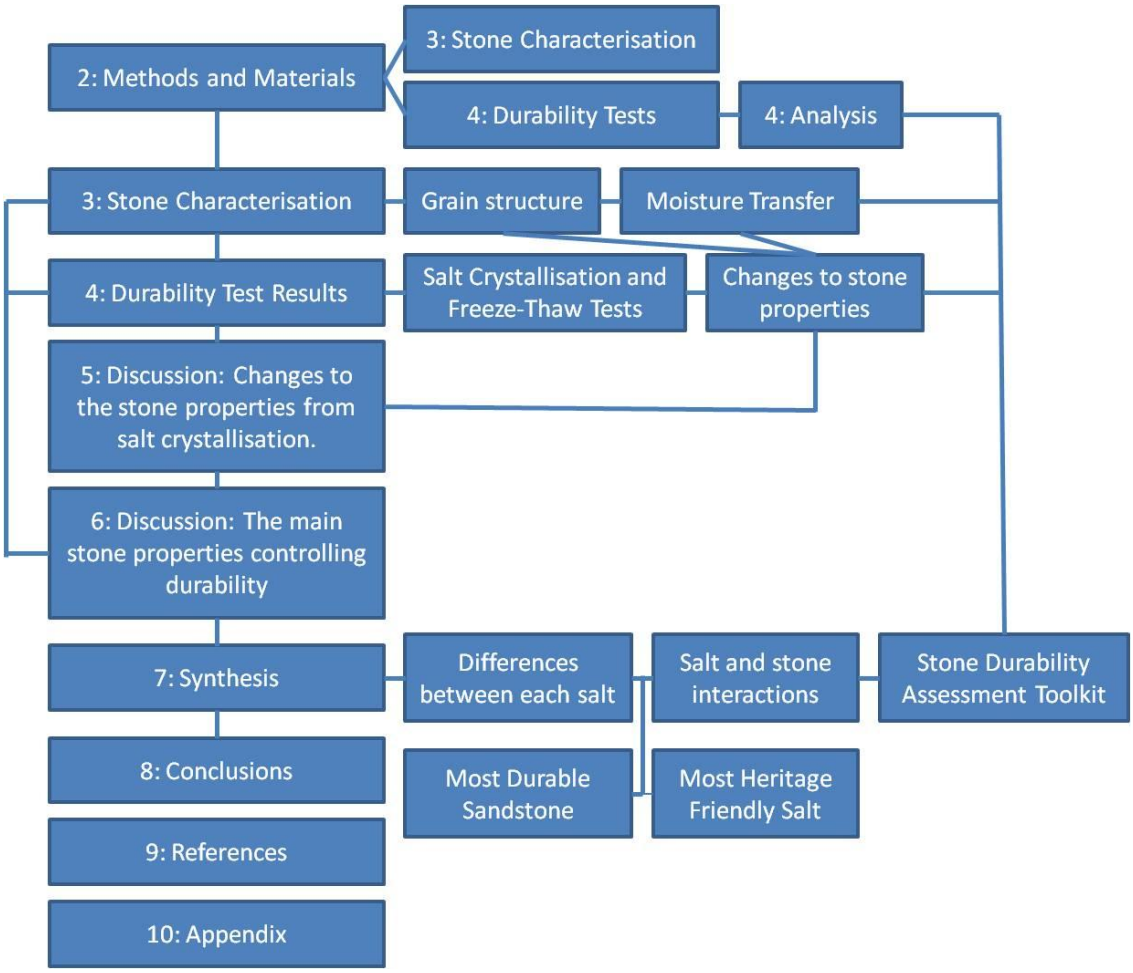

Figure 1-21: Flow chart documenting the thesis structure and highlighting the links between each chapter.

2 Materials and Methods

2.1 Materials

2.1.1 Sandstones

Samples of 12 different sandstones were used for hydric performance tests and salt crystallisation experiments. Ten of the stones are representative of common replacement stones throughout central Scotland and a further two are “used” samples taken from The University of Glasgow during repair work. These two are tentatively identified as Giffnock blond sandstone and Bonhill red sandstone. Stones were chosen in accordance to their importance in Scottish built heritage as common replacement stones and also to provide a broad petrographic and mineralogical range.

Before the project started, stone selection according to specific criteria had to be made. It was important that the samples used in the study were historically significant building stones, either locally or nationally, and would either be used as common replacement stone in historic buildings or used in the original construction of historically important buildings. The first five samples (Blaxter, Clashach, Cullalo, Giffnock (the first ‘used’ sample from the university) and Scotch Buff) were chosen from an original batch of seven that had been used previously in a similar PhD project, researching the effects of climate change on the blond sandstones of Glasgow. These first five stones and two others (Locharbriggs and Stanton Moor) were chosen after initial consultation with stone matching experts at the British Geological Survey (BGS). An eighth sample (Bonhill) was later acquired as used sandstone from restoration work that was being carried out on the main building of Glasgow University. Following initial salt crystallisation tests and after recommendations from experts in the field, the final three samples were added: Corsehill, Hazeldean and Doddington. Sandstone descriptions, quarry locations and geological origins are discussed in Chapter 3.

2.1.2 Salts

2.1.2.1 *Sodium Chloride (NaCl)*

The most common de-icing salt is NaCl and is used as a pure salt, or commonly as “rock salt”; which is a mixture of salt with sand-grade silicate mineral grains. NaCl is the cheapest and most extensively available salt and is used extensively worldwide. Depending on conditions, NaCl can be utilised as either a solid salt or a brine, and can be deployed as both a de-icer and anti-icer. It has been shown to work best at temperatures above -11^{o}C (Transport Scotland, Winter Service Plan, 2010), although under ideal laboratory conditions it may continue to melt ice down to the eutectic temperature of -21^{o}C (Nixon et al. 2007).

NaCl is used as a reference salt within the study as it is the most universally used and commercially available de-icing salt and one of the most common salts associated with masonry decay. It is frequently used in decay experiments (Rothert et al. 2007) and does not present any complicated phase changes as is observed with Na_2SO_4, therefore allowing its behaviour within sandstone to be accurately recognised and understood as it should behave in relatively predictable way. (Gomez-Heras and Fort, 2007). Rocksalt was used within the study, and from SEM analysis it is identified as a gritty mixture of NaCl (≥80%) and abrasive sands, rock fragments and fly ash (20%) (Figure 2-1).

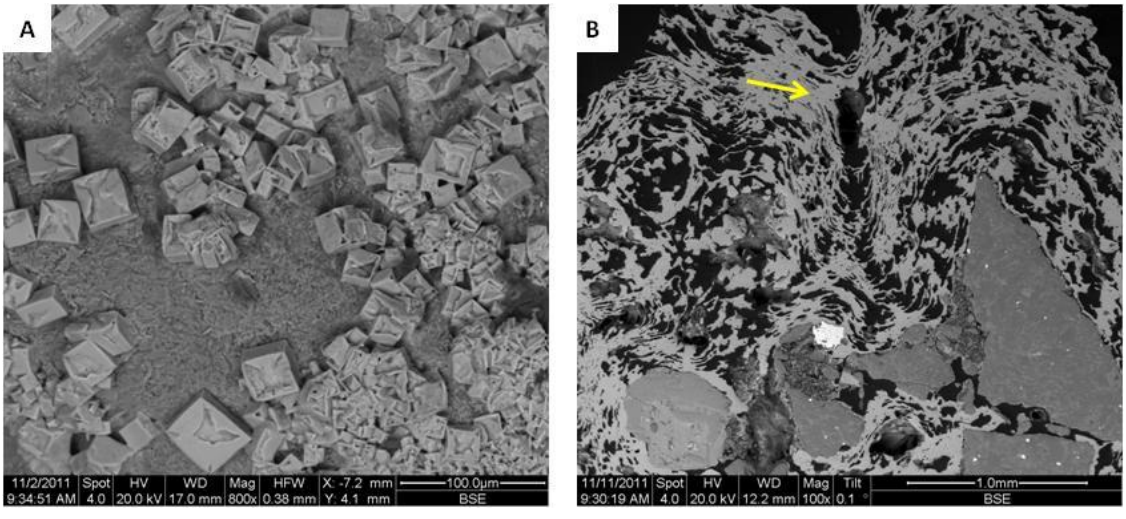

Figure 2-1: SEM images of “rocksalt”.

(A): Individual salt crystals. (B): Thin section showing salt (yellow arrow) and rock fragments composing 20% of rocksalt mixture.

2.1.2.2 *Magnesium Chloride ($MgCl_2$) and Calcium Chloride ($CaCl_2$)*

$CaCl_2$ and $MgCl_2$ are secondary chloride de-icers, and are commonly used in the UK as a replacement for NaCl or are applied alongside it. They have lower eutectic temperatures than NaCl, increasing their ability to effectively de-ice at lower temperatures (NCHRP, 2007). Tests have shown both greater reaction times and greater depths of penetration at lower temperatures when compared to NaCl (Nixon et al. 2007). $CaCl_2$ is a by-product in the manufacturing of soda ash (sodium carbonate), known as the Solvay process, and has recently been mined directly and more economically from Trona deposits within the USA (Effler, 1996). $MgCl_2$ is the most soluble component within natural brines and is obtained from natural salt deposits, for example, the Great Salt Lake, Utah, USA (Tripp, 2009).

Although performance results provide evidence of a greater de-icing ability of $CaCl_2$ and $MgCl_2$ compared to NaCl, there are also a number of disadvantages in the prolonged use of these salts. There have been many published compilations highlighting the relevant costs of different de-icing compounds (Fischel, 2001; Salt Institute, 2004) and both $CaCl_2$ and $MgCl_2$ can cost as much as 7 times that of NaCl, with other alternative de-icers costing more than 20 and 30 times the price of standard NaCl (Salt Institute, 2004).

Through numerous laboratory experiments, $CaCl_2$ and $MgCl_2$ have been shown to be more effective than NaCl at melting ice at lower temperatures, with tests indicating both greater reaction times and greater depths of penetration at lower temperatures (Nixon et al. 2007). This finding echoes data provided by Dickinson (1959), who documented greater rates of ice melt, and data by Sinke et al. (1976) and McElroy et al. (1988) who documented increased ice under-cutting rates at various concentrations and temperatures. $CaCl_2$ is used as the primary de-icer on priority routes at Stirling and Edinburgh Castles, while Transport Scotland trialled $MgCl_2$ on a road in Aberdeen in 2012 to determine whether it would be a suitable alternative de-icing salt to NaCl during times of extremely low temperatures.

2.1.2.3 *Envirothaw® ($NaCl.MgCl_2.6H_2O$)*

Envirothaw® is a blended, granular chloride de-icer manufactured by Envira Products Limited that was chosen in the study to represent an increasingly popular line of commercially available, “environmentally friendly” chloride-blend de-icers. Similar products are advertised as being more economical, faster acting and “pet friendly” alternatives to standard rock salt. SEM X-ray microanalysis (Figure 2-2) and X-ray diffraction (XRD) on both powder and coarsely crystalline forms of Envirothaw® show a base composition of NaCl (≥90%) combined with bischofite, which is a magnesium chloride hydrate additive, and several other trace minerals (Figure 2-3). It is referred to as ‘chloride blend’ herein.

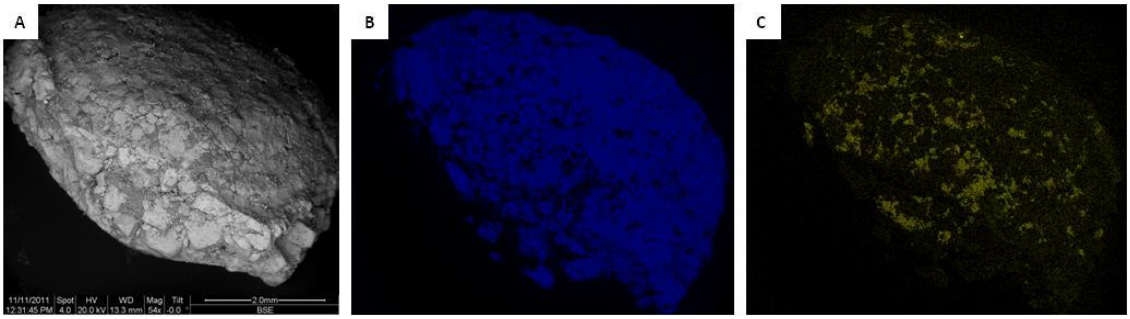

Figure 2-2: Image and X-Ray maps of chemical composition of Envirothaw salt grain. (A):SEM image of envirothaw grain. (B): Na distribution. (C): Mg distribution.

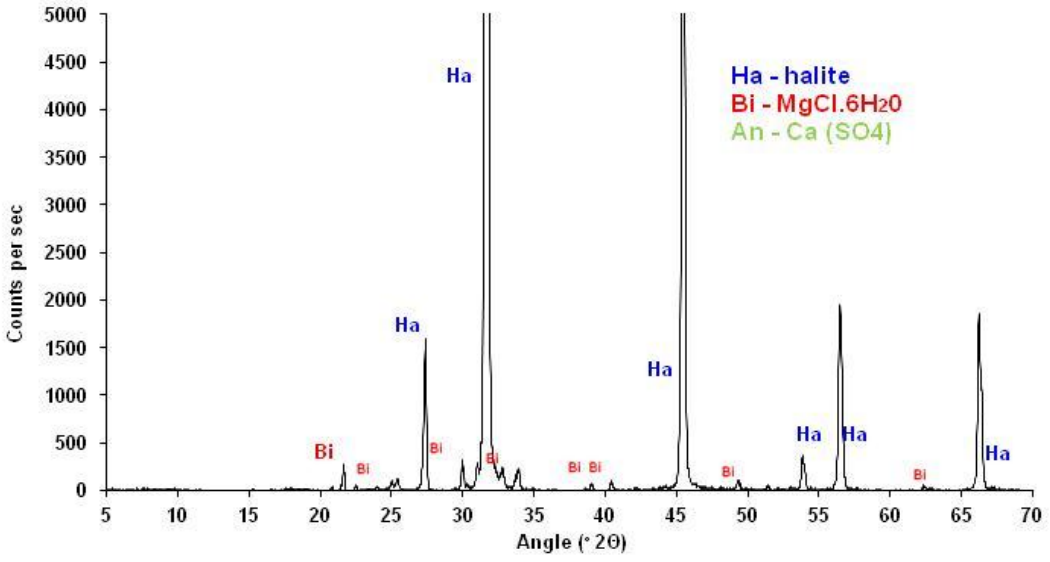

Figure 2-3: XRD spectrum of “Envirothaw” salt showing a match for NaCl and bischofite.

2.2 Methods

Several analytical techniques were used in order to characterise fresh replacement sandstones and to understand their behaviour after crystallisation tests using different de-icing salts. Table 2-1 lists the use of each methodology.

Method	Use	Fresh Stones	Post Crystallisation	Salts
SEM	Grains, salt damage	X	X	
ESEM	Salt crystallisation			X
DIA	Grain size	X		
µCT	Pore network	X	X	
USV	Grain compaction	X	X	
Hydric Tests	Moisture movement and porosity	X	X	
Drying Test	Drying efficiency	X		
MIP	Porosity, PSD	X		
Colour	Surface colour	X	X	
Laser Scanning	Surface roughness	X	X	
IC	Cation analysis			
AAS	Anion analysis			
Ice Melting Capacity	Ice melting capacity of salts			X

Table 2-1: The use of each methodology within the research.
SEM: scanning electron microscope, ESEM: environmental scanning electron microscope, DIA: digital image analysis, µCT: micro computed tomography, USV: ultrasonic velocity, MIP: mercury intrusion porosimetry, IC: ion chromatography, AAS: atomic absorption spectroscopy. IC and AAS were used for measuring salt concentrations in the case study site and not for characterising the salt content of fresh stone samples as initial salt values within fresh stones would be too variable to quantify.

2.2.1 Stone Characterisation

The most important stone properties that influence durability were measured using various methods in order to understand their effect on the stone's behaviour in response to salt crystallisation and freeze-thaw weathering. These properties include: porosity, permeability, pore size distribution, strength and mineralogy.

2.2.1.1 *Scanning Electron Microscopy (SEM)*

Polished thin sections of clean sandstones, blocks of select sandstones from the salt crystallisation tests and intermediate state sandstones from the freeze-thaw test, were analysed by SEM imaging and X-ray microanalysis. Dry-

cut, rough samples were studied to investigate the distribution and morphology of salt crystals within the pore network, while polished thin sections were used to analyse changes to the pore network from salt crystallisation damage and for grain size analysis. Imaging used a Carl Zeiss SIGMA FE SEM in the department of Geographical and Earth Sciences at The University of Glasgow using both secondary electron (SE) and backscatter electron (BSE) modes operating at 20 kV. Analysis of rough samples was undertaken in low vacuum and thin sections under high vacuum. SE images are produced by the detection of low energy electrons that are ejected from an extremely small area surrounding the point of contact between the electron beam and the sample. BSE images are produced through the detection of backscattered electrons that originate from deeper in the sample from the interaction of the electron beam and the nucleus of the sample atoms.

2.2.1.2 *Digital Image Analysis*

Digital image analysis of polished thin sections enables the quantification of grain shape, grain size and porosity. The pore network of a stone, as mentioned previously, is an extremely important determinant of weathering processes. The pore network, including total porosity, effective porosity, pore size distributions, tortuosity and permeability are controlled by sedimentary depositional factors, such as the mineralogy, grain size, grain shape, orientation, sorting, and by digenetic processes including as grain compaction, cementation, dissolution and recrystallisation. These features also influence the density and strength of the rock and thus must be taken into account in this research work (Götze and Siedel, 2007; Nabawy, 2014).

The technique reported here follows a similar one as reported by Hashimoto and Minamizawa (2009) for measuring quartz grain size distributions. Polished thin sections of each stone type were analysed using a Sigma Zeiss SEM in BSE mode at a magnification of 99x, giving a resolution of 0.37 µm/pixel. Mosaic pictures were composed from 8-12 individual SEM micrographs that were taken in a step-wise fashion so that the width of each thin section was analysed in a two row tier segment (Figure 2-4 A). It was found that a mosaic of ten images, covering an area of 123 mm^2, was sufficient to accurately

determine grain shape parameters. Plain images of each micrograph were stitched to create a mosaic using Adobe Illustrator CS3. Each mosaic was then imported into the image processing and quantification software image-J. Grains were segmented from the pore space using the grey-scale values of each mosaic.

In these images, pores are black while detrital grains and diagenetic clays appear as different shades of grey and white. Visual estimations were used to define the segmentation intervals, leaving a binary image once processed. Due to the sometimes high compaction of grains within each sandstone type, it was difficult to separate individual grains from each other after segmentation. The “watershed” tool was therefore used in image-J to roughly separate and determine individual grains from the mosaic. The watershed tool works by calculating a Euclidian distance map, whereby black pixels are replaced by grey pixels of intensity that is proportional to their distance from a white pixel. The ultimate eroded points are then calculated as the centre of each grain (the pixels of greatest intensity that are equidistant from the edges). Each ultimate eroded point is then dilated until it touches the edge of another growing region and the watershed line is drawn (Figure 2-4 B).

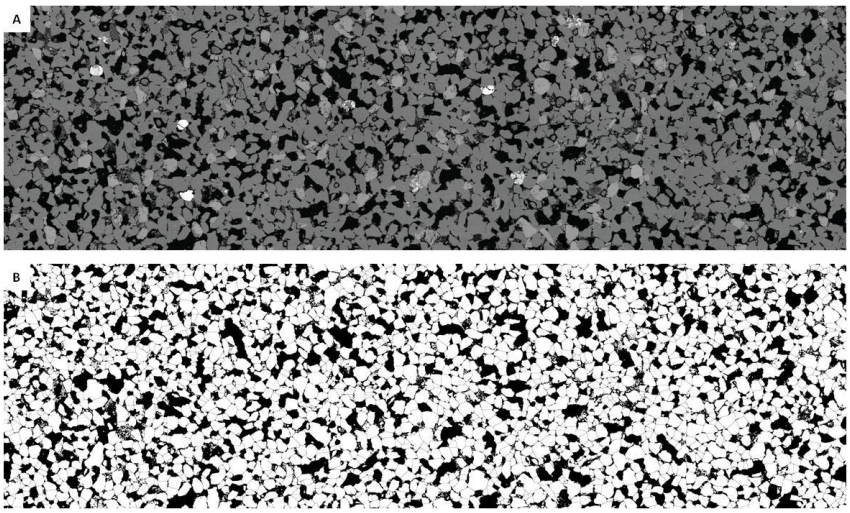

Figure 2-4: Mosaic images of Locharbriggs sandstone used for digital image analysis.

Mosaic images of Locharbriggs sandstone. (A): Mosaic of 10 stitched SEM micrographs, (B): the same mosaic after subsequent segmentation and watershed application. The black areas are pores and the white areas are grains. The area in both images is 123 mm^2.

After the watershed tool had been applied, the mosaic was then imported into Microsoft Paint, whereby corrections to the watershed process were made to define the correct shape and size of specific grains and to “clean

up" the image, removing clay particles and infilling microporous grains. This process was undertaken to ensure a more accurate response of the grain quantification, as small clay particles and microporous grains would be counted as individual grains, and multiple grains, respectively, during the final analysis. In a study by Barraud (2006) limitations to the watershed technique are identified and improvements suggested. Jungmann et al. (2014) describe alternative segmentation techniques and report on a modified method. The final, cleaned up image was then re-imported into image-J, the correct scale was set and quantification was performed. The grain greyscale phase was selected using the threshold selector and analysed using the "measure particles" tool. Grains under the size of 200μm^2 were excluded from analysis as these represent clay fractions, with the remaining grains analysed for: grain area (μm^2), maximum axial length (μm), minimum axial length (μm) and circularity.

Circularity is a measure of how circular an object is, ranging from 0 (an elongated polygon) to 1 (a perfect circle) and is calculated as 4π x (area)/ (perimeter) ^{2}. The number of grains measured range from 2598 to 5024 per mosaic. For Locharbriggs and Blaxter samples, results from two mosaics are combined, resulting in the measurement of 6800 and 7622 grains for each stone, respectively. Grain size is estimated by using the maximum axial length of each grain and plotted using the Wentworth (1922) scale of grain size. Using the method of point counting to determine grain size parameters it is recommended to analyse a minimum of 300 grains to ensure of accurate results (Dryden, 1931), of which this study far exceeds. Point counting, although time consuming in comparison to digital image analysis, does allow the quantification of mineralogy to be made with greater accuracy. Due to similarities in greyscale values of BSE images, it is sometimes difficult to distinguish certain minerals from each other (eg quartz and albite). An example of the results that the technique yields is given in Figure 2-5 and Figure 2-6.

Porosity is measured using a similar analysis in Image-J, but using the mosaic images in their pre-watershed state. Due to many of the pores being connected within the thin section, analysis using image-J cannot separate

individual pores. Mercury intrusion porosimetry (MIP) provides a greater accuracy of pore size distribution over a greater range of pore sizes and is used in this thesis as the preferred technique for pore size analysis.

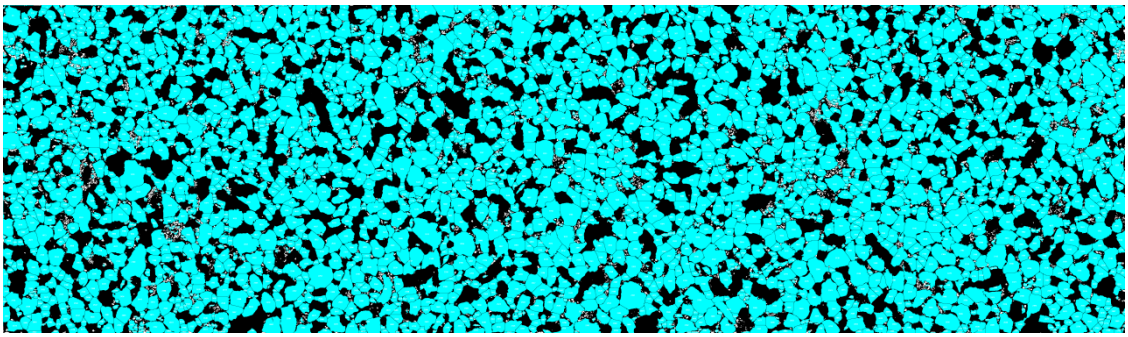

Figure 2-5: Output from Image-J quantification of Locharbriggs sandstone. Area of image is 123 mm^2.

Blue areas are individually numbered grains that were quantified separately.

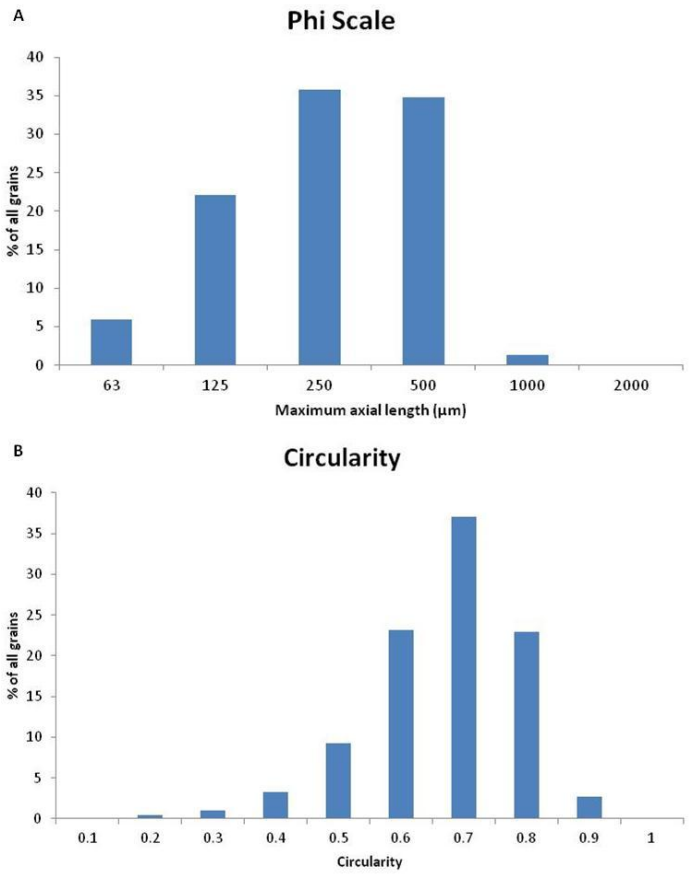

Figure 2-6: Image-J analysis results for Locharbriggs sandstone.

(A): Phi grain scale analysis. (B): Circularity analysis. Measurements are from the image in Figure 2-5.

2.2.1.3 *Ultrasonic Velocity Tests*

Ultrasonic velocity measurements were made to provide a non-destructive means of determining physical-mechanical parameters of the samples. This method works on the principle of quantifying the time of flight of longitudinal p waves emitted from a piezoelectric pulser transducer and received by a receiving transducer as they traverse the sample. The travel time of both primary waves (p waves) and secondary, shear waves (s waves), are influenced by a number of mechanical properties of the stone including: porosity, mineralogical composition, grain size, grain compaction, mineral alignment and water content. Ultrasonic velocity measurements are therefore an extremely useful tool for detecting: (i) the degree and direction of anisotropy within rocks (Vasconcelos et al. 2008); (ii) internal changes in porosity (Sousa et al. 2005); (iii) cracks, fissures and the degree of decay within rocks (Christaras et al. 2014).

The ultrasonic velocity is measured by dividing the travelled distance of the p waves (length of the material) by the measured time of flight between both detectors. It is possible to measure both p waves and s waves in order to quantify a variety of important coefficients and parameters. Such parameters include: the Poisson's ratio, elastic modulus, acoustic impedance, reflection coefficient and the transmission coefficient. In this study only the p waves were measured due to instrumental constraints. It was not possible under these circumstances to measure the elastic or acoustic properties of the samples; however it is possible to indirectly measure the effects of salt crystallisation on the porosity and petrographic properties of the stone.

Measurements were made by clamping the transducer and receiver to opposite sides of the secured stone sample using two G clamps. K-Y Jelly was used as a coupling agent ensuring that both detectors were in firm and secure contact with the sample. A PUNDIT ultrasonic velocity tester was used to carry out the measurements and operates at a 50 KHz frequency. All samples were tested consecutively under stable conditions of room temperature and RH after prior drying at 80^{o}C. Measurements were made in three orientations per sample and the average taken. For each stone type eight samples (5cm^{3} cubes) were tested equating to 24 measurements. Each sample was then re-

analysed after salt crystallisation tests to determine the effect of salt growth on the petrographic properties and grain structure of the stone. The ultrasonic velocity testing apparatus and experimental design is shown in Figure 2-7.

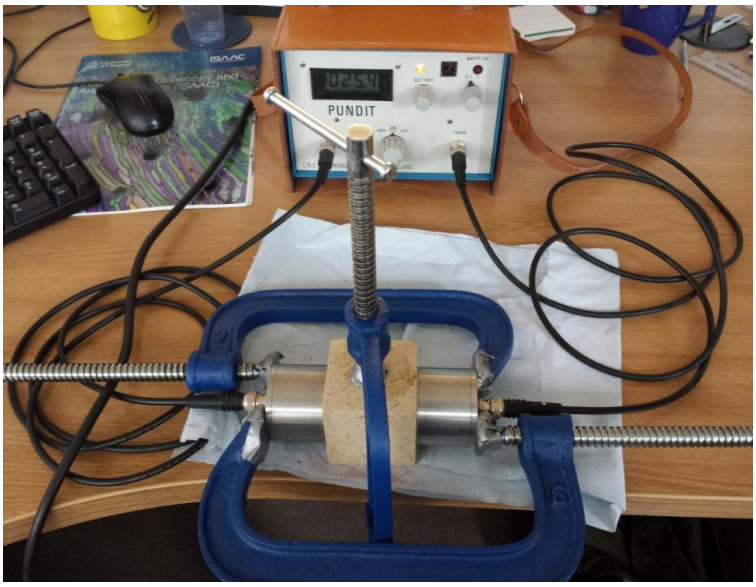

Figure 2-7: Ultrasonic velocity testing apparatus and design.

The PUNDIT receiver and transmitter are held in contact with a block of sandstone by two G clamps (blue).

2.2.1.4 *Compressive Strength Tests*

To determine the uniaxial compressive strength of each sample, tests were performed in accordance with British standard BS EN1926:2006. Experiments were performed at The University of Glasgow using a Zwick/Roell 250 uniaxial tension compression machine (Figure 2-8), capable of a 250kN tension capacity and testxpert II data collection software. 40 mm and 50 mm edge length cubic samples were used, providing a consistent sample size across each stone characterisation and durability test. Samples were oven dried at 60^{o}C for 24 hrs and left to cool and equilibrate to room temperature for a further 24 hrs. The cross-sectional areas in contact with the platens were calculated by the measurement of two medians using callipers to the nearest 0.01 mm. Samples were then loaded onto the platens (flat metal sample platforms) and a constant stress rate of 0.5 MPa/Sec was applied. A computer linked to the test machine then recorded, in real time, the stress applied

against travel. From this result, the applied force at the time of failure/averaged cross-sectional area equals the uniaxial compressive strength of the sample. Each sample the exception of Bonhill (due to limited sample availability) was tested between six to nine times.

Figure 2-8: Example of Zwick/Roell compressive strength test equipment. (www.zwick.co.uk)

Red box indicates the platens and the sample placement.

2.2.2 Surface analysis

2.2.2.1 *Colour Measurements*

Colour and surface texture are two important properties of building stones that greatly influence their economic and aesthetic value. Colour is influenced by the stone's mineralogy and these factors may also play an important role in heat propagation through stone, thus influencing decay processes (Gomez-Heras et al. 2006; Hall et al. 2008). Colour can also be significantly altered through weathering processes such as salt efflorescence, crust development, mineral dissolution, chemical staining and biological growth. Colour is a very subjective parameter and so to avoid potential human errors, it must be quantified.

This quantification was performed using a portable Konica CR-400 chroma meter. The chroma meter works by flashing a light onto an enclosed section of the stone surface. The colour is measured by comparing the reflectance to a standard. This method is based on the CIELAB system (Commission Internationale de l'Eclairage) that was introduced as an international standard in 1976. According to this technique, there are three measurable components: L*: the luminescence lightness value, a*: a measure of the red-green colour scale, and b*: a measure of the yellow-blue colour scale. Each scale provides an opposing colour that can be measured by reflectance values of known wavelength. Each stone sample that was subject to salt crystallisation tests was measured six times ensuring an even coverage of one of the sample faces. These results were compared to measurements made on fresh blocks of each stone type.

2.2.2.2 *3D Laser Scanning*

Repeat 3D laser scanning was undertaken on the drying surfaces of specific blocks in the second and third crystallisation tests in order to quantify the grains lost during each crystallisation cycle, and to accurately map surface decay features. Reference screws were drilled into the samples that allow repeat scans to be matched and compared. Scans were undertaken at The University of Glasgow using a "Next Engine" 3D laser scanner at an X-Y resolution of 130µm/pixel. Blocks were scanned once before and once after the second crystallisation test, and at intervals of 10 cycles in the third test. XYZ files were exported from the scanner software into "cloud compare" software where scans were referenced and compared. The results provide a colour-coded surface map of the change in height between repeat scans. The software is capable of measuring changes at a resolution of 0.3µm. Laser scanning has been used previously as a powerful non-destructive tool for monitoring weathering rates in a variety of materials (Birginie and Rivas, 2005; Gomez-Heras et al. 2008; Graham, 2011).

2.2.3 Void Space analysis

The total connected porosity (effective porosity) is an important stone property that directly controls both the total volume capacity of moisture

absorption, and also influences the strength of the stone. Porosity can be measured by a variety of techniques, but many are constrained in their effectiveness by their resolution of measurable pore sizes. The various techniques used within this study are described below.

2.2.3.1 *Determination of Open Porosity and Apparent Density*

To determine the apparent density and open porosity of each sample, hydric tests were performed, and guided by the buoyancy procedure outlined in British standard BS EN1936:2006. Cubic samples of 40 mm and 50 mm edge length were oven dried to constant mass at 80°C over 48 hrs. Each sample was then cooled to room temperature and placed in a vacuum oven for 2 hrs at 4 ± 2 kPa to eliminate any air trapped within the pores. These samples were then slowly returned to atmospheric pressure and introduced into beakers of demineralised water at 20°C on non-absorbent supports. They were then re-introduced to the vacuum at 4 ± 2 kPa for no less than 15 minutes to allow full saturation of the open porosity. Samples were then brought back to atmospheric pressure and left fully immersed in a water bath for 24 hrs. Each sample was then weighed while immersed in water and in a saturated state to the nearest 0.01 g. Open porosity is expressed as a percentage of sample volume and apparent density, in values of Kg/m^3. The apparatus is shown in Figure 2-9. It must be noted that the drying process (at 80°C) may impact on the micro-structure of the stone by imposing thermal stresses on the grains, which could slight alter the measurement readings.

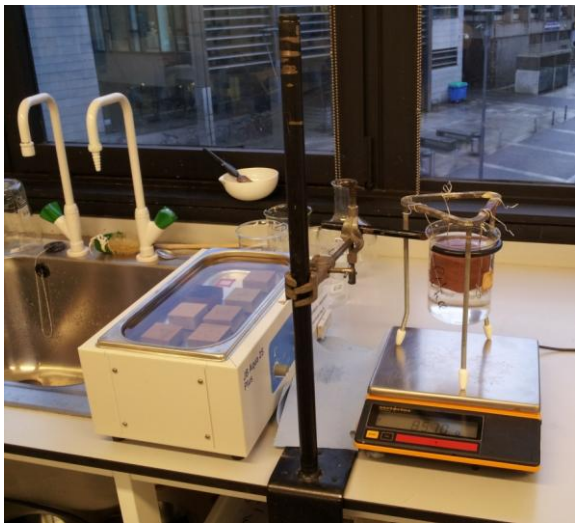

Figure 2-9: Porosity measurements using the British standard buoyancy technique.

2.2.3.2 *Mercury Intrusion Porosimetry (MIP)*

Mercury intrusion porosimetry (MIP) was used to quantify pore size. Work was carried out in the Advanced Materials Research Laboratory at Strathclyde University, UK using a Quantachrome Poremaster 60. This instrument is capable of measuring pore size in the range of 900 µm - < 3.5 nm. Samples of 5 mm x 20 mm were used in these tests (Figure 2-10). Mercury intrusion porosimetry works on the basis that because mercury is a non-wetting fluid, it will only invade capillaries under pressure, as described by the Washburn equation:

$$D = -4\gamma\cos\theta / p$$

Equation 2-1: Washburn equation

Where D= pore diameter, γ= superficial tension of mercury, θ= contact angle, and p= induced pressure. The pore size distribution can then be calculated from the volume of mercury intruded into the sample at different pressure increments. The total connected porosity is then calculated as the difference between the additions of the amount of mercury intruded at each pressure interval and the original bulk mercury volume at atmospheric pressure in the chamber before the test. MIP has been used extensively over the last 30 years in many applications, both within academic research and industry (Cnudde et al. 2009).

Figure 2-10: MIP samples. Samples measure ~ 5mm x 20 mm.

There are, however, a few contentious issues surrounding the use of MIP. These involve assumptions in the equation that every measured pore is cylindrical in shape, the surface tension and contact angle of the mercury is constant and the so-called “Ink-bottle effect”; this is where the porosimeter only measures the pore throat value and not the actual pore size itself. This issue is extremely important for materials that contain large pores that are separated by narrow or tortuous pore throats. Mercury intrusion is controlled by the smallest opening/entry into a pore and will intrude into both large pores with a narrow opening and small pores simultaneously. This property means that MIP measurements of pores can overestimate the percentage of small pores and significantly underestimate the percentage of large pores. Additionally, MIP only considers cylindrical pores, which is a measurement of the pore diameter/radius, and will therefore not accurately account for elongated pores. In the case of sandstones, an assumption is that most pores will follow this cylindrical shape. By using MIP in this study in combination with complimentary methods such as thin section analysis, CT scanning and hydric testing, it is a reliable and important technique.

2.2.3.3 *Helium Porosimetry*

Helium porosimetry was undertaken using a Corbey-Stevens design helium porosimeter at Aberdeen University, UK. Helium porosimetry works on the concept of Boyle's law, in which gas displacement is measured in the sample and used to calculate bulk density and open porosity. Any gas can be used, however helium is the most common due to the extremely small size of the helium molecules, allowing the infiltration and measurement of commensurately small pores and voids.

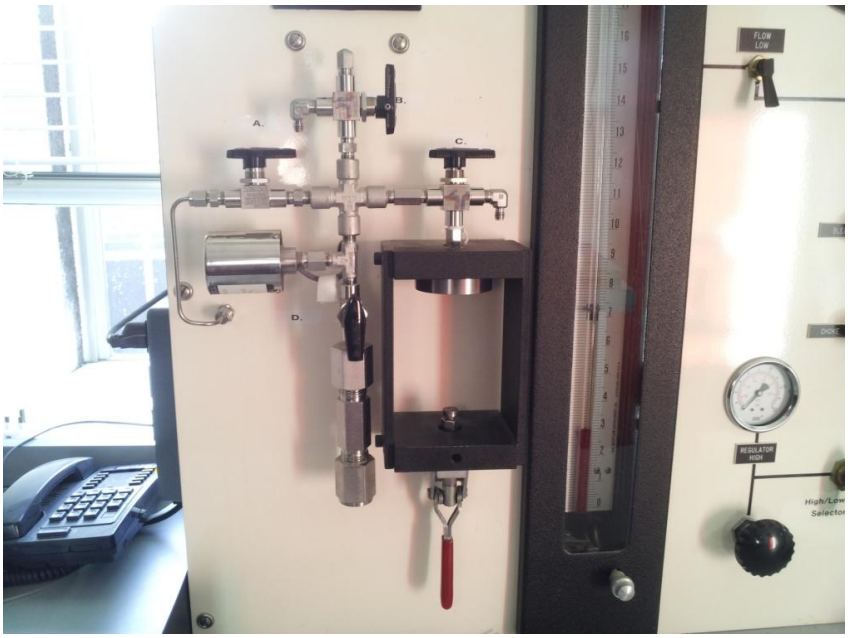

Figure 2-11: Corby-Stevens design helium porosimeter.

Cylindrical cored samples of maximum length 50 mm and diameter of 25 mm were used. The bulk volume of each sample was initially measured to the nearest 0.01 mm^3 using callipers and placed into a sealed holder at atmospheric pressure; the initial pressure (P1) was noted. In a second vessel connected by a valve to the sample holder, the pressure was increased to 100 psi and the pressure (P2) was noted. The valve connecting the pressurised vessel to the sample holder was then slowly opened and the pressure allowed to equilibrate to (P3) as it entered the sample holder. By using pressure values (P1, P2 and P3), the total volume of the sample holder (previously calculated during calibration), the bulk volume of the sample and the porosity can be calculated. The experimental rig is shown in Figure 2-11.

2.2.4 Hydric and Hygric Tests

Hydric performance tests have been used extensively in the stone decay field, and alongside thin section analysis and MIP to characterise the texture, pore structure and physical properties of natural porous materials. These tests have also been utilised in stone durability estimations (Benavente et al. 2006; Anania et al. 2012; Cultrone et al. 2012; Vazquez et al. 2013). A typical sample set up is shown in Figure 2-12.

Figure 2-12: Typical capillary coefficient test set-up with 4cm^3 cubes.

2.2.4.1 *Capillary absorption coefficient*

To provide information on the capillary uptake of solution, water absorption tests were performed on each sample following the specifications of British standard BS EN1925:1999.

Cubic samples of 60mm edge length were used for each sample. After drying to a constant mass, the area of the base to be immersed in water was calculated by the measurement of two medians to the nearest 0.1 mm. The base of each stone was then immersed in de-ionised water to a depth of 3 mm on non-absorbent supports (so that they rest only partly on their base) in a covered water tank at 20^{o}C. At time intervals of 1, 3, 5, 10, 15, 30, 60 (1 hr), 300 (5 hrs) and 1440 (24 hrs) mins each sample was removed from the

water bath and weighed to a precision of 0.01 g. Water was maintained at the same level throughout the test procedure. The results are an expression of the mass of water absorbed (g) divided by the area of the immersed base of the sample (m^2) as a function of the square root of the time (sec).

2.2.4.2 *Absorption Coefficient at Atmospheric Pressure*

Information regarding the absorption coefficient of stone at atmospheric pressure was determined using the test procedure outlined in British standard BS EN13755:2008. Water absorption relates to how much moisture can access the pore network without force.

Each hydric test was performed consecutively using the 40 mm, 50 mm and 60 mm cubic samples in order to maintain consistent results and to minimise any deviation caused by heterogeneities within the stone. After drying to a constant mass, samples were placed in a water bath on non-absorbent supports (insuring that each sample had at least 15mm clearance from adjacent samples) and were immersed to a depth of 20 mm at 20^{o}C. At time intervals of 60 mins and 120 mins water levels were increased to depths of 30 mm and 65 mm, respectively. After 48 hrs from the start of the experiment, each sample was removed from the bath and weighed to the nearest 0.01 g, with repeat measurements taken every 24 hrs until a constant mass was obtained. The results are expressed as a percentage, by the ratio of the weight of the saturated specimen, to the weight of the dry specimen.

Results of absorption coefficient tests allow the measurement of water absorption at atmospheric pressure and by the effect of capillarity. This property provides information regarding intrinsic characteristics of the stone, including effective porosity, permeability and water saturation. It must be noted however that these factors themselves are not solely sufficient to explain or estimate stone durability to salt induced damage.

2.2.4.3 *Saturation Coefficient*

Determination of the saturation coefficient follows a similar procedure as the water absorption method. After initial oven drying at 80^{o}C for 24 hrs, samples

were left to cool and equilibrate to room temperature and weighed (give the dry value). Following the same procedure as the water absorption test, each sample was then immersed to a depth of 20 mm at 20°C. At time intervals of 60 mins and 120 mins water levels were increased to depths of 30 mm and 65 mm respectively. Samples were then left for 24 hrs, removed, surface dried and reweighed to give the wet value. Samples were then dried for 24 hrs at 80°C, removed from the oven and cooled to room temperature. The samples were then put through the same vacuum procedure as in the determination of open porosity method to provide the water saturated value (i.e. were water-saturated under vacuum). The results are expressed by the fraction of water absorbed under atmospheric pressure to the maximum saturated amount possible.

2.2.4.4 *Nitrogen Permeability*

Nitrogen permeability measurements were undertaken at Aberdeen University, UK, using the same samples as for the helium porosimetry tests. Permeability is defined as the property of the porous material that determines the ease by which fluid flows through it in response to an applied pressure gradient. Permeability is not measured directly and must be calculated from physical measurements that are related to theoretical and empirical assumptions and relationships. Permeability is related to Darcy's law, an equation used to calculate fluid flow through a porous medium. The movement of water and vapour through stone is an important process that significantly influences the resistance of stone to various forms of decay. Although permeability is related to the pressure-induced movement of fluid, which is an unlikely occurrence within building stone, it is a complimentary method that is used to quantify anisotropy within the sample and is an indication of how well connected the pores are. It is important to note that permeability does not provide information on porosity, pore shapes, pore sizes or pore size distributions. Within a building façade, moisture is commonly transferred by capillary forces as opposed to a saturated, pressure gradient induced flow.

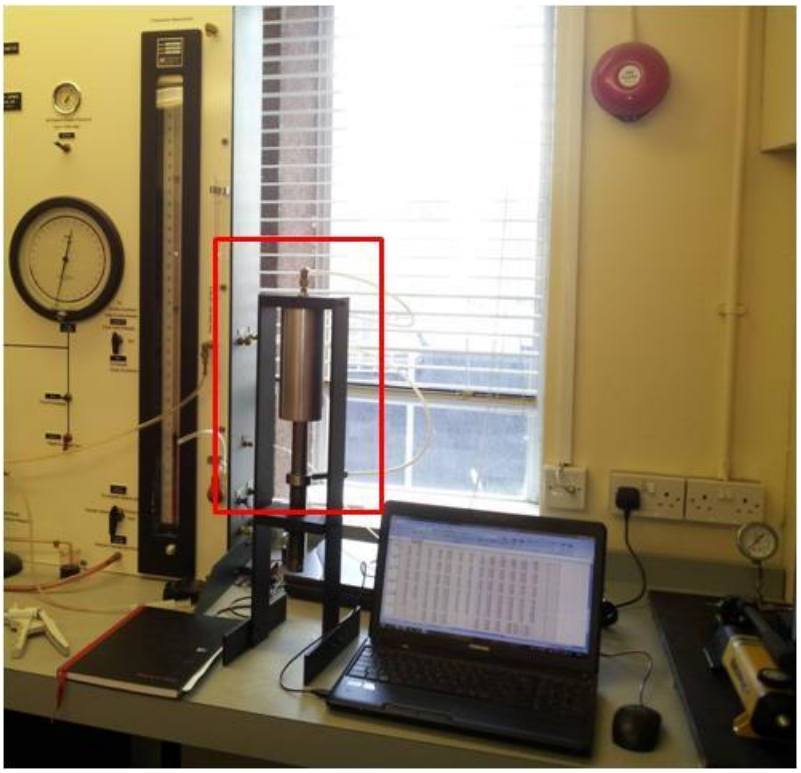

Figure 2-13: Nitrogen porosimeter. Highlighted in red is the Hassler core holder.

Core samples (50 mm length x 20 mm diameter) were placed in a hassler core holder (Figure 2-13) and a 400 psi confining pressure was applied. This is an equivalent pressure to what a stone block may experience in a building façade. The Hassler core holder consists of a rubber sleeve in which a confining pressure is applied, a gas inlet valve and gas outlet valve. At incremental steps relative to each sample, the nitrogen input pressure was raised and the subsequent outward flow rate from the other side of sample was measured. At low confining pressures, the mean free path of gas molecules is greater than the pore dimensions; therefore fluid flow cannot be considered as a continuous saturated flow. A correction, known as the Klinkenberg effect, can be applied to determine a more accurate permeability value. This correction involves the repeat measurement of different gas inlet and outlet pressures at incremental steps, ensuring a wide range of inlet and outlet pressures. The mean gas pressure throughout the core at each pressure step is then calculated and the inverse plotted against the measured permeability. The resulting transect point between these points is the corrected Klinkenberg permeability.

2.2.4.5 *Drying/Evaporation Test*

Drying/evaporation experiments were performed on 40 mm cubes of each sandstone. Five sides of each sample were sealed with rubber and adhesive tape to ensure that drying occurred on only one face. Each sample was dried to constant mass at 80°C for 24 hrs, cooled to room temperature and weighed. The sample was then water saturated under vacuum in the same procedure outlined in the determination of the apparent density and the open porosity test (section 2.2.3.1), and then submerged in water for a further 48 hrs. The water saturated sample was then weighed and the test initiated. The test consists of the drying of water saturated samples over 69 hrs under constant temperature and RH conditions.

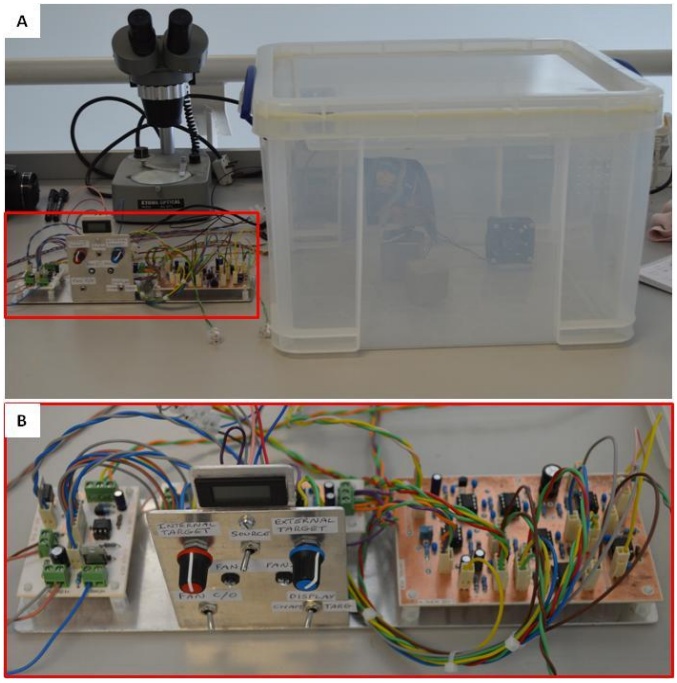

Figure 2-14: (A) RH chamber, (B) Circuit board controlling RH in the chamber. (A) RH chamber, (B) Circuit board that controls the RH within the chamber.

The test was performed under room temperature (20-25°C) and at a RH of 33%. The RH was controlled by a bespoke RH chamber (Figure 2-14), whereby two fans connected to a small circuit board control the humidity. Fan 1, situated inside the chamber, circulates air over $CaCl_2$ desiccant, while fan 2, situated outside of the chamber, introduces humid, ambient air. The design was based on a similar, smaller design as published by Harris et al. (2002). A slightly modified circuit board as proposed by Harris et al. (2002) was used, and is shown in Figure 2-15.

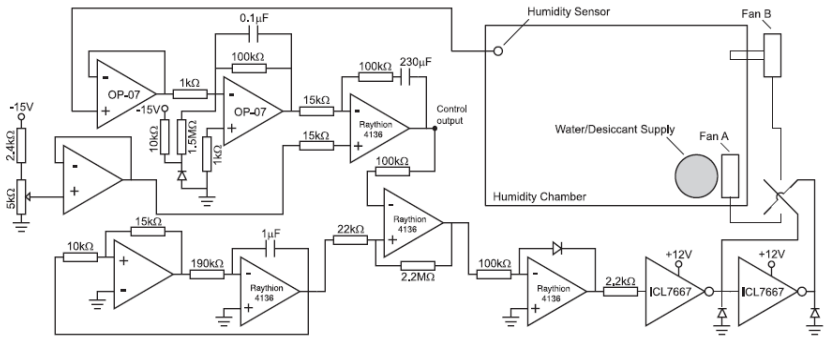

Figure 2-15: RH chamber circuit board diagram.
Circuit board diagram as proposed by Harris et al. (2002).

The RH is kept constant by varying the speed of each fan. Figure 2-16 is a graph of RH and temperature within the chamber over one day as measured by a “tinytag” RH logger. The weight loss of each sample was measured at 1 min intervals using a 0.01 g precision balance connected to a near-by laptop to allow constant logging of the data. From the obtained weight loss graphs, the constant drying rate, falling drying rate, critical moisture content and residual moisture content can be calculated by dividing the remaining moisture content by the drying surface area.

During the first stages of drying, water evaporates from the surface of the stone and is transported through the stone to the surface by hydraulic flow; this process is known as ‘the constant drying rate’. Water evaporation at this stage is roughly constant and is not controlled by the fluid parameters of viscosity and surface tension. After a period, the hydraulic connection to the surface is broken and the drying front moves beneath the stone surface. This stage is controlled by capillary flow and is the falling rate period. This change in evaporation rate represents the point of critical moisture content; the amount of moisture left within the sample as the drying front recedes. After 69 hrs of drying, the remaining moisture is calculated as the residual moisture content.

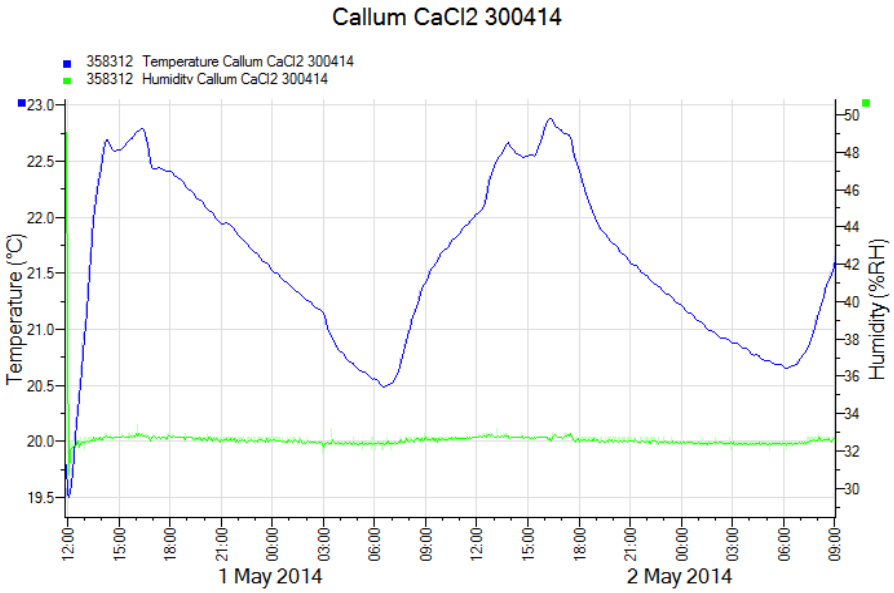

Figure 2-16: Measured temperature and RH graph from RH chamber.

2.2.4.6 *Synchrotron µCT Scanning*

Synchrotron µCT experiments were undertaken in order to visualise and better understand the capillary uptake mechanisms of different sandstones used within the study. Although the principle of µCT scanning is the same in the lab systems and Diamond synchrotron, the generation of X-rays and available X-ray energies are characteristically different. X-rays produced at synchrotrons are part of a generated synchrotron light that encompasses infrared light, radio waves, ultraviolet and visible light. Electrons are generated by an electron gun and fired through a linear accelerator known as a linac. The linac increases the speed of electrons by subjecting them to a series of oscillating electric potentials. The electrons are then passed into a booster synchrotron where they are sped up to an even greater velocity. By the use of powerful magnets, the electron beam is injected into the storage ring. At this point the electrons are travelling at near the speed of light following a circular path around the storage ring. It is this part that gives synchrotron light sources their distinct shape (Figure 2-17); however the storage ring is not a true circle. It contains 24 straight beamline sections that are bent using powerful magnets and it is these magnets that force the electrons around the storage ring.

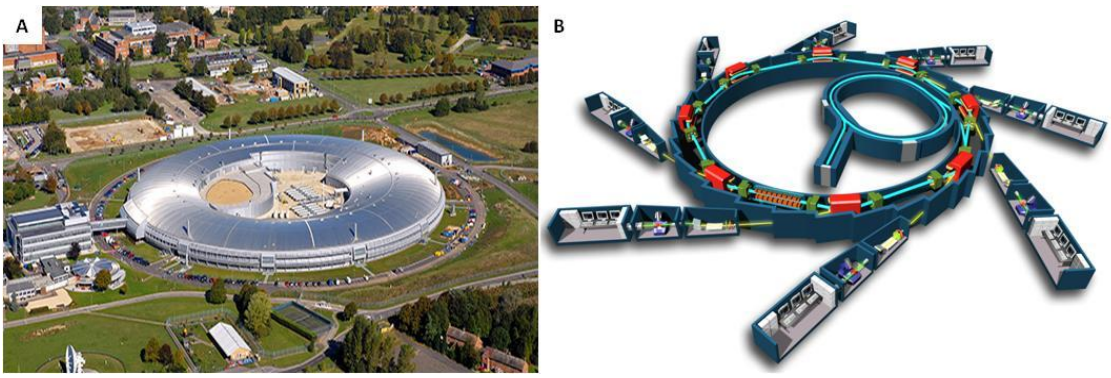

Figure 2-17: Diamond Light Source synchrotron, Didcot, Oxfordshire, UK.

(A) Diamond Ligh Source synchrotron, Didcot, Oxfordshire, UK. (B) Schematic synchrotron structure.

Insertion devices, known as wigglers, are placed in each linear beamline section and are used to further increase the velocity of the electron beam. This velocity increase is achieved by subjecting the electrons to a set of opposing magnets that cause them to undulate as they pass through them. Unlike lab μCT systems whereby X-rays are generated by electron-atom collisions, synchrotron radiation is created when the acceleration of electrons change in direction and not in velocity (Bertrand et al. 2012). As electrons are bent around the storage ring by powerful magnets, they lose energy in the form of synchrotron light. This extremely bright light is then focussed and filtered by a series of beamlines that extend out from the main storage ring to produce a high energy monochromatic X-ray beam. Unlike the polychromatic beam produced by lab CT systems, the monochromatic synchrotron beam lowers the signal-noise ratio and allows the use of substantially higher X-ray intensities. This greater intensity allows greater sample penetration, with the resolution dependant on the detector, rather than the distance ratio to the source or the beam focal point size.

This higher energy, monochromatic synchrotron beam has greater penetration that in return allows faster scanning times. In this case, scanning times are controlled by detector camera, the connected computer systems and the rotation speed of the sample stage. As a result, synchrotron μCT can produce higher quality images than lab systems, with a superior spatial resolution and a lower signal-noise ratio. Experiments were undertaken on the I12 beamline of the Diamond Light Source Synchrotron. Diamond generates electrons

through a 90 keV electron gun and a 100 MeV linac, with the conversion from 100 MeV – 3 GeV within the booster synchrotron. Diamond is the largest medium energy synchrotron light source in the world.

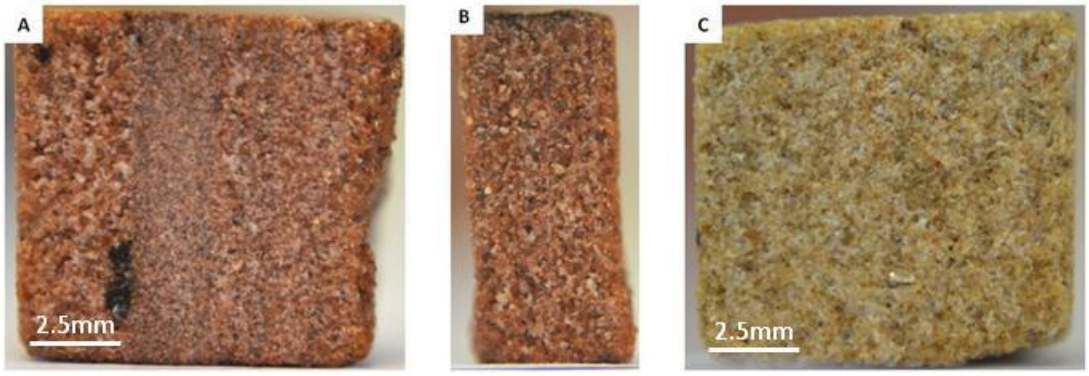

Figure 2-18: Sandstone samples analysed used in synchrotron experiment. (A) Locharbriggs fine grained, (B) Locharbriggs coarse grained, (C) Blaxter.

The sandstone samples used at Diamond were cubes with an 8-10 mm edge length, and cylinders >10 mm height by 8 mm diameter. From the data presented in this thesis, the Blaxter and one Locharbriggs sample were cut into cubes and the remaining two Locharbriggs samples were made into cylinders. The fine grained Locharbriggs, coarse grained Locharbriggs and Blaxter samples used in the experiment are shown in Figure 2-18. The experiment design consisted of a bespoke cylindrical chamber 110 mm in height by 50 mm in diameter that was constructed from 2 mm thick Perspex. It consisted of two sections: a top part containing a small platform that was used to hold sandstone specimens, and a bottom section that housed a small reservoir of salt solution. Both parts of the chamber were connected and sealed together using a large, tight rubber band, with small holes drilled into the platform in the upper section to allow the circulation of air and connection with the reservoir in the lower section. The chamber was sealed using a large rubber bung. The chamber design is shown in Figure 2-19. In all experiments, samples were held in place using moulded foam to ensure their stability during stage rotation.

The initial experimental proposal called for a process whereby solution that was contained in a small reservoir in the bottom section of the chamber was transferred by a filter-paper wick to a piece of 1 mm thick filter paper situated on the platform in the top section. Salt solutions would then enter

the sample via non-forced capillary uptake from the saturated filter-paper. This design would provide solution at a rate that gave a five minute delay before solution entered the stone, during which time safety checks and sample stage positioning could take place. Due to poor contrast between the solution and stone at low solution concentrations (1M and 3M), a 6 M concentrated calcium iodide (CaI_2) solution, as used in previous studies of this type (Shokri et al. 2010), was chosen to ensure sufficient contrast. At this high concentration however, wicking between the lower reservoir and the filter paper prior to safety checks did not take place. In order to solve this problem, saturated filter-paper was used. This provided a second problem as by the time scanning was initiated, capillary intrusion into the sample had already started. As a consequence the field of view had to be moved to a higher position on the sample to enable fluid movement through the stone to be imaged.

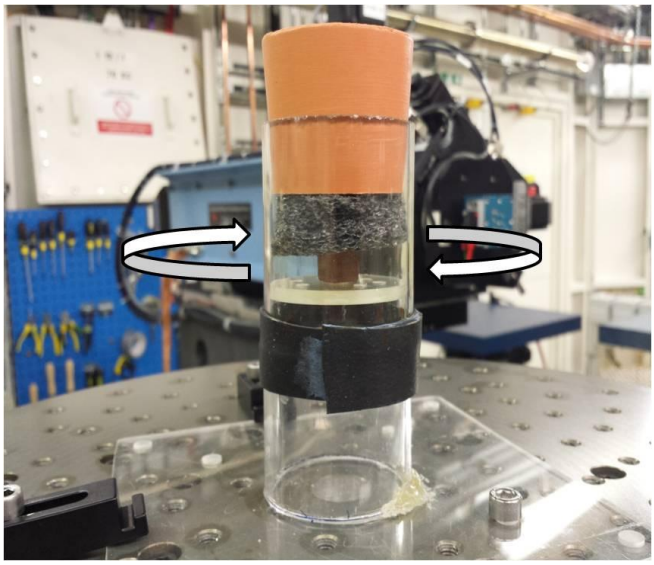

Figure 2-19: Sample chamber with arrows indicating direction of movement.

Dynamic, high speed tomography scanning was performed on the I12 beamline. Images were captured using module 2 of the Phantom v7.3 camera. This camera had a field of view of 9.8 mm by 7.3 mm and a resolution of ~12 µm/pixel. With this arrangement the sample stage rotation was set as to ensure that one 360^{o} scan took only 7 seconds to complete and therefore the dynamic movement of solution into and throughout the sample could be imaged. 580 projections were captured in each 360^{o} scan, however specific images from either the start or end of each scan were omitted due to poor definition of phase boundaries.

Reconstructed scans were visualised in Avizo 7 software. Each scan was placed through two filters to enhance contrast between greyscale phases and to enhance the edge detection of each separate phase. By using the greyscale distribution of each scan, grain, pore and solution phases were separated and quantified to provide the porosity and solution values through each slice. Each separate scan was then registered to a reference scan to ensure that it was aligned in each scan set. In order to visualise the change in solution movement from two neighbouring scans, the arithmetic tool of Avizo was used to calculate the difference between each scan. The resulting difference field was used to visualise and quantify the movement of solution between scans. Samples L2 and L3 were also cropped prior to any analysis to eliminate background “porosity” from out-with the sample.

2.2.5 Durability Tests

Durability tests are used as the quickest and most comprehensive means of understanding the response of each sandstone to severe weathering processes. These testing techniques do not always provide ‘realistic’ testing environments and are not always representative of ‘real world’ conditions. The behaviour and reaction of the stone to these tests will not necessarily accurately predict their behaviour/durability within a building. Test utilising more realistic temperatures, salt concentrations, moisture uptake regimes and a longer, more representative cycle-period will produce more realistic and accurate weathering/decay development. Furthermore, the use of large-scale test walls within a monitored environmental scenario over an extended test period, of up-to several years, will allow the durability of stone to different weathering agents to be made without compromising temperature, sample size and time. What accelerated durability tests compromise in test conditions (temperature, moisture, humidity etc) they compensate for in convenience, allowing durability prediction to be in short time constraints, which is generally a major issue experienced in scientific research.

Sandstones samples in this study were placed through salt crystallisation and freeze-thaw tests following British standard procedures.

2.2.5.1 *Crystallisation Tests*

In order to assess the mechanisms of salt decay and their impacts on the internal structure and integrity of the various sandstones, salt crystallisation tests were performed in accordance with British standard BS EN12370.1999. Cubic stone samples of 40 mm edge length, cut using a lubricated rotary saw were used. Samples were first washed to remove loose material and traces of lubricating oils. Specimens were then dried in an oven to a constant mass at a temperature of 105^{o}C for 48 hrs assuring that the difference in weight after two weighings at an interval of 24 hrs was no more than 0.1% of the first weighing. Samples were then cooled to room temperature (20^{o}C (+/- 1^{o}C)) and weighed to a precision of 0.1 g. Each dried sample was placed in a container and covered to a depth of 8 mm above its top surface in a 0.5 molar concentrated salt solution, and left for 2 hrs at room temperature (molar concentrations for each salt solution were calculated using the British standard guideline of a 14% solution of sodium sulphate decahydrate).

The wet samples were then oven dried for 16 hrs at 105^{o}C. Cooling of the samples at room temperature for 2 hrs completed one cycle. Impacts on the stone were documented by measuring mass gain/loss and by photographing after each cycle. Samples were photographed using a Fujifilm Finepix S4080, 14 MP 30X optical zoom digital camera, with any signs of variable damage and decay documented. Each sample was then weighed to a precision of 0.1 g and the result was recorded. Due to the difficulty in collecting all detached material from each sample, only the decayed cubic samples were weighed, with values representing the competition between both a weight increase from addition of salts and weight decrease by material loss from stone decay. NaCl, $CaCl_2$ and “Envirothaw” salts were used, with de-ionised water as a control within the experiment. This control batch is representative of any damage caused only by thermal contraction and expansion of saturated stone samples.

A second and third crystallisation test was undertaken on a similar sample set, but with a variation from the previously outlined test procedure. Four cubic samples of 50 mm edge length were used for each stone type subject to each salt solution. Both of these tests used NaCl, anhydrous $CaCl_2$ and

$MgCl.6H_2O$ de-icing salts. 150 samples, comprising eight sandstone types, were used in this second test. Each sample was prepared using the same procedure as outline above before having four faces sealed by gaffer tap, leaving only a front face and bottom face exposed for drying and capillary uptake, respectively. Each cycle consisted of the capillary uptake of 0.5 M concentrated solutions of each salt at a depth of 3-5 mm for 2 hrs (Figure 2-20), 16 hrs of drying at 90°C, a cooling period at room temperature for 2 hrs before being weighed to a precision of 0.01 g. Molar concentrated solutions with equivalent weight % are listed in Table 2-2. Water absorption, capillary uptake and saturation coefficients were determined for two samples of each stone subject to each salt solution before the test started, and were measured again on completion of the test. In Locharbriggs, Blaxter and Cullalo stones, two extra samples were included per salt solution (eight in total per stone type) that were subject to capillary uptake parallel to bedding and drying perpendicular to bedding to investigate the influence of anisotropy on stone behaviour. High precision laser scans of the drying surfaces of select samples were made before and after the test to quantitatively capture the decay patterns. Due to problems associated with glue from the tape absorbing into the pores of the sandstones, the second test was abandoned after 16 cycles. The area of contamination was restricted to the outer 3 mm of each face in contact with tape but caused considerable discolouration and cohesion of grains in the contaminated areas.

Salt	Molar concentration (M)	Weight %
NaCl	0.5	2.83%
$CaCl_2$	0.5	5.24%
$MgCl_2.6H_2O$	0.5	9.11%

Table 2-2: Salt concentrations used in the crystallisation tests.

Figure 2-20: Capillary uptake of salt solution in crystallisation test 2.

As a result of these problems, a third crystallisation test was performed on five of the most susceptible sandstones from the second test. The same numbers of samples per stone per salt were used (6 samples for Locharbriggs, 7 samples for Stanton Moor and 4 samples for the remaining stone types); with the same hydric and ultrasonic velocity tests performed on the same number of samples before and after the test (2 samples for each stone type). Each sample was sealed on four sides with rubber, leaving two opposite faces free for drying and capillary uptake of solution. After 2 hrs of capillary immersion, samples were dried for 2-3 hrs using halogen lamps and a heater fan ensuring that the drying surfaces (those used for capillary uptake) reached a temperature no higher than 70°C while fan assisted convective heating took place at a temperature range of 30-40°C and 30-40% RH. The drying sample set-up is shown in Figure 2-21.

Figure 2-21: Drying period set-up of $CaCl_2$ saturated blocks.
The blocks were positioned in a metal frame ensuring that each block was exposed to equal amounts of radiative heating from the halogen lamp and convective heating from the fan

Samples were then placed in the oven for 16 hrs at 90°C and cooled for 2 hrs before being weighed to complete one cycle. In this experimental design, each stone absorbs solution by a mechanism mimicking that expected in a building and from a drying regime that comprises both convective and radiative heating, whereby drying takes place predominantly through one face. The oven used for water-saturated and NaCl-saturated samples was too small to allow for lower temperatures to be used (as the oven retained too much moisture); while these higher temperatures were chosen to ensure $MgCl_2$ and $CaCl_2$ crystallisation took place. Photographs of each sample were

re-taken after every ten cycles in this test using a Nikon D3200 DSLR camera. Different sample sets were used in each test due to a combination of: (i) stone availability, (ii) their importance as replacement sandstone (Hazeldean as preferred matching sandstone for Craigleith in Edinburgh), (iii) their observed behaviour in previous tests, with resistant sandstones dropped for the following test. The general procedure for all three crystallisation tests and the differences between each test are shown in Figure 2-22, Figure 2-23 and Figure 2-24.

Salt crystallisation tests have been used extensively within built heritage and construction sciences to assess the performance and durability of building materials. Numerous standard methods have been proposed for this same test and are distinguished by differences in: (i) the duration and type of immersion and drying (Goudie, 1993; Gomez-Heras and Fort, 2007; Espinosa-Marzal and Scherer, 2010); (ii) the temperature of drying; (iii) the used salt concentrations; (iv) the sample dimensions (Angeli et al. 2007). Various salts have been used in salt crystallisation tests: sodium sulphate (Ruedrich and Siegesmund, 2007), magnesium sulphate (Rothert et al. 2007) and sodium chloride (Rothert et al. 2007; Gomez-Heras and Fort, 2007).

The results of each salt crystallisation test are the consequence of the combination of different weathering processes experienced the stone; including thermal and hydric expansion/contraction, which is influenced by the temperature regime and temperature range in each test. The influence of these additional weathering mechanisms cannot be easily identified or isolated from these tests. Aditionally, the observed decay morphologies within the tests are significantly influenced by both the additional weathering mechanisms and sample specific properties, including their preparation, size and moisture content at the end of each uptake cycle. Although the standard crystallisation test used within the present study may use parameters that the stone is unlikely to experience in the natural environment, it does provide, importantly, solid initial results by accelerating salt enrichment and decay, therefore giving an even comparison across each stone type. The isolated influence from each salt, without test-specific influences, cannot be accurately identified however.

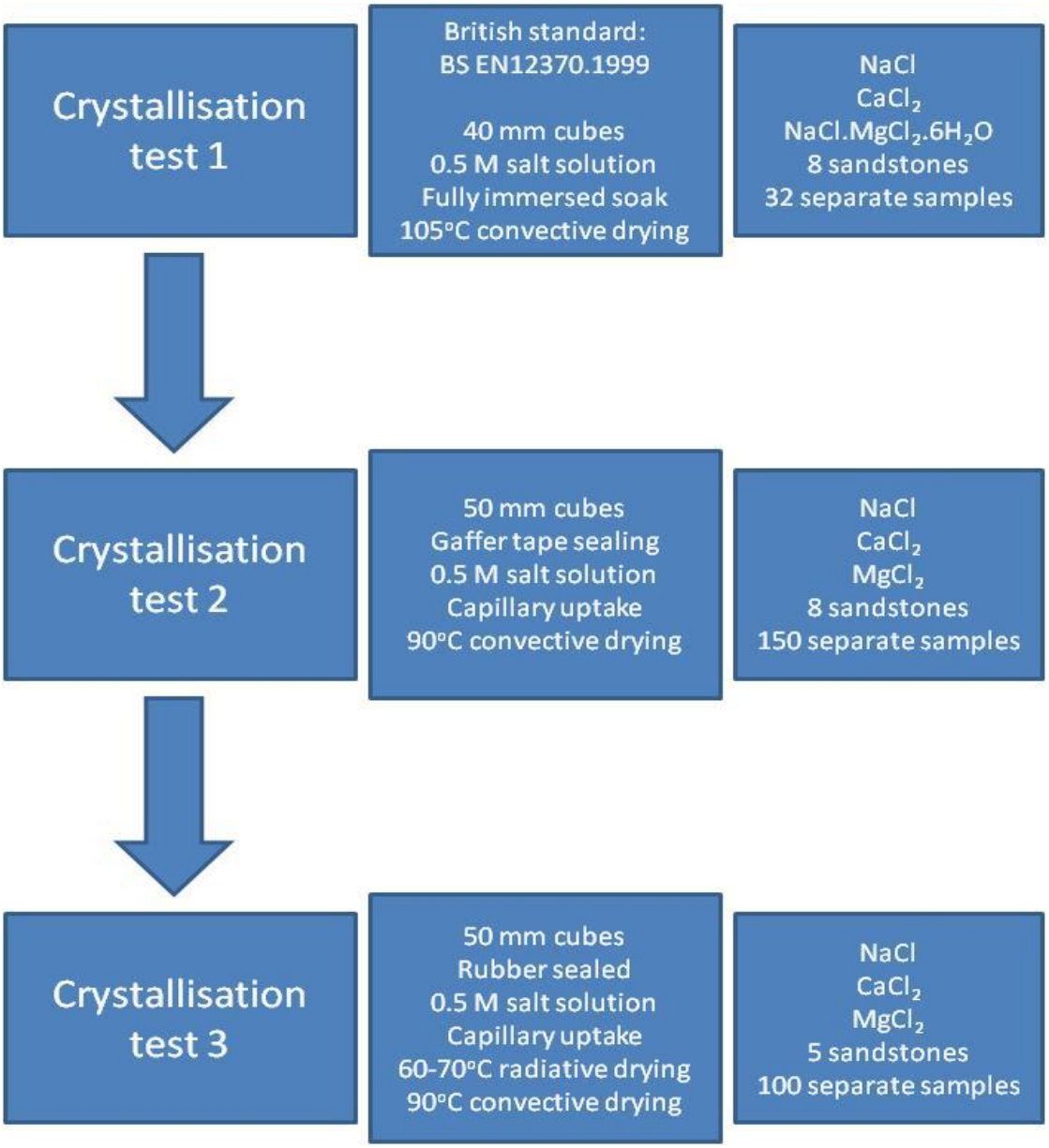

Figure 2-22: Flow diagram highlighting the main procedure differences between each crystallisation test.

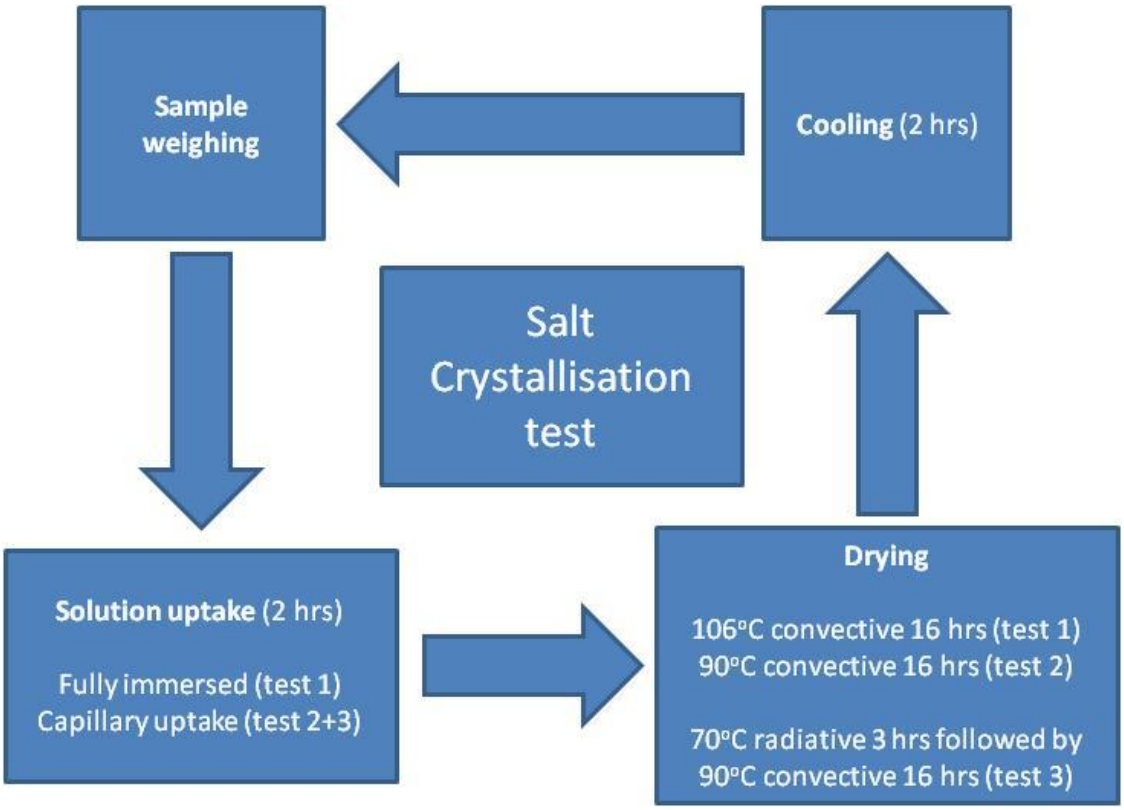

Figure 2-23: General salt crystallisation test procedure.

Each cycle represents one revolution of the flow chart in each crystallisation test. Each cycle starts and ends with sample weighing (top left). Each cycle duration is 24 hours.

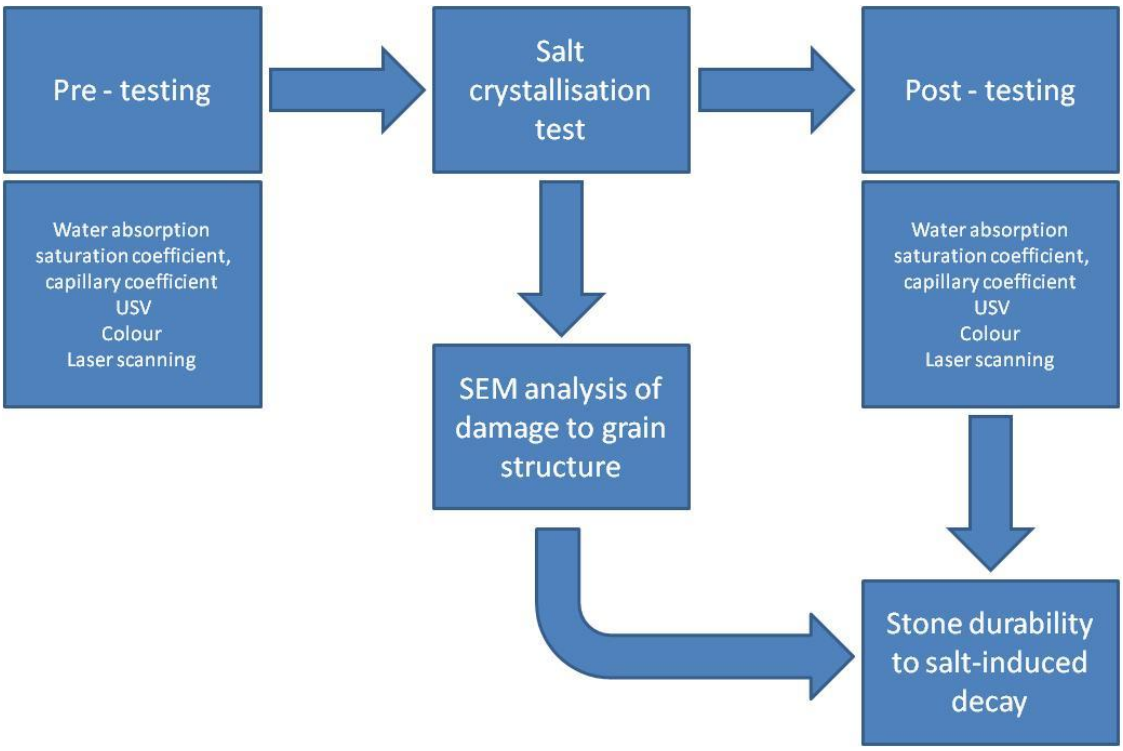

Figure 2-24: Overall salt crystallisation test procedure (tests 2 and 3) that was used to determine the stone durability to salt-induced decay.

2.2.5.2 *Freeze-thaw Tests*

In order to assess the durability of sandstone samples to frost attack, repeated freezing and thawing cycles were conducted in a similar procedure to the British standard BS EN12371:2010. 50 mm edge length cubic samples of Locharbriggs, Corsehill, Blaxter and Cullalo were used. Specimens were oven dried at ~70^{o}C until they reached constant mass. The specimens were then immersed in de-ionised water. The base of each sample was immersed to half the depth of the sample. At one hour intervals after initial immersion the water level was raised to depths of 30 mm and 65 mm respectively. The samples were then left for 48 hrs to allow partial saturation at atmospheric pressure. A large upright freezer, capable of reaching -10^{o}C was used for the freezing of the samples. Each sample was placed in the freezer ensuring that there was a gap of at least 10 mm was present between each sample. A sample containing a thermocouple was placed at the centre of the freezer to provide core temperature readings for each of the samples. Each 24 hour cycle consisted of a four hour freezing period followed by a two hour thawing period during which the samples were fully immersed in water, then a further 16 hour freezing period and a final two hour thawing period. This sequence ensures that each sample is water-saturated at the start of each freezing cycle. A total of 100 freeze-thaw cycles were carried out on three batches of samples; one containing water impregnated samples, a second batch containing samples impregnated with 0.5 M and 3 M NaCl solutions, and a third with 0.5 M and 3 M $CaCl_2$ solutions.

Following 60 and 100 cycles, each specimen was visually inspected, de-salinated for one month in de-ionised water, undergoing regular water changes and finally subjected to repeat capillary coefficient and water absorption tests to evaluate any changes to the pore structure of the stone.

2.2.6 Environmental Monitoring and Salt Ion Analysis

In order to accurately predict the changing salt behaviour from increased de-icing salt levels in Glasgow's sandstone buildings, a good understanding of current salt ion levels and environmental conditions experienced by the sandstone is needed. This was achieved by measuring the salt ion

concentrations, temperature and RH at different depths within the chosen stone blocks from around the campus of The University of Glasgow.

2.2.6.1 *Salt Ion Extraction*

Analysis of ions in depth profiles from buildings across the University of Glasgow campus was undertaken using Ion Chromatography (IC) and Atomic Absorption Spectroscopy (AAS). The dust used for analysis was collected by drilling into specified areas in step-wise increments to create a depth profile of salt ion concentration. These drillings used a 10 mm diameter bit and the dust was collected using a dust bubble (a sealed package surrounding the drill bit that collects the drilling dust) at depths of 0-1 cm, 1-3 cm and 3-5 cm (Figure 2-25 A). Before each phase of drilling, any residual dust was removed by blowing air into the drill hole. Through this process, dust samples within the range of 85 mg – 1.2 g were collected for each depth. This process was used following similar methods used elsewhere (Godts et al, 2012). Once collected, the dust was weighed, emptied into small re-sealable cellophane plastic bags and diluted in 50 ml of deionised water. These samples were then left for 24 hrs to ensure all of the salt ions had dissolved into solution (Figure 2-25 B). The samples were then passed through a 0.2 µm cellulose acetate filter into 50 ml centrifuge tubes to remove any larger dust particles. This 50 ml of solution was then analysed for anions using IC and cations using AAS.

2.2.6.2 *Ion Chromatography (IC)*

IC analysis was undertaken using a Dionex Ion Chromatograph at The University of Glasgow, with 5 ml of solution being used per sample for analysis using the auto-sampler function. In certain samples further dilutions were made prior to measurement. A standard of 10:1:10 mg/l of Cl^-, NO^{3-} and SO_4^{2+} respectively was used throughout the analysis. IC works by passing the solution through a positively charged ion exchanger containing an ion exchange resin, whereby negatively charged molecules are attracted to the positively charged stationary phase of the ion exchange column. An ion extraction liquid known as eluent is then passed through the column, separating the absorbed ions from the column. The ions, now within the

eluent, are analysed by conductivity measurements within the detector. Different ions have specific retention times when absorbed to the ion exchange column and it is through using this retention time that different ions are detected. The output takes the form of peaks on a graph with each peak representing a separate ion determined by retention time on the exchange column and the height of each peak correlates to the concentration.

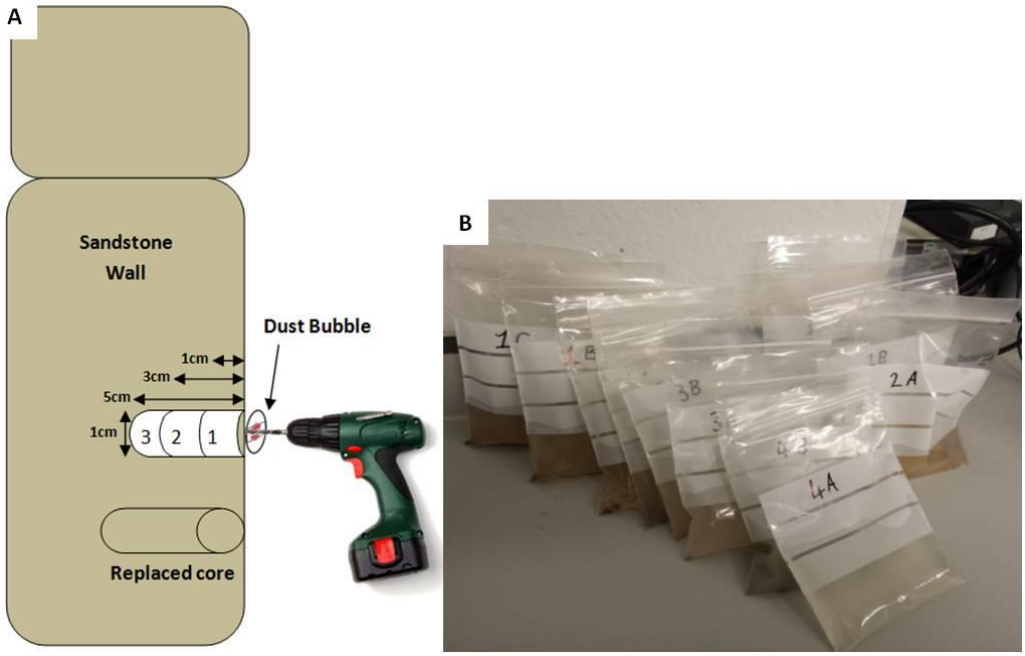

Figure 2-25: Salt ion extraction and analysis.
(A): Drilling schematic for powder extraction. (B): Extraction of ions from dust using deionised water.

2.2.6.3 *Atomic Absorption Spectroscopy (AAS)*

AAS was used to measure cation concentrations within the dust generated by drilling. Samples were acidified prior to analysis by adding 5% hydrochloric acid to the extracted solution to minimise the potential for precipitates forming, which could affect the instrument. AAS analysis was undertaken using a Thermo Scientific iCE 3000 series AA spectrometer at The University of Glasgow. AAS analysis requires the use of standards with known ionic content to enable a relationship between the measured absorbance and concentration. Table 2-3 shows the standards used for each ion. AAS works on the principle that atoms of particular elements can absorb specific wavelengths of light and by measuring the amount of absorbed light, concentrations of ions can be made. A hollow cathode lamp containing the

element of interest emits light of particular wavelengths by exciting the element atoms. The particular wavelengths of this light will be absorbed only by the atoms of the same element within the sample. The sample, once fed into the spectrometer, is passed through a flame as an aerosol where it is atomised and separated into free atoms in the vapour state. The emitted light from the cathode lamp is then passed through the flame as electromagnetic radiation. Atoms corresponding to the same element used within the lamp will then absorb this radiation. The amount of radiation absorbed is proportional to the abundance of atoms within the sample and is proportional to the concentration. The measured absorption values are then compared to the standards used and a final concentration of a particular element within the sample can be measured. Final values from both IC and AAS methods are in mg/l.

Ion	Standards used (mg/l)
Na^+	0.5, 1.0, 1.5, 2.5
Ca^{2+}	0.4, 0.8, 1.2
Mg^{2+}	0.4, 0.8, 1.2
K^+	0.4, 0.8, 1.2

Table 2-3: Ion standards as used for AAS analysis.

2.2.6.4 *RunSalt®*

Computer modelling of measured ion concentrations was performed using the chemical equilibrium thermodynamic model system ECOS RunSalt® (Bionda, 2002). RunSalt is a computer programme that is capable of predicting the behaviour of aqueous salt solutions within porous materials under equilibrium conditions of variable temperature and RH. RunSalt requires the user input of ion data (Na^+, K^+, Mg^{2+}, Ca^{2+}, Cl^-, NO^{3-} and SO_4^{2+}) as either weight % or molar concentration, temperature and RH. From this data it plots the expected solid salt phases (by volume or molar mass), salt pathways and salt transitions under specific temperature and RH conditions. RunSalt works by using two separate models that: (i) calculate the activity coefficients of an electrolyte solution; (ii) calculate the phase changes of salts under environmental conditions. An ionic charge balance is necessary for RunSalt analysis to work

and can be influenced by the accuracy of the analytical measurements, sample preparation and ions that were not measured. In the case of charge imbalances within the data, the auto charge balance facility in RunSalt was used. This facility makes a correction for either all the cations or anions based on which values are smaller. Due to the low solubility of gypsum under changing environmental conditions, RunSalt will exclude gypsum from calculations by removing calcium or sulphate, depending on the smallest values. Both corrections were used in several of the calculations. Some examples of the use of RunSalt are discussed below.

Benavente et al. (2011) investigated the micro-climatic factors and petrophysical properties of the stone used in construction of the Postumuis Tomb in the Roman Necropolis of Carmona, Spain, in order to understand the high susceptibility of the tomb to salt decay. Analysis of weathered material showed that gypsum, thenardite and halite were the salts present in the tomb. Salt crystallisation-dissolution cycles were then calculated for the tomb using environmental monitoring data collected from the tomb over a two year period, and deliquescence values for each salt. The authors revealed that the seasonality of salt crystallisation cycles were similar for both thenardite and halite, with most intensive damage likely to take place in spring and autumn and less so in winter and summer months.

Over a six year period, the “petraSalt” project has investigated the weathering damage of rock cut monuments in Petra, Jordan, by studying the weathering patterns, the micro-climate and salt concentrations and distributions of selected monuments. The team quantified a weathering index for the monuments using petrographic analysis of the stone, thermal imaging of rock surfaces and damage mapping of monument façades. It was initially found that salt originating from rain water was the main weathering agent (Heinrichs, 2008). By using a wireless sensor network, they were able to remotely measure at high resolution the internal and external environmental factors experienced by the monuments. By measuring the internal and external temperature and RH values, precipitation rates, wind strength, wind direction and salt concentrations profiles into the monuments, the exact salt phase transitions in time and space were calculated (Heinrichs et al. 2012).

By using ECOS RunSalt they found that halite was the most damaging salt, with maximum damage focussed at the outer cm's of the monuments. Maximum depth crystallisation cycles were reached in the summer months, with the outer 4.5 cm of the monument affected by recurrent salt crystallisation nearly every day during this period (Heinrich and Azzam, 2014).

Zehnder and Schoch (2009) in a similar effort to Heinrichs et al. (2012), managed the near-continuous monitoring of salt efflorescence cycles within an historic building by using automated, computer controlled photography and climate sensors. The evolution of efflorescence was traced accurately by visualisation and was in good agreement with theoretical (by RunSalt) and experimental IC data from the same site. They found that crystallisation-dissolution cycles of the measured salt mixture (Na_2SO_4, $MgSO_4.7H_2O$ and $CaSO_4.2H_2O$) were triggered by small changes in a moderately small RH range measured in the room. It was concluded that minimising the salt decay risk by environmental management would be extremely difficult unless the same temperature and RH conditions were kept completely constant and/or salts were removed by poulticing.

RunSalt was used to measure the expected salt phase changes from buildings around Glasgow University under measured environmental conditions in Glasgow and analogues from cities from around the world. Measured ion concentrations were then used as raw data to input increased de-icing salts levels to measure the effect of these on salt phase transitions.

2.2.6.5 *Temperature and Relative Humidity (RH) Monitoring*

Temperature and RH were measured over a ten month period from March, 2014 – December, 2014 at two sites in Glasgow University (Figure 2-26). At both sites, Ibutton data loggers were used to record temperature and RH at 2 hour intervals, at a height of 1m at site 1 and 0.5m at site 2 and at the surface of the stone and at a depth of 5 cm. The Ibuttons placed at depth were sealed using a cored piece of sandstone and exterior polyfill material. Silicon sealant was used to attach the Ibuttons to the outer surface of each site. Maxima Ibutton data loggers are small loggers that are 5 mm thick by 17

mm in diameter. The Ibuttons measure temperature and RH by monitoring these values from the sealed, internal circuit board. The stated accuracy of temperature and RH are 0.5°C and 0.6% respectively. An example of previous applications of Ibuttons is to help understand the weathering of coastal structures in the intertidal zone on the southern coast of England (Coombes et al. 2013).

By using meteorological data and climate prediction models for Western Europe, Grossi et al. (2011) were able to parameterise salt crystallisation-dissolution cycles for NaCl and thenardite-mirabilite phase transitions for Na_2SO_4 using daily temperature and RH values. They show that it is possible to estimate the frequency of salt transitions using the Koppen-Geiger climate classifications. It was found that humid summer environments present the most damaging situations for salt crystallisation cycles as they have continuously higher RH values that cross over the NaCl and Na_2SO_4 deliquescence points more often. Climate projections predict that areas experiencing high humidity summers will become drier and thus the amount of salt transitions over the summer in these regions will be reduced.

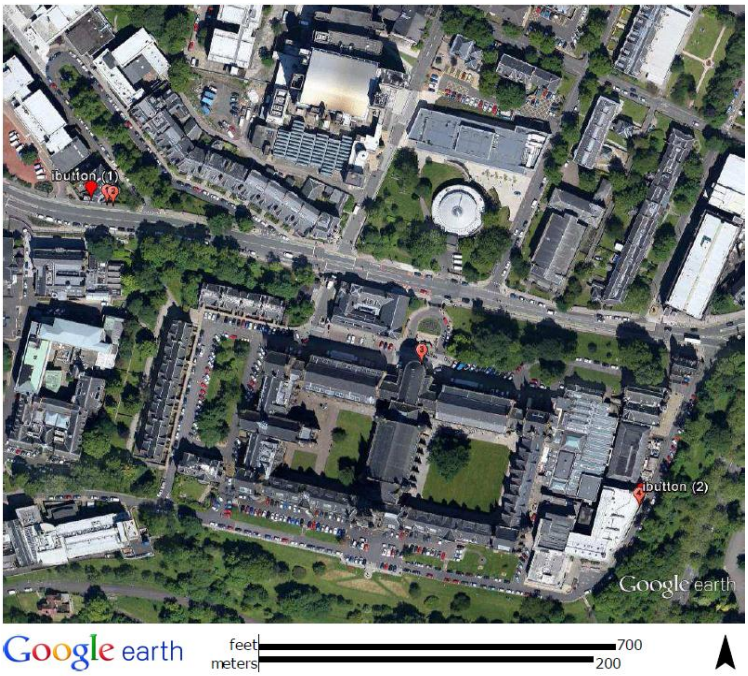

Figure 2-26: Locality map of ibutton placement and drilling locations.

This study built on earlier work by Grossi, et al. (2007) who used measured climate data and HadCM3 climate models to predict the long term freeze-thaw risk for archaeological sites in Europe. They concluded that as climate

models predict warmer climates in the future, the risk from freeze-thaw weathering, especially in northern Europe will be reduced. This change would lead to an overall wetter climate for many areas in northern Europe, specifically Northern Ireland, Scotland and Northern England. According to Smith et al. (2010) the result would be prolonged deep-wetness for buildings. That could have profound implications for increased salt penetration into building stones, with reduced frequency but higher amplitude salt crystallisation events taking place.

2.2.7 Salt Tests

2.2.7.1 *Ice Melting Capacity Test*

Ice melting capacity tests were conducted to assess the ice melting rate and overall effectiveness of the chosen salts. The test followed the procedure and guidelines established by Nixon et al. (2007) and Fay et al. (2008). The three de-icing compounds used throughout this study were utilised in this test. A covered Plexiglas dish was filled with 60 ml of deionised water and left to freeze at the working temperature of -15^{o}C. A large walk-in cold room was used for this experiment with in-situ thermometers relaying immediate changes in temperature. 1 g of salt was distributed over the surface of the ice and the ice weighed. Results are expressed as a function of the amount of brine generated by 1 g of salt at recorded intervals of 10, 20, 30, 45 and 60 mins. Brines were removed at each interval and measured using a suitable syringe before being reintroduced to the dish, assuring that each measurement took no longer than one minute to complete. Tests were repeated three times for each salt with separate Plexiglas dishes used for each salt to avoid cross-contamination.

2.2.7.2 *Environmental SEM (ESEM)*

Environmental SEM (ESEM) was used to record in real time the in-situ crystallisation mechanisms and crystal growth of the three de-icing salts. Experiments took place using an FEI Quanta 200F SEM using a 20 kV accelerating voltage and at a constant temperature of 3^{o}C and variable Relative Humidity (RH) in the Department of Geographical and Earth Sciences at The University of Glasgow. Crystallisation of $CaCl_2$ and NaCl was studied as

individual saturated droplets on a sample holder and between quartz grains (Figure 2-27). RH was chosen as a variable as the equilibrium RH of NaCl is well documented. Samples were introduced at an initially high RH of 90% and temperature of 3°C. The RH was subsequently lowered in step-wise increments. The RH is controlled within the ESEM sample chamber by varying the pressure. The phase diagram for water, which was used to control the RH, is given in Figure 2-28.

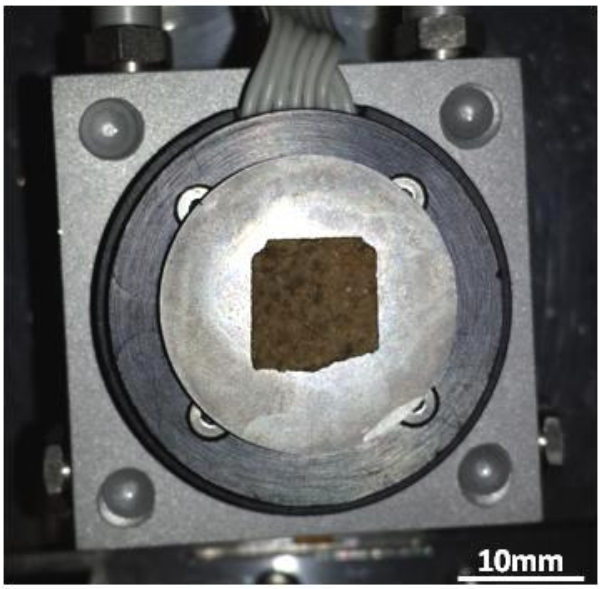

Figure 2-27: Stanton Moor sample saturated with concentrated $CaCl_2$ solution on a peltier heating and cooling stage for ESEM analysis.

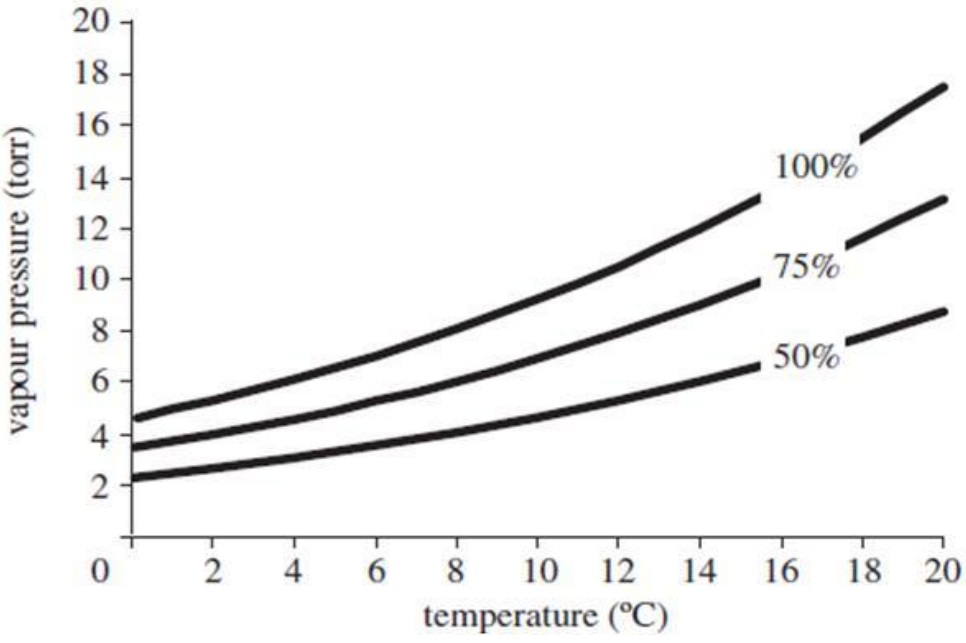

Figure 2-28: Phase diagram for water (Stokes, 2003). Lines (100%. 75%, 50%) represent the RH.

3 Stone and Salt Characterisation Results and Discussion

Sandstones were characterised using a range of complimentary methods. These methods are essential for stone durability prediction and reveal important information on stone mineralogy, pore space quantification, and the transfer of moisture within the stone. Stone durability is defined as “the measure of the ability of natural building stone to endure and maintain its essential and distinctive characteristics of strength, resistance to decay and appearance in relation to a specific manner, purpose and environment of use” (Anon, 1983 in Benavente et al., 2004). Understanding the petrographic and petrophysical properties of the stone is essential for both durability estimation and mitigation and for understanding the feedback mechanisms between the pore structure properties and salt-induced decay.

Averaged petrographic and petrophysical data on each sandstone was collected from sub-sets of different sized blocks from several repeat tests, constituting, on average, 20 repeat samples per stone/test. These results provide a range of values for each stone that are representative of their natural heterogeneities, and the errors associated with each test procedure. This chapter shows that the comparative differences of each property between each sandstone are sufficient to understand, explain and estimate the durability of each stone type to salt-induced decay. Samples are comparatively classified, with each stone ranked in order of their average values for each test. This rank order shows that both high and low estimates for each stone property can explain stone durability behaviour, highlighting that average values for each stone property are sufficiently representative for each stone type.

3.1 Petrographic Descriptions, Historical Significance and Geological Backgrounds

The petrographic descriptions of each sandstone were undertaken by digital analysis of thin sections using transmitted light and scanning electron microscopy, with results compared to data on the same stones from the Building Research Establishment (BRE, 2000). The mineralogy and porosity of each stone is listed in Table 3-1.

3.1.1 Clashach

Clashach is Permian (299 – 251Ma) sandstone quarried in Elgin, Moray. It is a fine-medium grained, texturally and mineralogically mature sandstone composed mainly of quartz, with smaller quantities of similar sized feldspar grains. It is buff coloured in hand specimen with an open porosity of ~10%. Quartz grains are mono and poly-crystalline, from igneous, sedimentary and metamorphic provinces. It is highly compact sandstone bound by silica cement, which is found commonly as quartz overgrowths throughout (Figure 3-1). Quartz grains are tightly packed showing concave-convex and sutured contacts with evidence of grain dissolution by pressure solution contacts, which possibly supplied silica for quartz cement precipitation. Fe-oxide staining and pore filling clays are also evident but to a lesser degree. Clashach has been used extensively in the Edinburgh new town as replacement sandstone and was used in the construction of The National Museums of Scotland Building in Edinburgh (Figure 3-2).

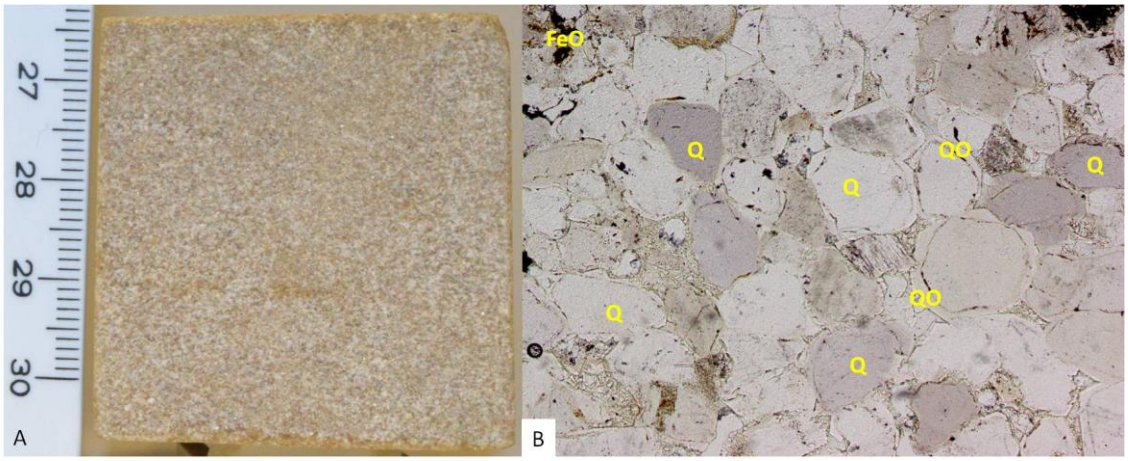

Figure 3-1: Hand specimen and thin section of Clashach sandstone.

(A) Image of Clashach hand specimen. (B) Plane polarised thin section of Clashach. Q: quartz, QO: quartz overgrowth, FeO: Fe-oxides.

Figure 3-2: National Museums of Scotland; constructed using Clashach sandstone and emphasising the heterogeneity within the different beds of the quarry.

Clashach sandstone identified geologically as Hopeman Sandstone of the same named formation is Permo-Triassic sandstone that outcrops along a 10 km section on the southern coast of the Moray Firth. Hopeman Sandstone comprises part of the initial infill sequence of the inner Moray Firth Basin, situated south of the Great Glen Fault. The stratigraphy of the coastal section from Burghead to Lossiemouth consists of five Permian - Jurassic formations resting unconformably on upper Old Red Sandstone (Edwards, 1993). Hopeman sandstone is the oldest in this sequence, underlying the Burghead beds formation of sandstone, Lossiemouth sandstone, Triassic chert and sandstone/marls of Jurassic age, respectively. South of the Lossiemouth Fault this sequence rests unconformably on Old Red Sandstone of Devonian age. Hopeman sandstone outcrops to the north of the fault on a large coastal section, containing frequent joint zones and minor faults. To the east, younger rocks outcrop south of the fault and older rocks to the north. This results in Jurassic rocks lying unconformably with Devonian rocks (Edwards et al., 1993).

The Hopeman sandstone itself is a >70 m thick sequence of dune bedded aeolian sands (Frostick et al., 1988). Studies have interpreted these as being a formation of complex star dunes created by a south – south-west sand transport direction (Clemmensen, 1987). Two main types of aeolian sandstone units are evident: one composed of trough-formed high-medium-angle cross-bedding of dune deposits (<1 m - >10 m) and the second consisting of oppositely dipping and more wedge-shaped cross-bedding of a similar scale (1->10m) (Clemmensen, 1987). Many contortion features are

observable in the sequence caused by liquefaction structures associated with heavy rainfall episodes and related small inter-dune river channels and slumping on dune flanks (Frostick et al., 1988). Much research has been undertaken looking at the fault movement and subsequent porosity and permeability change of the Hopeman sandstone as a good quality proxy of reservoir sandstones of the southern North Sea (Edwards et al., 1993; Ngwenya et al., 2000; Main et al., 2001).

3.1.2 Cullalo

Cullalo is Carboniferous (359 – 299Ma) sandstone that is extracted at Cullalo Quarry, near Burntisland, Fife (Figure 3-3). It is a very fine grained, texturally and mineralogically mature sandstone composed of a bulk composition of similar sized, sub-rounded quartz grains, with lower amounts of feldspar and muscovite present. It has a porosity of ~18% with over 70% of this total porosity being open and accessible. Quartz grains are relatively well compacted showing an abundance of line contacts, bound by quartz cement including quartz-overgrowths (Figure 3-4). Overall, quartz grains are very clean, showing no alteration or dissolution. Kaolinite is present, and is found between quartz grains and filling available pore spaces. A weak mineral fabric is evident within the stone through the accumulation and layering of small, rounded, well aligned quartz grains. Cullalo has been used as replacement sandstone on buildings on the Royal Mile, Edinburgh, as replacement stone for the High Kirk of St Giles, Edinburgh and as building stone for the Forth Estuary Buildings, Leith.

Figure 3-3: Cullalo quarry, Fife.

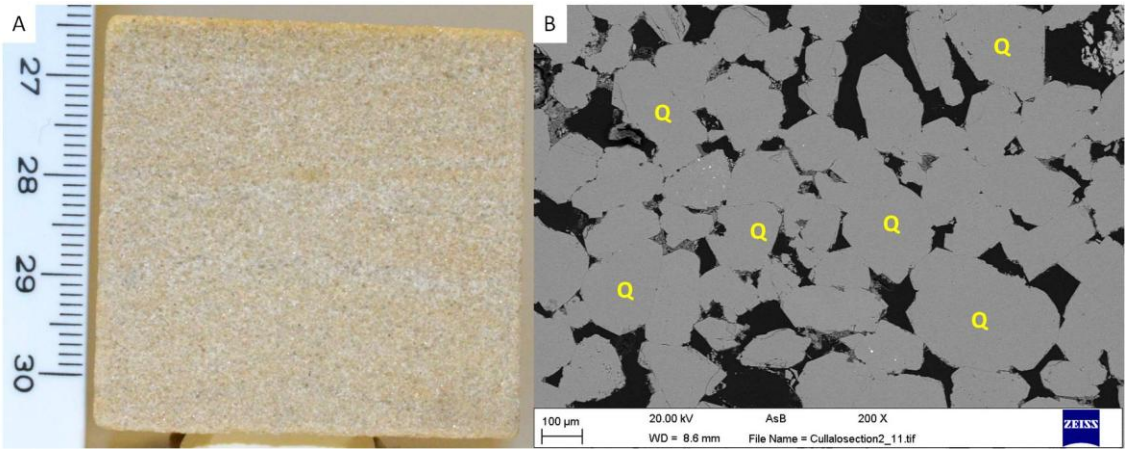

Figure 3-4: Hand specimen and thin section of Cullalo.

(A) Hand specimen of Cullalo sandstone. (B) SEM BSE thin section image of Cullalo. Q: quartz, pore space is black.

Cullalo sandstone is of Lower Carboniferous age and stratigraphically located in the Sand Craig Formation of the Strathclyde Group of the Midland Valley of Scotland; its outcrop extends from Ayrshire in the West to East Lothian on the Eastern coast. The Strathclyde Group overlies the Inverclyde Group and underlies the Clackmannan Group. The Strathclyde Group itself changes laterally from west to east across the Midland Valley. In the west it is found in small patches in Ayrshire and sporadically across the central belt, whereby the Clyde Plateau Volcanic, Kirkwood and Lawmuir Formations of subaerial basalts, volcanic detritus and marine sedimentary rocks are found respectively. In Fife, the Strathclyde Group is split into five main formations. Cullalo sandstone is found within the Sand Craig formation that overlies the Pittenweem Formation and is overlain by the Pathhead Formation. The Sandy Craig Formation is ≥670 m thick and is characterised by a range of sedimentary rocks; usually as cycles of mudstone, siltstone and sandstone (Hyslop et al., 2009). Beds of algal-rich oil-shale are common but minor, with beds of non-marine limestone and dolostone also present. Most of the succession is interpreted as cycles of upward coarsening deltaic cycles, capped by thinner upward-fining fluvial units (Read et al., within Trewin, 2002).

3.1.3 Scotch Buff

Scotch Buff is Carboniferous (359 – 299Ma) sandstone quarried near Scotch Corner in Richmondshire, Northern England. It is medium-grained,

mineralogically mature sandstone composed of sub angular- sub-rounded quartz grains, showing a range of grain sizes and shapes (Figure 3-5). Quartz grains are mono and poly-crystalline, show minor fracturing, some dissolution at grain boundaries and Fe coated rims. There is a minor percentage of feldspar grains, some of which show evidence of decomposition. Quartz overgrowths are present with evidence of silica cement between many of the quartz grains. It is a clay-rich stone with evidence of a high percentage of pore filling clays, which probably serve as supporting cement throughout the stone. Porosity is generally high (~18%), as determined from a suite of porosity tests, containing many large, poorly connected pores. Scotch Buff has been used in new retail and residential developments at Glasgow Cross, Glasgow and at the Western Harbour, Goosander Place, Leith.

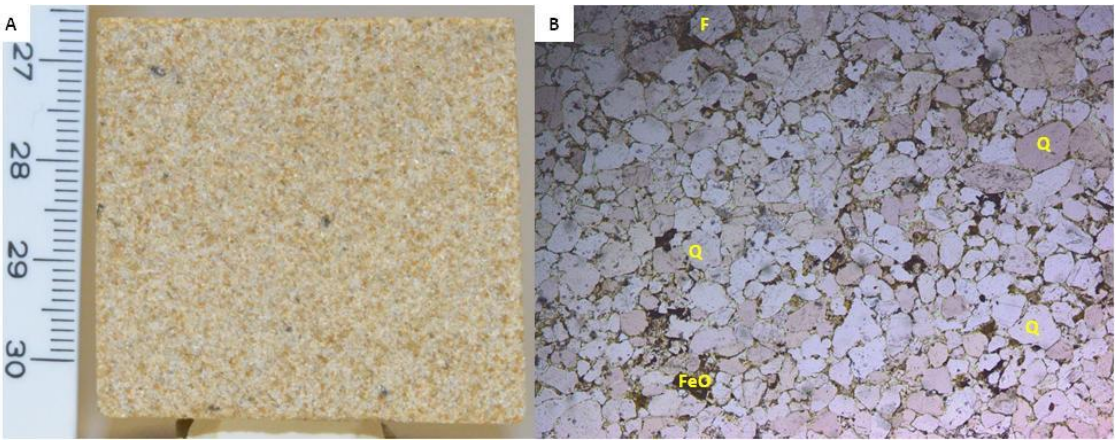

Figure 3-5: Hand specimen and thin section of Scotch Buff sandstone. Field of view is 3.3mm

(A) Hand specimen of Scotch Buff sandstone. (B) Optical thin section image Scotch Buff. Q: quartz, F: feldspar, FeO: iron oxide.

Scotch Buff sandstone is part of the Alston Formation of cyclic bioclastic limestones, sandstones, mudstones, siltstones and coals (King, 2012). The Alston Formation is part of the Yordale Group within the Alston Block, a structure located south of the Northumberland half-graben Basin. It is underlain by the Tyne Limestone Formation and overlain by the Stainmore Formation. The structural high of the Alston Block provided a topography that led to the development of shallow seas and the formation of the platform carbonates of the Yordale Group. The Alston Formation is split into numerous limestone units that dominate the Alston Formation. These units vary in thickness but are laterally persistent and are known as the Yoredale Cyclothems (King, 2012). The marine-shelf carbonate limestones are separated by units of deltaic sandstones and siltstones, marine shales and

pro-delta mudstones; grouped together as the general Alston Formation. Tucker (2009) proposed that these cyclothems are attributed to short, millennial-scale, eccentricity Milankovitch cycles, resulting in high frequency, arid-humid climatic fluctuations (Tucker et al., 2009). Scotch Buff sandstone is therefore attributed to a deltaic depositional environment; similar to that of Blaxter, Doddington and Hazeldean sandstones (Tucker et al., 2009).

3.1.4 Stanton Moor

Stanton Moor is Carboniferous (359 – 299Ma) sandstone from the Millstone Grit series and is extracted from Dale View Quarry near Matlock in Derbyshire, England. It is a medium grained, mineralogically and texturally immature buff coloured lithology. The mineralogical framework of Stanton Moor comprises detrital quartz grains with feldspar and muscovite distributed throughout. Detrital grains are sub-angular and poorly sorted. A proportion of the feldspar and muscovite grains show a significant degree of decomposition and alteration into authigenic clays, likely to be kaolinte (Figure 3-6). These clays cause a reduction in effective porosity and coat detrital grains throughout. Quartz grains commonly show pitting and fracturing. A variation in compaction is evident throughout the stone, with evidence for both brittle and chemical compaction. Areas of tightly interlocking quartz grains show line contacts and areas of chemical dissolution between grain boundaries. Quartz and calcite cement is common throughout (Figure 3-7); with quartz cement commonly occurring as quartz overgrowths. Stanton Moor is used extensively within Scotland for new build projects, such as Our Dynamic Earth in Edinburgh and as a cost effective match for many original blond sandstones in restoration projects, including at The University of Glasgow as a match for original Giffnock stone.

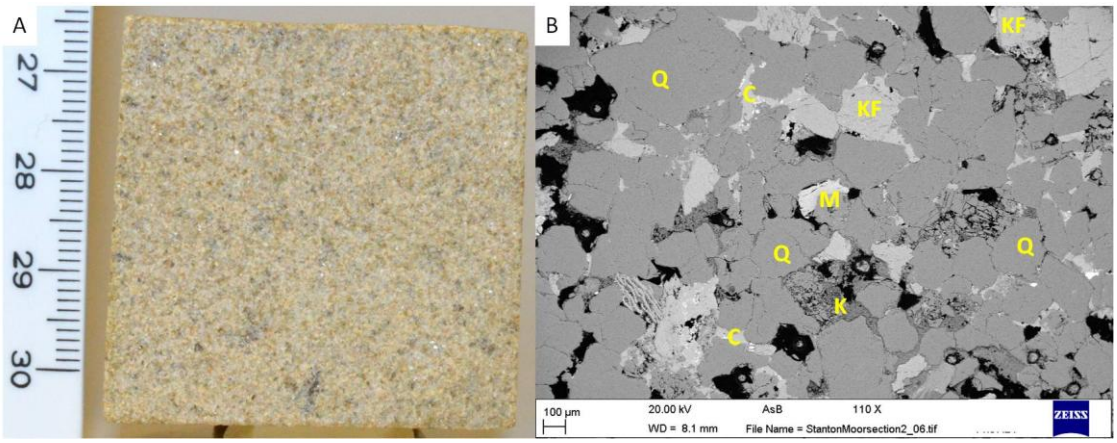

Figure 3-6: Hand specimen and thin section of Stanton Moor sandstone.

(A) Hand specimen of Stanton Moor sandstone. (B) SEM BSE thin section image of Stanton Moor. Q: quartz, KF: k-feldspar, M: muscovite, K: kaolinite, C: calcite cement, pore space is black

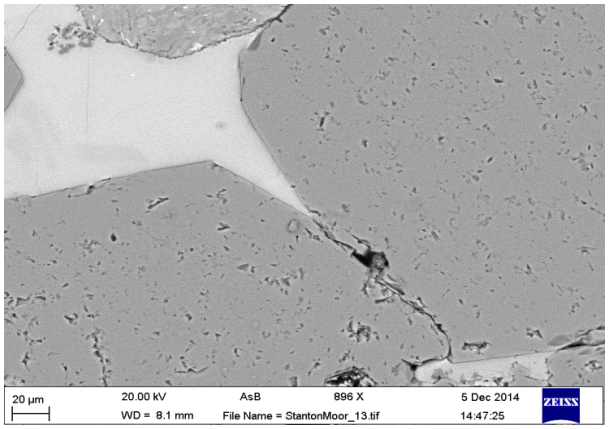

Figure 3-7: Calcite cement (white) between two quartz grains (grey).

Stanton Moor sandstone is part of the Ashover Grit series of the Millstone Grit Group which is Upper Carboniferous in age. The Millstone Grit Group overlies the Craven Group, which is composed of shale and mudstone, and underlies the Penine Coal Measures Group. The Millstone Grit Group was deposited in the Pennine Basin, which formed in consequence of previous tectonic activity related to the subsidence of the graben and half-graben basins (the Craven Basin, Gainsborough Trough and Widmerpool Gulf) (Waters, 2010). The upland areas of the Wales-Brabant High and the Southern Uplands formed the southern and northern boundaries of the Pennine Basin, respectively. The Millstone Grit group is characterised by fluvial-deltaic and thick turbidity fronted delta systems, depositing sediments within the basin (Waters, 2010). The Ashover Grit series is proposed to have been formed by a turbidite-fronted delta system, with sediment likely transported by braided rivers into the delta (Waters, 2010).

3.1.5 Blaxter

Blaxter is yellow-buff coloured, medium grained Carboniferous (359 – 299Ma) sandstone quarried near Otterburn, Northumberland. It is mineralogically immature sandstone containing a high abundance of feldspar and muscovite grains which are visible in hand specimen. Most grains are sub-angular and are poorly sorted. A high proportion of the muscovite and feldspar grains show extensive alteration and many have fully or partially decomposed into kaolinte and illite clay. Feldspar decomposition is highlighted in Figure 3-8. Much of the clay is pore filling, lowering the effective porosity throughout the stone. There are variable grain contacts seen throughout, ranging from line to concavo-convex and sutured contacts between quartz grains. Quartz overgrowths provide cement between grains, but are generally uncommon throughout. Authigenic clays provide secondary cement, binding large grains in the main matrix framework, and are situated within smaller pores between grains. Pores are generally quite large in what is a stone of variable properties, with large pores separated by areas of highly compact and clay supported quartz grains. Many Fe-oxides are present in the stone, coating feldspar and quartz grains, giving the stone its yellow colour in hand specimen. Blaxter is used widely within Scotland for both new buildings, including the National Library of Scotland and the Jenners department store on Princess Street in Edinburgh, and as replacement stone in restoration projects, including restoration work on the Holyrood Hotel, Edinburgh.

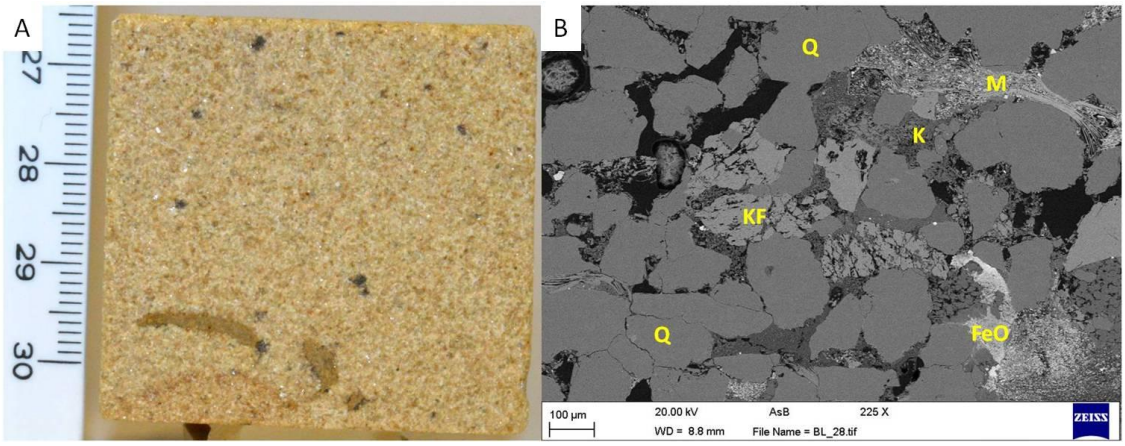

Figure 3-8: Hand specimen and thin section of Blaxter sandstone.

(A) Hand specimen of Blaxter sandstone. (B) SEM BSE thin section image of Blaxter. Q: quartz, KF: K-feldspar, M: muscovite, K: kaolinite, FeO: Fe-oxides, pore space is black.

Blaxter sandstone is extracted from the Tyne Limestone Formation (within the Scremerston Coal member), formally the Scremerston Coal Formation, comprising the lowest and thickest formation in the Yordale Group of the Lower Carboniferous in the Northumberland Basin (King, 2012). The sandstone is quarried in the Otterburn District of Northumberland, which is a complexly faulted syncline situated south-west of the Bolton-Swindon and Cragend-Chartner shear zone (Frost, 1969). The area is heavily faulted to the south but diminishes closer to the basin centre where the influence from the basin rocks is lessened owing to a greater depth of sedimentation (Frost, 1969). The formation outcrops in western and central Northumberland (King, 2012). The Tyne Limestone Formation which incorporates the Scremerston Coal member contains various rock types from grey, fine-grained and micaceous sandstones to pink, medium-grained siliceous sandstones, coal bands, shales, mudstones, cementstones and laminated siltstone-shale beds (Smith, 1967). Most of the sandstones found within the Tyne Formation are quartz arenites, commonly showing cross-laminations above erosive bases, with massive-laminated beds above this (Smith, 1967). South - south-west palaeocurrent directions are consistently recorded within the Tyne Formation (Smith, 1967). It is believed that the Tyne Limestone formation continues in a similar deposition environment to that of the Fell Sandstone and Cementstone groups of delta – delta-front platforms, mud plains and associated braided rivers (Smith, 1967). Due to the high abundance of micas within the sandstones of the Tyne formation, Smith (1967) reports that these sandstones (including Blaxter) would have been formed from point bar deposits in stream channels.

3.1.6 Giffnock

Giffnock is a local and now weathered sandstone originally used in the construction of the University of Glasgow at the present Gilmorehill campus in 1870. It is blond, medium grained Carboniferous (359 – 299Ma) sandstone; first quarried in 1835. This sample represents the typical Glasgow sandstone, estimated to be used in 43% of the blond sandstone buildings in the Glasgow area (Hyslop and Albornoz-Parra, 2009). The stone is composed primarily of sub-rounded quartz grains of variable size with a lower proportion of feldspar and muscovite; some of these grains show decomposition and pitted

weathering features (Figure 3-9). Quartz overgrowths are present on some grains, and the rock is cemented by a dolomite throughout, with pore filling clays also evident and partially infilling the porosity. Two different clay textures are distinguished and are likely to represent detrital and authigenic clays infilling pores and acting as a secondary cement binding the matrix material. Fe-oxides also coat quartz grains. Many of the famous and grand buildings within Glasgow are constructed using very similar blond sandstone, including the Glasgow Savings Bank on Ingram Street, and the interior of the Kelvingrove Art Gallery.

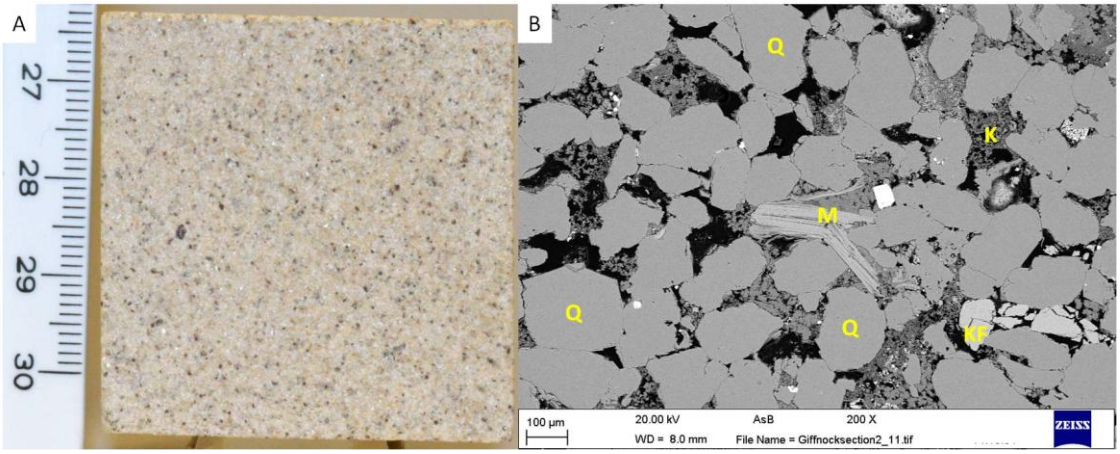

Figure 3-9: Hand specimen and thin section of Giffnock sandstone.
(A) Hand specimen of Giffnock sandstone. (B) SEM BSE thin section image of Giffnock. Q: quartz, KF: K-feldspar, M: muscovite, K: kaolinite, pore space is black.

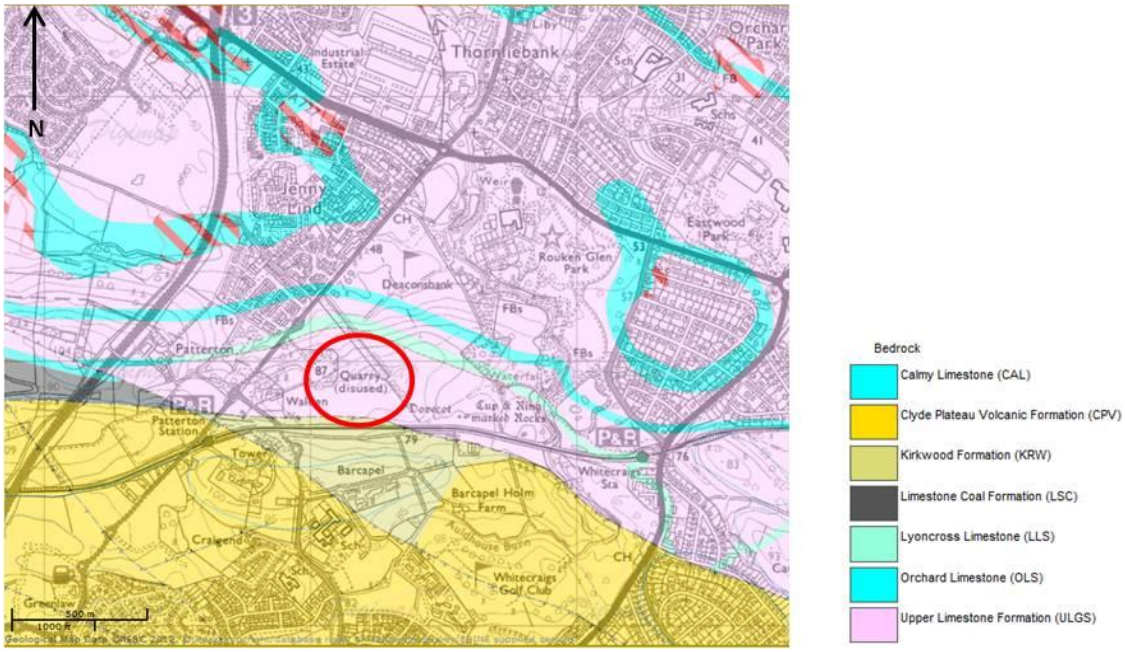

Figure 3-10: Historic Giffnock Quarry, Giffnock, south-west Glasgow.

Highlighted in the red box is one of the former Giffnock quarries. There were numerous historic quarries within the Giffnock area, with the map showing the urbanisation of the area post closure of the quarries. Map taken from Digimap.

Giffnock sandstone was quarried at a number of sites in the Giffnock area of Glasgow throughout the 19th and 20th centuries. These include: Braidbar Quarry, New Braidbar Quarry, Williamwood Quarry, Giffnock Quarry and New Giffnock Quarry. These quarries produced two types of stone, known as "liver rock" and "Moor rock". The "liver rock" was a preferred stone for both quarry men and stone masons due to its lack of stratification, allowing it to be extracted and cut at much greater ease to the "Moor rock" which was a harder and more porous stone (Portal to the Past website, East Renfrewshire Council; Shaw, 2007). The sandstone was quarried from the Upper Limestone Formation of the Bathgate and Clackmannan Groups of Lower Carboniferous age. The geology of the Giffnock area of Glasgow is shown in Figure 3-10.

The Clackmannan Group comprises the Lower Limestone, Limestone Coal, Upper Limestone and Passage Formations consisting of alternating cycles of marine and fluviodeltaic sedimentary rocks (in the first three formations) and a more fluvial dominated environment in the Passage Formation (Read et al., within Trewin, 2002). The Clackmannan Group overlies the Strathclyde Group and underlies the Coal Measures Group, and is only recognisable in the Midland Valley. The lithostratigraphy of the Clackmannan Group and its subsequent formations are well understood owing to the amount of available borehole data and underground coal workings that took place throughout Ayrshire, Glasgow and Lanarkshire. The structural geology of the Midland Valley, which subsequently controlled sedimentation processes during the Carboniferous, is less straightforward however (Read et al., 2002 within Trewin, 2002). A number of faulted basins and blocks were responsible for the sedimentation processes that dominated the Clackmannan Group. The Upper Limestone Formation comprises three sets of allocycles that are related to low, intermediate and high-frequency sea level oscillations. These oscillations lead to the deposition of numerous limestone, mudstone and sandstone beds of marine, deltaic and fluvial origin (Read et al., 2002 within Trewin, 2002). Giffnock sandstone itself is a river channel deposit; part of a larger river channel system during times of sea-level oscillations.

3.1.7 Locharbriggs

Locharbriggs is red sandstone of Lower Permian age (299 – 251Ma) that is extracted at Locharbriggs quarry, Dumfries and Galloway, southern Scotland. This is the oldest and largest red sandstone quarry in Scotland, and was opened in 1759. It is mineralogically immature, medium grained sandstone containing abundant clean, sub-rounded quartz grains and a smaller percentage of feldspar grains. Quartz occurs as mono and poly-crystalline grains from a range of geological provinces. There is a variable size and shape to the quartz grains, with most having hematite rims and some containing quartz-overgrowths. The stone matrix is composed of poorly sorted and broken lithic fragments, quartz grains and clay. Grains are cemented by silica and hematite throughout, and show a range of grain-grain contacts in what is a variably compacted rock. There is a strong and clearly distinguishable fabric throughout the stone with narrow layers of poorly sorted quartz grains, small Fe-oxides and small pores separated by layers composed of larger quartz grains, larger Fe-oxides and larger pores (Figure 3-11 and Figure 3-13).

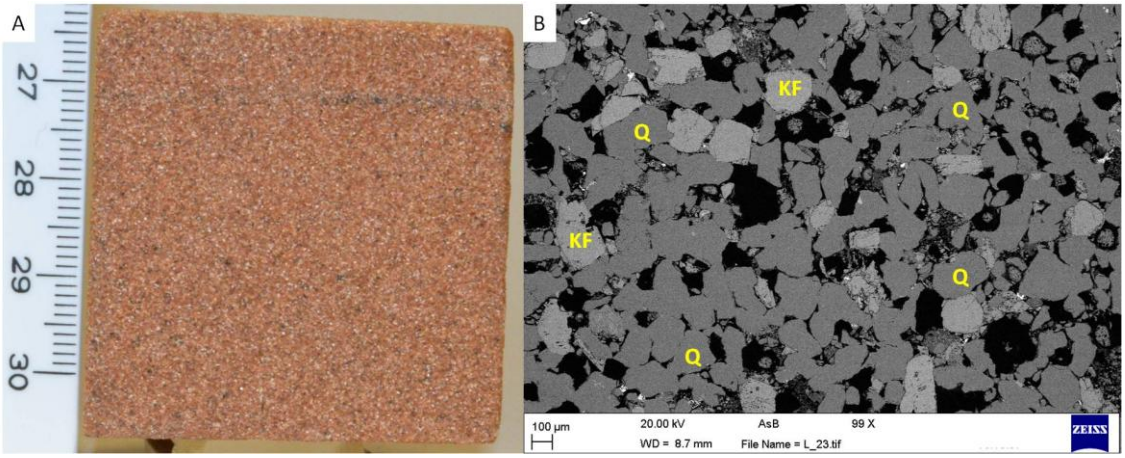

Figure 3-11: Hand specimen and thin section of Locharbriggs sandstone.

(A) Hand specimen of Locharbriggs sandstone. (B) SEM BSE thin section image of Locharbriggs. Q: quartz, KF: K-feldspar, pore space is black.

The grain structure creates a high porosity and high pore connectivity, with a wide range of pore sizes and pore throat distributions throughout the stone. Locharbriggs is an extremely important and popular building stone throughout the UK. The lists of buildings that were constructed from Locharbriggs date back to the 1700's and includes the Kelvingrove Art Gallery, The Royal Scottish Academy of Music and Drama, the Burrell Museum, Glasgow and the Caledonian Hotel and College of Art in Edinburgh. Many of the red sandstone

tenement buildings within Glasgow are built using Locharbriggs sandstone (Figure 3-12).

Figure 3-12: Tenement town house in the West End of Glasgow built using Locharbriggs sandstone.

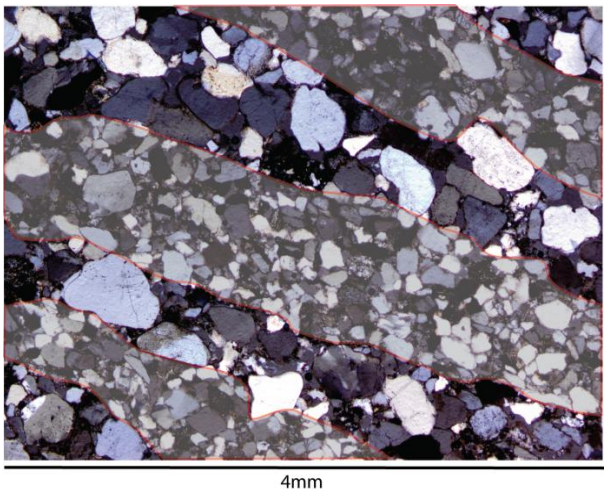

Figure 3-13: Layers highlighted in Locharbriggs cross-polarised thin section.

Locharbriggs is located in the Dumfries Basin in southern Scotland. The basin contains the Doweel Breccia Formation and Locharbriggs Sandstone Formation. The Doweel Breccia is composed of mainly sedimentary breccias interbedded with thin beds of sandstone and underlies the western part of the basin (McMillan et al., 2011). The Doweel Breccia Formation extends eastwards where it makes contact with and overlies the Locharbriggs sandstone. The Locharbriggs Sandstone Formation is comprised by two distinct facies: orange-red, cross-bedded sandstones that were likely to have formed as a migrating dune field in arid desert conditions, and the second is characterised by thin-bedded and laminated, orange-red and more silty

sandstones that contain pebbles of local origin, generated by fluvial reworking of breccia and local sandstone (Akhurst and Monro, 1996). Foresets within the formation show a consistent south-westerly dip, indicating a palaeo wind direction from the North East (Brookfield, 1978). The Dumfries Basin is underlain in the south east by Carboniferous strata that extends east into the adjacent Annan Basin. It is estimated from gravity survey data that the infilling sequence of the Dumfries Basin is between 1.1 km and 1.4 km in thickness and is bound in the west and northeast by a range of faults (Arkhurst et al., 2006). Similar sedimentary sequences within the Appleby Formation in the Vale of Eden Basin are thought to have originated in the same depositional environment; however it is unlikely that continuity exists between these rock units (Holliday et al., 2004).

The first scientific descriptions of vertebrate trackways from anywhere in the world was made in the red Aeolian sandstones of the Lochmaben and Dumfries Basins. These were first described in 1831, and have been followed since by several other finds from the Locharbriggs and Corncockle quarries (McKeever, 1994; Lucas and Hunt, 2006). The infill of clays within these footprints (which consequently allowed the good preservation) is likely to have been caused by short wet periods during mainly arid conditions.

3.1.8 Bonhill

This sample is tentatively identified as Bonhill red sandstone, a now weathered sample originally used in the construction of the University of Glasgow at its present site in Gilmorehill. This stone would have been originally quarried in Dunbartonshire, western Scotland. The sample is a mineralogically and texturally mature, moderately sorted sandstone composed mainly of sub-rounded, medium sized quartz grains with smaller percentages of lithic fragments, Fe-oxides and feldspars. Quartz grains are both mono and poly-crystalline and show a well-developed Fe-oxide coating, with a moderately high percentage of grains having a quartz overgrowth cement. These overgrowths are not necessarily syntaxial and some grains show Fe staining on the rim between the original grain and overgrowth suggesting a gap in time between oxidation reactions creating hematite rims and the development of quartz overgrowths. Feldspar overgrowths are also

present, with both quartz and feldspar grains showing a range of grain contacts, including a high percentage of point and line contacts. Pore filling clays are common and are associated with lithic fragments in the stone matrix. The sample has a high open porosity with many large, irregular pore chambers connected by narrow pore throats. (Figure 3-14). The geologic history of this sandstone is unknown.

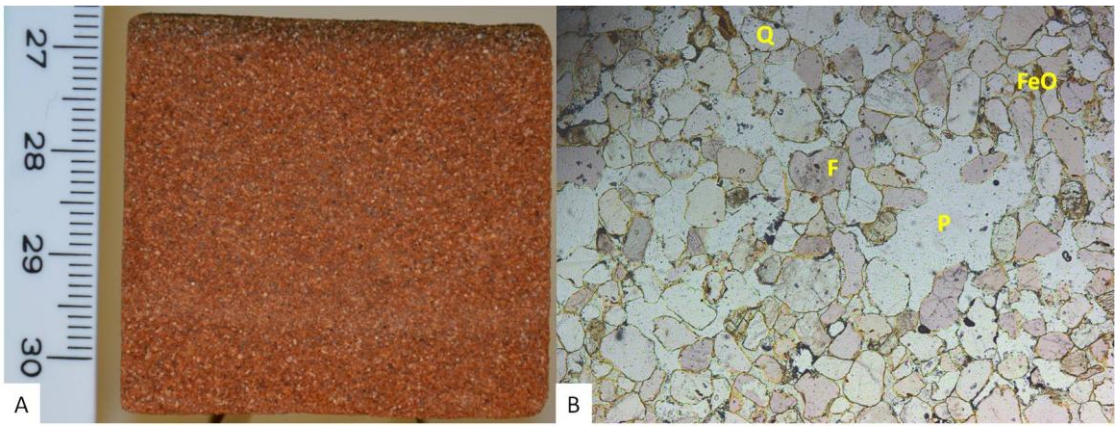

Figure 3-14: Hand specimen and thin section of Bonhill sandstone. Field of view is 3.3 mm.

(A) Hand specimen of Bonhill sandstone. (B) Plane polarised thin section of Bonhill. Q: quartz, F: feldspar, P: pore, FeO: Fe-oxides.

3.1.9 Hazeldean

Hazeldean is cream – pale white, medium-grained Carboniferous (359 – 299Ma) sandstone extracted at Hazeldean Quarry near Alnwick, Northumberland. Hazeldean is texturally and mineralogically mature, well sorted sandstone, containing an abundance of similar sized, mono-crystalline quartz grains and a lower percentage of poly-crystalline quartz. Smaller, sub-rounded feldspar grains are present but to a much lower percentage than quartz, with muscovite displaying lineations and a weak fabric in areas throughout the stone. Detrital grains show little decomposition, and there is a high proportion of pore filling clays throughout; likely kaolinite (Figure 3-15). Pores tend to be small and irregular, and the porosity is inter-granular, with a clay-filled proportion. There is also evidence of small rock fragments found within pores, likely from an igneous and metamorphic origin. Silica cement is common throughout the stone, but with limited quartz overgrowths present. It is a relatively well compact stone, showing a range of point contacts, small sutured contacts and a majority of tight line contacts between quartz grains (Figure 3-15). Overall, Hazeldean is a relatively

mature, well sorted sub-feldspathic arenite. Hazeldean Quarry was recently re-opened in response to calls to find a suitable match for Craigleith sandstone: an extremely important and popular stone used throughout Edinburgh. Hazeldean has since been used as the best match replacement stone for Craigleith sandstone, including its use at Holyrood Palace, Edinburgh, Register House, Edinburgh and the University of Edinburgh Old College, Edinburgh.

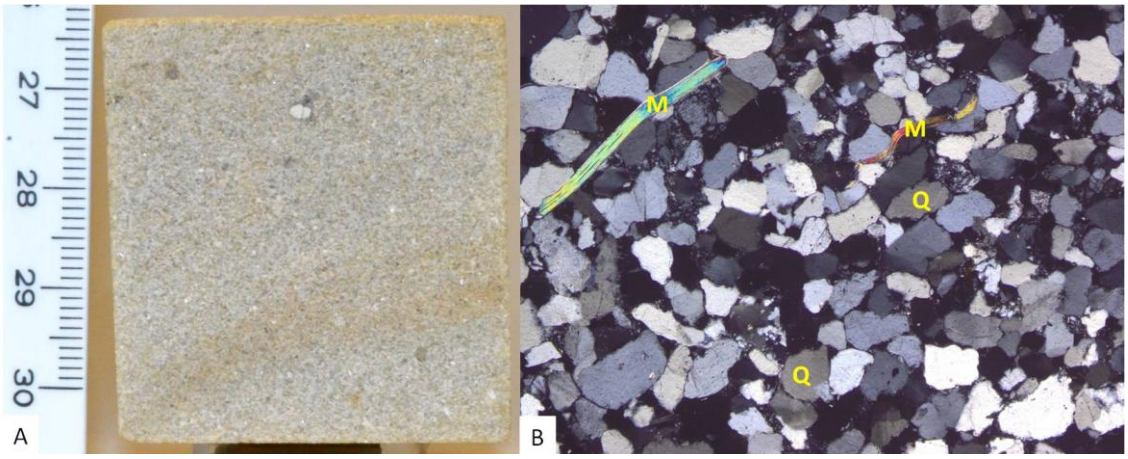

Figure 3-15: Hand specimen and thin section of Hazeldean sandstone.

(A) Hand specimen of Hazeldean sandstone. (B) Cross polarised image of a thin section of Hazeldean. Q: quartz, M: muscovite. Field of view is 3.3 mm.

3.1.10 Doddington

Doddington is very distinctive pink, medium-grained Carboniferous (359 – 299Ma) sandstone that is extracted from Doddington Quarry, near Wooler in Northumberland. The quarry has been worked consistently since the 1950's and likely for a number of years before then. It is a texturally and mineralogically mature sandstone composed of rounded to sub-rounded quartz grains and a smaller percentage of fractured and decomposed feldspar grains, muscovite, Fe-oxides and lithic fragments. Quartz grains show a wide range of sizes with no visible bedding features present in hand specimen or in thin section. There are a range of grain contacts, spatially variable, composed of mainly point contacts and line contacts between quartz grains (Figure 3-16). A high abundance of pore filling clays occur throughout, with minor amounts of clays coating quartz grains. Broken lithic fragments combine with clays to infill large areas of porosity, thus disconnecting areas of the pore network.

Doddington has been used extensively throughout Edinburgh since 1880 (McMillan et al., 1999), with few other sandstones quite as distinguishable as the pink-purple colours found within this lithology. It has been used as both the main building stone within many buildings but also used for dressings with other sandstones.

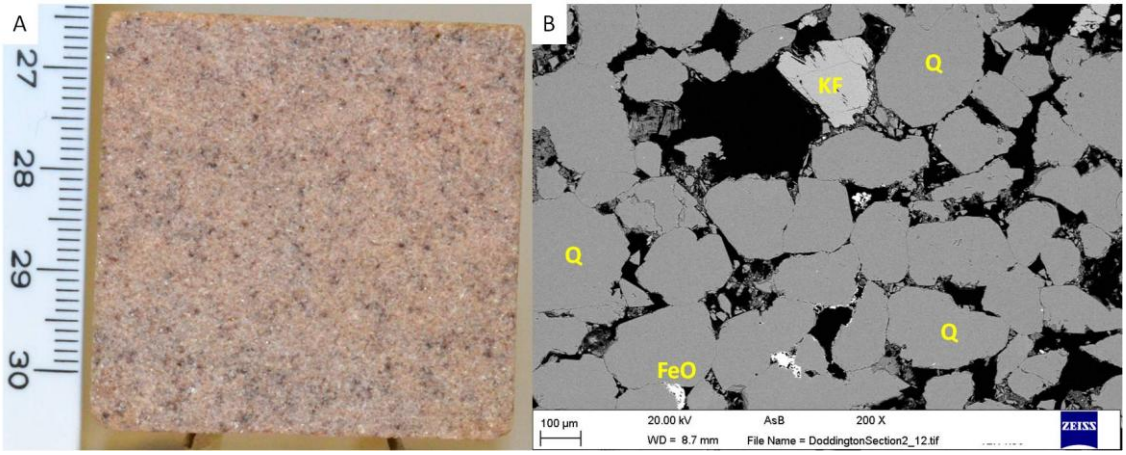

Figure 3-16: Hand specimen and thin section of Doddington sandstone.
(A) Hand specimen of Doddington sandstone. (B) SEM BSE thin section image of Doddington. Q: quartz, KF: K-feldspar, FeO: iron oxide, pore space is black.

Hazeldean and particularly Doddington are very distinctive sandstones found within the Fell Sandstone Formation of the Border Group of rocks in the Lower Carboniferous delta complex which infills the Northumberland Basin. The basin comprises a half-graben structure and is bound with the geomorphological high Alston Block in the south by the east-west trending Maryport-Stublick-Ninety Fathom fault system (Chadwick et al., 1993). The Fell sandstone group itself extends in a large arc from Burnmouth in south-east Scotland through Northumberland and into the Brampton-Bewcastle areas of Cumbria and west towards the north coast of the Solway Firth (Hodgson, 1978).

The group ranges in thickness from around 230 m – >330 m in the central areas of the basin. It is underlain by the Cementstone Group of sandstones and overlain by the Tyne Limestone Formation (formally the Scremertson Coal Formation, comprising extensive coal seems, limestones and sandstones). The beds on average have a gentle dip of around 5 - 10^{o} away from the central dome (Hodgson, 1978). The Fell Sandstone Formation comprises a majority of white, yellow and pink cross-stratified quartz arenite sandstones with thin bands of quartz pebbles and thin, discontinuous bands of

mudstones. The main sedimentary structures found within the formation are planar cross-laminations, convoluted laminations and overturned foreset beds that are spatially discontinuous (Smith, 1967). There has been much previous sedimentological research undertaken on the Fell Sandstone with several depositional environments proposed. Robson (1956) inferred a deltaic environment with a northern provenance for material. Smith (1967) proposed a large shallow marine environment and Hodgson (1978) proposed a fluvio-deltaic alluvial plain with periods of meandering braided stream systems as part of a larger deltaic environment encompassing much of the Lower Carboniferous.

3.1.11 Corsehill

Corsehill is red coloured, fine-grained Triassic (250 – 200Ma) sandstone that is extracted at Corsehill Quarry, near Annan, Dumfriesshire. The quarry re-opened due to increased demand in 1982 having originally closed in 1946. Corsehill is texturally immature sandstone, containing a majority of poorly sorted, sub-rounded to sub-angular mono-crystalline quartz grains. The stone contains decomposed feldspars, occasional highly decomposed muscovite and small rock fragments. Many of the feldspar and micas are highly weathered, creating authigenic clays (likely kaolinite) that fill much of the intergranular pores between the main framework minerals. Most grains show a ferruginous clay coating and hematite rims throughout. Visible, open pores are mainly round and elongated, with significant dolomite cement present throughout the stone. Much of the dolomite cement presents slight zoning on the outer edges of the crystal structure and is heavily stained by ferruginous clays. There is little grain-grain compaction in the stone, with most grains supported by clay filling pores and an abundance of dolomite cement. Figure 3-17 shows an SEM thin section highlighting the feldspar decomposition, the range of pore sizes and pore filling clays. Historically, Corsehill has been a very important building stone used nationally and internationally in a variety of buildings. Corsehill has been used more recently to build the Scottish National Portrait Gallery in Edinburgh, the Falkirk Sheriff Court, and was used internationally to construct the Million Dollar staircase at the New York State Capitol Building, New York.

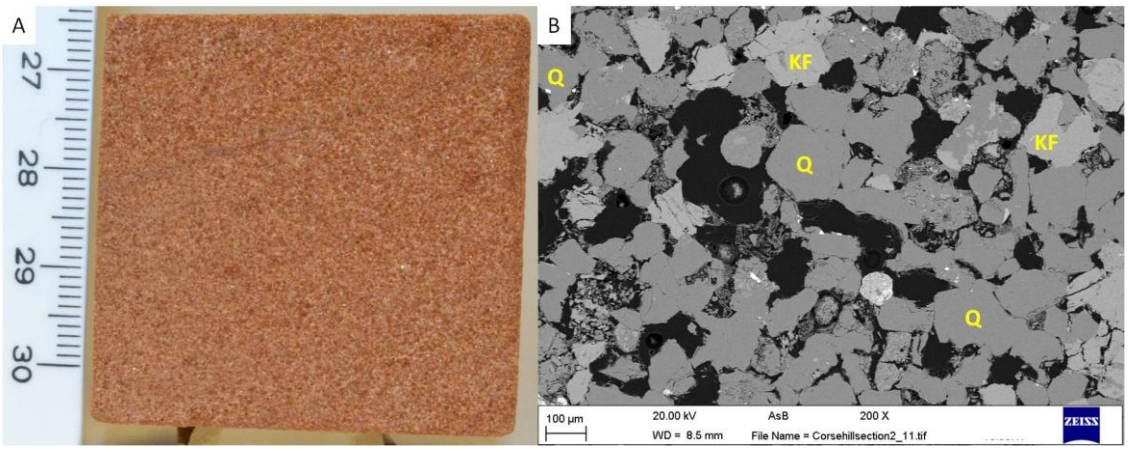

Figure 3-17: Hand specimen and thin section of Corsehill sandstone.

(A) Hand specimen of Corsehill sandstone. (B) SEM BSE thin section image of Corsehill. Q: quartz, KF: K-feldspar, pore space is black.

Corsehill sandstone occurs in the St Bees Formation of the Triassic Sherwood Sandstone Group within the Annan sub-basin of the Carlisle Basin in Dumfriesshire, southern Scotland. The St Bees formation consists of a thick sequence of reddish-brown, fluvial, fine-grained sandstones, locally silty or micaceous containing claystone and siltstone partings, overlain by coarser grained aeolian and fluvial sandstones (Holliday et al., 2008). It has been subsequently separated into two distinct formations; the St Bees and the Calder Sandstone Formations (Barnes et al., 1994). The Sherwood Sandstone Group overlies the Cumbrian Coast Group; consisting of the Eden Shale and mudstone formations and the Appleby and Yordale groups of sandstones and limestones respectively. A transition from the Eden Shale of the Cumbrian Coast Group to the St Bees Formation of the Sherwood Sandstone Group within the Carlisle Basin shows a change from aeolian to aqueous processes in the Eden Shale to the overlying fluviatile processes seen within the St Bees Formation and a progressive aeolian environment within the Calder Sandstone member. The Sherwood Sandstone group has been well researched as it constituted a principle reservoir target within the East Irish Sea Basin (Meadows and Beach, 1993). Lower parts of the St Bees Formation are seen within Corsehill Quarry and contain similar features to those found at Cove Quarry (Cove Sandstone): sheet sandstones, containing trough and planar tabular cross-bedding and ripple cross-laminations interbedded with laterally continuous mudstones and desiccation cracks (Holliday et al., 2008). Ripple marks within the Corsehill Quarry are shown in Figure 3-18. These ripple marks are likely caused by sheetflood sandstones inter-bedded with playa

mudstones and minor channel sandstones, interpreted as part of a terminal fan deposit overlain by a sandy braidplain, associated with a large north-west flowing braided fluvial system (Holliday et al., 2008).

Figure 3-18: A quarry worker at Corsehill quarry.
A quarry worker at Corsehill Quarry shows the dimensions of blasted stone. Ripple marks on the surface acts as a natural bed where clays collect allowing stone to break away

Name	Quartz (%)	K-Feldspar + mica+ (%)	Fe-oxide+ other (%)	Clay/ Cement (%)	Average Porosity (%)
Blonde					
Blaxter	69.0	6.6	0.7	5.7	18
Clashach	83.9	1.2	1.6	3.3	10
Cullalo	77.0	1.0	nd	2.0	20
Scotch Buff	73.0	2.0	2.0	5.0	18
Stanton Moor	73.5	3.5	2.0	7.0	14
Giffnock	75.5	1.5	1.0	6.0	16
Hazeldean	73.0	5.0	2.0	5.0	16
Doddington	69.0	5.0	2.0	5.0	19
Red					
Bonhill	68.4	2.0	1.5	2.6	26
Locharbriggs	70.5	3.0	3.5	2.0	21
Corsehill	69.0	2.0	5.0	5.0	19

Table 3-1: Mineralogy and average porosity.

Average porosity of the sandstones is calculated by helium porosimetry, water absorption and MIP. Mineralogy was determined by point-counting from blue-stained thin sections. Nd denotes not detected.

3.2 Hydraulic and Pore System Properties

The hydraulic properties of the stone provide information relating to moisture transport within the stone and are indirect measurements of specific petrographic properties.

3.2.1 Drying Tests

Drying tests provide information on the drying kinetics of each sandstone under set RH and temperature conditions. The drying of stone is a complex process influenced by external environmental conditions (temperature, RH), solution properties and the stone itself. The main transport mechanisms controlling this process are hydraulic capillary flow and vapour diffusion, with an important stage marking the transition between these processes. Several parameters are identified from the graphs of weight loss vs time that are generated in the test.

To normalise the data, weight loss is divided by the drying surface area for each sample. The initial slope of the drying curve corresponds to the constant drying rate period, where the drying boundary is located on the stone surface and hydraulic continuity exists throughout the stone. Water during this period is transferred to the surface by capillarity.

The critical moisture content (CMC) relates to the point in the graph where the weight loss gradient changes and the drying rate decreases. The CMC is a measure of the remaining moisture in the sample as the drying boundary retreats into the sample and the stone is no longer surface wet. Hydraulic connectivity to the surface is now discontinuous and is initially controlled by unsaturated capillary flow. This second stage of capillary flow is short lived in most samples and it represents an important phase change from a liquid to gas state, whereby vapour diffusion throughout the sample becomes the limiting factor. The moisture remaining in the sample at the end of the test is calculated as the residual moisture content, representing the remaining moisture trapped within the pores.

Most of the samples have similarly high constant drying rates ranging from 302 g/m^2/hr to 348 g/m^2/hr, while Corsehill and Clashach have the lowest values of 275 g/m^2/hr and 286 g/m^2/hr, respectively. Cullalo has the highest CMC at 62% and Doddington the lowest at 25%. Stanton Moor, Giffnock and Clashach samples also exhibit high CMC values. Stanton Moor and Corsehill samples have the largest residual moisture contents after 62 hrs of drying, with Doddington, Hazeldean and Blaxter samples showing the lowest residual moisture contents of 4%, 5% and 9%, respectively. Doddington and Hazeldean sandstones are the most efficient drying stones, and are characterised by high constant drying rates, low CMC values and low residual moisture contents. These values suggest that Doddington and Hazeldean sandstones have well connected pore structures that permit high hydraulic flow rates and ensure that the greatest amount of moisture is lost during the first stage of drying. Low residual moisture contents after this first drying stage contribute to lower falling drying rates. Averaged drying values are given in Table 3-2.

Locharbriggs on the other hand is characterised by a high constant drying rate and a high average falling drying rate. This result indicates that Locharbriggs, like Hazeldean and Doddington, permits fast hydraulic flow to the surface and efficient vapour diffusion throughout the stone. The relatively high residual moisture content at the end of the test is related to the overall high porosity of Locharbriggs sandstone.

Corsehill and Clashach sandstones have lower constant drying rates, leading to larger CMC values. As shown in Figure 3-19, Cullalo sandstone reaches its CMC before every other sample, while Corsehill is characterised by a prolonged and slow initial drying stage. Cullalo sandstone experiences a long capillary flow phase, characterised by a high average falling rate and a high residual moisture content. In this situation, the drying boundary recedes into the stone at an earlier stage than other stones but hydraulic continuity continues between moisture at depth and the stone surface. This same behaviour is seen in Locharbriggs and Corsehill sandstones, whereby this second phase of capillary flow is extended when compared to Hazeldean, Blaxter and Stanton Moor sandstones.

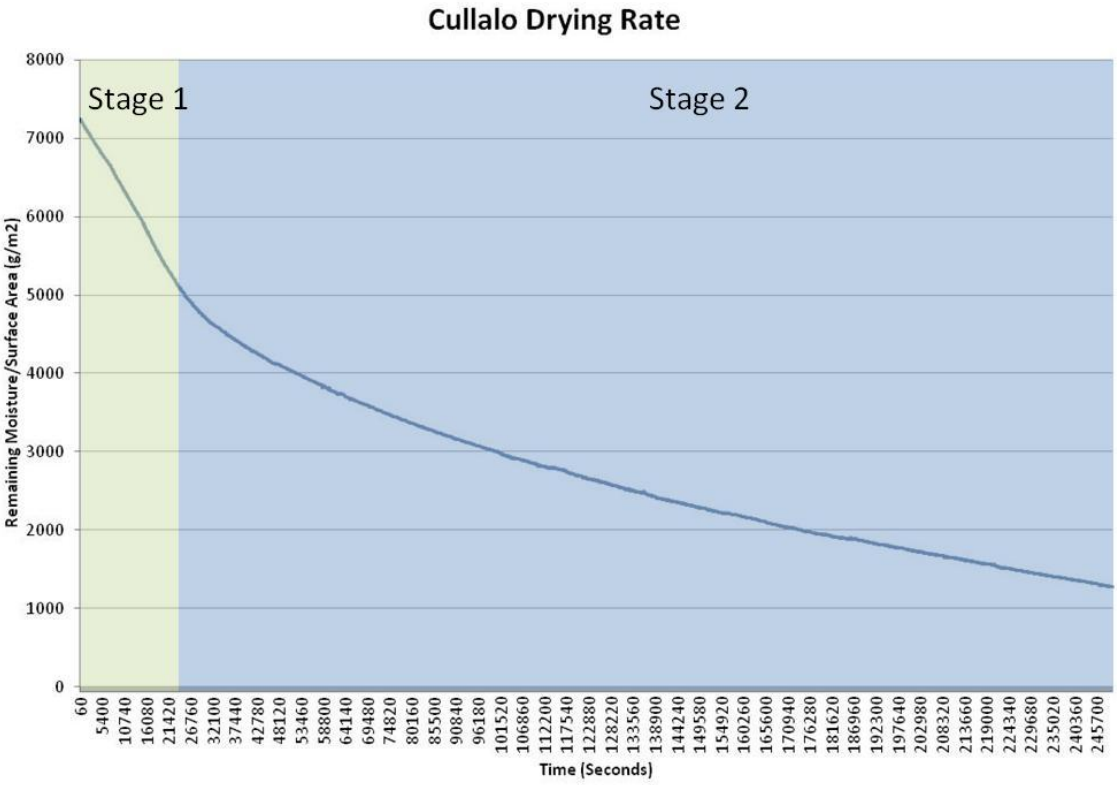

Figure 3-19: Drying curve for Cullalo sandstone, showing a 2 stage drying profile. The test lasted 68 hours.

Unfortunately, due to the complex interactions taking place within the drying regimes of porous materials, it is not always possible to identify the exact points where these phase transitions occur. Low permeability values of Stanton Moor and Blaxter samples suggest that they may experience slow drying rates once hydraulic flow is disrupted. High permeability values of Hazeldean, Cullalo and Locharbriggs samples also indicate reasons as to why these stones have both relatively high constant drying rates and in Cullalo and Locharbriggs samples, extended capillary dominated flow and high falling rates.

If time had permitted, the tests would have continued until all stones had completely dried out. In this situation, identifying each separate phase would be much easier. Despite these uncertainties, results show that Hazeldean is dried efficiently (Figure 3-20), while Stanton Moor (Figure 3-21) has a slower drying rate and is dominated by a longer vapour diffusion regime. Cullalo on the other hand, although exhibiting a high CMC, continues to have an efficient drying regime with prolonged capillary flow to the surface.

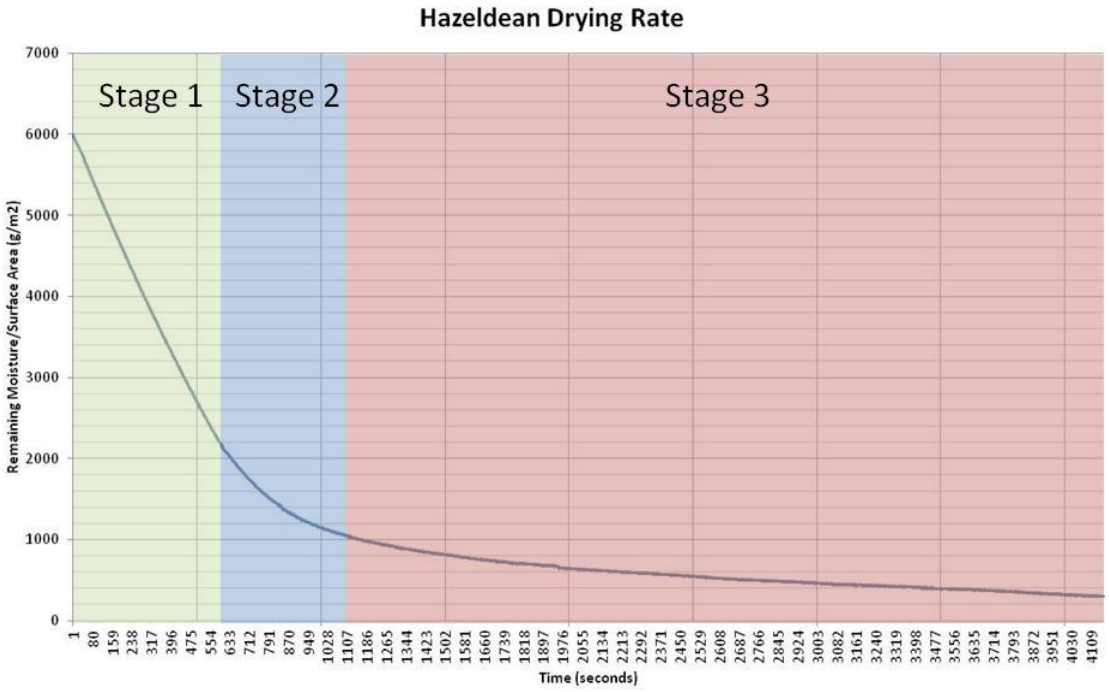

Figure 3-20: Drying curve for Hazeldean sandstone, showing the typical 3 stage drying profile

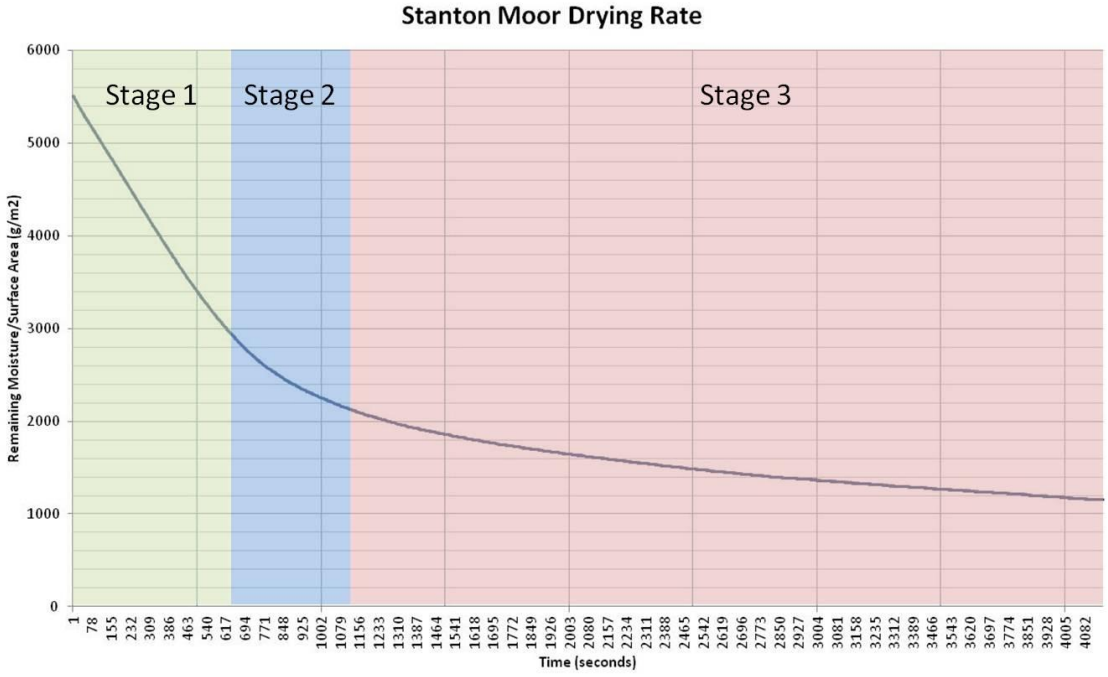

Figure 3-21: Drying curve for Stanton Moor sandstone, showing the 3 stage drying profile.

Stone Type	Constant Rate ($g/m^2/hr$)	Falling Rate ($g/m^2/hr$)	CMC (%)	Residual Moisture Content at end (%)
Blaxter	343	30	31	9
Clashach	286	28	57	13
Corsehill	275	43	40	15
Cullalo	336	60	62	12
Doddington	318	34	25	4
Giffnock	302	38	65	13
Hazeldean	348	27	30	5
Locharbriggs	333	45	31	10
Stanton Moor	311	34	57	18

Table 3-2: Drying rates for sandstone samples. CMC: critical moisture content.

3.2.2 Water Absorption and Saturation Coefficient

Stone Type	Water Absorption (%)	Saturation Coefficient
Blaxter	5.6 – 6.5	0.71 – 0.75
Bonhill	8.0 – 10.2	0.65 – 0.76
Clashach	2.4 – 3.3	0.61 – 0.62
Corsehill	6.0 – 12.2	0.75 – 0.78
Cullalo	5.4 – 6.2	0.64 – 0.76
Doddington	6.0 – 7.3	0.68 – 0.78
Giffnock	3.7 – 6.8	0.64 – 0.75
Hazeldean	4.3 – 4.6	0.64 – 0.68
Locharbriggs	9.4 – 10.5	0.73 – 0.83
Scotch Buff	6.8 – 7.2	0.77 – 0.78
Stanton Moor	4.3 – 4.9	0.80 – 0.99

Table 3-3: Water absorption and saturation coefficient values for each sandstone.

Water absorption is the measure of the maximum amount of water absorbed by a stone under atmospheric pressure and is directly influenced by the total porosity. The effective open porosity and the saturation coefficient are calculated by comparing the maximum water uptake values and the total porosity of each stone. The water absorption values are shown in Table 3-3 and Figure 3-22. Clashach, Hazeldean and Stanton Moor stones have the lowest values averaging between 2.4% – 4.9%, while Cullalo, Blaxter, Scotch Buff and Doddington stones have similar mid-range values falling between 5.4% – 7.3%. The largest average values belong to Corsehill and Locharbriggs sandstones and are over double the values of Clashach, Hazeldean and Stanton Moor sandstones. Both Corsehill and Giffnock stones show an extremely large variation of values between 6 – 12.2% and 3.7 – 6.8%

respectively. These results were obtained from the averages of measurements of 16 x 5 cm^3 cubes and 6 x 6 cm^3 cubes of each sandstone. All of the samples absorb over 90% of the total amount during the first 48 hrs, with a plateau of values reached after this. The largest and most accessible pores are filled during the first 48 hrs and only the most inaccessible and air trapped pores are filled after this.

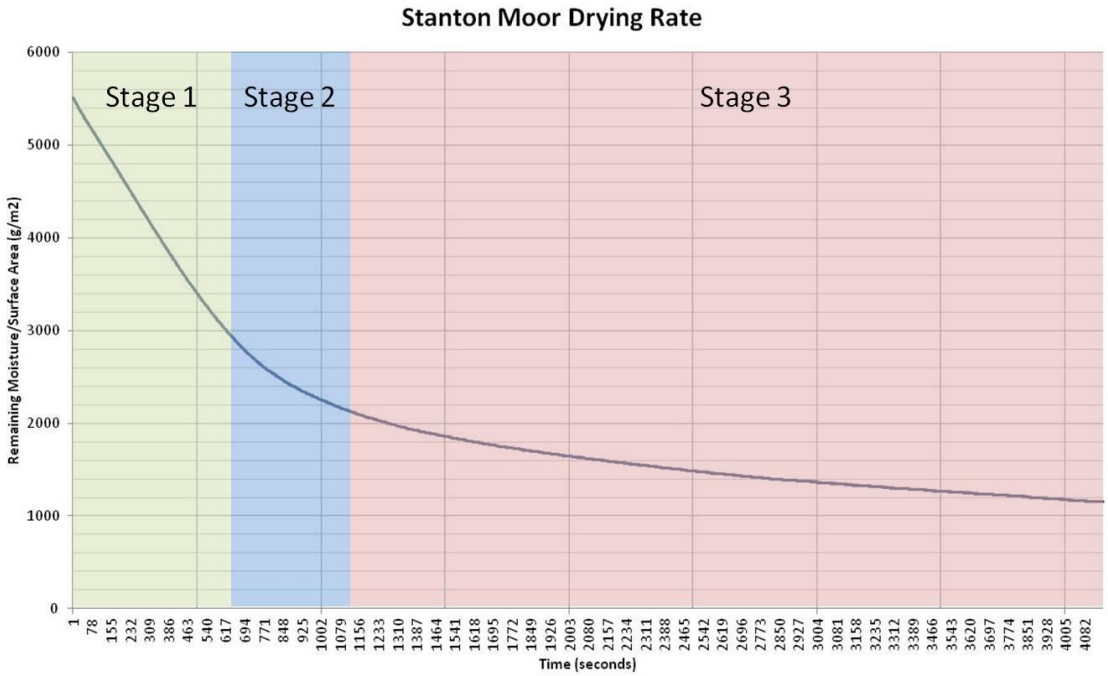

Figure 3-22: Average water absorption plot with standard deviation error bars. Sandstones are divided into three groups of high values (red), medium values (blue) and low values (green). Bonhill = 6x4cm^3. Locharbriggs, Corsehill, Doddington, Cullalo, Stanton Moor = 22 samples. Scotch Buff = 4x6cm^3. Blaxter and Hazeldean = 6x6cm^3 and 8x5cm^3. Giffnock = 14x5cm^3. Clashach = 6x5cm^3.

The saturation or "Hirschwald's" coefficient is measured as the ratio of pores filled under atmospheric pressure to the volume of pores filled under vacuum and is used to calculate the effective open porosity. Hirschwald made observations that suggested that those stones with a saturation coefficient greater than 0.8 (80% saturation) were most susceptible to frost damage (Ingham, 2005). Most of the measured stones have a saturation coefficient that lies within the 0.61 – 0.78 range and could therefore be considered as being relatively frost resistant (i.e.. only 61-78% of the total porosity is likely to be water-filled). A low saturation is the result of poor connectivity between the filled and unfilled pores due to extremely small pore throats or a tortuous pore network. Locharbriggs and Stanton Moor have the highest saturation values of 0.73 – 0.83 and 0.80 – 0.99, respectively. These samples, during complete immersion, will have a greater % of their porosity filled,

however this does not directly equate to the overall volume of moisture absorbed into the stone. The water absorption and saturation coefficient values do not provide information on rates of moisture uptake and are representative of maximum values expected for each stone type. Average saturation values are presented in Table 3-3.

3.2.3 Capillary Coefficient

Capillary coefficient measurements provide information on the rate of water uptake by capillarity; that is the transfer of water through pores <20 μm (Mamillan, 1981 in Tomasic et al., 2011). The capillary coefficient is measured from the initial slope of the capillary uptake curve. This curve is represented by two distinct parts; an initial linear slope that is a function of the square root of time; and a second stage comprised of a plateau, where little or no weight increase is recorded. The initial slope represents the uptake of solution by the free porosity in the stone, where the vertical capillary rise of solution is the dominant transport mechanism. The second part of the curve, represented by a plateau, develops once the open porosity is filled and the sample is essentially saturated in regards to capillary absorption. The further filling of micro-pores continues during this stage but is negligible in regards to a measurable weight increase. Capillary uptake values are given here as the averages from 3-4 separate tests utilising on average 6/12 x 6 cm^3 samples and 16 x 5 cm^3 samples per stone type.

The highest values are recorded for Locharbriggs and Bonhill samples, followed by Cullalo, Scotch Buff, Corsehill and Doddington. Locharbriggs shows a large variation between all measured samples, with several samples characterised by a two-stepped gradient profile, indicating an initial very fast capillary uptake followed by a break before another increase in the capillary uptake. This stepped profile suggests a very heterogeneous pore structure, whereby layers within the stone that have different pore properties significantly influence the movement and uptake of water. Bedding planes within the Locharbriggs sandstone provide layers of different pore sizes that can directly influence both the vertical intrusion of water and the rate of absorption. The first plateau is reached once the vertical intrusion of water encounters a bedding plane. Once water has penetrated through this bed,

increased capillary flow is restored as hydraulic connectivity will now operate through this plane (Figure 3-23). Average capillary coefficient values are given in Table 3-4 and Figure 3-25.

The second stage plateau is reached after 10-15 minutes for the Locharbriggs and Doddington samples and attained after 30 minutes for Cullalo, Scotch Buff and Corsehill samples. Saturation levels after one hour are in the range of 96-100% for these sandstones, with only the smallest pores and pore throats being filled after this time. This finding is in contrast to Hazeldean, Blaxter, Stanton Moor and Giffnock samples where 5 hours are needed before saturation is met, with one hour saturation ranging from 40% in Giffnock to 97% in Blaxter. A substantial percentage of absorption continues to take place in Stanton Moor and Giffnock samples between one and five hours and is highlighted by the shape of the slope in Figure 3-24.

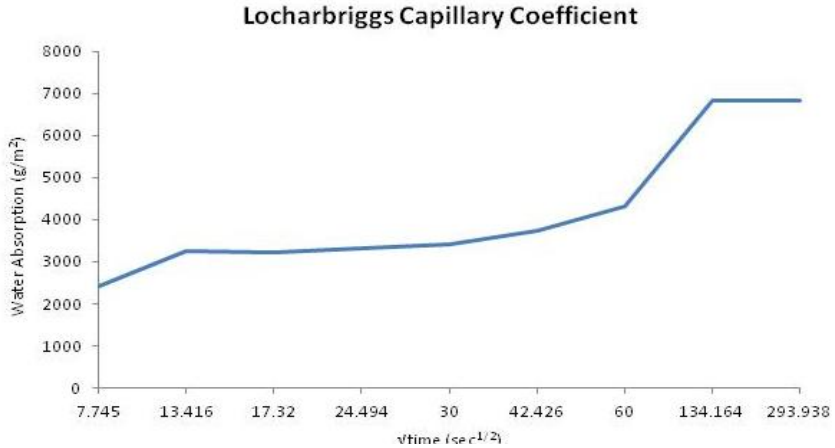

Figure 3-23: Capillary uptake profile for Locharbriggs sandstone. Two stepped gradient profile indicating low connectivity between bedding planes within the

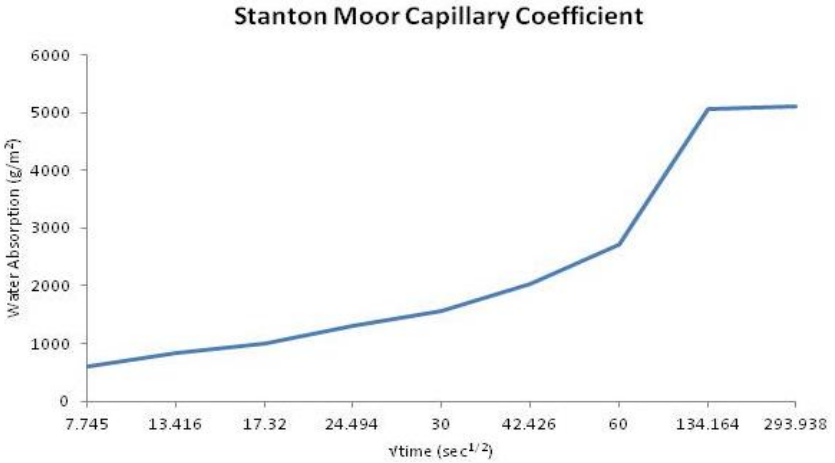

Locharbriggs sandstone. X-axis is the square root of time in seconds.

Figure 3-24: Capillary uptake profile for Stanton Moor sandstone.

Stone Type	Capillary Coefficient (g/m^2)	Standard Deviation	Variance
Blaxter	52	13	25
Bonhill	332	32	10
Clashach	28	12	44
Corsehill	171	68	40
Cullalo	108	51	47
Doddington	172	41	24
Giffnock	44	17	38
Hazeldean	51	22	43
Locharbriggs	310	143	46
Scotch Buff	134	24	18
Stanton Moor	32	12	37

Table 3-4: Capillary coefficient values for each sandstone.

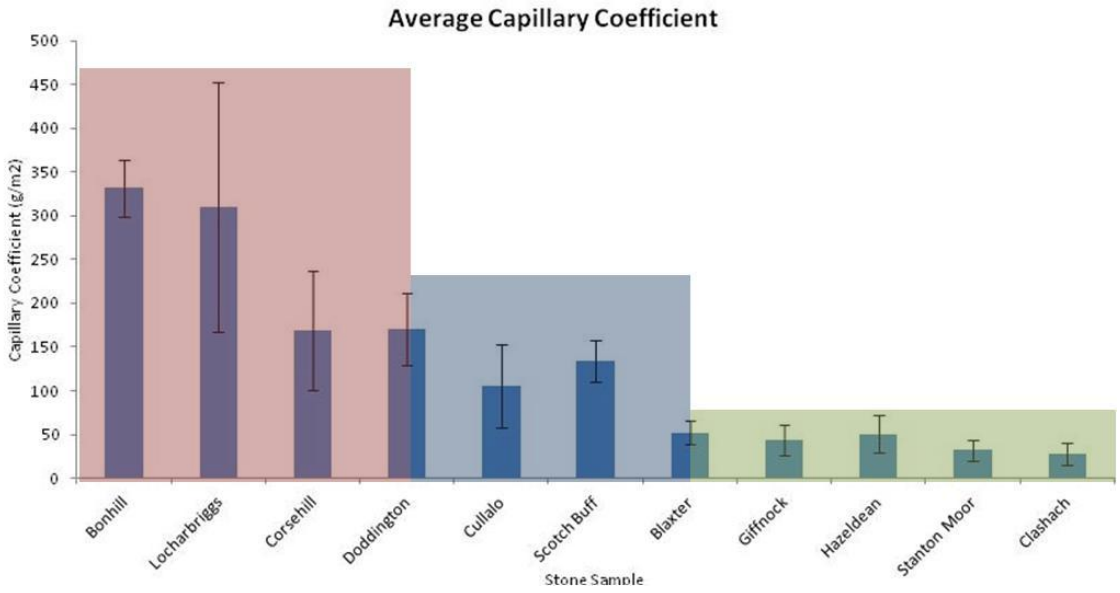

Figure 3-25: Plot of average capillary coefficient values with standard deviation error bars.

Sandstones are divided into three distinct groups of high values (red), medium values (blue) and low values (green). These groups relate to similar groups from water absorption tests and final ranking orders. Bonhill = 6x4cm^3. Locharbriggs = 10x6cm^3 and 16x5cm^3. Corsehill = 6x6cm^3 and 16x5cm^3. Doddington and Cullalo = 12x6cm^3 and 16x5cm^3. Scotch Buff = 4x6cm^3. Blaxter and Hazeldean = 12x6cm^3 and 8x5cm^3. Giffnock = 14x5cm^3. Stanton Moor = 12x6cm^3 and 22x5cm^3. Clashach = 6x5cm^3.

The capillary coefficient is directly related to pore network characteristics; most importantly the pore shapes, sizes and connectivity. Correlation

coefficients (R) of 0.8 and r^2 values of 0.6 and 0.7 are evident between: (i) the capillary uptake values; (ii) the percentage of porosity volume <0.1 μm diameter, (iii) the actual porosity <0.1μm diameter respectively. There is no correlation between capillary uptake values and any other pore size classes, suggesting that pores <0.1 μm have the greatest influence on the capillary uptake of water. It is likely that the measured pore values of <0.1 μm diameter correspond to pore throats and pore openings. It is through these narrow pore throats that steep pressure gradients will exist, leading to a faster uptake of water.

Other important factors influencing the capillary uptake include the tortuosity of the pore network and the spatial distribution of the small capillary pores. Lower capillary coefficient values suggest either low pore connectivity or a tortuous pore network. The lack of complete linearity during the initial slopes of the graphs indicates heterogeneities within the pore network, causing certain areas within the stone to absorb moisture at a greater rate than others. The shape and orientation of minerals, pores and pore openings can have an effect on the capillary uptake rate and movement of solution through the stone. Locharbriggs sandstone showed an increase in capillary uptake when measured parallel to bedding in certain samples, while changes were also measured in specific samples of Hazeldean and Cullalo when measured perpendicular to the original uptake plane. In both Cullalo and Hazeldean samples planes of preferential orientation cannot be viewed in hand specimen or under thin section. Locharbriggs showed a difference of roughly 35%; Hazeldean a difference of roughly 55% and Cullalo a difference of roughly 46%.

3.2.4 Ultrasonic Velocity Testing

Ultrasonic velocities were measured in three orientations for each sample, allowing the identification of any anisotropy within the stone. Table 3-5 shows the values and errors for each stone type. Cullalo, Doddington, Hazeldean, and Stanton Moor samples have the highest velocities, with Corsehill and Locharbriggs showing similar mid-range values, while Blaxter has the lowest measured velocity. High velocities indicate a high density and well compacted rock, while lower values are indicative of higher porosities and lower densities. Locharbriggs and Corsehill are both high porosity red sandstones with a high percentage of large pores and a relatively large volume of clay. Conversely, Cullalo, Doddington, Hazeldean and Stanton Moor stones have a greater degree of grain compaction.

As regards the high velocity stones, Cullalo is a mineralogically and texturally mature sandstone, containing a high proportion of clean, highly cemented quartz grains and a relatively low clay content. Due to the maturity of the stone, the grains are well compact, leading to a high ultrasonic velocity, even with high porosity values (20%). Stanton Moor also exhibits high ultrasonic velocities which are linked to the high apparent density of the stone (2.25 kg/m^3), caused by a very tortuous pore network that contains a high percentage of micro-pores. Stanton Moor is poorly sorted, with evidence of sutured contacts and dissolution boundaries occurring between grains. This high grain compaction gives the stone a very low permeability, with a high percentage of micro-pores situated between large and small grains.

Giffnock and Stanton Moor samples show low standard deviations and low variance coefficients, highlighting less spatial petrographic variability, with

no indication of anisotropy. Cullalo and Locharbriggs samples both have higher standard deviations and variance coefficients, linked to anisotropies within the stones. Clearly defined orientations of anisotropy are evident in both stone types, whereby one measurement per Locharbriggs sample has a reduced velocity measurement of ~100-400m/sec on average, while the remaining orientations are within a 100m/sec range of difference. Cullalo samples show three distinctive planes, where differences of ≥100 m/sec on average are found for each orientation. These differences are highlighted in Table 3-6. Variance values of ≤10% provide confidence within the data set for each sample. Ultrasonic velocity measurements are mainly used as a non-destructive tool for determining change in samples after crystallisation tests.

Stone	Mean velocity (m/sec)	Standard Deviation	Variance (%)	No of measurements
Blaxter	2522	112	4	12
Corsehill	2616	152	6	24
Cullalo	3708	356	10	24
Doddington	3107	237	8	24
Giffnock	2816	155	5	12
Hazeldean	3125	176	6	12
Locharbriggs	2654	195	7	24
Stanton Moor	3079	152	5	24

Table 3-5: Ultrasonic velocity measurements for each sandstone, indicating the standard deviation from the mean values of 8 samples, variance and total number of measurements made for each sandstone (3 measurements x 8/4 samples). Extra measurements were made for the 5 samples used in the third crystallisation test to allow for changes to their USV from salt decay to be quantified.

Stone	O1	O2	O3
Cullalo	3592	3307	3144
	4013	3809	3645
	4190	4065	3652
	3514	3405	3312
Locharbriggs	2943	2688	2997
	2652	2369	2518
	2516	2468	2521
	3038	2705	2908

Table 3-6: Ultrasonic velocity measurements for three orientations (01. 02, 03) in Cullalo and Locharbriggs sandstone. Values are in m/sec.
Differences of >100m/sec for each orientation in Cullalo sandstone suggests an anisotropic pore structure controlled primarily by a weak fabric within the stone. Differences in one orientation (O2) in Locharbriggs sandstone highlight the bedding planes that indicate spatial differences in the pore size distribution, grain size and grain shape.

3.2.5 Colour Measurements

Stone colour is an important surface property of masonry sandstone that influences both building aesthetics and the thermal properties of the stone by altering the albedo of its surface. Measuring the colourimetric parameters of the stone is important for assessing what aesthetic impact de-icing salts have on each stone type. The L*, a* and b* values and standard deviations are given for each type in Table 3-7. Six measurements were made on 12 different samples for each stone type, giving a total of 72 measurements for each stone type. These values are used as a baseline standard in order to quantify the effect of salt crystallisation on stone colour.

Stone	L*	L* Std Dev	a*	a* Std Dev	b*	b* Std Dev
Blaxter	63.84	2.31	4.43	1.35	21.8	1.43
Corsehill	46.65	1.33	14.93	0.60	20.77	0.87
Cullalo	71.25	2.43	2.02	0.77	12.64	1.97
Doddington	61.48	1.25	7.03	0.76	8.77	1.18
Giffnock	69.92	2.05	2.28	0.74	11.02	2.04
Hazeldean	70.58	2.41	1.41	0.94	11.82	3.73
Locharbriggs	50.81	1.25	13.85	1.04	18.1	1.07
Stanton Moor	67.19	1.28	2.29	0.65	14.09	1.38

Table 3-7: Colour measurements for each sandstone. Corsehill, Doddington and Locharbriggs are red sandstones. L*: lightness, a*: red-green spectrum, b*: blue-yellow spectrum.

3.2.6 Porosity and Pore Size Distribution

Porosity, density and pore size distributions were obtained from mercury intrusion porosimetry (MIP) measurements. It must be noted that MIP does not provide a true representation of pore size distribution and in some situations may correspond to the measurement of pore throats as opposed to actual pore sizes. The results from MIP (Table 3-8) are herein referred to as measurements of actual pore sizes and are reported as pore diameter.

In all stones apart for Stanton Moor, the greatest percentage of pores lie in the 10 μm – 50 μm range, while Stanton Moor contains the greatest percentage of pores between 5 μm – 10 μm. Stanton Moor has a unimodal distribution and a large range of pore sizes, with 88.1% of all pores situated within the range of 0.1 μm – 10 μm and only 10.1% of pores greater than 10

μm. In comparison, all other samples contain ≥49.9% of pores greater than 10μm.

Blaxter sandstone shows a bimodal pore size distribution, with peaks situated between 0.1 μm – 1 μm (15.8%) and 10 μm – 50 μm (42.2%). Blaxter shows a similarly large range of pore sizes to Stanton Moor, with 90.8% of pores situated in the range of 0.1 μm – 50 μm, but only 48.7% of pores between 0.1 μm – 10 μm, nearly half of the Stanton Moor value.

Giffnock sandstone, like Blaxter, shows a bimodal pore size distribution, with two main peaks situated in the same range as Blaxter; 0.1 μm – 1 μm (17.3%) and 10 μm – 50 μm (46.2%). Giffnock contains a slightly lower % of pores between 0.1 μm – 10 μm (46.3%), but shows a similar distribution trend to Blaxter.

Fine grained Locharbriggs sandstone has a unimodal pore size distribution, with a maximum percentage of pores in the 10 μm – 50 μm range. It shows a large distribution of values below 10 μm, containing the greatest percentage of the sample set between 0.01 μm – 0.1 μm. Coarse grained Locharbriggs on the other hand shows a contrasting distribution, containing a greater % of larger pores, with an increase of 21.5% within the 10 μm – 50 μm range and a significant reduction in pores ≤1 μm.

Corsehill, Bonhill and Scotch Buff sandstones show a similar distribution trend to coarse grained Locharbriggs. Each stone contains the largest pore fraction between 10 μm – 50 μm, with Scotch Buff and Bonhill sandstones showing smaller secondary peaks between 0.1 μm – 1 μm (9.1% and 6.7% respectively) and Corsehill being the only sandstone in the sample set to contain pores of <0.01 μm (0.8%).

Clashach, Cullalo, Doddington and Hazeldean sandstones all show very similar pore size distributions, with Cullalo having the greatest % within the 10 μm – 50 μm range (77.1%) and Clashach the greatest % >100 μm (15.5%). These samples also have the largest % of values >50 μm, with each sandstone

exceeding 10% of pores in this class and the lowest % values <5 μm, ranging between 3.1% (Clashach) – 10.4% (Doddington).

Skewness and kurtosis values were measured for each sandstone and reveal similarities in pore size distribution trends. Bonhill, Hazeldean, coarse grained Locharbriggs and specifically Cullalo and Doddington all show similar kurtosis and skewness values, and all show unimodal distributions, negative skews and contain mean and median values within the 10 μm – 50 μm range.

Blaxter and Giffnock sandstones have near identical kurtosis and skewness values, highlighting their bimodal distribution, while Stanton Moor has significantly different values that show a symmetrical unimodal distribution, with mean and median values situated within the 0.1 μm – 10 μm range.

Stone	Pore Size Distribution % – Diameter (μm)								
	<0.01	0.01-0.1	0.1-1	1-2	2-5	5-10	10-50	50-100	>100
Blaxter	0.0	1.5	15.8	10.0	11.1	11.8	42.2	2.5	5.2
Bonhill	0.0	2.5	6.7	2.9	2.8	6.4	68.5	6.4	3.9
Clashach	0.0	0.9	0.7	1.0	0.5	4.2	73.3	4.3	15.1
Corsehill	0.8	2.3	5.0	3.5	5.2	15.6	63.2	1.2	3.2
Cullalo	0.0	0.2	2.5	1.2	1.6	5.8	77.1	3.9	7.6
Doddington	0.0	0.0	4.0	2.6	3.8	4.9	72.2	6.8	5.7
Giffnock	0.0	0.4	17.3	6.7	9.0	13.3	46.2	2.0	5.2
Hazeldean	0.0	0.0	0.7	0.7	2.4	10.8	74.6	3.5	7.3
Loch (Fine)	0.0	6.6	8.7	5.0	7.0	17.9	50.7	0.7	3.4
Loch (Co)	0.0	0.1	6.2	3.3	3.6	7.3	72.2	4.0	3.3
Scotch Buff	0.0	0.7	9.1	4.4	7.1	14.6	59.4	1.2	3.4
SM	0.0	1.8	26.2	13.1	20.8	28.0	4.8	1.1	4.2

Table 3-8: Pore size distribution (%) for each sandstone.
SM: Stanton Moor, Loch (Fine): fine grained Locharbriggs, Loch (Co): coarse grained Locharbriggs. These results are the mean values of 3 samples.

Porosity was determined by He porosimetry, MIP, vacuum water absorption, and digital image analysis. MIP and image analysis can also allow the measurement and quantification of pore size distribution and pore/grain shape, respectively. Each technique is constrained in its effectiveness by limitations on measurement resolution. By using complimentary techniques, different pore thresholds can be measured. Results presented here were calculated from He porosimetry on 25 mm diameter cores, vacuum water absorption image analysis.

Under vacuum immersion, water can penetrate pores greater than 100 nm (Meyer et al., 1994 in Cnudde et al., 2009), and when combined with water absorption at atmospheric pressure provides a measurement of the effective open porosity; the actual porosity that is likely to undergo repeat absorption and desorption under natural, non-forced conditions.

Bonhill had the largest porosity at 25% under vacuum immersion. Locharbriggs had the second largest porosity at 21.2%, while Doddington (19.3%), Cullalo (18.7%), Corsehill (18.5%) and Blaxter (18.1%) had similar values. Clashach (10%), Stanton Moor (13.5%) and Giffnock (14%) samples had the lowest average porosity values. The saturation coefficients for each sample were used to calculate effective open porosity. Clashach (6%), Giffnock (11%), Hazeldean (11%) and Stanton Moor (12%) had the lowest effective open porosities, while Bonhill (18%) and Locharbriggs (17%) had the highest effective open porosities. Every other sample had values between 13-14%. Results are presented in Table 3-9, Table 3-10 and in Figure 3-26.

Helium porosimetry was undertaken to provide complimentary porosity data. For many of the samples, repeat measurements were taken and averages calculated. As helium can penetrate extremely small pores, the helium porosity values are expected to be slightly higher than those calculated from the vacuum water absorption method. This was true for the Bonhill, Scotch Buff, Locharbriggs, Cullalo, Giffnock and Stanton Moor samples, while the Corsehill and Blaxter samples had significantly lower helium porosity values. To test the reliability of these values, vacuum porosity tests were undertaken on the same cores as used for helium porosimetry. For all but three samples (Corsehill, Blaxter and Hazeldean) vacuum porosity measurements gave slightly lower values from those calculated with He porosimetry, as expected. R^2 values of 0.7 were calculated for helium and hydric porosities of all the cores. This rose to 0.9 when Corsehill and Blaxter samples were removed. These values suggest significant heterogeneities across Corsehill and Blaxter samples and highlight the specific variations in the type and quality of Corsehill samples used within the study.

MIP is a versatile technique that can measure the porosity, pore size distribution and real densities of each stone. The results show very similar

porosities to those measured by He and vacuum saturated methods in all but Cullalo and Bonhill samples, whereby porosities were significantly lower than those recorded by other techniques.

Variance values for each stone type as calculated from MIP, He, image analysis and hydric testing on cores and cubes range from 37.3% in Corsehill to 8.2% in Clashach. Image analysis grossly overestimated Locharbriggs and Corsehill porosities, while every other test generally returned values falling within the final variance range.

Stone	Hg	He	Cores	WP4	WP5	SEM	Average	SD	Var
Blaxter	17	15	17	19	18	19	**18**	**1.5**	**8.5**
Bonhill	18	29	26	24	n/a	n/a	**24**	**4.6**	**19.2**
Clashach	10	10	9	11	n/a	n/a	**10**	**0.8**	**8.2**
Corsehill	21	12	17	20	n/a	33	**20**	**7.6**	**37.3**
Cullalo	13	23	19	18	19	19	**18**	**3.3**	**17.8**
Doddington	18	21	19	n/a	20	16	**19**	**1.9**	**10**
Giffnock	18	17	16	12	n/a	15	**16**	**2.4**	**15.3**
Hazeldean	12	15	15	17	15	n/a	**15**	**1.9**	**13.1**
Locharbriggs	23	20	19	19	26	31	**23**	**4.9**	**21.1**
Scotch Buff	18	20	19	16	n/a	n/a	**18**	**1.7**	**9.3**
Stanton Moor	12	16	14	14	13	10	**13**	**2.0**	**14.9**

Table 3-9: Porosity values for each sandstone as calculated by 4 separate techniques.

Hg: mercury porosimetry porosity, He: helium porosity, Cores: water buoyancy measurements of 25 mm cores, WP4: water buoyancy measurements of 40 mm cubes, WP5: water buoyancy measurements of 50 mm cubes, SEM: digital image analysis porosities from SEM micrographs.

Stone	Porosity	Effective Open Porosity	SD	Variance
Blaxter	18	13	1.5	8.5
Bonhill	26	18	2.5	9.6
Clashach	10	6	0.8	8.2
Corsehill	19	15	2.0	10.3
Cullalo	20	14	1.9	9.9
Doddington	19	14	1.4	7
Giffnock	16	11	1.5	9.3
Hazeldean	16	10	1.0	6.3
Locharbriggs	21	17	2.9	13.7
Scotch Buff	18	14	1.7	9.3
Stanton Moor	14	12	1.5	11.1

Table 3-10: Average porosity (minus outliers) and calculated effective open porosities as measured from the average porosity (minus outliers) for each sandstone.

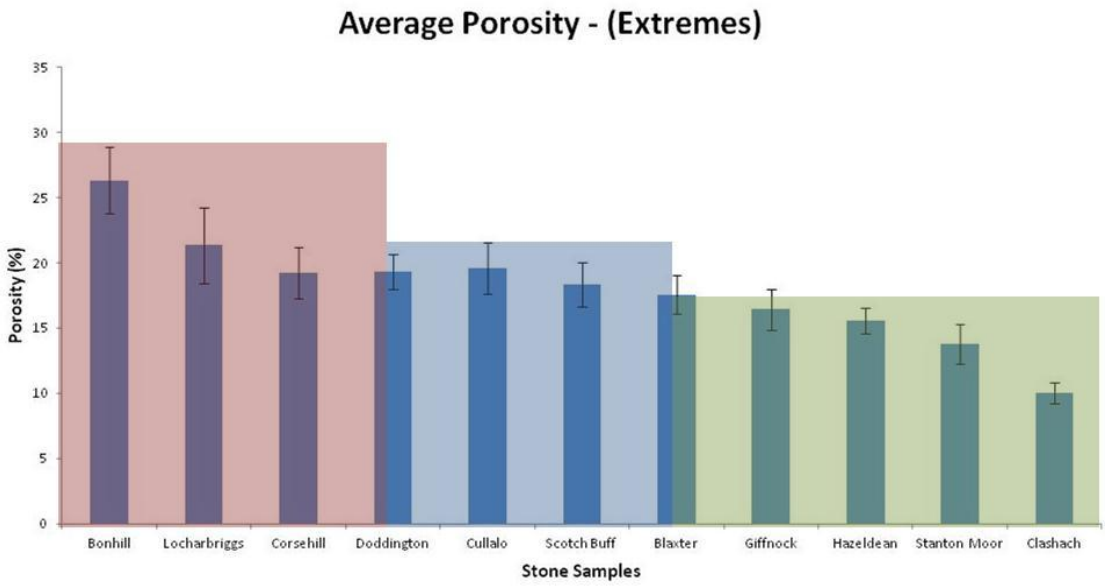

Figure 3-26: Plot of average porosity values (minus extremes/outliers) for each sandstone with standard deviation errors bars. Data in table 3-10.

Sandstones are divided into three groups of high values (red), medium values (blue) and low values (green).

3.2.7 Nitrogen Permeability

Nitrogen permeability measurements were carried out in three orientations on each sample where possible, and were limited by material quantity. Measurements were carried out on 25 mm diameter cores after they had been used in helium porosity tests. The flow of gas will behave differently to water and so these measurements are limited in their applicability to the topic of this thesis. Bonhill has the highest measured gas permeability value of 1749 milli Darcy (mD), while Stanton Moor had the lowest average permeability values. The Locharbriggs sample shows a strong anisotropy, with values of 8.11 mD, 204.48 mD and 297.81 mD measured at three different orientations with the highest permeability values parallel to the bedding planes. Hazeldean, Cullalo and Doddington samples all had values exceeding 100 mD, with Doddington having an average of 763 mD.

Two repeat Hazeldean and Corsehill samples were measured and were in extremely good agreement, with variance values of 1% and 2% respectively. Conversely, Locharbriggs, Doddington and Clashach samples had extremely high variance values, exceeding 30%. The high variance for Doddington is likely caused by the length difference of 3 cm between the two measured samples and a poor agreement between measured permeabilities at each pressure division in the shortest sample. The latter reason is the likely cause for the high variance values for Clashach. The high variance of Locharbriggs is caused by the spatial differences in permeability in all three orientations caused by the high anisotropy of this stone type. Results are presented in Table 3-11. There is no correlation between permeability and porosity/open porosity.

Stone Type	Permeability (mD)	Standard Deviation	Variance (%)
Blaxter	46	9	18
Bonhill	1749	-	-
Clashach	79	54	68
Corsehill	67	1	2
Cullalo	579	96	16
Doddington	763	242	32
Giffnock	93	26	28
Hazeldean	290	4	1
Locharbriggs	170/251	148/66	87/39
Scotch Buff	48	-	-
Stanton Moor	7	2	24

Table 3-11: Nitrogen permeability measurements for each sandstone. Two values are given for Locharbriggs that represent the average porosity from 3 orientations (170mD) and from 2 orientations perpendicular to bedding planes.

3.2.8 Compressive Strength Tests

Three uniaxial compressive strength tests were conducted using two different loading regimes. The first test used a continuous stress rate of 1 MPa/second, while the second and third tests used a more accurate and controlled rate of 0.5 MPa/second. Bonhill was not tested due to lack of sufficient sample. Results obtained from the second and third tests are thought to be more representative and generally show a smaller standard deviation between repeat measurements. The data show that Stanton Moor, Cullalo, Corsehill, Hazeldean and Clashach sandstones have the highest average strengths, while Locharbriggs has a much smaller value, which is around half of the Hazeldean value. The standard deviation and variance between repeat samples of Cullalo, Scotch Buff, Hazeldean and Locharbriggs are significant and emphasise the heterogeneities within these samples. Giffnock and Doddington samples show less variation between three and four repeat measurements respectively.

Measured values are therefore not accepted as being representative for each stone type due to the high variation in measurements. The results are shown in Table 3-12. It must also be noted that each test took place under dry stone conditions, unlikely to be experienced in a building façade. Rossana and Paola (2012) showed that the strength of metamorphic rocks were considerably reduced under wet conditions and they emphasise that the strength values of wet samples should be used when recommending suitable stone types for building façades. Stones were tested under dry conditions in order to follow the British standard procedure and so they could be compared to official Building Research Establishment (BRE) data on the same stones.

Official data from the BRE highlight the inaccuracies of the measured strength data in the present study. BRE values show that Clashach sandstone has the greatest compressive strength, followed by Hazeldean, Stanton Moor and Scotch Buff sandstones. The BRE data does show however that Locharbriggs sandstone is amongst the weakest in the study as also indicated by the values obtained here. Measurements made within this study generally underestimate the compressive strength of each sandstone (most notably with Clashach). However, the range of measured values for Blaxter, Corsehill

and Hazeldean agree with those given by the BRE. Official Cullalo strength values could not be found, while there is no data available for the weathered samples of Giffnock sandstone.

Many studies have investigated the relationship between stone strength and: (i) mineral composition (Price, 1966); (ii) porosity (Dunn et al., 1973; Benavente et al., 2004); (iii) fabric (Přikryl, 2001). Petrographic analysis and hydric testing of samples within the study show that many of the stones exhibit anisotropy that can significantly influence water movement and water absorption within the stone. As stones are commonly edge bedded and face bedded within a façade, these factors must also be adapted in strength testing.

Stone Type	Compressive Strength MPa	BRE Values MPa	Standard Deviation	Variance (%)
Blaxter	45 (32-53)	38-55	14	17
Clashach	45 (37 – 55)	132	7	15
Corsehill	62 (49 – 74)	68	22	17
Cullalo	49 (41 – 64)	-	12	22
Doddington	42 (38 – 44)	51 - 58	12	8
Giffnock	46 (40 – 50)	-	5	11
Hazeldean	58 (36 – 84)	84	2	43
Locharbriggs	28 (23 – 30)	47	7	14
Scotch Buff	45 (35 – 57)	76	7	24
Stanton Moor	51 (37 – 61)	79	6	16

Table 3-12: Measured compressive strength values and official BRE compressive strength values for each sandstone.
Standard deviation and variance values are given for measured compressive strengths within the study. The range of measured values is given in brackets following the averaged value.

3.3 Salt Characterisation

3.3.1 Ice Melting Capacity

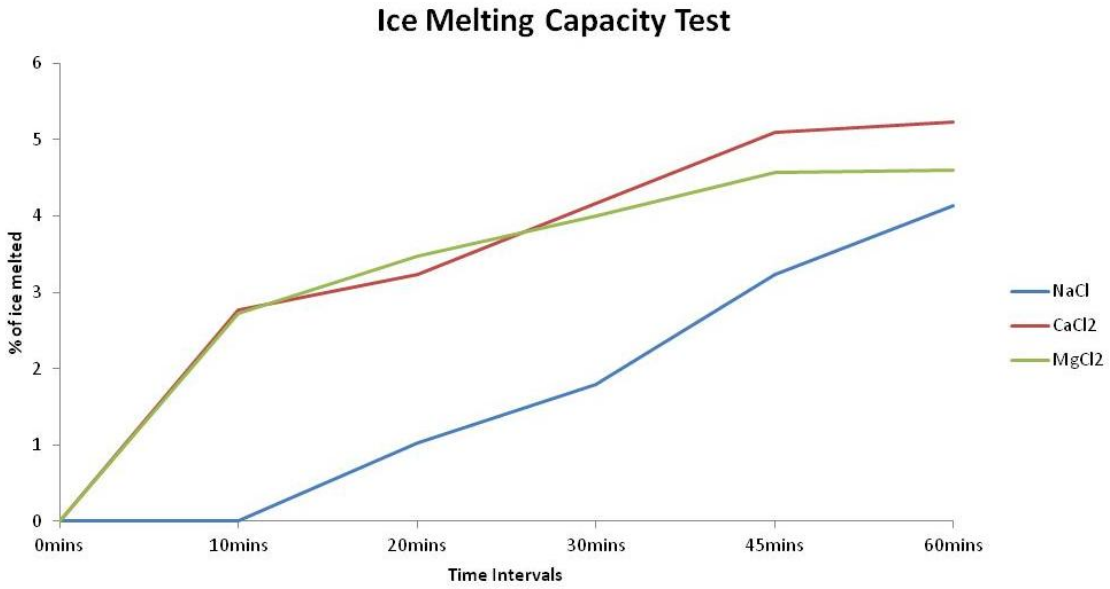

Figure 3-27: Average % of ice melted over 60mins for NaCl, $MgCl_2$ and $CaCl_2$.

Tests were conducted to assess the ice-melting effectiveness of each de-icing salt at a working temperature of -15°C using 1 g of each salt and 50 ml of water. Salt was evenly distributed over the surface of the ice, and the generated brines were measured after 10, 20, 30, 45 and 60 minutes. Six repeat samples were used for each salt, and averages were recorded. The test used $CaCl_2$, NaCl and $MgCl_2$.

Results indicate that both $CaCl_2$ and $MgCl_2$ are more effective and more responsive de-icing salts than NaCl (Figure 3-27). After the first 10 minutes, NaCl had a negligible effect on the ice, while both $CaCl_2$ and $MgCl_2$ started to melt ice immediately, with the two salts having very similar melting rates. Each salt showed similar melting rates over the following 20 minute period, with NaCl experiencing an increase in melting and $CaCl_2$ and $MgCl_2$ experiencing a slight decrease in their melting efficiency. After 30 minutes the ice melting rate of NaCl started to increase, while this decreased significantly for both $CaCl_2$ and $MgCl_2$ after 45 minutes. At the end of the test NaCl generated on average 2.1 g of brine, $CaCl_2$ 2.6 g and $MgCl_2$ 2.3 g.

A larger NaCl particle size contributed to greater undercutting and penetration rates, more focused melting and consequently better access to generated brines. Penetration and undercutting rates were reduced in the $CaCl_2$ and in particular $MgCl_2$ samples owing to the different particle sizes. It is thought that any generated brines here would have been trapped within the ice and were not accessible for weighing. Generally, values for $MgCl_2$ and $CaCl_2$ were lower than expected and are likely underestimated as a consequence of the entrapment of brine underneath and within the ice.

Importantly however, both $CaCl_2$ and $MgCl_2$ are faster acting than NaCl at -15^{o}C and have a greater ice melting capacity even with conservative measurements (i.e. not all of the generated brine was extracted for measurement). This was an expected result that confirms what is known in the literature about the three salts. These results demonstrate that particle size is an important function in the overall ice melting process. A larger particle size creates more focussed melting and a greater penetration rate. For salt to be efficient, it must penetrate through the ice and break the bond between the ice and the underlying substrate. This process will allow greater traction between vehicles and the road surface.

3.4 Hydric/Hygric Parameter Discussion

As discussed by authors including Benavente et al., (2004), the durability of building stone is influenced by the aggregate of a range of physical and mechanical parameters. It was for this reason that many analytical techniques were used to quantify the hydric, hygric, mechanical and petrographic properties of each stone type used in this study. It is important to summarise the properties of each stone type and to discuss the relationships between the most significant properties that are thought to influence decay.

Each stone type has been ranked in order of lowest – highest value for each individual test and results averaged for a basic rank order (Figure 3-28 and Figure 3-29). Stones were ranked on an ascending scale (1-11, with 11 being the number of stones in the study), with stones with the highest values for each test (high porosity, high water absorption, high capillary coefficient etc)

given low values, starting at 1. The stones with the lowest values for each test were given the highest numbered values. Results show a very similar pattern to the individual tests, with the highest ranking positions occupied by Bonhill, Locharbriggs, Corsehill and Doddington samples and the lowest by Hazeldean, Stanton Moor and Clashach. The comparative grouping of each sandstone is of more importance than the absolute ranking order. Interestingly, the top four samples with the highest average values are red sandstones, while the remaining samples are pale/blonde sandstones. Mineralogy and grain size/shape do not directly correlate to stone ranking placement. The two most mineralogically mature sandstones Cullalo and Clashach, are six places apart, while Stanton Moor, a mineralogically immature sandstone is located in the opposite end of the table to Corsehill and Locharbriggs sandstones. Using the ranking order, sandstones are organised into three separate groups (Table 3-13).

Group A samples have high porosities, ranging from 19 – 26%, connectivity values greater than 2.2, water absorption values generally above 8% and high capillary coefficient values, exceeding 170 g/m^2.

Group B samples have the greatest range in values, with both Doddington and Cullalo samples lying at the top end of this group, with capillary coefficient and porosity values close to those of group A. Average porosities range from 16 – 20%, connectivity values between 1.88 – 2.44, water absorption values between 5.5 – 7.02% and capillary coefficient values showing a large variation between 44 – 172 g/m^2.

Group C contains Hazeldean, Stanton Moor and Clashach, and is characterised by significantly lower values than those averaged in group A and B. Porosity ranges from 10-16%, and connectivity values are lower than 2.05, with an especially low value for Stanton Moor (0.67). There is no overlap between water absorption values, ranging from 2.97 – 4.64%, with only a slight overlap into group B with the Hazeldean capillary coefficient value. However, 70% of all Hazeldean capillary coefficient values are below the lowest Group B average of 44%. Clashach has the lowest average capillary coefficient value of 28 g/m^2, while 35% of all Stanton Moor samples showed values <22 g/m^2.

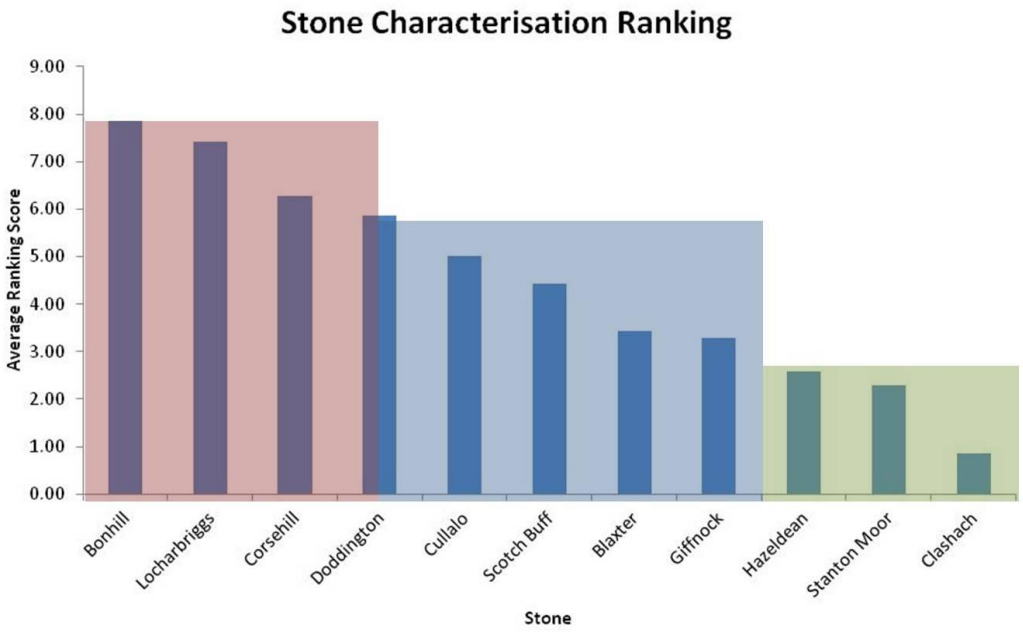

Figure 3-28: Stone characterisation ranking. Ranking is calculated from average capillary coefficient, water absorption, saturation coefficient, porosity and connectivity measurements.

Ranking calculated from average capillary coefficient, water absorption, saturation coefficient, porosity and connectivity measurements. Sandstones are ranked according to a ranking score, with 1: the highest values for each test and 11: the lowest value for each test. The sandstones are then comparatively ranked by subtracting the average ranking score from 10 and then divided into 3 distinct groups of average ranked high (red), medium (blue) and low values (green). Sandstones in the high (red) group show average high values for the above measurements and sandstones in the green group show consistent low values for each measurement.

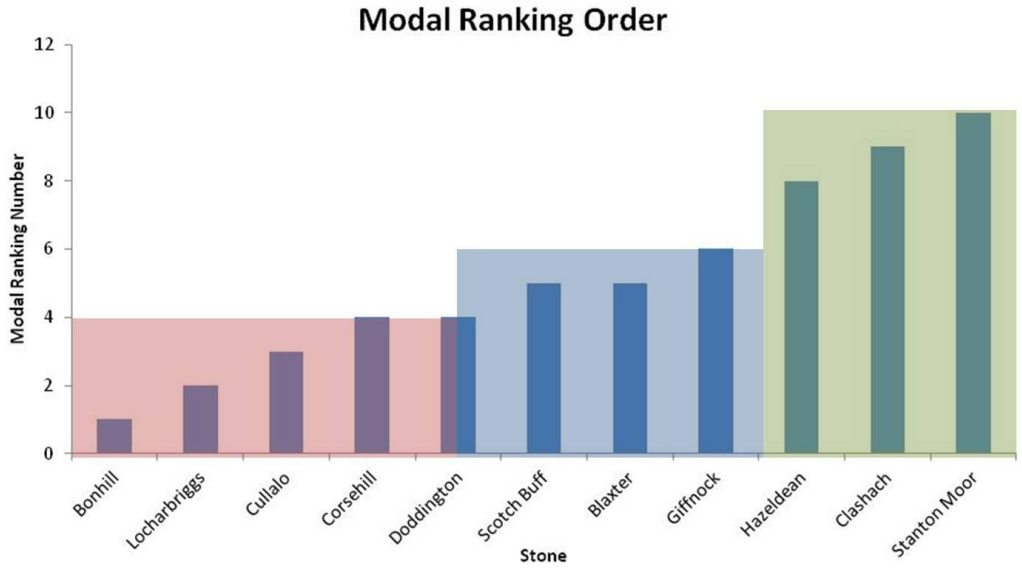

Figure 3-29: Modal ranking order for each sandstone.

The mode indicates the number that appears most often in the ranking scores for each stone. Modal ranking order highlights a similar trend whereby Bonhill, Locharbriggs and Corsehill had consistently low ranking numbers (indicating high values in each test) for and Hazeldean, Clashach and Stanton having consistently high ranking number (indicating low values in each test).

Large variations exist within many of the samples, most notably Corsehill, Locharbriggs and Cullalo sandstones. Figure 3-28 and Figure 3-29 indicate that even with the occurrence of high variance and standard deviation values in many of the hydric tests, most of the samples continue to fall within their designated groups (of high, medium and low hydric values), with minimal crossover. Furthermore, these high-medium-low groupings (as used throughout the chapter) show that both high and low estimates for most tests are sufficient to characterise each stone. Large variations within Locharbriggs, Cullalo and Hazeldean samples may be associated with anisotropy in the pore network.

Group A	Group B	Group C
Bonhill	Doddington	Hazeldean
Locharbriggs	Cullalo	Stanton Moor
Corsehill	Scotch Buff	Clashach
Doddington	Blaxter	
	Giffnock	

Table 3-13: Ranking groups for each sandstone. Group A: red, Group B: blue and Group C: green.

The assumption of normaility of sample was assessed, with results indicating a relatively normal distribution. Q-Q plots are provided in Appendix H. A clear correlation exists between water absorption and both the total and effective porosities. This correlation indicates that stones with a higher porosity can absorb a greater percentage of water under natural atmospheric pressures. Bonhill, Locharbriggs and Corsehill contain the highest of these values, while Stanton Moor and specifically Clashach samples have the lowest values. The addition of water into stone is an important parameter that can initiate many decay processes. The greater the pore space, the greater the amount of water that can infiltrate the stone. However, water absorption does not give information on fluid movement and transport within the stone, and what pore classes are filled under these conditions. The saturation and accessibility of micro-pores are shown to be extremely important factors influencing salt-induced decay (Buj and Gisbert, 2010).

Relationships exist between water absorption and total porosity, effective porosity and capillary coefficient. These parameters have correlation coefficients of 0.8, 0.9 and 0.9 and linear regression r^2 coefficient values of 0.64, 0.75 and 0.70, respectively. There are similar trends evident between

the capillary coefficient and (total porosity and open porosity) showing correlation values of 0.9 and r^2 values of 0.75 and 0.73, respectively.

It is difficult to draw on many of the aforementioned relationships (water absorption and porosity, capillary coefficient) without other sufficient knowledge of the pore structure itself. Clashach and Stanton Moor samples likely have low capillary coefficient values due to intense compaction between grains. Substantial quartz overgrowths are present in the Clashach sample and tightly interlocking calcite cement in Stanton Moor; the stones also have a tortuous pore network and a low effective and total porosity.

It must be noted that the existence of correlations between parameters do not imply a greater statistical influence of these parameters on stone durability/susceptibility, nor does it suggest the contrary, whereby values that deviate from the average trend are less important for stone durability.

The values of permeability, porosity, capillary uptake, water absorption and drying all help to explain the connectivity of the pore network, including the tortuosity and movement of moisture with the stone, which are of key concern to salt weathering processes. A combination of these factors will influence the expected durability/resilience of each stone to the crystallisation of different de-icing salts. The key properties each sandstone and their hypothesised durability to salt crystallisation are discussed in turn in this next section.

3.4.1 Bonhill

Bonhill is used red sandstone recovered from The University of Glasgow after recent renovation work. It is medium grained, mineralogically mature sandstone containing sub-rounded quartz and feldspar grains, lithic fragments and Fe-oxides. It contains the highest average porosity value of 24%, with a similar pore size distribution to Scotch Buff and Corsehill sandstones, containing a large pore size distribution, with 9.2% of pores within the 0.01 μm – 1 μm diameter range. It contains the highest permeability value, exceeding 1000 mD, the highest capillary coefficient and one of the highest water absorption coefficients. With an extremely high porosity and several

other subsequently high hydric values, Bonhill is regarded as a stone susceptible to salt-induced decay.

3.4.2 Locharbriggs

Locharbriggs is a medium grained, mineralogically immature red sandstone containing a high percentage of Fe-oxides and ferruginous clays. It has a clear fabric throughout, producing the anisotropy identified through hand specimen, capillary coefficient, permeability and ultrasonic velocity values. Locharbriggs has a high capillary coefficient, a high porosity of ~20%, high water absorption and high saturation coefficient values. This makes Locharbriggs an extremely absorbent stone, with a high salt absorption potential. The pore size distribution comprises 4.1 – 7.2% in the ≥50 μm pore range, while 13.2 – 27.3% is classified as microporosity (≤5 μm). The spatial distribution of this porosity is extremely important, with most of the micro-pores likely located within the narrow beds of the rock. Locharbriggs has a high constant drying rate and a high falling drying rate, with a moderate CMC and residual moisture level. This indicates that there must be a high connectivity throughout the sample for hydraulically connected drying and capillary dominated drying in the falling rate regime. The high water absorption and capillary absorption values, combined with a high percentage of spatially concentrated microporosity suggest that Locharbriggs is likely susceptible to salt-induced decay.

3.4.3 Corsehill

Corsehill is a texturally and mineralogically immature, fine grained sandstone, containing a high abundance of ferruginous clays. It has a similar clay abundance, and comparable porosity and ultrasonic velocity measurements with both Locharbriggs and Blaxter sandstones. Corsehill has a high porosity, with extremely high water absorption and capillary coefficient values. It has a slightly lower than average saturation value due to the relatively high amount of pore filling clays. The pore blocking effect of the clays also serves to reduce the constant drying rate of the stone. Corsehill has the fourth highest CMC value and the second highest residual moisture content measured here owing to the high porosity of the sandstone. These

values show that Corsehill has a poor drying efficiency, retaining a high percentage of moisture that when combined with a high porosity leaves Corsehill vulnerable to salt-induced decay.

3.4.4 Doddington

Doddington is a highly compacted, medium grained sub-arkose sandstone with a relatively high clay content. It has a high porosity with high water absorption, capillary coefficient and moderate-high saturation coefficient values, and contains a high proportion of macropores (12.5% >50 μm and 5.7% >100 μm). Doddington has the second lowest constant drying rate but has a low CMC value. It also has a lower falling drying rate than most other stones but contains a low residual moisture content at the end of the test. Due to the lack of micro-pores within the stone, but with a high porosity and a high water absorption capacity, it is likely that Doddington has a moderate-high resistance to salt decay.

3.4.5 Cullalo

Cullalo is a fine grained, mineralogically and texturally mature sandstone that contains an abundance of well rounded and compacted quartz grains. These properties give Cullalo with a large unimodal pore size distribution, with a high proportion of large pores (11.5% >50μm). High ultrasonic velocity measurements result from the high levels of compaction and anisotropy within the stone. Cullalo has a high porosity, with moderate water absorption and saturation coefficient values. It has an initial low constant drying rate but with a high CMC and high falling rate, Cullalo maintains hydraulic connectivity through capillarity. This drying regime prevents the onset of vapour dominated drying, whereby subflorescence would take place, and provides a regime whereby efflorescence on the surface of Cullalo is likely. With a lack of micro-pores, moderate water absorption and saturation values and high compaction between the quartz grains, it is predicted that Cullalo is resistant to salt-induced decay.

3.4.6 Scotch Buff

Scotch Buff sandstone is a medium grained, mineralogically mature sandstone composed of sub-angular – sub-rounded quartz grains of variable size. It is characterised by mid-range hydric values for almost all tests. It contains a relatively high percentage of micro-pores, with 9.1% of pores within the 0.1μm - 1μm diameter range, making it potentially vulnerable to salt-induced decay.

3.4.7 Blaxter

Blaxter, like Corsehill, is a mineralogically and texturally immature sandstone with a high clay content, as seen in hand specimen and thin section analysis. It is a stone with a medium porosity of around ~15%, with moderate water absorption and saturation values. MIP data reveals that Blaxter contains a high proportion of micro-pores (38.4% <5 μm) and a bimodal distribution, but does not contain any extreme hydric or hygric test values. Low saturation and capillary coefficient values suggest that much of this microporosity is inaccessible or poorly connected to the rest of the pore network, possibly due to tortuous pore connections and pore filling clays. Blaxter is likely to be a moderately durable stone.

3.4.8 Giffnock

Giffnock is a used sample taken from The University of Glasgow and is a sub-arkose sandstone, containing a majority of quartz grains with a dolomite cement throughout. It has high ultrasonic velocity values and a high apparent density, with low-medium porosity and low-medium water absorption values. It has a low saturation and capillary coefficient values. MIP analysis shows a high microporosity (33.4% <5μm) and drying experiments reveal slow drying rates, with a high CMC. A high microporosity and slow drying rates suggest that Giffnock is potentially vulnerable to salt decay. However, low saturation coefficient values suggest that much of this microporosity is inaccessible under atmospheric conditions, limiting the vulnerability of Giffnock sandstone to salt-induced decay.

3.4.9 Hazeldean

Hazeldean is a mineralogically mature sandstone, containing small amounts of feldspar and mica, with micas showing a weak linearity throughout. It has a highly compact texture with high ultrasonic velocity values. Hazeldean has low hydric values, with the lowest porosity, water absorption capacity, saturation and capillary coefficient values. It contains a high proportion of macropores, with the second highest constant drying rate amongst the sample set and both the lowest CMC and residual moisture content. Hazeldean dries in a similar way to Cullalo, with hydraulic flow connecting moisture at depth to the drying boundary. Low CMC and residual moisture contents are also caused by low water absorption and saturation values. These combined properties render Hazeldean as salt resilient sandstone.

3.4.10 Stanton Moor

Stanton Moor is a mineralogically and texturally immature sandstone, with a high clay content. There is a high distribution of grain sizes that show intense compaction throughout, as evidenced by high ultrasonic velocity values. It has a low-moderate porosity of ~13-15% and a high proportion of micro-pores. High saturation values show that much of this microporosity is accessible, but with low permeability, connectivity and capillary coefficient values, it is likely that Stanton Moor has a very tortuous pore network. Low drying values, high CMC and high residual moisture content is caused by this high tortuous porosity, with much of the drying taking place within the vapour phase. This could lead to crystallisation within the pores under non-equilibrium conditions. Stanton Moor is therefore predicted to be susceptible to salt-induced decay.

3.4.11 Clashach

Clashach is a mineralogically and texturally mature, fine-medium grained sandstone, containing a large proportion of well cemented quartz grains. It has some of the lowest hydric values, with extremely low total and effective porosities of 10% and 6% respectively and the lowest water absorption and capillary uptake coefficients. It contains a bulk percentage of large pores, with the highest percentage of pores >100 μm in diameter. The high

compaction and low porosity of Clashach sandstone contributes to a high compressive strength and high predicted durability.

4 Stone Durability Results

Stone durability tests are commonly used to artificially accelerate natural processes that affect building stone by exposing samples to extreme weathering regimes under controlled laboratory conditions. From these tests, the key mechanisms of decay can be identified and understood, and predictions made regarding stone behaviour and long-term durability.

The aim of this thesis is to understand the mechanisms of salt crystallisation within sandstone and to identify the most important stone properties governing these mechanisms. Results from three salt crystallisation tests and one freeze-thaw test on several sandstone types are reported.

Repeat salt crystallisation tests were performed in order to optimise the test procedure by better replicating natural weathering regimes experienced by the stone. Two hypotheses were proposed at the start of these experiments:

- (1) The main factor controlling dry weight loss and alteration of the stone samples is salt type and the various mechanisms of salt crystallisation.

- (2) The main factor controlling dry weight loss and alteration of the stone samples is the stone type and the petrographic properties of the samples.

The reality of salt crystallisation within porous materials is, however, a far more complex process than is alluded to by these hypotheses. An awareness of experimental influences on stone behaviour within these tests is essential in understanding and identifying the natural responses to salt crystallisation that are less influenced by the experimental procedure. A critique of durability test procedures is presented in Chapter 8.

A consistent sample naming system is used across each salt crystallisation test for clarity. The first letter corresponds to the sandstone type (i.e. Blaxter = B), the second letter to the salt treatment (i.e. NaCl = N), and the number to differentiate the number of repeat samples (i.e. 1, 2, 3 and 4). In samples that contain an inherent anisotropy (Blaxter, Cullalo and Locharbriggs), two repeat samples per salt type were used in tests 2 and 3 whereby these samples absorbed salt solution perpendicular to planes of anisotropy, and dried parallel to their planes of anisotropy (opposite to the other remaining samples). These samples are identified with a 'P' placed prior to the sample number (i.e. LNP2 = the second parallel/perpendicular Locharbriggs sample subject to NaCl). In addition, the notation '$_1$' corresponds to test 1, '$_2$' to test 2, '$_3$' to test 3, and '$_{ft}$' to the freeze-thaw test. Lastly, when giving property values of samples prior to salt treatment, the prefix '$_{pre}$', is used, while '$_{post}$', is used for property values after salt treatment. This naming system is given in Table 4-1.

Sandstone	Notation			
	Treatment			
	NaCl (N)	$MgCl_2$ (M)	$CaCl_2$ (C)	Chloride blend (CB)
Blaxter (B)	BN	BM	BC	BCB
Bonhill (BO)	BON	-	BOC	BOCB
Clashach (CH)	CHN	-	CHC	CHCB
Corsehill (C)	CN	CM	CC	-
Cullalo (CL)	CLN	CLM	CLM	CLCB
Doddington (D)	DN	DM	DC	-
Giffnock (G)	GN	GM	GC	GCB
Hazeldean (H)	HN	HM	HC	-
Locharbriggs (L)	LN	LM	LC	LCB
Scotch Buff (SB)	SBN	-	SBC	SBCB
Stanton Moor (SM)	SMN	SMM	SMC	SMCB

Table 4-1: Sandstone sample notation. (-) indicates that these samples were not submitted to testing by the corresponding salts.

Numerical values of weight loss/gain and hydric properties are given as mean values for each sandstone type, generally from four repeat samples unless otherwise stated. Error bars on graphs are given as the upper and lower ranges of measured values for each sandstone. NaCl and $CaCl_2$ were used throughout every crystallisation test, while the chloride blend was used in the pilot study and $MgCl_2$ in the second and third tests. Not all sandstone types were exposed to every salt due to the progression of each test. New

samples were introduced into the second test, while sample availability dictated what stones were dropped for this test. Stones identified as durable from the first and second tests were also dropped from the third crystallisation test.

4.1 Salt Crystallisation Test (II)

The second salt crystallisation test builds on results from the first by using a modified procedure. Eight sandstone types, with four samples per salt type (7 samples for Locharbriggs, and 6 samples for Blaxter and Cullalo), were tested against the effects of NaCl, $CaCl_2$ and $MgCl_2$, using 117 samples in total. The resistance to salt crystallisation is expressed by the weight change after every cycle, observed damage characteristics on the stone surface by photography after every fourth cycle, and changes to their hydric properties and by laser scanning after completion of the test. This test was discontinued after 16 cycles due to contamination from the tape that was used to seal the samples. The same number of water control samples was also included per stone type.

4.1.1 Weight change

Weight change was measured for each sample after every cycle, highlighting the characteristic three stage weight development as described in section 11.1.1. The results reported in this section are averaged values from between 4 and 7 samples per stone type. Water control samples showed negligible mean weight change for each sandstone.

4.1.1.1 *NaCl*

Maximum weight values were recorded after cycle 16 (the end of the test) in all but Giffnock sandstone, where an average maximum was reached after 10 cycles. Locharbriggs, Cullalo, Giffnock and Blaxter sandstones show two stages of weight evolution, with Locharbriggs, Cullalo and Blaxter reaching stage two after 12 cycles, and Giffnock after 10 cycles. Both Blaxter and Cullalo show a slight increase in weight between cycles 15 and 16 and indicate a movement back to stage one increase. Stage two is more defined in Locharbriggs and Giffnock sandstones, while Corsehill, Hazeldean and

Doddington show a continued linear trend in salt uptake. Stanton Moor also shows a linear increase but with greater variability in weight change and a slight drop in weight recorded between cycles 10 and 11.

Corsehill had the greatest uptake of NaCl with an average maximum weight increase of 4.17%, with Locharbriggs, Stanton Moor and Doddington also accumulating similar values of NaCl at 2.50%, 2.45% and 2.26%, respectively. Hazeldean, Giffnock and Cullalo had the lowest average maximum weight gain values of 1.33%, 1.52% and 1.66%, respectively. Only Locharbriggs, Stanton Moor and Giffnock experienced any notable weight loss throughout the test following NaCl crystallisation and subsequent material loss. Periods of weight loss are identified in Figure 4-1 by falls in weight gain. Stanton Moor had the greatest total average weight loss, while Locharbriggs was more variable (with two samples experiencing total losses of 0.73% and 0.46% and a further three samples experiencing no loss). Average final weight values are directly influenced by maximum accumulation values, with Corsehill having the greatest final weight and Hazeldean the lowest. The weight evolution of NaCl samples is shown in Figure 4-1.

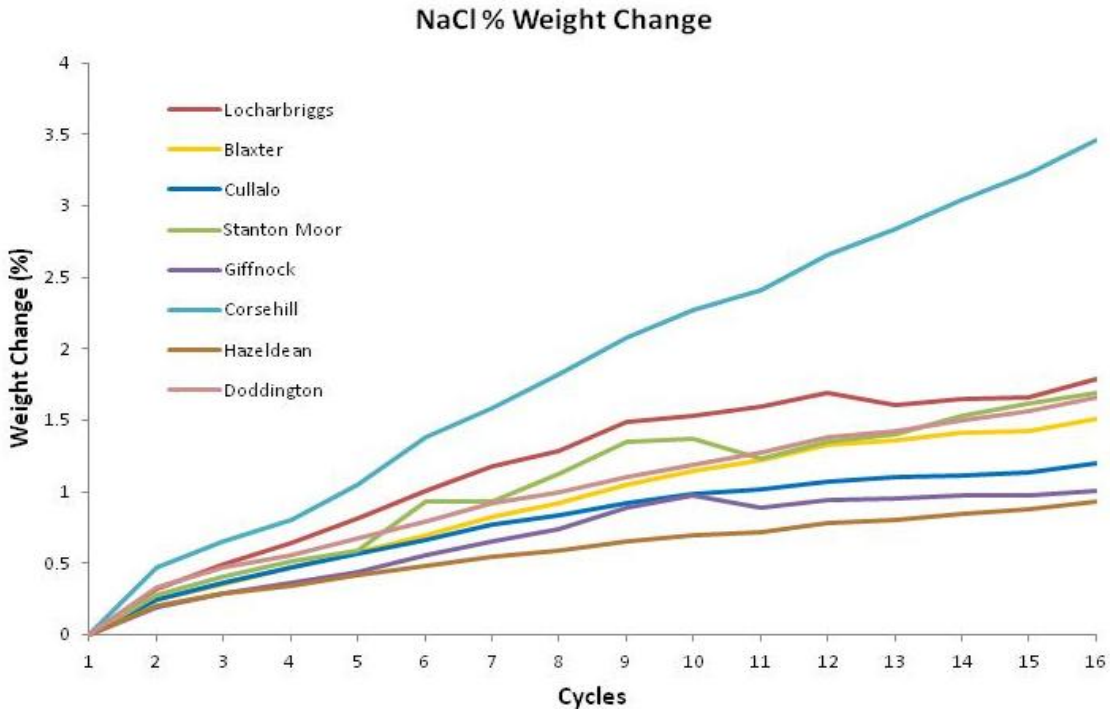

Figure 4-1: Mean percentage weight evolution of NaCl treated sandstones.

4.1.1.2 *$MgCl_2$*

All $MgCl_2$ samples apart from Hazeldean progressed into stage two. Stage two was reached after 14 cycles in Blaxter, Cullalo, Stanton Moor, Giffnock and Doddington sandstones, while Locharbriggs and Corsehill reached stage two after 11 and 12 cycles, respectively. Doddington, Corsehill and Locharbriggs start to show weight loss after 14 cycles, with Locharbriggs and Corsehill showing initial weight loss after 12 cycles.

Similar trends of averaged maximum salt uptake to NaCl are evident in Corsehill sandstone, with an average weight increase of 5.05%. Locharbriggs and Doddington have the second and third highest uptake values of 3.17% and 2.88% respectively. Hazeldean has the lowest value with an increase of 1.65%, while Cullalo, Stanton Moor and Giffnock sandstones all show similar average uptake values. The weight evolution of $MgCl_2$ samples is presented in Figure 4-2.

$MgCl_2$ induced greater decay than NaCl in most sandstones, with the exception of Giffnock and Stanton Moor, which experienced greater weight loss in the NaCl test. Corsehill and Locharbriggs experienced the greatest weight loss relative to their continued weight gain from salt accumulation, with Hazeldean and Giffnock encountering very little decay. Final weights were directly related to the magnitude of salt absorption in each sample, with Corsehill presenting the highest average final weight, even in the presence of material loss, and Hazeldean the lowest. The remaining stones had similar values ranging between 1.59% and 1.93% weight increase.

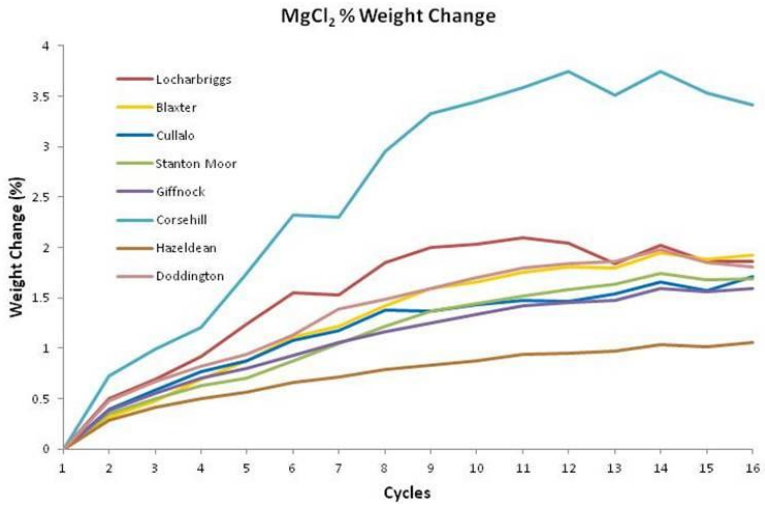

Figure 4-2: Mean percentage weight evolution of $MgCl_2$ treated samples.

4.1.1.3 *$CaCl_2$*

$CaCl_2$ produced similar trends in weight change to $MgCl_2$ samples, with every sandstone characterised by a well defined plateau in the weight change graph, indicative of the second stage (Figure 4-3). Furthermore, $CaCl_2$ was absorbed to a greater extent and at a faster rate than $MgCl_2$ and NaCl salts in every sample. The second stage of weight progression is met after cycle 8 in Locharbriggs, cycle 9 in Corsehill and Doddington and after cycle 10 in Giffnock and Stanton Moor, with the remaining samples reaching stage two between 12 (Cullalo and Blaxter) and 14 cycles (Hazeldean). Locharbriggs shows the greatest variability in weight change, with weight losses recorded in certain samples after only six cycles and then continuously, in most samples, after cycle 11. In addition to Locharbriggs, both Corsehill and Doddington progress into the third stage of weight loss. Sustained decay occurs in Corsehill and Doddington samples after 10 and 14 cycles, respectively.

$CaCl_2$ produced the greatest average weight loss of all three salts in all but Stanton Moor and Giffnock sandstones, while every sandstone showed an increase in their average maximum salt accumulation with $CaCl_2$. In particular, Locharbriggs and Cullalo exhibit increases of 1.55% and 1.26% respectively over equivalent $MgCl_2$ values. Higher average final weights were also recorded in all but Corsehill sandstone, which suffered the greatest weight loss of any stone across the full test.

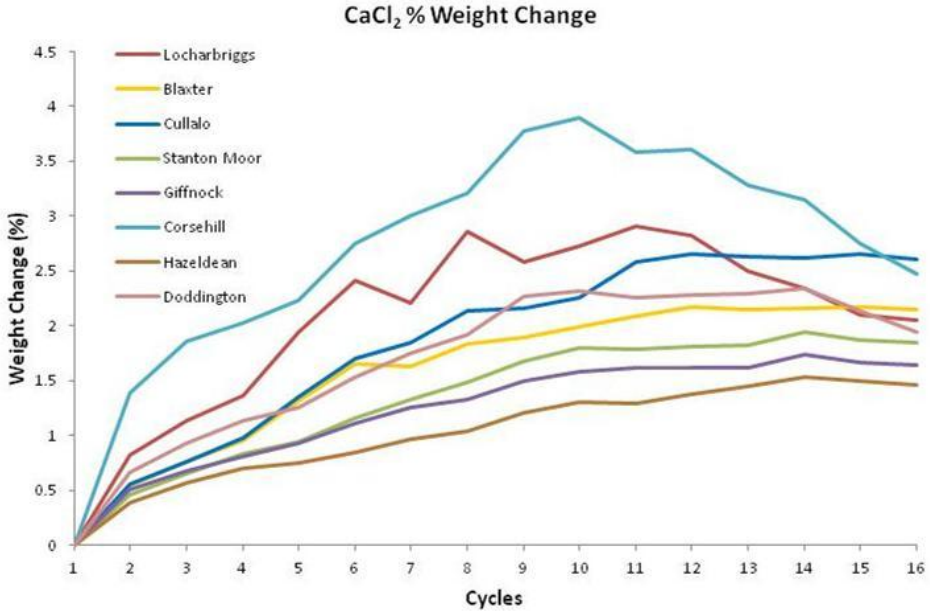

Figure 4-3: Mean percentage weight evolution of $CaCl_2$ treated samples.

4.1.1.4 *Weight change summary*

Corsehill experienced the greatest weight change across all three salts, including the greatest average maximum salt accumulation in each salt (Figure 4-4), the greatest average maximum weight loss with $MgCl_2$ and $CaCl_2$ (Figure 4-5) and the highest average final weights with NaCl and $MgCl_2$ salts (Figure 4-6). Stanton Moor (SMN_{2post}), Locharbriggs (LN_{2post}), and Giffnock (GN_{2post}), were the only sandstones to experience weight loss with NaCl (Figure 4-5), while Giffnock and Stanton Moor had some of the lowest weight changes with $MgCl_2$ and $CaCl_2$. Hazeldean had the lowest values of maximum salt accumulation, maximum weight loss and average final weights across every salt, while Locharbriggs experienced, on average, the greatest variability in weight change between repeat samples for each salt as illustrated by the large error bars for averaged Locharbriggs data (Figure 4-4, Figure 4-5 and Figure 4-6).

$CaCl_2$ treatment caused a greater salt accumulation in every sample, with substantially higher weight loss values in all but Giffnock and Stanton Moor sandstones. NaCl had the lowest average weight change, while $MgCl_2$ had mid-range values in weight loss, weight gain and final average weights but followed a near identical weight evolution trend to $CaCl_2$ in all sandstones.

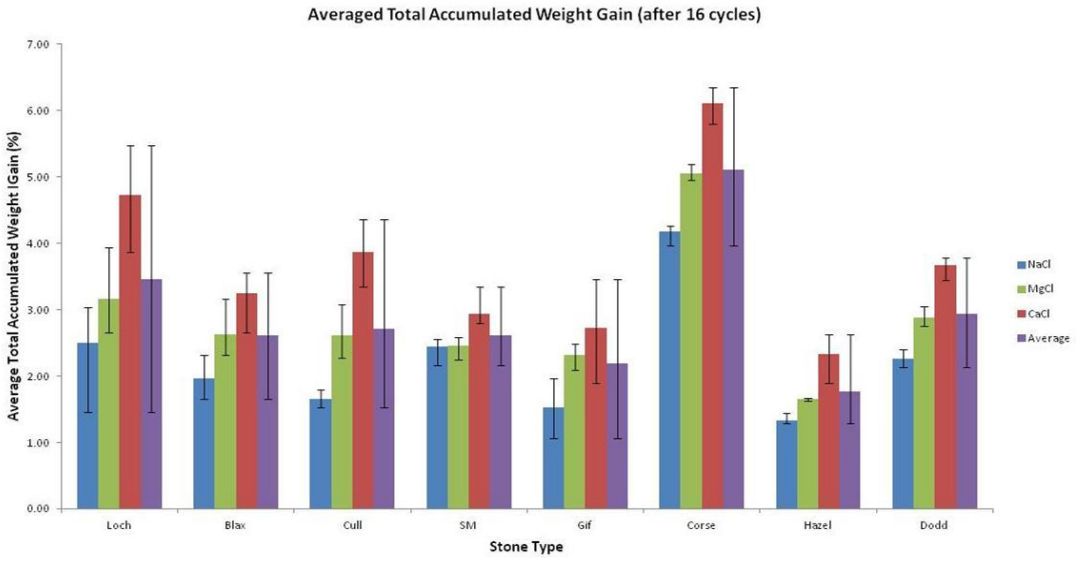

Figure 4-4: Average total accumulated percentage weight gain of eight sandstones subject to NaCl, $MgCl_2$ and $CaCl_2$ throughout 16 salt crystallisation cycles.

Loch: Locharbriggs, Blax: Blaxter, Cull: Cullalo, SM: Stanton Moor, Gif: Giffnock, Corse: Corsehill, Hazel: Hazeldean, Dodd: Doddington. Error bars represents the range of measured values for each sandstone. These values were calculated as the percentage difference in the final weight in relation to the original pre-test weight for each stone subject to each salt.

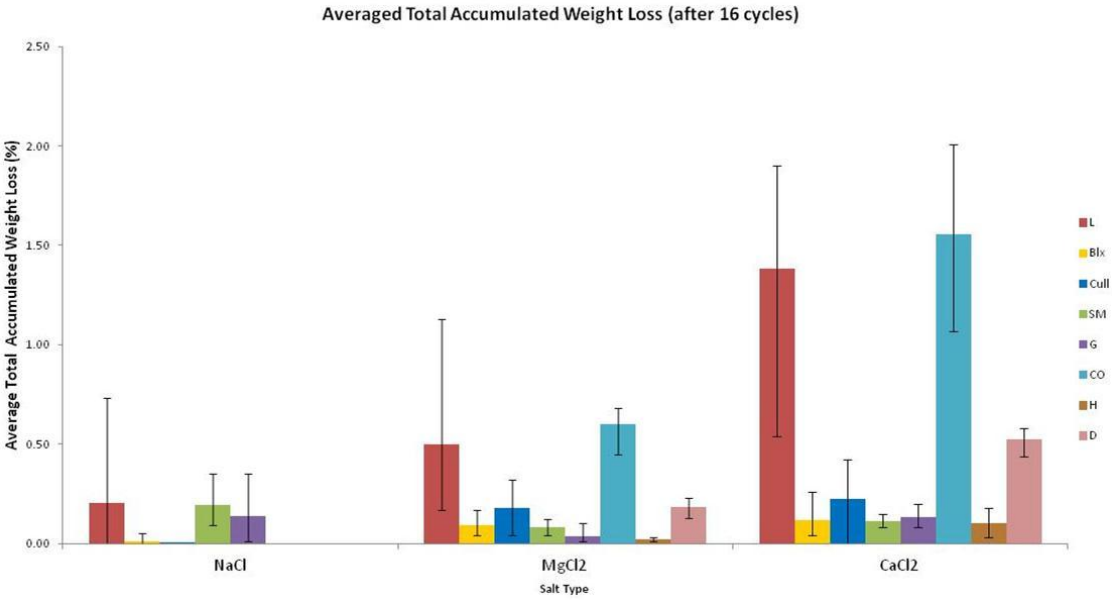

Figure 4-5: Average total accumulated percentage weight loss of eight sandstones subject to NaCl, $MgCl_2$ and $CaCl_2$ throughout 16 salt crystallisation cycles.

L: Locharbriggs, Blx: Blaxter, Cull: Cullalo, SM: Stanton Moor, G: Giffnock, CO: Corsehill, H: Hazeldean, D: Doddington. Error bars represents the range of measured values for each sandstone. These values were calculated by adding the total amount of percentage weight loss at any point during the test, neglecting any weight gain for each repeat sandstone block subject to each salt. This should therefore represent the total quantifiable amount of material that was lost on average for each sandstone subject to each salt and does not concern the weight gain.

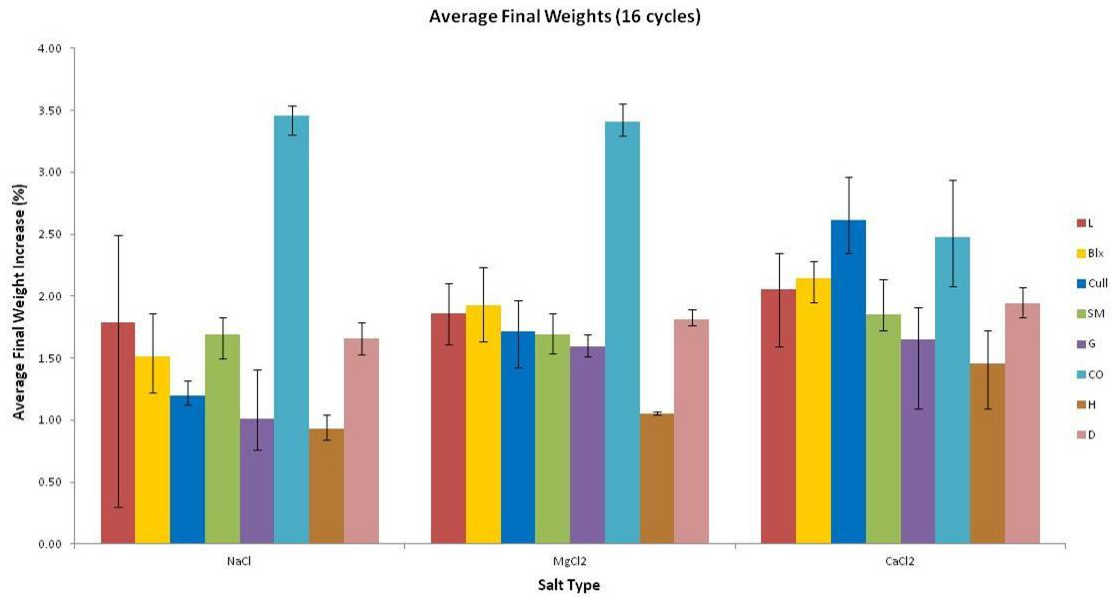

Figure 4-6: Average percentage final weights of eight sandstones subject to NaCl, $MgCl_2$ and $CaCl_2$ after 16 salt crystallisation cycles.

L: Locharbriggs, Blx: Blaxter, Cull: Cullalo, SM: Stanton Moor, G: Giffnock, CO: Corsehill, H: Hazeldean, D: Doddington. Error bars represents the range of measured values for each sandstone. The values are the same as those in Figure 4-4 but presented in order to highlight the differences in each salt on average.

4.1.2 Visual surface change

The visual change to each sample surface was monitored by photography after 2, 8 and 16 cycles in the second test. After the second cycle, every NaCl and $MgCl_2$ sample showed efflorescence on the drying face, while $CaCl_2$ samples appeared darker and had no visible efflorescence. A small fracture caused by the drilling of reference screws in sample $BN4_{2post}$ started to be exposed, with salts preferentially crystallising within the fracture. Interestingly, there is the early onset of a salt efflorescence horizon located ~35 mm above the base of most NaCl and $MgCl_2$ samples. With NaCl, this horizon indicates a change in efflorescence morphology, while in $MgCl_2$ samples, it represents the limit of efflorescence coverage.

By the eighth cycle most $CaCl_2$ samples of every stone type had started to show small amounts of surface efflorescence located in the same lower regions as in the NaCl and $MgCl_2$ samples. Corsehill $CaCl_2$ samples showed granular decay affecting the bottom edge of the blocks extending to roughly 20 mm above their base. A similar change is also evident in Corsehill $MgCl_2$ and one Locharbriggs $MgCl_2$ sample but to a lesser extent. Cullalo samples had significantly greater $MgCl_2$ efflorescence, with salt crystallisation following the internal structure of the stone. Other $MgCl_2$ samples continue to show the same efflorescence distribution as cycle 2 but with a higher volume of salt crystallisation. The NaCl efflorescence boundary becomes more pronounced with each cycle, and a greater contrast in salt texture becomes evident on either side of the boundary by cycle 8. The upper area of efflorescence is characterised in Doddington (DN_2) and Cullalo (CLN_2) samples by a thin salt crust extruding ~5 mm from the surface, while smaller salt crystals dominate the lower section.

After 16 cycles Corsehill $CaCl_2$ samples start to show greater signs of decay, characterised by granular disintegration near their base. One Corsehill sample also shows the detachment of ~1 mm thick layers from the top 25 mm of the sample as highlighted in Figure 4-7. Locharbriggs $CaCl_2$ samples continue to show substantial material loss through granular decay that is restricted to the capillary zone of the stone. $MgCl_2$ shows similar decay trends to $CaCl_2$ with most granular decay focussed in the lower edges and corners of the samples.

By the 16th cycle, every sample has experienced an increase in surface efflorescence, with Cullalo NaCl and $MgCl_2$ samples in particular, displaying the largest accumulations (Figure 4-8). Locharbriggs NaCl samples experience evenly distributed granular decay across their exposed face, while Blaxter NaCl samples have decay focussed on the bottom corners and edges. Giffnock, Hazeldean and Stanton Moor show little visual change and low volumes of efflorescence across every salt, with the exception of Hazeldean NaCl samples that show increased efflorescence located near the top of the samples and one Giffnock NaCl sample that shows extension and increased roughness of the front face. Other sandstones show a continued trend in efflorescence and decay from earlier cycles.

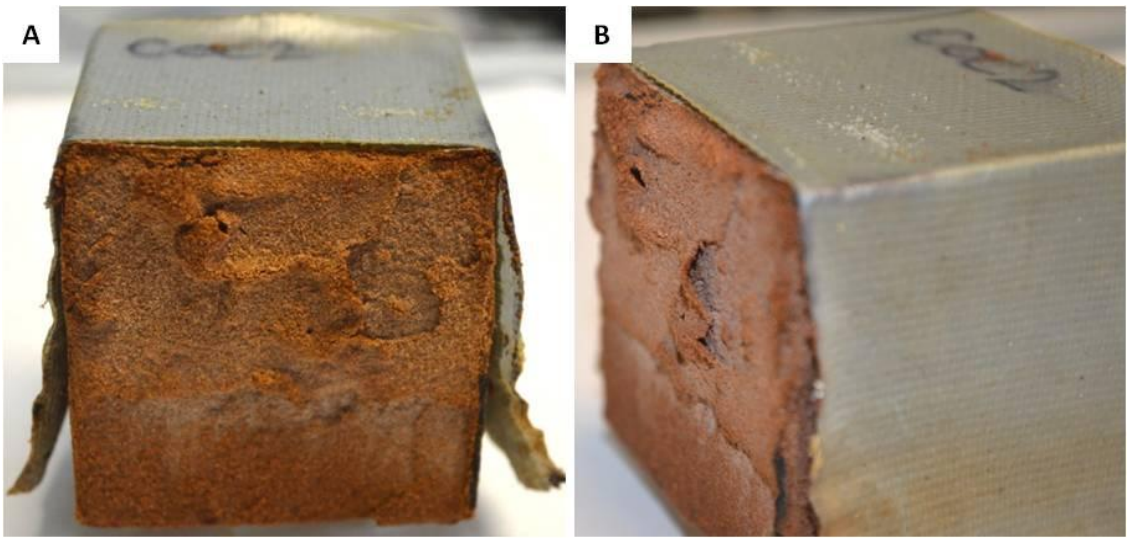

Figure 4-7: $CC2_{2post}$ sample after 16 salt crystallisation cycles.
$CC2_{2post}$ samples after 16 $CaCl_2$ salt crystallisation cycles. (A): Front face showing detachment of flakes from the top 25 mm, with substantial granular taking place below this level. (B): Side view showing the relief and estimation of the thickness of the flakes.

NaCl and $MgCl_2$ salts cause more efflorescence than $CaCl_2$, with a greater percentage of $CaCl_2$ crystallising internally in each sandstone. Most decay was focussed in the lower sections of the samples in what is the main capillary zone, containing the greatest volume of moisture during the absorption phase. Interestingly, it is above this zone that a change in NaCl efflorescence texture is located. Efflorescence in this top section is characterised by a thin hollow salt crust extruding several mm's from the stone surface. This salt crust is explained by a decrease in salt concentration at this level and the absence of repeat wetting and drying cycles continually dissolving it; as experienced in the lower sections of the stone. This process generates a hardened salt crust that continually dries out over time. The bottom section

of each stone experiences greater material loss due to the blocking of surface pores from substantial crystallisation. The blocking of surface pores can induce increased subflorescence as the drying boundary recedes into the stone.

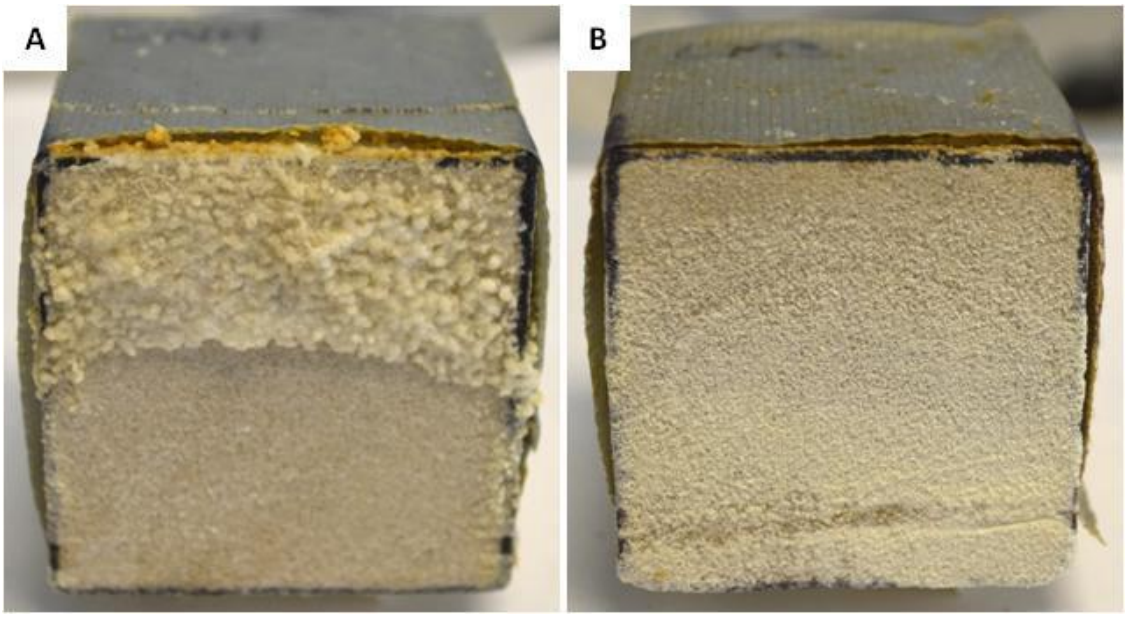

Figure 4-8: Cullalo samples after 16 salt crystallisation cycles.
(A): $CLN1_{2post}$ sample illustrating the distinctive salt horizon that separates the bottom capillary zone and a drier top section. The top section is characterised by a dry hollow salt crust and the bottom capillary zone by a thinner salt crust. (B): $CLM3_{2post}$ sample showing a large $MgCl_2$ efflorescence completely covering the front face of the block.

Cullalo experienced the greatest efflorescence with every salt, while Stanton Moor and Giffnock samples on average, with the exception of one Giffnock NaCl sample, had the lowest visual change across every salt. Corsehill had the greatest $CaCl_2$ decay, followed by pronounced visual changes in Locharbriggs and Doddington $CaCl_2$ samples. Table 4-2 summarises the notable visual changes to each sandstone.

Stone Type	Notable visual changes to each sandstone subject to each salt		
	NaCl	**$MgCl_2$**	**$CaCl_2$**
Blaxter	GD, F, E_{thin}	E_{minor}	-
Corsehill	E_{thick}, GD_{minor}	GD_b, E_{minor}	Significant GD, S
Cullalo	Significant E_{thick}	Significant E_{thin}	E_{minor}
Doddington	E_{thick}	E_{thin}	GD
Giffnock	E_{minor}, GD in 1 sample / -	-	-
Hazeldean	E_{thin}	-	-
Locharbriggs	E_{thick}, GD	E_{minor}, GD	GD
Stanton Moor	E_{thin} / GD	-	-
NaCl	Granular decay, some fracturing between screws, and efflorescence in every stone type.		
$MgCl_2$	Thin, minor efflorescence coverage, and some granular decay in Locharbriggs and Corsehill.		
$CaCl_2$	Generally very low change in most stones and minor efflorescence coverage. Granular decay in Doddington, Locharbriggs and especially Corsehill.		

Table 4-2: Summary of main visual changes in each stone type and for each salt. GD: granular decay, E: efflorescence, E_{minor}: minor efflorescence coverage, E_{thin}: thin efflorescence coverage (generally in lower capillary zone), E_{thick}: thick efflorescence coverage (generally in top zone), F: fracturing of stone surface, S: scaling surface decay, (-): no change.

4.1.3 Changes to fluid movement within the pore network

The hydric properties of the stones were measured on completion of the crystallisation test, with results compared to the pre-tested values of the same samples. Repeat hydric tests were performed on desalinated samples after the test in order to understand the effects of salt crystallisation on water absorption capacity and capillary uptake rates. Select samples were chosen to be analysed, with post-analysis carried out after one month of desalination in de-ionised water and after each sample was trimmed using a lubricated trim saw to remove pore blocking contaminants.

4.1.3.1 *Capillary coefficient changes: pore sizes*

Most samples showed a decrease in their capillary coefficient after 16 cycles with each salt. Only Locharbriggs, Giffnock and Hazeldean samples experienced increases in their capillary coefficient across different salts. Locharbriggs (LM_{2post}) and Giffnock (GM_{2post}) only experienced increases from $MgCl_2$, while Hazeldean experienced increases from $MgCl_2$ and $CaCl_2$. Changes to the Giffnock $MgCl_2$ and Hazeldean $CaCl_2$ samples are not accepted as representing statistically significant change due to the extremely large deviation between two repeat samples of each sandstone subject to $MgCl_2$ and $CaCl_2$, respectively.

$CaCl_2$ caused the greatest average decrease in capillarity across every stone type (minus one Hazeldean sample), with $CaCl_2$ samples showing a combined average decrease of 19.59%, compared to a decrease of 17.14% for NaCl and an average increase of 12.80% for $MgCl_2$ (minus one Giffnock sample). Doddington (DN_{2post}) and Corsehill (CN_{2post}) showed the greatest decrease in capillarity with NaCl, while Doddington (DM_{2post}) and Cullalo (CLM_{2post}) experienced the greatest decrease in capillarity with $MgCl_2$ and Doddington (DC_{2post}) and Blaxter (BC_{2post}) with greatest decrease in capillarity with $CaCl_2$. Stanton Moor had the lowest change in capillarity across all three salts, while Giffnock, with the exception of one repeat $MgCl_2$ sample, experienced limited change in capillarity across all three salts. The percentage difference in capillary coefficient for each sandstone across each salt is shown in Figure 4-9.

In general, NaCl caused a decrease in the capillary coefficient across all sandstones. Stanton Moor had the lowest average change with each salt, while Hazeldean and Doddington had the greatest average change across all three salts. Interestingly, the large changes experienced by Hazeldean (HC_{2post}), Cullalo (CLC_{2post}) and Blaxter (BC_{2post}) $CaCl_2$ samples were unexpected, due to their low weight change values and absence of visual damage.

The control samples for sandstone type, with the exception of Stanton Moor ($SMCON_{2post}$), experienced large changes to their capillary coefficient, often exceeding the values of change in each salt treated stone. Locharbriggs ($LCON_{2post}$), Cullalo ($CLCON_{2post}$) and Doddington ($DCON_{2post}$) experienced the greatest reductions in their capillary coefficient, while Hazeldean ($HCON_{2post}$) and Giffnock ($GCON_{2post}$) control samples both had large increases in theirs. Smaller changes in the capillary coefficient in Stanton Moor ($SMCON_{2post}$), Blaxter ($BCON_{2post}$) and Corsehill ($CCON_{2post}$) control samples results from a reduction in the total amount of water absorbed as opposed to a reduction in the rate of water absorption.

Only Locharbriggs $MgCl_2$, Blaxter $CaCl_2$, Corsehill NaCl, $CaCl_2$, Hazeldean $MgCl_2$ and all Doddington samples treated with each salt experienced average changes greater than their control counterparts. The significance of these results are unclear and do not definitively explain, nor differentiate between the effects of heating and cooling, wetting and drying and salt crystallisation on water uptake rate and the associated stone properties that influence this.

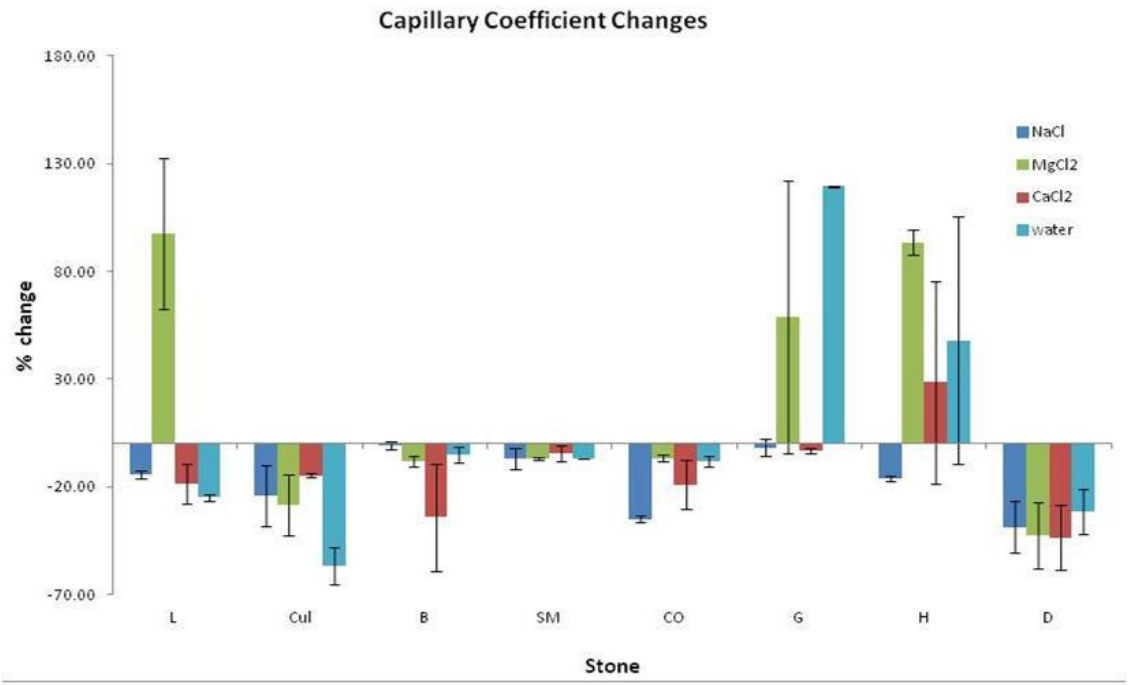

Figure 4-9: Mean percentage change in capillary coefficient relative to pre-tested values on the same samples. (Average of two repeat samples per stone type).

L: Locharbriggs, Cull: Cullalo, B: Blaxter, SM: Stanton Moor, CO: Corsehill, G: Giffnock, H: Hazeldean, D: Doddington. Error bars represent the upper and lower ranges of measured values for each sandstone.

4.1.3.2 *Water absorption changes: connected porosity*

Most samples show a consistent decrease in their water absorption capacity after the experiments. All three salts on average cause similar decreases in water absorption, with the average changes for each salt within 1% of each other. Cullalo and Doddington had the greatest average decrease with all salts which were over double the value of other stones. Giffnock on the other hand showed a small increase in some samples across each salt. Stanton Moor had the lowest change of 2.54% averaged across all three salts and no change associated with NaCl. Locharbriggs had similar values of decrease with every salt (~-7%), while Hazeldean recorded high values of -6.1%, -10.23% and- 9.7% with NaCl, $MgCl_2$ and $CaCl_2$ salts respectively.

Locharbriggs, Cullalo, Corsehill and Doddington control samples experienced a decrease to their water absorption coefficient, while the remaining sandstones all experienced increases. The greatest changes to control samples were experienced by Cullalo, Stanton Moor, Giffnock and Hazeldean. After the subtraction of these errors, Doddington continued to experience the greatest reduction of water absorption across every salt, while Locharbriggs

and Corsehill also expressed larger decreases than the remaining sandstones. The results from Giffnock and Stanton Moor were not corrected to incorporate these errors, as control samples experienced larger changes than those measured for all three salts. It is considered that only Doddington sandstone, after the correction for errors, presents values representing change in water absorption due to salt crystallisation. Only Doddington presented values of change that exceeded 10% decrease after the correction for errors. The percentage difference in water absorption for each sandstone across each salt is shown in Figure 4-10.

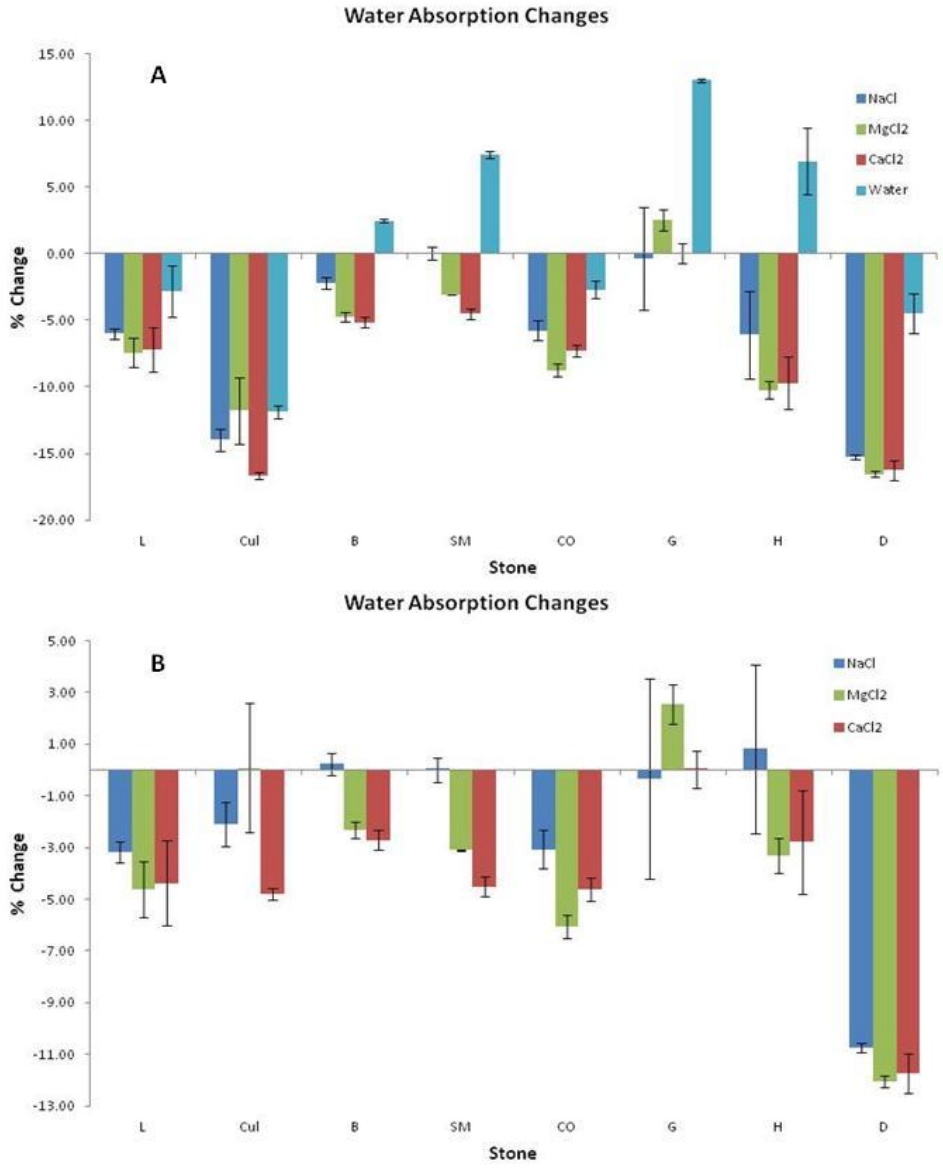

Figure 4-10: Mean percentage change in water absorption relative to pre-tested values on the same samples. (Average of two repeat samples per stone type).

L: Locharbriggs, Cull: Cullalo, B: Blaxter, SM: Stanton Moor, CO: Corsehill, G: Giffnock, H: Hazeldean, D: Doddington. Error bars represent the upper and lower ranges of measured values for each sandstone. A: Mean percentage change in water absorption relative to pre-tested values on the same samples. B: Mean percentage change in water absorption relative to pre-tested values on the same samples minus control values.

4.2 Salt Crystallisation Test (III)

A final crystallisation test was undertaken following the contamination problems experienced in the second test. Five sandstones were used in this test in accordance to their performance from the second test. Two batches of Stanton Moor samples were used; namely Stanton Moor (1) and Stanton Moor (2). Two batches were utilised due to the extremely low capillary absorption rate of this stone compared to other samples, preventing an accurate comparison between stone types to be made. The first batch (1) were subjected to the same capillary absorption conditions as the other sandstone types, while the second batch (2) were submerged to a greater depth, allowing more solution to be absorbed, and therefore a more comparable regime to the other sandstone types. Samples that were deemed salt resilient, such as Hazeldean, were omitted, while Blaxter and Giffnock were not considered due to lack of sample availability. Four repeat samples per stone type were tested against each salt over 50 crystallisation cycles. Resistance to salt crystallisation was analysed by: the weight change after each cycle; visual inspection by: photography, colour measurements and laser scanning; changes to the ultrasonic velocity; changes to the hydric properties after desalination at the end of the test; and SEM observations of dry cut samples.

4.2.1 Weight change

Weight measurements were made after every cycle, following the same procedure as in the previous tests. Water control samples showed negligible mean weight change for each sandstone.

4.2.1.1 *NaCl*

There is a distinct trend in the average weight evolution of NaCl samples in every sandstone. NaCl samples show a continuous linear gain in weight across every stone, with Stanton Moor (1), Cullalo and Doddington samples showing stage one weight increase throughout all 50 cycles. The Stanton Moor (1) samples show more variability, with minor oscillations superimposed on a continued weight increase. These oscillations represent small, short-lived episodes of weight loss and salt absorption. Cullalo and Doddington weight

change graphs show very similar trends, with little variation in their absorption rate across 50 cycles. Locharbriggs and Corsehill also show similarities, with an initial convex trend line that evolves into a plateau (and second stage weight change). This second stage plateau is attained after 33 cycles in Locharbriggs and after ~45 cycles in Corsehill. Weight loss was recorded between cycles 38 and 39 in Corsehill, with a loss of 1.53% caused by the detachment of a large corner section in one of the samples. Stanton Moor (2) shows a slightly different trend to the other Stanton Moor samples, presenting a concave-convex trend-line, whereby a period of salt enrichment is followed by a small plateau before a further period of salt uptake. This pattern represents stage one salt enrichment, followed by a second stage of increased weight loss and decay and then a return back to the first stage. The high variability in weight change is similar to Stanton Moor (1) samples and shows the dynamic competition taking place within the stone between continuous salt enrichment and weight loss. The NaCl weight evolution is shown in Figure 4-11.

Small decreases in weight between cycles 8 and 9 (Figure 4-11) in all NaCl samples were caused by the loss of surface efflorescence during the drying stage, as moisture that was expelled from control samples dripped onto NaCl samples in the oven.

Corsehill had the greatest average maximum NaCl accumulation (expressed as weight gain) of 11.15%, followed by Locharbriggs and Stanton Moor (2), with values of 6.58% and 6.15%, respectively. The remaining samples fell within a range of 1.3%, from 3.8% in Stanton Moor (1) to 5.2% in Doddington. Stanton Moor (2) had the greatest average maximum weight loss of 3.85%, followed closely by Locharbriggs and Corsehill, with values of 3.66% and 3.25%, respectively. Cullalo and Doddington had minimal weight losses of 0.38% and 0.63%, respectively. Corsehill and Locharbriggs had the greatest range of maximum accumulation values; however, the lowest maximum accumulation value recorded for Corsehill was still greater than the average values of both Locharbriggs and Stanton Moor (2) (Figure 4-16). Corsehill and Locharbriggs also experienced the greatest range of maximum weight loss values. One Locharbriggs sample experienced no weight loss, while samples of Corsehill

and Locharbriggs showed higher weight loss values than the equivalent Stanton Moor (2) average (Figure 4-17).

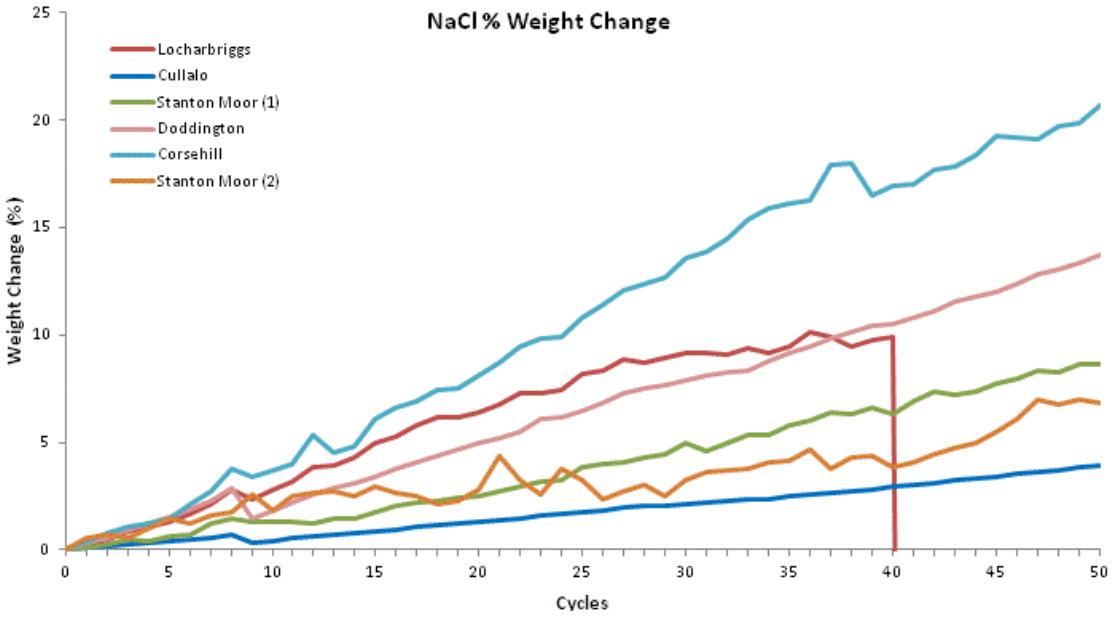

Figure 4-11: Mean percentage weight evolution of the NaCl treated samples. The drop in weight change for Locharbriggs at cycle 40 represents the catastrophic decay of one of the samples.

4.2.1.2 *$MgCl_2$*

All $MgCl_2$ samples experienced a greater salt accumulation rate than NaCl, with every sandstone attaining the second stage plateau at between 7 and 12 cycles. Locharbriggs and Corsehill experienced similar trends in their weight change, characterised by a prolonged second stage plateau before the sudden and substantial loss of material. A small blip in the Corsehill weight change is evident between cycles 46 and 47, explained by the loss of 6% weight from one sample, before experiencing catastrophic scaling-decay after cycle 48. Two Locharbriggs samples also suffered similar damage, with the complete detachment of similar sized sections of stone after cycles 36 and 47, triggered by the development of planar fractures extending parallel to the front drying face. Doddington in contrast, experienced each distinct stage of weight change. Stage one increase took place within the first 15 cycles; stage two between cycles 15 and 33, and stage three in the following cycles. Stage three is characterised by substantial granular decay and the complete destruction of several samples and is illustrated by the gradual loss of weight in Figure 4-12.

Cullalo had the greatest average total accumulated weight gain from salt absorption, experiencing an average increase of 5.98% over 50 cycles, while both Locharbriggs and Corsehill showed similar values of 4.78% over 50 cycles. Both Stanton Moor sample sets had the lowest accumulation values over 50 cycles, with Stanton Moor (1) experiencing 1.06% average accumulated weight gain. Locharbriggs, Corsehill and both Stanton Moor sets have substantially smaller standard deviations than equivalent NaCl values. In contrast, large standard deviations in Cullalo are associated with the dynamic loss and gain of surface efflorescence. $MgCl_2$ efflorescence extended outwards by several millimetres from the sample surface and was vulnerable to detachment between cycles. This texture is in contrast to the hard-packed and dry efflorescence of NaCl, and will be discussed in greater detail later in the chapter.

Doddington had the greatest average maximum weight loss of 7.89%, associated with a long period of granular decay before the complete breakdown of the stone. Locharbriggs and Corsehill samples also suffered significant damage but as granular decay was not operating, maximum weight loss values are significantly lower than for Doddington. However, large errors associated with Locharbriggs do show that some samples experienced granular decay, which lead to high total accumulated losses in these samples. Relatively high accumulated losses in Cullalo are caused by the loss of surface efflorescence and not through damage to the stone. Both Stanton Moor stones suffered negligible weight loss and no visible decay.

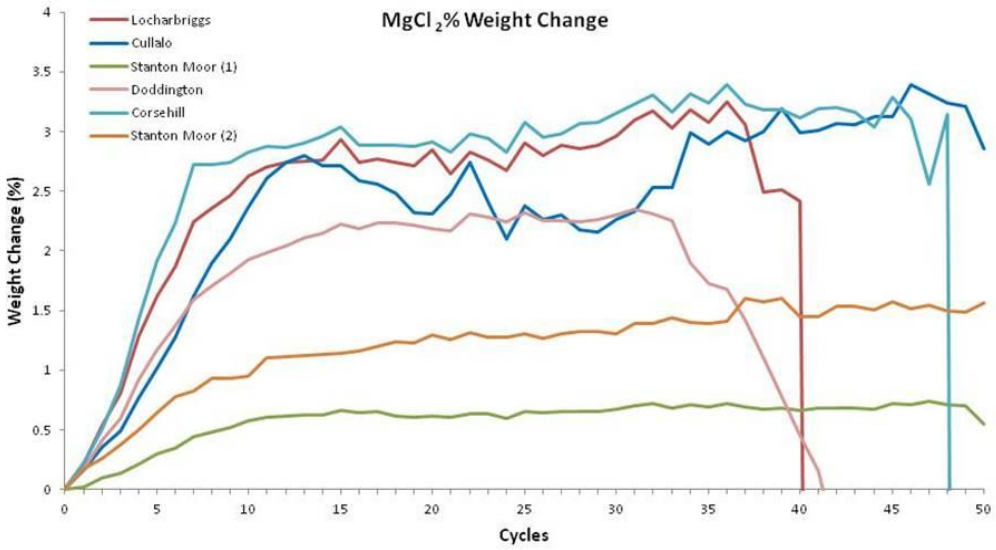

Figure 4-12: Mean percentage weight evolution of the $MgCl_2$ treated samples.

4.2.1.3 *$CaCl_2$*

$CaCl_2$ shows a very similar weight change trend to $MgCl_2$, with all sandstones having a clearly defined stage one weight increase and stage two plateau. Both Stanton Moor sets and Corsehill have near identical $CaCl_2$ and $MgCl_2$ trends, while Doddington has a similar trend that shows three defined stages, with decay initiating after the 43rd cycle. A steep weight loss curve takes place after this, with 3.55% recorded between cycles 47 and 50. It is likely that if the tests had continued, complete breakdown of these samples would have taken place. Cullalo shows a movement into stage two after ~18 cycles, with further weight increase taking place between cycles 30 and 43. Locharbriggs had a greater uptake rate than $MgCl_2$ samples, but reached the second stage plateau at the same time. Movement into weight loss initiates after cycle 23 and again after cycle 33 in Locharbriggs, with 3.65% lost over the final six cycles. The complete breakdown of one Locharbriggs sample took place after 47 cycles, while granular decay affected most Locharbriggs samples from cycle 30 onwards. The % weight loss curves for $CaCl_2$ are shown in Figure 4-13.

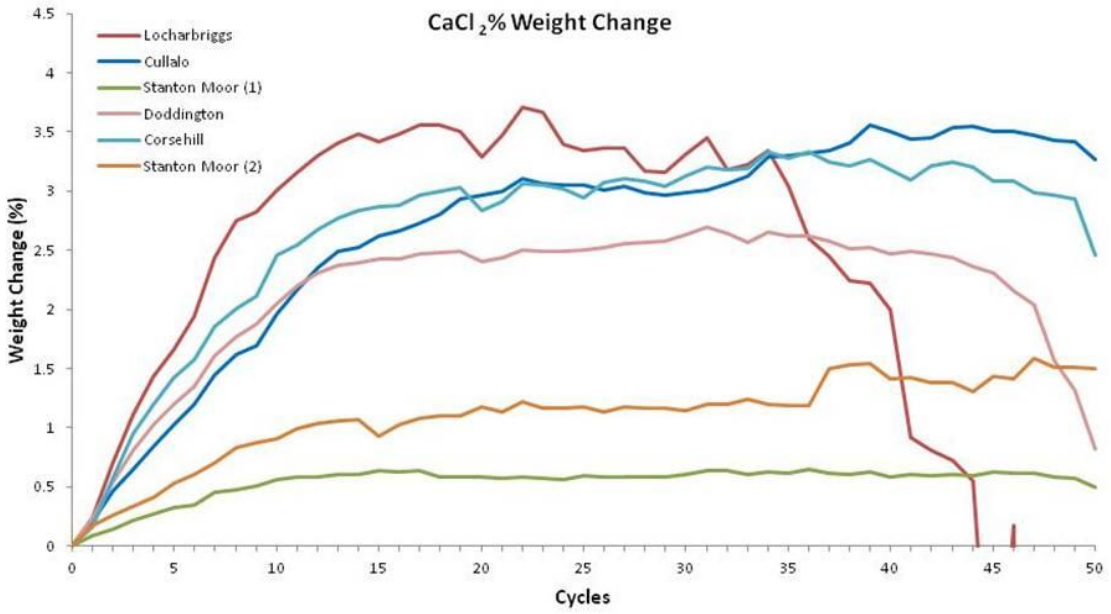

Figure 4-13: Mean percentage weight evolution of the $CaCl_2$ treated samples.

Locharbriggs shows the greatest change with $CaCl_2$, suffering sustained granular decay and experiencing the highest maximum accumulation and maximum weight loss values. It has the highest average maximum weight loss value, over four times higher than the second highest value of Doddington. The lowest measured weight loss value of a Locharbriggs sample is also nearly 2% higher than the average Doddington value. Doddington and Corsehill have similar values of average maximum weight loss, while both Stanton Moor sets have negligible average maximum weight loss values of between 0.41% and 0.78%.

4.2.1.4 *Weight change summary*

There are distinct differences in the weight change between (i) NaCl, and (ii) $MgCl_2$ and $CaCl_2$. NaCl caused the greatest weight gain across every sandstone, with higher average final weights (Figure 4-14) and higher average maximum weight accumulations in all but Cullalo sandstone (Figure 4-15). Locharbriggs, Corsehill and Cullalo had the greatest average weight increases with $MgCl_2$ and $CaCl_2$ (Figure 4-15 and Figure 4-16), while both Stanton Moor sample sets had the lowest weight gain across both salts (Figure 4-15 and Figure 4-16). $MgCl_2$ and $CaCl_2$ caused greater average maximum weight loss in all but the Stanton Moor samples (Figure 4-17). Doddington and Corsehill experienced greater loss with $MgCl_2$, while Locharbriggs had greater $CaCl_2$ weight loss.

Stanton Moor samples were only affected by NaCl, with little weight change and visual change associated with $MgCl_2$ and $CaCl_2$. In contrast, Cullalo and Doddington suffered little weight loss and no decay associated with NaCl, while there was the complete destruction of Doddington $MgCl_2$ samples and surface damage to Cullalo $CaCl_2$ samples. Locharbriggs and Corsehill were equally affected by all three salts, with Locharbriggs experiencing greater $CaCl_2$ decay, and Corsehill experiencing greater NaCl decay.

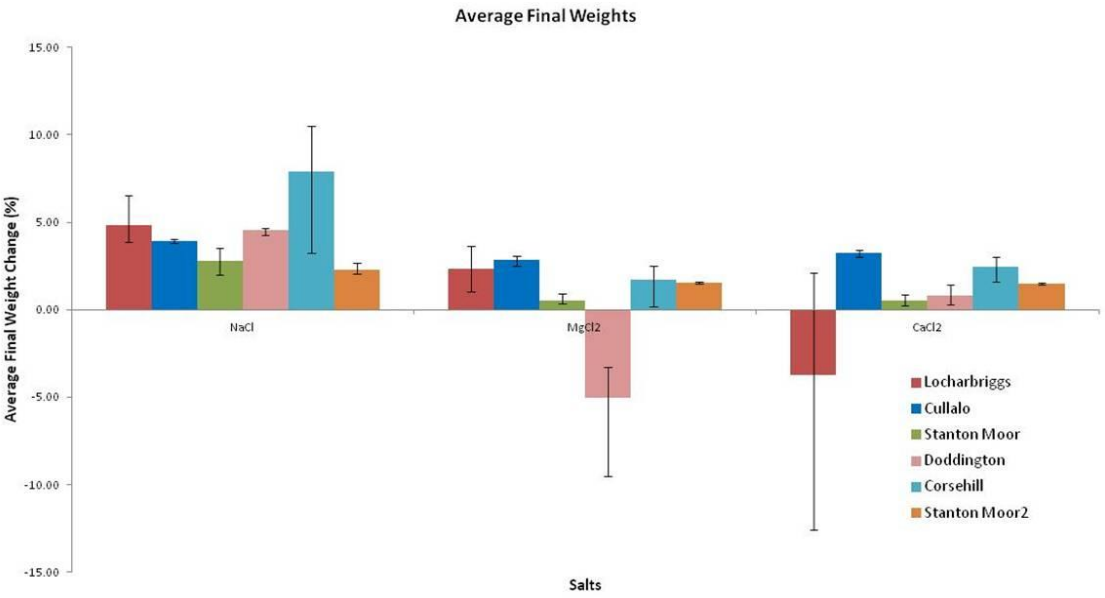

Figure 4-14: Average percentage change in final weights over original weights after 50 cycles.

Error bars represent the range of measured values. These values were calculated as the percentage difference in the final weight in relation to the original pre-test weight for each stone subject to each salt. These values are the difference between the values calculated for Figure 4-15 and Figure 4-17 after 50 cycles.

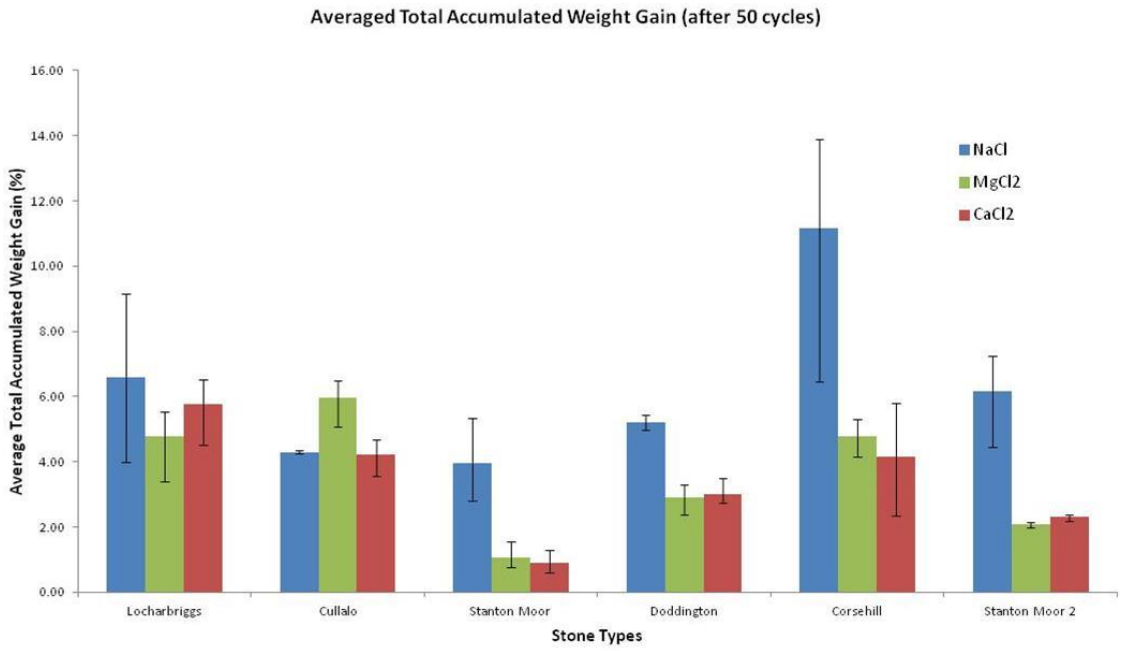

Figure 4-15: Average total accumulated weight gain over 50 cycles (by stone type).

Error bars represent the range of measured values. These values were calculated by adding the total amount of percentage weight increase at any point during the test, neglecting any weight loss for each repeat sandstone block subject to each salt. This should therefore represent the total quantifiable amount of salt that was absorbed on average for each sandstone subject to each salt and does not concern the weight loss caused by salt-induced damage.

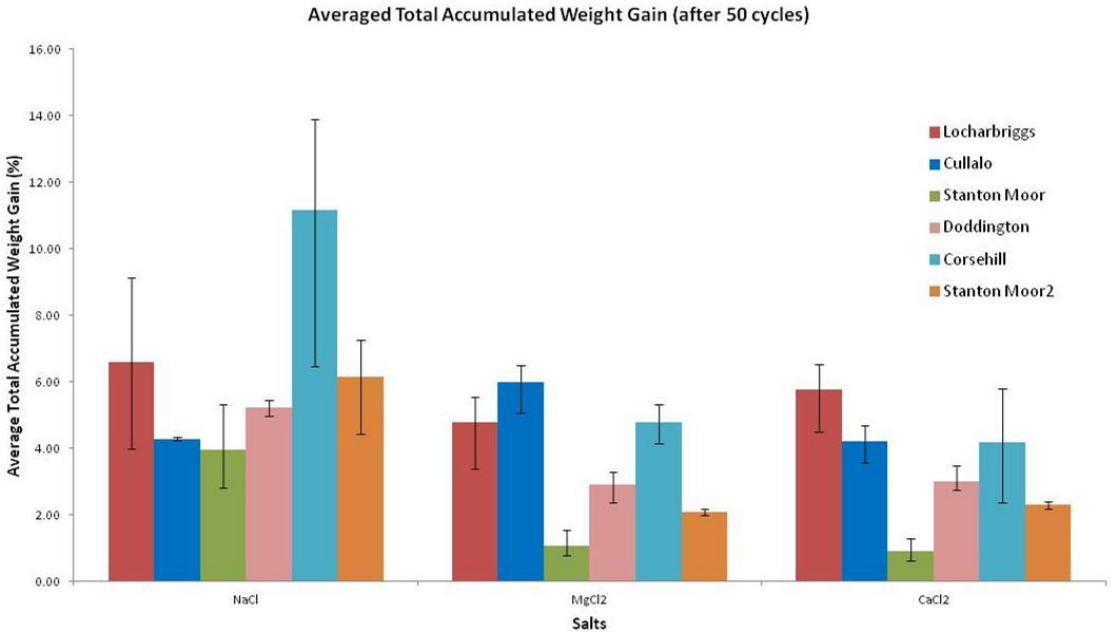

Figure 4-16: Average total accumulated weight gain over 50 cycles (by salt type). Error bars represent the range of measured values. The values are the same as those in Figure 4-15 but presented in order to highlight the average differences between salts.

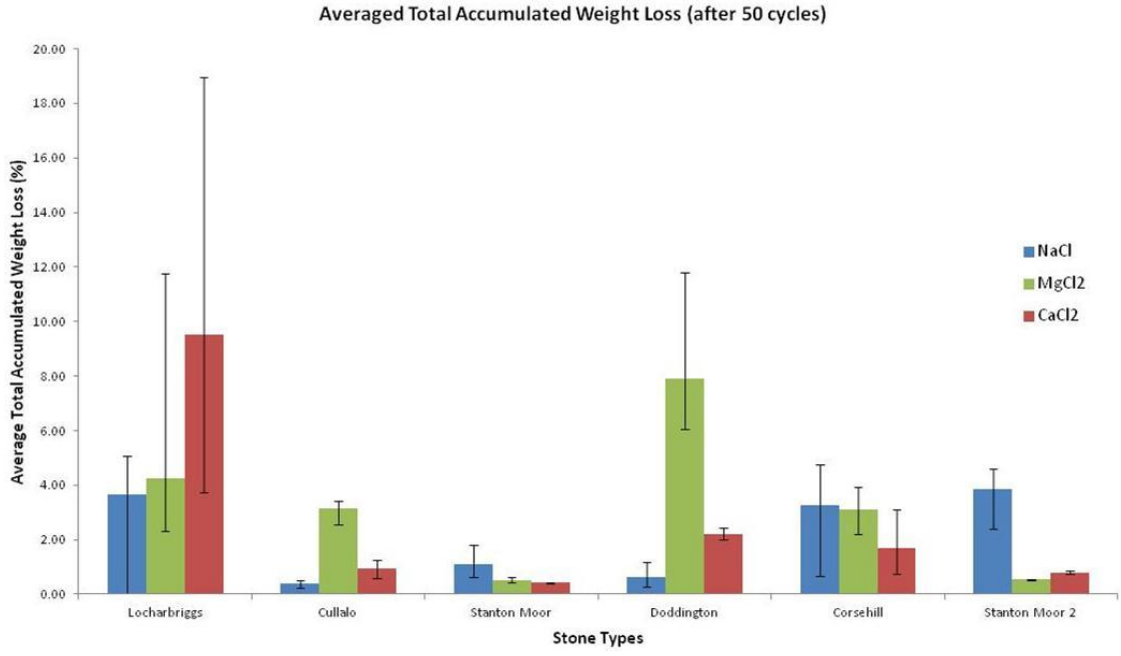

Figure 4-17: Average total accumulated weight loss over 50 cycles.

Error bars represent the range of measured values. These values were calculated by adding the total amount of percentage weight loss at any point during the test, neglecting any weight gain for each repeat sandstone block subject to each salt. This should therefore represent the total quantifiable amount of material that was lost on average for each sandstone subject to each salt and does not concern the weight gain.

4.2.2 Visual and surface change

The visual changes to each sample were analysed by photography after every ten cycles and after the complete destruction of specific samples.

After ten cycles there was minimal change to most $CaCl_2$ samples, with only Locharbriggs (LC_3) and Corsehill (CC_3) showing any evidence of surface efflorescence, while in most other blocks salt was limited to the surface pores. Every Locharbriggs $MgCl_2$ (LM_3) sample showed a thin and continuous surface efflorescence, with Corsehill (CM_3), Doddington (DM_3) and Cullalo (CLM_3) showing discontinuous and patchy efflorescence across several samples, and Stanton Moor (SMM_3) showing no surface changes with $MgCl_2$. Locharbriggs (LN_3), Corsehill (CN_3), Doddington (DN_3) and Cullalo (CN_3) had similar NaCl efflorescence coverage, with thick accumulations across most repeat samples while Stanton Moor (SMN_3) experienced no surface modification with NaCl after ten cycles.

There were no obvious surface changes to Corsehill (CC_3), Doddington (DC_3), Stanton Moor (SMC_3) and Cullalo (CLC_3) $CaCl_2$ samples after 20 cycles. $LC3_3$ and $LC4_3$ samples began to show granular decay, and the initiation of contour scaling revealing the subsurface crystallisation of salts in the outer pores. There was complete $MgCl_2$ surface coverage in all Locharbriggs (LM_3) samples, with granular decay evident on the lower edges of several of them. Corsehill (CM_3) and Doddington (DM_3) showed increased efflorescence located predominantly on the edges and corners of the blocks, with central areas remaining unaffected. Stanton Moor (SMM_3) efflorescence was patchy and did not preferentially crystallise in any specific areas. By this time (20 cycles) Cullalo (CLM_3) started to show significant surface efflorescence, with hollow, “bubbly” textures located along the bottom edge of blocks. Furthermore, a continued increase in NaCl efflorescence was evident in all samples, with granular decay at this point now apparent in Locharbriggs (LN_3).

After 30 cycles, Locharbriggs continued to show granular decay in all but $LCP1_{3post}$ and $LCP2_{3post}$ samples, with all other $CaCl_2$ sandstone samples showing no significant additional surfaces changes. Similar trends of $MgCl_2$ change now become apparent across most sandstones, with most

efflorescence limited to the outer edges and corners of the front faces (Figure 4-18). Cullalo (CLM_3) samples continue to show "bubbly" surface efflorescence, with small bubbles following the fabric of the stone. Significant efflorescence is also evident on the back faces of each Cullalo (CLM_3) sample, extending several millimetres above the rear surface of the stone. The surface changes in Locharbriggs NaCl samples now become more dynamic, with the opening of surface fractures taking place within several samples (Figure 4-19). A large fracture extends between both reference screws in $LN4_{3post}$, while smaller cracks are evident in the rear faces of samples $LN1_{3post}$ and $LN3_{3post}$. Similar fractures between reference screws are evident in the $CN4_{3post}$ sample, while other Corsehill NaCl samples lack any relationship in salt coverage. In contrast, Stanton Moor (SMN_3) samples continue to show little surface modification, while an increase in salt coverage now takes place in most Doddington (DN_3) and Cullalo (CLN_3) samples.

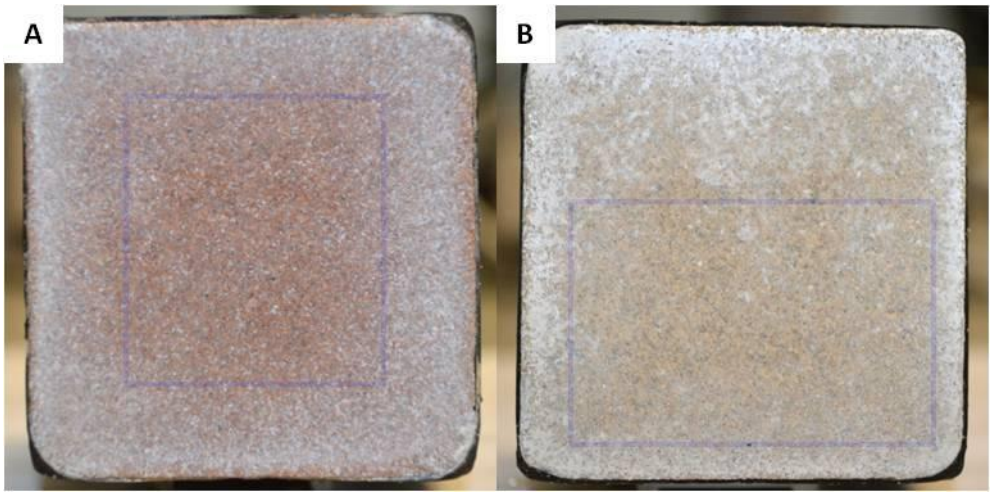

Figure 4-18: Efflorescence distribution after 30 $MgCl_2$ crystallisation cycles. (A): $LM1_{3post}$ sample. (B): $DM1_{3post}$ sample. Blue boxes highlight internal areas unaffected from $MgCl_2$ efflorescence. Blocks are 50mm edge length.

Figure 4-19: Sample $LN1_{3post}$ showing the initiation of surface fractures on the rear face.

Greater surface modifications were evident after 40 cycles in Locharbriggs $CaCl_2$ samples that exceed the changes seen between previous photographic intervals. Substantial granular decay from the rounding of edges and corners is evident in all but one Locharbriggs $CaCl_2$ sample, with the loss of 5-6 mm of surface material from the face of one of the samples. The same trends continue in the remaining sandstones across each salt, with most $MgCl_2$ efflorescence continuing to be located near to the surface corners and edges and with NaCl efflorescence and damage continuing at a similar rate.

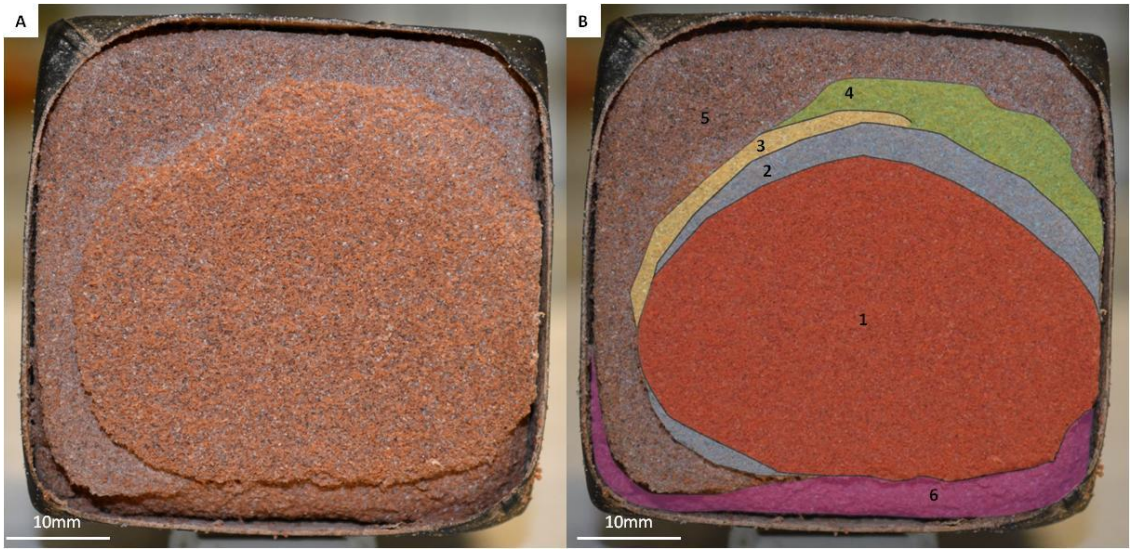

Figure 4-20: Sample $LC1_{3post}$ after 50 cycles showing scaling decay processes. (A): Sample $LC1_{3post}$ after 50 cycles. White patches on the 5th layer indicate salt crystals. (B): Separate scaled layers are highlighted and numbered. Six separate layers can be identified.

After 50 cycles, sample $LC1_{3post}$ shows the formation of six distinct layers on the front drying face where significant material loss has taken place. The majority of this decay is located on the corners and edges of the sample (Figure 4-20). An additional large fracture located 15 mm from the back face of the sample and running parallel to the drying face has appeared but not yet triggered complete block failure (Figure 4-21). Samples $LCP1_{3post}$ and $LCP2_{3post}$ show significantly reduced material loss, with damage limited to the corners and top edge of the samples. Corsehill samples show limited surface change, with two samples displaying no change at all. Doddington $CaCl_2$ (DC_3) samples all show consistent rounding of their corners and edges, while Stanton Moor (SMC_3) and Cullalo (CLC_3) continue to lack any significant modifications and have no surface efflorescence.

Figure 4-21: Sample $LC1_{3post}$ after 50 crystallisation cycles.

Large fracture running parallel to the rear drying face. The dark surface is caused by the dye used within the rubber sleeve.

$MgCl_2$ samples continue to show efflorescence located preferentially along surface edges, with any damage limited as granular decay at the corners of the blocks. Sample $CM4_{3post}$ has lost two large pieces of rock from the top corners of the front drying face (Figure 4-22), while the other Corsehill (CM_3) samples experience increased surface efflorescence. The one remaining Doddington (DM_3) sample has lost large quantities of material in the form of individual quartz grains from the rounding of corners and edges, while Stanton Moor (SMM_3) samples, although showing increased efflorescence, show no signs of surface damage. Cullalo (CLM_3) samples continue to gain surface efflorescence on their rear faces and lose material through granular decay from the block corners.

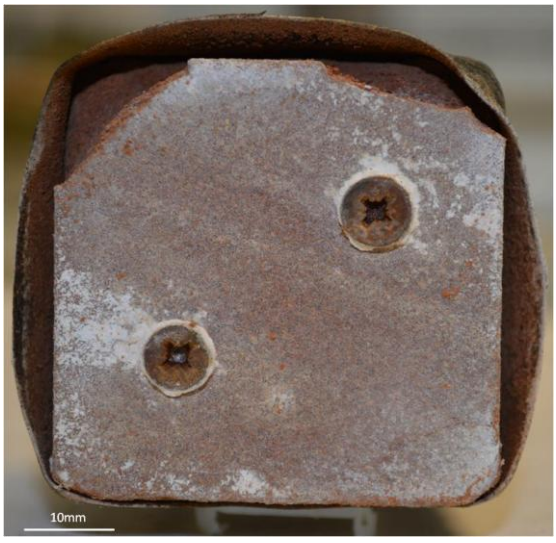

Figure 4-22: Sample $CM4_{3post}$ after 50 crystallisation cycles.

Locharbriggs NaCl samples $LN2_{3post}$ and $LN3_{3post}$ show significant bulk changes to their overall appearance, with multiple fractures located at 15 mm from the rear face of $LN2_{3post}$ extending parallel to drying face (Figure 4-23). The top section of the rear face of $LN3_{3post}$ shows considerable lateral extension of ~7 to 8 mm, with salts preferentially crystallising in this large hollow section (Figure 4-23 D). Samples $LNP1_{3post}$ and $LNP2_{3post}$ show granular surface decay and efflorescence but lack any further flaws or damage.

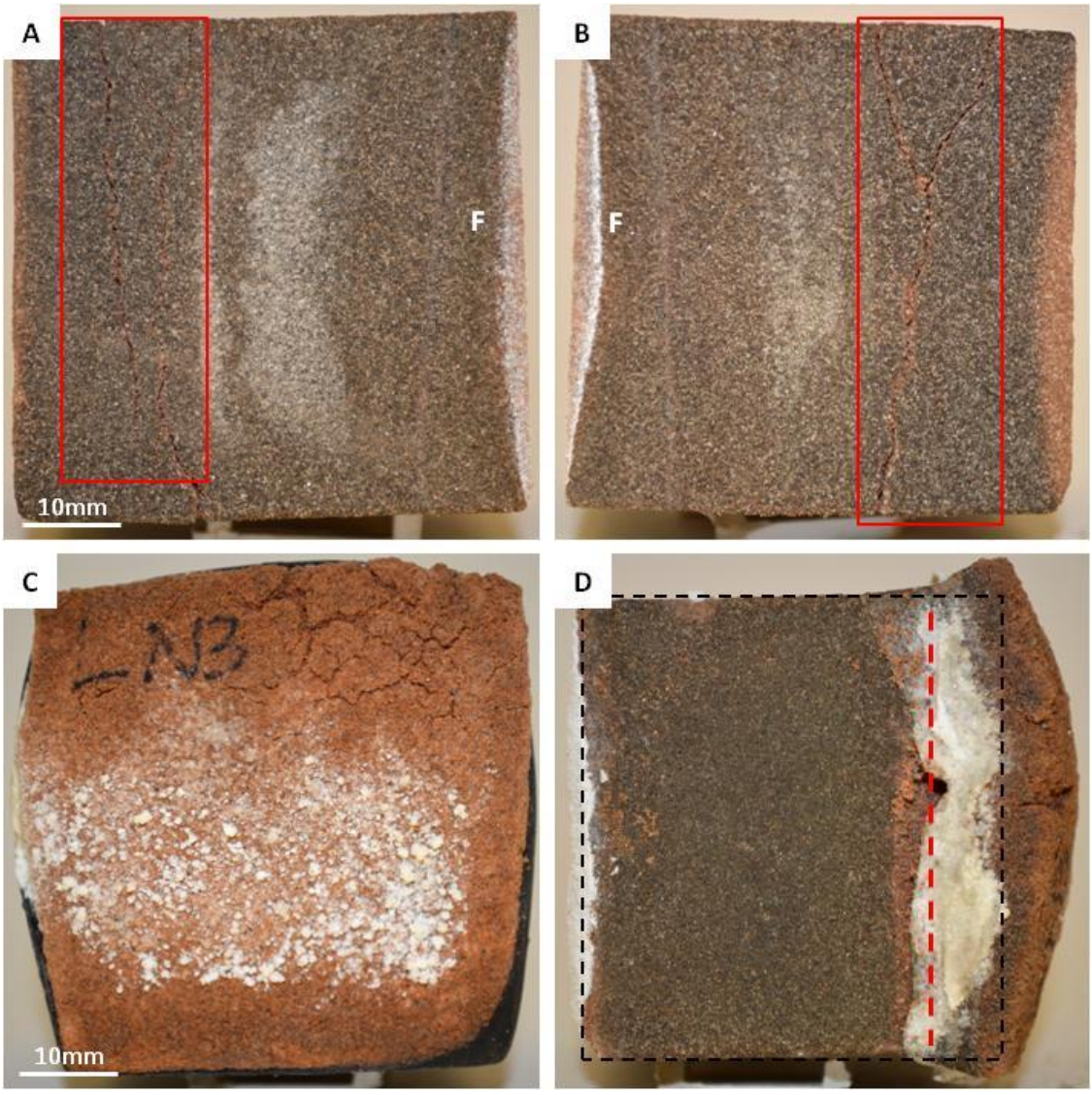

Figure 4-23: Locharbriggs samples $LN2_{3post}$ and $LN3_{3post}$ after 50 crystallisation cycles. (A): Left side of sample $LN2_{3post}$. Red box highlights the small fractures within the block. (B): Right side of sample $LN2_{3post}$ with red box highlighting small fractures. F denotes the front drying face of the block. (C): Rear face of sample $LN3_{3post}$. White efflorescence is visible underneath the top bowed section containing multiple fractures and cracks. (D): Top view of sample $LN3_{3post}$. Black dashed box represents the original dimensions of the stone, with areas out-with this box showing areas of extension. Red dashed line represents the original fracture plane. A large area of salt accumulation is shown to be preferentially crystallising within this location. The scale is the same for all four images.

Corsehill (CN_3) samples continue to experience granular surface decay, with large sections extending 20-25 mm from the back face that show significant surface crystallisation (Figure 4-24). The surface fractures between reference screws in $CN4_{3post}$ have increased in size, with similar extension to $LN3_{3post}$ taking place on the rear face (Figure 4-24).

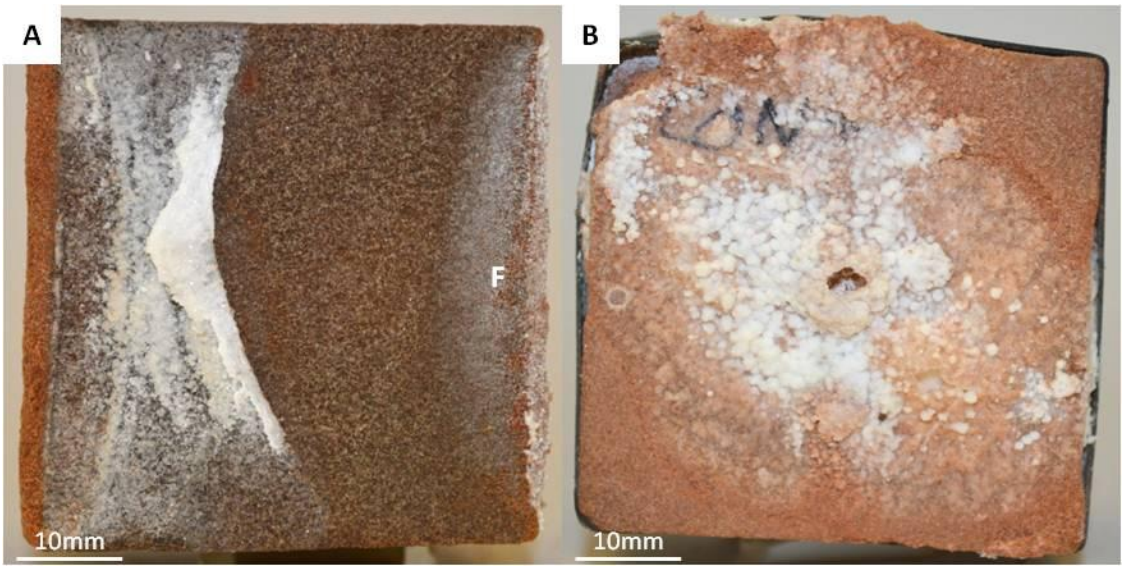

Figure 4-24: Corsehill NaCl samples after 50 crystallisation cycles.
(A): Sample $CN3_{3post}$ with efflorescence occurring near to the rear face of the block. F denotes the front face. (B): The rear face of sample $CN4_{3post}$ showing efflorescence and significant lateral extension focussed near the top of the sample.

Stanton Moor (SMN_3) experienced no significant surface modification but suffered internal micro-fracturing along planes parallel to the drying face in all four samples (Figure 4-25). Greater surface decay and efflorescence is seen on the Stanton Moor (2) (SMN_3) samples, with evidence of both surface contour scaling and the creation of micro-fractures at depth within the stone (Figure 4-25). The fractures in Stanton Moor samples $SMN1_{3post}$ – $SMN4_{3post}$ were located ~10 mm from the rear face, while fractures in Stanton Moor (2) samples $SMN5_{3post}$ – $SMN7_{3post}$ were located closer to the front drying faces.

Doddington NaCl samples experienced similar continued rates of granular decay and efflorescence accumulations, with salts crystallising in similar locations to Corsehill NaCl samples. Cullalo (CLN_3) on the other hand, although accumulating large quantities of surface efflorescence, experienced no stone material loss. Front face efflorescence appears as a thin crust covering the full face, while efflorescence on the rear face is formed by a thick hard salt crust (Figure 4-26).

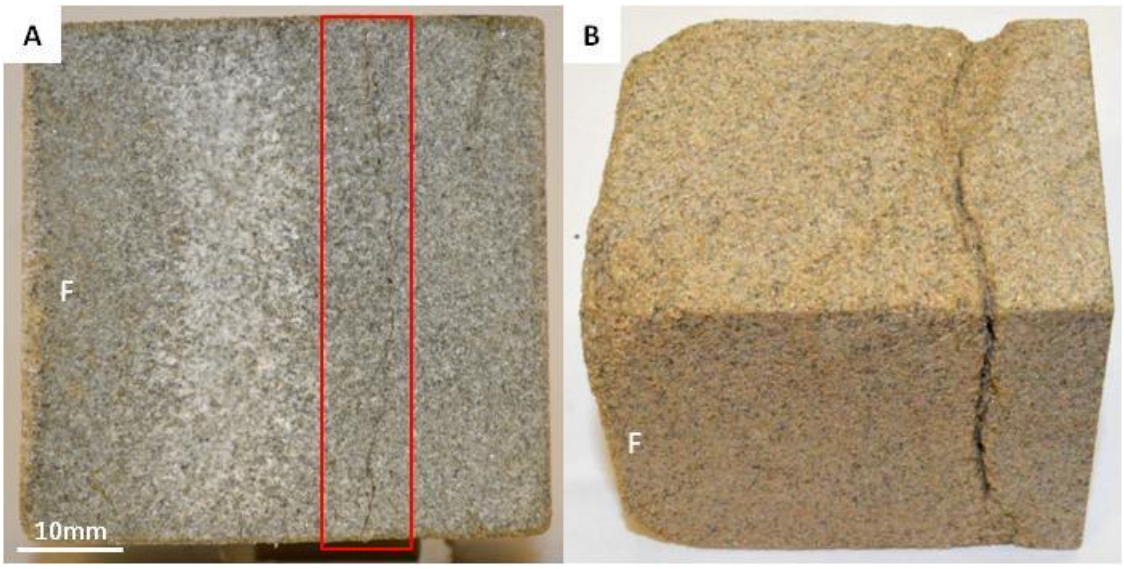

Figure 4-25: Stanton Moor NaCl samples after 50 crystallisation cycles.

(A): Sample SMN2$_{3post}$ after 50 crystallisation cycles showing internal fracturing as highlighted by the red box and minimal surface alteration. (B): Sample SMN6$_{3post}$ after 50 crystallisation cycles, showing significant internal fracturing and granular surface decay. F denotes the front face in both blocks.

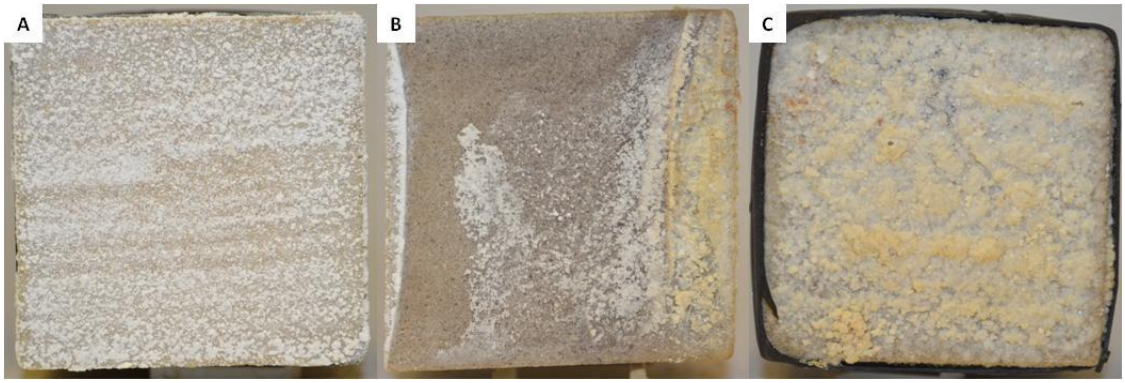

Figure 4-26: Cullalo sample (CLN4$_{3post}$) after 50 crystallisation cycles.

(A): Front face of sample CLN4$_{3post}$ showing efflorescence following the fabric of the stone. (B): Right side of the same sample showing no physical decay but significant efflorescence. (C): Rear face of the same sample showing a large quantity of thick halite efflorescence.

Several samples were removed from the test at specific cycles after experiencing critical material losses. Critical losses were determined as the failure of large sections of the stone that contributed to over 20% of the original sample weight. Locharbriggs samples LM4$_{3post}$ and LN1$_{3post}$ suffered critical material loss after 36 cycles, with both samples experiencing fracturing parallel to their drying face (Figure 4-27). LM4$_{3post}$ failed at a depth of ~10 mm from the rear face, while LN1$_{3post}$ suffered failure at the same depth from the front face.

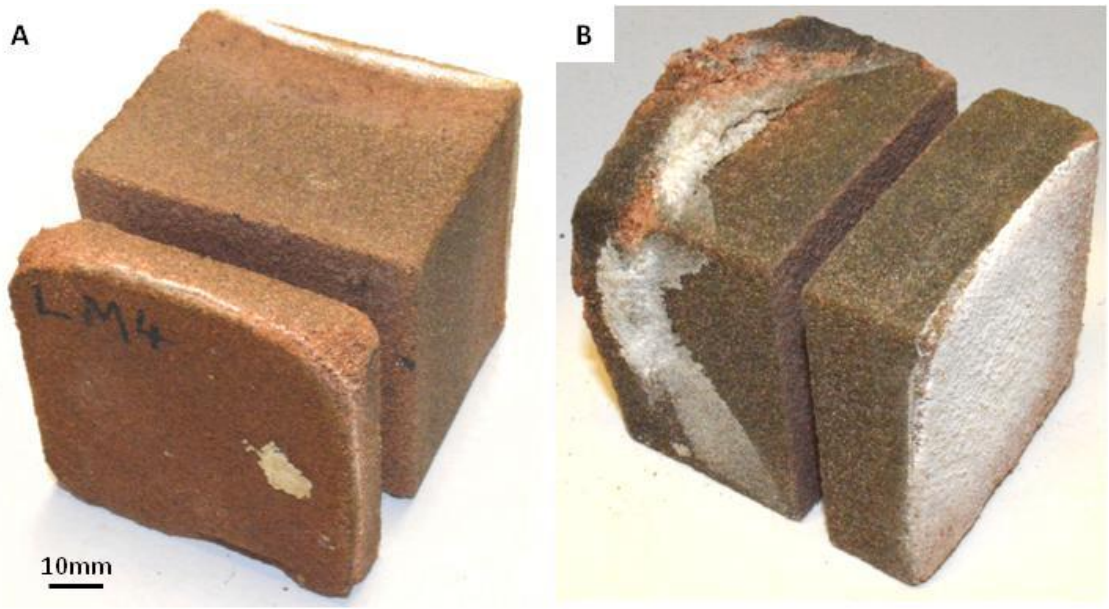

Figure 4-27: Locharbriggs samples showing critical failure after 36 crystallisation cycles.

(A): Sample $LM4_{3post}$ showing critical failure along a bedding plane after 36 crystallisation cycles. Efflorescence is located near the edges of the front drying face, with the rounding of the corners and edges of the rear face. (B): Critical failure of sample $LN1_{3post}$ across a bedding plane. Significant fracturing and extension is shown on the rear face, with a thin efflorescence crust on the front drying face. Both pictures have the same scale.

Critical failure was observed on sample $LN4_{3post}$ after 37 cycles; $LC4_{3post}$ and $DM1_{3post}$ after 45 cycles; on samples $LC2_{3post}$, $LC3_{3post}$, $DM3_{3post}$ and $CM2_{3post}$ after 47 cycles and on sample $DM4_{3post}$ after 49 cycles. Critical decay was characterised by the complete removal of large sections of the stone along fracture planes running parallel to the front and rear faces of samples: $LN4_{3post}$, $LC4_{3post}$, $LC2_{3post}$, $LC3_{3post}$ and $CM2_{3post}$, while significant granular decay of over 20% of the original weight caused the removal of samples $DM1_{3post}$, $DM3_{3post}$ and $DM4_{3post}$ from the test (Figure 4-28). Fracture planes were located in similar positions for each sample, at a depth of 7-12 mm from the exposed faces and were accompanied in samples $LN4_{3post}$, $LC2_{3post}$, $LC3_{3post}$ and $LC4_{3post}$ by granular decay and surface scaling (Figure 4-28).

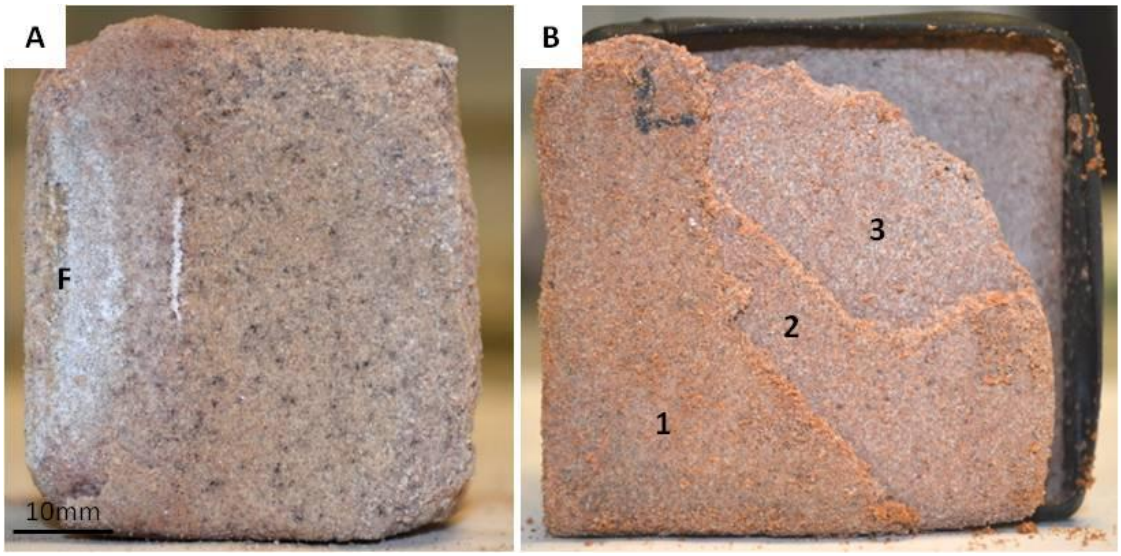

Figure 4-28: Doddington $MgCl_2$ and Locharbriggs $CaCl_2$ samples after removal from the test.

(A): Doddington sample $DM2_{3post}$ suffering granular decay and the critical loss of a large section from the rear of the sample after 49 crystallisation cycles. (B): Locharbriggs sample $LC1_{3post}$ after 47 crystallisation cycles. Numbers highlight three distinct scales from the rear face of the sample. Complete removal of the rear face contributed to the retirement of this sample from the test. F denotes the front face of the sample. Both pictures have the same scale.

4.2.2.1 *Visual surface change summary*

Locharbriggs $CaCl_2$ experienced the largest mean and maximum height change, which is associated with surface retreat. Most decay is focussed on the edges and corners of the stone, extending 4-5 mm into the centre of the face. In contrast, Corsehill $CaCl_2$ had one of the lowest mean changes in surface height. Both Locharbriggs and Corsehill NaCl samples had preferential decay that exploited small drilling-related fractures in the stone. Locharbriggs $MgCl_2$ was the only sample to experience no surface height loss, with a maximum height increase of 1.17 mm/mm^2 corresponding to an estimated salt volume of 501.25 mm^3. Corsehill $MgCl_2$, although experiencing one event of substantial decay, had similarly low surface alteration values to Locharbriggs $MgCl_2$. A summary of the main visual changes is given in Table 4-3.

Stone Type	Notable visual changes to each sandstone subject to each salt		
	NaCl	**$MgCl_2$**	**$CaCl_2$**
Corsehill	E_{thin}, GD and fracturing in 1 sample	E_{thin}, fracturing in 1 sample	-, fracturing in 1 sample
Cullalo	Significant E_{thick}	Significant E_{thick}	- / minor GD
Doddington	E_{thin}	E_{thin}, Significant GD	GD
Locharbriggs	E_{thick}, GD, significant F	E_{thin}, GD, F	GD, S and significant F
Stanton Moor	$E_{minor/thin}$, GD, F	-	-
NaCl	Generally large efflorescence accumulations in all stones bar Stanton Moor, with granular decay and catastrophic fracturing		
$MgCl_2$	Large, thick efflorescence accumulations in all stones bar Stanton Moor, granular decay and fracturing of select samples		
$CaCl_2$	No visible efflorescence, generally minor granular decay and fracturing in Corsehill and Locharbriggs		

Table 4-3: Summary of main visual changes in each stone type and for each salt. GD: granular decay, E: efflorescence, E_{minor}: minor efflorescence coverage, E_{thin}: thin efflorescence coverage, E_{thick}: thick efflorescence coverage, F: fracturing of the stone, S: scaling surface decay, (-): no change.

$CaCl_2$ did not cause surface efflorescence in any of the sandstones, instead, it crystallised throughout the stone blocks, with subflorescence likely located in the outer few millimetres in most samples, as supported by visual observations of samples (Figure 4-20 and Figure 13-9F). $CaCl_2$ caused significant material loss in Locharbriggs, with multiple flaking and contour scaling. Rounding of corners and edges was evident in Doddington and towards the end of the test in Cullalo. There was no surface modification caused by $CaCl_2$ in both of the Stanton Moor sub-sets or the Corsehill samples.

$MgCl_2$ caused efflorescence in all sandstones, with high accumulations focussed along the edges and corners of the samples, extending towards the centre of most sandstones. Decay was suppressed in most samples until after the 45^{th} cycle, whereby most damage was focussed along fracture planes in the middle of blocks and as granular decay affecting Doddington sandstone.

NaCl caused a greater average surface change through thick efflorescence accumulations, granular decay and surface fracturing in Locharbriggs samples. Although there was greater surface modification in general across each sandstone, critical decay and the complete destruction of samples was limited to Locharbriggs, with Stanton Moor experiencing complete fracturing during the desalination process.

Locharbriggs experienced the greatest surface modification across each salt through large efflorescence accumulations, granular decay, contour scaling, multiple flaking, surface fracturing, and the highest number of samples experiencing critical breakdown before the end of the test.

Corsehill showed high variations in visual change throughout the test, with repeat $CaCl_2$ samples showing contrasting behaviour. Damage developed as granular decay on the corners and edges of samples, with the critical destruction of one $MgCl_2$ sample through the development of a subsurface fracture. NaCl efflorescence was also shown to crystallise on the sides of the samples underneath the rubber jacket (Figure 4-24).

Stanton Moor showed the lowest surface change in all but the Stanton Moor (2) NaCl samples, with no efflorescence in $CaCl_2$ samples and no surface damage across all three salts. Importantly however, was the development of micro-fractures in all NaCl samples after 50 cycles, leading to structural instability, with two samples suffering critical decay during the desalination process.

Doddington $MgCl_2$ samples suffered critical breakdown through extensive granular decay from the rear face of each sample. Granular decay extended to the front face along the edges of the samples. The rounding of corners and edges of $CaCl_2$ samples was apparent after 40 cycles, while large NaCl efflorescence accumulations were established in most samples by 20 cycles, but with no subsequent decay of these samples.

Cullalo experienced no substantial material losses across any salt but was characterised by the large, thick efflorescence in $MgCl_2$ (Figure 4-29) and NaCl samples. Efflorescence formed on both exposed faces, with thin crusts emerging on the front face and thick accumulations on the rear face. By the end of the test, the rear NaCl efflorescence had dried out and formed a hard-packed crust, likely sealing this rear face from further drying and salt growth.

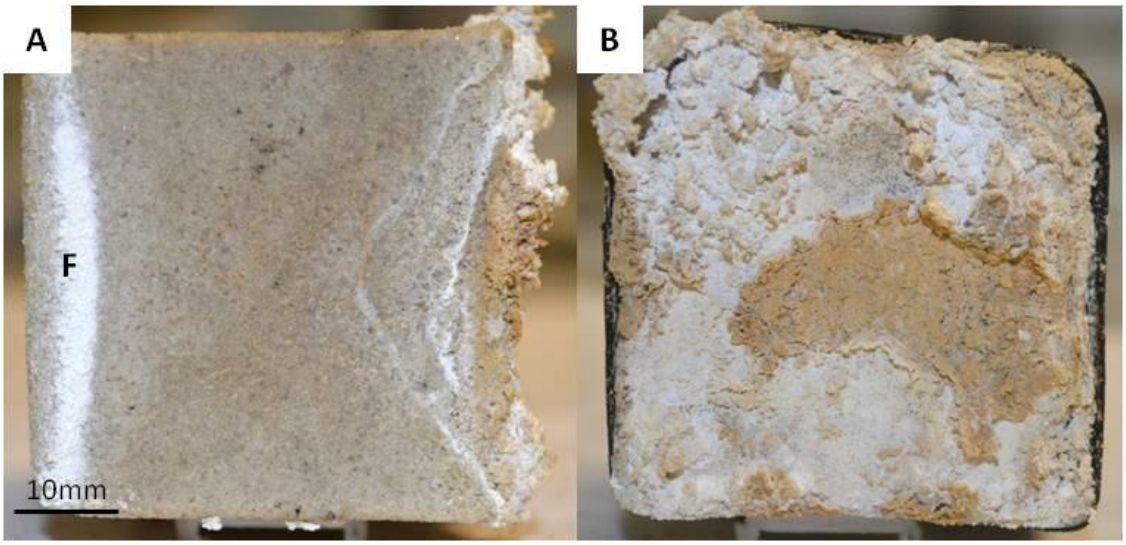

Figure 4-29: Cullalo sample $CLM2_{3post}$ after 50 crystallisation cycles.

(A): Right side view of sample $CLM3_{3post}$ after 50 crystallisation cycles. Notice the difference in efflorescence between the front and rear faces. F denotes the front face. (B): Rear view of the same sample showing significant efflorescence coverage extending several mm above the stone surface. Both pictures have the same scale.

4.2.3 Salt crystallisation damage to the grain structure

SEM analyses of rough dry-cut samples were made on completion of the test to visualise the morphology and distribution of salt crystals and the associated internal crystallisation damage. Analysis is arranged by stone type.

4.2.3.1 *Corsehill NaCl*

Halite is found completely infilling near-surface pores and extending to depths of several mm. The infilling of near-surface pores is seen on every face, with greater penetration evident towards the rear corners. A large area at the rear of the stone block shows lateral extension of the stone. This area has extended above a 500-600 μm thick salt horizon as shown in Figure 4-30A. From the surface this area appears as an accumulation of salt efflorescence but is actually an extended piece of rock that has been broken and detached from the main stone block (Figure 4-30B). A similar broken outer layer is evident on the lower side of the stone, characterised by a large accumulation of salt crystals enclosing displaced quartz grains (Figure 4-31). Surface cracks caused by weaknesses in the stone from the drilling of reference screws extend to nearly 50 mm depth, with thin salt crusts developing on the fracture walls. Surface efflorescence on the other hand is composed of the accumulation of similar sized individual halite crystals.

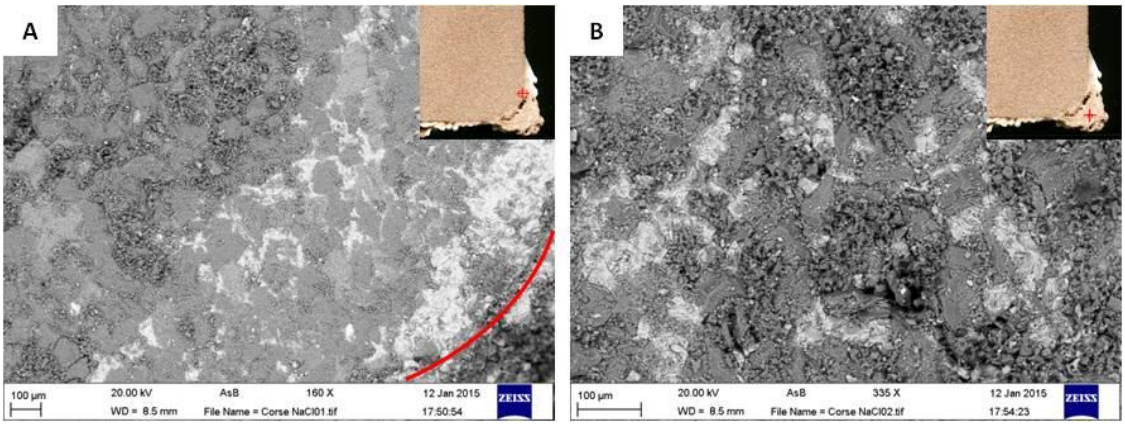

Figure 4-30: Backscatter electron SEM images of sample $CN4_{3post}$ after 50 cycles. (A): Sample $CN4_{3post}$ showing 500-600μm thick salt horizon. Red line indicates a small fracture disconnecting a small salt filled section of rock. (B): A small detached section of stone containing a high salt concentration. White areas in both images correspond to halite. The insert at the top right hand side of A and B shows the location of the SEM images: indicated by the small red box.

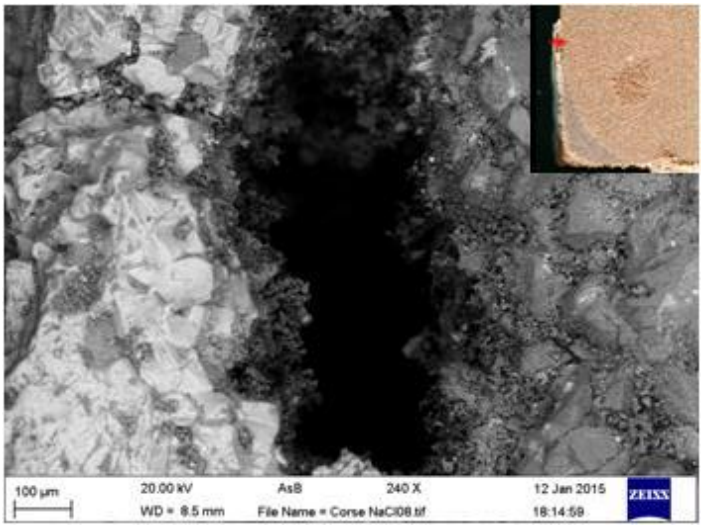

Figure 4-31: Backscatter electron SEM image of salt crust within sample $CN4_{3post}$ after 50 cycles.
Detachment of a thin salt crust from the surface of sample $CN4_{3post}$. Salt crust contains individual detached quartz grains. Salt is the white material. The insert at the top right hand side shows the location of the SEM images: indicated by the small red box.

4.2.3.2 *Cullalo NaCl*

There is evidence of halite crystallisation at depth within the block, coating quartz grains and breaking grain surface overgrowths. Broken and fractured quartz grains are found close to the sample edges, with halite crystallising in neighbouring pores (Figure 4-32). Halite crystals are also found within secondary micro-pores located in small cracks of individual quartz grains (Figure 4-32). Efflorescence on the front face is similar to the thin crust found in the Cullalo samples in the second crystallisation test (Figure 4-8) and the above Corsehill sample. Efflorescence near the rear face is in the form of a large accumulation of salt crystals, extending ~800 µm – 1 mm above the surface, infilling surface pores and coating quartz grains.

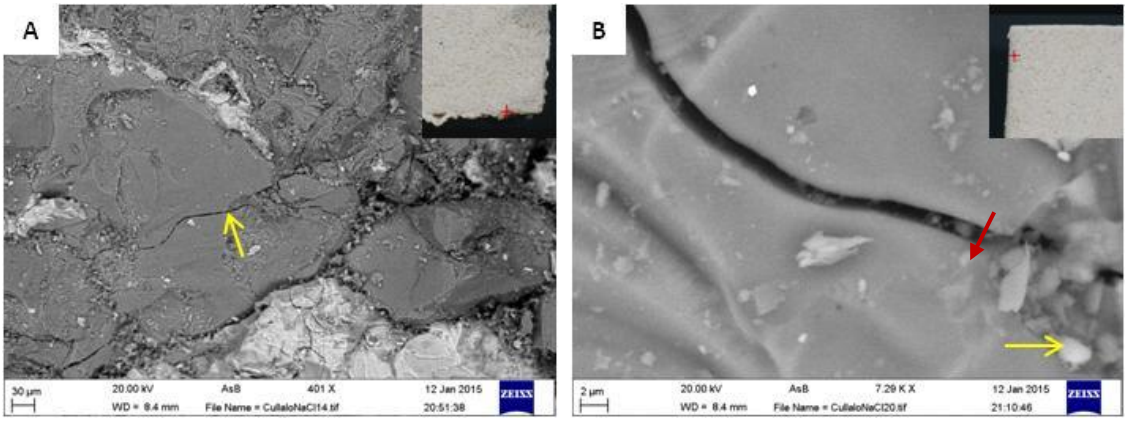

Figure 4-32: Backscatter electron SEM images of sample CLN4$_{3post}$ showing salt crystallisation damage after 50 cycles.

(A): Yellow arrow indicates small fracture within a quartz grain. Related damage is also found within neighbouring quartz grains and salt crystals. This area is located at the back face of the sample. (B): Extremely small fracture within a quartz grain near the front face of the sample acting as a secondary pore allowing salt crystallisation to take place. Yellow arrow highlights nearby halite crystals and red arrow highlights salt within the secondary pore. This site is located near the front face of the sample.

4.2.3.3 *Stanton Moor NaCl (1)*

This sample reveals the damage caused to Stanton Moor after low salt absorption levels (in relation to Stanton Moor (2) samples). These samples experienced less salt uptake, less weight loss and less visual change than Stanton Moor (2) due to their slower solution uptake regime. Stanton Moor (1) is characterised by minimal surface alteration, with most salt limited to a ~1 cm thick horizon located in the centre of the blocks (Figure 4-34). Represented by a dark section of stone, this horizon is located in front of a large fracture extending the width of the block. Halite is found in extensive accumulations surrounding quartz and feldspar grains and completely infilling the open porosity and forming fracture chains of laterally connected salt filled pores within, and above the fracture (Figure 4-33). A cross-section transecting the area indicates that this horizon represents the depth of maximum salt penetration and signifies the importance of drying mechanics on salt crystallisation distribution and behaviour (Figure 4-34).

The location of salt crystallisation sites is limited by the pore network characteristics, which influence solution distribution, solution penetration depth (through capillary uptake) and the evaporation pathways and drying boundaries within the stone. The distribution of micro-pores, which ultimately determine the magnitude of salt crystallisation pressures within

the stone, will only cause significant structural damage once a substantial stress field is established. This process is achieved by the interconnection of isolated pressure regions throughout a substantial volume of stone (Scherer, 2002). It is evident that in Stanton Moor, a combination of capillary penetration depth and poor drying efficiency presents a situation whereby large structural flaws can materialise through the development of salt fracture chains.

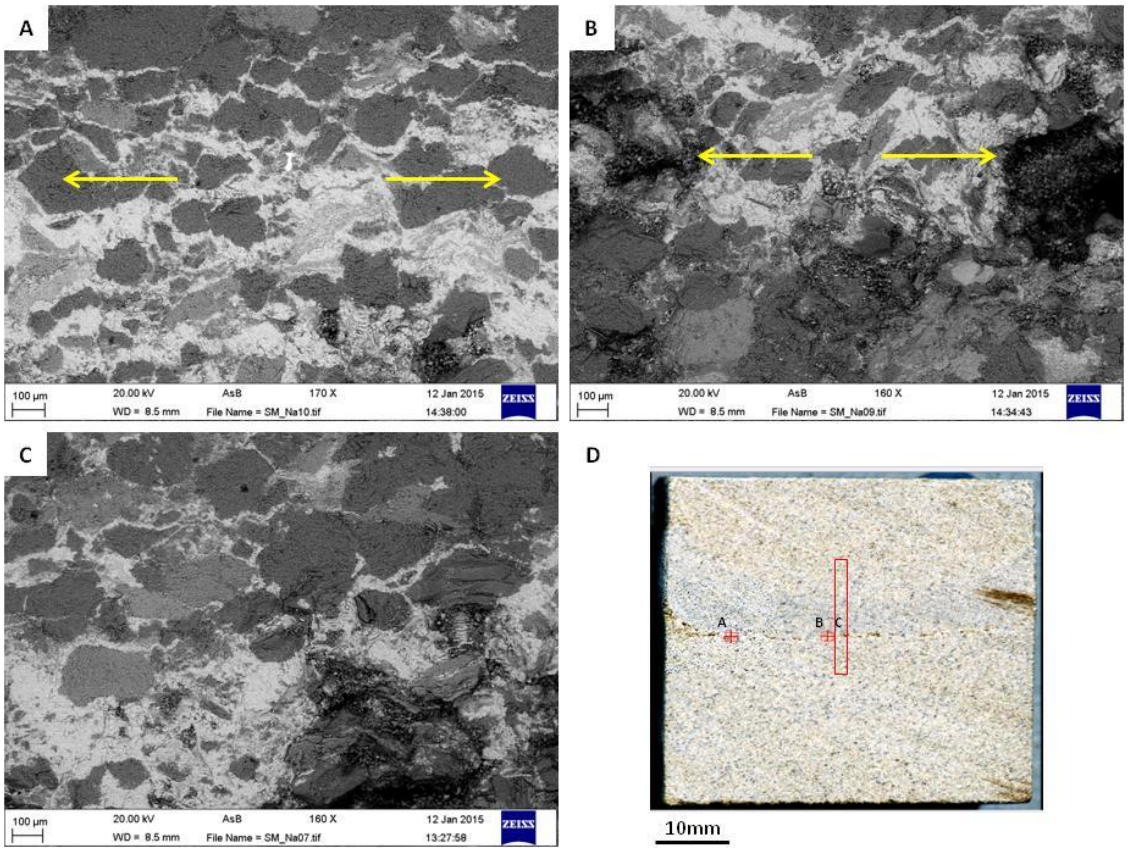

Figure 4-33: Backscatter electron SEM images of halite distribution and damage in Stanton Moor (1) sample SMN4$_{3post}$ after 50 cycles.

(A): SEM image of connected salt filled pores with yellow arrows showing the direction of connection. (B): A small area of connected salt filled pores between a larger fracture within the block. Yellow arrows show the direction of salt connection. (C): A small section of connected salt filled pores in front of the large fracture. (D): image of the rough-cut section of Stanton Moor sandstone that was analysed showing the locations of each separate image. The top of this image represents the front face of the sample. The red box represents the mapped section shown in Figure 4-34. The top of this image is the front of the sample. The connection of salt filled pores creates "fracture chains" that are responsible for the formation of the large internal fracture.

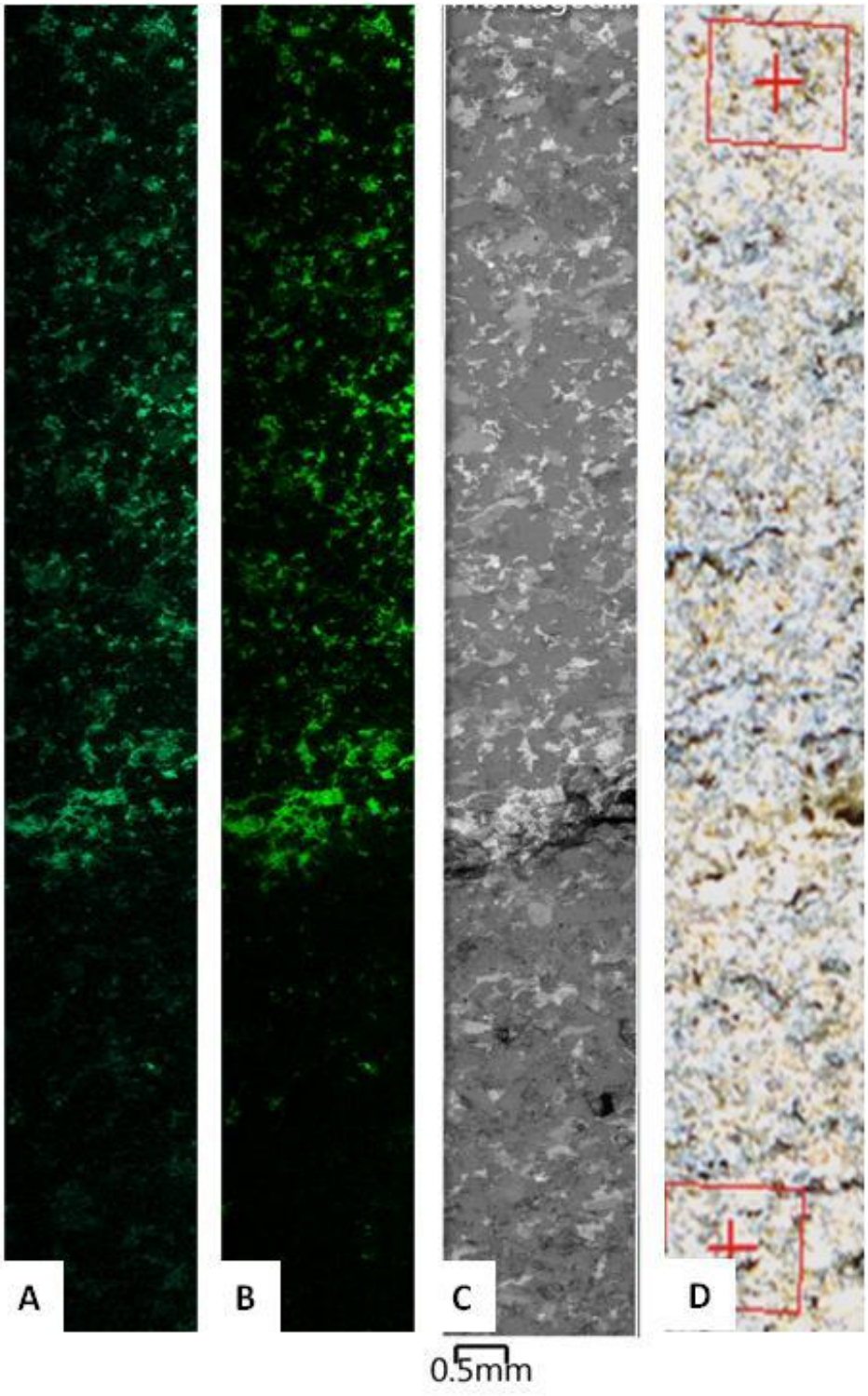

Figure 4-34: SEM EDX mapped section through Stanton Moor (1) sample $SMN4_{3post}$ after 50 cycles.

(A): Na distribution. (B): Cl distribution. (C): Backscatter electron SEM image of mapped section. (D): Photograph of mapped section. The mapped section is shown in Figure 4-33 D. High concentrations of halite are located in front of the fracture, with increased

salt concentrations within the fracture itself. The fracture is located ~ 20mm from the front surface of the stone. Significantly reduced concentrations are found behind the fracture, indicating the depth of maximum salt penetration and subsequent crystallisation. The top of each image is extending towards the front face of the sample.

4.2.3.4 *Stanton Moor NaCl (2)*

Stanton Moor (2) samples experienced greater capillary uptake rates than Stanton Moor (1) samples, which ultimately increased salt absorption and produced greater weight loss through granular disintegration of the stone surface and contour scaling. Contour scaling is associated with surface decay processes whereby an open surface pore structure is partially detached from a horizon of high salt concentration by an open fracture. Granular disintegration of the surface is caused by the dislodgement of individual quartz and feldspar grains by small isolated pockets of trapped salt crystals located between grains.

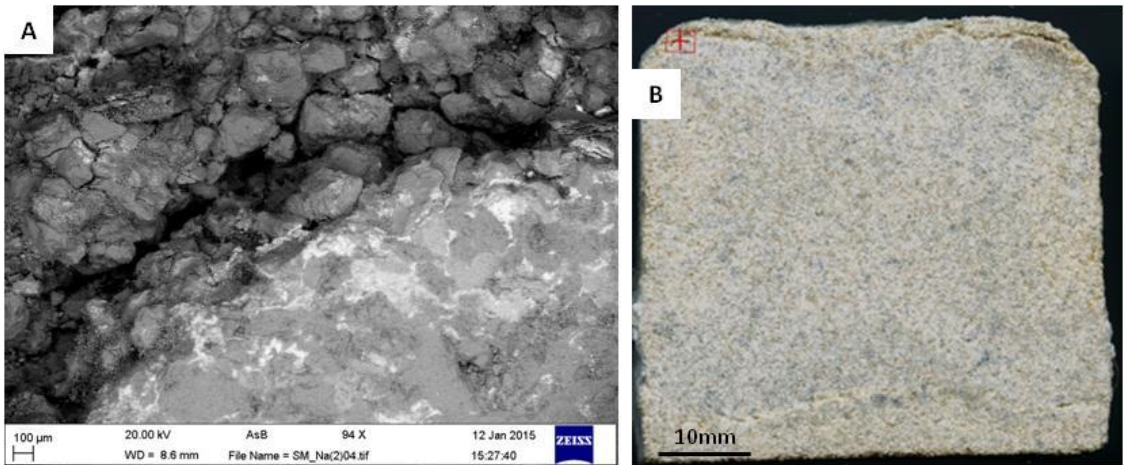

Figure 4-35: Images of salt crystallisation damage in Stanton Moor (2) sample $SMN7_{3post}$ after 50 cycles.

(A): Backscatter electron SEM image of contour scaling damage within sample $SMN7_{3post}$. A small section of the surface of the stone containing an open pore structure is disconnected from an area of high salt concentration (in white), shown to infill most of the open porosity in this section. (B): Photograph showing the location of the SEM image highlighted by the red box. Contour scaling is visible at the top of the sample, with the creation of a large fracture also noticeable near the bottom of the sample.

Contour scaling (Figure 4-35) and granular decay are the dominant surface decay process affecting the front face of the stone, while the early stages of further contour scaling and internal fracture development (Figure 4-36) are evident on the side and rear faces of the block. Greater salt efflorescence is evident in sporadic clusters across the sides of the stone, formed as the accumulation of individual halite crystals (Figure 4-37).

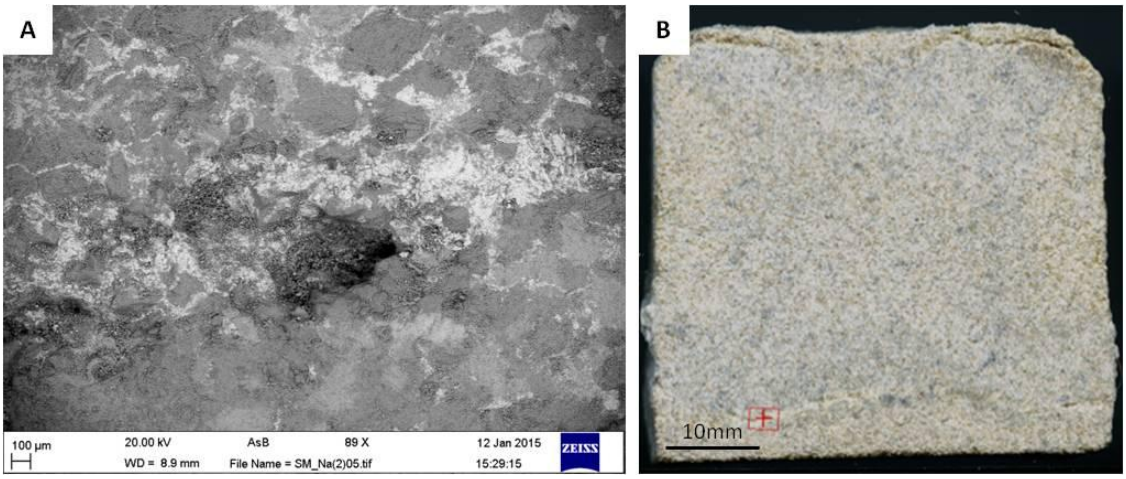

Figure 4-36: Images of salt crystallisation damage in Stanton Moor (2) sample SMN7$_{3post}$ after 50 cycles.

(A): Backscatter electron SEM image of fracture development through contour scaling in sample SMN7$_{3post}$. Salt is the white material. (B): Photograph of sample SMN7$_{3post}$, with location of SEM image highlighted by the red box.

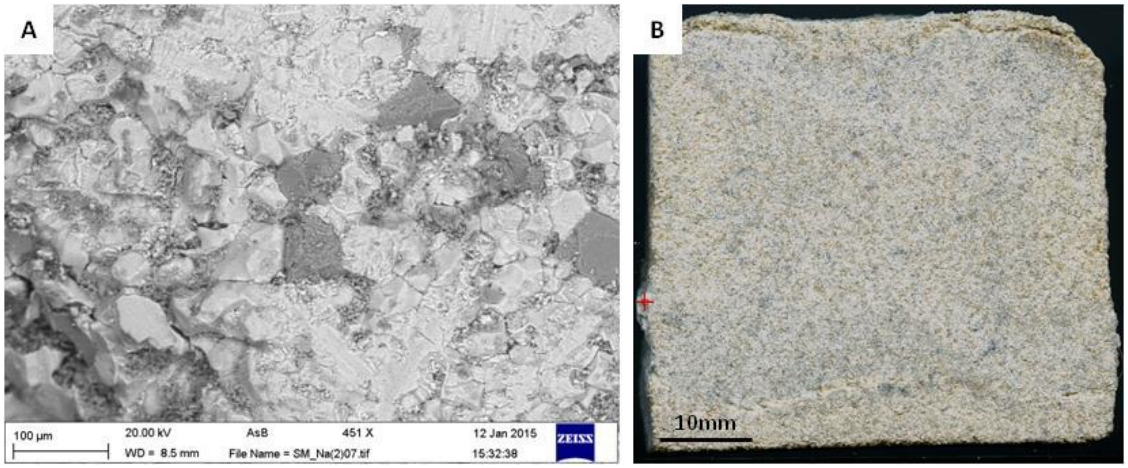

Figure 4-37: Images of salt efflorescence in Stanton Moor (2) sample SMN7$_{3post}$ after 50 cycles.

(A): Backscatter electron SEM image of salt efflorescence on the surface of sample SMN7$_{3post}$. Efflorescence is comprised of the accumulation of individual halite crystals (white), containing detached quartz grains. (B): Photograph showing in red, the location of the SEM image.

4.2.3.5 *Locharbriggs NaCl*

Locharbriggs suffered considerable damage from the subsurface crystallisation of NaCl. Salts crystallised in two distinct horizons within the stone: (i) a 4 mm thick salt horizon located directly beneath the rear face of the block (see also Figure 4-23 of similar damage in another Locharbriggs NaCl sample) and (ii) within a bedding plane in the centre of block (Figure 4-27 B). At the rear of the block, salt accumulated as individual halite

crystals (Figure 4-38 A), completely filling the open porosity and causing damage by fracturing of quartz grains (Figure 4-39) and from the partial detachment of surface scales and flakes of salt-contaminated stone (Figure 4-38 B and C). This damage was probably the consequence of near-surface pore blocking by substantial efflorescence, which caused the retreat of the drying boundary into the stone interior and created this zone of high salt concentration and the subsequent fracture chain development on the rear face of the block. Elsewhere, Figure 4-40 highlights the large fractured bedding plane within the stone, whereby a change in stone texture, from the increased spatial concentration of micro-pores, indicates a narrow horizon of

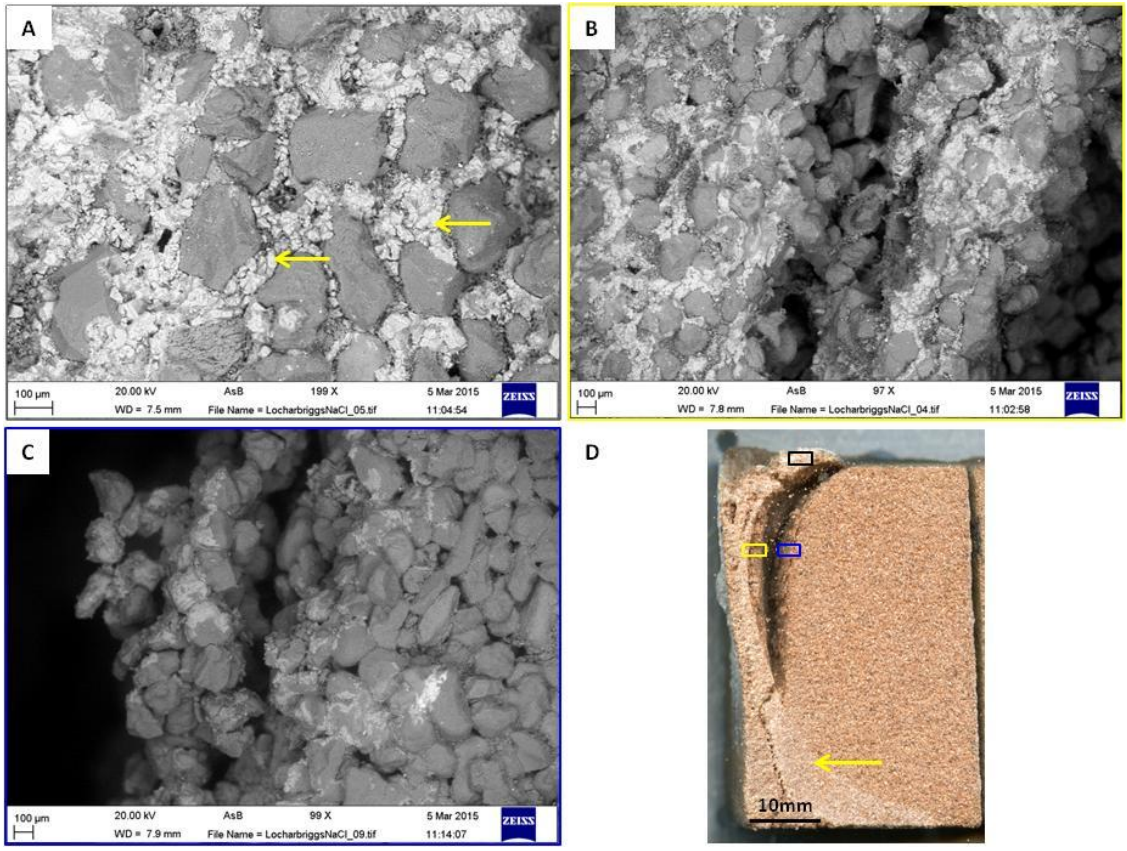

increased salt crystallisation and further fracture development from the same processes.

(A): Backscatter electron SEM image showing that pores are completely filled by halite crystallisation (white). Yellow arrows indicate individual halite crystals. (B): Backscatter electron SEM image showing the development of small broken flakes on the side of the large fracture separating the main surface scale from the main sandstone block. (C): Backscatter electron SEM image showing similar flake development on the opposite side of the main rear fracture. (D): Photograph the analysed sample. The black, yellow and blue boxes highlight the locations of SEM images A, B and C respectively. The yellow arrow indicates the continued salt horizon (white) below the main fracture.

Figure 4-38: Images of salt crystallisation damage within sample $LN1_{3post}$ after 36 cycles.

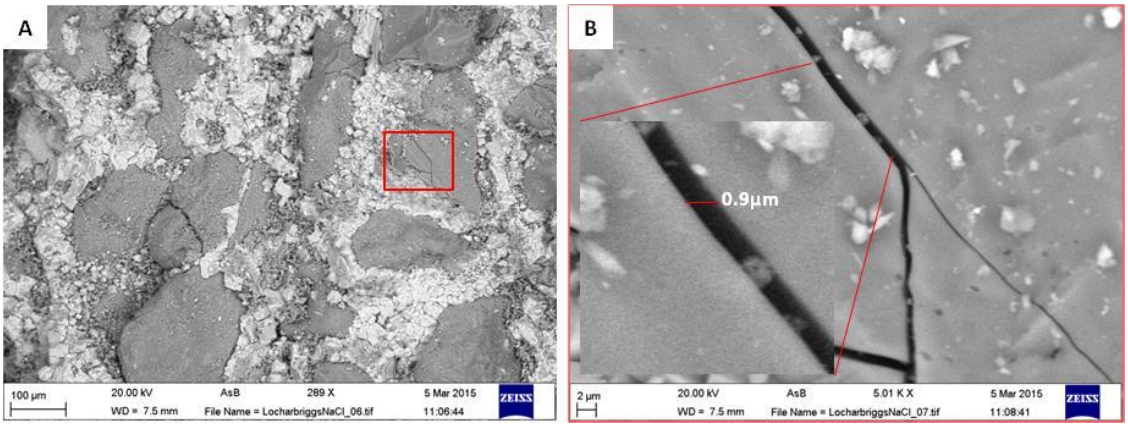

Figure 4-39: Backscatter electron SEM images of damage and salt crystallisation within sample $LN1_{3post}$ after 36 cycles.

(A): Backscatter electron SEM image of complete filling of porosity with halite crystals and 2 fractured quartz grains. (B): Magnified view of the red box in image A showing a fractured quartz grains. The inset image highlights the width of a typical fracture within quartz sandstone and the crystallisation of halite within. These images are located close to image B from Figure 4-38. Halite is white.

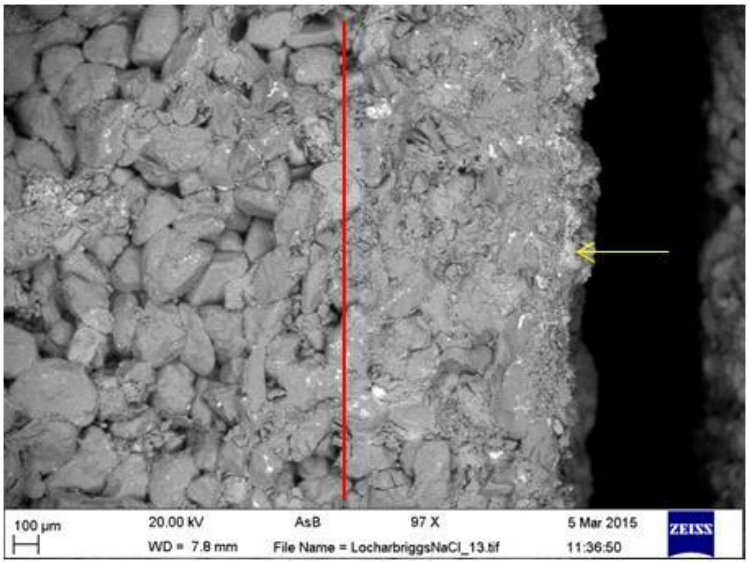

Figure 4-40: Backscatter electron SEM image of damaged fracture plane within sample $LN1_{3post}$ after 36 cycles.

Red line indicates the boundary between the fractured bedding plane (on the right side of the red line) and the bulk pore network of the stone (on the left side of the red line). A clear change in stone texture is identified, with higher grain compaction, lower porosity/reduction in large pores and greater salt content as highlighted by the yellow arrow.

4.2.3.6 *Locharbriggs $MgCl_2$ and Doddington $MgCl_2$*

Unlike the NaCl contaminated samples, $MgCl_2$ salts were not identified by SEM in either the Locharbriggs or Doddington samples. This absence may have been caused by the high ambient relative humidity prior to sample analysis

that would have caused salt dissolution. Mg and Cl were recorded by X-ray microanalysis throughout the samples, possibly coating grains as a thin salt film. Two distinct areas of decay are identified in the Locharbriggs sample as shown in Figure 4-41. These are identified as the front fracture plane, and the initial development of a second fracture horizon close to the rear face of the sample. Figure 4-42 shows the difference in stone texture between salt damaged stone within the fracture, and undamaged stone surrounding it. Damaged stone is characterised by an open pore structure, with a reduction in cement and pore filling clays. This leads to the removal of material through granular decay as inter-granular material is lost and grains are easily displaced.

Doddington samples were especially vulnerable to $MgCl_2$ decay through substantial granular disintegration. SEM analysis of a broken fracture plane shows similarities to those imaged within Locharbriggs. Figure 4-43 provides evidence for broken quartz overgrowths, while the bulk volume of the stone shows an open texture, with no further alterations to the mineralogy.

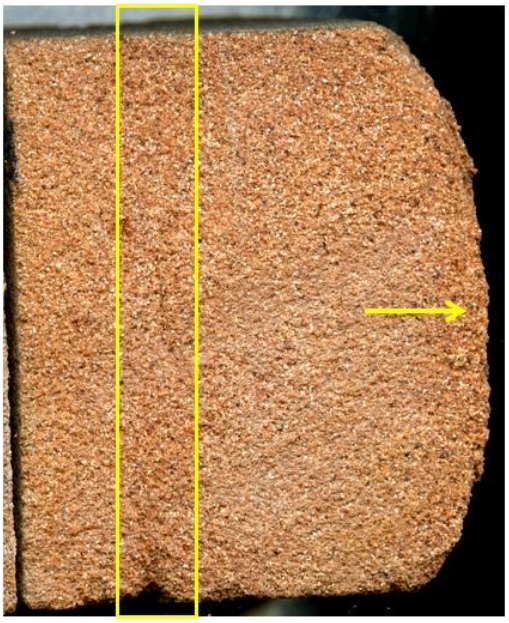

Figure 4-41: Photograph of Locharbriggs sample $LM1_{3post}$ after 50 cycles. Yellow box highlights the development of a fracture chain near the rear face of the sample. The yellow arrow indicates the main fracture plane within the centre of the stone.

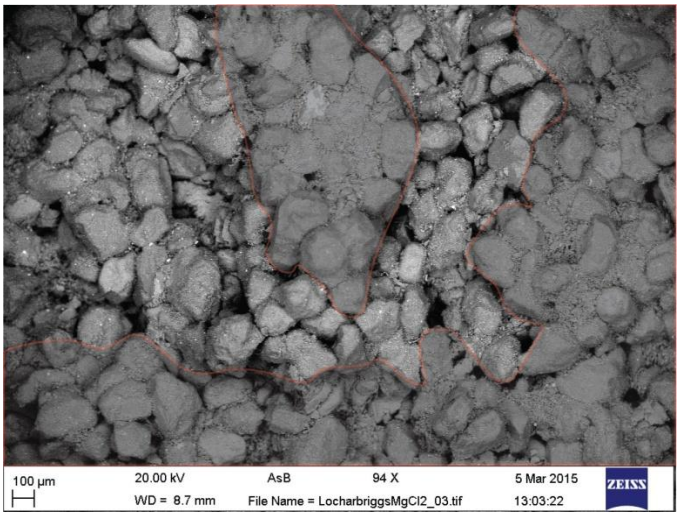

Figure 4-42: Backscatter electron SEM image of a decayed area within Locharbriggs sample $LM1_{3post}$ after 50 cycles.

Dark shaded area shows non decayed sandstone with clays and cements between grains. Lighter area shows a more open porosity, where there has been removal/loss of inter-granular material leading to granular decay.

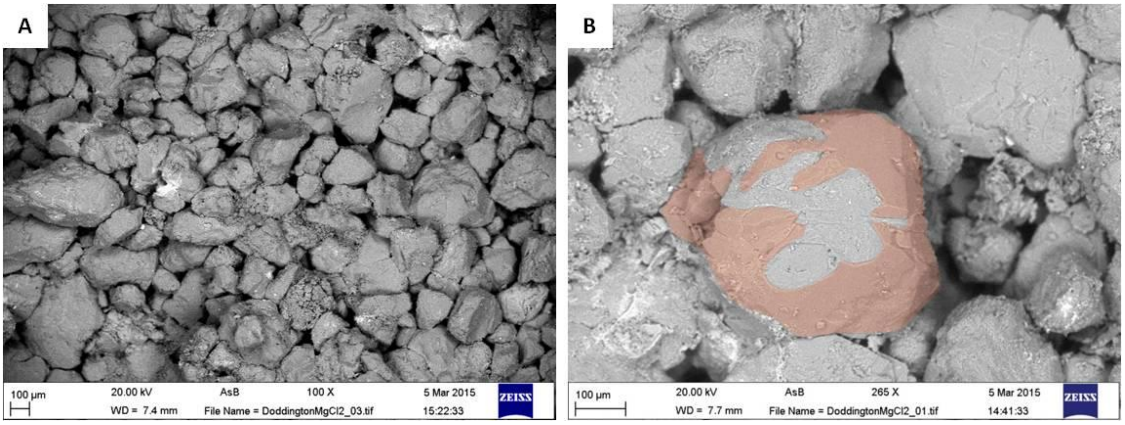

Figure 4-43: Backscatter electron SEM image of Doddington sample $DM2_{3post}$ after 49 cycles.

(A): Backscatter electron SEM image of the bulk pore network showing an open porosity low cementation and clay content between grains. (B): Red shaded area highlights a broken quartz overgrowth where a quartz grain has been lost to granular decay.

4.2.4 Ultrasonic velocity change

The change to ultrasonic velocity was measured after the completion of the third crystallisation test. Each sample was measured in three different directions and the average of these measurements taken as the final value. Samples were measured immediately following crystallisation tests while still containing salts within the pores, and again after desalination. For stones that that had sample completely destroyed during the test, different samples were measured after the test and compared against the average values for each stone type (as measured in chapter 3) to ensure that two samples of each stone were analysed for each salt.

Most of the salt-loaded samples showed an increase in average velocity. $CaCl_2$ treated stones had the greatest average increase in ultrasonic propagation of 260.65 m/s and $MgCl_2$ the lowest increase of 58.98 m/s. Corsehill and Stanton Moor had the greatest average increase in ultrasonic velocity of 16% and 12% respectively, while Cullalo showed a negligible reduction of 1%. Stanton Moor and Corsehill have the greatest increase in ultrasonic velocity from NaCl treated samples of 19% and 20%, while both Doddington and Cullalo showed decreases of 2% and 12%, respectively. Similar trends of increase and decrease are also evident in $MgCl_2$ samples, while all samples experienced an increase in ultrasonic velocity with $CaCl_2$. Consistent increases were expected due to the addition of salt crystals filling pore spaces. In samples that experienced an average decrease (additional samples of Cullalo and Doddington), these were still within the standard deviation of pre-test samples. These samples were not measured before the test, and therefore direct comparisons from before the test cannot be made. In this situation, the damage caused to the stone compensated for any salt increase, and due to the lack of direct comparisons, less reliability is placed on results from these samples. The percentage change in ultrasonic velocity for each sandstone when containing salt is shown in Figure 4-44.

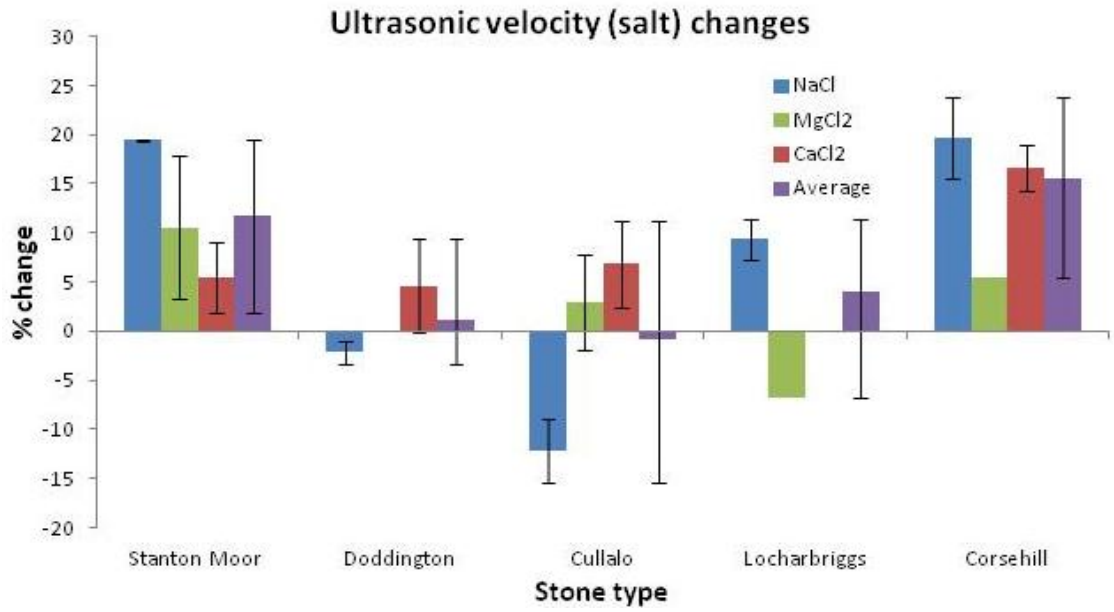

Figure 4-44: Mean percentage change in ultrasonic velocity.
Error bars represent the upper and lower ranges of measured values for each sandstone.

Every sample showed a decrease in ultrasonic velocity after desalination. On average, $MgCl_2$ samples had the greatest reduction in velocity of 562.44 m/s; 78 m/s lower than NaCl values. After the removal of extremely large Locharbriggs $MgCl_2$ values, the average $MgCl_2$ desalinated value was in line with both NaCl and $CaCl_2$. The removal of Locharbriggs values is justified to the poor contact between the pundit transmitter/receiver and the stone surface. This problem would significantly lower the measured velocity by introducing a gap between the transmitter/receiver and the stone surface. Stanton Moor had the lowest average values in desalinated samples, while Doddington, Cullalo, Stanton Moor (2) and Corsehill had similarly high average values. These changes are shown in Figure 4-45.

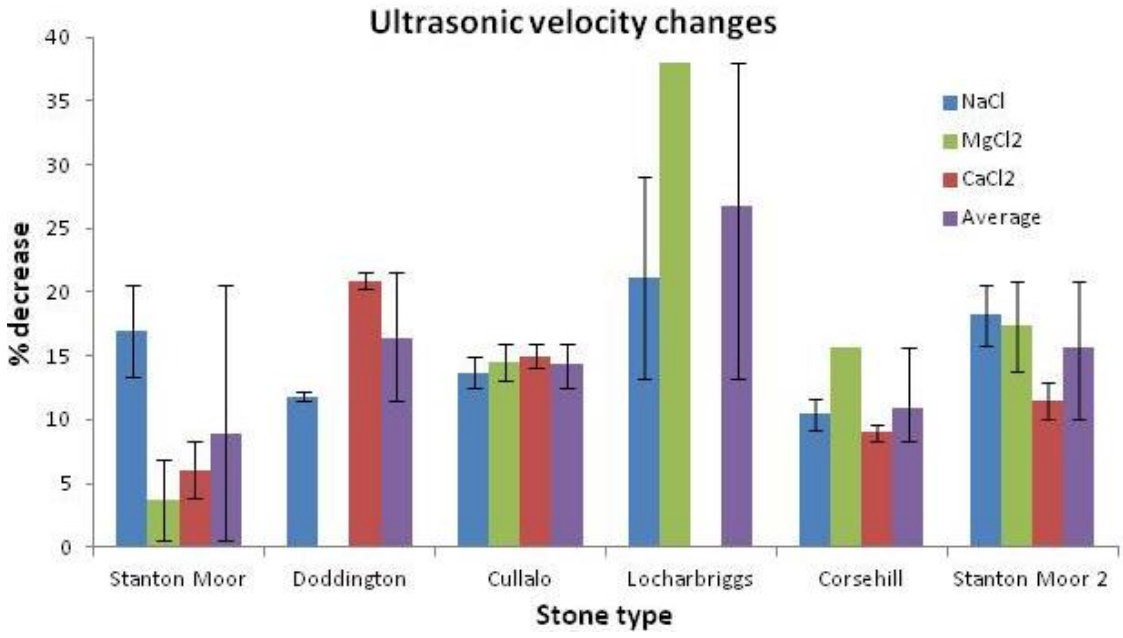

Figure 4-45: Mean percentage decrease in ultrasonic velocity of samples after desalination compared to pre-tested values of the same samples.

Error bars represent the upper and lower ranges of measured values for each sandstone.

Stanton Moor, Stanton Moor (2) and Locharbriggs experienced the greatest reduction in NaCl samples relative to their initial pre-tested values, with each stone registering average losses ≥17%, with the remaining stones all having reductions ≤14%. Stanton Moor showed preferential reduction in one direction, corresponding to the large damage plane through the sample. Doddington $MgCl_2$ samples were not measured due to the complete destruction of these samples. Stanton Moor (2), Corsehill and Cullalo had high decreases of 17%, 16% and 15% respectively and Stanton Moor the lowest reduction of 4% relative to their initial pre-tested values. Doddington had the greatest average reduction in $CaCl_2$ samples of 21%, while Stanton Moor continued to register the lowest changes. In one Stanton Moor sample of $MgCl_2$ and $CaCl_2$, the reduction in velocity was within the averaged standard deviation of the clean Stanton Moor value, further indicating a lack of change in Stanton Moor $MgCl_2$ and $CaCl_2$ samples.

Extremely large decreases in ultrasonic velocity relative to pre-tested values in both Locharbriggs and Corsehill $MgCl_2$ desalinated samples are due to large gaps created by the loss of material at distinct damage planes. These gaps would significantly increase the length of sound propagation and decrease the calculated velocity, as the sound would have a larger exterior section of air to penetrate. As these voids are located on the exterior section of the stone, these errors are external measurements and not an internal measurement of change.

Lastly, the need for good contact between the transmitter/receiver and stone surface must be acknowledged. Samples such as Locharbriggs $MgCl_2$ had significant surface irregularities and were extremely rough. This property lowered the quality of the transmitter/receiver surface contact and introduced errors that likely decreased the measured velocity. In contrast, Stanton Moor and Cullalo samples had relatively low surface alteration that likely yielded more reliable results by providing better contact surfaces.

A collective reduction in the ultrasonic velocity of desalinated samples relative to their initial pre-test values shows that every stone experienced alteration to their internal pore structure. In some situations this alteration was not visible in hand specimen, with little observed surface change. A reduction in ultrasonic velocity propagation suggests the formation of internal cracks and fractures that decrease the cohesion and surface contacts of grains. Every sample experienced a decrease in their ultrasonic velocity, with changes generally lying out-with the standard deviation (as measured in Chapter 3) for each sandstone. Error values are generally quite high for each sandstone, specifically in Stanton Moor and Locharbriggs samples. This feature is explained by the difference in stone size and the lack of sufficient repeat measurements.

4.2.5 Changes to fluid movement within the pore network

Hydric properties of the desalinated stones were analysed to reveal any changes in water absorption and capillary coefficients. Samples were reanalysed after one month of desalination in de-ionised water and after each sample was trimmed to remove discolouration and any possible

contaminants. End values were calculated after the subtraction of errors that were measured as the percentage change of control samples subject to each test. This approach was in order to remove the effects of surface contamination and heating – cooling and wetting - drying on the samples as these were the processes that affected the control samples. Results reported herein refer to the average changes experienced by each sandstone after the subtraction of the changes to control samples. This approach will therefore highlight the changes caused by salt crystallisation alone.

4.2.5.1 *Capillary coefficient changes: pore sizes*

There is a general decrease in the capillary coefficient after the crystallisation tests across every stone type subject to NaCl and $CaCl_2$ (also control samples). Corsehill (N_{3post}) and Locharbriggs (N_{3post}) experienced the greatest reductions of 55.1% and 44.2% respectively with NaCl. Cullalo (N_{3post}), Stanton Moor (2) (N_{3post}) and Doddington (N_{3post}) experienced reductions of 29.4%, 21.1% and 5.3% respectively while Stanton Moor (1) (N_{3post}) samples were not measured due to the breakdown of these samples during desalination. $CaCl_2$ also induced reductions to the capillary coefficient, with Locharbriggs (C_{3post}) and Stanton Moor (2) (C_{3post}) experiencing similar reductions to NaCl of 46.2% and 20.5%, respectively, while Cullalo (C_{3post}) experienced a greater fall in capillary coefficient, of 44.9%. Locharbriggs (M_{3post}), Cullalo (M_{3post}) and Stanton Moor (M_{3post}) were the only samples repeat tested for $MgCl_2$, with Locharbriggs (M_{3post}) and Cullalo (M_{3post}) experiencing average increases of 92.3% and 2.7%, respectively, while Stanton Moor (M_{3post}) once again experienced a negligible change. Control samples for each sandstone type experienced a reduction to their capillary coefficient. Stanton Moor and Cullalo control samples had greater reductions in their capillary coefficient than their equivalent $MgCl_2$ samples (CLM_{3post}) (SMM_{3post}) and in Stanton Moor, greater reductions than equivalent NaCl (SMN_{3post}) and $CaCl_2$ (SMC_{3post}) samples.

NaCl and $CaCl_2$ caused similar decreases in capillary coefficient across every stone type, with Locharbriggs typically experiencing the highest change and Doddington and Stanton Moor the lowest. Large errors are associated with Corsehill and Stanton Moor samples, taken as the average change in control

samples in the test, as outlined earlier. Stanton Moor and Corsehill control samples experienced reductions of 24.7% and 12.9%, respectively which significantly changed the final post-test values in desalinated samples of NaCl and $CaCl_2$ treated samples of both sandstones. Due to the unavailability of samples $LN1_{3post}$, $LM1_{3post}$ and $LC1_{3post}$ due to their critical breakdown, these were replaced with samples $LNP2_{3post}$, $LMP2_{3post}$ and $LCP2_{3post}$ and were measured against the original Locharbriggs average. The combined errors for each stone are therefore substantial and less reliability is placed on these results. The results of changes to the capillary coefficient after the reduction of control values are given in Figure 4-47.

Disregarding the influence of these errors, Locharbriggs, Corsehill and Cullalo generally showed the greatest change in capillary coefficient following desalination after salt-loading tests, while Stanton Moor and Doddington samples showed smaller changes to their capillary coefficient. The changes are shown Figure 4-46. By comparing both the final capillary coefficient values for each sandstone and the percentage of change, it is considered that only Cullalo NaCl (CLN_{3post}), Locharbriggs NaCl (LN_{3post}), Corsehill NaCl (CNa_{3post}), Locharbriggs $MgCl_2$ (L), Cullalo $CaCl_2$ (CLC_{3post}) and Locharbriggs $CaCl_2$ (LC_{3post}) samples experienced significant changes. These samples experienced changes >20% after error reduction, however the final capillary uptake values were still within the standard deviation and measured range of values for each sandstone. The range of values for Doddington $CaCl_2$ (DC_{3post}) and Stanton Moor $MgCl_2$ (SMM_{3post}) indicate that these samples experienced both an increase and decrease in the capillary coefficient and are therefore disregarded as being representative of accurate change. Extremely large error values are also associated with Locharbriggs $MgCl_2$ (LM_{3post}) samples; however both samples show a consistent increase in the capillary coefficient.

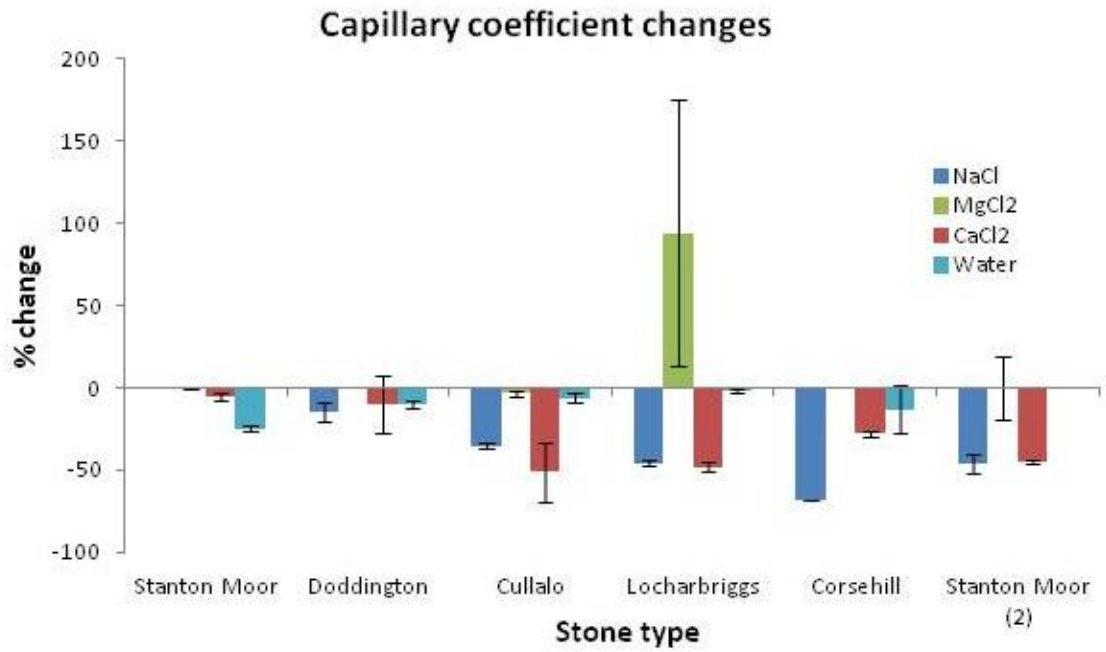

Figure 4-46: Mean percentage change in capillary coefficient relative to pre-tested values on the same samples. (Average of two repeat samples per stone type).

Error bars represent the upper and lower ranges of measured values for each sandstone. Changes to Stanton Moor control samples are also used as errors for Stanton Moor (2) samples. In all but Stanton Moor, the average decrease in the capillary coefficient for water samples is lower than each salt.

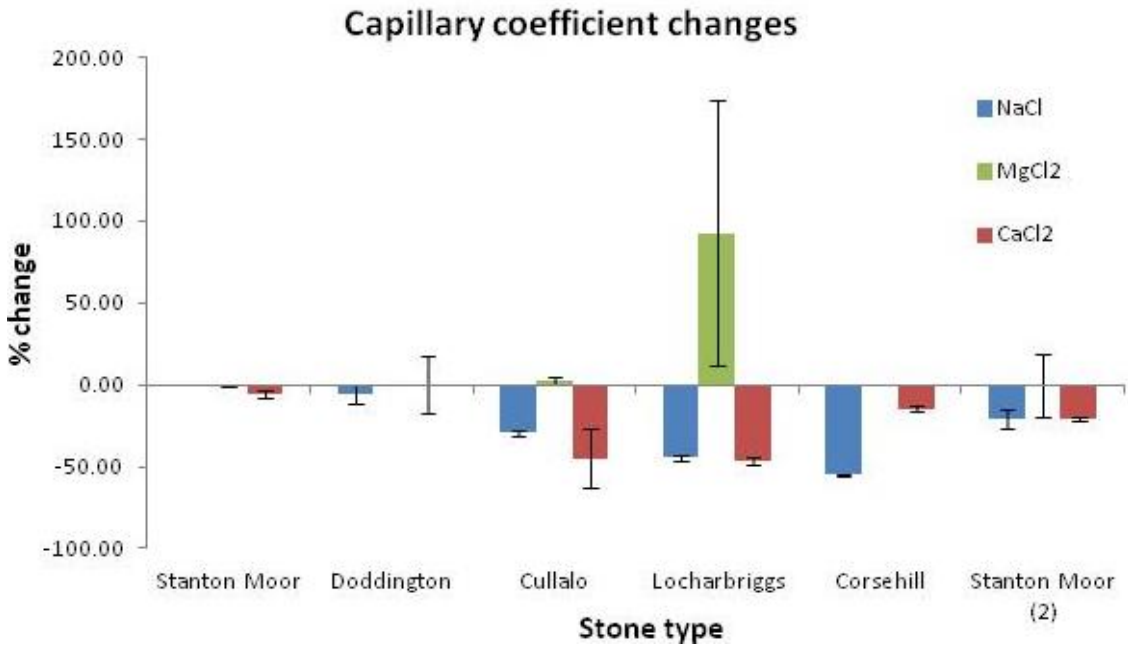

Figure 4-47: Mean percentage change in capillary coefficient relative to pre-tested values on the same samples (after subtracting changes to control values). (Average of two repeat samples per stone type).

Error bars represent the upper and lower ranges of measured values for each sandstone.

4.2.5.2 *Water absorption changes: connected porosity*

Changes to the water absorption capacity of de-salinated samples relative to their pre-tested values show similar trends to capillary coefficient changes, with both NaCl and $CaCl_2$ samples experiencing similar decreases and $MgCl_2$ samples experiencing smaller changes. Doddington, Locharbriggs and Corsehill experience the largest reductions with NaCl, with Doddington (DN_{3post}) showing a fall of 10.3%, while Cullalo (CLN_{3post}) had a lower reduction of 5.2% on average, and Stanton Moor (2) (SMN_{3post}) experiencing an average increase. Doddington (DC_{3post}), Locharbriggs (LC_{3post}) and Corsehill (CC_{3post}) had the highest reductions with $CaCl_2$ of 8.2%, 10.9% and 12.9%, respectively, while Stanton Moor (SMC_{3post}) and Cullalo (CLC_{3post}) had negligible change after the subtraction of controls. $MgCl_2$ caused changes <4% in Stanton Moor (1) (SMM_{3post}), Cullalo (CLM_{3post}) and Locharbriggs (LM_{3post}), while Stanton Moor (2) (SMM_{3post}) experienced a larger reduction of 8.1%. The remaining sandstones were not measured due to the unavailability of samples. High values of change were measured for each control sample relative to pre-tested samples in this test, ranging from reductions of 3.1% in Corsehill ($CCON_{3post}$) to 12.8% in Cullalo ($CLCON_{3post}$). Stanton Moor (2) (SM_{3pre}) values were not measured before the test, with the difference in post-test values for each different salt-induced sample measured against the pre-test values of Stanton Moor (1) ($SMCON_{3pre}$) samples and therefore do not represent exact change to the water absorption capacity in these samples. The final water absorption values are comparable to those of Stanton Moor (1) (SM_{3post}) samples. Only the control samples of Stanton Moor experienced an increase in water absorption relative to the control samples of other stones. The remaining control samples for every other sandstone type experienced reductions in their water absorption value, with Cullalo and Locharbriggs control samples having a greater decrease than their equivalent $MgCl_2$ samples (CLM_{3post}) (LM_{3post}). The changes to the water absorption coefficient relative to pre-tested values of the same samples are shown in Figure 4-48 and Figure 4-49 (after the subtraction of control values).

The changes to Doddington (DN_{3post}/DC_{3post}), Cullalo (CLN_{3post}/CLC_{3post}), Locharbriggs (LN_{3post}/LC_{3post}) and Corsehill (CN_{3post}/CC_{3post}) NaCl and $CaCl_2$ samples are significant, with measured values (before the reduction of

control values) lying out-with the standard deviations and expected minimum ranges for each sandstone (as measured on fresh samples, as given in Chapter 3): Doddington NaCl (DN_{3post}), Locharbriggs $CaCl_2$ (LC_{3post}) and Corsehill $CaCl_2$ (CC_{3post}) experiencing changes ≥10% after the subtraction of control values. Stanton Moor $MgCl_2$ (SMM_{3post}) and $CaCl_2$ (SMC_{3post}) samples experience changes that signify both an increase and decrease in the water absorption, leading to extremely high errors in these measurements. These samples are therefore disregarded.

$MgCl_2$ (M_{3post}) samples experienced changes of <10% that continue to lie within the standard deviations (as measured on fresh samples, as given in Chapter 3) of each sandstone and are therefore not considered significant. Changes to the initial saturation coefficient values on the other hand are considered significant, with most values showing changes >10%, lying out-with the measured standard deviation and minimum range values for most sandstones. Furthermore, Doddington NaCl (DN_{3post}), Doddington $CaCl_2$ (DC_{3post}) and Corsehill $CaCl_2$ (CC_{3post}) samples show changes ≥9% after the subtraction of control values.

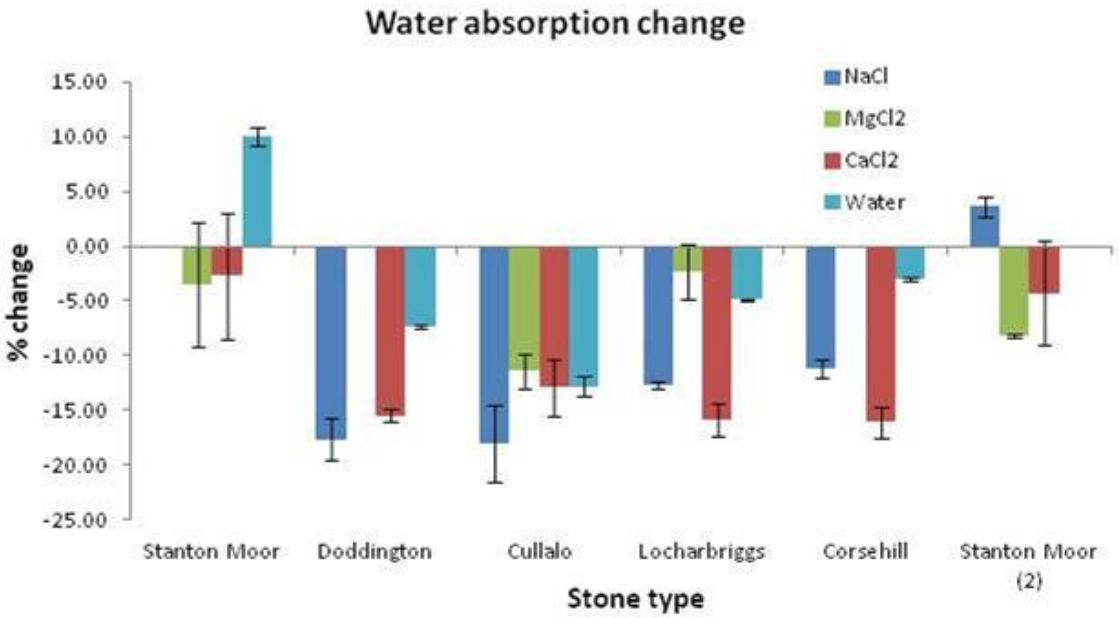

Figure 4-48: Mean percentage change in water absorption relative to pre-test values on the same samples. (Average of two repeat samples per stone type).

Error bars represent the upper and lower ranges of measured values for each sandstone.

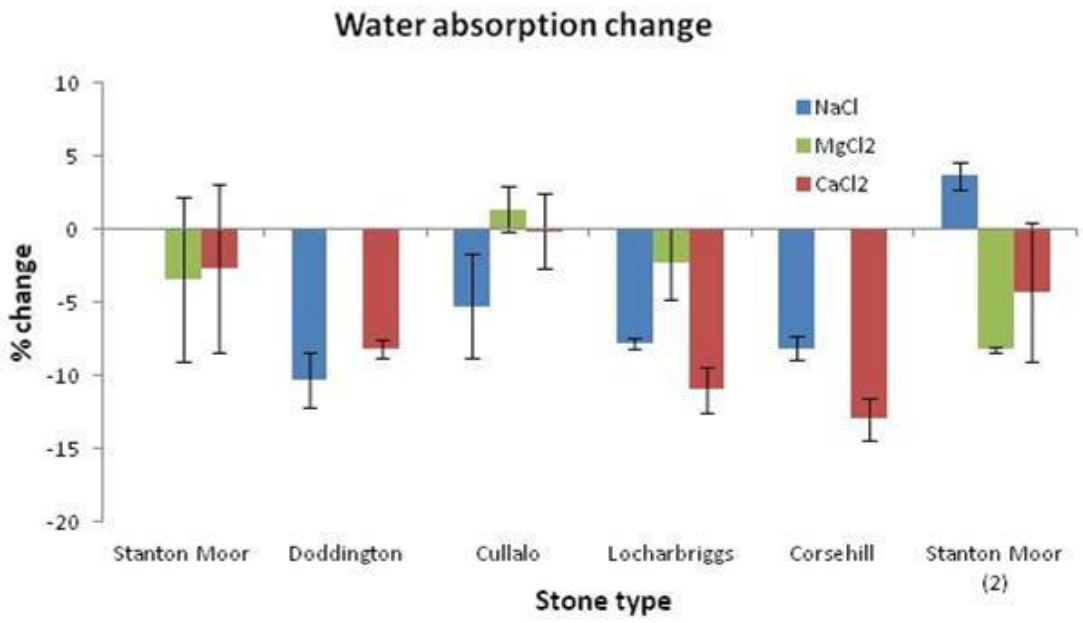

Figure 4-49: Mean percentage change in water absorption relative to pre-test values on the same samples (on subtraction of changes to control values). (Average of two repeat samples per stone type).

Error bars represent the upper and lower ranges of measured values for each sandstone.

4.2.5.3 *Hydric change errors and reliability*

Large magnitudes of change to the capillary coefficient and water absorption of control samples are likely to be associated with a number of processes. The changes to the capillary coefficient and water absorption of control samples include the stresses developed within these stones during the heating /cooling and wetting/drying cycles, with samples experiencing repeat expansion and contraction cycles (Hall and Hall, 1996; Summer and Loubster, 2008). A second explanation is from the contamination of these samples during cycle 9, whereby control samples were contaminated by excess salt solution during the drying stage as surface waters from NaCl samples dripped onto them in the oven. The repeat crystallisation and dissolution of this extremely small salt content could have been sufficient to damage the stone, thus decreasing the capillary coefficient and water absorption values. The actual value of change to the capillary coefficient and water absorption relative to pre-tested values corresponding to the effects of heating and cooling are therefore likely smaller than those reported but cannot be accurately determined. These errors are reported as maximum errors for each sample. In most samples, the change to control samples is smaller than those of salt loaded samples. This suggests that the trend of reductions in

capillary coefficient and water absorption measurements are due to salt loading, although the accurate measurement of exact changes cannot be made with confidence.

4.3 Freeze-Thaw Test

Freeze-thaw tests followed a similar procedure to the British Standard for frost resistance of natural stone: BS EN12371:2010, with batches of samples completely immersed in water, NaCl and $CaCl_2$ solutions of different concentrations. $MgCl_2$ was neglected due sample availability. Locharbriggs, Corsehill, Blaxter and Cullalo samples were subject to 100 freeze-thaw cycles, with samples analysed by visual inspections after every cycle, repeat hydric testing after desalination at 20, 40, 60 and 100 cycles and SEM rough-cut analysis of two samples of contrasting pore structure after 40 cycles before being re-introduced into the test. Stone types were selected in relation to stone availability and their anticipated durability performance. Two freeze-thaw cycles were carried out over 24 hours, with the internal stone temperature experiencing a freezing rate of 0.05°C/min and a minimum internal temperature of -8.9°C over a period of 16 hours. A minimum internal temperature of -5°C was recorded over a second freezing period of four hours, with each stone experiencing an external temperature of -10°C throughout. Thawing occurred over a two hour period whereby internal temperatures peaked at 18.4°C (Figure 4-50). Internal temperatures were measured using a thermocouple glued into the centre of a block of Locharbriggs sandstone that was previously immersed in water.

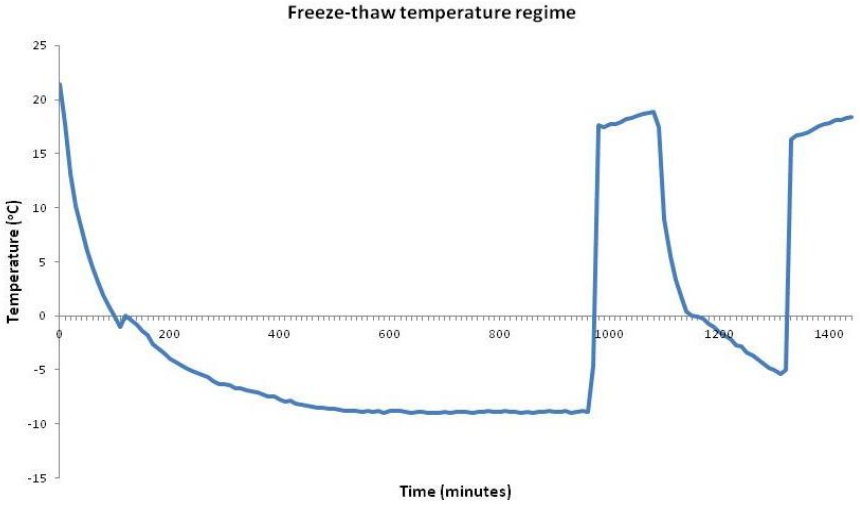

Figure 4-50: Internal temperature profile of sandstone samples during one complete freeze-thaw cycle.

4.3.1 Weight change

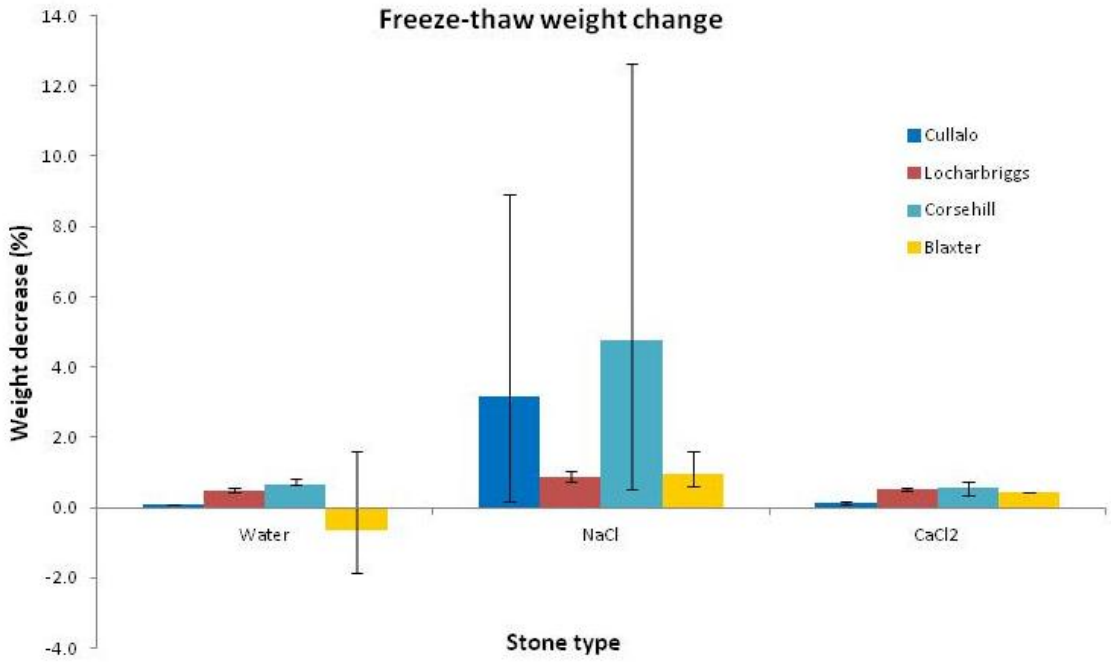

Figure 4-51: mean percentage weight loss after 100 freeze-thaw cycles.

Error bars represent the upper and lower ranges of measured values for each sandstone. Wide ranges for Cullalo and Corsehill NaCl represent the weight loss of samples subject to 3M solutions. Values below 0 represent weight gain.

Weight loss data was measured as the dry weights of repeat hydric tests at the 20, 40, 60 and 100 cycle intervals. Water samples across all four stone types experienced a gradual weight loss during the test. Larger losses of weight are recorded after 60 and 100 cycles but do not exceed 1% in any stone. Weight change data is shown in Figure 4-51.

0.5 M NaCl samples have a greater rate of weight loss at every interval than water samples and a greater overall loss after 100 cycles. A maximum average loss of 0.8% was recorded for Corsehill ($CN_{0.5ftpost}$) and Locharbriggs ($LN_{0.5ftpost}$) and a 0.7% loss was recorded for Blaxter ($BN_{0.5ftpost}$) after 100 cycles. 0.5 M $CaCl_2$ samples show slightly lower values of loss to NaCl across every stone type, with Cullalo ($CLC_{0.5ftpost}$) samples showing the lowest weight loss of 0.1% after 100 cycles.

Corsehill and Cullalo 3 M NaCl samples showed the greatest values of weight loss, with most loss occurring after 40 cycles in both samples. The Corsehill ($CN_{3ftpost}$) sample experienced a 12.6% loss and Cullalo ($CLN_{3ftpost)}$ an 8.9% loss. Locharbriggs ($LN_{3ftpost}$) and Blaxter ($BN_{3ftpost}$) samples also experienced an

increase in weight loss, with an increase over 0.5 M NaCl samples of 0.3% and 0.9% respectively.

The Locharbriggs 3 M $CaCl_2$ ($LC_{3ftpost}$) sample shows a very similar weight loss to 0.5 M ($LC_{0.5ftpost}$) samples. Corsehill ($CC_{3ftpost}$), Cullalo ($CLC_{3ftpost}$) and Blaxter ($BC_{3ftpost}$) 3 M $CaCl_2$ samples experienced the same weight loss as 0.5 M samples.

Corsehill experienced a greater weight loss across every solution (and solution concentration), with Cullalo experiencing the lowest weight loss with water and $CaCl_2$ saturated samples. Locharbriggs and Blaxter had similar weight loss values for all solutions. Freeze-thaw tests are comparable to the first crystallisation test results in that both sets of samples were uncovered and completely immersed in solution. This fact allows weight loss data over the first 40 cycles to be compared between them. Freeze-thaw 0.5 M NaCl weight loss values are lower than equivalent crystallisation test values, particularly with Locharbriggs and Blaxter samples. Freeze-thaw water samples experienced a slight increase in weight loss after 100 cycles when compared to the crystallisation test water samples after 36 cycles. Weight loss values are identical in water samples after the equivalent amount of freeze-thaw cycles, with only Locharbriggs experiencing a greater weight loss in the crystallisation test.

4.3.2 Visual change

Throughout the test, 3 M NaCl samples showed salt efflorescence after each 16 hour freezing period. 0.5 M NaCl samples also showed efflorescence in most samples, but this was lower than equivalent 3 M samples. Both $CaCl_2$ concentrations caused no visible efflorescence, with some samples still surface wet after 16 hours of freezing, suggesting that freezing of $CaCl_2$ solutions did not take place in the stone at surface temperatures of -10^{o}C. Water samples under both freezing regimes experienced ice formation on their surfaces but there was no distinct trend as to the extent of this ice formation between any sandstone.

4.3.3 Freeze-thaw damage to the grain structure

SEM analysis of dry rough-cut specimens of Corsehill ($CN_{0.5ftpost}$) and Cullalo ($CLN_{0.5ftpost}$) 0.5 M NaCl after 40 cycles highlights the influence of pore structure on salt distribution within both stones. Clusters of salt crystals are larger within the Corsehill sample, while Cullalo shows a well dispersed salt coverage of evenly sized crystals throughout the pore network.

4.3.4 Changes to fluid movement within the pore network

The hydric properties were measured by changes to the capillary coefficient and water absorption after 60 and 100 cycles. It is important to note the large variations between specific repeat samples across every stone type.

4.3.4.1 *Capillary coefficient change: pore sizes*

Two of the three Locharbriggs water samples show good agreement, with changes to the capillary coefficient relative to pre-tested values of between 2% and 3% after 100 cycles. The third sample shows a decrease of nearly 70% after 100 cycles. 3 M concentrated samples of NaCl ($LN_{3ftpost}$) and $CaCl_2$ ($LC_{3ftpost}$) show minimal capillary coefficient increases of 9.3% and 7.8%, respectively. There is a significant difference of 29% between the changes to the capillary coefficient relative to pre-tested values in both 0.5 M NaCl ($LN_{0.5ftpost}$) samples, however close final values of 329.66 gm^2 and 333.82 gm^2 show that the final uptake values are very similar. 0.5 M $CaCl_2$ ($LC_{0.5ftpost}$) samples show closer agreement, with a near identical increase in the capillary coefficient of 31.39% and 32.18%, with most change taking place between 60 and 100 cycles.

Cullalo water ($CLCO_{ftpost}$) samples show a consistent increase in capillary coefficient after 100 cycles, with an average increase of 36%. The 3 M NaCl Cullalo ($CLN_{3ftpost}$) sample shows a significant decrease of 51% after 100 cycles, while a large variation in the extent of change exists between 0.5 M NaCl ($CLN_{0.5ftpost}$) samples, with one sample showing a decrease of 56% and the other experiencing no change in capillary uptake. Similar variations are evident in $CaCl_2$ samples, with one 0.5 M $CaCl_2$ ($CLC_{0.5ftpost}$) sample showing a

similar increase in values as the equivalent 3 M ($CLC_{3ftpost}$) sample, while the other 0.5 M sample ($CLC_{0.5ftpost}$) showed minimal change.

There is no change in the capillary uptake of Corsehill water ($CCON_{ftpost}$) samples, while there is a consistent decrease in values with all Corsehill NaCl samples. Both Corsehill 0.5 M NaCl ($CN_{0.5ftpost}$) samples show decreases of 67% and 61% and are larger than the 3 M NaCl ($CN_{3ftpost}$) samples which saw a decrease of 22%. In common with the water samples, $CaCl_2$ caused no significant changes to the capillary coefficient.

In contrast to the other sandstones, Blaxter shows little variation between all measured samples, with all solutions having no measurable effect on capillary uptake values. A slight increase in the capillary coefficient is measured after 60 and 100 cycles in every sample, with values never exceeding 5.05%.

There is an increase in the capillary coefficient of water samples in all of the sandstones, excluding Locharbriggs, which varied greatly between samples. The water samples show the lowest change in values after 100 cycles, with only small increases in the capillary coefficient relative to pre-tested values recorded in Blaxter and Corsehill samples. Corsehill and Blaxter experienced the lowest changes with $CaCl_2$, with average increases of <5% recorded in both 0.5 M and 3 M samples. There is no trend between salt concentration and salt type across the sandstones, with high 3 M NaCl ($CLN_{3ftpost}$) and $CaCl_2$ ($CLC_{3ftpost}$) changes measured in Cullalo, and the greatest decrease in any solution recorded by 0.5 M NaCl Corsehill ($CN_{0.5ftpost}$) samples. Results are shown in Figure 4-52.

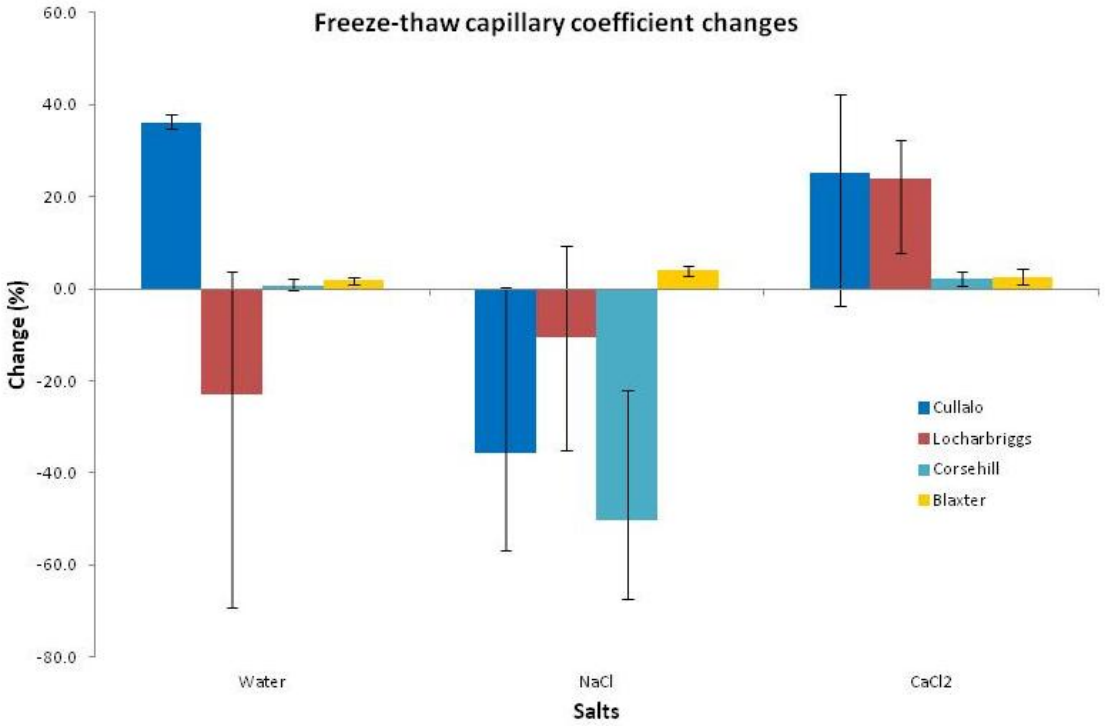

Figure 4-52: Mean percentage change in capillary coefficient.
Error bars represent the upper and lower range of measured values for each sandstone.

4.3.4.2 *Water absorption change*

A trend of gradual decrease in the water absorption capacity over 60 and 100 cycles is evident in all samples with the exception of three Locharbriggs samples which showed no significant change (<1%) after 60 cycles. Water samples had lower decreases in water absorption than salt samples, although one Blaxter water ($BCON_{ftpost}$) sample showed an extremely high decrease of 42% after 100 cycles. The two remaining Blaxter water samples were in better agreement and were both below 10%. Excluding Blaxter, the other sandstones suffered a greater reduction in water absorption with the 0.5 M solutions of both salts compared to 3 M solutions. NaCl caused the greatest decrease in Locharbriggs, Corsehill and Blaxter, while Cullalo experienced the greatest decrease with $CaCl_2$. Cullalo had the greatest decrease with every solution across each concentration, with an average water decrease of 10.3% and an average $CaCl_2$ decrease of 16.3%. Locharbriggs on the other hand experienced the smallest decrease across every solution, with changes never exceeding 10%. Blaxter and Corsehill had similar average decreases with every solution. Most of the repeat samples for each solution had variations of roughly 2-4%, with Blaxter generally having the highest variations between

repeat samples; with a difference of 30% between water samples, 10% in NaCl and 4% in $CaCl_2$.These results are shown in Figure 4-53.

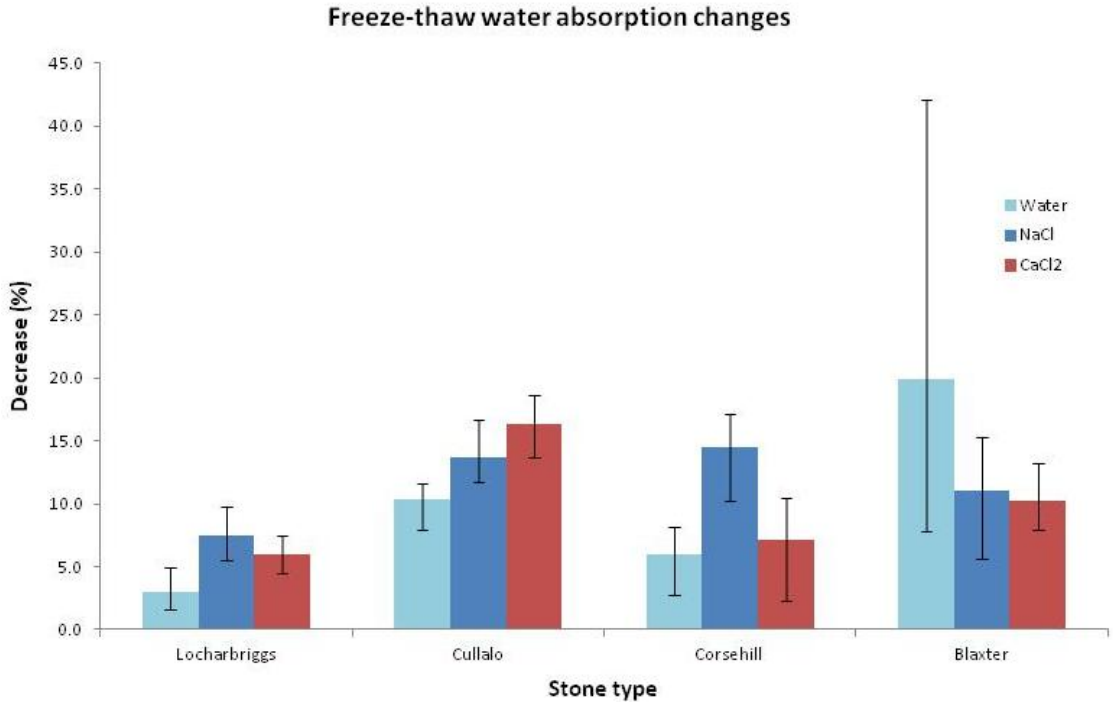

Figure 4-53: Mean percentage decrease in water absorption.
Error bars represent the upper and lower ranges of measurements for each sandstone.

4.4 Critical evaluation of stone characterisation testing

It is important to evaluate and critique the methodologies and techniques used within this thesis that were used to characterise each sandstone type. This is in order to distinguish between those that were and were not of value in understanding the salt-induced decay of each sandstone from the different salts. This evaluation will contribute to a stone durability assessment toolkit that will help recommend the best practice for future stone durability research and materials testing by classifying different techniques that are deemed essential, useful and not useful for stone durability assessment. This toolkit is discussed in greater detail in Chapter 7. Table 4-4 summarises: (i) the stone properties that each technique measured; (ii) the rationale for the use of each test; (iii) the usefulness of each test.

Test Methodology	Use for stone characterisation	Usefulness for understanding salt-induced decay from de-icing salts.
DIA (SEM)	To characterise the grain structure: grain size and grain shape, and to calculate the porosity. SEM is used to analyse salt crystallisation damage.	Did not provide information that helped to predict stone durability or understand salt crystallisation damage.
µCT	To help characterise the pore network by visualising the capillary uptake of salt solution into Blaxter and Locharbriggs sandstone.	Did not provide sufficient information to help understand or predict stone durability that wasn't available through other techniques.
USV	To quantify the grain compaction of each sandstone. Also used to quantify changes to the grain structure after salt crystallisation tests.	When used to quantify changes to the grain structure after salt crystallisation tests it was useful in helping to understand the response of specific stone types to salt-induced decay.
Colour	To quantify the colour of fresh sandstones and colour changes after salt crystallisation tests.	Did not provide information that helped to predict stone durability or understand salt crystallisation damage.
Laser Scanning	To characterise surface roughness and changes to the stone surfaces after salt crystallisation tests.	Did not provide sufficient information to help understand or predict stone durability that wasn't available through other techniques.
Buoyancy Weighing	To measure the porosity of each sandstone.	Useful in calculating porosity that was representative of each sandstone but was not used individually to understand or explain salt-crystallisation damage/durability.
Water Absorption	To measure the amount of water that is absorbed into the stone under atmospheric pressure. This helps to understand the connected porosity of the sample and was used to analyse the changes to the connected porosity from salt crystallisation damage.	Provided more useful results than porosity measurements for understanding salt-crystallisation damage and stone durability. An important parameter to measure.
Saturation	To measure the ratio of pores filled with water under atmospheric pressure to the volume of pores filled under vacuum. Helps to understand the connected porosity of the sample.	As useful as understanding the porosity of each stone, but not as important as the water absorption value, and was not used specifically to understand salt crystallisation damage or predict stone durability.
Capillary Coefficient	To measure the rate of moisture absorption from capillary processes. This helps to understand the movement of moisture through pores <20µm in diameter	A useful parameter that helped to explain the extent of salt-induced damage in specific sandstones but cannot be used in isolation to predict stone durability.

	and the amount of these pores that are accessible.	
Drying Test	To provide information on: (i) the rate of moisture loss over a specific period of time, (ii) the critical moisture content which describes the moisture content of the stone when the drying boundary retreats into the stone, (iii) the residual moisture content in the stone after a specific period of drying.	A useful parameter that helped to explain the extent of salt-induced damage in specific sandstones but cannot be used in isolation to predict stone durability.
MIP	Primarily to measure the pore size distribution within each sandstone and to measure the porosity. This data is used to calculate theoretical crystallisation pressures and help predict stone durability to NaCl.	When used to measure the pore size distribution of each sandstone was an extremely useful technique. Pore size distribution data was used as the basis of calculating theoretical NaCl crystallisation pressures and predicting stone durability to NaCl-induced decay.
He Porosimetry	To measure the porosity of each stone.	A good technique for measuring porosity, but these results were not used to help understand salt crystallisation damage or predict stone durability.
Nitrogen Permeability	To measure the permeability of each stone.	A good technique for measuring permeability, but these results were not used to help understand salt crystallisation damage or predict stone durability.
Compressive Strength Tests	To measure the compressive strengths of dry sandstone samples.	The results were made on dry samples and might not be representative of the strength values of wet samples within the salt crystallisation tests. Tensile strength is more important in understanding stone durability and should be measured instead. This was used as a reference for theoretical crystallisation pressures.

Table 4-4: Critical evaluation of stone characterisation testing.

The comments made for each test outlined within the table do not detail the effectiveness of each test at measuring its intended property. For example, the use of a chroma meter in quantifying stone colour is the most accurate and efficient process of this measurement, however this property was not found to be of value in understanding the durability of sandstone to salt-induced decay. Although the tests that were identified in Table 4-4 as not being of use in understanding the thesis research question, such as colour measurements and laser scanning, they continue to have their value within the field of stone weathering research and have been used effectively elsewhere to quantify the 'greening' of historic masonry (Cutler et al, 2013) and stone response to physical decay processes (Gomez-Heras at al, 2008), respectively. The tests that are identified in Table 4-4 as not being of value to this thesis are found in the attached appendix.

The remaining tests are all considered to have some value in answering the research question. The most important stone properties that help in the understanding of stone durability and salt-induced decay relate to the pore properties and moisture movement within the stone. Other techniques including USV and SEM are of value in quantifying and understanding the changes to the stone after salt crystallisation. These techniques by themselves however do not serve to help predict stone durability.

Each technique that was used throughout the thesis is critically evaluated in chapter 7, whereby the most and least important properties and techniques for estimating stone durability to salt-induced decay are discussed. Furthermore, the most efficient and effective techniques for measuring different and important stone properties are also discussed.

5 Discussion: changes to the stone properties from durability tests.

In order to fully understand and predict the long-term impacts of salt crystallisation on sandstone, a comprehensive analysis of changes to the various properties of the stone must be undertaken. The properties that are most important to the present study are those that control moisture movement and the structural parameters of the stone. These properties are generally interconnected, generating important feedback mechanisms that influence the continued durability of the stone to both salt crystallisation damage and several other weathering processes.

This chapter discusses the changes to the grain structure and fluid movement within sandstone from the crystallisation of NaCl, $MgCl_2$ and $CaCl_2$ de-icing salts after the completion of repeat salt crystallisation and freeze-thaw tests. The most important parameters of the stone that control its durability will be discussed along with the main salt crystallisation mechanisms that help govern the potential destructiveness of each salt.

5.1 Changes to the stone properties from NaCl crystallisation.

NaCl is the one of the most common salts within our environment and is used as the primary de-icing salt across the world due its low cost, availability and effectiveness. It is therefore extremely important that the main crystallisation mechanisms of NaCl are well understood, and the major changes to the stone caused by NaCl crystallisation are identified.

5.1.1 Changes to the grain structure from NaCl.

Grain structure is an important property controlling stone strength and moisture movement. Within this study grain structure refers to the mineralogy and grain size, shape and compaction.

The results of freeze-thaw and salt crystallisation tests are given in Chapter 4. NaCl causes similar decay features in most sandstones across each salt crystallisation test. Granular decay was the most prominent decay process linked NaCl, and involves the loss of individual grains from the surface of the stone. In all three crystallisation tests, granular decay focussed on the corners and edges of the blocks and especially so in the second test. This process was limited to the bottom capillary zone of the stones, as identified by laser scanning (Figure 12-1, Figure 12-7).

5.1.1.1 *Granular Decay induced by NaCl*

Granular decay develops on stone faces owing to the development of high crystallisation pressures within near-surface pores that over-time force the grains apart. Grains are generally cemented within the stone through quartz and feldspar overgrowths that, on the surface of the stone, have a limited influence due to the limited contact area between surface grains. Surface granular decay is therefore influenced by the cohesive strength of the grain overgrowths. Drying will preferentially take place on the corners and edges of the sample owing to a larger surface area. The cohesive strength of near-surface grains is also substantially reduced on the corners and edges of the samples due to a lack of supporting grains. This geometrical factor will lower the threshold crystallisation pressures required to break overgrowth cements

and will lead to preferential decay occurring at corners and edges (Figure 4-30 and Figure 4-31). Granular decay was evidenced throughout all three crystallisation tests (Figure 4-25 and Figure 11-9) and has been identified in other works as an important decay process (Warke et al., 2006; Angeli et al., 2007).

Broken quartz overgrowths on the surface of Locharbriggs sandstone provide evidence of granular decay, leading to the loss of individual grains from the stone surface (Figure 5-1). This process is evidenced further by SEM analyses in Section 11.1.3.

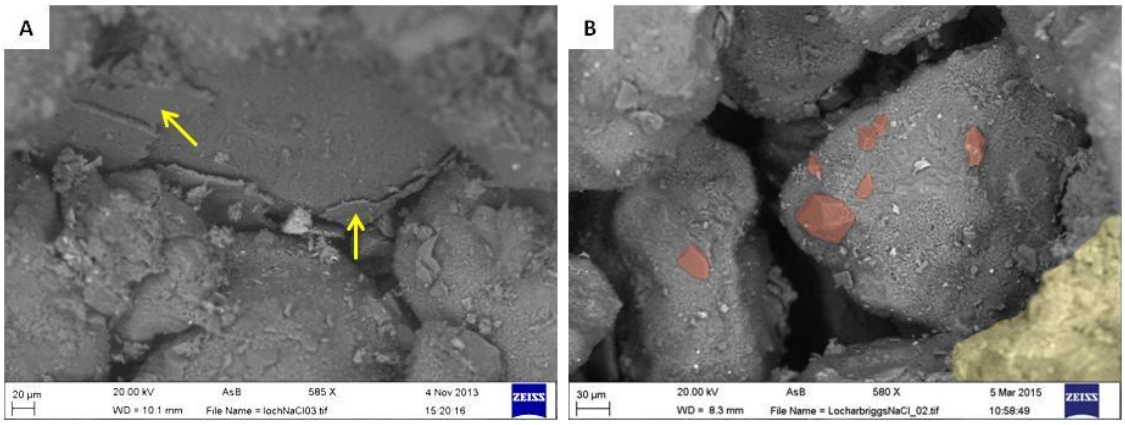

Figure 5-1: Backscatter electron SEM images of broken quartz overgrowths on the surface of Locharbriggs sandstone from crystallisation test 3.

(A): Yellow arrows indicate broken fragments of quartz overgrowths. (B): Highlighted in red are remnants of quartz overgrowths. Shaded in yellow is a cluster of NaCl.

Granular decay has been described previously as a homogenous process when comparing the behaviour of blocks of the same sandstone (Angeli et al., 2007). In reality, granular decay is a spatially heterogeneous process that is influenced by the drying pathways and inherent flaws within the stone. In many cases this process leads to the development of a rough stone surface and an elevated near-surface porosity (Figure 4-34 and Figure 5-2). Warke et al. (2006) suggest that continued granular decay may lead to increased stone weathering potential through positive feedbacks of increased surface-area-to-volume ratio and greater penetration of weathering agents into the stone. Certainly, the Stanton Moor (2) NaCl weight change graph (Figure 5-3) is consistent with operation of positive feedbacks. This process is identified by an increase in salt accumulation after 40 cycles, having followed a short period of weight loss between cycles 20-26. This positive feedback mechanism likely originates from an increase in the near-surface porosity by

granular decay, and precedes further increased weight gain, as a higher near-surface porosity permits increased salt uptake and further internal damage.

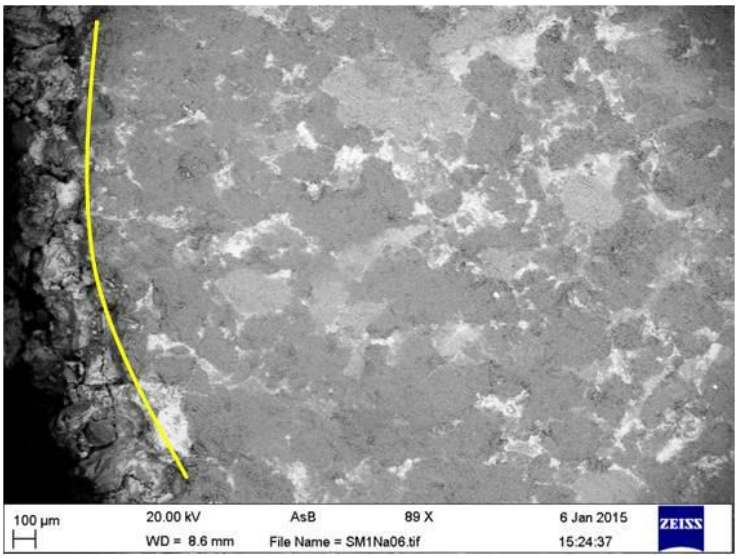

Figure 5-2: Backscatter electron SEM image of the surface of Stanton Moor sandstone after 50 NaCl crystallisation cycles.
The yellow line indicates the outer weathering boundary which is characterised by a more open pore structure and higher porosity.

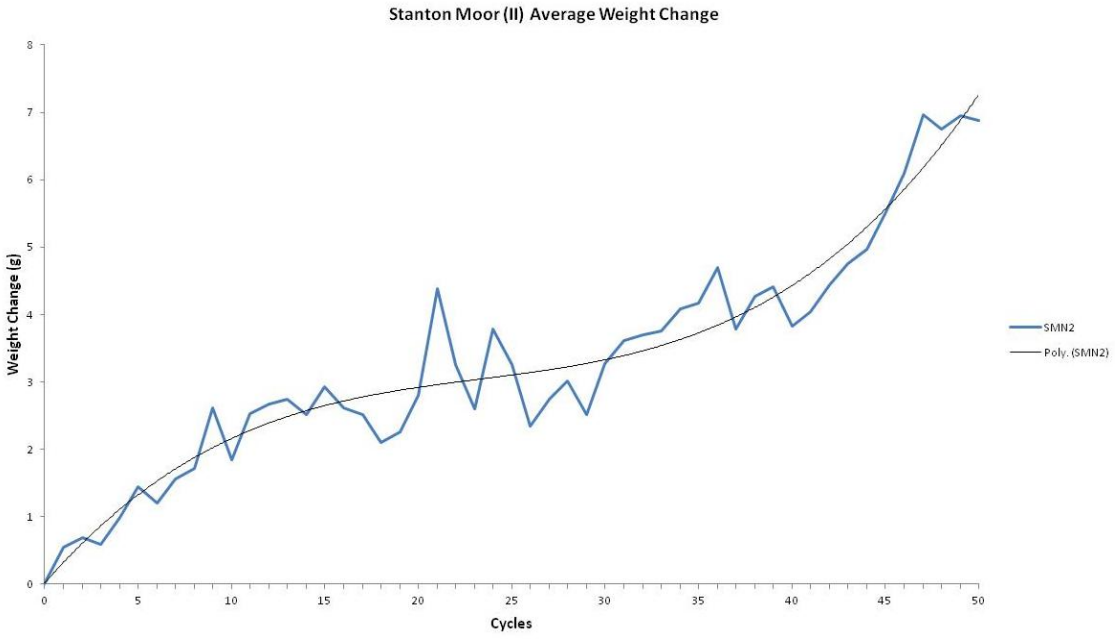

Figure 5-3: Average weight change of Stanton Moor (2) samples over 50 NaCl crystallisation cycles.

Increased surface roughness through granular decay has further consequences, with continued positive feedback mechanisms occurring through several other weathering processes. Hall et al. (2008) suggest that surface roughness is an important intrinsic stone parameter that induces complex near-surface intra-mineral stress fields through time-transient, latitudinally dependent surface shadowing from high relief areas on the stone surface. This process could provide a positive feedback for continued granular decay through increased thermal stress. It is unknown however, what effect increased surface roughness of fine-medium sandstones will have on intra-crystal thermal stresses. The study by Hall et al. (2008) considers a maximum topography of 2 cm height by 150 cm length (13 cm/m) which is far greater than those expected from weathered sandstone surfaces. There is also supporting evidence to suggest that the presence of salt may increase the thermal expansion coefficient of stone (Cnudde et al. 2013).

A second important weathering response to granular decay concerns the increased secondary bioreceptivity of weathered sandstones owing to their increased surface roughness. Bioreceptivity, as originally defined by Guillitte (1995), describes the capacity of a material to be colonised by living organisms without prior biodeterioration, as a cumulative influence of the material properties that control the development of biological growth on stone. As bioreceptivity concerns the changing material properties, the bioreceptivity will also develop with the weathering response of the stone. Several authors have identified the significance of near-surface porosity and surface roughness to increased secondary bioreceptivity (Tiano et al., 1995; Silva et al., 1997; Tomaselli et al., 2000; Dubosc et al., 2001; Prieto and Silva, 2005; de los Rios, 2009).

Guillitte and Dreesen (1995) explain that a greater surface roughness, and a rise in the near-surface porosity, can increase the number of available anchoring points for algae and mosses to colonise the stone. Papida et al. (2000) also show that increased salinity, through salt crystallisation, does not negatively affect the colonisation of sandstone by mixed microbial populations. This outcome is due to microbes producing extrapolymeric substances, which facilitate colonisation. The production of these extrapolymeric substances was actually stimulated in the presence of salts. It

is unknown however, what lasting effect increased “greening”, as stimulated by granular decay, will have on building stone, other than the obvious aesthetic consequences.

Evidence from around Glasgow shows that granular decay is an important process, with Figure 5-4 highlighting a similar sandstone response to differential decay across the corners and edges of several stone blocks, as also observed in crystallisation tests. This weathering response limits central areas of individual blocks from experiencing significant decay, and gives the blocks a very rounded appearance. The high moisture availability and exposure to salts from the adjacent busy road is thought to have influenced the differential damage within these two sites, but without further investigation the influence from de-icing salts from ‘normal’ ground accelerated decay cannot be confirmed.

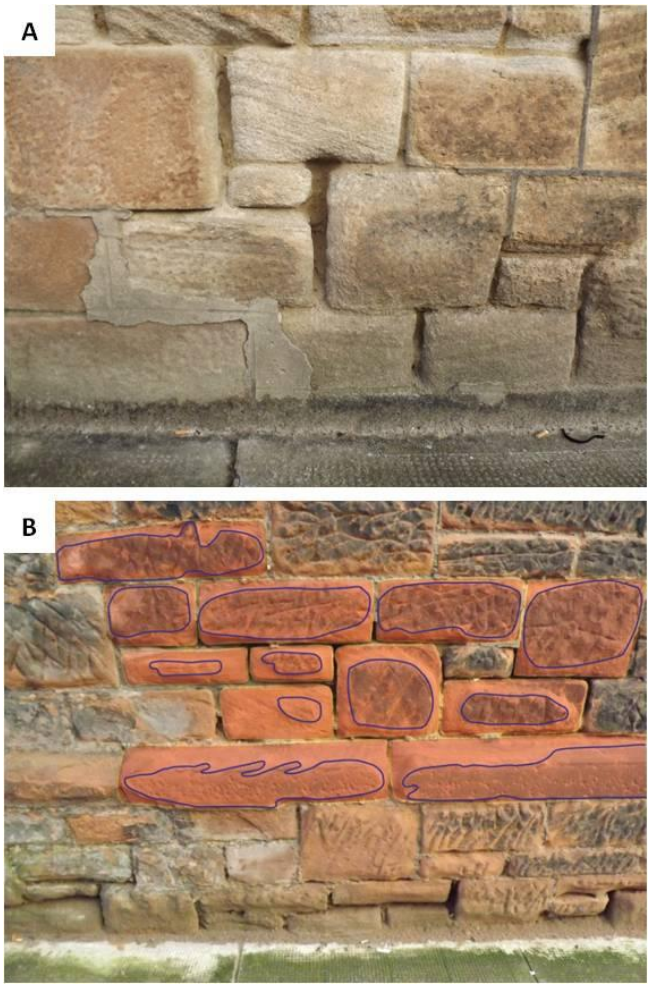

Figure 5-4: Granular decay of buildings in Glasgow.

(A): Granular decay of blonde sandstone in Glasgow. (B): Granular decay of red sandstone in Glasgow. The original block size and shape are highlighted in red, with non decayed central parts of each block outlined in blue. This building is characterised by thin black gypsum crusts, similar to the Bonhill used sample within the study.

5.1.1.2 *Scaling Decay induced by NaCl*

A second important decay feature identified amongst Locharbriggs and Stanton Moor samples in the third crystallisation test is scaling, and specifically contour scaling. Unlike the sporadic and heterogeneous behaviour of granular surface breakdown, scaling can be thought of as a structured or "organised" failure (Warke et al., 2006). Areas of high salt accumulation are eventually linked, creating fracture chains parallel to the drying surfaces.

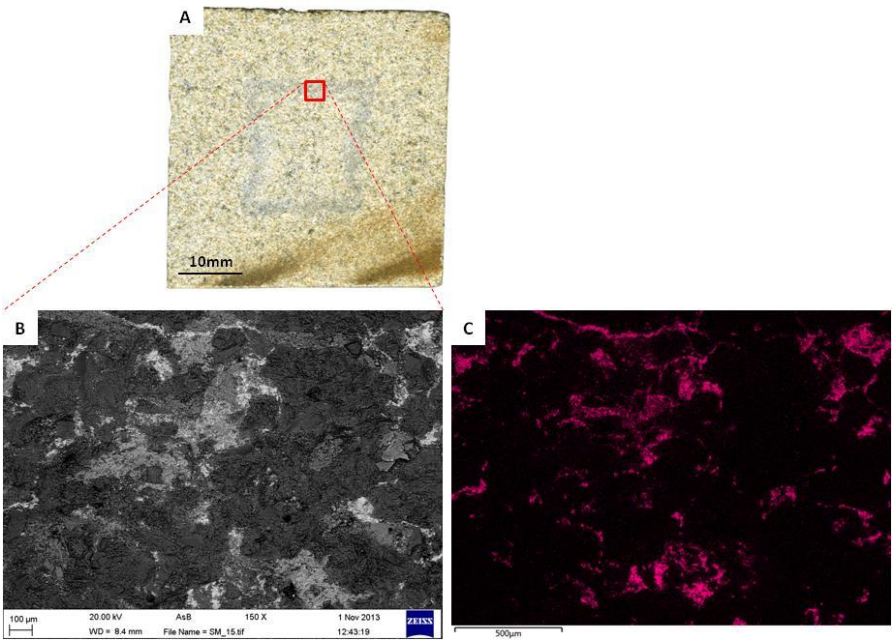

Figure 5-5: Backscatter electron SEM images of NaCl crystals in test 1 Stanton Moor sandstone.

(A): Optical scanner image of Stanton Moor sandstone. The dark square represents a salt horizon in the stone. Red box identifies the location of images B and C. (B): Backscatter electron SEM image of salt crystals. (C): EDX map data showing chloride distribution from the SEM image in B.

Different stages of scaling severity and formation are traced through the changes to Stanton Moor sandstones across each test. Dark halite-rich layers within Stanton Moor highlight salt crystallisation horizons (Figure 5-5). Salt crystallisation sites are influenced by the drying pathways in the stone and will indicate the drying direction to the stone surface. A clear change in the locality of the salt horizon is evident between each crystallisation test as influenced by the different test parameters. Figure 5-5 shows a distinctive salt horizon within the test 1 Stanton Moor sample. This horizon closely resembles the drying pathways of moisture in stone as proposed by Angeli et al. (2007). In this situation, the salt horizon in Stanton Moor is thought to

create a barrier to flow through pore blocking, trapping salt internally within the “wet” zone, as suggested in Figure 5-6.

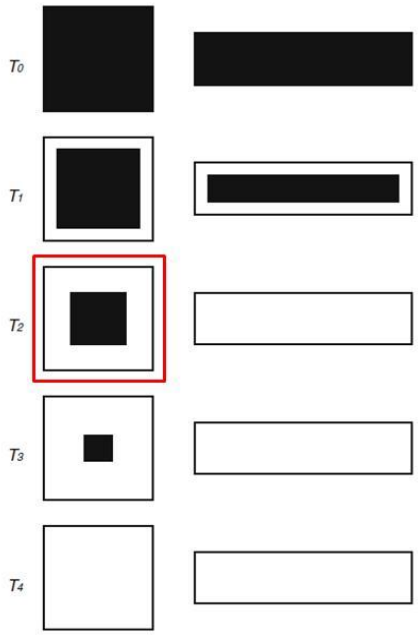

Figure 5-6: Schematic taken from Angeli et al. (2007) showing the simplified drying kinetics of stone of different dimensions.

The black areas highlight wet areas of the stone. The red box highlights a similar pattern of NaCl crystallisation in the Stanton Moor Test 1 sample (Figure 5-5). T_1 – T_4 is the progression in time.

Figure 5-5 highlights the early stages of scaling decay, characterised by a distinctive, but still largely disconnected salt horizon. As discussed originally by Amoroso and Fassina (1983) and later by Smith and McGreevy (1988), the initial development of salt chains is primarily controlled by the pore network properties. These properties determine the capillary movement of moisture within the stone, influencing moisture absorption and the evaporation kinetics. During second stage drying, the evaporation boundary progresses into the stone interior (Figure 5-6). Over time, this process would lead to an internal salt reservoir as salt continually crystallises within the pores. Influenced in part by the surface weathering processes, surface efflorescence and the grain texture, salts would eventually concentrate at a specific depth within the stone. By initially forming small individual crystals (Figure 11-12), salts will, over time, and through diffusion within this disconnected outer layer, form connected “chains” of crystals. Pore blocking from these connected salt chains would prevent further moisture penetration, trapping salts internally (Figure 5-5 and Figure 5-6) and focus further repeat

crystallisation cycles within this outer layer. Crystallisation pressures will only produce internal structural damage once a substantial stress field is established. High crystallisation pressures are achieved from the interconnection (Figure 4-33) of isolated (Figure 5-5) pressure regions throughout a substantial volume of stone (Scherer, 2002). Figure 5-7 is a diagram illustrating changes in the drying regime throughout the third crystallisation test that eventually produced the observed fracture chains of interconnected salt crystals in Stanton Moor (2) samples.

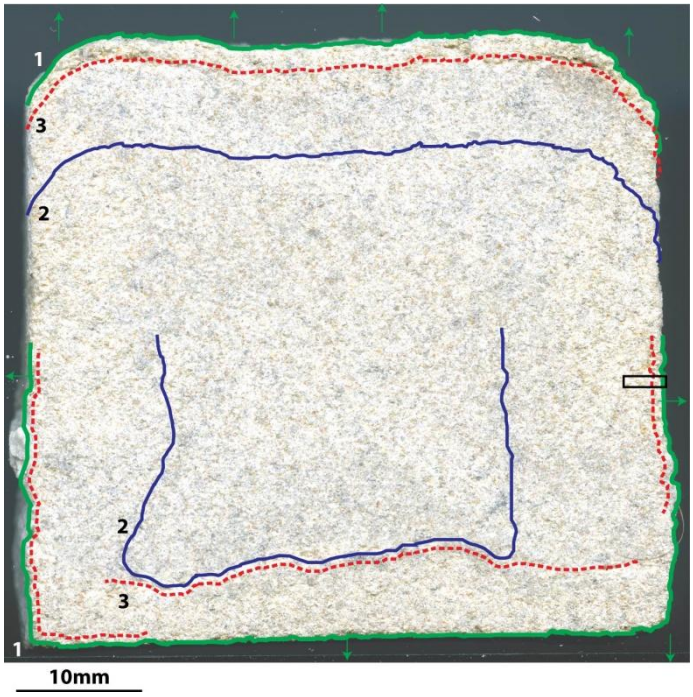

Figure 5-7: Schematic representation of the changing evaporation boundaries within Stanton Moor sandstone ($SMN7_{3post}$).
(1: green solid line and arrows): Surface phase 1 drying. (2: blue solid line): Preferential internal crystallisation and phase 2/3 drying. This is the internal crystallisation boundary evident within Stanton Moor test 1 samples. (3: red dashed line): Fractures within the stone that highlight the subsequent damage after the preferential crystallisation of salts at depth within the stone, as shown by the blue line. The black box defines the analysed region described in Figure 5-8.

SEM EDX maps of parts of Stanton Moor samples reveal the preferential accumulation of halite crystals within distinct boundaries in the stone, with significant volumes crystallising in front of a prominent fracture plane in Figure 4-33. Fracture chains are produced by the intrusion of a uniform drying front from one specific drying face. The development of this fracture chain was achieved in Stanton Moor through minimal surface alteration. Surface alteration has been shown elsewhere to significantly alter the drying pathways within stone (Gupta et al., 2014). Figure 5-8 shows the salt

crystallisation distribution and sustained damage to the same Stanton Moor (2) sample as in Figure 5-7. Increased moisture absorption through greater capillary uptake in Stanton Moor (2) samples changed both the depth of moisture penetration, and the subsequent drying pathways within the stone. Due to evaporation taking place on all six faces of the stone (to a limited extent on covered side faces), a similar salt distribution to Figure 5-5 is evident. Greater moisture absorption and penetration has lead to the development of an internal fracture chain located close to the rear face of the sample, as indicated in Figure 5-7, and contour scaling focused predominantly on the front face (Figure 4-34), but also on the side faces as shown by Figure 5-8. The location of the analysis shown in Figure 5-8 is highlighted by the black box on the right-side of the image in Figure 5-7.

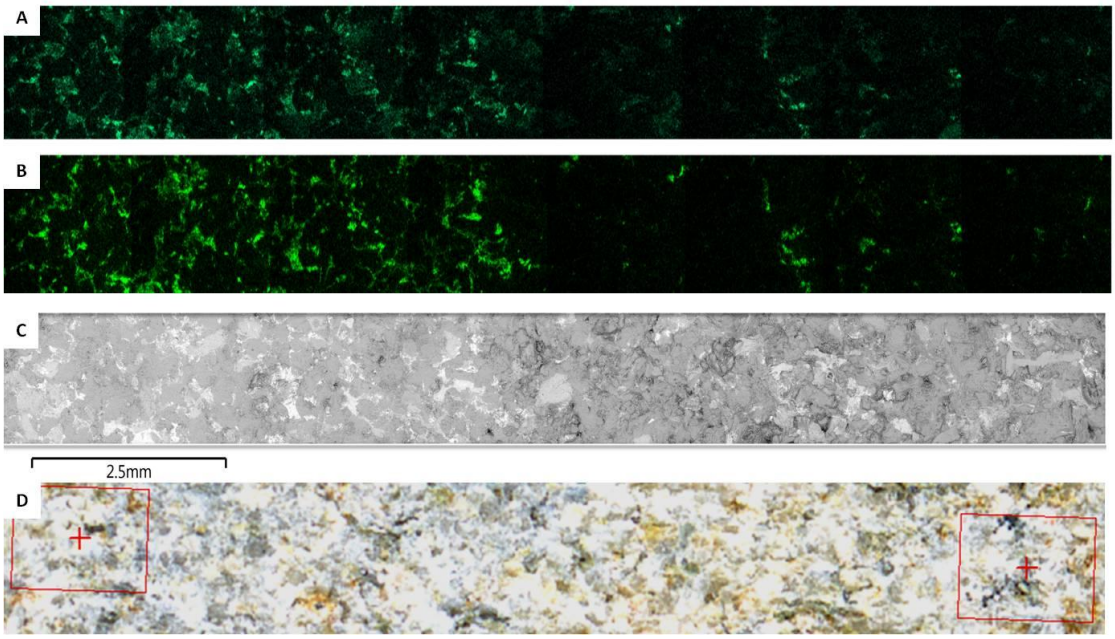

Figure 5-8 SEM EDX mapped section through Stanton Moor NaCl sample ($SMN7_{3post}$). (A): Na distribution. (B): Cl distribution. (C): Backscatter electron SEM image of mapped section. (D): Photograph of the mapped section. The location of this analysis is highlighted by the black box in Figure 5-7.

The outer 2.5 mm of the Stanton Moor NaCl ($SMN7_{3post}$) sample has a depleted salt content relative to the internal salt horizon, with a slight increase in salt measured at a depth of 2.5 mm – 5 mm below the surface. A further gap of salt depletion is encountered at a depth of 5 mm – 7.5 mm before further continued salt enrichment at a depth of ~7.5 mm. Over time, the first salt horizon would continue to increase in salt content through repeated crystallisation cycles. Salt-filled pores will gradually link up and create

fracture chains. The detachment of the outer 2.5 mm of the stone through grain dislodgement and scaling from high crystallisation pressures would subsequently follow. Secondary scaling would then proceed through the positive feedback of the same process at a depth of 7.5 mm below the surface, as a new surface is exposed for further salt enrichment. Smith et al. (2003) identified similar positive feedbacks leading to episodes of repeat contour scaling taking place on limestone buildings in Budapest, Hungary.

The development of structurally damaging fracture chains was prevalent in Locharbriggs sandstone, leading to critical failure in two blocks after 36 and 37 cycles (Figure 5-9). Damage was incurred through the connection of volumes with high crystallisation pressures within narrow bedding planes of relatively low porosity and permeability. A high pore tortuosity, as measured previously for the same sandstone (McCabe et al., 2013), and a relatively low porosity and permeability of bedding planes characterise a pore structure that is vulnerable to salt crystallisation.

Tortuosity is an important parameter that describes the connectivity of the pore network. Although tortuosity does not explicitly relate to pore size or grain properties, these are important variables that influence pore connectivity. As described by McCabe et al. (2013), a high value of tortuosity will slow down ion diffusion and will provide a relatively high number of salt nucleation sites. Salt crystallisation within a highly tortuous region of the stone will generate positive feedbacks by further decreasing the connectivity in the stone by pore blocking. Pore blocking may lead to the non-equilibrium growth of salts, whereby brief episodes of high crystallisation pressures develop as non-forced crystals elsewhere in the stone cannot relieve the increasing crystallisation pressures of compressed crystals within the disconnected bedding planes (Scherer, 2002; Section 1.3.3.1).

Figure 5-9: Photographs of a fractured Locharbriggs NaCl sample from the third crystallisation test. An area of high halite concentration is highlighted. F: front face. B: rear face.

Buj and Gisbert (2010) suggest that stones with a low porosity and high tortuosity could be resilient to salt decay owing to the poor connection and low moisture absorption of the pore network. This might hold true for stones that are entirely characterised by these properties. However, in stones such as Locharbriggs, the “background” pore structure permits high moisture absorption and therefore the poorly connected pores within thin beds have a greater influence than background porosity on the drying pathways and salt crystallisation sites in the stone. This feature leads to non-equilibrium growth and the creation of connected stress fields in narrow planes of the stone.

The importance of spatially concentrated areas of high pore tortuosity to the distribution of salt crystallisation is supported by results of SEM work on Locharbriggs sandstone showing higher grain compaction, a lower porosity and increased salt content within bedding planes (Figure 4-40). Synchrotron CT analysis, capillary uptake measurements and permeability measurements parallel to bedding planes (Appendix A and Chapter 3) also show a disconnected pore network within the bedding planes. This property would certainly disrupt the uptake of water, slow ion diffusion and alter internal drying dynamics of the stone. A greater volume of micro-pores within connected planes and the volume of swelling clays would also increase the salt weathering potential of this sandstone (as discussed later).

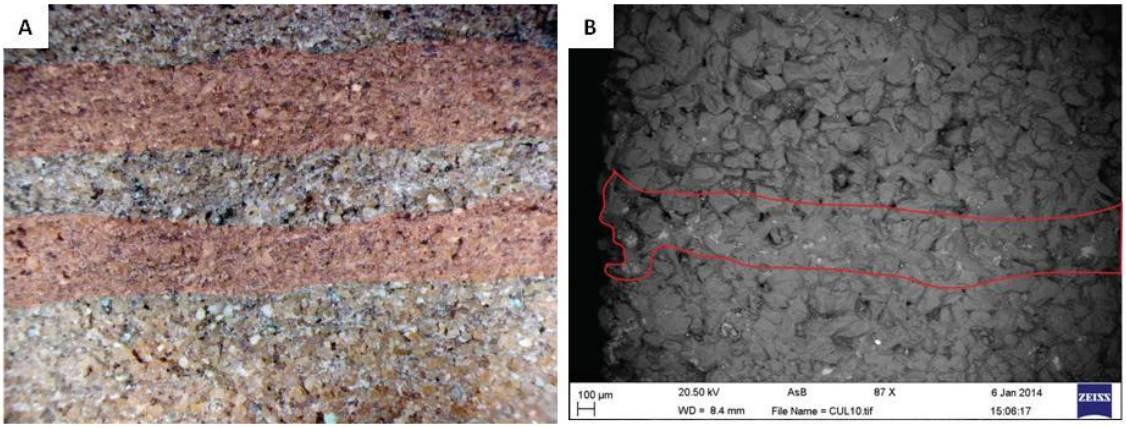

Figure 5-10: Microscope images of Locharbriggs and Cullalo sandstones showing preferential halite crystallisation within layers and bedding planes.

(A): Photograph of Locharbriggs sample LN_{1post}. Red shaded areas highlight layers of high halite accumulation. (B): Backscatter electron SEM image of Cullalo NaCl test 1 sample showing narrow area of high halite concentration (in white).

Preferential crystallisation of halite within distinct boundaries in both Cullalo and Locharbriggs sandstone in the first crystallisation test (Figure 5-10), and the focussing of decay located in specific beds (Figure 4-40), is further evidence for the importance of anisotropy and stone heterogeneity with regards to susceptibility to salt crystallisation.

Planes within sandstone with well connected porosity may however also be viewed as conduits for elevated solution movement towards the surface. This process would permit the growth of “harmless” efflorescence on the stone surface and limit crystallisation pressures within the stone, provided that the stone was “naturally bedded” or “edge bedded”. There is evidence to support this claim, with Figure 5-11 showing salt efflorescence within narrow bedding planes in Locharbriggs sandstone in Glasgow.

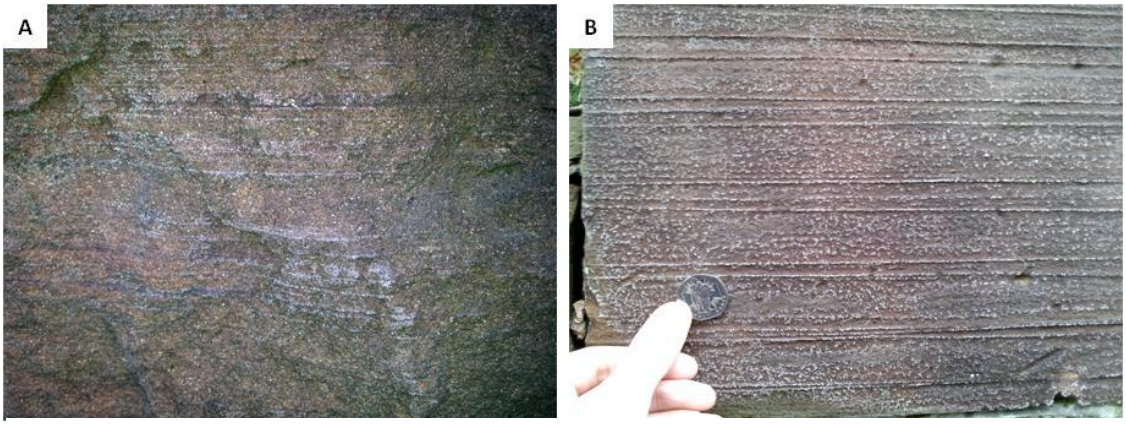

Figure 5-11: Edge bedded Locharbriggs sandstone in Glasgow showing efflorescence focussed within narrow bedding planes in the stone.

(A): Thin bands of halite crystallisation in Locharbriggs sandstone at Kelvingrove Museum, Glasgow, UK. (B): Thin bands of halite crystallisation in Locharbriggs sandstone in a tenement building in Glasgow, UK.

5.1.1.3 *Efflorescence pore blocking induced by NaCl*

Efflorescence is the surface crystallisation of salts. It is generally considered to be a harmless deposit that impacts mainly on the aesthetic properties of buildings. In some situations this is the case, as it represents “efficient” drying, whereby drying takes place on the stone surface as indicated in Figure 5-11. Several authors (Pel et al. 2004; Sghaier and Prat, 2009) have however identified efflorescence as an important transient salt crystallisation feature that has a dynamic interplay and influences the drying regime within the stone and changes the salt crystallisation behaviour.

NaCl efflorescence was prominent on all test samples apart for Stanton Moor, with salt growing as thin crusts on the top sections of most samples in the second and third tests due to the capillary uptake regime. Macroscopic observations reveal efflorescence as thin accumulations on the front drying faces of most samples, with thick dry accumulations forming on the rear faces of Cullalo and Doddington samples in the third test. SEM observations showed that most efflorescence is through the accumulation of individual halite crystals (Figure 5-12). Cullalo in particular formed substantial efflorescence on both drying faces early in the third crystallisation test. This feature is explained by efficient drying in Cullalo through a prolonged stage 2 capillary regime, thus moisture is kept in hydraulic connectivity for a prolonged period of time, allowing a thick efflorescence to accumulate on the stone surface.

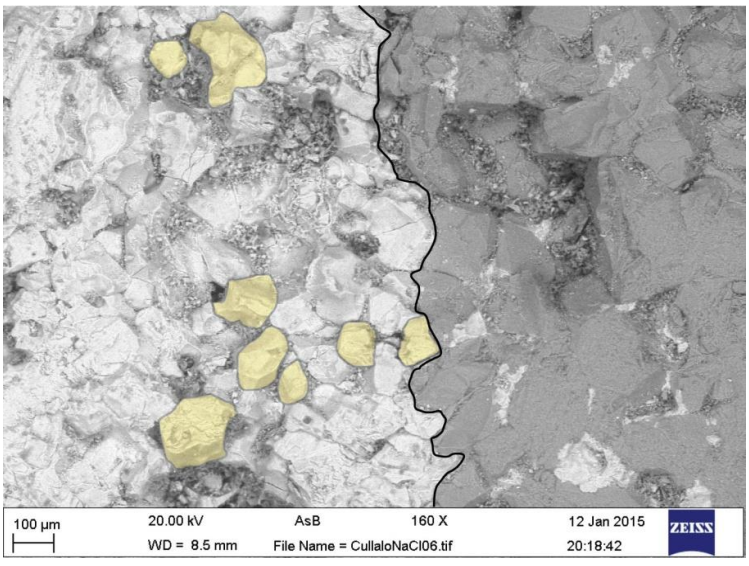

Figure 5-12: Backscatter electron SEM image of a Cullalo NaCl Test 3 sample. Yellow areas highlight individual halite crystals within a large surface accumulation.

Initial efflorescence formation must have been porous in order to have allowed the continued drying of the stone and development of such extensive efflorescence. Drying would have occurred on the outermost surface of the efflorescence (Sghaier and Prat, 2009; Veran-Tissoires et al. 2012) and in spaces on the stone surface between efflorescence accumulations (Eloukabi et al., 2013). Gupta et al. (2014) reveal, through nuclear magnetic resonance techniques, that the drying regime is influenced by drying rate as a function of temperature, RH and the efflorescence texture. A change to the drying regime of Cullalo, and also Doddington sandstone, is shown to follow a similar pattern, whereby the evaporation boundary retreats into the stone as the outer efflorescence crust thickens and eventually dries out; later it creates a barrier to fluid flow (Nachshon et al. 2011). Subflorescence would then commence in these stones, with salt crystallisation damage being observed in central locations within Cullalo (Figure 5-13). The retreat of the evaporation boundary by extensive surface pore blocking is also the likely source of multiple flaking and surface scaling in Locharbriggs sandstone (Section 4.2.3.5) (Figure 4-37).

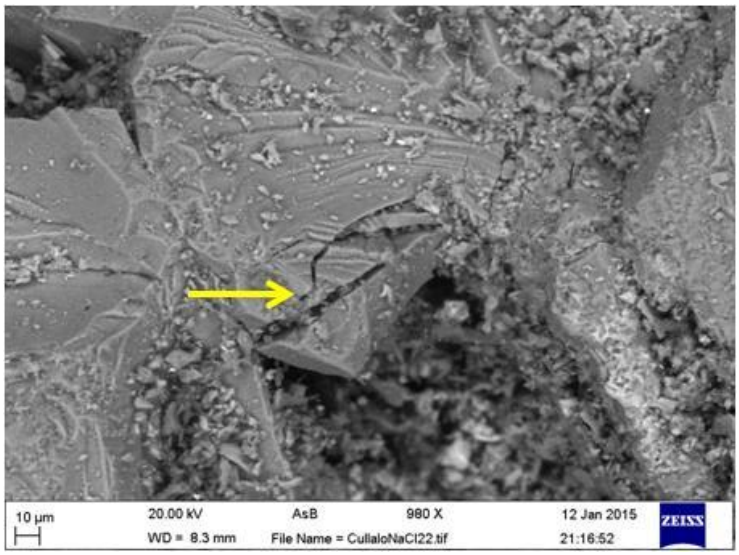

Figure 5-13: Backscatter electron SEM image of Cullalo NaCl Test 3 sample ($CLN4_{3post}$) showing a fractured quartz grain (arrow).

5.1.1.4 *Ultrasonic velocity changes from NaCl*

Changes to ultrasonic velocity following salt tests will reveal any grain structure alterations that have taken place. Generally, ultrasonic velocity is a measure of how compact the stone is, thus describing grain contacts, cementation and cohesion throughout the stone. A decrease in ultrasonic velocity after salt tests is an expression of the reduction in the number and quality of grain contacts in the stone.

Stanton Moor (SMN_{3post}) and Locharbriggs (LN_{3post}) showed the greatest decreases in ultrasonic velocity after the tests; 21% and 18%, respectively. These reductions are in response to the development of large fracture chains in the stone, locally increasing the pore space and reducing grain contacts. A decrease of over 200 m/s in one direction of measurement within the Stanton Moor (SMN_{3post}) sample highlights a prominent porous fracture chain (Figure 4-33) reducing the ultrasonic velocity. Broken quartz grains and fractured overgrowths also lower ultrasonic velocity as these processes disrupt the contact between grains, and increase the air fraction within the stone that the sound pulses pass through. The subsequent infill of pores with broken lithic fragments will likely lower the effective porosity, while increasing the pore sizes and decreasing the percentage of grain contacts.

Reductions of ultrasonic velocity in Cullalo (CLN_{3post}) by 14% show that although surface damage was limited, with no substantial weight loss recorded, internal damage took place through broken and fractured quartz grains (Figure 5-13). Blocked near-surface pores forced the retreat of the evaporation boundary into the stone, leading to the homogenous crystallisation of halite throughout the pore network. In a sense, the substantial efflorescence, although unsightly, protected the outer surface from granular decay and other subsequent alteration.

Corsehill (CN_{3post}) on the other hand, although experiencing the highest salt accumulation and high weight loss values, had the lowest average reduction in ultrasonic velocity (10%). These contradictory results are explained by the distribution of salt within Corsehill sandstone. As shown by SEM analysis (Figure 4-30, Figure 4-31), salt crystallisation was focussed on the outer

edges and corners of Corsehill, with fewer crystallisation sites identified at depth within the stone. Focussed decay along certain edges and specifically the corners may have minimised the impact of this damage on ultrasonic propagation. It is expected that because the sandstone cubes are larger than the pundit transmitter and receiver, corner sections of the stone would have been excluded from the measurements. Therefore the 10% ultrasonic velocity is likely an underestimation of the true reduction in ultrasonic velocity within Corsehill.

As Corsehill sandstone (CN_{3pre}) samples prior to the tests had a low ultrasonic velocity, subtle changes to the grain structure following salt tests would be hard to identify by ultrasonic velocity measurements. Figure 5-14 highlights the immature mineralogy and grain structure of Corsehill sandstone, which is characterised by large pores, a wide range of grain shapes and grain sizes, and a poorly connected and poorly cemented grain structure (Section 3.1.11). The breaking of grain contacts by salt crystallisation is therefore unlikely to make much of a difference to an already poorly connected grain structure. Greater damage is therefore required to create significantly large changes to the ultrasonic velocity propagation

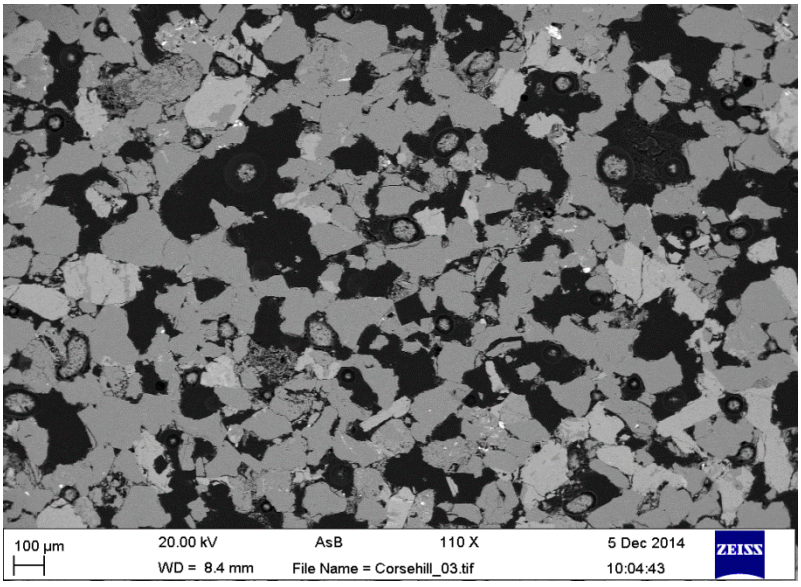

Figure 5-14: Backscatter electron SEM image of untreated Corsehill sandstone in thin section.

Cullalo sandstone by contrast has a well cemented and highly compact grain structure, as identified by digital image analysis (Section 3.2.14). Changes to

the grain structure through the breaking of grain contacts will therefore significantly modify grain structure and be more easily identified by ultrasonic velocity changes. Therefore the changes following salt tests in Cullalo (CLN_{3post}) may be overestimated, while the opposite might be true in Corsehill (CN_{3post}), with ultrasonic velocity measurements underestimating grain network changes in relation to the other sandstones.

Importantly, every measured sandstone sample showed a fall in ultrasonic velocity following salt tests. This finding suggests damage to the internal grain structure for every sandstone subject to halite crystallisation. Importantly, the technique is capable of identifying grain structure changes that are otherwise not discernible by conventional photography and weight analysis techniques.

5.1.2 Changes to fluid movement within the pore network from NaCl

In order to quantify changes to moisture movement and pore network properties of the sandstones from salt crystallisation, selected samples were analysed before and after the tests for changes to several properties that control moisture uptake and moisture movement. Changes to the hydric properties, including water absorption, saturation coefficient and capillary coefficient, are important because they provide information relating to grain compactness, pore size and pore connectivity. Changes to these properties may alter stone behaviour within a building considerably by altering moisture movement, which leads to increased decay rates through other weathering processes.

Contamination of some samples by sealants in crystallisation tests 2 and 3 could have altered each hydric property and so make measurements unrepresentative. The influence of contamination was identified on control samples for each sandstone. The changes in the hydric properties of the control samples were subtracted from stones used in salt loading tests in order to provide more representative values of change. In specific stone samples this process reduced the magnitude of change to the hydric properties substantially so that they were not accepted as representing true

change from salt crystallisation within the stone. Therefore, the average trends of change to the hydric properties after salt tests are discussed, as they illustrate more representative change to the moisture movement.

5.1.2.1 *Water absorption and saturation coefficient changes from NaCl*

There is a consistent decrease in the water absorption and saturation across most sandstone types by the end of each test, with only Giffnock (GN_{2post}) and Stanton Moor (SMN_{2post}) samples in test 2 and Stanton Moor (SMN_{3post}) samples in test 3 showing an increase in both values. Cullalo (CLN_{2post}), Locharbriggs (LN_{2post}), Hazeldean (HN_{2post}) and Corsehill (CN_{2post}) experienced the greatest reductions in the second test, with Doddington (DN_{3post}), Locharbriggs (LN_{3post}) and Corsehill (CN_{3post}) experiencing the greatest reductions in the third test. Larger decreases were found in the third than second crystallisation test, which show a progressive evolution of continued decrease in the water absorption over each cycle. Small differences between each test in results from some sandstone types suggest that substantial internal crystallisation damage happens within the first 16 cycles. On the other hand, this result may be an artefact of the crystallisation test conditions, whereby the focussed drying through one face causes greater damage in response to an earlier retreat of the drying boundary into the stone interior.

Water absorption is an indication of the available and accessible pore space within the stone. A reduction in the water absorption value suggests a decrease in the available and accessible porosity for moisture uptake. Saturation on the other hand relates to the connectivity of the pore network. SEM micro analysis of dry rough-cut sections and polished thin sections of salt damaged stone provide insights as to the reduction in the water absorption and saturation for each sandstone type after crystallisation tests. Most sandstones suffered internal crystallisation damage as indicated by common falls in ultrasonic velocity. Damage to the grain structure is through the fracturing and dislodgement of individual quartz and feldspar grains.

Figure 11-13, Figure 11-16and Figure 11-17 highlight the salt crystallisation damage in Locharbriggs (LN_{1post}) and Blaxter (BN_{1post}) sandstone from the first crystallisation test. They show an extremely convoluted pore structure with

larger debris-filled pores having formed through the substantial fracturing of quartz and feldspar grains. The mobilisation of broken lithic material throughout the pore network probably reduces overall porosity, water absorption and the saturation capacity, by increasing tortuosity and by trapping areas of pores with small broken fragments and mobile clay fractions.

Further analysis of dry rough-cut samples of Cullalo (CLN_{1post}) and Locharbriggs (LN_{1post}) show similar crystallisation damage through the breaking of quartz overgrowths and fracturing of individual grains. Figure 4-32, Figure 5-1 and Figure 5-3 show the fracturing of individual grains and broken quartz overgrowths that have resulted in granular surface decay and the increased mobilisation of lithic material through the pore network. Thin sections (Section 11.1.3) show that this mobile lithic and clay material infills and separates volumes of open porosity, leading to a reduction in the water absorption capacity.

On the other hand, fractured quartz grains create secondary micro-pores that may provide a positive feedback to salt crystallisation, whereby increased crystallisation pressures may arise through the crystallisation of small salt crystals within these micro-pores, as shown in Figure 4-32 and Figure 4-39.

The increase in the water absorption of Stanton Moor (2) samples over Stanton Moor (1) samples in the third salt test is thought to stem from the creation of fracture chains and surface scales within the stone. Figure 5-15 shows the dimensions of newly established secondary pores in the fractured surface zone. Contour scaling creates large open pores that could increase the open porosity for increased water absorption.

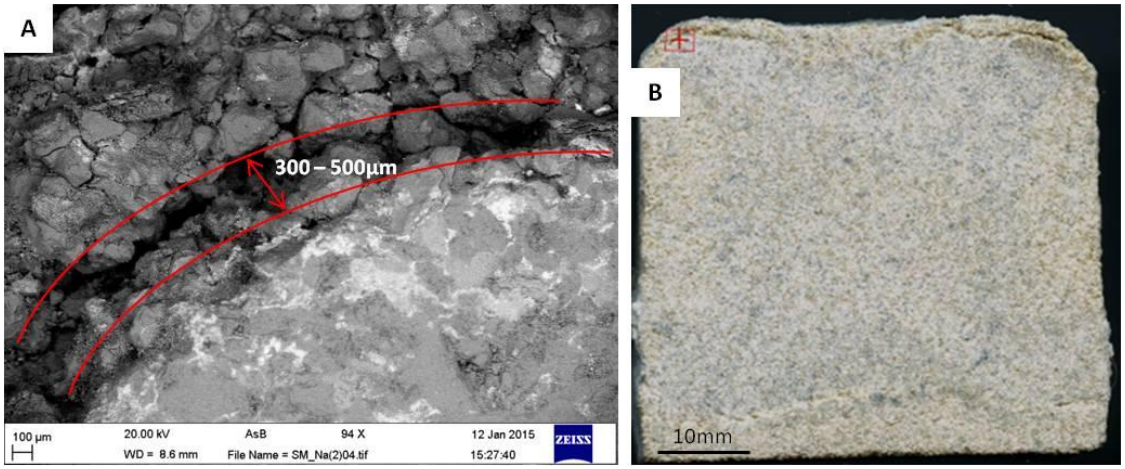

Figure 5-15:Backscatter SEM image of halite crystallisation damage in Stanton Moor test 3 ($SMN7_{3post}$) sample.

(A): SEM image showing surface contour scaling and the creation of secondary porosity. The red area highlights the fracture plane, measuring between 300-500µm in width. (B): Photograph of $SMN7_{3post}$ sample, with the analysed fracture highlighted by a thin red box.

5.1.2.2 *Capillary uptake changes from NaCl*

There was a consistent decrease in capillary coefficient across all samples in all tests bar Blaxter in the freeze-thaw test. Corsehill and Cullalo both showed substantial reductions across every test. Capillary absorption is related to the pore size distribution, especially the fraction of pores and porosity with a diameter <0.1µm, as described in Section 3.2.3. Any change to the capillary coefficient must be related to a modification to the absolute pore size distribution, the accessibility of micro-pores (<0.1µm diameter) and the water absorption capacity. A decrease in the capillary coefficient is attributed to a reduction in the micro-porosity through either a decrease in the micro-porosity fraction by the creation of larger pores, or by a reduction in the accessibility of the micro-pores.

Significant or "genuine" changes to the capillary coefficient (those that are still significantly large after the subtraction of control values), as identified in Hazeldean (HN_{2post}) and Doddington (DN_{2post}) in crystallisation test 2 and Corsehill (CN_{3post}), Cullalo (CLN_{3post}) and Locharbriggs (LN_{3post}) in crystallisation test 3, are attributed to changes in the uptake rate through a shift in the capillary uptake plateau, as depicted in Figure 5-16. Smaller changes to the capillary uptake, as highlighted in Figure 5-17, correspond to a reduction in the water uptake value, rather than a reduced rate of uptake.

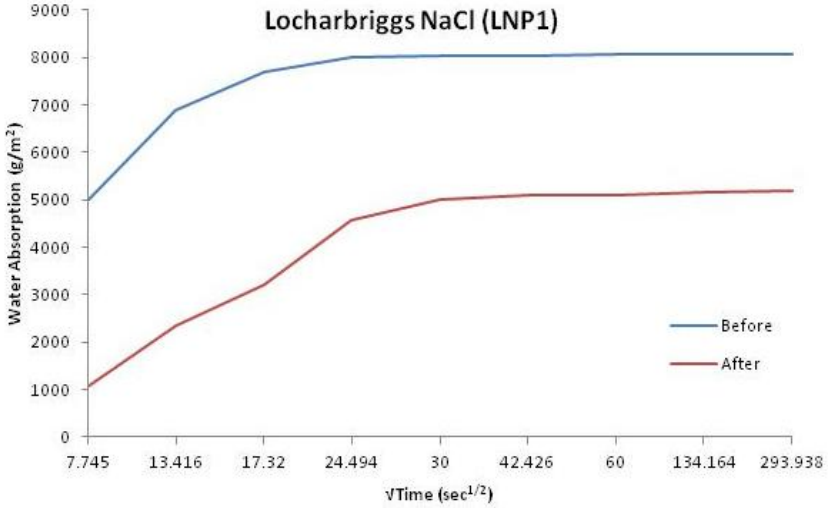

Figure 5-16: Comparison of the capillary uptake curves of Locharbriggs NaCl sample ($LNP1_{3post}$) from before and after the third salt crystallisation test.

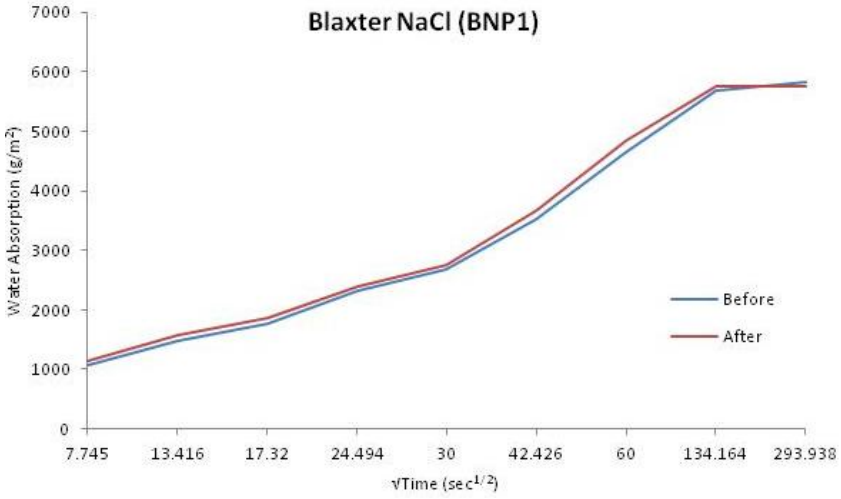

Figure 5-17: Comparison of the capillary uptake curves of Blaxter NaCl sample ($BNP1_{2post}$) from before and after the second salt crystallisation test.

The reduction in the capillary uptake in Locharbriggs sample $LNP1_{3post}$ is from a combination of two main pore network changes: a decrease in the total volume of smaller pores, and a reduction in the water absorption capacity from the infill and disconnection of porosity by mobile lithic material. It must be noted that in certain samples, including Locharbriggs, Cullalo and Corsehill, the original range of measured capillary uptake coefficients exceeds variance values of 45%. Only sandstones that experienced changes out-with their standard deviation and their upper and lower range of values actually experience a significant change to their moisture transport regime that could significantly alter their initial predicted durability in a building. Only Stanton Moor NaCl, $CaCl_2$ and Cullalo $MgCl_2$ samples experienced values that were out-with the standard deviation and measured range of values on clean, control samples as presented in Chapter 3.

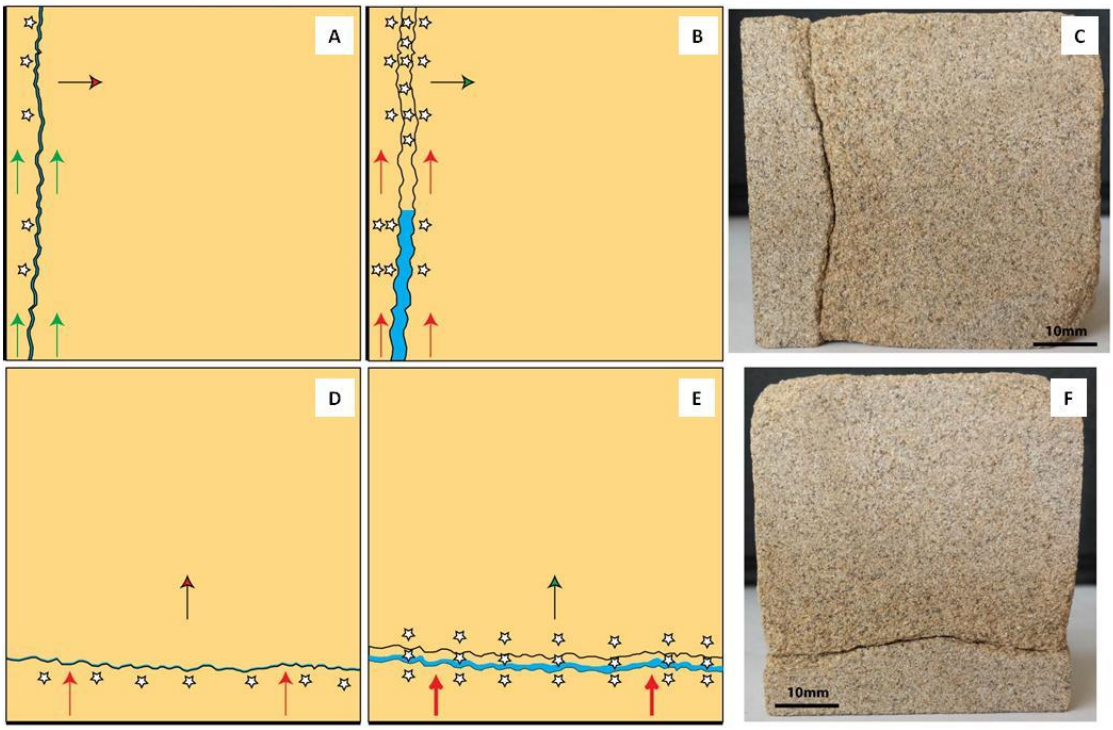

Figure 5-18: Schematic diagram highlighting the effect of secondary pore creation from "fracture chains" on capillary uptake in sandstone.

(A): During the initial stages of fracture chain development, small secondary capillary pores are created that may increase the capillary uptake of water into the stone (green arrows), creating a positive feedback. A thin red arrow indicates low salt penetration into the stone. (B): Over time, further crystallisation continues to take place within this boundary and the chain widens. At this point, the secondary pores within the chain are larger than capillary pores, resulting in a slower capillary uptake of water (red arrows). The thin green arrow indicates high salt penetration into the stone. (C): A photograph of Stanton Moor sandstone highlighting the vertical orientation of the fracture chain. A-C are representative of early fracture chain development in the second crystallisation test. D and E are the equivalent to boxes A and B, illustrating the effect of horizontal fracture chain orientation on fluid flow. Red arrows highlight an initial drop in the capillary uptake at the onset of fracture chain development, even with the creation of smaller, capillary pores. A thin red arrow indicates low salt penetration into the stone. Capillary flow is severely hindered as the fracture chain develops. A thin green arrow indicates a greater salt penetration into the stone. (F): a photograph of Stanton Moor sandstone highlighting the horizontal orientation of the fracture chain.

Figure 11-13and Figure 11-17 show the creation of large lithic-filled pores and pore "chains" in Locharbriggs sandstone. Measuring >500μm in diameter, these large connected pore regions would likely reduce capillary movement within sandstone, while other, smaller near-by pores would slow capillary uptake rate owing to increased tortuosity. Figure 5-18 shows, very simply, the effect of pore chain orientation on capillary uptake. Initially, the capillary uptake rate may be increased through the early creation of pore chains as a salt drying boundary is established within the stone. As salt crystallisation continues, the average pore chain diameter increases, as shown in Figure 11-13 and Figure 11-17, and will eventually inhibit flow

within this region. In Figure 5-18 D and E, capillary flow would be immediately interrupted by the fracture chain.

Water absorption, saturation and capillary coefficients all show a reduction across the freeze-thaw and crystallisation tests. This common pattern indicates a decrease in overall water absorption and moisture movement within the stone through changes to both the pore and grain networks. Water is the key weathering agent in building stone, and therefore a reduction in water absorption could be an important negative feedback, limiting stone decay processes. However, water is always present within building stones, with some studies suggesting increased moisture retention within building stone through an anticipated increase in future annual rainfall (Smith et al. 2011). Changes to the movement of inherent moisture is thought to be of great importance as this process will influence the rate and location of repeat crystallisation cycles within the stone, even without the increased absorption of salt.

A decrease in the saturation coefficient in the freeze-thaw and salt tests suggests a reduction in pore connectivity throughout the stone, while lower capillary coefficients indicate slower movement of moisture. As mentioned previously (Section 5.1.1.2), a reduction in connectivity and flow rate by increased pore tortuosity could lead to the non-equilibrium growth of salt in isolated regions of the stone. Non-equilibrium growth could quickly lead to the development of high crystallisation pressures throughout a now considerably weaker stone (as suggested by reductions in ultrasonic velocity). Fractures and pore chains would provide barriers to hydraulically connected drying through decreased capillary movement, which would provide a positive feedback, leading to further subflorescence of salt at particular areas within the stone.

In a proportion of the stone samples (Cullalo, Hazeldean and in some cases Locharbriggs) the onset of subflorescence is initiated through efflorescence blocking surface pores, while in other stones the microtexture of the stone and the original pore network have a greater initial influence of salt crystallisation. These processes are discussed in Chapter 7.

5.2 Changes to the stone properties from $MgCl_2$.

Changes to stone properties are caused, certainly in part, by the crystallisation of $MgCl_2$, which is a process unlikely to occur naturally within a maritime temperate climate such as Scotland (as discussed in Chapter 5). A second hypothesis accounting for the changes to stone properties concerns the osmotic swelling of clays through the absorption of Mg^{2+} into the clay structure. This process is less dependent on precise RH and temperature conditions and could therefore be a more important process regarding the conservation of Scottish building stone.

The process of $MgCl_2$ crystallisation is more relevant for buildings within the localities identified in Chapter 5: Denver, Colorado, USA, Salt Lake City, Utah, USA and Toronto, Ontario, Canada etc. Salt efflorescence accumulating on the stone surfaces signifies that crystallisation was achieved in the second and third salt test, making it difficult to separate the effects of salt crystallisation from other processes, such as clay swelling. It is likely that a combination of these processes (salt crystallisation and clay swelling) results in the observed decay characteristics in certain sandstones.

5.2.1 Modifications of grain structure.

Three main alteration features in the $MgCl_2$-loaded samples were identified across different sandstone types and will be discussed in turn below. $MgCl_2$ caused significant efflorescence on every sample bar Stanton Moor and within the second and third salt tests, while granular decay was focussed on the corners and edges of most sandstones throughout the third test. Lastly, catastrophic decay affected Doddington (DM_{3post}) and Locharbriggs (LM_{3post}) samples through the loss of large sections of stone by crystallisation occurring in specific planes of weakness in the stone.

5.2.1.1 *Granular decay induced by $MgCl_2$*

Granular decay occurs through a similar process as described in Section 5.1.1.1, but with important differences in the crystallisation and chemical behaviour of $MgCl_2$ resulting in different sandstone behaviour. $MgCl_2$ is shown in this research thesis to grow in very different crystal habits to NaCl, forming

contrasting efflorescence morphologies and affecting sandstones differently. Plane polarised microscope analysis of $MgCl_2$ crystals has identified one distinct $MgCl_2$ crystal morphology that is stable under moderate RH (40-60%) and room temperature conditions (20°C). $MgCl_2$ formed a large continuous salt crust characterised by a rough texture of interconnected salt ridges (Figure 5-19) that is in contrast to NaCl; a salt known to form individual isometric hopper crystals. It is thought in this research that $MgCl_2$ crystallises within the stone by coating grains and infilling the open porosity. Granular decay was limited to the front and rear corners and edges in the third salt test, while drying faces were largely unaffected by the granular loss of material. The difference in the crystallisation behaviour of NaCl and $MgCl_2$/$CaCl_2$ is highlighted by a schematic in Figure 5-19. The crystallisation of several individual halite crystals will cause the internal fracturing of individual grains at the points of crystal growth. In contrast, $MgCl_2$ and $CaCl_2$, by forming large crystalline sheets that coat grains, spread their crystallisation pressure over a larger area, causing the disaggregation of grains without their prior fracturing.

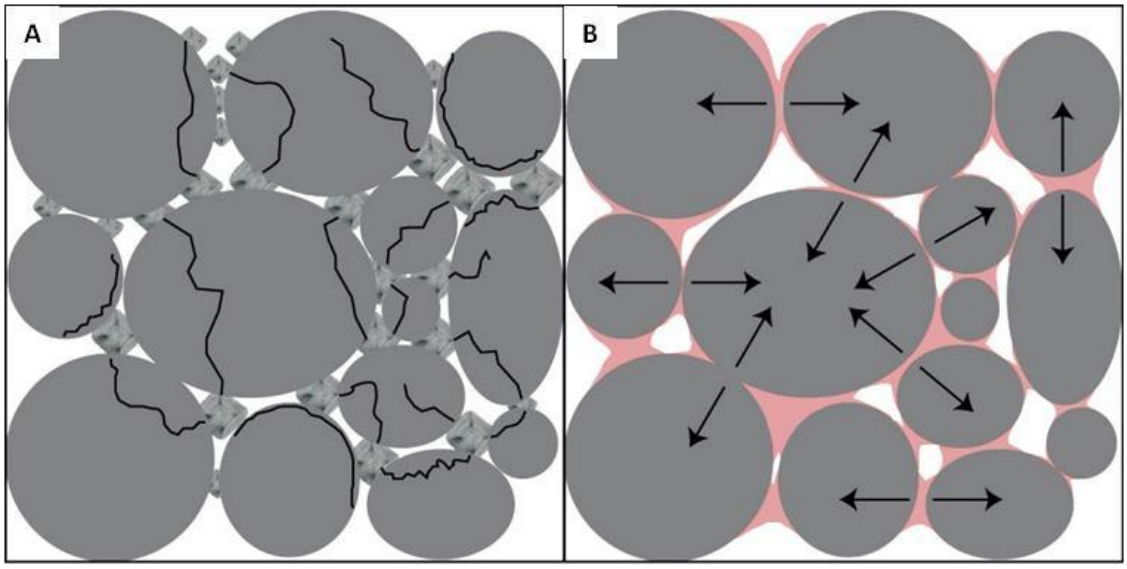

Figure 5-19: Schematic diagram highlighting the differences between the crystallisation behaviour of NaCl (A) and $CaCl_2$ and $MgCl_2$ (B).
(A): NaCl forms individual hopper crystals, with pressures that increase with a diminishing pore size. Quartz grains (grey) break and fracture from high pressures at point contacts. (B): $CaCl_2$ and $MgCl_2$ crystallise as sheets that coat grains and block pore throats. Pressures are spread across a larger contact area with the quartz grains. Grains are forced apart with the absence of broken and fractured grains.

Doddington (DM_{3post}) was the most susceptible sandstone to $MgCl_2$-induced breakdown, experiencing an extreme loss of material through granular decay in the third salt test, which was focussed on the covered side faces of the

stone. SEM analysis of Doddington sandstone (DM_{3post}) (Figure 4-43) shows the loss of grains through the detachment of quartz overgrowths, while further intra-granular fracturing, as previously identified in NaCl samples, was largely absent. Grains were lost through the removal of inter-granular material, including cements and clays. This process produced an open pore network whereby grains were easily displaced through the gentle brushing of the stone surface. It is assumed that only pressures produced from the crystallisation of salts and clay expansion can explain this weak surface loss of material in Doddington, and also Corsehill (CM_{3post}) and Locharbriggs (LM_{3post}) sandstones. The chemical dissolution of cements is an unlikely mechanism for the observed decay; due to the short test duration and the longer time-scales needed for this extent of chemical decay. There is also a lack of damage in, what are deemed to be more chemically vulnerable stones, such as Stanton Moor (calcite cement), Giffnock and in some Corsehill samples (containing dolomite cement).

Figure 5-20 is a diagram taken from Sebastian et al. (2008) illustrating the differences between crystalline and osmotic clay swelling.

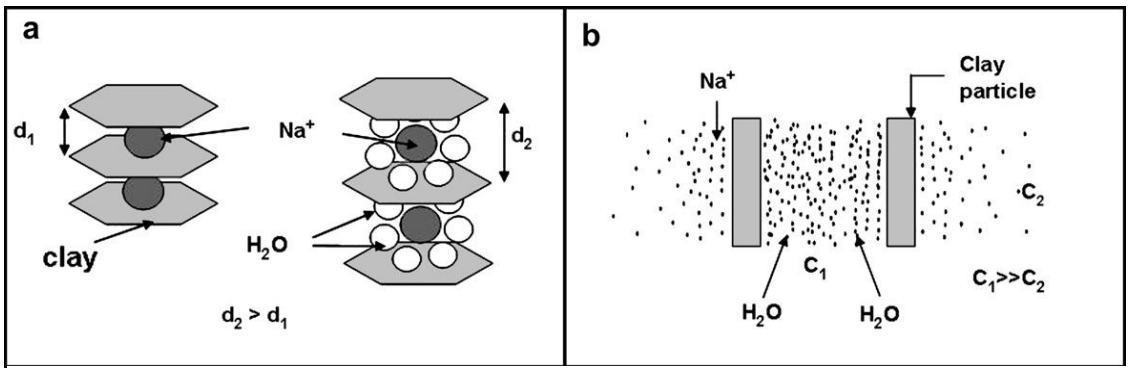

Figure 5-20: Clay swelling processes.

(a): Intracrystalline swelling of clay. (b): Osmotic swelling of clay. In (a) d indicates the basal spacing of clay, whereas in (b) C indicates the concentration of Na^+ ions.

There is evidence to suggest that both the swelling of smectite crystals and the osmotic swelling of generally non-swelling clays including illite through Mg^{2+} absorption could induce high pressures. Certainly, NaCl has been thought to increase the swelling capacity of clay-rich, smectite-bearing sandstone through crystalline swelling (Sebastian et al., 2008), while a study by Rao et al. (2013) found that NaCl increased the swelling of clay-rich soils through crystalline swelling at high NaCl concentrations, and through both crystalline

and osmotic swelling at lower concentrations. It is known that Mg^{2+} and Ca^{2+} have a stronger clay absorption affinity than Na^{+} owing to their smaller hydrated ionic radii and higher valences. Zhang and Norton (2002) show that Mg^{2+} has a strong absorption affinity for illite and vermiculitic clays, which could lead to osmotic swelling pressures.

The absorption of Mg^{2+} by clay could produce the breakdown pattern observed in Locharbriggs samples (Figure 4-41) by disconnecting individual grains from cement through high clay swelling pressures, and from clay mobilisation that would reduce the cementation of grains. Together, these mechanisms could: (i) produce sufficient internal pressures, and (ii) reduce the tensile strength in the stone (from clay dispersal reducing cementation). It is unknown exactly which clays are present in each sandstone; however, there must be a mechanism for the Doddington (DM_{3post}) and Corsehill (CM_{3post}) samples to have suffered catastrophic breakdown that was not seen in the NaCl samples. One possibility is that pore blocking near to the rear face of Doddington (DM_{3post}) samples hindered their efficient drying; this process forced all of the drying to continue through the front face and side faces. Pore blocking would lead to substantial internal crystallisation of $MgCl_2$ in Doddington samples. Rear faces were relatively unaffected and remained fairly cohesive in comparison to the rest of the block. Figure 5-21 is a schematic diagram explaining this decay process.

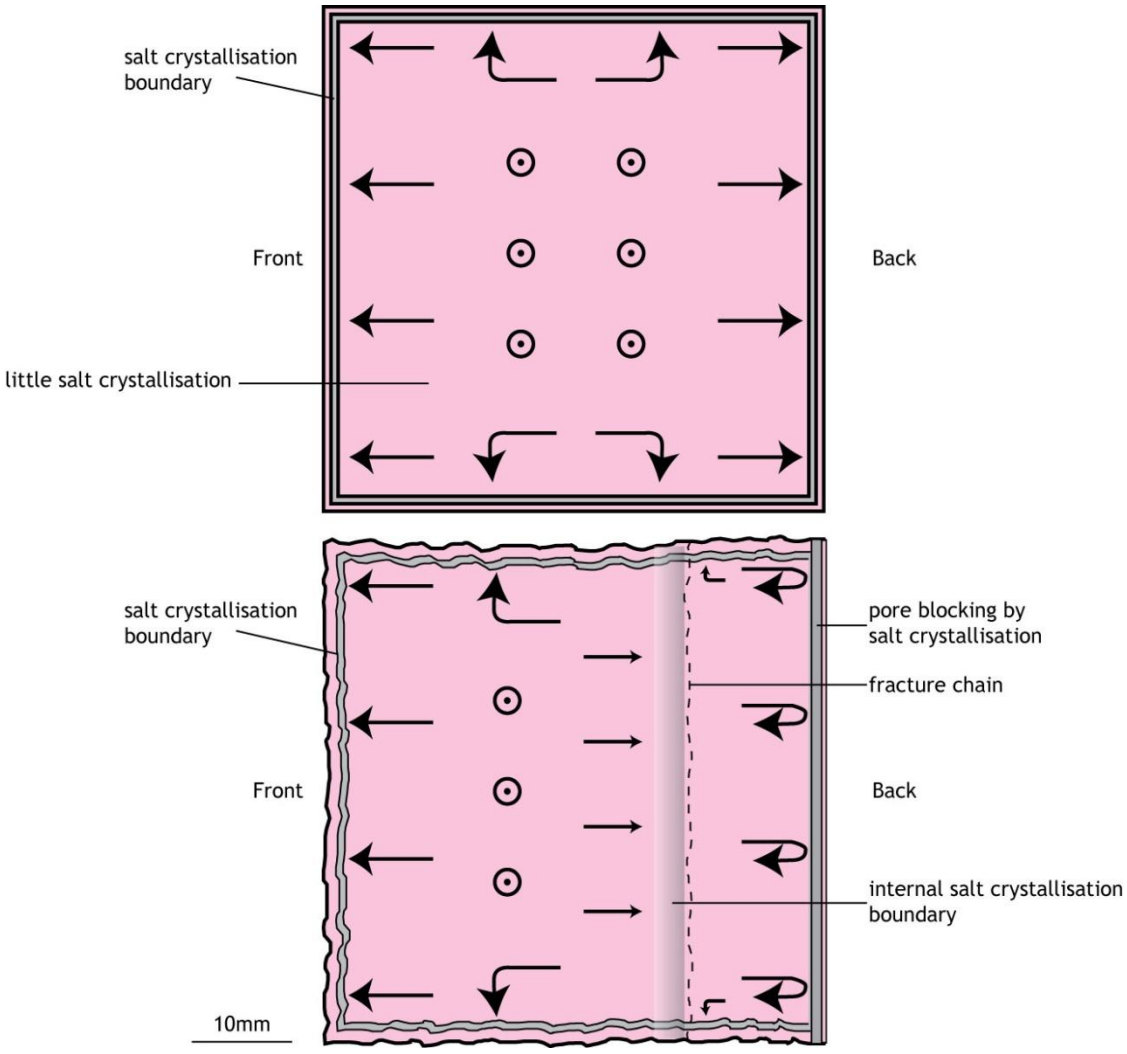

Figure 5-21: Schematic diagram of the changing drying process in Doddington sandstone subject to $MgCl_2$ crystallisation.

(A): Arrows highlight the initial drying pathways of solution within Doddington sandstone. Circles with dots represent a "head-on" view of arrows, indicating that drying takes place through every face (to some extent), with greatest drying taking place through the front and rear faces. (B): Pore blocking takes place on the rear face of the sample through salt crystallisation. Pore blocking forces drying to recede and to continue through the remaining surfaces as indicated by the arrows. A change to the drying direction establishes a drying boundary within the stone, whereby salt crystallisation takes places. This process creates a fracture chain and the eventual catastrophic failure of the stone. Elsewhere, solution can move towards the stone surface causing granular decay on the remaining five faces.

The process of $MgCl_2$ crystallisation is likely to be the same across all sandstone types, with the rate of decay and observed damage related to the test procedure and the tensile strength of each stone. Doddington and Locharbriggs are substantially weaker stones than Corsehill, Cullalo and Stanton Moor. This difference in resilience means that lower crystallisation pressures can initiate decay, and is thought to be the process occurring in the third crystallisation test, in which Locharbriggs (LM_{3post}) and Doddington (DM_{3post}) sandstones were extremely vulnerable to $MgCl_2$ induced decay. Weak

and more porous Corsehill sandstone than usual was used in the second crystallisation test due to differences between received samples from the supplier between each test, owing to the heterogeneities within Corsehill sandstone which likely increased its susceptibility to decay in that case.

5.2.1.2 *Scaling induced by $MgCl_2$*

A second prominent decay feature identified in Locharbriggs (LM_{3post}), Corsehill (CM_{3post}) and Doddington (DM_{3post}) sandstones was the loss of large sections of stone by the development of fracture chains. As formed by a similar process as described in Section 5.1.1.2, fracture chain development was influenced by the microscopic texture of Locharbriggs sandstone and by the drying boundary location in Corsehill and Doddington. Catastrophic decay in Corsehill and Doddington from the internal retreat of the drying boundary favours the crystallisation pressure hypothesis. Pore blocking through surface efflorescence (Figure 5-22) and near-surface crystallisation would have initiated the retreat of the drying boundary into the stone, causing the repeated crystallisation of $MgCl_2$ along the length of the drying boundary and elsewhere.

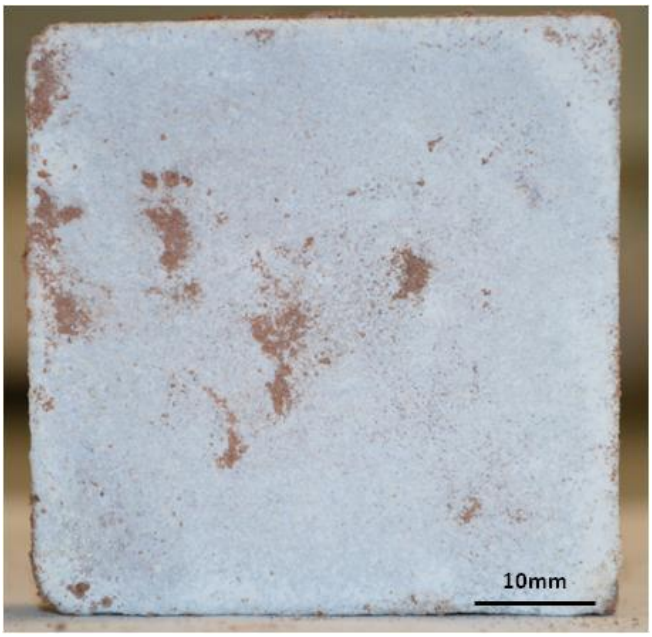

Figure 5-22: Photograph showing $MgCl_2$ efflorescence (white) on the front face of Corsehill (CM_{3post}) sandstone in test 3.

Locharbriggs on the other hand is characterised by layers that have a relatively low porosity, permeability and a different grain structure. Previous work has found that the distribution of clays within building sandstone can

cause severe decay through flaking and contour scaling (Rodriguez-Navarro et al., 1997; Sebastian et al., 2008). Locharbriggs has a relatively high content of clays, principally smectite, illite and kaolinite (Baraka-Lokmane et al., 2009). Pandey et al. (2014) considered the influence of ion exchange processes on salt transport in Locharbriggs sandstone, concluding that Locharbriggs has a large cation exchange capacity (CEC), with both Mg^{2+} and Ca^{2+} experiencing high exchange affinities within the stone. Pandey et al. (2014) suggest that ion exchange may alter both the physical properties of clays within the stone and the flocculation of clays within pores; essentially making them mobile throughout the pore network. It is therefore concluded that the combined osmotic and crystalline swelling of illite and smectite through Mg^{2+} absorption and from $MgCl_2$ crystallisation pressures within layers induced high pressures within Locharbriggs sandstone, resulting in the detachment of large sections of the stone across bedding planes.

5.2.1.3 *$MgCl_2$ Efflorescence*

Samples used in the $MgCl_2$ crystallisation tests were characterised by significant surface efflorescence. Cullalo experienced the greatest surface efflorescence in the second and third crystallisation tests, with the largest accumulations forming on the rear drying face in the third test. $MgCl_2$ formed a thin efflorescence crust across all sandstones in tests 2 and 3, with the exception of Stanton Moor. Early efflorescence formation was loosely focussed along the edges and corners of some sandstones (Figure 4-18), with Cullalo experiencing dynamic changes in both the structure and distribution of efflorescence throughout the tests. Initial efflorescence was largely limited to the front drying face of Cullalo (CLM_{3post}), showing a “bubbled” pattern of different sized hollow salt bubbles (Figure 5-23).

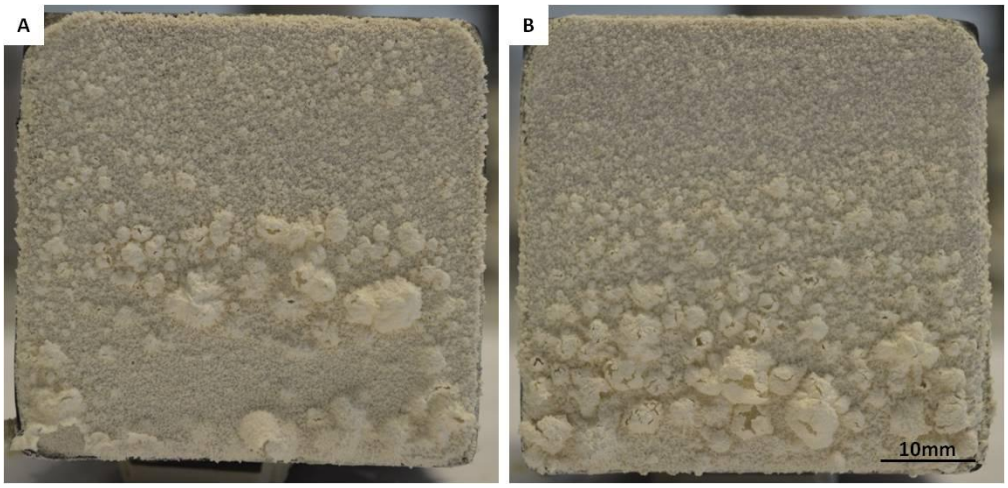

Figure 5-23: $MgCl_2$ efflorescence on Cullalo sandstone (CLM_{3post}) in test 3. (A and B): $MgCl_2$ efflorescence on two samples of Cullalo sandstone in test 3 showing a distinctive "bubbled" appearance.

Substantial efflorescence, particularly across Cullalo (CLM_{3post}) and Locharbriggs (LM_{3post}) samples in the third test, signifies the successful transport of moisture through the pore system, allowing salts to crystallise on the stone surface. This process is explained simply, in the case of Cullalo sandstone, by efficient drying kinetics that allow the prolonged capillary flow of solution to the stone surface, especially in the absence of significant clay content that would slow the migration of salts (Pandey et al., 2014). High moisture migration rates prior to salt formation suggests a slow onset of crystallisation, generally allowing the transportation of large quantities of salt towards the surface. Once a substantial salt efflorescence crust is developed, as evident in Cullalo (CLM_{3post}), pore blocking would cause the retreat of crystallisation into the stone interior.

In contrast to Cullalo, Doddington sandstone (DM_{3post}) displayed limited efflorescence, while suffering the greatest weight loss and the complete disintegration of most samples. This study has shown that Doddington has a fast and efficient drying rate, with low critical moisture content (CMC) values (Section 3.2.1). Such properties indicate that the pore network alone does not explain the behaviour of Doddington sandstone to $MgCl_2$ decay and a secondary mechanism must surely account for it. SEM images and EDX analysis of Doddington thin sections reveal the occurrence solely of kaolinite infilling porosity and forming important cement throughout the stone (Figure 5-24 and Figure 5-25). Kaolinite has a low CEC of 3-15 meq/100 and therefore osmotic

swelling through cation exchange would not provide a suitable mechanism for increased decay susceptibility. It is therefore assumed that damage within Doddington sandstone was influenced by the blocking of near-surface pores by salts on the rear face. In common with Cullalo NaCl and $MgCl_2$ samples, this process would drive the crystallisation of $MgCl_2$ further into the stone, with substantial decay taking place due to the preferential crystallisation of salt along the drying boundary and on side faces of the stone.

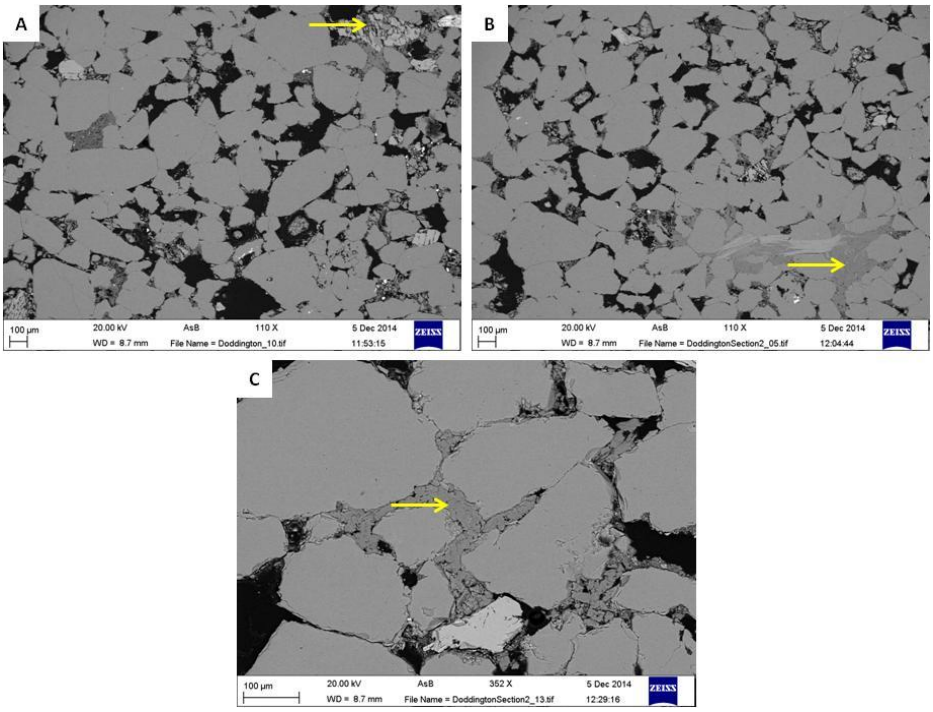

Figure 5-24: Backscatter electron SEM thin section images showing clay accumulations in Doddington (arrows indicate pore-filling clays). A, B and C are from different locations throughout the stone.

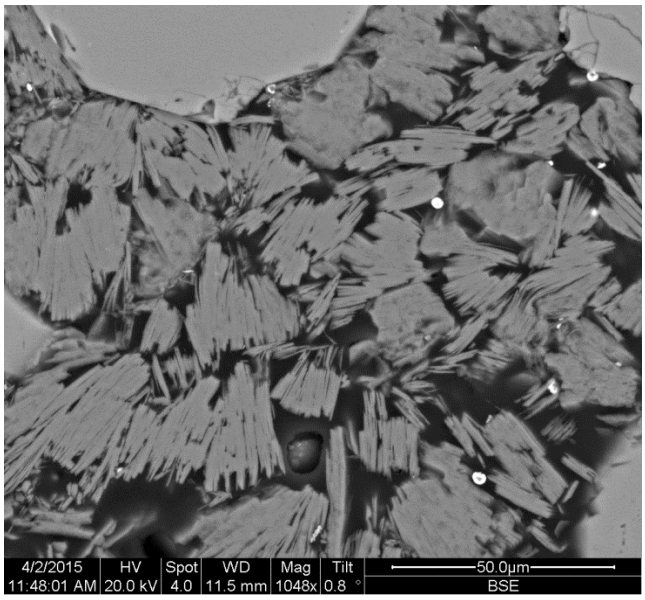

Figure 5-25: Backscatter electron SEM image of kaolinite clay in Doddington sandstone.

5.2.1.4 *Ultrasonic velocity changes from $MgCl_2$*

Greater decreases in the ultrasonic velocity were measured for the $MgCl_2$ samples than those subjected to NaCl crystallisation. Locharbriggs (LM_{3post}) experienced the greatest decrease, of 38%, while Cullalo (CLM_{3post}), Corsehill (CM_{3post}) and Stanton Moor (2) ($SM(2)_{3post}$) experienced similar decreases that were within 2% of each other. The large decreases in Locharbriggs (LM_{3post}) and Corsehill (CM_{3post}) sandstones (6% greater than NaCl (LN_{3post}/CN_{3post}) and 7% greater than $CaCl_2$ (LC_{3post}/CC_{3post})) are explained by the rough surface textures as caused by salt-induced damage, that create large air gaps on the surface. These are external reductions, and do not represent changes to the internal grain structure. Furthermore, due to the complete disintegration of repeat samples, only one sample was measured for both Locharbriggs (LM_{3post}) and Corsehill (CM_{3post}). Stanton Moor (SMM_{3post}) experienced lower decreases than NaCl (SMN_{3post}); this is explained by the low susceptibility to $MgCl_2$-induced damage and low weight change of Stanton Moor samples. An average reduction of 15% in Cullalo (CLM_{3post}) indicates discontinuities within the grain structure produced by crystallisation pressures as the drying boundary retreated into the stone by surface pore blocking. Doddington (DM_{3post}) stones on the other hand were not measured due to the complete destruction of all four repeat samples.

5.2.2 Changes to fluid movement within the pore network from $MgCl_2$

$MgCl_2$ samples in general experience a similar, and in some sandstones, a smaller change to their hydric behaviour in relation to NaCl samples. These hydric changes are primarily thought to occur from the distribution of salt crystallisation damage within the stone.

5.2.2.1 *Water absorption and saturation coefficient changes from $MgCl_2$*

Trends show that every sandstone (bar Giffnock) experienced a decrease in their water absorption in the second and third crystallisation tests. Stanton Moor experienced the smallest reductions in both tests, while Hazeldean, Doddington and Cullalo had the largest reductions. Cullalo (CLM_{3post}) and Locharbriggs (LM_{3post}) in test 3 and Cullalo (CLM_{2post}), Blaxter (BM_{2post}) and

Stanton Moor (SMM_{2post}) in the second test experienced lower reductions in their water absorption compared to other salts. Due to high errors between repeat measurements (Figure 4-48) and from high errors associated with control samples, there are no statistically significant changes in water absorption identifiable in the third test, while changes to only Hazeldean (HM_{2post}) and Doddington (DM_{2post}) are considered significant in the second test.

On the other hand, saturation changes are generally more significant than water absorption values across most sandstones in both tests, with larger decreases and lower variance values measured between repeat samples. This pattern reveals a consistent reduction and disconnection of effective porosity through pore blocking by mobile lithic material and clays from crystallisation damage.

5.2.2.2 *Capillary coefficient changes from $MgCl_2$*

Changes to the capillary uptake coefficient show a greater variability between sandstones in relation to water absorption and saturation tests, with Locharbriggs (LM_{2post}), Giffnock (GM_{2post}) and Hazeldean (HM_{2post}) experiencing increases of >50% in the second $MgCl_2$ test, and Locharbriggs (LM_{3post}) showing an increase in the third test. Stanton Moor (SMM_{2post}), Blaxter (BM_{2post}) and Corsehill (CM_{2post}) in the second test and Stanton Moor (SMM_{3post}) and Cullalo (CLM_{3post}) in the third $MgCl_2$ test show changes of <10% which is not counted as significant as these values still lie within the standard deviation and their expected range of values (as measured in Chapter 3). These sandstones therefore do not experience a change to their capillary uptake regime after $MgCl_2$ loading, with the main changes explained by reduced water uptake owing to decreased water absorption. Giffnock (GM_{2post}) is also not significant due to the large variation in results between repeat samples. Doddington (DM_{2post}) on the other hand had the greatest reduction, of 42%, in the second test, signifying substantial changes to the pore network and capillary uptake regime.

Changes to the capillary coefficient are a consequence of the concentration of salt crystallisation damage within the stone. Large efflorescence

accumulations indicate transportation of salt to the stone surface: especially in Locharbriggs (LM_{3post}), Cullalo (CLM_{3post}) and Corsehill (CM_{3post}) samples. It is reasonable to assume that the greatest percentage of salt crystallisation will therefore take place close to the stone's surface (Figure 5-26). If crystallisation damage is limited to regions immediately beneath the drying faces, the remaining pore network may be unaffected and so not limit capillary flow within the stone (Figure 5-27). Near-surface crystallisation of $MgCl_2$ can only explain the small capillary coefficient changes in sandstones that contain low contents of damaging clays (i.e. low smectite and illite contents). As explained in Figure 5-18, the initial development of narrow fracture chains within the stone may cause an initial increase in the capillary coefficient through the increased connection of smaller pores. An increase in the Locharbriggs capillary coefficient will stem from the crystallisation and localised accumulation of clays within the bedding planes in the stone creating small fracture chains that increase the capillary uptake, while the rest of the pore networks remains relatively unaffected (Figure 5-28).

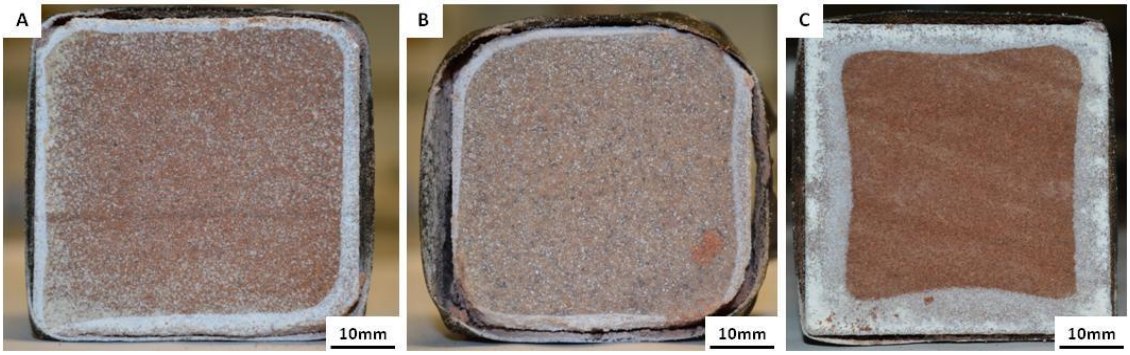

Figure 5-26:Photographs showing $MgCl_2$ efflorescence distribution on their front drying face after 49 crystallisation cycles in the third crystallisation test.
(A): Locharbriggs sandstone (LM_{3post}). (B): Doddington sandstone (DM_{3post}). (C): Corsehill sandstone (CM_{3post}).

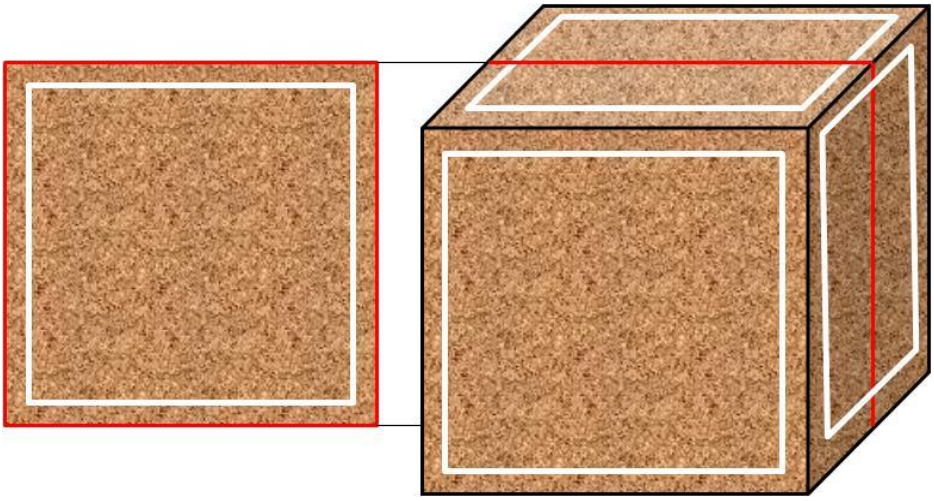

Figure 5-27: Schematic diagram highlighting the location of the drying boundary (in white).

Solution movement to the stone surface generates significant efflorescence and concentrates most of the crystallisation in a layer close to the stone faces. Areas beneath this layer experience less $MgCl_2$ crystallisation and remain relatively unaffected throughout the salt crystallisation test.

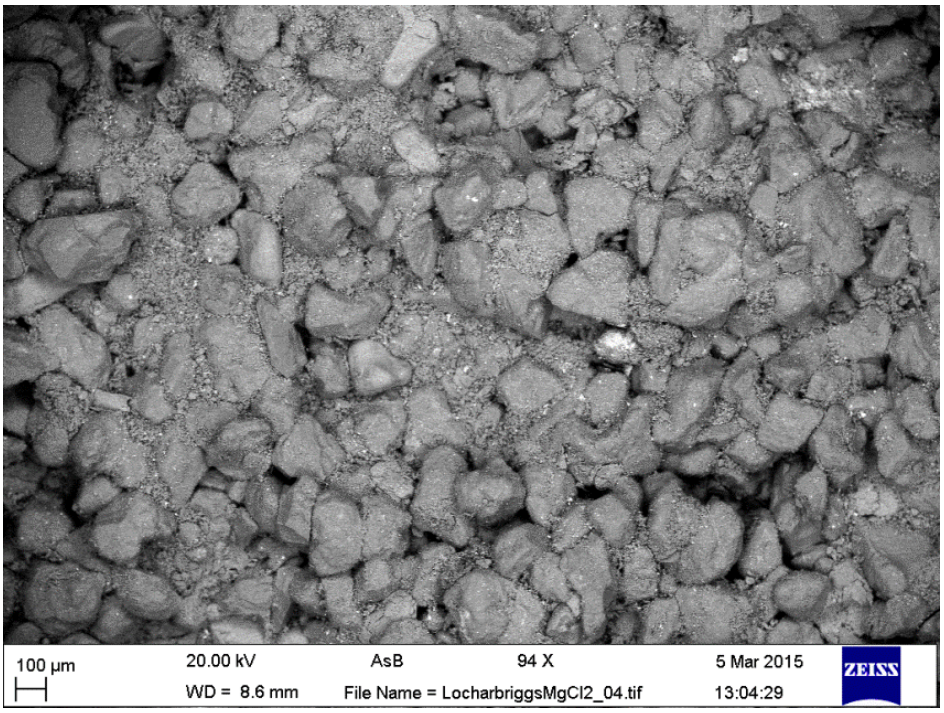

Figure 5-28: Backscatter electron SEM image of a Locharbriggs $MgCl_2$ (LM_{3post}) sample from the third salt test showing a relatively unaffected pore structure after 50 crystallisation cycles.

5.3 Changes to stone properties from $CaCl_2$ crystallisation.

Changes to stone from $CaCl_2$ crystallisation closely follow those of $MgCl_2$, with salt crystallisation processes not expected to take place in the stone under environmental conditions expected in Scotland.

5.3.1 Changes to the grain structure induce by $CaCl_2$.

$CaCl_2$ produced similar changes to the sandstone grain structure as $MgCl_2$, with granular and scaling decay identified as the most significant processes. Importantly, $CaCl_2$ did not cause significant efflorescence on any sandstone, with most samples experiencing limited efflorescence across three crystallisation tests and one freeze-thaw test. Unfortunately there is no SEM data on $CaCl_2$-induced samples in the second or third tests to help substantiate the hypotheses discussed in the following section.

5.3.1.1 *Crystallisation and absorption behaviour of $CaCl_2$*

It is thought through research in this thesis that $CaCl_2$ has a similar behaviour within sandstones as $MgCl_2$, causing breakdown through the same mechanisms, but with the rate of decay influenced by the location of salt crystallisation. This was previously identified as an important factor in $MgCl_2$ behaviour. In contrast to $MgCl_2$, $CaCl_2$ is likely to have crystallised internally throughout the stone, with little transportation of salt towards the surface. This internal crystallisation can be explained by the operation of two different processes: (i) a slow movement of Ca^{2+} towards the stone surface as a result of greater cation absorption onto clay particles; (ii) a fast rate of $CaCl_2$ crystallisation, causing the in-situ growth of $CaCl_2$ crystals over a very short period under precise temperature and RH conditions.

Espinosa et al. (2008) showed, through an innovative crystallisation test, that the supersaturation and subsequent crystallisation of hydrated $CaCl_2$ phases is achieved under precise temperature conditions, and proceeds very quickly once initiated. They showed that high supersaturation ratios were required before the onset of crystallisation of $CaCl_2.6H_2O$ at temperatures of $<30^oC$. This crystallisation behaviour is due to the high nucleation energies required

for the uptake of water into the crystal lattice before crystallisation can progress. Rapid crystallisation of $CaCl_2$ could take place before substantial movement of the salt ions towards the stone surface as the water within the stone is incorporated into the crystal lattice. The lack of $CaCl_2$ efflorescence certainly demonstrates that internal crystallisation was taking place across every sandstone type.

ESEM analysis of $CaCl_2$ crystallisation (Figure 5-29) shows that crystal growth started at low RH conditions (<25% RH), initially forming large thin sheets within solution that coated grains. Some of these sheets (20-40μm thickness) appear layered, however at lower RH conditions (<10% RH) the layers are thinner. At extremely low RH conditions (5%), dynamic crystallisation and dissolution reactions were evident, forming small, unstable globules on quartz grains, likely caused by an increase in the surface tension and viscosity of the solution. Solution movement and "bubbling" also took place, with areas of solution showing a hollow, bubbly and globular morphology. Grain coating also leads to the partial infilling of pores, as thick crystalline layers growing on-top of grains would narrow pore throats. A fractured texture dominates crystalline sheets at very low RH conditions (5% RH), showing possible evidence of zoned crystallisation, with channels or elongated crystals separating the zoned areas. During the hydration of $CaCl_2$ in a simple droplet test, dendritic crystals were observed, growing from an initial nucleation site at 30% RH. SEM imaging of dry rough-cut sections of Locharbriggs and Scotch Buff used in test 1 reveals a third crystal morphology, characterised by small clusters of irregular shaped, ridged crystals (Figure 5-30). An increased solution viscosity, combined with pore blocking crystallisation characteristics and a high Ca^{2+} absorption affinity, would impede the flow of salt to the surface and cause subflorescence.

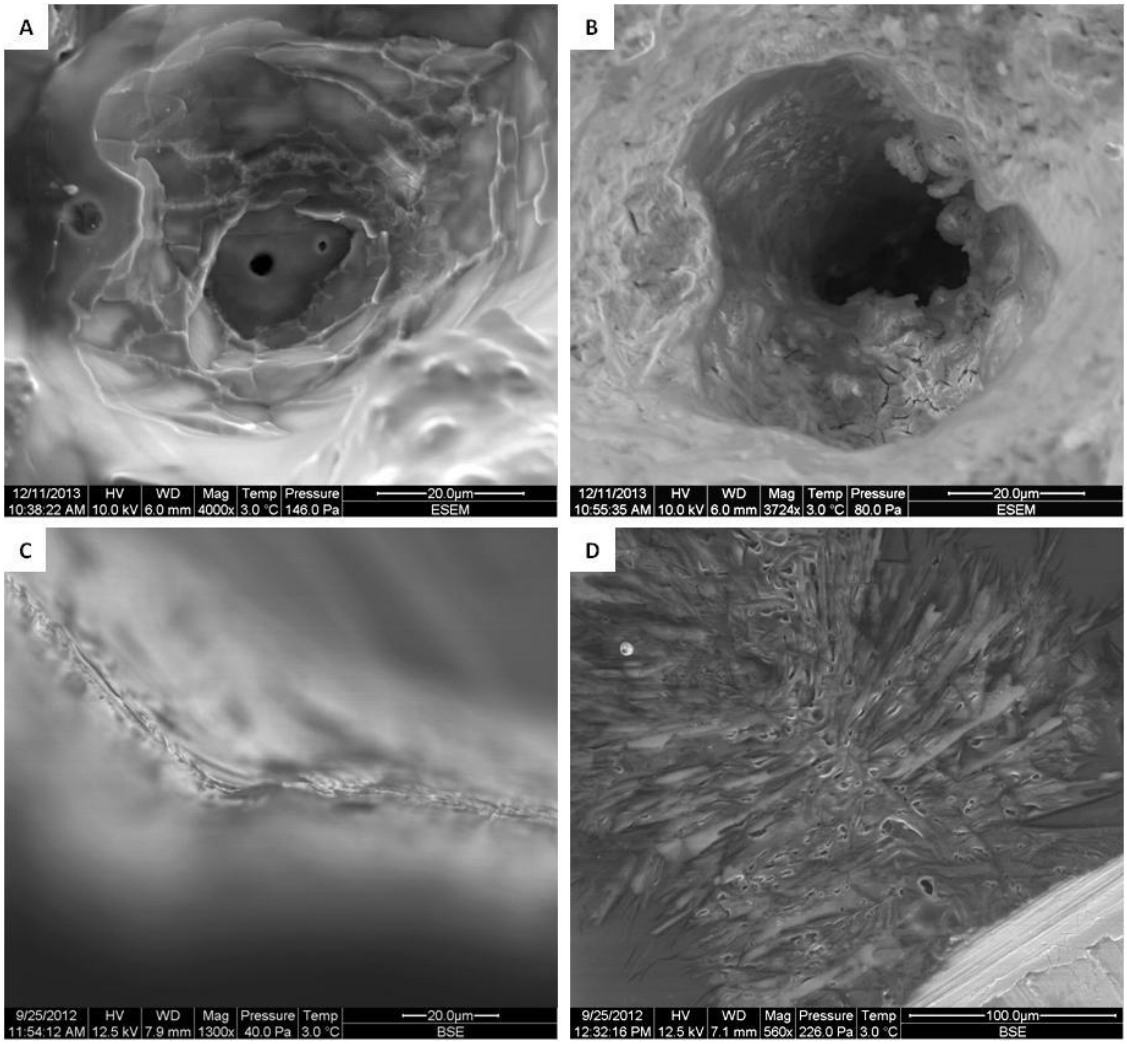

Figure 5-29: ESEM images of $CaCl_2$ crystallisation under stable temperature (3°C) and different RH conditions.
(A): Layered sheet structure at 20% RH. (B): $CaCl_2$ crystallisation infilling and narrowing pores at 10% RH. (C): Thin sheet of $CaCl_2$ at 5% RH. (D): Dendritic $CaCl_2$ crystal growth at 30% RH that grew extremely quickly.

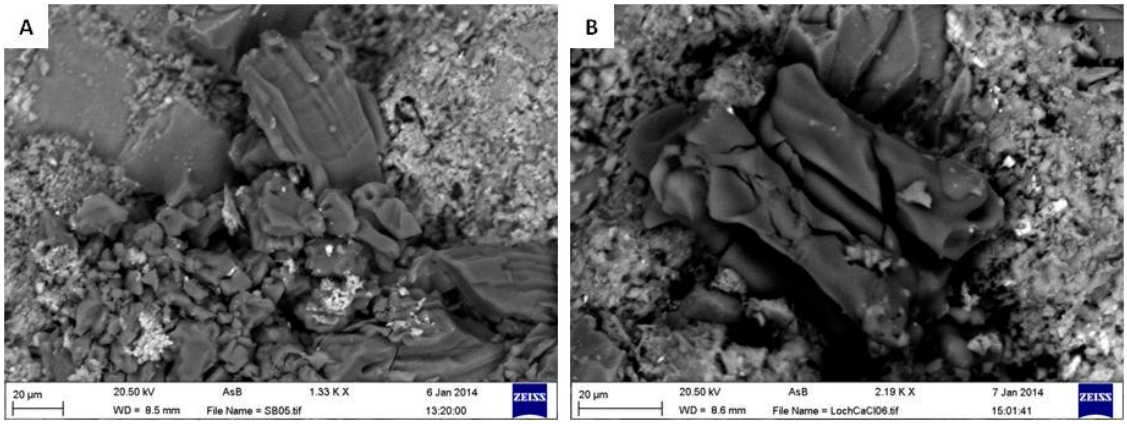

Figure 5-30: Backscatter electron SEM images of $CaCl_2$ samples from crystallisation test 1.

(A): $CaCl_2$ crystals in Scotch Buff sandstone (SBC_{1post}). (B): $CaCl_2$ crystals (dark grey) in Locharbriggs sandstone (LC_{1post}).

$CaCl_2$ crystallisation caused granular decay located predominantly in the lower capillary zones in the second test, affecting Locharbriggs (LC_{2post}) and Corsehill (CC_{2post}), and as granular decay located along the corners and edges of Locharbriggs (LC_{3post}), Cullalo (CLC_{3post}) and Doddington (DC_{3post}) in the third test. The removal of near-surface scales was evident in two Locharbriggs (LC_{3post}) samples in the third test and across two Corsehill (CC_{2post}) samples in the second test. Figure 4-2 and Figure 4-3 show the average weight change of $MgCl_2$ and $CaCl_2$, respectively, in the third test and demonstrate similar weight change profiles for each sandstone, distinguished by the onset of the third weight change stage. Decay focussed near to the stone surface, as hypothesised for the $MgCl_2$ samples, would cause more substantial material loss via granular decay. $CaCl_2$ is thought to have crystallised homogeneously throughout the pore network, causing damage through salt crystallisation, and clay swelling and dispersal, as hypothesised to occur in Locharbriggs. Near surface crystallisation pressures may then have taken longer to develop, with Figure 4-3 indicating that decay was likely to continue at an increased rate in Doddington (DC_{3post}), Corsehill (CC_{3post}), Cullalo (CLC_{3post}) and Locharbriggs (LC_{3post}) sandstones.

Changes to ultrasonic velocity reveal similar patterns as those measured for $MgCl_2$ samples, with smaller changes in Stanton Moor (2) ($SM(2)C_{3post}$) and Corsehill (CC_{3post}), with the latter explained by the inaccuracies in the measurement of the $MgCl_2$ sample. Doddington (DC_{3post}) shows the greatest reduction, suggesting the greatest internal damage, and correlates with the low durability of Doddington to both $MgCl_2$ and $CaCl_2$ through the same crystallisation processes. Decreases to the ultrasonic velocity propagation result from the same reductions in grain cohesion as described in Sections 5.1.1.4 and 5.2.1.4.

5.3.2 Changes to fluid movement within the pore network from $CaCl_2$.

All $CaCl_2$ samples in the second and third salt tests experienced a decrease in their water absorption, saturation and capillary uptake coefficients (apart for Hazeldean) in both crystallisation tests.

5.3.2.1 *Water absorption and saturation coefficient changes from $CaCl_2$*

Every sandstone type experienced a reduction in their water absorption and saturation coefficient values (except Stanton Moor 2) across both crystallisation tests. $CaCl_2$ caused a similar reduction in values as did $MgCl_2$ in the second test, while Cullalo (CLC_{3post}) and Locharbriggs (LC_{3post}) registered greater decreases in the third test. Reductions to water absorption and saturation coefficient are in response to the same hypothesised mechanisms that affected $MgCl_2$ samples (Section 5.2.2.1); through clay swelling, clay dispersal and from crystallisation pressures.

Interestingly, Doddington continues to display some of the greatest reductions in saturation and water absorption across both tests, while Stanton Moor, Giffnock and Blaxter experience the lowest changes in both tests. Reductions are similar across the second and third tests, indicating that changes were experienced after only 16 cycles in most sandstone types.

5.3.2.2 *Capillary coefficient changes from $CaCl_2$*

In general, most $CaCl_2$-loaded samples experienced a similar decrease in their capillary uptake as those treated with $MgCl_2$, with only Cullalo (CLC_{2post}) in the second test decreasing less and Hazeldean (HC_{2post}) experiencing an increase on average. The remaining sandstones had a greater decrease in their capillary coefficient than those treated with $MgCl_2$. These greater reductions in capillary coefficient are explained by the fast crystallisation behaviour of $CaCl_2$, and slow migration of Ca^{2+} throughout the pore network. This process would lead to $CaCl_2$ preferentially crystallising internally within the pore network, as strongly suggested from the absence of surface efflorescence across all three tests. Relatively slow solution movement combined with rapid crystallisation would prevent $CaCl_2$ from accumulating within specific regions of the stone and therefore salt crystallisation damage would be more homogenously distributed. As suggested by Espinosa-Marzal and Scherer (2010), the generation of large supersaturation ratios prior to crystallisation (as identified by Espinosa et al., 2008 for $CaCl_2.6H_2O$ crystallisation in brick under specific environmental conditions) makes $CaCl_2$ a theoretically damaging salt.

It is assumed that the widespread distribution of salt crystallisation and clay swelling damage throughout the pore network would have a greater impact than localised damage (as thought to occur with $MgCl_2$) on the overall moisture movement throughout the stone. Reductions in the capillary coefficient result from a change in pore size distribution, through either a fall in the accessibility and overall proportion of smaller pores, or from an increase in the fraction of larger pores. In contrast to $MgCl_2$, this process would have a greater impact on the capillary uptake coefficient, causing a lower capillary uptake rate and lower degree of water absorption.

5.4 Differences between $MgCl_2$ and $CaCl_2$ crystallisation damage

$MgCl_2$ and $CaCl_2$ are thought to cause damage through the same processes, by forming similar crystal habits and morphologies. Both salts crystallise under low values of RH, forming extensive crystal sheets that coat grains and narrow pores. The main differences in behaviour of sandstone samples subject to both salts in tests 2 and 3 results from test-specific parameters that influence both the flow of salt solution and the sites of crystallisation. The “gentle” radiative drying phase in the third test provides an environment that permits movement of $MgCl_2$ to the stone surface before subsequent crystallisation taking place in the longer, “intense” convective heating stage. In contrast, the radiative heating stage did not impact on $CaCl_2$ movement within the samples; thus leading to homogeneous crystallisation at depth throughout the stone blocks. This process is evidenced by the extensive $MgCl_2$ efflorescence accumulations and the absence of $CaCl_2$ efflorescence. There was evidence of a thin $MgCl_2$ efflorescence after 2-4 hours of radiative heating on certain sandstones, whereas it was absent from $CaCl_2$ samples. Near surface crystallisation leads to faster decay rates associated with granular decay and near-surface fracture chain development.

In the second test, both salts would have undergone rapid internal crystallisation during the convective heating stage. Limited $MgCl_2$ efflorescence accumulations show that less salt than the third test was migrating to the stone surface, with greater internal crystallisation taking place. Under the same conditions, where both salts experienced greater

internal crystallisation, $CaCl_2$ was shown to be a more damaging salt/produce a greater decay rate than $MgCl_2$. Certainly, extensive damage to the Corsehill samples is likely influenced by their relatively high porosity and low tensile strength. These properties explain the high weight losses of $CaCl_2$ samples in test 2 and the higher weight loss values of $MgCl_2$ samples in test 3.

5.5 Summary of the main stone property changes from NaCl, $MgCl_2$ and $CaCl_2$-induced decay

Several trends are evident between sandstones and salts throughout each test that relate to specific stone properties, salt behaviour and test conditions. Locharbriggs and Corsehill consistently displayed alteration, damage and high salt absorption across every salt type in every test, including granular and surface scaling decay. Locharbriggs in particular experienced significant decay focussed within thin clay-rich layers in the stone that differ to the bulk of the sample in grain and pore network properties and clay concentrations.

Stanton Moor on the other hand was only affected by NaCl, experiencing extensive salt uptake and suffering granular and scaling decay. This damage was clearly identified in cross-sections, highlighting different stages of fracture chain and scale development. Stanton Moor was resistant to $MgCl_2$ and $CaCl_2$ in tests 2 and 3, experiencing low salt uptake, minimal surface change and minor alterations to moisture transportation.

Doddington, although absorbing relatively high volumes of NaCl in the second and third crystallisation tests, suffered minimal physical alteration and so remained relatively undamaged. This outcome was in contrast to $MgCl_2$ and $CaCl_2$, whereby Doddington suffered some of the highest weight loss values and complete destruction of every $MgCl_2$ sample in test 3 owing to substantial granular disintegration.

Giffnock, Blaxter, and specifically Cullalo, Hazeldean and Clashach, showed minimal surface alteration across each salt in all three tests and generally experienced low salt uptake and low weight loss across the different salts. According to the British standard salt crystallisation test procedure, these are categorised as ‘salt resistant’ sandstones; however this designation may be

slightly misleading. Hazeldean and Cullalo sandstones, although experiencing little physical alteration and lower uptake and weight loss, did show extensive modifications to their hydric properties, including some of the largest recorded changes across water absorption, saturation and capillary uptake values. In addition, Cullalo experienced large ultrasonic velocity changes across all three salts in test 3. Both Hazeldean and Cullalo are relatively mature sandstones having a “clean” pore network, with low clay and feldspar contents. Cullalo in particular, is well sorted and well cemented, with well rounded quartz grains. Thus both sandstones are sensitive to grain and pore network changes and show a larger contrast than poorly sorted and texturally immature sandstones between original and post-test values even in the absence of high decay rates. Therefore, extensive changes in the ultrasonic velocity and hydric test measurements are an artefact of the high contrast in these properties between original and post-treated samples rather than the occurrence of significant pore and grain network damage. In contrast, smaller changes to Corsehill values for example, may be explained by the lesser contrast between original and post-test values due to the mineralogical immaturity and “unclean” pore network of this sandstone.

Each salt produced similar decay patterns across most sandstones that were influenced, in part, by the test procedures. Most NaCl samples were characterised by a similar efflorescence pattern across each test. In the second crystallisation test, the location of efflorescence was controlled by the extent of the capillary wetting zone and by the mechanisms of capillary uptake; as previously explained by Scherer (2004) and witnessed in similar crystallisation tests by Benavente et al. (2001). NaCl produced significant granular decay and contour scaling, specifically within Stanton Moor and Locharbriggs in all three tests.

$MgCl_2$ and $CaCl_2$ on the other hand are interpreted to have caused damage through a combination of similar salt crystallisation processes and by clay swelling and dispersal. These can be likened to the mechanisms of formation-damage within hydrocarbon reservoir sandstones (Wilson et al., 2014). The main factors influencing the rate of decay concern the distribution of salt crystallisation pressures and possible clay swelling within the stone. A

relatively high transportation rate of $MgCl_2$ within the pore network produced significant efflorescence in Cullalo and Locharbriggs sandstone, and caused the preferential crystallisation of salts near to the drying surfaces; these processes subsequently increased the rates of granular decay in these stones.

Water samples were used as controls in each test in order to determine the effects of heating-cooling and wetting-drying on the stone. It is concluded that every sandstone type is sensitive to heating-cooling and wetting-drying cycles in the presence of water, with large changes to the hydric properties of control samples recorded across the second and third crystallisation tests. It must be noted that surface contamination from sealants used in the second and third tests may have altered the hydric properties of control samples for each stone. Regardless, the control samples for each sandstone suffered changes to their moisture transportation regimes, highlighting sensitivity of every sandstone to heating-cooling and wetting-drying cycles, and from surface contamination/alteration processes.

Furthermore, the specific crystallisation test conditions influenced the stone behaviour, specifically in relation to the rate of decay, and the decay processes experienced by each sandstone. Importantly however, this result did not affect conclusions about the overall durability of each sandstone, as consistent trends of salt accumulation and weight loss were recorded for each stone in every test.

6 Discussion: The main stone properties controlling durability to salt-induced decay.

By understanding the most important properties that control and influence stone durability to natural weathering processes, more informed recommendations can be made towards the suitable choice of appropriate replacement sandstone for historic buildings. It is clear throughout the literature that this is not a simple task, and several important properties are known to influence moisture movement and salt crystallisation within stone. There are an inter-connected network of stone properties that influence salt-induced decay, while crucial feedbacks exist between these properties during the natural weathering of sandstone.

The grain network comprises the stone mineralogy, grain shape, grain size and cementation: These properties are influenced by the diagenesis of the stone during sedimentation and burial. The grain network also impacts on the pore network and the uptake and migration of moisture through the stone. The influence of these sandstone properties on salt-induced decay is discussed in the following section.

6.1 Structural properties

The most important structural properties of sandstones relevant to decay are the compressive strength, ultrasonic velocity propagation, mineralogy, grain shape and grain size. The size and shape of grains and their compaction can significantly influence both the stone's compressive and tensile strength and the pore network properties that govern moisture movement within the stone. Therefore, the grain network influences a range of weathering processes; from chemical and biological decay to the physical breakdown from salts and ice formation.

Three main grain structure classes of sandstone are identified from the analysed samples (Section 3.1 and 3.4): (i) Cullalo (also Hazeldean and Clashach): generally well compacted sandstones that are well sorted and containing moderately-well rounded quartz grains, with a low clay and feldspar content. (ii) Corsehill, Blaxter, Locharbriggs: these are generally

poorly compacted and poorly sorted sandstones with a high clay and feldspar content. (iii) Stanton Moor: a well compacted, but poorly sorted sandstone showing sutured grain contacts and a tight interlocking cement throughout, with mainly sub-angular - angular shaped grains. Doddington, Giffnock and Scotch Buff sit somewhere between all three classes: showing greater feldspar and clay contents than Cullalo but lower than those of Blaxter and Corsehill, with lower cement content and generally lower compaction than Stanton Moor.

Ultrasonic velocity (USV) is an important technique that is used to determine the compaction and anisotropy within the sandstones. High USV values (Section 3.2.4) correspond to well compact sandstones, with the greatest belonging to Cullalo, Doddington, Hazeldean and Stanton Moor. The lowest USV values are obtained from Blaxter, Corsehill and Locharbriggs; all of these stones have medium-high porosities and a low degree of grain compaction. Interestingly, the grain network and USV values do not correlate directly with compressive strength values (Section 3.2.8), with Corsehill giving high compressive strength values and Doddington having a lower than expected strength. The compressive and tensile strength of a stone together control its mechanical breakdown. Crystallisation and swelling pressures must therefore overcome the bulk tensile strength of the stone before breakdown initiates. As stated by Benavente et al. (2004), it is imperative to acknowledge and understand the strength of stone as this can be used to estimate its resistance to salt crystallisation. Different authors have successfully used USV measurements to calculate the modulus of elasticity for different materials in order to estimate their durability to salt and ice crystallisation (Valdeon et al., 1996; Goudie, 1999).

There is a relationship between grain size, grain shape and the pore size distribution (PSD) whereby a stone with an organised and well sorted grain structure has a smaller range of pore sizes. Cullalo, Hazeldean, Doddington and coarse-grained Locharbriggs have the highest PSD skewness and kurtosis values, representing a unimodal, negatively skewed and typically large pore sizes, with mean and median values lying within the 10μm - 50μm range. Similar sized and generally well-rounded grains will deform in a stable

configuration through slip-rotational compaction, while grains showing a wider range of grain size and shape (and likely a more diverse mineral assemblage) will undergo a less organised compaction, leading to a greater distribution of pore sizes throughout the stone. Corsehill, Blaxter and Stanton Moor all have a wide range of grain size and grain shape distributions that correlate with a relatively large PSD (Figure 6-1).

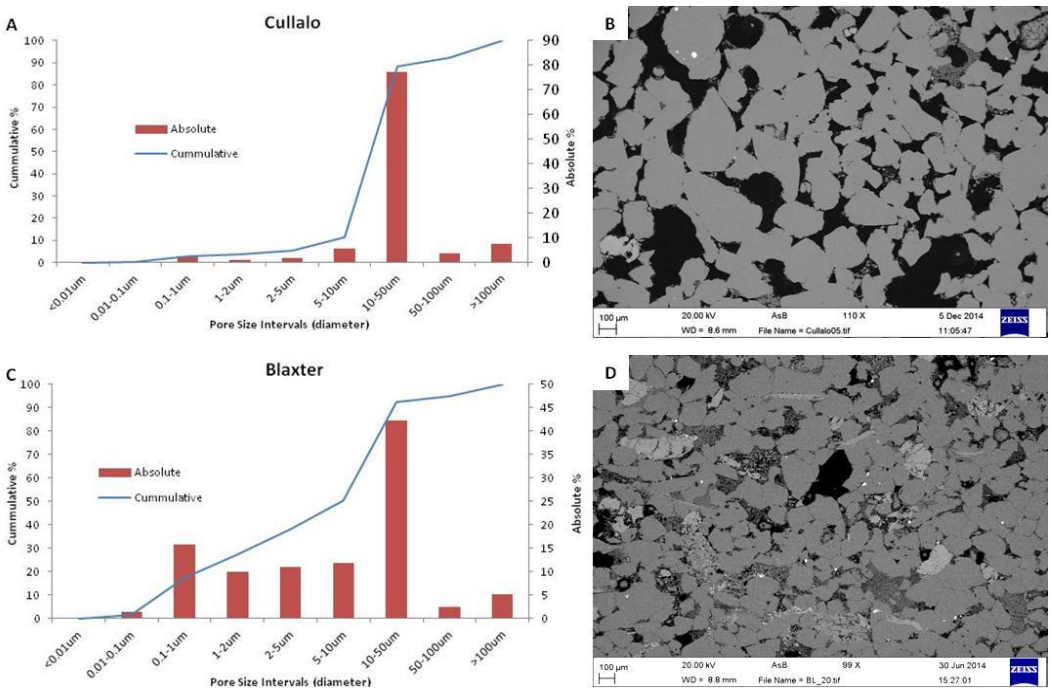

Figure 6-1: Pore size distribution data (A and C) and backscatter electron SEM thin section images (B and D).

(A): Cullalo mean pore size distribution. (B): Cullalo SEM thin section image. (C): Blaxter mean pore size distribution data. (D): Blaxter SEM thin section image. Dark grey: quartz, light grey: feldspar, pore space is black.

Generally, texturally and mineralogically mature sandstones have a lower PSD owing to the organised compaction of similar sized grains. This property increases the accessibility of the main pore network to moisture and so permits a greater moisture flow throughout the stone. The open pore networks of Hazeldean, Cullalo and Doddington influence the efficient drying regimes of these sandstones, allowing prolonged capillary connection to the stone's outer surface and a continuously high drying rate. In contrast, Stanton Moor has an extremely slow drying rate, with a short-lived stage 2 capillary regime and prolonged vapour controlled drying. As will be discussed further in this chapter, this is not a simple relationship, with several factors other than grain compaction influencing moisture movement within the stone.

High USV values typify well compacted and cemented sandstones, and low USV values are indicative of texturally and mineralogically immature sandstones. Importantly, sandstones characterised by a well organised grain structure are shown by this research to have a lower PSD and more open pore network, permitting faster drying regimes and generally better moisture flow.

6.2 Pore network properties and moisture movement

The pore network directly controls moisture movement within the stone and influences the rate and total volume of moisture absorption. The principal mechanisms controlling moisture absorption and distribution are well established (Hall, 1977; Gummerson et al., 1980; Scherer, 1990), while various authors have identified crucial durability estimators that rely significantly on pore structural properties (Mod'd et al., 1996; Benavente et al., 2004; Yu and Oguchi, 2010).

Several key pore properties and subsequent feedback mechanisms are identified here as essential factors influencing the durability of sandstone to different salt decay processes. These properties are discussed in the context of salt crystallisation mechanisms and important issues relating to the appropriate choice of suitable replacement stone.

It is well established that porosity and PSD significantly influence stone durability. These two properties primarily control the migration and distribution of moisture and weathering agents throughout the stone and have been used to successfully estimate and predict the durability of various building materials to weathering processes (Richardson, 1991; Bell, 1993; Buj and Gisbert, 2010; Török and Vásárhelyi, 2010).

Everett (1961) first proposed the idea that crystallisation pressures within stone are influenced by pore dimensions, with subsequent work building on these foundations. Zehnder and Arnold (1989) observed that salt preferentially crystallises in larger pores, with later studies successfully calculating theoretical crystallisation pressures using measured pore dimensions and porosity values. Rossi-Manaresi and Tucci (1991) in their

pioneering paper, presented results of theoretical NaCl crystallisation pressure calculations using known pore dimension values of limestone and interfacial tensions of NaCl.

Following from these studies, crystallisation pressures were here estimated in each stone type using empirical PSD data. According to previous thermodynamic models of salt crystallisation, salts will preferentially grow in the largest pores first. Once the largest pores are filled, solution will move into connected smaller pores where crystallisation will continue. This process will generate a crystallisation pressure that has been postulated to scale with a decreasing pore size; it was calculated by Wellman and Wilson, as expressed in equation 1-4 and below (Equation 6-1).

$$P=2\ \gamma_{cl}(1/r_1 - 1/r_2)$$

Equation 6-1

Where γ_{cl} = the interfacial tension between the solution and the growing crystal, r_1 = the radius of the small pores and r_2 = the radius of the large pores. The calculated pressure (P) is the excess pressure when crystallisation moves from larger pores into smaller pores. Higher crystallisation pressures will therefore develop in smaller pores. Since the larger pores will be filled first and little excess crystallisation pressure generated, a simpler equation can be used (Equation 6-2):

$$\Delta P=2\ \gamma_{cl}(1/r_1)$$

Equation 6-2

In order to calculate the effective pressure for each pore class and ultimately the overall generated pressure, the volume percent of each class must be considered; as shown in Equation 6-3.

$$Vr/VR$$

Equation 6-3

Where Vr = volume of the pores in each class and VR = the volume of the largest pores. The overall crystallisation pressure is calculated by multiplying Equation 6-2 and Equation 6-3 for each pore class. The chosen pore classes were (in diameter): (1) >50μm; (2) 25-50μm; (3) 5-25μm; (4) 2.5-5μm; (5) 1-2.5μm; (6) 0.5-1μm; (7) 0.05-0.5μm; (8) 0.005-0.05μm; (9) <0.005μm. Table 6-1 shows the theoretical crystallisation pressures for each stone type used in this study.

Sandstone	Theoretical Crystallisation Pressure MPa	Compressive Strength MPa (average and range)	Estimated Tensile Strength MPa
Corsehill	216	62 (49-74)	6.2
Locharbriggs (fine grained)	143	28 (23-30)	2.8
Stanton Moor	79	51 (37-61)	5.1
Blaxter	44	45 (32-53)	4.5
Scotch Buff	37	45 (35-57)	4.5
Giffnock	31	46 (40-50)	4.6
Locharbriggs (coarse grained)	20	28 (23-30)	2.8
Doddington	8	42 (38-44)	4.2
Cullalo	5	49 (41-64)	4.9
Hazeldean	3	58 (36-84)	5.8
Clashach	7	45 (37-55)	4.5

Table 6-1: Theoretical crystallisation pressures, measured compressive strengths and estimated tensile strengths for each sandstone.

Crystallisation pressures calculated in Table 6-1 for Corsehill, fine-grained Locharbriggs and Stanton Moor exceed their measured compressive strength of clean, control samples, and suggest that these sandstone types will be vulnerable to salt-induced decay. Crystallisation pressures for Blaxter and Scotch Buff are within the range of measured compressive strength values and so render these stones potentially vulnerable. Hazeldean, Cullalo and Doddington on the other hand have extremely small crystallisation pressures that are significantly lower than their compressive strength.

Importantly, tensile strength is thought to be the mechanical property that more accurately reflects the cohesive strength of a solid material and is the value in which mechanical resistance to processes such as salt crystallisation should be evaluated (Cardell, 2003). Griffith's theory (Griffith, 1924 in Cardell, 2003) assumes that compressive strength values may be up to ten

times the tensile strength of a material. Therefore, with this in mind, and by using measured compressive strength values, we see that the Hazeldean theoretical crystallisation pressure remains below the limiting tensile strength of the stone, while Cullalo is shown to be on the limit of its tensile strength. The other sandstones in Table 6-1 are predicted to experience crystallisation pressures well in excess of their estimated tensile strength.

Additionally, several studies have indicated the importance of specific pore diameter classes on salt uptake and durability. Yu and Oguchi (2010) introduced the salt susceptibility index (SSI) (Equation 6-4) that is used to predict the durability of a stone to salt crystallisation through two specific pore classes. The SSI is defined as:

$$SSI = (I_{pc} + I_{pm0.1})(P_{m5}/P_c)$$

Equation 6-4: Salt Susceptibility Index.

Where I_{pc} = the index of the total connected porosity, $I_{pm0.1}$ = the index of the microporosity of pores smaller than 0.1μm radius, P_{m5} = the microporosity of pores smaller than 5μm radius, and P_c = the total connected porosity. The connected porosity (I_{pc}) is an extremely important parameter influencing the susceptibility of stone to salt crystallisation, as it indirectly, amongst other parameters, encompasses mechanical properties of the stone including the tensile strength. However, as shown previously, the ratio of microporosity in the stone has the greatest impact on crystallisation pressures and therefore the microporosity ($I_{pm0.1}$) will indicate how much of this porosity is responsible for damaging crystallisation pressures. The second part of the equation relates to the active stress field within the stone, with the microporosity of pores smaller than 5μm generally controlling the capillary uptake of salts. The second part of the equation provides a ratio of the absorbed salt to the overall volume of porosity, and therefore the volume of the stone that will experience damaging crystallisation pressures. Table 6-2 presents calculated SSI values for each sandstone, with Yu and Oguchi's interpretation given for each SSI interval.

Sandstone	SSI	SSI Interpretation
Stanton Moor	6	Salt prone
Locharbriggs (fine)	4	Salt prone
Giffnock	4	Salt prone
Blaxter	4	Salt prone
Scotch Buff	3	Salt resistant
Corsehill	2.5	Salt resistant
Locharbriggs (coarse)	1.5	Very salt resistant
Doddington	1	Very salt resistant
Hazeldean	0.7	Exceptionally salt resistant
Cullalo	0.6	Exceptionally salt resistant
Clashach	0.3	Exceptionally salt resistant

Table 6-2: SSI classification and their interpretation as given by Yu and Oguchi, (2010).

The SSI data predict that Stanton Moor, fine-grained Locharbriggs, Giffnock and Blaxter will be the only salt prone sandstones, with Hazeldean and Cullalo the most resistant. Pore fractions, estimated crystallisation pressures, SSI values and specific hydric properties for each sandstone were correlated against dry weight losses (DWL) and maximum weight gain values (MWG) across each crystallisation test for all stones to examine the relevance and significance of these estimators. Table 6-3– Table 6-8provide the correlation coefficient values across each test.

NaCl DWL	% P_{m5}	P_{m5}	% $P_{m0.1}$	$P_{m0.1}$	SSI	ΔP	D	*P*	C_o	S	W_{abs}	C_{abs}
T1	0.08	0.28	**0.90**	**0.91**	0.29	**0.81**	0.59	0.60	0.41	0.22	**0.82**	**0.80**
T2	**0.70**	**0.73**	0.57	0.53	**0.81**	0.26	0.43	-0.17	-0.44	0.61	0.08	0.20
T3	**0.75**	**0.90**	**0.75**	0.67	**0.88**	**0.77**	0.55	-0.33	-0.24	**0.82**	0.36	0.14

Table 6-3: Correlation coefficients for all stones in crystallisation test 1 (T1), test 2 (T2) and test 3 (T3) between mean % NaCl dry weight loss (DWL) and the mean values of % pores <5µm (%P_{m5}), microporosity <5µm (P_{m5}), % pores <0.1µm (%$P_{m0.1}$), microporosity <0.1µm ($P_{m0.1}$), salt susceptibility index (SSI), theoretical crystallisation pressure (∆P), durability (D), porosity (P), connectivity (C_o), saturation coefficient (S), water absorption (W_{abs}) and capillary coefficient (C_{abs}). Bold values represent those over 0.7.

$CaCl_2$ DWL	% P_{m5}	P_{m5}	% $P_{m0.1}$	$P_{m0.1}$	SSI	ΔP	D	*P*	C_o	S	W_{abs}	C_{abs}
T1	0.12	0.25	-0.04	-0.05	0.08	-0.05	0.19	0.36	0.33	-0.07	0.23	-0.05
T2	-0.19	0	**0.78**	**0.81**	0.01	**0.87**	**0.71**	0.68	0.60	0.27	**0.97**	**0.84**
T3	-0.01	0.29	**0.86**	**0.89**	0.20	0.34	**0.96**	0.59	0.26	0.05	0.63	**0.90**

Table 6-4: Correlation coefficients between mean % $CaCl_2$ DWL and each parameter. T1: test 1, T2: test 2, T3: test 3. Bold values represent those over 0.7.

$MgCl_2$ DWL	% P_{m5}	P_{m5}	% $P_{m0.1}$	$P_{m0.1}$	SSI	ΔP	D	*P*	C_o	S	W_{abs}	C_{abs}
T1	-0.02	0.16	**0.72**	**0.72**	0.14	0.60	0.53	0.65	0.49	0.10	**0.74**	0.66
T2	-0.18	-0.01	**0.76**	**0.79**	0.01	**0.88**	**0.73**	**0.71**	0.59	0.29	**0.97**	**0.82**
T3	-0.67	-0.59	-0.18	-0.08	-0.65	-0.32	0.18	0.62	0.45	-0.57	0.23	0.51

Table 6-5: Correlation coefficients between mean % $MgCl_2$ (chloride blend in T1) DWL and each parameter.
T1: test 1, T2: test 2, T3: test 3. Bold values represent those over 0.7.

NaCl MWG	% P_{m5}	P_{m5}	% $P_{m0.1}$	$P_{m0.1}$	SSI	ΔP	D	*P*	C_o	S	W_{abs}	C_{abs}
T1	**0.73**	**0.78**	0.17	0.20	**0.76**	0.47	**0.77**	0.58	-0.14	**0.75**	0.51	0.24
T2	0.11	0.16	0.53	0.51	0.21	**0.90**	0.57	0.32	0.33	0.53	**0.77**	0.46
T3	0.05	0.21	0.42	0.41	0.18	**0.92**	0.16	0.05	0.46	0.21	**0.70**	0.19

Table 6-6: Correlation coefficient between mean % NaCl maximum weight gain (MWG) and each parameter.
T1: test 1, T2: test 2, T3: test 3. Bold values represent those over 0.7.

CaCl2 MWG	% P_{m5}	P_{m5}	% $P_{m0.1}$	$P_{m0.1}$	SSI	ΔP	D	*P*	C_o	S	W_{abs}	C_{abs}
T1	**0.72**	**0.87**	0.57	0.57	**0.77**	**0.76**	**0.88**	0.62	-0.07	**0.77**	**0.76**	0.53
T2	-0.20	-0.06	0.62	0.63	-0.06	**0.84**	0.66	**0.70**	0.62	0.25	**0.93**	**0.70**
T3	-0.42	-0.13	**0.73**	**0.79**	-0.20	0.41	0.65	**0.83**	0.67	-0.39	**0.77**	**0.85**

Table 6-7: Correlation coefficient between mean % $CaCl_2$ MWG and each parameter.
T1: test 1, T2: test 2, T3: test 3. Bold values represent those over 0.7.

$MgCl_2$ MWG	% P_{m5}	P_{m5}	% $P_{m0.1}$	$P_{m0.1}$	SSI	ΔP	D	*P*	C_o	S	W_{abs}	C_{abs}
T1	**0.93**	**0.84**	0.18	0.14	**0.90**	0.51	0.66	0.19	-0.65	**0.96**	0.25	0.05
T2	-0.07	0.06	0.50	0.50	0.04	**0.86**	0.54	0.52	0.57	0.30	**0.85**	0.52
T3	-0.68	-0.57	0.19	0.26	-0.57	0.15	0	**0.72**	**0.74**	**-0.73**	0.46	0.39

Table 6-8: Correlation coefficient between mean % $MgCl_2$ MWG and each parameter.
T1: test 1, T2: test 2, T3: test 3. Bold values represent those over 0.7.

The correlation coefficient values provide an understanding of the linear relationship between different variables. Values >0.7 are generally considered strong relationships, while values <0.5 are regarded as weak relationships. 31% of the measured correlations provide medium – strong relationships (>0.7), suggesting the existence of casual relationships whereby highly absorbent stones and those with a high microporosity are more

susceptible to salt absorption and salt crystallisation damage. Further analysis of R^2 values, which represent the fraction of the data that fit the linear regression, of each measured correlation coefficient shows that only 34% of those initial strong relationships are of statistical significance by providing R^2 values that are generally >0.8. It was found that the correlation coefficient was unsuccessful in detecting outliers within the small datasets.

Figure 6-2 presents two specific situations, whereby high correlation (R) and R^2 values imply a strong relationship between the DWL values of $MgCl_2$ and ΔP, and the DWL of $CaCl_2$ and % $P_{m0.1}$. This interpretation is misleading however, as the values of Stanton Moor, Cullalo and Doddington in both graphs do not accurately follow this trend. Results from the third crystallisation test reveal that Doddington is the most vulnerable to both $MgCl_2$ and $CaCl_2$ crystallisation, while Stanton Moor is shown to be resistant to both salts.

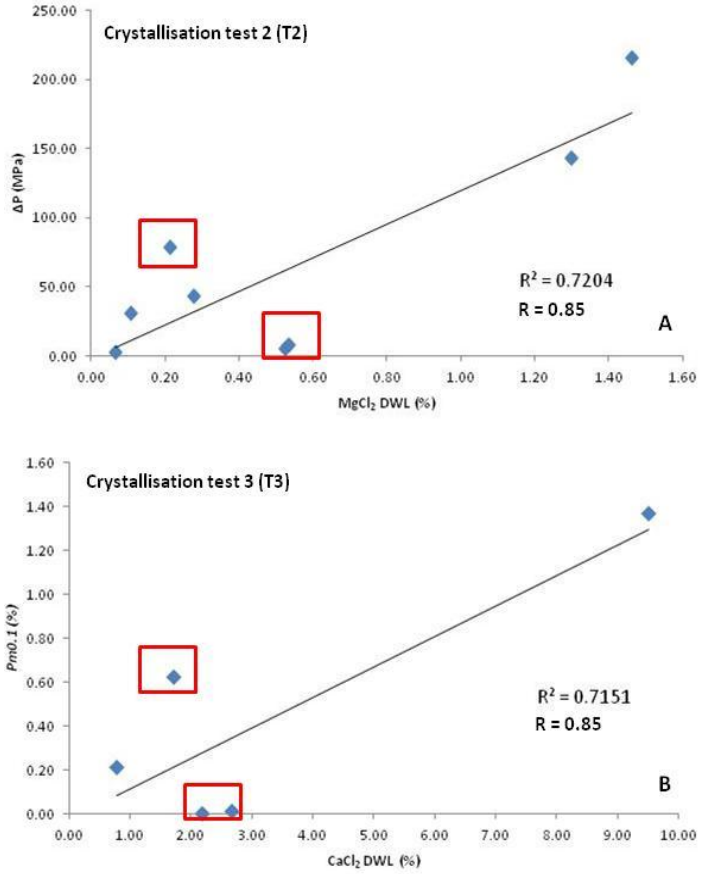

Figure 6-2: Correlations between DWL values of salts and stone parameters. (A): Correlation between $MgCl_2$ and theoretical crystallisation pressure in crystallisation test 2. (B): Correlation between $CaCl_2$ DWL and microporosity <0.1µm in crystallisation test 3. Red boxes highlight Stanton Moor, Cullalo and Doddington. Stanton Moor is located above the trend line in both graphs.

Weak and misleading relationships between most of the measured pore structure properties and the DWL and MWG values of $CaCl_2$ and $MgCl_2$ suggests either the absence of, or a change to the pore dimensional controls on the crystallisation of these salts. The poor relationship between the DWL and MWG of $CaCl_2$, $MgCl_2$ and the pore properties is expected considering the contrasting crystallisation behaviours of $CaCl_2$, $MgCl_2$ to NaCl.

The moderate - strong correlations that exist between the MWG of chloride blend treated stones and their SSI and % P_{m5} suggests the importance of the PSD and in particular, the microporosity, on NaCl accumulation in all samples subject to full immersive uptake. From the known continued behaviour of each sandstone in tests 2 and 3, it is postulated that certain samples contain a 'salt accumulation threshold', whereby continued salt crystallisation over several more cycles in test 1 would have lead to the eventual breakdown of sandstones, in particular Locharbriggs, Stanton Moor, Blaxter and Scotch Buff. Certainly, the Locharbriggs and Blaxter NaCl and envirothaw samples had already shown signs of surface granular decay, while Stanton Moor showed the early advancement of scaling decay and fracture chain development. Additionally, it is thought that due to the short duration of the second test, DWL values may demonstrate greater significance in relation to the rate of decay of the sandstones as opposed to their overall resilience to salt induced decay.

There are further strong correlations evident between the MWG and DWL values of NaCl in the third test and the SSI, % P_{m5} and P_{m5} as shown in Figure 6-3. The graphs show strong trends of increased salt accumulation (graph C) and increased dry weight loss that correlate with increasing P_{m5} and SSI (graphs 7-3 A, B and D). These correlations imply that greater salt accumulation and damage are expected in sandstones that have a relatively large proportion of pores in the <5µm diameter range. Green circles in graphs 7-3 A, B and D highlight the position of Locharbriggs sandstone, while green dashed lines represent the best fit and idealised line through Doddington, Cullalo and Stanton Moor samples. The higher DWL values shown by Locharbriggs and Corsehill are influenced by the increased solution uptake through faster capillary suction and high water absorption values, and in Locharbriggs sandstone in particular, the spatial concentration of micro-pores

within bedding planes in the stone. Strong linear correlations signify the strong relationship between the DWL and MGW of NaCl and the microporosity. Strong relationships exist because the crystallisation pressure of NaCl is inversely related to the pore size. Figure 6-3 however, highlights that this is not a simple relationship. The relationship between PSD and salt crystallisation damage is influenced by various other properties of the stone, as well as the test parameters themselves.

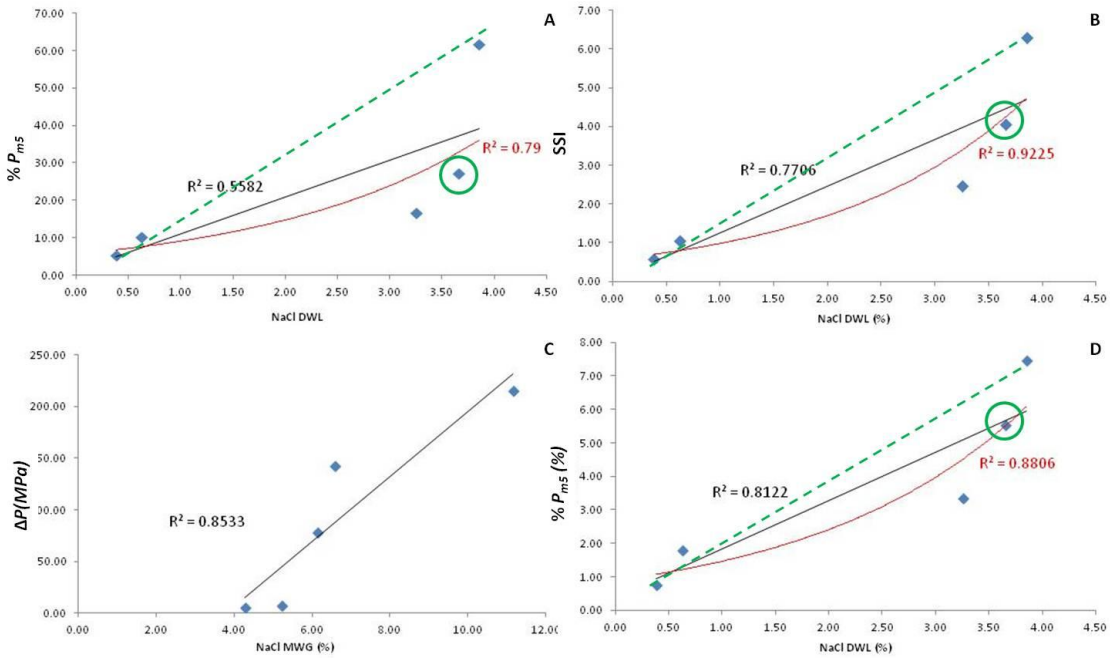

Figure 6-3: Correlations between NaCl DWL and MWG values from crystallisation test 3 and various stone parameters.
(A): Correlation between NaCl DWL and % porosity <5µm. (B): Correlation between NaCl DWL and SSI. (C): Correlation between NaCl MWG and theoretical crystallisation pressure. (D): Correlation between NaCl DWL and microporosity <5µm. Green circles highlight the location of Locharbriggs. Green dashed line represents the idealised trend line through Stanton Moor, Cullalo and Doddington. Red line represents exponential trendline through each sample. Black line represents linear trendline through each sample. Red R^2 values correspond to red exponential trendline.

Cardell (2003) and Benavente et al. (2008) discuss that the abundance and complexity of mineralogical, hydric, environmental and durability test specific data severely limits the extent to which generalisations on durability predictions can be made. Several important and key feedback processes are identified in the literature, and in this thesis that can be used to predict and understand the observed damage phenomena and the stones resilience to salt-induced decay.

6.2.1 Hydric properties on salt crystallisation induced damage

Several important processes that control and influence salt induced-decay have been identified in the literature. Félix (1995) proposed a durability estimator based on the correlation between the decreasing strength of the stone and the increasing water content. Richardson (1991) and Bell (1993) successfully predicted the DWL in salt crystallisation tests by using the durability factor which is based on the saturation coefficient and porosity of the stone. The use of the capillary absorption coefficient has also been suggested as a durability estimator as it is closely related to pore structure through the overall porosity and PSD (Benavente et al., 2004). Water absorption and the saturation coefficient are also highlighted as important properties that influence stone decay processes (Cultrone et al., 2012). Estimators that provide the most complete and comprehensive information on the mechanical, hydric and pore properties of stone will give a greater understanding of its durability behaviour. Hydric and pore properties influence the moisture absorption and extent of crystallisation pressures within the stone, while the mechanical properties provide the resistance to salt crystallisation damage.

The PSD encompasses some of the most important properties that control the development of high crystallisation pressures within the stone; however, PSD cannot fully explain moisture absorption and migration. As shown in Figure 6-3 and Table 6-3 – Table 6-8, there is no simple linear relationship between microporosity, SSI, theoretical crystallisations and the DWL and MWG of different NaCl-loaded samples. The PSD can help estimate the vulnerability of a stone to the development of high crystallisation pressures, but does not describe the connectivity of this microporosity within the stone. A poorly connected, tortuous pore network may prevent or inhibit the rapid intrusion of moisture into the micro-pores during natural, unsaturated conditions that are experienced within a building. The PSD may therefore provide an overestimation of the stone's vulnerability to high crystallisation pressures.

High water absorption allows the greater uptake of salts in solution into the stone and influences its susceptibility to damaging crystallisation pressures by increasing the potential stress field within the stone (Figure 6-4). The

saturation and capillary absorption coefficients, particularly in the second and third tests, will certainly influence the amount of absorbed solution as capillary absorption was the principle mechanism of solution uptake.

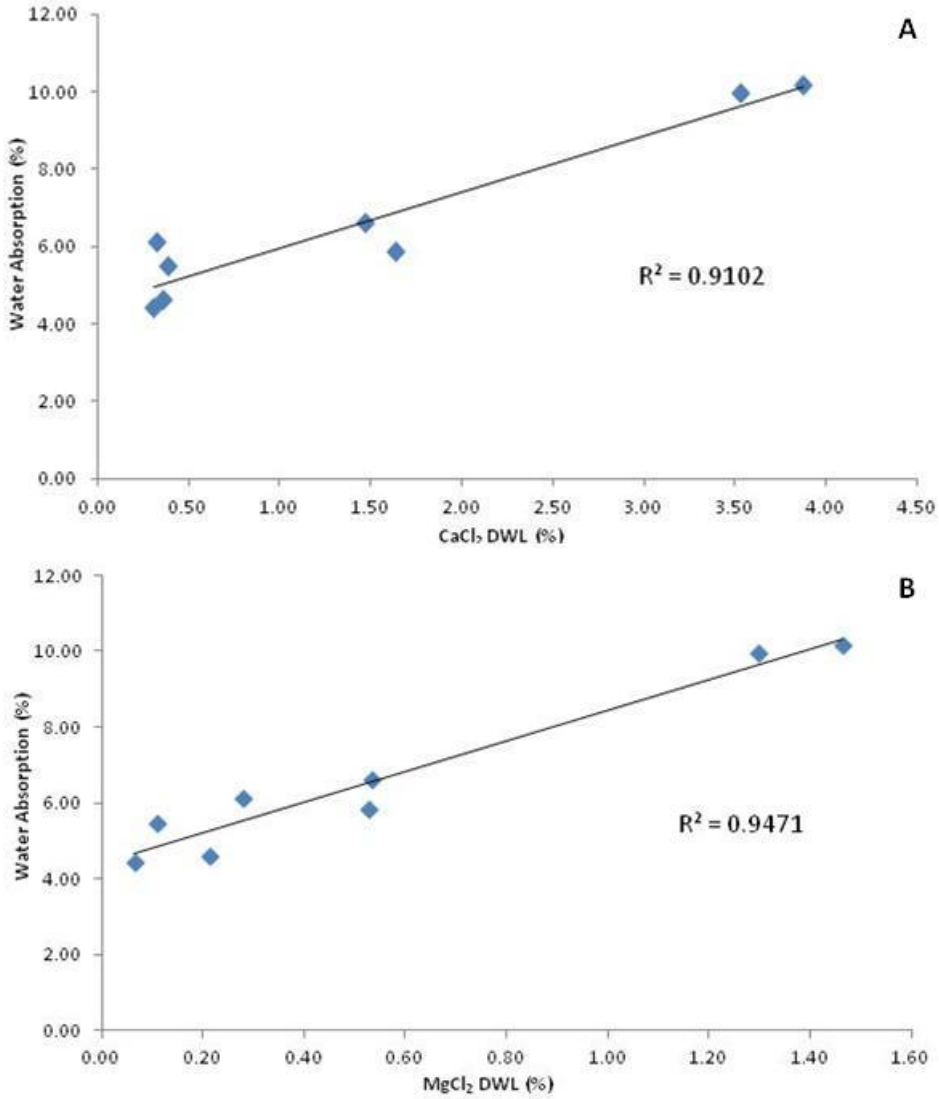

Figure 6-4: Correlations between $CaCl_2$ and $MgCl_2$ DWL values in crystallisation test 2 and water absorption.

(A): Correlation between $CaCl_2$ DWL and water absorption. (B): Correlation between $MgCl_2$ DWL and water absorption.

In the second and third tests, Corsehill displayed the greatest NaCl uptake, but suffered no DWL in the second test and high DWL in the third test. The absence of DWL in the second test corresponds to the short number of cycles, but suggests an anticipated susceptibility of Corsehill over several more cycles; as confirmed in test 3. The high water absorption capacity of Corsehill makes this stone vulnerable to NaCl induced decay by allowing a greater volume of salt to crystallise within the pore network, even in the absence of a substantial volume of micro-pores.

Locharbriggs suffered comparable NaCl DWL and decay patterns to Stanton Moor in the second and third crystallisation tests. The DWL is higher than that the ΔP, SSI and P_{m5} values would predict for Locharbriggs in comparison to values for Stanton Moor. Increased susceptibility to salt-induced decay is explained by the large water absorption, capillary uptake, porosity and low compressive and estimated tensile strength values of Locharbriggs. Furthermore, the spatial concentration of micro-pores within the bedding planes of Locharbriggs provide preferential crystallisation sites for NaCl, as described in Section 5.1.1.2. Increased crystallisation across specific areas within the stone will provide the ideal environment for elevated cation exchange capacity (CEC) (Pandey et al., 2014) and the development of fracture chains.

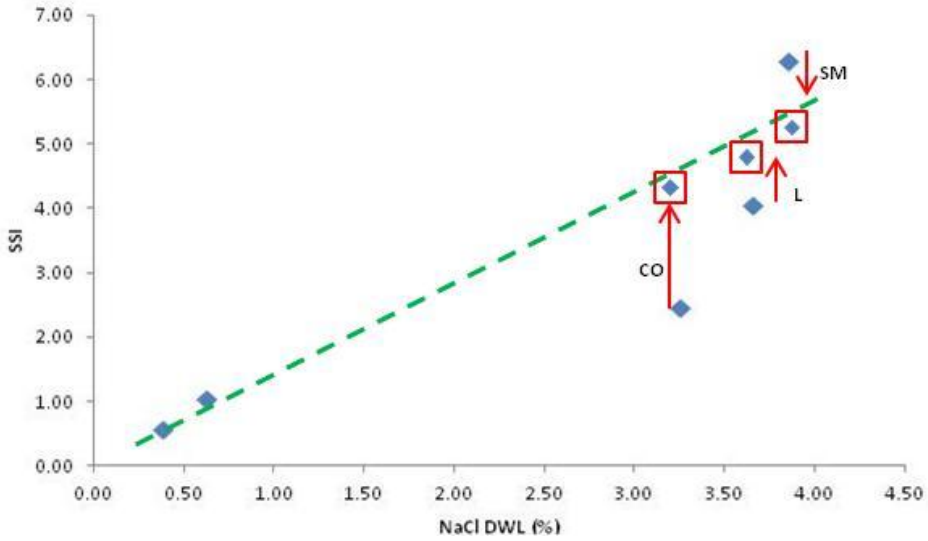

Figure 6-5: Expected changes to the correlation between NaCl DWL and SSI by incorporating water absorption values into the SSI calculation for Corsehill, Locharbriggs and Stanton Moor.
Red arrows indicate the movement of each value with the inclusion of water absorption values into the SSI calculation. CO: Corsehill, L: Locharbriggs, SM: Stanton Moor.

Figure 6-5 shows the expected change to the SSI values of Stanton Moor, Locharbriggs and Corsehill from the influence of total water absorption and porosity in the stone. High water absorption values in Locharbriggs and Corsehill increased their susceptibility to salt crystallisation damage. It was found that by incorporating the water absorption with % P_{m5} and SSI values, stronger correlations between the DWL and pore structure were found in the third test (Figure 6-6). There was an increase of 0.213 (from 0.747 to 0.960) and 0.068 (from 0.877 to 0.945) in the correlation coefficient and an increase of 0.364 (from 0.558 to 0.922) and 0.122 (from 0.770 to 0.893) in the

R^2 value for the NaCl DWL to $\%P_{m5}$ and SSI, respectively, after incorporating water absorption data into the $\%P_{m5}$ and SSI calculations.

Additionally, the difference in DWL and MWG values between Stanton Moor and Stanton Moor (2) samples in the third crystallisation test signify the importance of the absolute moisture absorption and the depth of moisture penetration on the overall susceptibility to salt-induced decay. Greater capillary uptake in Stanton Moor (2) samples resulted in greater depths of salt penetration and subsequently changed the drying regime of the stone, leading to more substantial granular decay and the relocation of fracture planes in the stone.

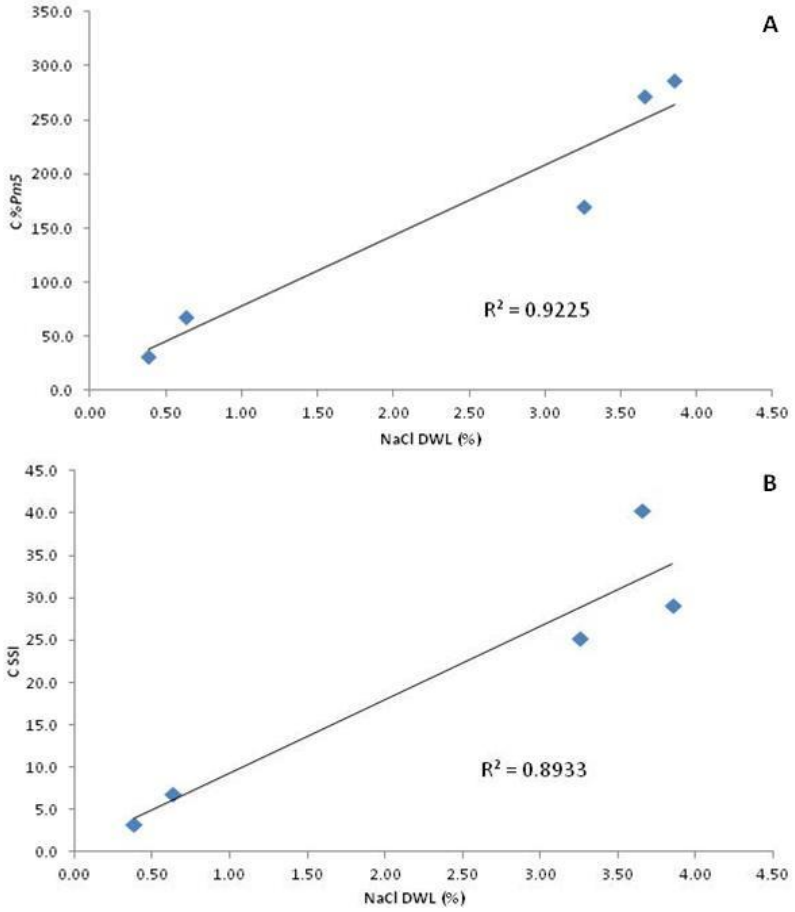

Figure 6-6: Correlations between NaCl DWL in the third crystallisation test and corrected SSI and porosity values.

(A): Correlation between NaCl DWL and corrected $\%P_{m5}$ value (P_{m5} x W_{abs}). (B): Correlation between NaCl DWL and corrected SSI value (SSI x W_{abs}).

Statistical correlations are largely absent from the data collected in tests 1 and 2 due to the relative incompleteness of these datasets. Rather, tests 1 and 2 are seen as predicting the rate of change in each sandstone. The overall susceptibility is based on the total change of each sandstone in the third crystallisation test.

6.2.2 Spatial distribution of microporosity on salt crystallisation induced damage

As suggested in Section 5.1.1.2, the spatial distribution of micro-pores within sandstone is likely to be an important influence on salt crystallisation damage. The concentration of micro-pores within bedding planes of Locharbriggs is recognised as a vital structural control on salt crystallisation. Figure 6-7 highlights the contrast between layers in Locharbriggs, whereby the narrow layers are characterised by smaller, angular quartz grains and a greater fraction of micro-pores. Crystallisation is thought to occur preferentially within these layers owing to their relatively low permeability and high tortuosity, which slows ionic diffusion and moisture transport. Substantial crystallisation within the layers would create natural planes of failure and increase the potential for substantial material loss. Figure 4-79 and Figure 6-8 illustrate the feedbacks between the structural properties of the stone and the drying process, which may also contribute to substantial damage.

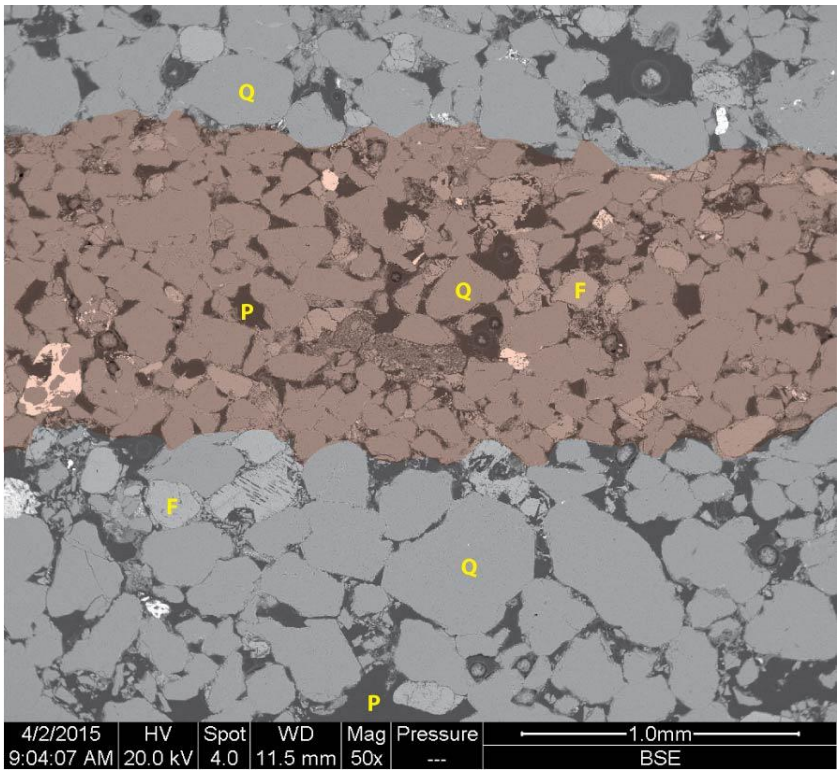

Figure 6-7: SEM BSE thin section image highlighting a layer with Locharbriggs sandstone.

F: Feldspar grains. Q: Quartz grains. P: Pores. Red shaded area highlights the layer.

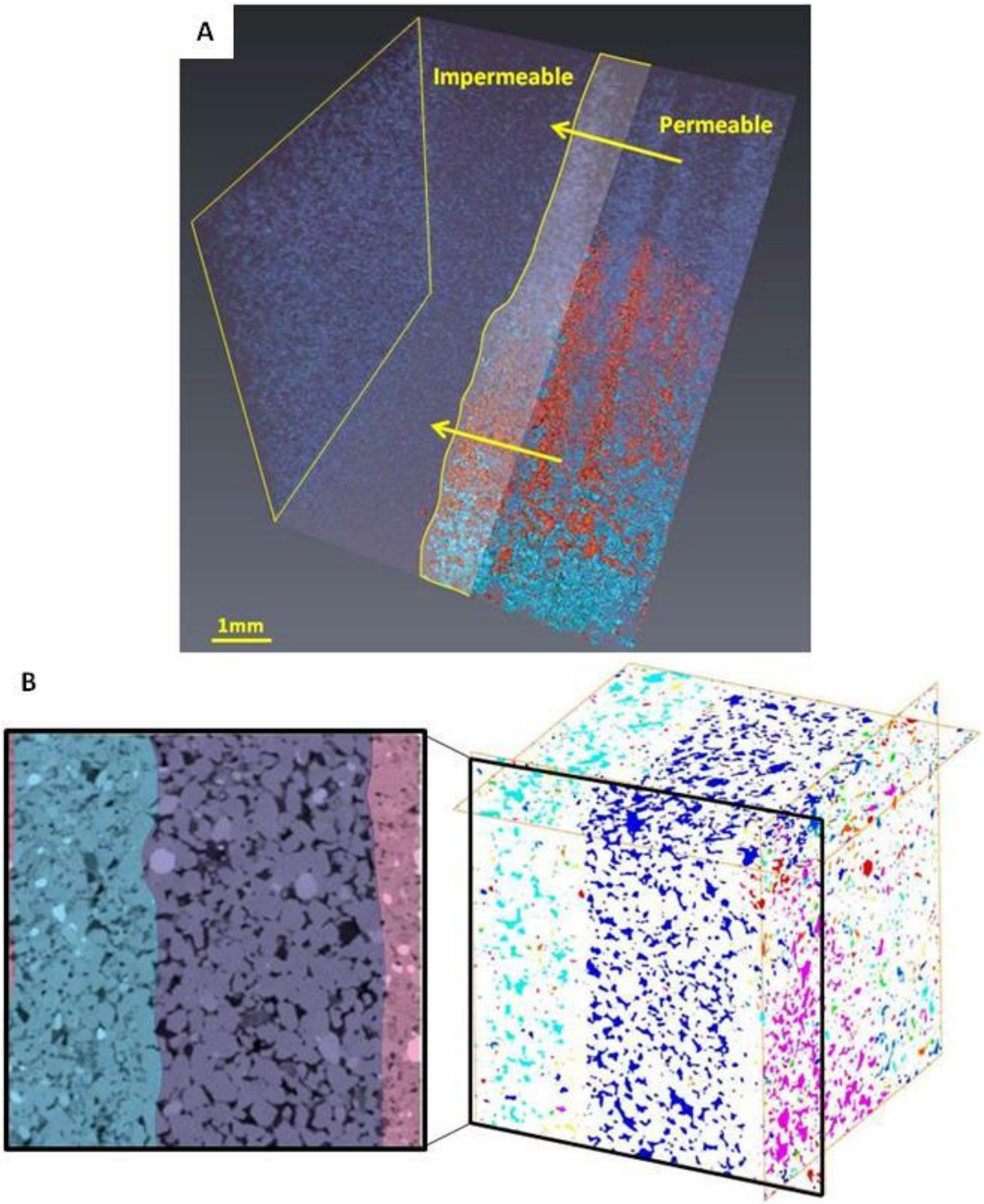

Figure 6-8: Moisture movement through layers in Locharbriggs sandstone. (A): Synchrotron µCT image of salt solution in fine-grained Locharbriggs. (B): µCT analysis of pore connectivity in Locharbriggs sandstone. Blue areas correspond to well-connected pores, ranging through turquoise to magenta and red; representing disconnected pores. Grains have an average size of ~190µm.

The stone in this scenario is characterised by the existence of two layers of different permeability. In the hypothetical situation where the drying front is located to the left side of the sample (thin yellow box), capillary flow through the stone would be severely disrupted owing to the low connectivity between the different layers. This would necessitate a change to the drying regime, whereby the drying boundary would retreat into the stone, relocate at this position, and prompt the preferential crystallisation of salts in this small zone adjoining the layers. Even in the absence of significant volumes of micro-pores within this crystallisation zone, damaging, differential pressures could develop through long fractures between the layers, causing considerable structural damage.

6.2.3 Drying process on salt crystallisation induced damage.

This last section primarily discusses the influence of pore properties that control moisture ingress on the DWL and MWG of stones exposed to de-icing salts. A second important aspect to consider when assessing the durability of materials to salt crystallisation damage is the drying process. Results from the drying test reveal information on several important and dynamic phase changes taking place within the stone. Due to the complexity of the drying process, several of the generated results from the drying tests are needed to accurately explain and characterise the drying process within the different sandstones. This caution explains the absence of drying test results in the statistical analysis.

The drying process impacts considerably on the behaviour of sandstone to salt-induced decay by influencing the location of salt crystallisation within the stone. The drying process is controlled partly by the pore properties of the stone, and partly by environmental conditions (as controlled by the salt crystallisation test procedure). Drying is primarily influenced by the pore connectivity and tortuosity, as this dictates the length of the drying pathway and therefore the rate of moisture movement to the stone surface.

Cullalo, Doddington, Hazeldean and Blaxter sandstones dry the most efficiently, and are generally characterised by: (i) high and prolonged constant drying rates that represent the evaporation of free water from the sample surface; (ii) low CMC values that represent the critical moisture content when the surface is no longer surface wet; (ii) low residual moisture contents (although this value can be influenced by the overall porosity of the stone to provide misleading results). The CMC represents both the point in time when salt crystallisation is likely to start but also the amount of remaining moisture that still contains salt; i.e., the reservoir of potentially damaging salts in solution still available in the stone.

Fast and efficient drying rates of Cullalo, Doddington, Hazeldean and Blaxter explain the low NaCl DWL values in tests 2 and 3 (after accounting for anomalies in Cullalo samples from the loss of efflorescence early on in the test that increased the Cullalo DWL value). High efflorescence accumulations

also represent the successful migration of salts through the pore network and onto the stone surface (Figure 4-29), forming the generally stated “harmless” efflorescence (Gupta et al., 2012). To some extent this is certainly true: those salt crystals within the efflorescence cannot exert damaging pressures on the pore structure themselves; however, thick efflorescence accumulations can drive important feedback mechanisms that initiate subflorescence via surface pore blocking. The development of hard, strongly adhered efflorescence on the stone surface creates a barrier to flow, causing the retreat of the drying boundary into the stone and the likely onset of internal salt crystallisation. This process was witnessed for Locharbriggs, Cullalo and certain Doddington ($MgCl_2$) and Corsehill samples (Figure 4-30). It generates a positive feedback for further potential salt crystallisation damage to Locharbriggs and Corsehill samples, which are already potentially vulnerable stones. In Doddington and Cullalo samples however, this process presents a situation whereby there is new potential of salt crystallisation damage. Changes to the USV of Doddington and Cullalo samples after NaCl crystallisation show that even with exceptionally resistant pore networks (as described by the SSI value), the development of crystallisation pressures capable of altering the pore network are possible through internal crystallisation caused by efflorescence pore blocking.

Figure 6-9 highlights the drying pathways within Cullalo sandstone, whereby high drying rates through continued capillary flow to the surface allows the formation of thick salt crusts. Initial efflorescence is porous; it forms during the drying process and dissolves during capillary immersion. Drying would have taken place on the efflorescence surface, and hydraulic connectivity would have been preserved through “capillary pumping” (Sghaier and Prat, 2009; Veran-Tissoires et al., 2012). At higher salt concentrations (after several cycles of salt uptake), efflorescence became a permanent feature on the rear faces of Cullalo (NaCl and $MgCl_2$) and Doddington (NaCl) sandstones. At this point, the efflorescence layer will have dried out and the drying rate would have been significantly reduced, with drying taking place either on the efflorescence surface or on the underlying substrate. In either case, the drying rate would have been reduced, with the onset of stage 2, with stage 3 drying taking place as the efflorescence became less porous (Nachshon et al.,

2011a; Nachshon et al., 2011b). Gupta et al (2014) showed that under low RH conditions (expected for high drying rate conditions), there was an unexpected reduction in the drying rate experienced by the stone due to the formation of a thin, impermeable salt crust. The formation of a thin salt crust blocked surface pores and reduced hydraulically connected stage 1 and stage 2 drying. At this point, subflorescence would have started to form in Cullalo and Doddington sandstones, and even in the absence of a high percentage of micro-pores, substantial pressures may have developed due to non-equilibrium salt growth and the sheer volume of salt present within the stone. Table 6-1 shows that crystallisation pressures exceeding the tensile strength of the stone are expected to develop within both Cullalo and Doddington sandstones.

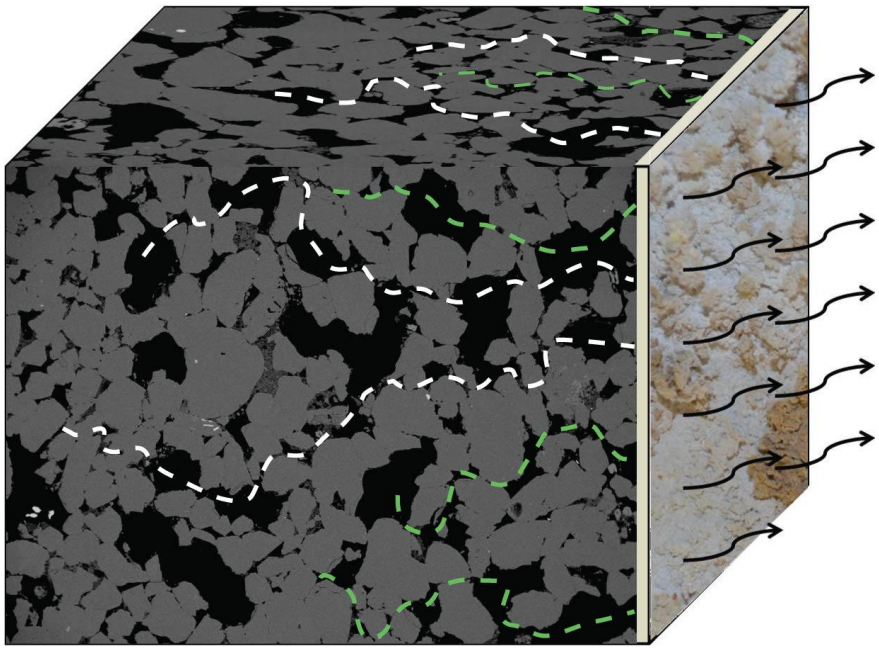

Figure 6-9: Hypothetical drying pathways in Cullalo sandstone.

Green lines: stage 1 drying pathways, with evaporation of free water taking place on the stone surface. White lines: stage 2 drying pathways, whereby prolonged drying takes place through continued capillary connection to the stone surface, allowing the drying of "deep" section in the stone.

On the other hand, Stanton Moor is an extremely slow drying stone, experiencing a high CMC, high residual moisture contents and low receding drying rates. Stanton Moor in particular experienced no significant efflorescence accumulation across any salt in every crystallisation test. Connected areas of high salt concentrations in samples from tests 1 and 3 clearly highlight the locations of drying boundaries within Stanton Moor

(Figure 11-11, Figure 11-12, Figure 4-33, Figure 4-34) and signify the poor drying efficiency of this stone. The location of the drying boundary was influenced by the crystallisation test procedure (drying and capillary uptake regimes), creating fracture chains and eventual scaling decay. Poor drying efficiency makes Stanton Moor a highly vulnerable stone to NaCl crystallisation damage even before the onset of subsequent pore structure changes that would certainly have provided positive feedbacks leading to increased vulnerability as experienced by Cullalo and Doddington. The grain structure as identified in Section 6.1 influenced the PSD and drying regime experienced by Stanton Moor, with a high tortuosity and poor connectivity between pores severely disrupting drying pathways within the stone (Figure 6-10).

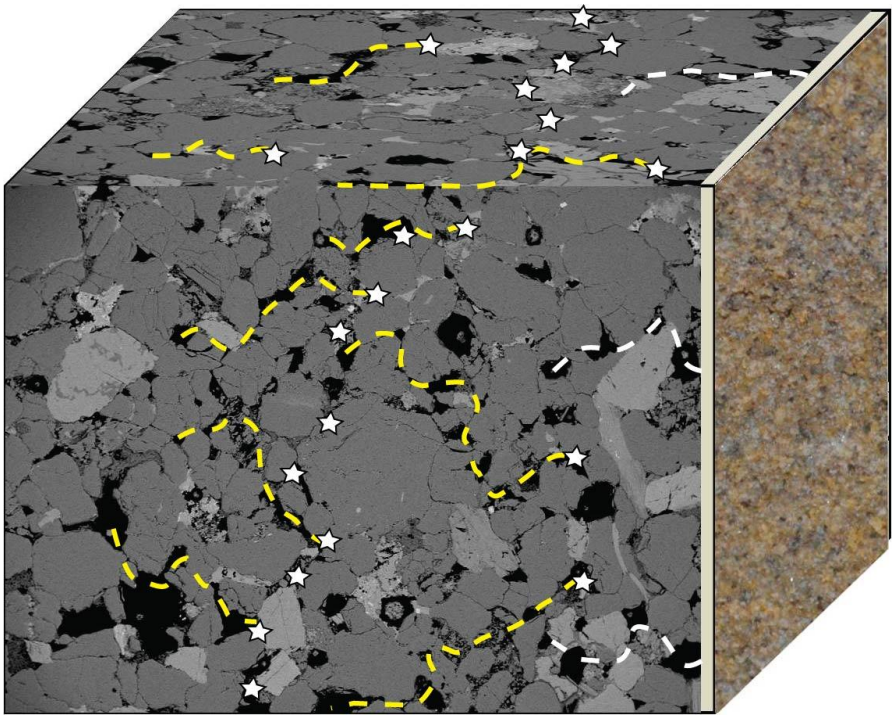

Figure 6-10: Hypothetical drying pathways in Stanton Moor sandstone.

White lines: stage 2 drying with short-lived capillary connection of moisture to the stone surface. Yellow lines: stage 3 drying, whereby capillary flow is disconnected from the stone surface and vapour diffusion controlled drying dominates. White starts denote where salt crystallisation is expected to take place.

In order to make a quantitative assessment of drying behaviour on the response of stone to salt-induced decay, several drying parameters were combined to produce an overall salt-decay susceptibility value for each sandstone. This task was achieved by combining the falling and constant rate values, as they provide the actual rates of moisture loss at different times

during the drying test. The CMC and remaining moisture contents were then subtracted as they indicate the moisture/salt reservoir remaining in the stone at different stages. High values of falling and constant drying rates represent fast drying throughout each drying stage, while low CMC and remaining moisture values indicate the remaining moisture within the stone after a substantial period of drying. Combined, high values indicate fast, efficient drying and a likely high resistance to salt induced decay. In contrast, lower values indicate a poor drying efficiency and the likelihood of subflorescence occurring. Figure 6-11 shows the various drying parameters and the overall calculated susceptibility value. Locharbriggs, Cullalo, Hazeldean and Doddington have similar high values, while Corsehill, Giffnock, Stanton Moor and Clashach are all characterised by low drying efficiency, with generally low constant and falling drying rates and low CMC values. This pattern helps to explain the high durability of Hazeldean, Cullalo and Doddington sandstones to NaCl crystallisation and the low resistance of Corsehill, Stanton

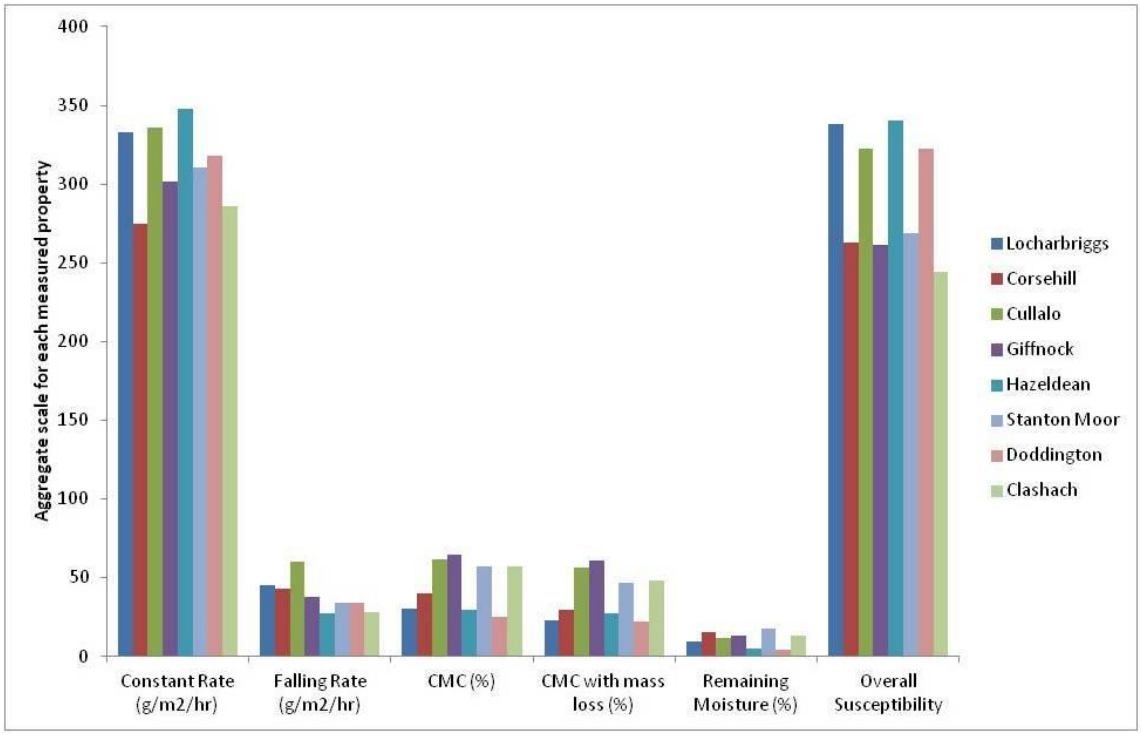

Moor and to an extent some Giffnock samples in test 2.

Figure 6-11: Drying test parameters. Y-axis values are given for each property.

Constant drying rate and falling drying rate: g/m^2/hr, CMC, CMC with mass loss and remaining moisture: %, Over Susceptibility is an accumulated coefficient value. High values represent greater durability to NaCl-induced decay and low values, greater susceptibility to NaCl-induce decay on average (with the exception of Locharbriggs due to its spatial concentration of micro-pores and Clashach due to its high strength and low proportion of micro-pores). The 'overall susceptibility' values correctly predict the

durability for Corsehill, Cullalo, Hazeldean, Stanton Moor and Doddington sandstones throughout the different salt crystallisation tests.

6.2.4 Combination of factors influencing salt crystallisation induced damage.

The poor durability of Locharbriggs is primarily due to the spatial distribution of micro-pores, its high porosity, and low compressive and tensile strength, while the high durability of Clashach is explained by its low microporosity, low total porosity, low water absorption, low capillary uptake and high compressive strength. Nonetheless, drying behaviour provides extremely valuable information relating to salt crystallisation distribution and the changing stone behaviour throughout the crystallisation tests.

The changing drying behaviour of most sandstones (especially Cullalo, Doddington, Stanton Moor, Locharbriggs) introduces an important dynamic variable, whereby changes to important stone properties significantly alter the response of the stone to salt-induced decay through positive feedback processes. Efficient drying sandstones will experience significant changes to their drying behaviour from the blocking of surface pores (such as case-hardening; Figure 6-12), leading to previously salt-resilient sandstones becoming increasingly sensitive to salt crystallisation damage and other weathering processes (Figure 6-12).

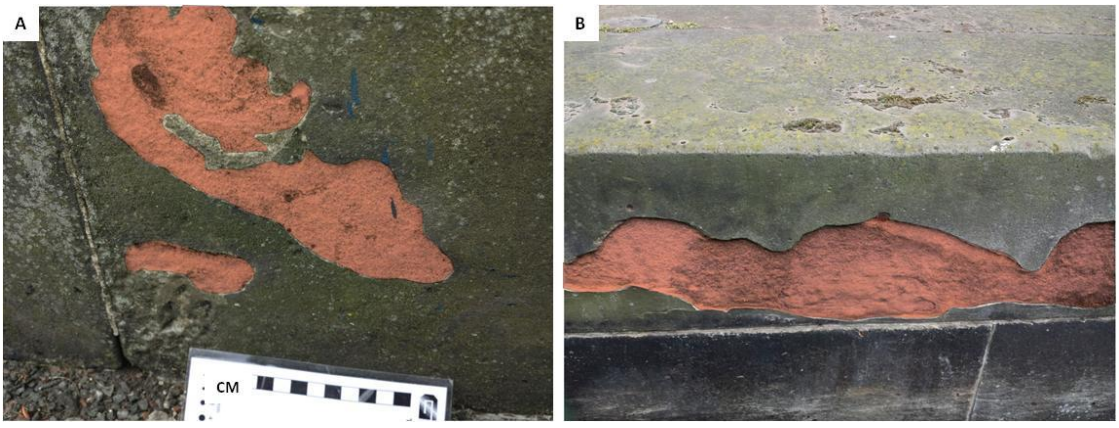

Figure 6-12: Granular decay of Cullalo following breaching of the case-hardened surface.

(A): Granular decay of Cullalo sandstone highlighted in red. Melville Tower, St Andrews Square, Edinburgh, UK. (B): Granular decay of Cullalo sandstone highlighted in red. National Gallery and Royal Scottish Academy, Edinburgh, UK. The remaining stone in both images shows evidence of surface staining and discolouration from case-hardening that is likely blocking surface pores and reducing the surface vapour permeability. This can cause the accumulation of salts beneath the impermeable surface, leading to accelerated decay, but is not exclusive to salt-induced decay.

Initial stone properties (porosity, permeability, PSD, drying rate etc) provide clear “starting properties” that will influence the initial durability of the stone to specific weathering agents. However, these properties will change in response to continued weathering, creating a dynamic, changing system of stone properties throughout the life-span of a building that becomes increasingly heterogeneous in time between the surface and sub-surface layers of the stone. This dynamic system makes the long-term prediction of building stone durability an extremely challenging task, whereby the use of freshly quarried stone properties is not always a true indication of how the stone will behave in-situ over the life-span of a building.

7 Synthesis discussion

7.1 Introduction

Much of Scotland's historic built heritage is now severely suffering from years of decay and weathering. In some cases this has been exacerbated by neglect, poor maintenance and bad building management through the recommendation and use of inappropriate repair strategies and materials. In particularly acute situations, this can lead to certain buildings losing a significant proportion of their original fabric, causing a considerable aesthetic impact and altering the future performance of the construction materials in an unknown and unpredictable fashion.

It is of great importance for the future protection of our built heritage that we understand the continued weathering behaviour and durability of newly replaced stone. Stone weathering is a complex and dynamic system comprising a suite of inter-related physical, chemical and biological processes that work to overcome the integrity of the stone. These processes are almost always aided by the presence of water (in the form of different phases: ice, liquid, vapour).

We regularly quantify the magnitude of change to stone in relation to its durability or resilience. Durability describes the ability of a material to withstand and resist weathering or decay over time by retaining its original mechanical, chemical and aesthetic properties, however durability as a general term to describe and understand the behaviour of a stone within a building is misleading. Just like the complexity of stone weathering systems; durability is influenced by a multitude of material properties, including tensile and flexural strength, mineralogy and pore structure.

Durability is generally regarded as a fixed value based on the measured properties of fresh stone. For durability values that are based on known static parameters of the stone to be accurate, the weathering and decay forces acting on it must also be invariant. However in reality, most stones

experience complex threshold and feedback-driven processes that vary spatially in their intensity and over time, while constantly altering the properties of the stone. The properties of the stone are in continuous change as the stone weathers and decays, which slowly alter the initially defined durability value of the stone. This dynamic weathering response was recognised in Cullalo and Hazeldean samples treated with NaCl. Promoted by efficient drying kinetics in these samples, significant surface efflorescence contributed to the blocking of surface pores and the onset of subflorescence which produced detectable changes (via USV testing and SEM) to their pore and grain structure.

Furthermore, when the durability of stone is described, it is only usually associated with one or two specific weathering agents. Durability can therefore be seen as a general indicator that is normally based relative to one or two of these associated decay processes. This has always been a necessary over simplification, since in reality the complexities of these weathering systems make it extremely difficult to measure and model stone weathering behaviour to any great certainty.

Attempts have been previously made to determine ‘durability estimators’ that can efficiently assess durability, and therefore the suitability of stone to resist specific weathering agents and environments, respectively, under short time constraints. These estimators are based on correlations between measured petrophysical properties of the stone (saturation, porosity, pore size distribution, tensile strength etc) and their behaviour to durability testing from specific weathering agents (freeze-thaw, salt crystallisation etc). These estimators are therefore only applicable to specific lithologies as well as specific weathering agents. Some of the most prominent durability estimators that have been proposed include the ‘durability factor’ (Richardson, 1991), the ‘limestone durability estimator’ (Moh’d et al. 1996) and the ‘alteration index estimator’ (Angeli et al. 2007).

It was deemed appropriate and furthermore, beneficial for future building stone research that a critique and ranked toolkit of stone testing procedures (that were used within the thesis for durability estimation) was undertaken. This critique identifies the stone properties (and their associated tests) that

are deemed essential for the accurate estimation of stone durability from salt-induced decay by NaCl, $CaCl_2$ and $MgCl_2$. Each stone property is classified under three broad headings; those that are (i) essential, (ii) useful and (iii) not-useful for estimating sandstone durability to NaCl-induced decay, using quantitative data from this thesis in order to classify each property. The most effective and efficient techniques for measuring these essential and useful stone properties, as well as alternative methods are also recommended.

One of the major decay mechanisms affecting sandstone buildings concerns the crystallisation of soluble salts within the stone. De-icing salts provide one of the most important sources and pathways of salt into the lower courses of buildings. In buildings vulnerable to increased de-icing salt absorption (those close to busy heavily salted roads and pavements with high pedestrian traffic), salt crystallisation damage is the dominant decay mechanism that is present in the lower courses of stone; frequently overprinting other weathering processes. NaCl is the most commonly used de-icing salt in Scotland owing to its low price and high availability. The majority of salt-induced decay in the lower stone courses of buildings is therefore attributed to that of NaCl crystallisation from de-icing practices (Aberg et al. 1999).

The damaging processes of NaCl are well-known and have been thoroughly researched under various environmental conditions (Smith et al. 2005, Warke, 2007) and in different lithologies (Rothert et al. 2007). However, there has yet to be thorough research undertaken on the potentially harmful effects of other de-icing salts on sandstone masonry in order to ascertain whether alternative ‘heritage friendly’ compounds to NaCl could be used. $CaCl_2$ and $MgCl_2$ are common alternative de-icing salts, with most research into their use concerning their damage to cement and concrete (Darwin et al. 2007, Şahmaran and Li, 2007). Cnudde et al. (2013) make reference to the deleterious impact of de-icing salts on sandstone buildings in Belgium. They fail to utilise these salts in their research on the winter weathering resistance of sandstone to salt-induced decay, but continue to refer to the durability of the stone in relation to de-icing salt use.

Research undertaken in this thesis was commissioned by Historic Environment Scotland in order to recommend: (i) the most ‘heritage friendly’ de-icing

salts that are least damaging to sandstone masonry and (ii) the most salt-resilient replacement sandstone for use in salt-vulnerable buildings by understanding the most important stone properties that influence salt-induced decay through laboratory salt-crystallisation tests. It is hoped that results from this thesis will help to inform homeowners and industry bodies on the use of appropriate de-icing salts by contributing to policy decisions and information/technical guides on de-icing practices.

This synthesis chapter will initially summarise the different behaviours of each de-icing salt and their risk to the mechanical and chemical damage of sandstone using results from crystallisation and durability tests. The most important stone properties governing salt-crystallisation damage are then discussed, with a ranked stone durability toolbox of essential and non-essential stone properties required for stone durability estimation presented. Both of these strands are then combined in a final section that summarises the complex salt-stone interactions that were identified in the durability tests.

Results in this thesis on the behaviour of NaCl within sandstone under laboratory conditions build on the current understanding of NaCl crystallisation within the literature. They also reveal important and complex feedback processes and interactions between salt crystallisation pressures, pore size distributions, surface efflorescence and drying processes.

Results from $MgCl_2$ and $CaCl_2$ treated samples from the same salt crystallisation tests reveal interesting and contrasting behaviours of these salts relative to those for NaCl under the same conditions. The tightly controlled phase transition conditions for free solutions of $CaCl_2$ and $MgCl_2$ are well understood in the chemistry literature, however their behaviour within stone has not been previously examined. Results of salt crystallisation tests reveal that under the temperature and RH conditions likely to be experienced in Scotland, both salts remain as harmless solutions within the stone. Under higher temperature and lower RH conditions however, both salts show similar crystal morphologies. The sensitivity of different stones to salt-crystallisation damage of both salts is related to slight differences in their

rate of crystallisation, with less direct influence from specific stone properties (as also determined for NaCl).

By undertaking a comprehensive study of the mechanical and pore network properties of different sandstones, the most important stone properties that influence key primary and feedback processes controlling the crystallisation of different salts were identified. A critique of the methodologies used in measuring the different stone properties enables the recommendation of a stone durability assessment toolkit. This toolkit builds upon existing durability classifications, and identifies those properties (and their mode of measurement) of most importance for estimating resistance to the crystallisation of NaCl, $CaCl_2$ and $MgCl_2$.

Lastly, a summary of the most important salt-stone interactions are presented for each salt relative to the vulnerable stone types. This section summarises the key crystallisation behaviours for each salt as discussed in Section 7.2 and describes the complex interactions between salt crystallisation and those stone properties identified in Section 7.3 as being most responsible for salt-induced decay.

7.2 The different behaviour of each de-icing salt and its risk for mechanical damage

The crystallisation process differs between each salt type used in the tests, and is distinguished by environmental conditions of crystallisation reactions, crystal habit/morphology and the extent and texture of salt efflorescence and decay. The difference between the crystal habit of $CaCl_2$/$MgCl_2$ and NaCl, and its affect on grain structure damage is described in Figure 5-19.

Each salt generated damage by exerting high pressures against pore walls during crystallisation. The extent of damage to each sandstone is influenced by a multitude of variables that dictate: (i) the net damage magnitude; (ii) the location of damage; (iii) the rate of damage; (iv) the weathering texture. Damage, in any form, was influenced by: (1) environmental conditions that the sandstones were exposed to during the durability tests, including: (a) drying and immersion regimes; (b) the uptake of solution into the stone, as this influences the quantity of salts that can crystallise and exert damaging pressures; (c) the porosity and pore size distribution of the stone, as NaCl crystallisation pressures correlate inversely with pore size; (d) the drying pathways and drying regime within the stone, as this variable can determine the location of salt crystallisation; (e) the surface conditions and near-surface porosity of the stone blocks, including the texture and location of surface efflorescence as this influences the solution uptake and drying of the stone.

Stone- and test-specific parameters effectively controlled the location of salt crystallisation, which in some stones substantially influenced the process by which salts produced certain types of damage. This phenomenon was chiefly achieved through the emergence of positive feedbacks that increasingly controlled salt crystallisation damage by altering the initial salt crystal growth process within the stone. Thus, the potential susceptibility of each stone to future weathering processes was increased.

7.2.1 $CaCl_2$ and $MgCl_2$

$CaCl_2$ and $MgCl_2$ have a similar crystallisation behaviour, forming large sheets that coat grains and block pore throats (Figure 5-29). This behaviour was revealed by ESEM analysis of free $CaCl_2$ solution and $CaCl_2$ solution within stone. The sheets that formed from the free solution measured 20 -40µm in thickness, while at extremely low RH conditions (5% RH) dynamic crystallisation reactions developed, with the crystallisation and dissolution of unstable 'globules' of salt and 'bubbly', hollow crystals taking place (Figure 7-1). Near the $CaCl_2$ deliquescence RH value (35%) however, the salt behaviour was found to feed dendritic crystal growth (Figure 5-29D). Within the stone, $CaCl_2$ blocked pore throats by forming layered crystal sheets that coated grains and was found as irregular shaped 'ridged' crystals in other dry-cut samples of Scotch Buff and Locharbriggs sandstone (Figure 5-30).

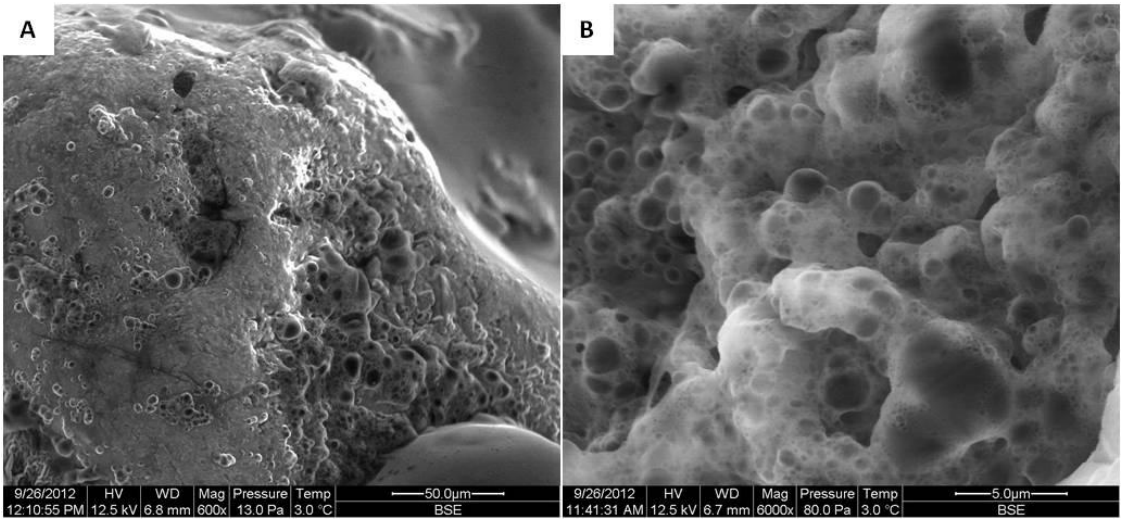

Figure 7-1: ESEM images of $CaCl_2$ crystallisation within Stanton Moor sandstone under stable temperatures (3°C) and different RH conditions.
(A): Small 'globules' of $CaCl_2$ at 2.5% RH. (B): 'Hollow' and 'bubbly' textured $CaCl_2$ crystals at 10%RH.

Substantial behavioural differences were revealed between the two salt types during the second and third crystallisation tests (which increase their potential for greater rates of decay). Both salts require either high temperatures or low RH conditions before crystallisation will commence. Prolonged drying under lower temperature, radiative heating conditions (50°C – 70°C) enabled the migration of $MgCl_2$ ions towards the surface, allowing the salt to crystallise as a thick efflorescence on certain stones (Cullalo, Locharbriggs) and increased the rate of decay in others (Doddington).

Increased $MgCl_2$ decay rates over $CaCl_2$ were due to the near surface crystallisation of the salt, leading to substantial granular decay. Figure 7-2 shows the differences between the crystallisation of $CaCl_2$ and $MgCl_2$ under radiative heating conditions as experienced in the third crystallisation test.

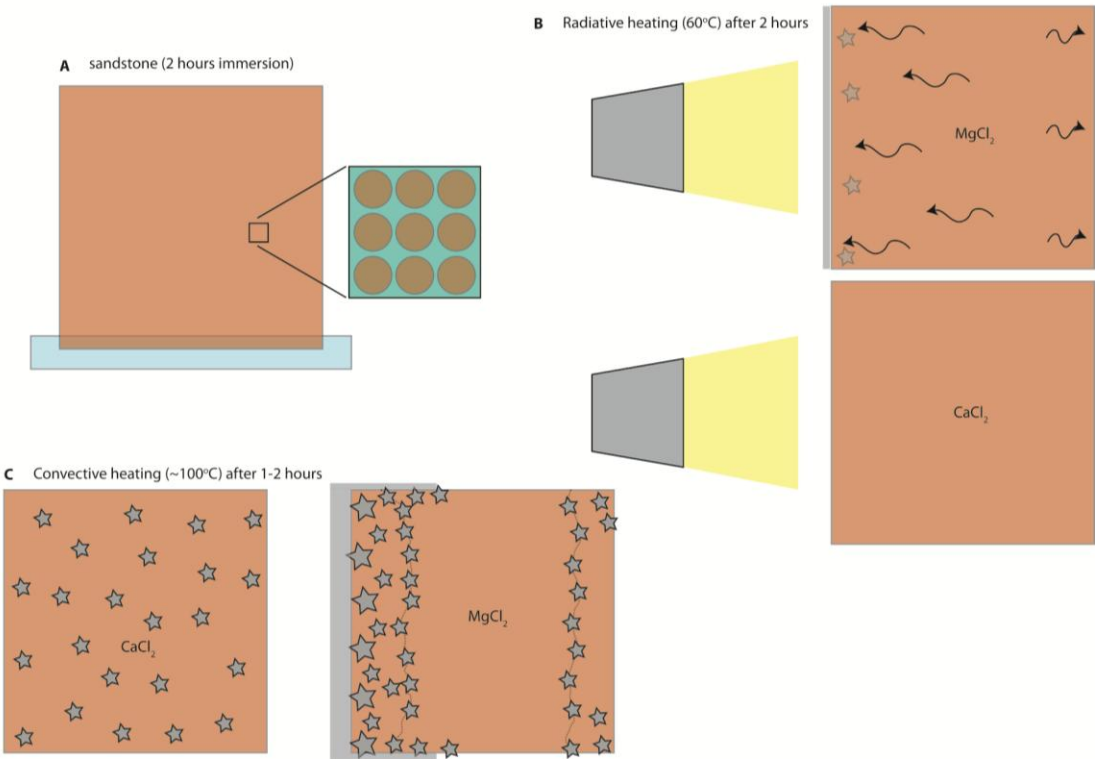

Figure 7-2: Differences in crystallisation behaviour between $MgCl_2$ and $CaCl_2$.

A: Sandstone after 2 hours of salt solution immersion. B: During the radiative heating regime at 60°C, $MgCl_2$ starts to slowly migrate towards the drying/heating surfaces, crystallising as efflorescence. Nothing happens during this period in $CaCl_2$ treated samples. C: After a period of high temperature convective heating, $CaCl_2$ crystallises homogeneously throughout the stone, while $MgCl_2$ concentrates close to the stone surfaces and along drying boundaries within the stone.

Under the same environmental test conditions, $CaCl_2$ solutions were unaffected at lower temperatures and only crystallised under extremely high temperatures and fast drying conditions. Although both salts have similar growth forms, homogeneous crystallisation of $CaCl_2$ produced lower DWL values than $MgCl_2$ on average (section 4.1.1.4), with reductions of ~70% in the DWL of $CaCl_2$ Cullalo and Doddington samples and a reduction of ~50% in the DWL of $CaCl_2$ Corsehill samples compared to equivalent $MgCl_2$ samples in the third test. However, $CaCl_2$ did produce greater internal change as identified from repeat hydric tests, owing to the greater internal crystallisation of the salt. There was considerable modification to the capillary coefficient and water absorption of $CaCl_2$ Cullalo and Locharbriggs and $CaCl_2$ Corsehill and

Locharbriggs samples, respectively, over equivalent $MgCl_2$ samples (section 4.2.5.1 and 4.2.5.2).

In the second crystallisation test and under high temperature drying conditions, both salts crystallised rapidly and showed limited solution and ion migration to the stone surface. Under these conditions, $CaCl_2$ was the more destructive salt, producing substantial increases in DWL relative to $MgCl_2$ in Locharbriggs, Corsehill and Doddington and smaller increases in the DWL of Giffnock and Hazeldean in relation to the DWL of equivalent $MgCl_2$ samples (Section 4.1.1.4). This result demonstrates the importance to the decay process of the location of crystallisation relative to the stone surface.

$CaCl_2$ and $MgCl_2$ caused decay to sandstones through the crystallisation of thick sheets that forced grains apart over a relatively large surface area, causing their disaggregation with limited grain fracturing or direct physical damage to minerals (Figure 5-19). At the stone surface this process leads to substantial granular decay in $MgCl_2$ samples, while at depth there would be an anticipated decrease in tensile strength as inter-granular cements are weakened, and secondary cements, in the form of swelling clays, are dispersed. Grains are ultimately forced apart from a combination of crystallisation and clay swelling pressures, leading in some stones to scaling decay. Substantial granular decay was evident throughout Doddington $MgCl_2$ samples in the third crystallisation test. Scaling decay was displayed by Locharbriggs and Corsehill samples from both salts in both tests owing to the accumulation of clays within layers in Locharbriggs, and changing drying kinetics leading to preferential salt crystallisation at specific boundaries in both stones.

7.2.1.1 *Clay swelling from $MgCl_2$ and $CaCl_2$*

The intracrystalline and osmotic swelling of clays by the absorption of Mg^{2+} and Ca^{2+} is also acknowledged, alongside crystallisation pressures, as a potential agent of salt-induced mechanical decay from both $CaCl_2$ and $MgCl_2$. High clay-related pressures could develop within sandstones that contain swelling (smectite) and certain non-swelling clays (illite) through the absorption of Mg^{2+} and Ca^{2+}. Pressures from the swelling of these clays within

the stone would force grains apart, while also lowering the tensile strength of the stone (leaving it increasingly vulnerable to crystallisation damage) by reducing the cementation of grains through their dispersal. The cation exchange capacity (CEC) of the stone is related to the types of clay and their overall proportions within the stone (as well as their spatial distribution) and will control the maximum clay swelling pressures experienced. Stones containing a high proportion of illite and smectite, such as Locharbriggs (Baraka-Lokmane et al., 2009; Pandey et al., 2014), are more vulnerable to this process, and this fact could account for the scaling decay in these samples. However, this process cannot explain the high decay rates experienced by Doddington $MgCl_2$ samples as swelling clays are absent from this stone.

Overall, $MgCl_2$ crystallisation has a lower dependency on precise temperature and RH conditions, while $CaCl_2$ crystallisation is determined by extremely tight environmental constraints. This difference gives $CaCl_2$ a more predictable crystallisation behaviour, while $MgCl_2$ damage varies according to the environmental conditions of the tests. Importantly, the behaviour of neither of the salts was influenced by precise pore structural parameters, with no statistical correlations evident between the pore parameters and DWL of either salt. In addition, the evolution of high clay swelling pressures from the absorption of Mg^{2+} and Ca^{2+} is potentially an important process affecting Locharbriggs sandstone, however further research is required to determine the potential impact this decay mechanism.

Significantly, both $MgCl_2$ and $CaCl_2$ are not expected to crystallise at any point under the annual RH and temperature conditions experienced in Scotland (Appendix F). This fact means that both salts will constantly stay in solution within a building, which will likely significantly lower, if not eliminate, their potential to cause damage through crystallisation, (which is the most likely cause of damage from these salts in each test). Based on the results from salt crystallisation tests, this crystallisation behaviour shows that both salts will likely be relatively harmless to Scottish sandstone buildings. However, further research needs to be undertaken on the complex interactions of salt phase changes within sandstone in relation to the effect of increased $MgCl_2$ and $CaCl_2$ on salt mixtures and their behaviour within

sandstone (Appendix F). A comprehensive study would reveal any latent processes/interactions that might affect the stone in the absence of salt crystallisation.

7.2.2 NaCl

Unlike $CaCl_2$ and $MgCl_2$, NaCl forms distinctive isometric hopper and euhedral cubic crystals (Figure 4-38, Figure 5-12 and Figure 11-12) in every sandstone type. In a free solution, NaCl forms numerous small crystals, with crystallisation tightly controlled by its RH deliquescence value (75%). On reaching this value, NaCl in a free solution will immediately crystallise from several nucleation sites (Figure 7-3), forming many small crystals. The reason for the development of several nucleation sites is related to the number of molecules that are needed to form a critical nucleus. This value is relatively low for NaCl, which allows it to form under low supersaturation levels and therefore produce lots of small crystals. This growth pattern was identified within the pores of Stanton Moor sandstone during ESEM analysis, with the accumulation of waxy-textured halite crystals (Figure 7-4) and the formation of hopper halite aggregates (Figure 7-4 and Figure 11-10A), as was identified by Rodriguez-Navarro and Doehne (1999) using similar ESEM techniques. The continued growth of hopper halite crystals is controlled by heat dissipation throughout the crystal structure, generating a higher relative supersaturation ratio on crystal edges, feeding further crystal growth (Chatterji, 2005). Halite crystals can only continue to grow if a thin film exists on their edges, and this is partly what limits further growth of individual crystals (Figure 7-3A).

The relatively high deliquescence point for NaCl (75%RH) means that its potential for crystallisation damage in maritime temperate climates, such as the UK, is extremely large. Annual RH continually fluctuates across 75% during the year, producing frequent repeat dissolution-crystallisation cycles (Appendix F).

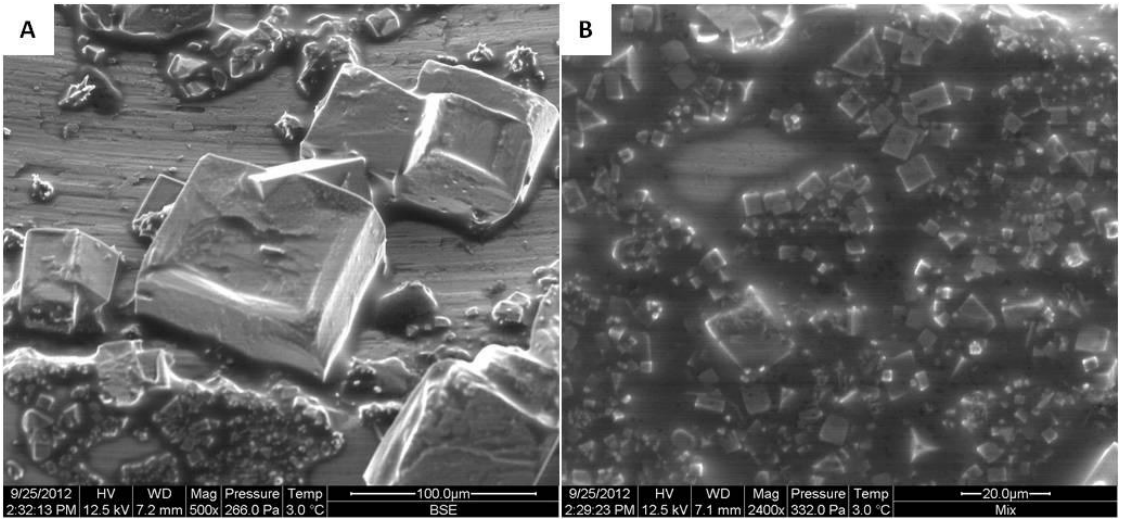

Figure 7-3: ESEM images of NaCl crystallisation in free solutions under stable temperature (3°C) and different RH conditions.

(A): NaCl crystallisation from free solution at 35% RH. (B): Crystallisation of several small NaCl crystals from free solution at ~70% RH.

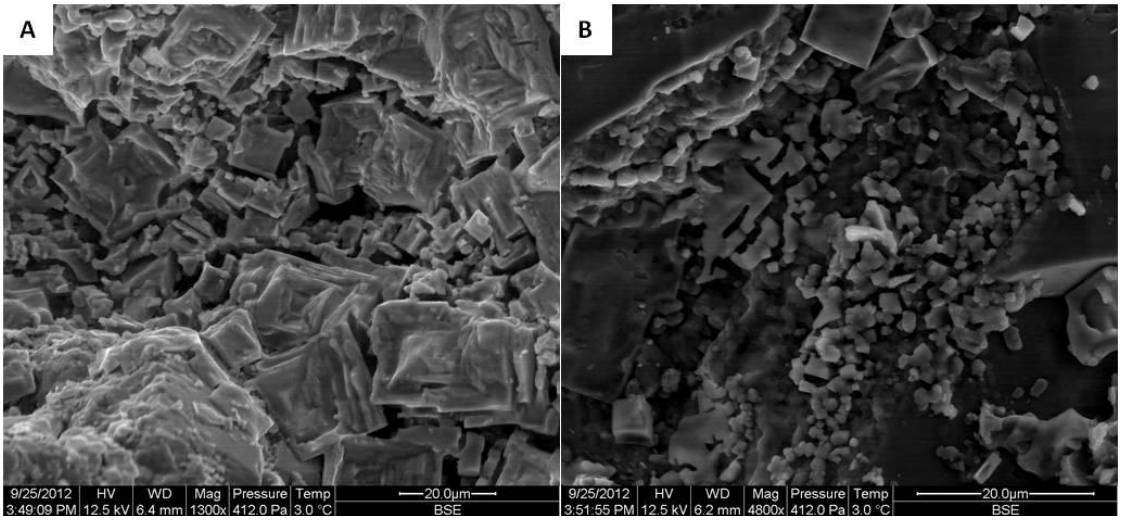

Figure 7-4: ESEM images of NaCl crystallisation in Stanton Moor sandstone under stable temperature (3°C) and different RH conditions.

(A and B): Accumulation of waxy textured isometric and hopper halite crystals at 75% RH.

Damage to sandstones was through the fracturing of individual mineral grains (Figure 4-32 and Figure 4-39) and overgrowths (Figure 5-1, Figure 11-10 and Figure 11-14). Pressures developed initially by the non-equilibrium growth of salts in trapped, isolated regions within the stone. Here the development of high supersaturation ratios could not be relieved by the growth of non-compressed crystals, and high crystallisation pressures were imposed on pore walls. This situation arose quicker in stones that experienced slow-drying regimes, which were generally those that contained tortuous and poorly connected pore networks. Eventually, high net crystallisation pressures evolved throughout the stone by the interconnection of these isolated

crystallisation pressure regions. The spatial concentration of these high pressure regions, such as along bedding planes, would also further increase the risk for mechanical damage by NaCl crystallisation.

An inverse relationship exists between crystallisation pressure and pore size, whereby higher crystallisation pressures develop in the smaller pores. This is due to the greater curvature and surface area of crystals in small pores compared to those in larger ones. The potential for NaCl-induced damage is therefore considerably elevated in those stones containing a greater proportion of micro-pores.

The most common NaCl-generated decay features were granular decay and contour scaling (Figure 5-15). Granular decay was produced, predominantly, by the near-surface crystallisation of salts that overcame the cohesive strength of inter-granular cements. Substantial near-surface crystallisation may also have forced the internal crystallisation of salts by inhibiting drying pathways to the stone surface. The surface crystallisation of halite was particularly prevalent in Cullalo samples (Figure 4-26 and Figure 5-12). As the surface efflorescence dried out, it blocked surface pores and caused internal crystallisation of halite (Figure 5-13) which was evidenced by measurable changes to the internal pore and grain structure as identified from changes to USV values (section 5.1.1.4). The internal crystallisation of NaCl also significantly altered the grain and pore networks of Locharbriggs and Blaxter sandstones in the pilot study (Appendix C). Extensive fracturing of matrix grains likely occurred at the point of contact on the grains between growing halite crystals and at the boundaries of near-by grains when in compression from high crystallisation pressures. Figure 11-13 describes this process, in which considerable volumes of broken lithic fragments and debris were released into the pore networks, significantly altering their water absorption potential and size distribution.

Scaling, and specifically contour scaling, on the other hand developed through the organised failure of connected salt planes within the stone (Figure 4-33). Their development was influenced by the spatial concentration of micro-pores within layers in the stone, specifically in relation to Locharbriggs, and by the dynamic feedback processes between the depth of

moisture penetration and the drying pathways from the stone (Figure 5-7). Stanton Moor was specifically vulnerable to scaling decay processes owing to its slow drying kinetics that prevented salt from crystallising at the stone surface.

$CaCl_2$, $MgCl_2$ and NaCl crystals have distinctive habits under diverse crystallisation conditions. These crystallisation processes control the observed breakdown patterns and DWL across each stone type. The development of high NaCl crystallisation pressures is tightly controlled by the pore network of the stone, including the proportion, absolute volume and spatial distribution of micro-pores. $CaCl_2$ and $MgCl_2$ on the other hand form crystal of similar habits under tightly-constrained environmental conditions, but the development of high crystallisation pressures is not significantly influenced by the precise pore properties of the stone.

7.2.3 Summary of the different behaviours of each salt

In order to recommend suitable de-icing salts to be used around buildings vulnerable to salt-induced decay, several aspects of the salt crystallisation process, as well as individual de-icing salt properties, have to be considered. The most important aspects include: (i) the risk salt poses to mechanical and chemical weathering of stone, (ii) how effective is each salt at melting snow and ice? and (iii) what are the associated costs of implementing each de-icing salt? Table 7-1 summarises the behaviour of each salt in respect to the aforementioned points.

Variable/Risk	NaCl	Confidence	$MgCl_2$ and $CaCl_2$	Confidence
Mechanical Damage	High Risk (GD, F, E_{thin}, E_{thick})	High	Low Risk (won't crystallise under expected RH)	High
Chemical Damage	Moderate to low / unknown	Low	Moderate to low / unknown	Low
De-icing Performance	Relatively slow and ineffective at low temperatures	High	Fast and effective at low temperatures	High
Cost of implementation	Cheap (baseline)	High	Expensive (up-to 3 or 4 times more expensive than NaCl)	High

Table 7-1 : Advantages and disadvantages of using each different de-icing salt. GD: granular decay, F: fracturing of the stone, E_{thin}: thin efflorescence coverage, E_{thick}: thick efflorescence coverage.

7.2.3.1 *Mechanical weathering*

Although all three salts damaged sandstone in the crystallisation tests, NaCl poses a greater risk for mechanical weathering than $MgCl_2$ and $CaCl_2$. This greater risk pertains to the much higher number of potential NaCl dissolution-crystallisation cycles likely to be experienced by stone in Scotland compared to $CaCl_2$ and $MgCl_2$ (ie none).

7.2.3.2 *Chemical weathering*

Mechanical weathering through salt crystallisation and clay expansion cycles are the most important processes affecting the deterioration of sandstones from each de-icing salts. Chemical weathering on the other hand may also present an important, yet possibly more latent process that could affect the durability of sandstone under specific environmental conditions. Warke et al, (2011) present results of a case study on the weathering on internal granite stone work from offshore, automated lighthouses in Ireland. It was discovered that on the automation of these lighthouses there was a significant increase in the reports of accelerated decay affecting their internal stone work.

Case studies of two automated offshore lighthouses reveal complex physical and chemical processes that are thought to contribute to their accelerated decay. Extremely high NaCl concentrations were measured in the outer 10 – 20 mm of the internal granite stone work, with their accumulation attributed to the high salinity sea air and high internal RH conditions on the sealing of the lighthouses when they became automated. The sealing of the lighthouses is thought to have significantly altered the internal micro-environment of the buildings; thus creating conditions that would facilitate the deposition of NaCl on stone surfaces through condensation and deliquescence. Under these extremely high salinity and high alkaline pore water conditions, increased corrosion and dissolution of silicate minerals (quartz, feldspar and mica) is thought to have occurred; significantly weakening the near-surface regions of the stone, leading to the observed granular decay of the granite.

Additionally, work by Vázquez et al, (2013) reveal that under laboratory conditions, sodium sulphate caused an increased in surface roughness of

granite and specifically marble samples by the dissolution of calcite and to a lesser extent, dolomite.

Chemical weathering, although a potentially destructive weathering process in crystalline rock, is not considered to have contributed to the observed breakdown of sandstone samples in salt crystallisation tests undertaken for this thesis. The observed extensive decay of internal granites from Irish lighthouses was shown to be facilitated by minor changes to their internal micro-environmental conditions, while external granite façades were unaffected. This result suggests a system that is dependent on precise environmental conditions of the type that are unlikely to be experienced on an extended time-scale by buildings identified as vulnerable to de-icing salt-induced decay. Furthermore, the highly alkaline pore waters needed for chemical decay are in some cases significantly greater than those measured elsewhere; in laboratory salt weathering simulations on sandstone (Warke et al., 2006; McCabe et al., 2008), sandstone buildings in city centre locations (Smith et al, 2002) and sandstone buildings in rural locations (Warke et al., 2003). The more frequent wetting and drying cycles and potential for regular washing of exterior building surfaces (Warke et al., 2011) will limit such high salt concentrations from occurring in the target buildings of this study.

There was no correlation found between what is deemed as stones more ‘mineralogically vulnerable’ and the observed salt-induced decay in $CaCl_2$ and $MgCl_2$ laboratory tests that would suggest the presence of chemical weathering processes. It is also considered that the time-scales experienced in durability tests would not be conducive to chemical weathering, with any chemical weathering that might have taken place being overprinted by physical decay processes.

7.2.3.3 *Ice melting capacity*

Ice melting capacity tests show that $CaCl_2$ and $MgCl_2$ are more efficient at melting ice than NaCl under low temperature conditions. Both salts melted a greater volume of ice and at a faster rate than NaCl. Furthermore, $CaCl_2$ and $MgCl_2$ can continue to work effectively at much lower temperatures than NaCl, therefore making them more effective de-icing salts.

7.2.3.4 *Cost*

In most economic situations, the cost of materials and procedures will dictate the most viable options. NaCl is currently used as the primary de-icing salt across the globe, due in part, to its low cost and abundance. $CaCl_2$ and $MgCl_2$ on the other hand are currently used as secondary de-icers within the UK, owing to their greater cost, which is in some cases double that of NaCl.

The potential savings from using 'heritage friendly' (ie less mechanically damaging) salts, such as $MgCl_2$ and $CaCl_2$ are reduced stone replacement/maintenance costs which may cover the increased price of using these salts in relation to NaCl. Hyslop et al, (2006) undertook a façade survey and building stone assessment of Glasgow in order to help understand Glasgow's built heritage skills and materials requirements. Although not quoting prices for the required maintenance of decayed stone in Glasgow, substantial Banker mason, Site mason and Carver days are suggested; totalling 1.5 million days and 389,000 tonnes of replacement stone. Any reduction in these values would mean a substantial cost saving. Table 7-2 highlights some potential costs of building stone replacement in Glasgow using the number of surveyed buildings suffering salt-induced decay taken from Hyslop et al, (2006) and an estimate of stone matching analysis work, which is a building management requirement for stone replacement. The number of surveyed buildings (and consequently the number of façades) represents less than 1% of the total population of stone façades in Glasgow. The overall price associated with stone analysis and replacement including masons days and the cost of stone will likely increase the value in Table 7-2 by at least three times. Multiplying this by 100 to take into account every building in Glasgow that might suffer from salt-induced decay gives a value of £8.4 million of repair work required from salt-induced decay (possibly associated with de-icing salts). It is thought that significant overall savings associated with the replacement of salt damaged stone could be made by using less damaging salts such as $MgCl_2$ and $CaCl_2$ based on this estimated monetary value.

Number of surveyed buildings showing salt damage	Overall cost of stone matching analysis
56	£28,000

Table 7-2: Cost of stone matching analysis for 240 surveyed buildings in Glasgow. Number of surveyed buildings is based on the number used in Hyslop et al, (2006) and the overall cost of the stone matching analysis is based on 1 stone analysis per building at £500/analysis.

7.3 Stone durability assessment toolkit

Standardisation is important to ensure a recognised high quality of workmanship and product specification. For example, it maintains high operational standards for quarry stone extraction, material characterisation and repair work. Academic research on the other hand has a level of freedom from industry protocols. This liberty allows the continued development of ideas, knowledge and understanding in the scientific field; bringing additional recommendations towards the standardisation of testing procedures for industry applications.

Furthermore, testing standards must allow the accommodation of a wide range of natural materials in their protocol, with certain tests tailored to specific stone types. The heterogeneity of natural stone, such as the huge differences between the pore structures of sandstone, limestone, granite and basalt for example, may not be suitably accommodated by one single testing method. Fine adjustments towards tailoring tests for specific stone types may be an important recommendation that reduces errors associated with the testing of different lithologies.

It is the aim of this section to critically evaluate the methodologies and techniques used within this thesis. This section also recommends the best practice for future stone durability research and materials testing by presenting those stone properties and their associated tests that are (i) essential, (ii) useful and (iii) not useful for stone durability assessment of salt-induced decay.

The efficient and accurate estimation of stone durability is of great practical importance in understanding how a stone will perform within a building when subjected to specific weathering agents. Specifically, this performance relates to the length of time that a stone can preserve its original

mineralogical composition, physical and mechanical properties, shape and aesthetic appearance (Přikryl, 2013).

The basic factors influencing stone durability include stone specific properties such rock fabric, mineralogical and chemical composition. External factors include environment and climatic conditions, their fluctuation and rate of change, the presence of water and other weathering agents (including salt) and its interaction with other materials (mortar, surrounding stone). Additional factors including the quarrying and finishing processes may also impart structural weaknesses into the stone that influence its durability.

Durability is regularly assessed by performing accelerated laboratory weathering tests, which when combined with quantitative data on the hydric properties of stone can produce durability estimators. Importantly, these durability values are not ‘fixed’ properties and will change over time at a rate proportional to the changing properties of the stone, owing to the complex internal weathering interactions and feedback processes. This toolkit is tailored to understanding the durability of sandstone to salt-induced decay using known quantitative properties of sandstone and its response to accelerated stone durability tests.

7.3.1 Essential properties and tests

The properties that are essential for differentiating between these sandstones that are the most and least vulnerable to salt-induced decay are related to their hydraulic and pore properties. These are the properties that influence the overall absorption of salt in solution into the stone and are the measureable physical properties that control the maximum pressures a stone can experience from growing salt crystals.

7.3.1.1 *Pore size distribution*

Pore size distribution (PSD), as measured by Hg intrusion porosimetry (MIP), was found to be an essential property in indentifying those stones that are most vulnerable to salt-induced decay from NaCl crystallisation. PSD data were used successfully to calculate theoretical crystallisation pressures and predict NaCl crystallisation damage via salt susceptibility index (SSI) values

and specific micropore ranges. Salt crystallisation pressures are related to measurable pore dimensions according to an adaptation of the Everett equation (Equation 1-4). MIP was found to be an important and efficient means of measuring a wide range of pore sizes; covering the range of 900μm to <3.5nm. Although other techniques are capable of measuring pore sizes, such as digital image analysis of SEM images and μCT Scanning, MIP is generally the most efficient in terms of cost, data acquisition and data analysis. MIP can additionally measure stone porosity (in pores < 900μm), density and tortuosity. The latter is an important property that influences stone durability as it relates to the specific surface area of grains (important for ion diffusion and nucleation sites) and influences the drying kinetics of the stone.

Alternative techniques such as SEM and μCT analysis may require similar sized samples and are likely more expensive to conduct, but they can also reveal other important information of the stone that is useful for understanding its durability. μCT analysis can reveal important spatial information relating to PSD data, as well as providing a useful method for quantifying changes to the stone from durability tests (Derluyn et al, 2014). μCT scanning does require additional equipment and skilled knowledge on data analysis software. Cnudde et al, (2009) discuss the differences between μCT Scanning and MIP for characterising the microstructure of building materials. They conclude that both techniques are difficult to compare owing to their different approach and physical basis, with μCT scanning providing greater information on pore sizes >10 - 60μm and MIP on pores smaller than this (shown here to be of most importance for salt crystallisation). Both sets of results can over- and under-estimate porosity in different ranges, but when combined can reveal additional valuable data.

An important drawback of MIP analysis originates from the premise that the technique does not accurately measure the true PSD due to the “ink-bottle” effect. Rather, the accurate representation of MIP data is through the measurement of pore openings. This fact can lead to erroneous measurements that may overestimate both the volume and size of the smaller pores. Regardless of these constraints, PSD data provided important

information that helped to explain salt crystallisation damage within the samples.

A major drawback of µCT scanning analysis relates to accessibility of high performance computers for data analysis. With the addition of a high performance, expensive computer and suitable high-end software, µCT scanning is an extremely powerful technique. However, regardless of this additional equipment, data analysis and interrogation is still significantly influenced by user inputs which can place further uncertainties on data accuracy.

7.3.1.2 *Water absorption*

Hydric properties that were measured in this thesis include the capillary absorption coefficient, water absorption, saturation coefficient and drying/evaporation properties. The capillary absorption coefficient and water absorption measurements followed the British standard testing protocols, while the saturation coefficient followed the established Hirschwalds' coefficient procedure. The design of the drying/evaporation test was based on similar tests used elsewhere (Colas and Mertz, 2012; Cnudde et al., 2013).

Water absorption under atmospheric pressure following BS EN13755:2008 was an especially important hydric property. It relates to the maximum amount of water that can be absorbed into the stone under non-forced conditions, and is an estimation of the available salt 'reservoir' within the stone. This parameter directly determines the amount of salt that can crystallise and ice that can form within the stone. As discussed earlier, the PSD and more importantly the proportion of micro-pores directly determines the maximum crystallisation pressures experienced by the stone. A stone characterised by a high proportion of connected micro-pores will experienced high NaCl crystallisation pressures, while this is not always true for stones characterised by a high water absorption coefficient. The water absorption value cannot determine the susceptibility of sandstone to salt-induced decay by itself, but when combined with PSD data, can help to explain the influence of potential crystallisation pressures within the stone as it represents the potential stress field in the stone. The water absorption coefficient is therefore a direct

measurement of the proportion of total porosity and an indication of the proportion of the micro-pores that can be filled under atmospheric pressure. PSD itself may provide overestimate the vulnerability of stone to high crystallisation pressures since it is unlikely that the full PSD range will ever be completely saturated.

The incorporation of the water absorption coefficient with SSI and the percentage of pores <5µm in diameter (%P_{m5}) provided stronger correlations with the dry weight loss of samples in the third crystallisation test. PSD data underestimated the vulnerability of Corsehill and Locharbriggs to salt-crystallisation damage, while it overestimated the vulnerability of Stanton Moor. High water absorption values for Corsehill and Locharbriggs, and the low water absorption value of Stanton Moor helped to explain their relative vulnerability to salt crystallisation. However, the high vulnerability of Stanton Moor to NaCl salt crystallisation indicates that the SSI, which is based on MIP data of porosity <5µm and 0.1µm radius, has the greater influence on stone durability.

7.3.1.3 *Drying tests*

The drying process influences the location of salt crystallisation within the stone, which can considerably impact on its durability. The drying test supplied information relating to the drying efficiency of the samples and provided insights into the distribution of salt crystals and changing stone behaviour throughout the crystallisation tests. Efficiently drying stones allow the majority of salt ions to migrate to the stone surface, where they grow as ‘harmless’ efflorescence. Conversely, slow drying stones trap salt internally where they grow as subflorescence, increasing the potential for high crystallisation pressures to develop. In similarity to the effects of the water absorption on crystallisation potential, the drying tests will reveal how much of this salt reservoir can efficiently migrate and crystallise on the stone surface. Drying tests conducted in this thesis were based on similar tests elsewhere (Cnudde et al., 2013) as there are no British Standard procedures for this test. The drying test provided four separate results associated to drying behaviour; namely, the constant drying rate, the falling drying rate, the critical moisture content (CMC) and the remaining moisture. The constant

and falling drying rates provide the actual rates of moisture loss while the CMC and remaining moisture contents indicate the moisture/salt reservoir remaining in the stone at different periods.

In combination, these values reveal two distinct groups of sandstone; those that are characterised by fast, efficient drying (likely durable to salt crystallisation) and those that are slow drying (likely vulnerable to salt crystallisation). The high drying efficiency of Hazeldean, Cullalo and Doddington help to explain their resistance to salt crystallisation, while the slow drying of Stanton Moor and Corsehill influences their vulnerability. The results from drying tests require careful user analysis and additional information relating to their pore structure (PSD, its spatial distribution and stone strength) in order to accurately interpret the results and how it might influence stone durability. Additionally, these results provided important information relating to feedback processes experienced by Cullalo, Stanton Moor and Doddington sandstones.

7.3.2 Useful properties and tests

The useful properties are those that provide important additional information on the stone that can help to explain the importance of the essential properties influencing salt crystallisation durability, but by themselves cannot predict stone durability.

7.3.2.1 *Strength*

A stone's strength limits the damage sustained from salt crystallisation, and so is a vital property to understand in order to predict durability. Strength is influenced by: the grain properties; porosity; PSD; and the water content among others. Only compressive strength was measured in the present study due to the unavailability of other testing equipment. It has been proposed that tensile strength controls stone durability (Cardell et al., 2003). Therefore, in order to translate durability estimations, compression strength values must be converted to tensile strengths. Flexural strength has been used previously as an indirect measurement of tensile strength (Benavente et al., 2004). It is recommended that tensile strength or flexural strength

measurements are made, with repeat measurements of both dry and capillary saturated samples undertaken.

7.3.2.2 *Porosity*

Porosity was measured by means of: (i) He porosimetry on 25 mm diameter cores; (ii) Hg porosimetry on 10 mm diameter fragments; (iii) buoyancy weighing following BS EN1936:2006 on 40 mm, 50 mm and 60 mm sandstone cubes; (iv) digital image analysis (DIA) of thin sections studied by SEM. Each technique is constrained by its resolution. DIA by SEM over-estimated the porosity of Corsehill and Locharbriggs sandstones, while Hg porosimetry calculations under-estimated the porosity in Cullalo and Bonhill. He porosimetry was expected to yield the highest porosity values due to the negligible restriction of He flow throughout the pore network, while on the other hand, DIA analysis is significantly influenced by user error when selecting suitable porosity thresholds in SEM images of thin sections. DIA is traditionally made using blue stained covered thin sections; however, problems were encountered during their preparation and therefore DIA was undertaken by SEM instead. Thin section analysis provides a 2D representation of porosity and grain size. It is suggested here that other techniques are more suited for accurate porosity measurements. Apparent porosity measurements from buoyancy weighing are reproducible between different sized samples and are obtainable using common, low cost laboratory equipment. Alternatively, DIA analysis of blue-stained thin sections and Hg porosimetry of rock fragments are recommended as useful techniques as they require a low quantity of material. Interestingly, every sandstone type fell into a similar relative order of porosity, even when comparing extreme values and outliers for each one. This result shows that the spread of the data was relative and comparatively consistent for each stone across each method used to determine porosity.

7.3.2.3 *Capillarity*

Capillary coefficient is an important hydric property. It is probably the primary mechanism of solution absorption into building façades and was used as the immersive process in the second and third crystallisation tests.

Furthermore, it was found that increased DWL and maximum weight gain (MWG) values for Stanton Moor 2 samples in the third test were the result of increased capillary uptake of NaCl. It is recommended that a similar capillary coefficient procedure as was used by Tomašić et al., (2011) is followed, as it allows a static water height to be maintained throughout the full testing period (Figure 7-5)

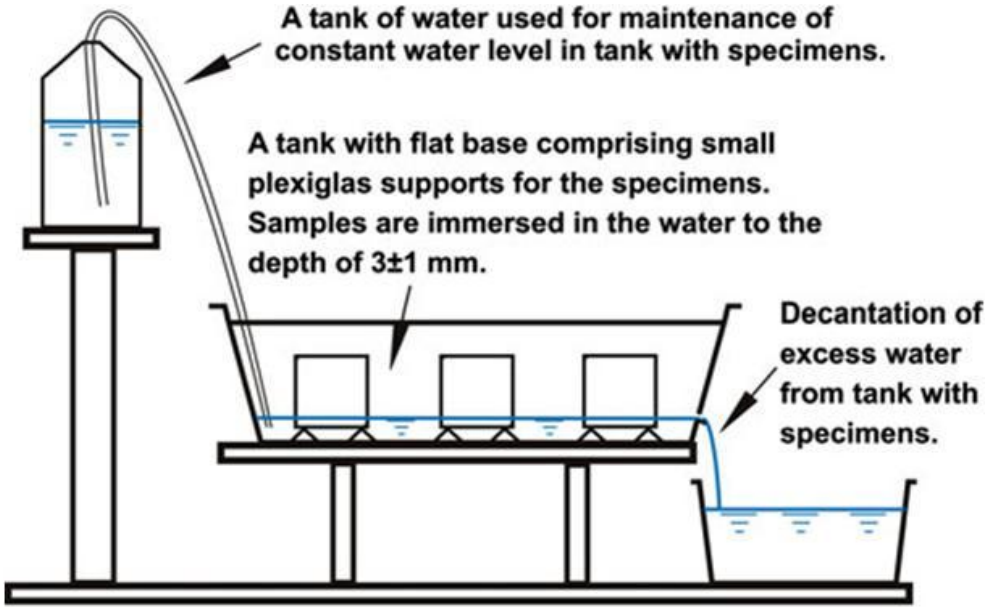

Figure 7-5: Capillary uptake coefficient procedure used by Tomašić et al., (2011).

7.3.3 Not useful properties and tests

These are the stone properties and associated tests that were not deemed to be useful for explaining salt crystallisation damage. Most of these tests relate to those that were undertaken in order to recognise and quantify changes to the stone from salt crystallisation.

7.3.3.1 *Grain properties*

There are relationships between pore size distribution (PSD) and: mineralogy, grain size and grain shape. PSD significantly influences the development of high crystallisation pressures within stone. Grain properties are therefore important, and should be analysed during stone durability testing. Grain properties have been traditionally characterised by point counting thin sections using plane polarised microscopy and SEM. Grain properties in this

thesis were analysed using SEM images from polished thin sections. Ten images were combined using Adobe Illustrator to make a collage that was subsequently analysed using imageJ. The acquisition of images was extremely rapid, with the subsequent segmentation of grains from pores being easily undertaken from greyscale BSE images, however, watershed segmentation of overlapping grains and the successive removal of erroneous grain boundaries and clay fractions were difficult, time-consuming and prone to human error. Nonetheless, the greater depth of analysis that is possible through digital image processing proves this to be an important technique for grain property identification.

SEM is a quick and accurate method of analysing pore and grain structure, providing high resolution information on grain contacts, clay distribution and internal, mineralogical weathering features. Digital image analysis (DIA) of thin sections by SEM can also be used to semi-quantitatively measure the mineralogy of stone through EDX mapping and greyscale segmentation in software such as imageJ.

Mineralogy was quantified by SEM and light microscope point counting of thin sections. X-ray diffraction (XRD) and X-ray fluorescence (XRF) have been shown elsewhere (Baraka-Lokmane et al., 2009) to be useful methods for quantifying the mineralogy of sandstone, specifically in relation to identifying its main constituents and accessory minerals. Initial XRD analysis of powdered sandstone samples was insensitive in identifying trace minerals or other constituent minerals due to the high quartz contents in most samples.

The clay fractions within sandstones were identified by analysing clay mineral textures and chemical compositions by means of plane polarised microscopy and SEM EDX analysis. SEM is a useful tool for analysing clay microtextures, mineralogy and distribution within a stone, while XRD analysis can provide quantitative analysis of clay volumes. Both techniques are valuable for understanding the overall clay content and its distribution, influence ion exchange processes, permeability and weathering behaviour of these minerals within sandstone.

DIA of polished thin sections by SEM, combined with quantitative XRD/XRF analysis of the stone mineralogy and clay fractions can provide additional in-depth understanding of the stone grain structure, however by themselves cannot accurately predict stone durability to salt crystallisation.

7.3.3.2 *Colour measurements*

Colour measurements were used to quantify any changes to the surface colour of samples after crystallisation tests. Results from the pilot study show that $CaCl_2$ caused a slight darkening of most samples while the chloride blend salt caused a distinct 'greening' of sample surfaces. There were no further correlations found in the remaining two crystallisation tests. Furthermore, it was not possible to quantify the differences in surface colour, as a surrogate for albedo, on the effect of the radiative drying regime on the third crystallisation test. Stone colour has been shown to alter the surface temperature of grains (Appendix G), which in turn could influence the temperature gradient through the stone and the drying regime experienced by it; the latter of which has been identified as an important process governing salt crystallisation damage. Quantifying the subtle colour parameters does not help to explain stone durability to salt crystallisation damage.

7.3.3.3 *Laser scanning*

Laser scanning allowed the quantification of change to the surface topography of samples as caused by salt crystallisation. Using the average surface area of sample faces and the average grain size, the average total loss of grains, the total loss of grains per mm^2/cycle could be calculated. Laser scanning managed to identify the main decay textures associated with each stone/salt type; however these were values that could be visually identified, while the loss of material was quantified by repeat weighing of samples. Laser scanning was not found to be a useful tool for predicting stone durability; however, it is important as a non-destructive technique for measuring stone decay in-situ.

7.3.3.4 *Ultrasonic velocity (USV) testing*

In common with laser scanning analysis, USV testing was primarily used to identify bulk changes to the grain structure from salt crystallisation. It successfully identified changes to the grain structure of Cullalo sandstone that were not visually evident or recognised from weight changes. USV provides information relating to the grain and pore structure of the stone, correlating to the compaction of grains within the stone. As previously discussed, the grain structure, although influencing important pore network and hydric properties of the stone does not solely explain or account for the behaviour of the stone to salt crystallisation.

7.3.4 Summary

The stone durability assessment toolkit is based on the results from salt crystallisation durability tests (4). Using quantitative data, I demonstrate that by using a combination of the three essential stone parameters/tests (PSD, water absorption and drying behaviour) it is possible to understand and predict the behaviour of each sandstone to NaCl crystallisation.

MIP provided important data on the distribution of pore sizes within each sandstone type. It was also used to estimate theoretical NaCl crystallisation pressures for each sandstone. Theoretical crystallisation pressures were calculated using an adaptation of the Wellman and Wilson equation (Equation 6-1) as defined by Rossi-Manaresi and Tucci (1991) (Equation 6-2 and Equation 6-3). By combining equations 7-2 and 7-3 and using defined pore classes (in diameter) of (1) >50μm; (2) 25-50μm; (3) 5-25μm; (4) 2.5-5μm; (5) 1-2.5μm; (6) 0.5-1μm; (7) 0.05-0.5μm; (8) 0.005-0.05μm; (9) <0.005μm, the overall crystallisation pressures expected to be experienced by each sandstone are calculated. These calculations show that Corsehill, fine-grained Locharbriggs and Stanton Moor are expected to experience crystallisation pressures exceeding their known compressive and estimated tensile strengths. On the other hand, Clashach, Hazeldean, Cullalo and Doddington should experience crystallisation pressure considerably lower than their compressive strength values (Table 6-1 and below).

The same PSD data were then used in the SSI equation (Equation 6-4), as described by Yu and Oguchi (2010), to predict the durability of stone to salt crystallisation. It uses only two specific pore size classes (0.1µm and 5µm radius) and the connected porosity as these are thought to represent the pores that experience the greatest crystallisation pressures, the active stress field throughout the stone and those that influence the overall tensile strength of the stone, respectively. The SSI classifies: (i) Stanton Moor, fine-grained Locharbriggs, Giffnock and Blaxter as 'salt prone'; (ii) Scotch Buff and Corsehill are 'salt resistant'; (iii) Clashach, Cullalo and Hazeldean as 'exceptionally salt resistant'.

In both sets of equations, fine-grained Locharbriggs and Stanton Moor sandstones are identified as being vulnerable to salt crystallisation, while Clashach, Cullalo and Hazeldean are always calculated as resistant stones. Moderate to high correlation coefficients are calculated between the SSI and the percentage of porosity that is lower than 5µm in radius (% P_{m5}) with the MWG of the chloride blend salt in the pilot study. High correlations are evident between the MWG and DWL of NaCl samples in the third test and the SSI and microporosity <5µm in radius.

The addition of water absorption values into SSI calculations (multiplying water absorption and SSI) increased the relative SSI value for Locharbriggs and Corsehill, and lowered it for Stanton Moor (Table 7-3). The incorporation of water absorption values makes sense as this parameter relates to the available 'salt reservoir' within the stone. Yu and Oguchi (2010) attempted to address this parameter using the connected porosity and 5µm radius pore class for each stone. It is thought that these values relate to the active stress field within the stone that would be affected by crystallisation as this pore class is thought to control the capillary uptake of salts. Water absorption values, as a direct measurement of the salt reservoir in the stone, improve the SSI by incorporating the amount of salt and moisture directly entering into the stone. The corrected SSI value therefore describes: (i) the amount of potentially damaging micro-pores within the stone that are responsible for the development of high crystallisation pressures; (ii) the active stress field within the stone; and (iii) the salt reservoir within the stone, which directly describes how much salt and moisture can enter the stone and so influence

its mechanical properties. MIP analysis calculates the PSD by forcing mercury into the pores and therefore does not necessarily acknowledge how much of this pore space will be accessed by water under non-forced conditions. The water absorption value therefore provides a direct indication of how much moisture/salt is absorbed by the stone. High water absorption values will increase the potential of a stone to salt-induced decay by increasing the amount of salt entering into the stone and by reducing the strength of the stone (and therefore the resistance to damage) (Rossana and Paola, 2012).

The high water absorption of Locharbriggs and Corsehill (Table 7-3) would allow more salt to enter the stone than equivalent blocks of Stanton Moor and therefore a greater proportion of the microporosity is likely to be accessed, while increased pore blocking of these higher values of salt would force increased internal crystallisation. Additionally, the greater volume of water in Locharbriggs and Corsehill sandstones would lower their compressive and tensile strengths and therefore lower their resistance to crystallisation pressures, allowing lower crystallisation pressures, under partially wet conditions to cause increased damage. The corrected SSI and % P_{m5} values increased their correlation coefficient with the DWL of NaCl samples in the third crystallisation test, indicating a relationship between the volume of absorbed moisture/salt and the accessibility of micro-pores and/or the strength of the stone.

Drying test results reveal that Stanton Moor and Corsehill are exceptionally slow drying stones characterised by low constant drying rates, low falling drying rates, high critical moisture contents and high remaining moisture contents (Table 7-3). These results provide additional evidence to support the assertion that substantial internal crystallisation is expected to occur in these stones. Fast drying rates and low moisture contents for Hazeldean, Cullalo and Doddington (Table 7-3) indicate that with a low proportion of micro-pores, the pore networks of these stones are well connected and allow the migration of salt to the stone surface where they will crystallise, as indicated by high efflorescence coverage in these samples. The combination of PSD and drying data would also suggest that even in the situation where pore blocking might lead to subflorescence in these samples, a lack of micro-pores should limit the extent of damage experienced by the stone. After 50

NaCl crystallisation cycles, both Doddington and Cullalo sandstones showed low significant aesthetic surface change.

Table 7-3 provides a summary of the PSD, water absorption and drying data as well as the NaCl MWG and DWL values from the second and third crystallisation tests. These data can accurately determine and predict the behaviour of different sandstones to NaCl crystallisation damage: stones characterised by a low proportion of micro-pores and high drying rates are resistant to salt crystallisation, whereas those containing a high proportion of micro-pores and having generally slow drying rates suffer higher rates of decay. Complimentary tests and analysis techniques such as µCT scanning, capillarity, drying, porosity and strength tests can reveal the subtle differences in the stone's behaviour.

Stone	Pore Size Distribution % - Diameter (μm)								
	<0.01	0.01 – 0.1	0.1 – 1	1-2	2-5	5-10	10-50	50-100	>100
Stanton Moor	0.0	1.8	26.2	13.1	20.8	28.0	4.8	1.1	4.2
Locharbriggs	0.0	6.6	8.7	5.0	7.0	17.9	50.7	0.7	3.4
Corsehill	0.8	2.3	5.0	3.5	5.2	15.6	63.2	1.2	3.2
Doddington	0.0	0.0	4.0	2.6	3.8	4.9	72.2	6.8	5.7
Cullalo	0.0	0.2	2.5	1.2	1.6	5.8	77.1	3.9	7.6

Stone	Constant Drying Rate ($g/m^2/hr$)	Falling Drying Rate ($g/m^2/hr$)	Critical Moisture Content (%)	Remaining Moisture (%)
Stanton Moor	311	34	57	18
Locharbriggs	333	45	31	10
Corsehill	275	43	40	15
Doddington	318	34	25	4
Cullalo	336	60	62	12

Stone	Water Absorption (%)	SSI	Corrected SSI	Theoretical Crystallisation Pressures (MPa)	Test2: NaCl MWG (%)	Test2: NaCl DWL (%)	Test3: NaCl MWG (%)	Test3: NaCl DWL (%)
Stanton Moor	4.64	6.0	29.1	79	2.45	0.19	6.15	3.85
Locharbriggs	9.99	4.0	40.4	143	2.50	0.20	6.59	3.66
Corsehill	10.18	2.5	25.2	216	4.17	0.00	11.15	3.25
Doddington	6.62	1.0	6.9	8.0	2.26	0.00	5.21	0.63
Cullalo	5.87	0.6	3.4	5.0	1.66	0.00	4.28	0.38

Table 7-3: Pore size distribution, drying and water absorption data, calculated SSI and corrected SSI values and MWG and DWL values for crystallisation tests 2 and 3. Representative sandstones shown.

7.4 Complex stone-salt interactions

The behaviour of salt within sandstone is an extremely complex process that is influenced by a plethora of processes and parameters that ultimately dictate the total damage sustained by the stone and the morphology of the decay process. It is possible to mitigate the damaging effects of salt crystallisation by carefully understanding the complex interactions that take place within the stone. Understanding the influence of these stone-salt interactions on stone durability is essential for differentiating between those stones vulnerable and resistant to salt-induced decay as this can help us to better manage buildings that are at risk to de-icing salt related decay. In particular, this knowledge will help to inform practitioners to the most appropriate replacement sandstone for building 'at-risk' and to those agencies, such as the BRE to efficiently and accurately identify the durability of sandstone to specific environmental conditions.

As discussed previously (Section 7.1 and 7.3), the performance of stone in response to weathering processes such as frost and salt can be determined through accelerated durability testing procedures. The behaviour of stone relative to different natural weathering phenomena is a complex process that will fluctuate according to the changing environmental conditions and stone properties; primarily the pore and grain network properties. This fact ensures an inherent difficultly in assessing the continued durability of stone over the lifetime of a building.

The durability performance of specific sandstones in response to mechanical weathering from different de-icing salts was analysed by placing each one through repeat salt crystallisation tests. The stone properties were analysed using a suite of complimentary techniques that provided information relating to the pore network, the stone's physical properties and the movement of moisture through the stone. The behaviour of each stone in repeat crystallisation tests is explained by complex interactions between: (i) the crystallisation behaviour of the different de-icing salts, which was in turn influenced by external environmental conditions experienced by the stone, including the drying regime (radiative/convective heating), drying rate and ambient RH, and (ii) the stone properties, which include the porosity, grain

structure and PSD, which together control the capillary uptake, water absorption and saturation coefficients, drying and moisture transportation regimes and the surface conditions/roughness of the stone blocks. Together these properties provide a multifaceted system of complex interactions between the different de-icing salts and sandstones.

In-spite of these complexities, it is possible using select measurable properties of the stones to determine two main groups of sandstone types, differentiated by their pore size distribution and main pore network properties, that are either vulnerable or resistant to NaCl-crystallisation damage. The intricate differences in the behaviour of each sandstone to different de-icing salts are also possible to study by augmenting these measured properties with complimentary information on observed salt crystallisation behaviour, salt efflorescence and subflorescence distribution, drying behaviour and the spatial distribution of pore sizes.

The impact of different de-icing salts on the range of sandstones can be initially differentiated by their crystallisation behaviour. NaCl forms individual isometric hopper crystals over a wide range of RH and temperature conditions, with their growth influenced by measurable pore properties of the stone. By contrast $MgCl_2$ and $CaCl_2$ have a similar crystallisation behaviour, forming as large crystalline sheets, that is tightly controlled by precise temperature and RH conditions, with less influence from the pore network properties of the stone.

7.4.1 $MgCl_2$ and $CaCl_2$

$MgCl_2$ and $CaCl_2$ produced similar values of MWG and DWL loss across equivalent sandstones in the second and third crystallisation tests. Both salts show similar crystallisation behaviours under precise RH and temperature conditions, forming thin crystalline sheets that coat grains. In Scotland, these precise conditions required for crystallisation are not expected to be met and therefore both salts will constantly stay in solution. However, under laboratory conditions in salt crystallisation tests, $MgCl_2$ was found to have a lower dependency on these precise temperature RH conditions, creating a

more complex system than for $CaCl_2$ which had a more predictable crystallisation behaviour.

7.4.1.1 *$MgCl_2$*

$MgCl_2$ produced significant efflorescence accumulations across every sample bar Stanton Moor, but especially in Cullalo and Locharbriggs samples in the second and third crystallisation tests. By contrast Locharbriggs, Corsehill and specifically Doddington samples experienced granular and scaling decay in the third test. Scaling decay through the loss of large sections of stone produced catastrophic decay in select Doddington and Locharbriggs samples in the third test, with continued granular decay seriously compromising the structural and aesthetic integrity of the remaining Doddington samples in the third test.

$MgCl_2$ crystallised under low RH (40 – 60%) and moderate to relatively low temperatures (20°C - 60°C) forming large continuous salt sheets/crusts in free solutions and forming thin efflorescence crusts in sandstone. $MgCl_2$ is thought to have crystallised in the stone by coating grains and infilling the open porosity. By completely coating grains and spreading the crystallisation pressure over a large area, $MgCl_2$ would have caused granular decay through the disaggregation and detachment of individual grains from quartz overgrowths without the prior intra-granular fracturing of grains. Under the less intense radiative heating regime in the third test, $MgCl_2$ successfully crystallised as efflorescence in every sandstone bar Stanton Moor, signifying the transportation of salt ions and their subsequent crystallisation on the surface. Over time, and in conjunction with continued efflorescence growth, salts would have concentrated close to the open stone surfaces, eventually causing granular decay on the stone corners and edges (owing to the lower cohesive strength of grains here). Salt also crystallised on the covered side faces of each sample, causing substantial granular decay in Doddington samples. As the side faces were not completely sealed, small air pockets existed between the high relief grains and allowed salt to crystallise.

The near-surface crystallisation of $MgCl_2$ during the radiative drying regime would have blocked these pores, forcing the drying boundary to recede into

the stone interior. Salt crystallisation would continue at this newly established drying boundary and overtime lead to the formation of a fracture chain (Figure 5-21). Scaling decay was a prominent decay feature identified in several Locharbriggs, Doddington and Corsehill samples. It is concluded that the granular and scaling decay recorded in Doddington and Corsehill samples was produced solely by the mechanical process of salt crystallisation, while it is thought that a combination of salt crystallisation and clay swelling of illite and smectite could have caused the decay in Locharbriggs sandstone. Figure 7-7 describes the joint clay swelling-salt crystallisation process that took place in Locharbriggs.

The process of $MgCl_2$ crystallisation was the same across every sandstone type used in the study, with the intensity of stone decay influenced by external environmental conditions and specific stone behaviours. The extent of $MgCl_2$ damage varied according to the environmental conditions experienced by the stone, whereby relatively low temperatures and moderate RH's enabled the slow migration of salt ions to the stone surface, influencing the location of efflorescence and internal salt crystallisation. On the other hand, a combination of stone strength, drying efficiency and clay content (and its spatial distribution) is thought to have influenced the vulnerability of specific stones to $MgCl_2$ – induced decay. A qualitative assessment of the durability of sandstone to $MgCl_2$ crystallisation is in Figure 7-6 which highlights the durability relationship between temperature and RH, stone strength and clay content.

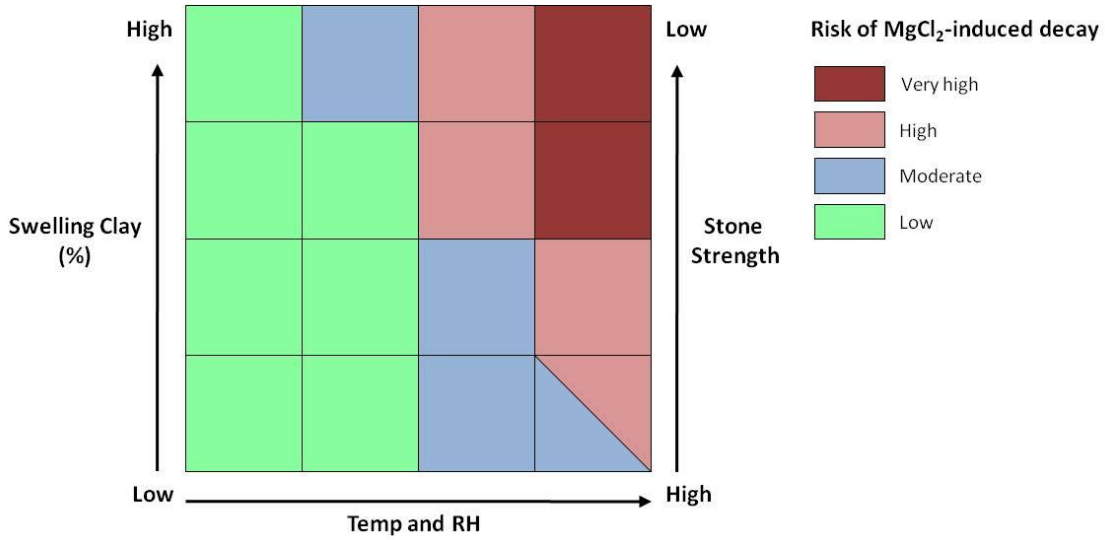

Figure 7-6: $MgCl_2$ crystallisation damage risk matrix.

Four distinct salt-stone interaction processes were identified in the third crystallisation test and are summarised in the following models.

7.4.1.1.1 Doddington

Figure 5-21 describes the salt crystallisation process that was prevalent in Doddington samples. Initially drying took place through every face of the stone, with the greatest rates occurring through the front and rear faces of the stone. As salt concentrations increased within the stone, surface efflorescence and near-surface crystallisation blocked the near-surface pores, forcing the drying boundary to recede into the stone, while near-surface crystallisation caused granular decay focussed on corners and edges of the stone. The internal crystallisation of salt weakened the stone through the disaggregation of grains and cements and caused the fracturing of the stone across fracture planes located at the internal drying boundary.

7.4.1.1.2 Locharbriggs

A similar process to that experienced by Doddington sandstone took place within Locharbriggs samples. The near-surface crystallisation of $MgCl_2$ produced granular decay, while forcing the drying boundary into the stone. It is thought that this drying boundary would have relocated to the low permeability/low porosity layers within Locharbriggs. The accumulation of swelling clays, such as smectite and illite, in these layers would have increased the stresses acting against the grains, causing the scaling decay that was evident in some of the samples. This process is described in Figure 7-7.

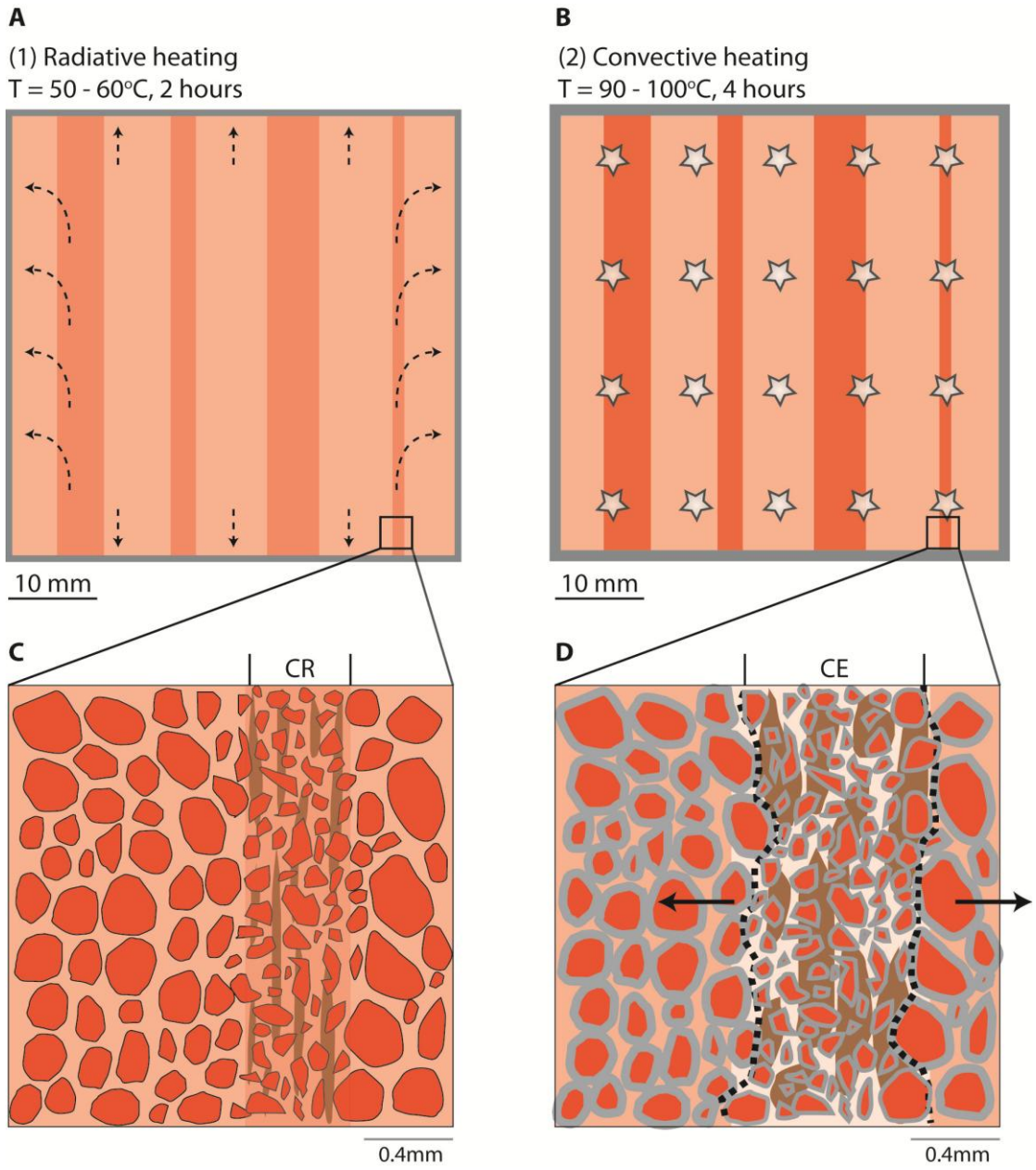

Figure 7-7: $MgCl_2$ crystallisation damage and clay expansion within Locharbriggs sandstone.
A: Radiative heating period whereby salt migrates towards the stone surface. Efflorescence starts to form a thin coverage. B: Convective heating period whereby salt starts to crystallise homogeneously throughout the stone and along beds of relatively high clay content and lower permeability. C: High magnification of the grain structure within a bedding plane highlighting the concentration of clays here. D: After repeated cycles of crystallisation, clay expansion combined with increased crystallisation within these beds causes fracturing and scaling to develop. $MgCl_2$ crystallises by coating grains and infilling pore spaces as highlighted in D. CR: clay rich, CE: clay expansion.

7.4.1.1.3 Cullalo

Cullalo experienced the greatest surface efflorescence in the second and third crystallisation tests. Early efflorescence formation was located across the front drying face of the sample as a thin ‘bubbled’ crust. In later cycles, thick efflorescence accumulations were located primarily on the rear faces of

samples. The growth of thick efflorescence within Cullalo sandstone is explained by the efficient drying kinetics that permitted the prolonged capillary flow of moisture to the stone surface. Early efflorescence formation must have been permeable, allowing this continued surface growth. As the efflorescence dried out and became impermeable, pore blocking would have resulted in the retreat of the drying boundary and instigated subflorescence. The high tensile and compressive strength of Cullalo sandstone resisted internal crystallisation pressures, preventing substantial decay. Figure 7-8 highlights this process.

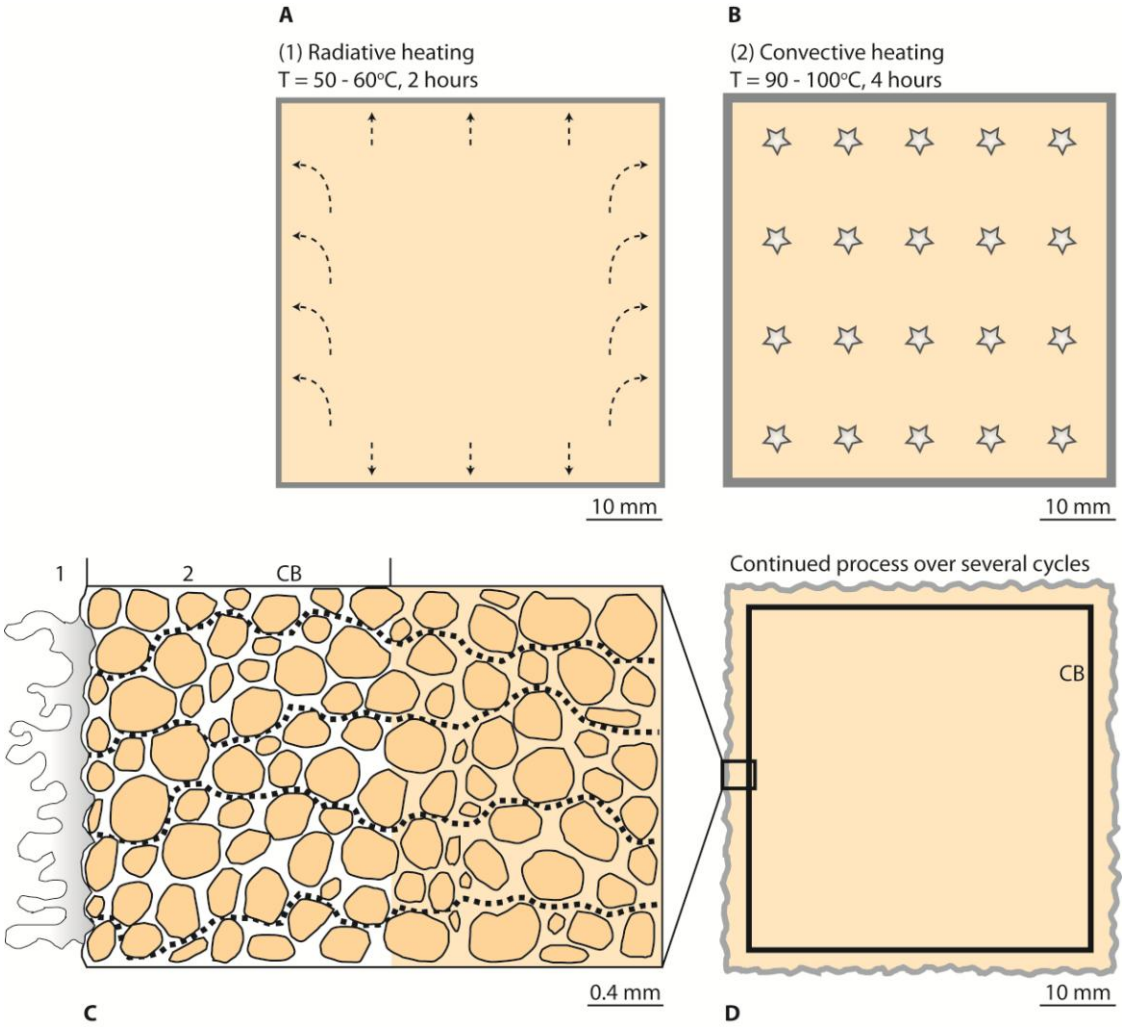

Figure 7-8: $MgCl_2$ crystallisation process within Cullalo sandstone.

A: Salt migrates towards the stone surface during the initial radiative heating stage. B: Homogenous crystallisation occurs throughout the stone during the high temperature convective heating stage. C: During the radiative heating stage efflorescence which is in hydraulic connectivity to the stone interior starts to form, allowing continued drying to take place through this salt crust. During the convective heating stage, a large salt gradient has developed, creating a crystallisation boundary (CB) close to the stone surface. D: Over several cycles, this continued process will eventually lead to granular decay on the stone surface owing to the high amount of salt located here.

7.4.1.1.4 Stanton Moor

Stanton Moor was extremely resistant to $MgCl_2$ crystallisation and remained aesthetically and mechanically intact after 50 cycles in the third crystallisation test. Low capillary absorption rates limited the uptake of $MgCl_2$, while slow drying kinetics prevented efflorescence formation. Low salt absorption rates combined with a high compressive and tensile strength would have resisted internal crystallisation pressures and ensured a high resistance to $MgCl_2$ crystallisation.

7.4.1.2 ***$CaCl_2$***

$CaCl_2$ produced similar decay morphologies and changes to the grain and pore structure as $MgCl_2$. The most prominent decay morphologies were granular and scaling decay, while $CaCl_2$ did not produce significant surface efflorescence on any sandstones. $CaCl_2$ has a relatively similar crystallisation behaviour to $MgCl_2$, forming thin crystalline sheets, but in contrast, its crystallisation is closely linked to precise temperature and RH conditions. $CaCl_2$ will only crystallise under low RH (<30%), or high temperature conditions (≥90 – 100^{o}C), whereby the onset and complete crystallisation of the salt takes place over a very short time period. This quick onset of crystallisation under extreme environmental conditions limits its transportation through the stone and prevents the near-surface crystallisation of salt and efflorescence from forming, as identified in $MgCl_2$ samples. The low extent of transportation of salt within the stone caused $CaCl_2$ to crystallise homogeneously throughout. Repeat crystallisation of salt that was initially located near to the stone surface would have produce the recorded granular decay in specific samples, while additional clay swelling and dispersal owing to the high cation exchange capacity (CEC) of Ca^{2+} would have produced the elevated decay rates of Locharbriggs samples. It is assumed that the spatial distribution of crystallisation significantly influences the rate of decay, and explains the differences in MWG between $CaCl_2$ and $MgCl_2$.

A qualitative assessment of the durability of sandstone to $CaCl_2$ crystallisation is presented in Figure 7-9, which highlights the durability relationship between temperature and RH, stone strength and clay content.

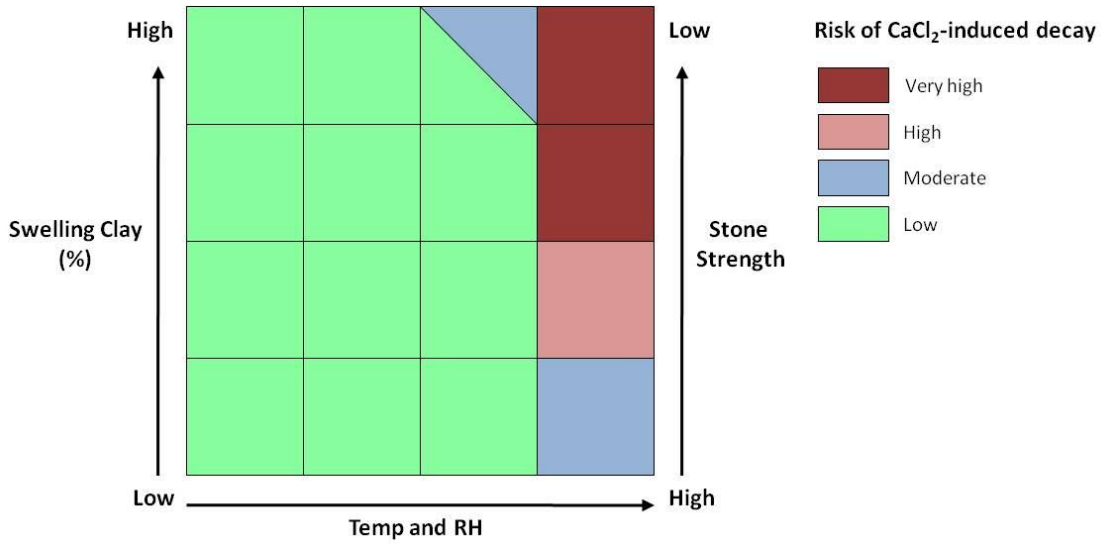

Figure 7-9: $CaCl_2$ crystallisation damage risk matrix.

Only two distinct salt-stone interaction processes were identified in the third crystallisation test, and are summarised in the following models. These processes are also relevant for both $CaCl_2$ and $MgCl_2$ in the second crystallisation test. The resistance of stone to decay from both salts in all tests is related to the cohesive strength and capillary absorption capacity of the stone.

7.4.1.2.1 $CaCl_2$ crystallisation process affecting every sandstone

Every sandstone in every test of the study experienced the same fundamental salt crystallisation process, which concerned the homogeneous crystallisation of $CaCl_2$. Most sandstone types experienced some change to their internal pore and grain structure as identified from results of repeat hygric and USV tests. Although damage was sustained internally across most sandstones, lower DWL values were recorded in relation to $MgCl_2$ in the third test owing to a lower proportion of samples experiencing granular surface decay. Over time, repeat crystallisation cycles of near-surface accumulations of salt (lower in relation to equivalent $MgCl_2$ samples), would eventually lead to granular decay and weight loss but at a reduced rate. Stones suffered similar internal damage to equivalent $MgCl_2$ samples. This process is described in Figure 7-2.

7.4.1.2.2 Locharbriggs

Locharbriggs experienced this same fundamental crystallisation process, however in common with $MgCl_2$ treated samples, also suffered from the expansion and flocculation of intra-granular clays; especially those concentrated in layers in the stone. This additional decay process lead to increased DWL values in Locharbriggs samples and the manifestation of multiple-scaling decay in the third test. Figure 7-7 also describes this process.

7.4.2 NaCl

NaCl caused damage in stone through the exertion of high pressures during the crystallisation of isometric hopper crystals. Damage was ultimately sustained by the stone when the net pressure of growing salt crystals exceeded its tensile strength. The magnitude of crystallisation pressures, the decay morphology, the rate of decay and its spatial distribution are primarily influenced by four key, interrelated factors: (i) the microporosity (and its spatial distribution); (ii) the water absorption coefficient; (iii) the tensile strength; and (iv) the drying rate.

The durability of select sandstones to NaCl crystallisation can be accurately classified using these easily measured stone properties, and the known thermodynamic crystallisation process of NaCl. Strong statistical correlations were found between the amended SSI and the DWL of samples from NaCl crystallisation, while the drying kinetics and spatial distribution of micro-pores successfully explain the decay morphology; including its spatial distribution and rate. Figure 7-10 is a qualitative assessment of the durability of sandstone to NaCl crystallisation in relation to these identified stone properties.

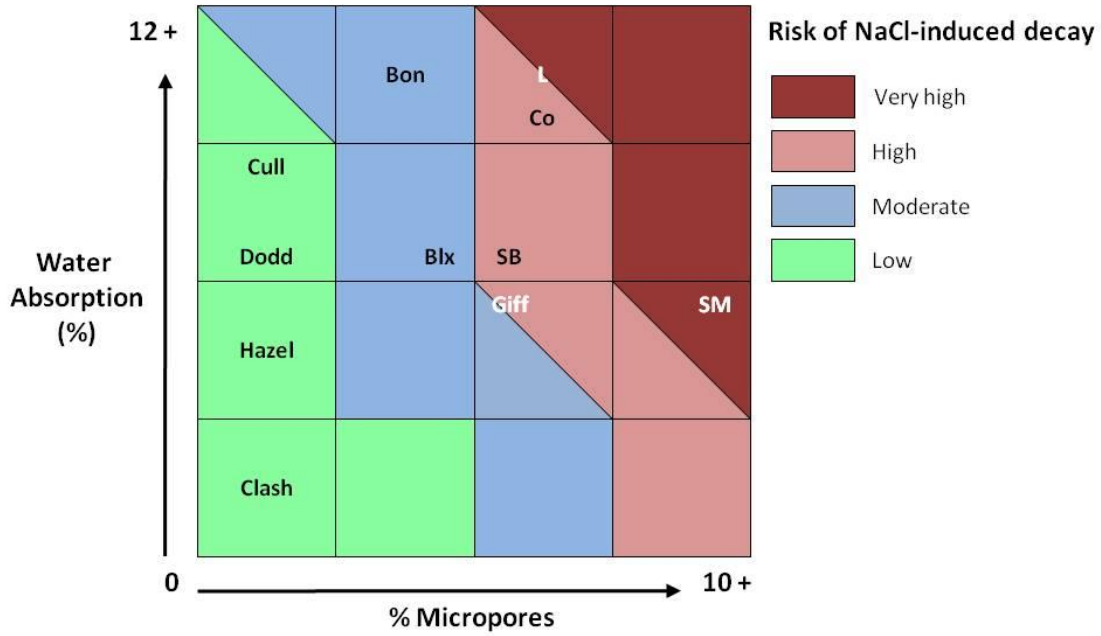

Figure 7-10: NaCl crystallisation damage risk matrix.
Clash: Clashach, Hazel: Hazeldean, Dodd: Doddington, Cull: Cullalo, Bon: Bonhill, Blx: Blaxter, Giff: Giffnock, SB: Scotch Buff, Co: Corsehill, L: Locharbriggs, SM: Stanton Moor.

The key salt-stone interactions are summarised below, highlighting the variable and complex nature of this process and how it is influenced by different combinations of stone properties.

7.4.2.1 *Locharbriggs*

Locharbriggs suffered substantial surface granular decay, catastrophic scaling decay and fracturing of near-surface regions in specific samples across all tests. Granular decay was initially focussed along the corners and edges of samples and within the bottom capillary zones through the loss of individual grains by the fracturing of quartz overgrowths and cement. This presented the first stage of visual decay in most samples and was the dominant process producing sustained weight loss in every test. Continued granular decay leads to the development of a rough stone surface and an increase in the near-surface porosity, which may promote positive feedback conditions through increased salt absorption, thermal stress and increased secondary bioreceptivity.

High water absorption and capillary coefficient values allowed the accelerated accumulation of salt within the stone, initially crystallising in the near-surface regions causing granular decay. Increased pore blocking at near

surface regions and on the stone surface through hard impermeable salt crusts eventually forced the retreat of the drying boundary into the stone interior. Layers characterised by low permeability, high pore tortuosity and a concentration of micro-pores provide a natural barrier to moisture flow, influencing the internal drying dynamics of the stone as the drying boundary receded. A decrease in pore connectivity (increased tortuosity) through the concentration of small angular grains, micro-pores and the accumulation of clays will lead to decreased ion diffusion and ultimately increase the relative number of nucleation sites in these layers. Salt crystallisation in these regions generates important positive feedbacks by further decreasing pore connectivity through pore blocking. Salt crystallisation initially leads to the non-equilibrium growth of salts and the development of brief episodes of high crystallisation pressures. The connectivity of these isolated regions of high crystallisation pressures through a substantial volume of stone (across bedding planes) eventually leads to the formation of scaling decay and the fracturing of the stone. The formation of scaling decay can be a latent process that occurs later than granular decay in the weathering process of a stone.

Locharbriggs is vulnerable to NaCl crystallisation owing to its high porosity, water absorption and capillary coefficient rate which permits the increased absorption of salt. The low compressive and tensile strength of Locharbriggs combined with a high drying efficiency leads to high rates of surface granular decay, while the spatial concentration of micro-pores within distinct layers presents an extremely vulnerable pore structure for crystallisation damage. Figure 7-11 summarises this process.

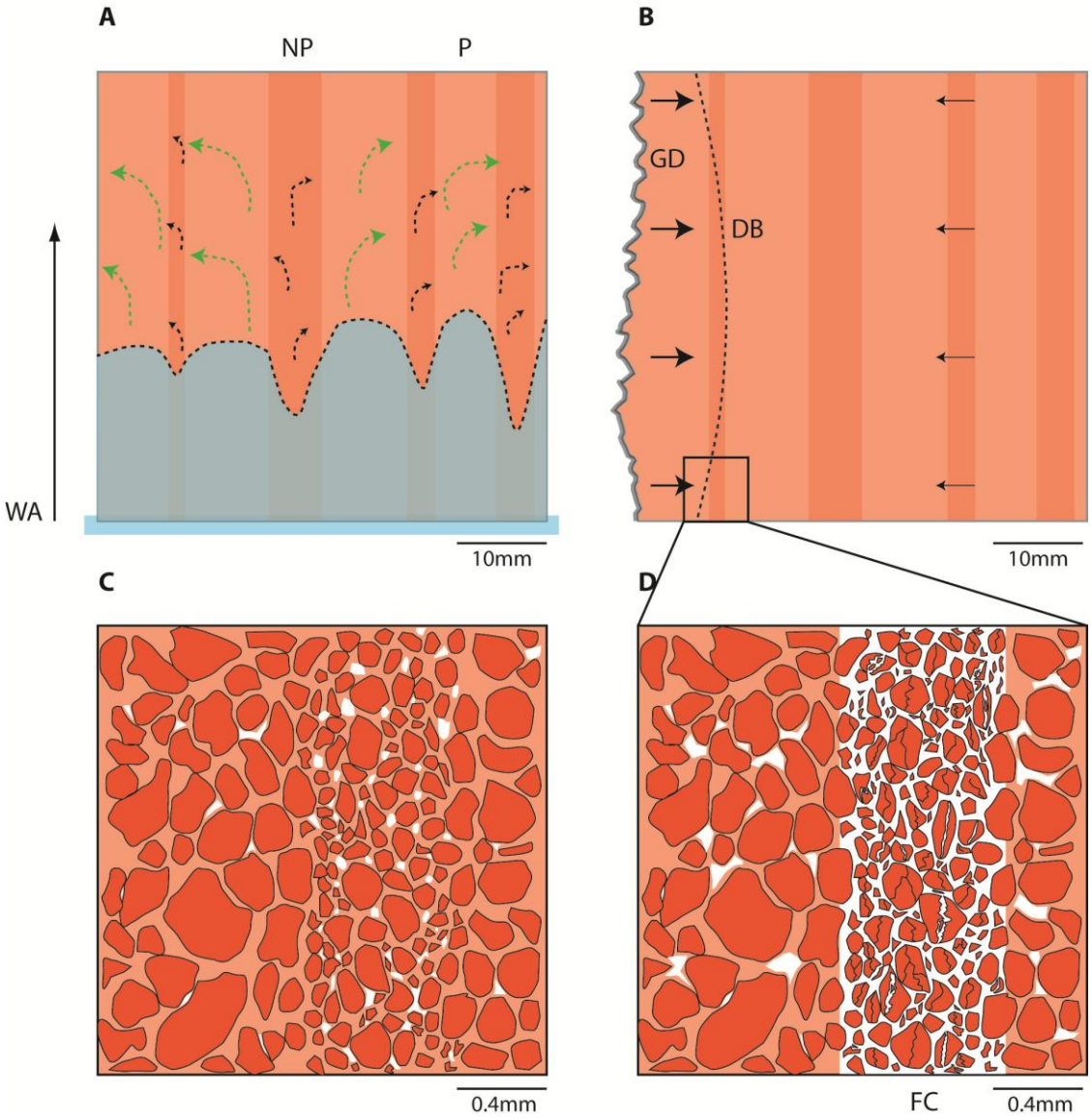

Figure 7-11: NaCl crystallisation damage in Locharbriggs sandstone.

A: Salt solution is absorbed into the stone at different rates, according to the permeability of layers within the stone and the water absorption (WA) capacity. P: porous, NP: non-porous. B: After several repeat crystallisation cycles, granular decay (GD) starts on the drying face of the stone and the drying boundary recedes owing to near-surface pore blocking. C: High magnification of the pore/grain structure across a layer within the stone. Salt preferentially accumulates within the higher concentration of micro pores in the layer. D: A fracture chain (FC) develops across this layer once a large enough volume of connected crystallisation pressures develop, causing significant damage and scaling to occur.

7.4.2.2 *Stanton Moor*

Stanton Moor was extremely vulnerable to NaCl crystallisation damage owing primarily to its high relative proportion of micro-pores, high saturation coefficient and low drying efficiency. Although Stanton Moor has a relatively low porosity, water absorption and extremely slow capillary absorption rate, its high saturation coefficient ensures that during long periods of moisture absorption an extremely high proportion of its porosity (and therefore micro-

porosity) is filled. The high relative proportion of micro-pores and the poorly connected, tortuous pore network within Stanton Moor presents an extremely vulnerable system that promotes the generation of high internal crystallisation pressures capable of significantly exceeding the stone's tensile and compressive strength.

Unlike the pore structure of Locharbriggs sandstone, the micro-porosity in Stanton Moor is uniformly distributed throughout the pore network. The distribution of salt crystallisation damage in Stanton Moor is therefore influenced by the external environmental conditions and stone surface condition, as these factors significantly control the drying behaviour of the stone. Stanton Moor is characterised by an extremely slow drying rate, experiencing high CMC and residual moisture levels. This slow drying rate prevents the formation of salt efflorescence as most salt crystallises somewhere within the internal pore network. As revealed by drying tests, the onset of the second drying stage initiates relatively early on and at high internal moisture contents (CMC) through the retreat of a uniform drying front. Over repeat crystallisation cycles a connected salt crystallisation front would extend across the drying plane, eventually developing into fracture planes and causing contour scaling.

The formation of several drying boundaries at different depths within the stone highlights the complexity of this system, whereby, early on, an initial salt horizon develops close to the stone surface due to repeat salt crystallisation cycles. Surface granular decay is prevalent during this period as isolated regions of salt crystallisation within the near-surface micro-pores force grains apart. This initial drying boundary and continued granular decay has two direct consequences on the continued weathering behaviour of the stone.

At first, granular decay increases the near-surface porosity, allowing more salt to be absorbed into the stone. This positive feedback accelerates the salt enrichment in this shallow salt horizon, eventually forming a large fracture chain that disconnects the surface from this salt horizon. At this point, the retreat of the drying boundary is forced deeper into the stone, where a second salt horizon develops, trapping salt deep within the stone. Scaling

decay then develops through the connection of substantial volumes of high crystallisation pressures within these horizons, repeating this same process at depth. The spatial extent of the drying boundary is influenced by the drying conditions and surface condition of the stone. The most prominent fracture chains will develop close to the primary drying surface, while smaller fractures and salt horizons develop parallel to the secondary drying surfaces (Figure 5-7).

Stanton Moor experienced lower damage and weight loss relative to other samples than what was estimated based on MIP results due to the low water absorption and capillary coefficient values of the stone. These results do reveal however, that even in the absence of high water absorption and porosity values, substantial decay can still occur if the stone is characterised by a tortuous pore network and a high proportion of micro-pores. Figure 7-12 highlights this complex process.

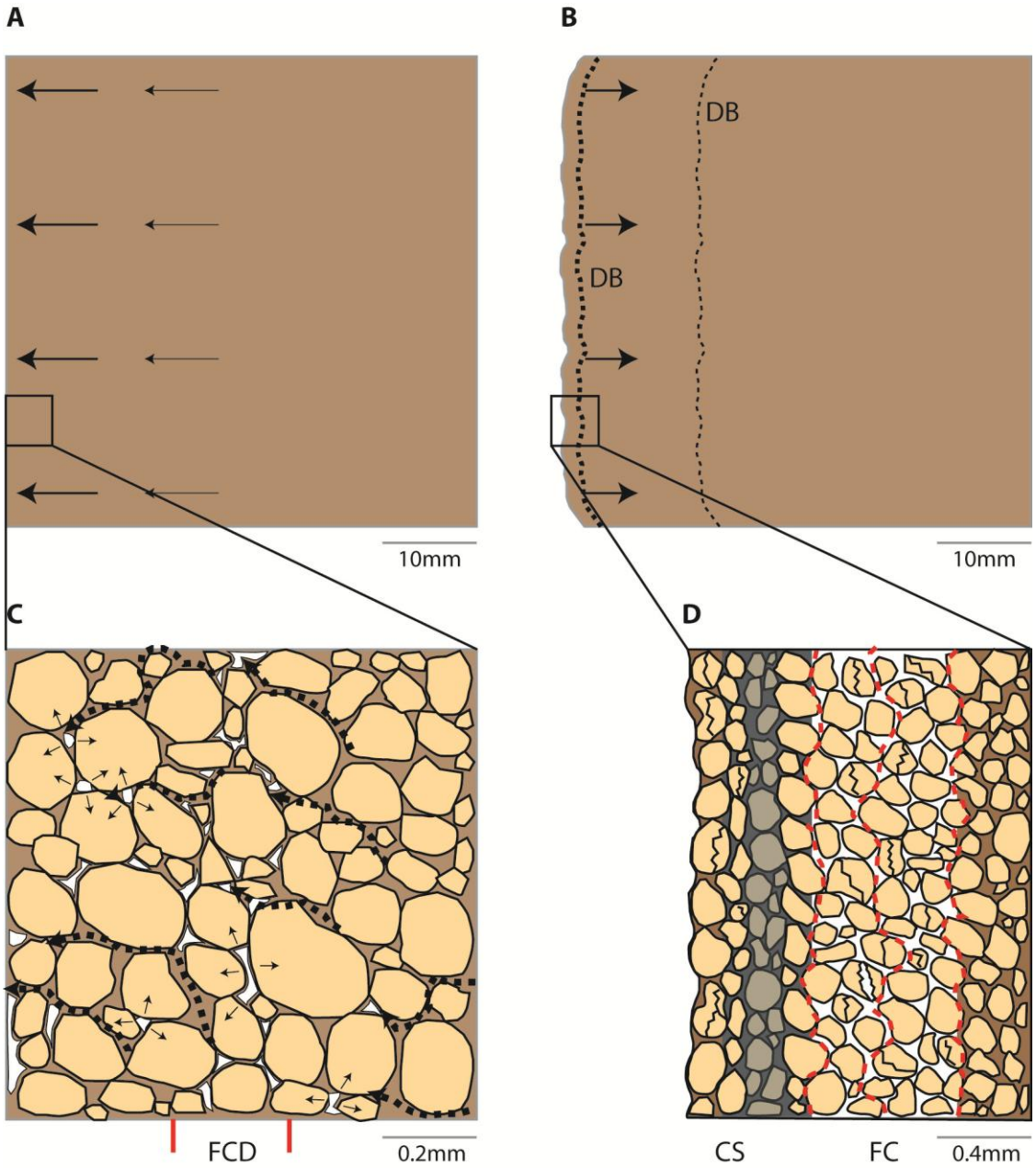

Figure 7-12: NaCl crystallisation damage within Stanton Moor sandstone.

A:Drying predominantly takes place through one drying face. There is no efflorescence the stone surface due to the poor drying efficiency of this stone, which forces internal crystallisation of the salt. B: Over several crystallisation cycles, granular decay at the stone surface develops and the drying boundary (DB) quickly retreats into the stone. A first drying boundary close to the stone surface develops initially. Over time and with continued pore blocking at this region, the boundary retreats further into the stone, creating a second and third crystallisation horizon/boundary. C: High crystallisation pressures develop with the micro-pores of the stone, placing stress on the detrital grains. A salt horizon starts to develop into a fracture chain across the first drying boundary. FCD: fracture chain development. D: Contour scaling (CS) develops as high pressures build across this initial fracture chain. As the drying boundary retreats further into the stone, a second fracture chain develops behind this region of high damage and increased secondary porosity.

7.4.2.3 *Cullalo (Hazeldean and Doddington)*

Cullalo, Hazeldean and Doddington sandstones all experienced very similar salt crystallisation interactions and can be grouped together as being resistant to NaCl crystallisation. All three salts are relatively texturally mature and are characterised by containing a low proportion of micro-pores, having fast and efficient drying regimes and a high tensile and compressive strength. Cullalo, Hazeldean and Doddington are generally well compacted sandstones that contain a well sorted grain structure; this property leads to a well organised compaction of similar-sized grains. Such organisation permits a high accessibility of moisture through the pore network and lowers the pore size distribution. An importance consequence of this grain structure is the high drying efficiency that ensures prolonged capillary connection of stage one drying, generally low CMC values and low residual moisture contents.

All three stones experienced high rates of surface efflorescence, indicating the efficient transportation of salt to the stone surface and limited subflorescence. Efflorescence must remain permeable in these stones to allow its continued formation; growing through a process of capillary pumping whereby permeable efflorescence connects the outer surface of the efflorescence crust to liquid regions within the stone interior (Figure 7-8).

As the efflorescence dried out and became impermeable, pore blocking would eventually force the internal crystallisation of salt and ultimately modify the drying behaviour of these sandstones. Over a prolonged period of internal crystallisation measurable changes to the pore and grain structure of each stone will eventually develop, creating an increasingly heterogeneous grain and pore network. The initial stone properties that characterised these stones as fast drying limit their vulnerability to salt crystallisation damage at this stage by successfully controlling the internal salt crystallisation pressures experienced through a lack of micro-pores and high pore connectivity (limiting non-equilibrium growth of salts). Figure 7-13 is a summary of this process.

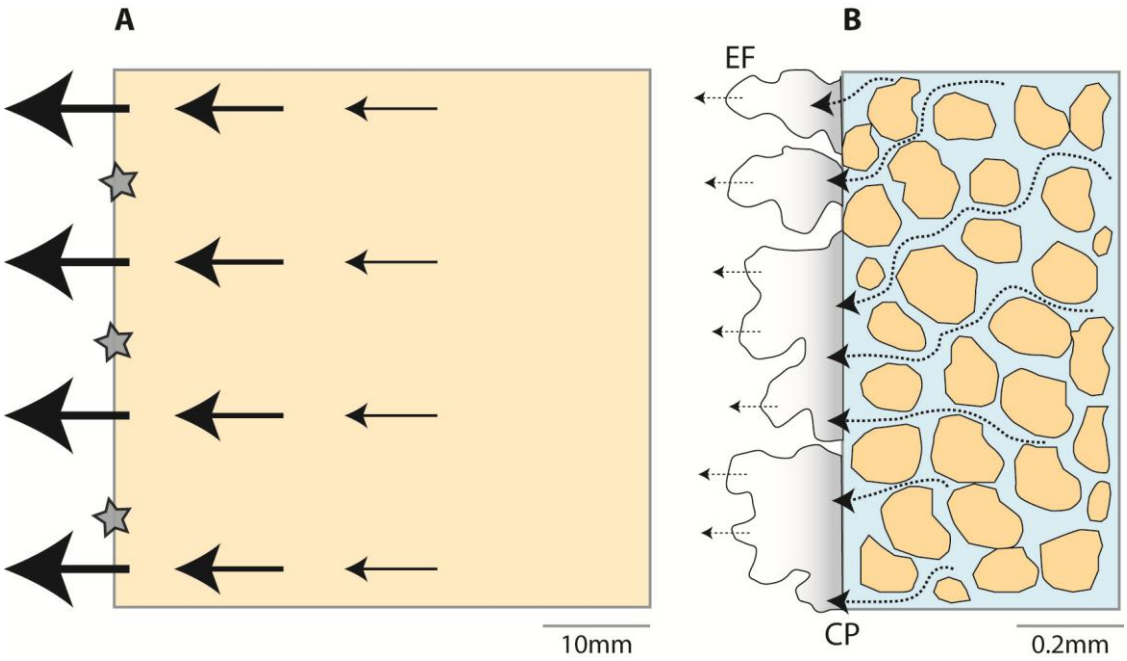

Figure 7-13: NaCl crystallisation process within fast drying sandstone (Cullalo and Hazeldean).

A: Fast drying efficiency allows salt to quickly migrate and crystallise as efflorescence on the stone surface. B: Permeable efflorescence (EF) allows the continued drying of the stone to take place on-top of the salt. Through a process of capillary pumping (CP), hydraulic connectivity is maintained for a long period between the efflorescence at the stone at depth.

7.5 Summary and key implications

The durability of select sandstones to salt-induced decay is a function of numerous interconnected stone properties that relate to: (i) stone strength, through grain shape, size, compaction and intergranular cement which promotes tensile strength of the stone; (ii) the transfer of moisture into and through the stone, such as the water absorption rate and drying behaviour, which relates to the effective salt reservoir and the location and rate of salt crystallisation, respectively; (iii) the magnitude of salt crystallisation pressures through the ratio and absolute volume of micro-pores within the stone. The incorporation of water absorption values into SSI calculations, which use the effective porosity and PSD, accurately identifies those stones vulnerable to NaCl crystallisation damage without the need to undertake time-consuming durability tests, and improves upon the original SSI. Stones such as Stanton Moor, Locharbriggs and Corsehill are identified as vulnerable to NaCl crystallisation damage, while Cullalo, Hazeldean and Doddington are resistant.

For the first time, a comprehensive study has been made into the effects of $CaCl_2$ and $MgCl_2$ on sandstone durability. Both salts are shown, under optimal and precise environmental conditions, to be damaging to certain sandstones as high crystallisation pressures and swelling clays force grains apart. Locharbriggs, Corsehill and Doddington were especially vulnerable to crystallisation, while Cullalo, Hazeldean and Stanton Moor were resistant. Under environmental conditions experienced in the UK however, both salts will stay as harmless solutions and not crystallise within the stone; rendering both salts as relatively harmless and safe. This work builds upon the scientific literature by understanding how both salts behave within the confined pore spaces of sandstone, as their crystallisation behaviour from free solutions is already known. Their interaction with swelling clays is less known however, and questions still remain regarding this process, plus what effect increased Ca^{2+}, Mg^{2+} and Cl^- ions have on other salt solutions found within building stone.

Results from this thesis are directly related to the behaviour of those sandstones used within the study, however it's thought that the crystallisation behaviour of each salt, and the most important stone properties governing salt crystallisation are relevant across most types of sandstone, with the proposed ranked toolkit having important implications for the durability assessment of building sandstone in the UK and elsewhere. Importantly, further research needs to take place regarding the suitability of this toolkit and implications of salt-stone interactions of other types of rock, including limestones and crystalline rocks, owing to their characteristically different pore structure relative to most typical sandstones.

Sandstones characterised by a high PSD and a high proportion of micro-pores are described as vulnerable to NaCl crystallisation damage, while the spatial distribution of micro-pores, water absorption values and drying kinetics can also significantly influence stone durability. Stones with a low proportion of micro-pores and those characterised by a clean, homogeneous pore network that permits high drying efficiency, with fast drying rates and low critical and residual moisture contents are generally very resistant to NaCl crystallisation damage. $MgCl_2$ and $CaCl_2$ are identified as not being damaging to sandstones within the UK, owing to the high annual RH and low annual temperatures.

8 References

ÅBERG, G. STRAY, H. AND DAHLIN, E., 1999, Impact of Pollution at a Stone Age Rock Art Site in Oslo, Normay, Studied using Lead and Strontium Isotopes: Journal of Archaeological Science. **26**, 1483 – 1488.

AKHURST, M. C. AND MONRO, S. K., 1996, Excursion 9. Dumfries: a Permian desert: In Stone, P. (eds) Geology in South-west Scotland: An Excursion Guide. British Geological Survey, Keyworth, Nottingham. 80 – 87.

AL-FARRIS, T. AND PINDER, K. L., 1987, Flow Through Porous Media of a Shear-Thinning Liquid with Yield Stress: The Canadian Journal of Chemical Engineering. **65**, 391 – 405.

AL-NADDAF, M., 2009, The effect of salts on thermal and hydric dilation of porous building stone: Archaeometry. **51**, 495-505.

AL-OMARI, ASAAD. BECK, KEVIN. BRUNETAUD. TÖRÖK, ÁKOS. AND AL-MUKHTAR, MUZAHIM., 2015, Critical degree of saturation: A control factor of freeze-that damage of porous limestones at Castle of Chambord, France: Engineering Geology. **185**, 71 – 80.

ALVES, CARLOS. FIGUEIREDO, CARLOS. MAURÍCIO, ANTÓNIO. AMÁLIA, MARIA. BRAGA, SEQUEIRA. AND AIRES-BARROS, LUÍS., 2011, Limestones under salt decay tests: assessment of pore network-dependent durability predictors: Environmental Earth Sciences. **63**, 1511 – 1527.

AMEY PLC. (2010), Winter Service Plan: 1st October 2010 – 15th May 2011 Transport Scotland, South West unit, 41 – 44.

AMOROSO, G. G. AND FASSINA, V., 1983, Stone Decay and Conservation: Atmospheric Pollution, Cleaning, Consolidation and Protection: Elsevier Science Publishers, Amsterdam.

ANANIA, LAURA. BADALÀ, ANTONIO. BARONE, GERMANA. BELFIORE, CRISTINA. MARIA. CALABRÒ, CHIARA. FRANCESCO LA RUSSA, MAURO.

MAZZOLENI, PAOLO. AND PEZZINO, ANTONINO., 2012, The stone in monumental masonry buildings of the "Val di Noto" area: New data on the relationships between petrographic characters and physical-mechanical properties: Construction and Building Materials. **33**, 122 – 132.

ANDERSON, S. H. WANG, H. PEYTON, R. L. AND GANTZER, C. J., 2003, Estimation of porosity and hydraulic conductivity from x-ray CT-measured solute breakthrough: Geological Society, London, Special Publications. **215**, 135 – 149.

ANGELI, MATTHIEU. BIGAS, JEAN-PHILIPPE. BENAVENTE, DAVID. MENÉNDEZ, BÉATRIZ. HÉBERT, RONAN. AND DAVID, CHRISTIAN., 2007, Salt crystallization in pores: quantification and estimation of damage: Environmental Geology. **52**, 205-213.

ANGELI, MATTHIEU. BENAVENTE, DAVID. BIGAS, JEAN-PHILIPPE. MENÉNDEZ, BÉATRIZ. HÉBERT, RONAN. AND DAVID, CHRISTIAN., 2008, Modification of the porous network by salt crystallization in experimentally weathered sedimentary stones: Materials and Structures. **41**, 1091 – 1108.

ARKHURST, M. C. BALL, D. F. BRADY, L. BUCKLEY, D. K. BURNS, J. DARLING, W. G. MACDONALD, A. M. MCMILLAN, A. A. DOCHARTAIGH, B. E. O. PEACH, D. W. ROBINS, N. S. AND WEALTHALL, G. P., 2006, Towards understanding the Dumfries Basin aquifer, SW Scotland: Geological Society, London, Special Publications. **263**, 187 – 198.

ATTIA, ATTIA. M., 2005, Effects of petrophysical rock properties on tortuosity factor: Journal of Petroleum Science and Engineering. **28**, 185 – 198.

BAI, Y. THOMPSON, G. E. MARTINEZ-RAMIREZ, S. AND BRÜEGGERHOFF, S., 2003, Mineralogical study of salt crusts formed on historic building stones: The Science of the Total Environment. **302**, 247 – 251.

BALBONI, ENRICA. ESPINOSA-MARZAL, ROSA. M. DOEHNE, ERIC. AND SCHERER, GEORGE. W., 2011, Can drying and re-wetting of magnesium sulphate salts lead to damage of stone?: Environmental Earth Science. **63**, 1463 – 1473.

BALLESTER, M. ALVAREZ DE BUERGO. AND GONZÁLEZ, R. FORT., 2001, Basic methodology for the assessment and selection of water-repellent treatments applied on carbonatic materials: Progress in Organic Coatings. **43**, 258 – 266.

BARAKA-LOKMANE, S., MAIN, I. G., NGWENYA, B. T., AND ELPHICK, S. C., 2009, Application of complimentary methods for more robust characterization of sandstone cores: Marine and Petroleum Geology. **26**, 39 – 56.

BARNES, R. P. AMBROSE, K. HOLLIDAY, D. W. AND JONES, N. S., 1994, lithostratigraphical subdivision of the Triassic Sherwood Sandstone group in west Cumbria: Proceedings of the Yorkshire Geological Society. **50**, 51 – 60.

BARRAUD, JOSEPH., 2006, The use of watershed segmentation and GIS software for textural analysis of thin sections: Journal of Volcanology and Geothermal Research. **154**, 17 – 33.

BASHAR, KHAIRUL. AND TELLAM, JOHN. H., 2011, Sandstones of unexpectedly high diffusibility: Journal of Contaminant Hydrology. **122**, 40 – 52.

BAYRAM, FATIH., 2012, Predicting mechanical strength loss of natural stones after freeze-thaw in cold regions: Cold Regions Science and Technology. **83 – 84**, 98 – 102.

BEAR SCOTLAND LIMITED., 2010, Winter Service Plan: 01 October 2010 to 15 May 2011: Transport Scotland, South East unit, 21 – 23.

BECK, KÉVIN. AL-MUKHTAR, M. ROZENBAUM, OLIVIER. AND RAUTUREAU, MICHEL., 2003, Characterization, water transfer properties and deterioration in tuffeau: building materials in the Loire valley-France: Building and Environment. **38**, 1151 – 1162.

BECK, KÉVIN. AL-MUKHTAR, MUZAHIM., 2010, Evaluation of the compatibility of building limestones from salt crystallization experiments: Geological Society, London, Special Publications. **333**, 111 – 118.

BELL, F. G., 1993, Durability of carbonate rock as building stone with comments on its preservation: Environmental Geology. **21**, 187 – 200.

BENAVENTE, D. GARCÍA DEL CURA, M. A. BERNABÉU, A. AND ORDÓÑEZ, S., 2001, Quantification of salt weathering in porous stones using an experimental continuous partial immersion method: Engineering Geology. **59**, 313 – 325.

BENAVENTE, DAVID. LOCK, PETER. GARCÍA DEL CURA, M. ÁNGELES. AND ORDÓÑEZ, SALVADOR., 2002, Predicting the Capillary Imbibition of Porous Rocks from Microstructure: Transport in Porous Media. **49**, 59 – 76.

BENAVENTE, D. GARCIA DEL CURA, M. A. AND ORDÓÑEZ, S., 2003, Salt influence on evaporation from porous building rocks: Construction and Building Materials. **17**, 113-122.

BENAVENTE, D. GARCIA DEL CURA, M.A. GARCIA-GUINEA, J. SANCHEZ-MORAL, S. AND ORDONEZ, S., 2004, Role of pore structure in salt crystallisation in unsaturated porous stone: Journal of crystal growth. **260**, 532 - 544.

BENAVENTE, D. MARTINEZ-MARTINEZ, J. ALGOZZINI, G. AND GARCIA DEL CURA, M. A., 2006, Influence of water transport and pore structure on the durability of porous building stones: Proceedings of IAEG Conference, The Geological Society of London, **233**.

BENAVENTE, DAVID. CULTRONE, GIUSEPPE. AND GÓMEZ-HERAS, MIGUEL., 2008, The combined influence of mineralogical, hygric and thermal properties on the durability of porous building stones: European Journal of Mineralogy. **20**, 673 – 685.

BENAVENTE, D. SANCHEZ-MORAL, S. FERNANDEZ-CORTES, A. CAÑAVERAS, J. C. ELEZ, J. AND SAIZ-JIMENEZ, C., 2011, Salt damage and microclimate in the Postumius Tomb, Roman Necropolis of Carmona, Spain: Environmental Earth Sciences. **63**, 1529 – 1543.

BERTRAND, LOÏC. THOURY, MATHIEU. AND ANHEIM, ETIENNE., 2012, Ancient materials specificities for their synchrotron examination and insights into their epistemological implications: Journal of Cultural Heritage. **14**, 277 – 289.

BIONDA, D. AND STOREMYR, P., 2002, Modelling the behaviour of salt mixtures in walls: a case study from Tenaille von Fersen, Suomenlinna, Finland: in T. Von Konow, ed., "The study of salt deterioration mechanisms. Decay of brick walls influenced by interior climate changes", Suomenlinnan hoitokunta, Helsinki. 95 – 101.

BIRGINIE, J. M. AND RIVAS, T., 2005, Use of a laser camera scanner to highlight the surface degradation of stone samples subjected to artificial weathering: Building and Environment. **40**, 1011 – 1020.

BLOCKSTONE LIMITED. (www.blockstone.co.uk). Accessed 2013.

BROOKFIELD, M. E., 1978 Revision of the stratigraphy of Permian and Supposed Permian Rocks of Southern Scotland: Heft. **67**, 110 – 143.

BRE, BUILDING RESEARCH ESTABLISHMENT., 2000, British Stone List, technical data sheets, (http://projects.bre.co.uk/ConDiv/stonelist/stonelist.html), Accessed 2012.

BUJ, OSCAR. AND GISBERT, JOSEP., 2010, Influence of pore morphology on the durability of sedimentary building stones from Aragon (Spain) subjected to standard salt decay tests: Environmental Earth Science. **61**, 1327 – 1336.

CAMUFFO, D., 1998, Microclimate for Cultural Heritage: Elsevier. Amsterdam and New York.

CAÑEDO-ARGÜELLES, MIGUEL. KEFFORD, BEN. J. PISCART, CHRISTOPHE. PRAT, NACRÍS. SCHÄFER, RALF. B. AND SCHULZ, CLAUS-JÜRGEN., 2013, Salinisation of rivers: An urgent ecological issue: Environmental Pollution. **173**, 157 – 167.

CARDELL, CAROLINA. YEBRA, AFRICA. AND VAN GRIEKEN, RENE. E., 2002, Applying Digital Image Processing to SEM-EDX and BSE Images to Determine and Quantify Porosity and Salts with Depth in Porous Media: Microchimica Acta. **140**, 9 – 14.

CARDELL, C. DELALIEUX, F. ROUMPOPOULOS, K. MOROPOULOU, A. AUGER, F. AND VAN GRIEKEN, R., 2003, Salt-induced decay in calcareous stone monuments and buildings in a marine environment in SW France: Construction and Building Materials. **17**, 165 – 179.

CARDELL, C. BENAVENTE, D. AND RODRÍGUEZ-GORDILLO, J., 2008, Weathering of limestone building material by mixed sulphate solutions. Characterization of stone microstructure, reaction products and decay forms: Materials Characterization. **59**, 1371 – 1385.

CARMELIET, JAN. DESCAMPS, FILIP. AND HOUVENAGHEL, GEERT., 1999, A Multiscale Network Model for Simulating Moisture Transfer Properties of Porous Media: Transport in Porous Media. **35**, 67 – 88.

CARTWRIGHT, TAMARA ANSON ET AL., 2008, Illustrated glossary on stone deterioration patterns: International Council on Monuments and Sites, 1 -86.

CEKSTERE, GUNTA. NIKODEMUS, OLGERTS. AND OSVALDE, ANITA., 2008, Toxic impact of the de-icing material to street greenery in Riga, Latvia: Urban Forestry and Urban Greening. **7**, 207 – 217.

CERIOTTI, MATTEO. MOTTOLA, LUCA. PICCO, GIAN. PIETRO. MURPHY, AMY. L. GUNÂ, STEFAN. CORRÀ, MICHELE. POZZI, MATTEO. ZONTA, DANIELE. AND ZANON, PAOLO., 2009, Monitoring Heritage Buildings with Wireless Sensor Networks: The Torre Aquila Deployment: Information Processing in Sensor Networks. 277 – 288.

CHABAS, A. JEANNETTE, D. AND LEFÈVRE, R. A., 2000, Crystallization and dissolution of airborne sea-salts on weathered marble in a coastal environmental at Delos (Cyclades-Greece): Atmospheric Environment. **34**, 219 – 224.

CHADWICK, R. A. HOLLIDAY, D. W. HOLLOWAY, S. AND HULBERT, A. G., 1993, The evolution and hydrocarbon potential of the Northumberland-Solway Basin: Petroleum Geology Conference series. **4**, 717-726.

CHAROLA, ELENA. A., 2000, Salts in the deterioration of porous materials: An overview: Journal of the American Institute for Conservation. **39**, **(3)**, **(2)**, 327 – 343.

CHAROLA, ELENA. A. AND WARE, ROBERT., 2002, Acid deposition and the deterioration of stone: a brief review of a broad topic: Geological Society, London, Special Publcations. **205**, 393 – 406.

CHAROLA, ELENA. A., 2003, Salt Deterioration: Open Questions: In Leitner, Laue and Siedel., Hochschule fur Bildende Kunste Dreseden. 19 – 24.

CHAROLA, ELENA. A. PÜHRINGER, JOSEF. AND STEIGER, MICHAEL., 2007, Gypsum: a review of its role in the deterioration of building materials: Environmental Geology. **52**, 339 – 352.

CHATTERJI, S. AND CRISTENSEN, P., 1979, A mechanism of break-down of limestone nodules in a freeze-thaw environment: Cement and Concrete Research. **9**, 741 – 746.

CHATTERJI, S., 2005, Aspects of generation of destructive crystal growth pressure: Journal of Crystal Growth. **277**, 566 – 577.

CHEN, T. C. YEUNG, M. R. AND MORI, N., 2004, Effect of water saturation on deterioration of welded tuff due to freeze-thaw action: Cold Regions Science and Technology. **38**, 127 – 136.

CHRISTARAS, BASILE. CUCCURU, FRANCESCO. FAIS, SILVANA. AND PAPANIKOLAOU, HELEN., 2014, Application of Non Destructive Ultrasonic Techniques for the Analysis of the Conservation Status of Building Materials in Monumental Structures: In G. Lollino et al. (eds), Engineering Geology for Society and Territory – Volume 8. 139 – 143.

CLEMMENSEN, L. B., 1987, Complex star dunes and associated Aeolian bedforms, Hopeman Sandstone (Permo-Triassic), Moray Firth Basin, Scotland: Geological Society, London, Special Publications. **35**, 213 – 231.

CNUDDE, V. CWIRZEN, A. MASSCHAELE, B. AND JACOBS, P. J. S., 2008, Porosity and microstructure characterization of building stones and concrete: Engineering Geology. **103**, 76 – 83.

CNUDDE, VEERLE. SILVERSMIT, GEERT. BOONE, MATTHIEU. DEWANCKELE, JAN. DE SAMBER, BJORN. SCHOONJANS, TOM. VAN LOO, DENIS. DE WITTE, YONI. ELBURG, MARLINA. VINCZE, LASZLO. VAN HOOREBEKE, LUC. AND JACOBS, PATRIC., 2009, Multi-disciplinary characterization of a sandstone surface crust: Science of the Total Environment. **407**, 5417-5427.

CNUDDE, V. DE BOEVER, W. DEWANCKELE, J. DE KOCK, T. BOONE, M. BOONE, M. N. SILVERSMIT, G. VINCZE, L. VAN RANST, E. DERLUYN, H.

PEETERMANS, S. HOVIND, J. MODREGGER, P. STAMPANONI, M. DE BUYSSER, K. AND DE SCHUTTER, G., 2013, Multi-disciplinary characterization and monitoring of sandstone (Kandla Grey) under different external conditions: Quarterly Journal of Engineering Geology and Hydrogeology. **46**, 95 – 106.

COLAS, ESTEL. AND MERTZ, JEAN-DIDIER., 2012, Influence of salt solution nature on the drying of clayey sandstone: Proceedings of The International Stone Conference. 13 – 22.

COLLINS, SARA. J. AND RUSSELL, RONALD. W., 2009, Toxicity of road salt to Nova Scotia amphibians: Environmental Pollution. **157**, 320 – 324.

COOKE, R. U., 1981, Salt weathering in deserts: Proceedings of the Geologists' Association. **92**, 1 – 16.

COOLING, L. F., 1930, The evaporation of water from brick: Transactions of the British Ceramic Society. **29**, 39 – 54.

COOMBES, MARTIN. A. NAYLOR, LARISSA. A. VILES, HEATHER. A. AND THOMPSON, RICHARD. C., 2013, Bioprotection and disturbance: Seaweed, microclimatic stability and conditions for mechanical weathering in the intertidal zone: Geomorphology. **202**, 4 – 14.

CORRENS, C. W. AND STEINBORN, W., 1939, Experimente zur Messung und Erklärung der sogenannten Kristallisationskraft: Z Krist (A). **101**, 117 – 133.

CORRENS, C. W., 1949, Growth and dissolution of crystals under linear pressure: Discussion of the Faraday Society. **5**, 267 – 271.

COSTA, EDUARDO. A. L. CAMPOS, VÂNIA. P. FILHO, LUIZ. C. P. DA SILVA. AND GREVEN, HÉLIO., 2009, Evaluation of the aggressive potential of marine chloride and sulphate salts on mortars applied as renders in the Metropolitan Region of Salvador – Bahia, Brazil: Journal of Environmental Management. **90**, 1060 – 1068.

COUSSY, OLIVIER., 2006, Deformation and stress from in-pore drying-induced crystallization of salt: Journal of the Mechanics and Physics of Solids. **54**, 1517 – 1547.

CULTRONE, G. RUSSO, L. G. CALABRÓ, C. UROŠEVIČ, M. AND PEZZINO, A., 2008, Influence of Pore system characteristics on limestone vulnerability: a laboratory study: Environmental Geology. **54**, 1271 – 1281.

CULTRONE, G. LUQUE, A. AND SEBASTIÁN, E., 2012, Petrophysical and durability tests on sedimentary stones to evaluate their quality as building materials: Quarterly Journal of Engineering Geology and Hydrogeology. **45**, 415 – 422.

CUTLER, NICK. A. VILES, HEATHER. A. AHMAD, SAMIN. MCCABE, STEPHEN. AND SMITH, BERNARD. J., 2013, Algal 'greening' and the conservation of stone heritage structures: Science of The Total Environment. **442**, 152 – 164.

DARWIN, DAVID. BROWNING, JOANN. GONG, LIEN. AND HUGHES, SEAN. R., 2007, Effects of deicers on concrete deterioration: Structural Engineering and Engineering Materials SL Report. The University of Kansas Center for Research Inc Lawrence, Kansas.

DE CLERCQ, HILDE. JOVANOVIC, MAJA. LINNOW, KIRSTEN. AND STEIGER, MICHAEL., 2013, Performance of limestone laden with Na_2SO_4-$NaNO_3$ and Na_2SO_4-K_2SO_4 mixtures: Environmental Earth Sciences. **69**, 1751 – 1761.

DE LOS RÍOS, ASUNCIÓN. CÁMARA, BEATRIZ. GARCÍA DEL CURA, M. ÁNGELES. RICO, VICTOR. J. GALVÁN, VIRGINIA. AND ASCASO, CARMEN., 2009, Deteriorating effects of lichen and microbial colonization of carbonate building rocks in the Romanesque church of Segovia (Spain): Science of The Total Environment. **407**, 1123 – 1134.

DEL MONTE, MARCO. AND ROSSI, PAOLA., 1997, Fog and gypsum crystals on building materials: Atmospheric Environment. **31**, **(11)**, 1637-1646.

DENECKER, MÉLANIE. HÉBERT, RONAN. BOURGÈS, ANN. MENENDEZ, BEATRIZ. AND DOEHNE, ERIC., 2012, Mirabilite and heptahydrate characterization from infrared microscopy and thermal data: Proceedings of The International Stone Conference. 14 – 23.

DERLUYN, HANNELORE. SAIDOV, TAMERLAN. A. ESPINOSA-MARZAL, ROSA. M. PEL, LEO. AND SCHERER, GEORGE. W., 2011, Sodium sulphate heptahydrate I: The growth of single crystals: Journal of Crystal Growth. **329**, 44 – 51.

DERLUYN, HANNELORE. DEWANCKELE, JAN. BOONE, MATTHIEU. N. CNUDDE, VEERLE. DEROME, DOMINIQUE. AND CARMELIET, JAN., 2014, Crystallization of hydrated and anhydrous salts in porous limestone resolved by synchrotron X-ray microtomography: Nuclear Instruments and Methods in Physics Research B. **324**, 102 – 112.

DEWANCKELE, J. DE KOCK, T. FRONTEAU, G. DERLUYN, H. VONTOBEL, P. DIERICK, M. VAN HOOREBEKE, L. JACOBS, P. AND CNUDDE, V., 2014, Neutron radiography and X-ray computed tomography for quantifying weathering and water uptake processes inside porous limestone used as building material: Materials Characterization. **88**, 86 – 99.

DICKINSON, WILLIAM E., 1959, Ice-Melting Properties and Storage Characteristics of Chemical Mixtures for Winter Maintenance: Highway Research Board Bulletin. **220**, 38th Annual Meeting.

DIXON, JOHN. C. AND THORN, COLIN. E., 2005, Chemical weathering and landscape development in mid-latitude alpine environments: Geomorphology. **67**, 127 – 145.

DOEHNE, ERIC., 2002, Salt Weathering: a selective review: Geological Society, London, Special Publications. **205**, 51 – 64

DOEHNE, ERIC., 2006, ESEM Applications: From Cultural Heritage Conservation to Nano-Behaviour: Microchimica Acta. **155**, 45 – 50.

DOEHNE, ERIC. AND PRICE, CLIFFORD. A., 2010, Stone Conservation: An Overview of Current Research: The Getty Conservation Institute. Chapter **1**, 1 – 25.

DRYDEN, A. L., 1931, Accuracy in Percentage Representation of Heavy Mineral Frequencies: Proceedings of the National Academy of Sciences. **17**, 233 – 238.

DUBOSC, A. ESCADEILLAS, G. AND BLANC, P. J., 2001, Characterisation of biological stains on external concrete walls and influence of concrete as underlying material: Cement and Concrete Research. **31**, 1613 – 1617.

DULLIEN, F. A. L., EL-SAYED, M. S. AND BATRA, V. K., 1977, Rate of capillary rise in porous media with nonuniform pores: Journal of Colloid and Interface Science. **60**, 497 – 506.

DUNN, D.E., LA FOUNTAIN, L.J. AND JACKSON, R.E., 1973, Porosity dependence and mechanism of brittle fracture in sandstones: Journal of Geophysical Research. **78**, 2403–2417.

DUTHIE, LAUARA. JANE., 2011, The Impact of Climate Change on Blond Sandstone Decay in Glasgow. PhD Thesis.

EDWARDS, H. EWART. BECKER, ANDREW. D. AND HOWELL, JOHN. A., 1993, Compartmentalization of an Aeolian sandstone by structural heterogeneities: Permo-Triassic Hopeman Sandstone, Moray Firth, Scotland: Geological Society, London, Special Publications. **73**, 339 – 365.

EFFLER, STEVEN. W., 1996, Limnological and Engineering Analysis of a Polluted Urban Lake: Prelude to Environmental Management of Onondaga Lake, New York: Springer-Verlag New York, Inc.

ELOUKABI, H. SGHAIER. BEN NASRALLAH, S. AND PRAT, M., 2013, Experimental study of the effect of sodium chloride on drying of porous media: The crusty-patchy efflorescence transition: International Journal of Heat and Mass Transfer. **56**, 80 – 93.

ENVIRONMENT AGENCY., 2010, Pollution Prevention Technical Information note – Safe Storage and use of de-icing products, December 2010, 1 – 5.

ESPINOSA, ROSA. MARIA. FRANKE, LUTZ. AND DECKELMANN, GERNOD., 2008, Phase changes of salts in porous materials: Crystallization, hydration and deliquescence: Construction and Building Materials. **22**, 1758 – 1773.

ESPINOSA, R.M. FRANKE, L. AND DECKELMANN, G., 2008, Model for the mechanical stress due to the salt crystallization in porous materials: Construction and Building Materials. **22**, 1350 – 1367.

ESPINOSA-MARZAL, R.M. AND SCHERER, G.W., 2010, Mechanisms of damage by salt: Geological Society, London, Special Publications. **331**, 61-77.

EVANS, M. BOOTH, C. JORDAN, R. AND CLEAVE, B., 2011, Guidance on the use in Scotland of five alternative de-icers to salt suitable for use in lower temperatures: Transport Research Laboratory Report. CPR1166

EVERET, D. H., 1961, The thermodynamics of frost damage to porous solids: Transactions of the Faraday Society. **57**, 1541 – 1551.

FAY, LAURA. VOLKENING, KEVIN. GALLWAY, CHASE. AND SHI, XIANMING., 2008, Performance and Impacts of Current Deicing and Anti-icing

Products: User Perspective versus Experimental Data: Proceedings of the 87th Annual Meeting of the Transportation Research Board.

FÉLIX, C., 1995, Choix de grès tenders du Plateau Suisse pour les travaux de conservation: In Pancella, R. (eds) Conservation et restauration des biens culturels. Actes du Congrès LCP. Laboratoire de Conservation de la Pierra, Dèpartement des matériaux, Ecole Polytechnique Fédérale, Lausanne. 45 – 71.

FISCHEL, MARION., 2001, Evaluation of selected deicers based on a review of the literature: Colorado Department of Transportation Research Branch. Report No CDOT-DTD-R-2001-15.

FITZNER, B. AND SNETHLAGE, R., 1982, Ueber Zusammenhange zwischen saltzkristallisationsdruck und Porenradienverteilung: G. P. News letter. **3**, 13 – 24.

FLATT, ROBERT. J., 2002, Salt damage in porous materials: how high supersaturations are generated: Journal of Crystal Growth. **242**, 435 – 454.

FLATT, ROBERT. J. STEIGER, MICHAEL. AND SCHERER, GEORGE. W., 2007, A commented translation of the paper by C.W. Correns and W. Steinborn on crystallization pressure: Environmental Geology. **52**, 187 – 203.

FISHER, R. A., 1923, Some factors affecting the evaporation of water from soil: Journal of Agronomy and Crop Science. **13**, **(2)**, 121 – 143.

FRANZEN, C. AND MIRWALD, P. W., 2004, Moisture content of natural stone: static and dynamic equilibrium with atmospheric humidty: Environmental Geology. **46**, 391 – 401.

FRANZEN, CHRISTOPH. AND MIRWALD, PETER. W., 2009, Moisture sorption behaviour of salt mixtures in porous stone: Chemie der Erde Geochemistry. **69**, 91 – 98.

FROST, D. V., 1969, The lower limestone group (Viscean) of the Otterburn District, Northumberland: Proceedings of the Yorkshire Geological Society. **37**, 277 – 309

FROSTICK, L. REID, I. JARVIS, J. AND EARDLEY, H., 1988, Triassic sediments of the Inner Moray Firth, Scotland: early rift deposits: Journal of the Geological Society. **145**, 235 – 248.

GABET, EMMANUEL. J. WOLFF-BOENISCH, DOMENIK. LANGNER, HEIKO. BURBANK, DOUGLAS. W. AND PUTKONEN, JAAKKO., 2010, Geomorphic and climatic controls on chemical weathering in the High Himalayas of Nepal: Geomorphology. **122**, 205 – 210.

GABRIELLI, ELENA. AND COLLA, CAMILLA., 2014, Monitoring of weathering effect evolution in porous masonry construction materials: NDT and mechanical tests: Proceedings of The 9th International Masonry Conference.

GHEDINI, NADIA. SABBIONI, CRISTINA. AND PANTANI, MARTA., 2003, Thermal analysis in cultural heritage safeguard: an application: Thermochimica. **406**, 105 – 113.

GLASGOW CITY COUNCIL., 2014, Glasgow Gritting Website: (http://gccgritting.iriss.org.uk/tracking). Accessed 2014.

GLASGOW CITY COUNCIL., 2014, Winter Maintenance Plan 2014 – 2015: Glasgow City Council.

GODTS, SEBASTIAN. DE CLERCQ, HILDE. HAYEN, ROALD. AND DE ROY, JUDY., 2012, Risk Assessment and conservation strategy of a salt laden limestone mausoleum and the surrounding funeral chapel in Boussu, Belgium: Proceedings of the International Stone Conference, 2 – 12.

GOMEZ-HERAS, MIGUEL. SMITH, BERNARD. J. AND FORT, RAFAEL., 2006, Surface temperature differences between minerals in crystalline rocks: Implications for granular disaggregation of granites through thermal fatigue: Geomorphology. **78**, 236 – 249.

GOMEZ-HERAS, MIGUEL. AND FORT, RAFAEL., 2007, Patterns of halite (NaCl) crystallisation in building stone conditioned by laboratory heating regimes: Environmental Geology. **52**, 259 – 267.

GOMEZ-HERAS, M. SMITH, B. J. VILES, H. A. MENEELY, J. AND MCCABE, S., 2008, HD Laser scanning for the evaluation of salt decay laboratory simulations of building limestone: Proceedings of the SWBSS conference.

GONCALVES, TERESA DIAZ. PEL, LEO. AND RODRIGUES, JOSE DELGADO., 2007, Drying of salt-contaminated masonry: MRI laboratory monitoring: Environmental Geology. **52**, 293 – 302.

GÖTZE, JENS. AND SIEDEL, HEINER., 2007, A complex investigation of building sandstones from Saxony (Germany): Materials Characterization. **58**, 1082 – 1094.

GOUDIE, A. S., 1974, Further experimental investigation of rock weathering by salt and other mechanical processes: Zeitschrift fur Geomorphologie Supplementband. **21**, 1 – 12.

GOUDIE, A. S., 1977, Sodium sulphate weathering and disintegration of the Mohenjo-Daro, Pakistan: Earth Surface Processes and Landforms. **2**, 75 – 86.

GOUDIE, A. S., 1993, Salt weathering simulation using a single-immersion technique: Earth Surface Processes and Landforms. **18**, 369 – 376.

GOUDIE, A. S. AND VILES, H. A., 1997, Salt Weathering Hazards: Chichester, Wiley.

GOUDIE, A. S., 1999, Experimental salt weathering of limestones in relation to rock properties: Earth Surface Processes and Landforms. **24** 715 – 724.

GRAHAM, CALLUM. JAMES., 2011, Quantifying the decay of Glasgow University by laser scanning: Unpublished Report.

GRATTONI, CARLOS. A. CHIOTIS, EFSTATHIOS. D. AND DAWE, RICHARD. A., 1995, Determination of Relative Wettability of Porous Sandstones by Imbibition Studies: Journal of Chemical Technology and Biotechnology. **64**, 17 – 24.

GROSSI, CARLOTA. M. BRIMBLECOMBE, PETER. AND HARRIS, IAN., 2007, Predicting long term freeze-thaw risks on Europe built heritage and archaeological sites in a changing climate: Science of the Totally Environment. **377**, 273 – 281.

GROSSI, C.M. BRIMBLECOMBE, P. MENENDEZ, B. BENAVENTE, D. HARRIS, I. AND DEQUE, M., 2011, Climatology of salt transitions and implications for stone weathering: Science of the Total Environment. **409**, 2577 – 2585.

GUILLITTE, O., 1995, Bioreceptivity: a new concept for building ecology studies: The Science of the Total Environment. **167**, 215 – 220.

GUILLITTE, O. AND DREESEN, R., 1995, Laboratory chamber studies and petrographical analysis as bioreceptivity assessment tools of building materials: The Science of the Total Environment. **167**, 365 – 374.

GUMMERSON, R. J. HALL, C. AND HOFF, W. D., 1980, Water Movement in Porous Building Materials – II. Hydraulic Suction and Sorptivity of Brick and Other Masonry Materials: Building and Environment. **15**, 101 – 108.

GUPTA, S. TERHEIDEN, K. PEL, L. AND SAWDY,A., 2012, Influence of ferrocyanide inhibitors on the transport and crystallization processes of sodium chloride in porous building materials: Journal of Crystal Growth. **12 (8)**, 3888 – 3898.

GUPTA, SONIA. HUININK, HENDRIK. P. PRAT, MARC. PEL, LEO. AND KOPINGA, KLASS., 2014, Paradoxical drying of a fired-clay brick due to salt crystallization: Chemical Engineering Science. **109**, 204 – 211.

GUPTA, SONIA. PEL, LEO. STEIGER, MICHAEL. AND KOPINGA, KLAAS., 2015, The effect of ferrocyanide ions on sodium chloride crystallization in salt mixtures: Journal of Crystal Growth. **410**, 7 – 13.

HALL, CHRISTOPHER., 1977, Water Movement in Porous Building Materials –I. Unsaturated Flow Theory and its Applications: Building and Environment. **12**, 117 – 125.

HALL, C. HOFF, W. D. AND NIXON, M. R., 1984, Water Movement in Porous Building Materials – VI. Evaporation and Drying in Brick and Block Materials: Building and Environment. **19**, (1), 13-20.

HALL, KEVIN. AND HALL, ALIDA., 1996, Weathering by wetting and drying: some experimental results: Earth Surface Processes and Landforms. **21**, 365 – 376.

HALL, CHRISTOPHER. AND HOFF, WILLIAM. D., 2002, Water Transport in Brick, Stone and Concrete: Taylor and Francis, London.

HALL, CHRISTOPHER. AND HOFFM WILLIAM. D., 2007, Rising Damp: capillary rise dynamics in walls: Proceedings of the Royal Society. **463**, 1871 – 1884.

HALL, KEVIN. GUGLIELMIN, MAURO. AND STRINI, ANDREA., 2008, Weathering of granite in Antarctica: II. Thermal stress at the grain scale: Earth Surface Processes and Landforms. **33**, 475 – 493.

HALL, CHRISTOPHER. AND HAMILTON, ANDREA., 2008, The Heptahydrate of sodium sulphate: Does it have a role in terrestrial and planetary geochemistry?: Icarus. **198**, 277 – 279.

HALL, KEVIN. AND THORN, COLIN., 2011, The historical legacy of spatial scales in freeze-thaw weathering: Misrepresentation and resulting misdirection: Geomorphology. **130**, 83 – 90.

HAMMECKER, CLAUDE. AND JEANNETTE, DANIEL., 1994, Modelling the Capillary Imbibition Kinetics in Sedimentary Rocks: Role of Petrographical Features: Transport in Porous Media. **17**, 285 – 303.

HANNEMAN, RICHARD L., 2010, Proof's in: salt management protects the environment: Salt Institute news letter (SHD).

HARRIS, K. D. HUIZINGA, A. AND BRETT, M. J., 2002, A simple and inexpensive humidity control chamber: Measurement Science and Technology. **13**, 10 – 11.

HASHIMOTO, YOSHITAKA, AND MINAMIZAWA., 2009, Data report: quantitative analysis of grain size distribution for coarse sediments in an accretionary prism: an example from the Cascadia accretionary prism: Proceedings of the Integrated Ocean Drilling Program. Volume 311.

HEINRICHS, KURT., 2008, Diagnosis of weathering damage on rock-cut monuments in Petra, Jordan: Environmental Geology. **56**, 643 – 675.

HEINRICHS, KURT. AZZAM, RAFIG. AND KRÜGER, MARKUS., 2012, The use of a wireless sensor network for high-resolution environmental monitoring of stone monuments in context with investigation of salt weathering – exemplified for rock-cut monuments in Petra/Jordan: Proceedings of The International Stone Conference. 2 – 11.

HEINRICHS, KURT. AND AZZAM, RAFIG., 2014, Quantitative Analysis of Salt Crystallization-Dissolution Processes on Rock-Cut Monuments in Petra/Jordan: In G. Lollino et al. (eds), Engineering Geology for Society and Territory – Volume 8. 507 – 510.

HENRY, JOHN J. BABOIAN, ROBERT. DUNLEAVY, JAMES W. GEOFFROY, DONALD N. GIDLEY, JEFFREY L. HORNER, RICHARD R. LARSON, MAURICE A. MANNING, DAVID G. MCCARTHY, PATRICK S. PEIPHO, LEE L. POLLOCK, SAMUEL J. ROY, DELLA M. WISE, DONALD L. AND ZOOK, RONALD L., 1991, Highway Deicing – Comparing Salt and Calcium Magnesium Acetate: Transportation Research Board, National Research Council, Special Report. **235**, 1 – 12.

HIRSCHWALD, J., 1908, Die Prufung der naturlichen Bausteine auf ihre Wetterbestandigkeit: Ernst and Sohn, Berlin.

HISTORIC SCOTLAND., 2009, Scotland's Historic Environment Vital to Economic Stability: (www.historic-scotland.gov.uk/news_search_results.htm/news_article.htm?articleid=23110). Accessed 2012.

HISTORIC SCOTLAND., 2011, Scottish Historic Environment Policy. December 2011: Historic Scotland.

HISTORIC SCOTLAND., 2012, Why is the historic environment important?: (www.historic-scotland.gov.uk/index/heritage/valuingourheritage/why-is-the-historic-environment-important). Accessed 2012.

HISTORIC SCOTLAND., 2013, Guide to the Protection of Scotland's Listed Buildings: What Listing Means to Owners and Occupiers.

HODGSON, A. V., 1978, Braided river bedforms and related sedimentary structures in the Fell sandstone Group (Lower Carboniferous) of north

Northumberland: Proceedings of the Yorkshire Geological Society. **41**, 509 – 532.

HOLLIDAY, D. W. WARRINGTON, G. BROOKFIELD, M. E. MCMILLAN, A. A. AND HOLLOWAY, S., 2001, Permo-Triassic rocks in boreholes in the Annan-Canobie area, Dumfries and Galloway, southern Scotland: Scottish Journal of Geology. **37**, 97 – 113.

HOLLIDAY, D. W. HOLLOWAY, S. MCMILLAN, A. A. JONES, N. S. WARRINGTON, G. AKHURST, M. C., 2004, The evolution of the Carlisle Basin, NW England and SW Scotland: Proceedings of the Yorkshire Geological Society. **55**, 1 – 19.

HOLLIDAY, D. W. JONES, N. S. AND MCMILLAN, A. A., 2008, Lithostratigraphical subdivision of the Sherwood Sandstone Group (Triassic) of the north-eastern part of the Carlisle Basin, Cumbria and Dumfries and Galloway, UK: Final Revision Paper, 1 – 37.

HOUSKA, CATHERINE., 2007, De-icing Salt – Recognising the Corrosion Threat: TMR Consulting, 1 – 11.

HOWARD, KEN. W. F. AND MAIER, HERB., 2007, Road de-icing salt as a potential constraint on urban growth in the Greater Toronto Area, Canada: Journal of Contaminant Hydrology. **91**, 146 – 170.

HUESTON, FREDERICK M., 1998, Subflorescence: the Deterioration of Historic Stone & Masonry through Crystallization of Water-Soluble Salts: The National training Centre for Stone & Masonry Trades, Special Report. **1018**, 1 – 3.

HYSLOP, EWAN. K. ALBORNOZ-PARRA, LUIS. J. FISHER, LYDIA. C. AND HAMILTON, SARAH. L., 2006, Safeguarding Glasgow's Stone Built Heritage Skills and Materials Requirements: Façade Surveys and Building Stone Analysis. British Geological Survey Commissioned Report.

HYSLOP, EWAN. K. AND ALBORNOZ-PARRA, LUIS., 2009, Developing a future repairs strategy for a sandstone city: A petrographic investigation of building stone in Glasgow, Scotland: Materials Characterization. **60**, 636 – 643.

HYSLOP, EWAN. K. ALBORNOZ-PARRA, LUIS. J. AND TRACEY, EMILY. A., 2009, Assessing the potential for reopening a building stone quarry: Newbigging Sandstone Quarry, Fife: British Geological Survey Minerals Programme Open Report, 1 – 37.

HYSLOP, EWAN. MCMILLAN, ANDREW. CAMERON, DON. LESLIE, ALICK. AND LOTT, GRAHAM., 2010, Building stone databases in the UK: A practical resource for conservation: Engineering Geology. **115**, 143 – 148.

IGLESIA, A. LA. GONZÁLEZ, V. LÓPEZ-ACEVEDO, V. AND VIEDMA, C., 1997, Salt crystallization in porous construction materials I Estimation of crystallization pressure: Journal of Crystal Growth. **177**, 111 – 118.

INGHAM, J.P., 2005, Predicting the frost resistance of building stone: Quarterly Journal of Engineering Geology and Hydrogeology. **38**, 387 – 399.

JAMSHIDI, AMIN. NIKUDEL, MOHAMMAD. REZA. AND KHAMEHCHIYAN, MASHALAH., 2013, Predicting the long-term durability of building stones against freeze-thaw using a decay function model: Cold Regions Science and Technology. **92**, 29 – 36.

JEFFERSON, D. P., 1993, Building stone: the geological dimension: Quarterly Journal of Engineering Geology. **26**, 305 – 319.

JENKS, CHRISTOPHER. W. JENCKS, CRAWFORD. F. HEDGES, CHRISTOPHER. J. DELANEY, EILEEN. P. AND FREER, HILARY., 2007, Guidelines for the Selection of Snow and Ice Control Materials to Mitigate Environmental Impacts: National Cooperative Highway Research Program. Report 577.

JONES, N. S. AND AMBROSE, K., 1994, Triassic sandy braidplain and Aeolian sedimentation in the Sherwood Sandstone group of the Sellafield area, west Cumbria: Proceedings of the Yorkshire Geological Society. **50**, 61 – 76.

JUNGMANN, MATTHIAS. PAPE, HANSGEORG. WIßKIRCHEN. CLAUSER, CHRISTOPH. AND BERLAGE, THOMAS., 2014, Segmentation of thin section images for grain size analysis using region competition and edge-weighted region merging: Computers and Geosciences. **72**, 33 – 48.

KHANLARI, GHOLAMREZA. SAHAMIEH, REZA. ZAREI. AND ABDILOR, YASIN., 2014, The effect of freeze-thaw cycles on physical and mechanical properties of Upper Red Formation sandstone, central part of Iran: Arabian Journal of Geosciences.

KING, ANDY., 2012, Strategic Stone Study: A Building Stone Atlas of Northumberland: English Heritage.

KIRK, S. S. AND WILLIAMSON, D. M., 2012, Structure and thermal properties of porous geological materials: Proceedings of the AIP conference. **1426**, 867 – 870.

KLOPPMANN, W. BROMBLET, P. VALLET, J. M. VERGÈS-BELMIN, V. ROLLAND, O. GUERROT, C. AND GOSSELIN, C., 2011, Building materials as intrinsic sources of sulphate: A hidden face of salt weathering of historic monuments investigated through multi-isotope tracing (B, O, S): Science of the Total Environment. **409**, 1658 – 1669.

KO KO SOE, AUNG. OSADA, MASAHIKO. AND WIN, THANDAR. THETOE. NWE., 2009, Drying-induced deformation behaviour of Shirahama sandstone in no loading regimes: Engineering Geology. **114**, 423 – 432.

KOENIG, RICH. AND RUPP, LARRY., 1999, Deicing Compounds and Utah Landscapes: Utah State University. **HG-511**, 1 – 4.

KOTSICK, DENNIS S., 2008, Salt: U.S Geological Survey 2008 Minerals Yearbook. **63**, 1 – 23.

KOSTICK, DENNIS S., 2011, Salt: U.S Geological Survey Mineral Commodity Summaries, 134 – 135.

LABUS, MAŁGORZATA. AND BOCHEN, JERZY., 2012, Sandstone degradation: an experimental study of accelerated weathering: Environmental Earth Sciences. **67**, 2027 – 2042.

LAGO, MARCELO. AND ARAUJO, MARIELA., 2001, Capillary Rise in Porous Media: Journal of Colloid and Interface Science. **234**, 35 – 43.

LARSEN, POUL. KLENZ., 2007, The salt decay of medieval bricks at a vault in Brarup Church, Denmark: Environmental Geology. **52**, 375 – 383.

LASAGA, A. C., 1998, Kinetic theory in the Earth Science: Princeton, Princeton University Press.

LAVALLE, J., 1853, Recherches sur la formation lente des cristaux à la temperature ordinaire: Compt. Rend. Acad. Sci. **34**, 493 – 495.

LAWSON, JUDITH., 1981, Building Stones of Glasgow: Geological Society of Glasgow.

LEE, MARTIN. R. HODSON, MARK. E. AND PARSONS, IAN., 1998, The role of intragranular microtextures and microstructures in chemical and mechanical weathering: Direct comparisons of experimentally and naturally weathered alkali feldspars: Geochimica et Cosmochimica Acta. **62**, 2771 – 2788.

LEE, HYOMIN. CODY, ROBERT. D. CODY, ANITA. M. AND SPRY, PAUL. G., 2010, Effects of Various Deicing Chemicals on Pavement Concrete Deterioration: Proceedings of the Mid-Continent Transportation Symposium. 151 – 155.

LEHMANN, PETER. ASSOULINE, SHMUEL. AND OR, DANI., 2008, Characteristic lengths affecting evaporative drying of porous media: The American Physical Society. **77**, 1 – 16.

LEWIN, S. Z., 1982, The mechanism of masonry decay through crystallization: Conservation of Historic Stone Buildings and Monuments. 120 – 144.

LINNOW, KIRSTEN. STEIGER, MICHAEL. LEMSTER, CHRISTINE. DE CLERCQ, HILDE. AND JOVANOVIĆ, MAJA., 2013, In situ Raman observation of the crystallization in $NaNo_3$-Na_2SO_4-H_2O solution droplets: Environmental Earth Sciences. **69**, 1609 – 1620.

LONG, HAILI. SWENNEN, RUDY. FOUBERT, ANNELEEN. DIERICK, MANUEL. AND JACOBS, PATRIC., 2009, 3D quantification of mineral components and porosity distribution in Westphalian C sandstone by microfocus X-ray computed tomography: Sedimentary Geology. **220**, 116 – 125.

LOPEZ-ARCE, P. GARCIA-GUINEA, J. BENAVENTE, D. TORMO, L. AND DOEHNE, E., 2009, Deterioration of dolostone by magnesium sulphate salt: An example of incompatible building materials at Bonaval Monastery, Spain: Construction and Building Materials. **23**, 846 – 855.

LOPEZ-ARCE, P. DOEHNE, E. GREENSHIELDS, J. BENAVENTE, D. AND YOUNG, D., 2009, Treatment of rising damp and salt decay: the historic masonry buildings of Adelaide, South Australia: Materials and Structures. **41**, 827 – 848.

LOTT, GRAHAM., 2013, Sourcing stone for the conservation and repair of historical buildings in Britain: Quarterly Journal of Engineering Geology and Hydrogeology. **46**, 405 – 420.

LUBELLI, BARBARA. VAN HEES, ROB. P.J. AND GROOT, CASPAR. J. W. P., 2004, The role of sea salts in the occurrence of different damage mechanisms and decay patterns on brick masonry: Construction and Building Materials. **18**, 119 – 124.

LUBELLI, B. VAN HEES, R. P. J. AND BROCKEN, H. J. P., 2004, Experimental research on hydroscopic behaviour of porous specimens contaminated with salts: Construction and Building Materials. **18**, 339 – 348.

LUBELLI, BARBARA. VAN HEES, ROB. P. J. AND GROOT, CASPAR. J. W. P., 2006, The Effect of Environmental Conditions on Sodium Chloride Damage: A step in the development of an effective weathering test: Studies in Conservation. **51**, 41 – 56.

LUBELLI, BARBARA. AND DE ROOIJ, MARIO. R., 2009, NaCl crystallization in restoration plasters: Construction and Building Materials. **23**, 1736 – 1742.

LUCAS, SPENCER. G. AND HUNT, ADRIAN. P., 2006, Permian tetrapod footprints: biostratigraphy and biochronology: Geological Society, London, Special Publications. **265**, 179 – 200.

MAIN, IAN, MAIR, KAREN. KWON, OHMYOUNG. ELPHICK, STEPHEN. AND NGWENYA, BRYNE., 2001, Experimental constraints on the mechanical and hydraulic properties of deformation bands in porous sandstones: a review: Geological Society, London, Special Publications. **186**, 43 – 63.

MALLIDI, SRINIVASA. REDDY., 1996, Application of mercury intrusion porosimetry on clay bricks to assess freeze-thaw durability – a bibliography with abstracts: Construction and Building Materials. **10**, 461 – 465.

MARTÍNEZ-MARTÍNEZ, JAVIER. BENAVENTE, DAVID. GOMEZ-HERAS, MIGUEL. MARCO-CASTAÑO, LUZ. AND GARCÍA-DEL-CURA, M. ÁNGELES., 2013,

Non-linear decay of building stones during freeze-thaw weathering processes: Construction and Building Materials. **38**, 443 – 454.

MATSUOKA, NORIKAZU. AND MURTON, JULIAN., 2008, Frost Weathering: Recent Advances and Future Directions: Permafrost and Periglacial Processes. **19**, 195 – 210.

MAURICIO, ANTONIO. M. PACHECO, ADRIANO. M. G. BRITO, PAULO. S. D. CASTRO, BRUNO. FIGUEIREDO, CARLOS. AND AIRES-BAROS, LUIS., 2005, An ionic conductivity-based methodology for monitoring salt systems in monument stones: Journal of Cultural Heritage. **6**, 287-293.

MAXWELL, INGVAL., 2010, Building Scotland: Celebrating Scotland's Traditional Building Materials: John Donald, an imprint of Birlinn Ltd, Historic Scotland.

MCCABE, S. MCKINLEY, J. M. AND SMITH, B. J., 2008, Simulating initial stages of salt accumulation and organization within building sandstones. In: Lukaszewicz, J. W. And Niemcewizc, P. (eds), 11th International Congress on the Deterioration of Stone. Nicolaus Copernicus University Press, Torun: 173 – 180.

MCCABE, S. MCKINLEY, J. M. GOMEZ-HERAS, M. AND SMITH, B. J., 2011, Dynamical instability in surface permeability characteristics of building sandstones in response to salt accumulation over time: Geomorphology. **130**, 65 – 75.

MCCABE, S. SMITH, B. J. MCALISTER, J. J. GOMEZ-HERAS, M. MCALLISTER, D. WARKE, P. A. CURRAN, J. M. AND BASHEER, P. A. M., 2013, Changing climate, changing process: implications for salt transportation and weathering within building sandstones in the UK: Environmental Earth Sciences. **69**, 1225 – 1235.

MCELROY, A.D. BLACKBURN, ROBERT. R. HAGYMASSY, JULES. AND KIRCHNER, HENRY., 1988, Comparative Study of Chemical Deicers –

Undercutting and Disbondment: Transportation Research Board Annual Meeting, January (1988).

MCGREEVY, J. P., 1982, 'Frost and Salt' Weathering: Further Experimental Results: Earth Surface Processes and Landforms. **7**, 475 – 488.

MCKINLEY, J.M. AND WARKE, P.A., 2007, Controls on permeability: implications for stone weathering: Geological Society, London, Special Publications. **271**, 225 – 236

MCKEEVER, PATRICK. J., 1994, A new vertebrate trackway from the Permian of Dumfries and Galloway: Scottish Journal of Geology. **30**, 11 – 14.

MCMILLAN, ANDREW. GILLANDERS, RICHARD. J. AND FAIRHURST, JOHN. A., 1999, Building stones of Edinburgh: Edinburgh Geological Society.

MCMILLAN, ANDREW. HYSLOP, EWAN. MAXWELL, INGVAL. AND MCKINNEY, ALAN., 2006, Indigenous stone resources for Scotland's Built Heritage: Proceedings of the IAEG conference. Paper number 825.

MCMILLAN, ANDREW. AND HYSLOP, EWAN., 2008, The City of Edinburgh – Landscape and Stone: Proceedings of the ICOMOS Scientific Symposium.

MCMILLAN, A. A. MERRITT, J. W. AUTON, C. A. AND GOLLEDGE, N. R., 2011, The Quaternary Geology of the Solway: Geology and Landscape (Scotland) Programme Research Report. British Geological Survey.

MEADOWS, N. S. AND BEACH, A., 1993, Controls on reservoir quality in the Triassic Sherwood Sandstone of the Irish Sea: Petroleum Geology Conference series. **4**, 823 – 833.

MENZIES, THOMAS R., 1992, Overview of National Research Council study on the comparative costs of using rock salt and CMA for highway deicing: Resources, Conservation and Recycling. **7**, 43 – 50.

MICHIGAN TECH TRANSPORTATION INSTITUTE., 2008, The Deleterious Chemical Effects of Concentrated Deicing Solutions on Portland Cement Concrete: South Dakota Department of Transportation, Office of Research, Study SD2002-01 Executive Summary, 1 – 56.

MILLER, A. Z. SANMARTÍN, P. PEREIRA-PARDO, L. DIONÍSIO, A. SAIZ-JIMENEZ, C. MACEDO, M. F. AND PRIETO, B., 2012, Bioreceptivity of building stones: A review: Science of the Total Environment. **426**, 1 – 12.

MOH'D, BASEM. K. HOWARTH, RICHARD. J. AND BLAND, CHRISTINE. H., 1996, Rapid prediction of Building Research Establishment limestone durability class from porosity and saturation: Quarterly Journal of Engineering Geology. **29**, 285 – 297.

MONGY, T., 2014, Application of Neutron Tomography in Culture heritage Research: Applied Radiation and Isotopes. **85**, 54 – 59.

MOROPOULOU, A. KOULOUMBI, N. HARALAMPOPOULOS, G. KONSTANTI, A. AND MICHAILIDIS, P., 2003, Criteria and methodology for the evaluation of conservation interventions on treated porous stone susceptible to salt decay: Progress in Organic Coatings. **48**, 259 – 270.

MORTENSEN, H., 1933, Die Salzsprengung und ihre Bedeutung fur die regionalklimatische GLiederung der Wusten: Petermann's Mitteilungen aus Justus Perthes geographischer Ansalt. **79**, 130 – 135.

MOSES, CHERITH. ROBINSON, DAVID. AND BARLOW, JOHN., 2014, Methods for measuring rock surface weathering and erosion: A critical review: Earth-Science Reviews. **135**, 141 – 161.

MUNCK, ISABEL. A. BENNETT, CHANDALIN. M. CAMILL, KIM. S. AND NOWAK, ROBERT. S., 2010, Long-term impact of de-icing salts on tree health in the Lake Tahoe Basin: Environmental influences and interactions with

insects and diseases: Forest Ecology and Management. **260**, 1218 – 1229.

MUTLUTÜRK, M. ALTINDAG, R. AND TÜRK, G., 2004, A decay function model for the integrity loss of rock when subjected to recurrent cycles of freezing-thawing and heating-cooling: International Journal of Rock Mechanics and Mining Sciences. **41**, 237 – 244.

NABAWY, BASSEM. S., 2014, Estimating porosity and permeability using Digital Image Analysis (DIA) technique for highly porous sandstones: Arabian Journal of Geosciences. **7**, 889 – 898.

NACHSHON, URI. WEISBROD, NOAM. DRAGILA, MARIA. I. AND GRADER, ABRAHAM., 2011A, Combined evaporation and salt precipitation in homogeneous and heterogeneous porous media: Water Resources Research. **47**, 1 -16.

NACHSHON, URI. SHAHRAEENI, EBRAHIM. OR, DANI. DRAGILA, MARIA. AND WEISBROD, NOAM., 2011B, Infrared thermography of evaporative fluxes and dynamics of salt deposition on heterogeneous porous surfaces: Water Resources Research. **47**, 1 -16.

NEUGEBAUER, J., 1973, The diagenetic problem of chalk. The role of pressure solution and pore fluid: Neues Jahrbuch fur Geologie und Palaontologies. **143**, 223 – 245.

NGWENYA, B. T. ELPHICK, S. C, MAIN, I. G. AND SHIMMIELD, G. B., 2000, Experimental constraints on the diagenetic self-sealing capacity of faults in high porosity rocks: Earth and Planetary Science Letters. **183**, 187 – 199.

NICHOLSON, DAWN. T. AND NICHOLSON, FRANK. H., 2000, Physical deterioration of sedimentary rocks subjected to experimental freeze-thaw weathering: Earth Surface Processes and Landforms. **25**, 1295 – 1307.

NIXON, WILFRID A. KOCHUMMAN, GEORGE. QIU, LIN. QIU, JU. AND XIONG, JING., 2007, Iowa Highway research Board Technical Report. **463**, 1 – 61.

ORDÓÑEZ, S. FORT, R. AND GARCÍA DEL CURA, M. A., 1997, Pore size distribution and the durability of a porous limestone: Quarterly Journal of Engineering Geology. **30**, 221 – 230.

PADILLA, VICTOR. GHODS, POURIA. AND ALFANTAZI, AKRAM., 2013, Effect of de-icing salts on the corrosion performance of galvanized steel in sulphate contaminated soil: Construction and Building Materials. **40**, 908 – 918.

PANDEY, SATISH. C. POLLARD, A. M. VILES, H. A. AND TELLAM, J. H., 2014, Influence of ion exchange processes on salt transport and distribution in historic sandstone buildings: Applied Geochemistry. **48**, 176 – 183.

PAPIDA, SOPHIA. MURPHY, WILLIAM. AND MAY, ERIC., 2000, Enhancement of physical weathering of building stones by microbial populations: International Biodeterioration and Biodegradation. **46**, 305 – 317.

PEL, L. HUININK, H. KOPINGA, K. VAN HEES, R. P. J. AND ADAN, O. C. G., 2004, Efflorescence pathway diagram: understanding salt weathering: Construction and Building Materials. **18**, 309 – 313.

PEL, LEO. SAWDY, ALISON. AND VORONINA, VICTORIA., 2010, Physical principles and efficiency of salt extraction by poulticing: Journal of Cultural Heritage. **11**, 59 – 67.

PEL, LEO. AND SAIDOV, T., 2012, Crystallization of sodium sulphate in porous media by drying: proceedings of The International Stone Conference. 34 – 42.

PENG, SHENG. HU, QINHONG. DULTZ, STEFAN. AND ZHANG, MING., 2012, Using X-ray computed tomography in pore structure characterization for a Berea sandstone: Resolution effect: Journal of Hydrology. **472 – 473**, 254 – 261.

PERRET, JOHAN. PRASHER, S. O. KANTZAS, A. AND LANGFORD, C., 1999, Three-Dimensional Quantification of Macropore Networks in Undisturbed Soil Cores: Soil Science Society of America Journal. **63**, 1530 – 1543.

PERRY, S.H. AND DUFFY, A.P., 1996, The Short-term effects of mortar joints on salt movement in stone: Atmospheric Environment. **31**, **(9)**, 1297 – 1307.

PERUZZI, ROBERTO. POLI, TOMMASO. AND TONIOLO, LUCIA., 2003, The experimental test for the evaluation of protective treatments: a critical survey of the "capillary absorption index": Journal of Cultural Heritage. **4**, 251 – 254.

PIGEON, M. AND PLEAU, R., 1995, Durability of Concrete in Cold Climates: Chapman and Hall, London.

POPE, GREGORY. A. MEIERDING, THOMAS. C. AND PARADISE, THOMAS. R., 2002, Geomorphology's role in the study of weathering of cultural stone: Geomorphology. **47**, 211 – 225.

PORTAL TO THE PAST. East Renfrewshire Council: (www.portaltothepast.co.uk). Accessed 2013.

POWERS, T. C., 1945, A working hypothesis for further studies of frost resistance of concrete: American Concrete Institute Journal. **41**, 245 – 272.

PRICE, N.J., 1966, Fault and Joint Development: Pergamon Press, Oxford, 172.

PRIETO, B. AND SILVA, B., 2005, Estimation of the potential bioreceptivity of granitic rocks from their intrinsic properties: International Biodeterioration and Biodegradation. **56**, 206 – 215.

PŘIKRYL, R., 2001, Some microstructural aspects of strength variation in rocks: International Journal of Rock Mechanics and Mining Science. **38**, 671–682.

PŘIKRYL, R. AND SMITH, B. J., 2007, Diagnosing decay: the value of medical analogy in understanding the weathering of building stones, Building Stone Decay: From Diagnosis to Conservation: Geological Society, London, Special Publications. **271**, 1 – 8.

PŘIKRYL, RICHARD. WEISHAUPTOVA, ZUZANA. NOVOTNA, MIROSLAVA. PRIKRYLOVA, JIRINA. AND ST'ASTNA, ANETA., 2011, Physical and mechanical properties of the repaired sandstone ashlars in the facing masonry of the Charles Bridge in Prague (Czech Republic) and an analytical study for the causes of its rapid decay: Environmental Earth Science. **63**, 1623 – 1639.

PŘIKRYL, RICHARD., 2013, Durability assessment of natural stone: Quarterly Journal of Engineering Geology and Hydrogeology. **46**, 377 – 390.

RAO, SUDHAKAR. M. THYAGARAJ, T. AND RAO, P. RAGHUVEER., 2013, Crystalline and Osmotic Swelling of an Expansive Clay Inundated with Sodium Chloride Solutions: Geotechnical and Geological Engineering. **31**, 1399 – 1404.

RAMAKRISHNA, DEVIKARANI M. AND VIRARAGHAVAN, THIRUVENKATACHARI., 2005, Environmental Impact of Chemical Deicers – A Review: Water, Air, and Soil Pollution. **166**, 49 – 63.

RICHARDSON, B. A., 1991, The durability of porous stones: Stone Industries. **26**, 22 – 25.

RIJNIERS, LOURENS. A. PEL, LEO. HUININK, HENK. P. AND KOPINGA, KLAAS., 2005, Salt crystallization as damage mechanism in porous building materials – a nuclear magnetic resonance study: Magnetic Resonance Imaging. **23**, 273 – 276.

RIVAS. T. POZO, S. AND PAZ, M., 2014, Sulphur and oxygen isotope analysis to identify sources of sulphur in gypsum-rich black crusts developed on granites: Science of the Total Environment. **482 – 483**, 137 – 147.

RODRIGUEZ-NAVARRO, CARLOS. HANSEN, ERIC. SEBASTIAN, EDUARDO. AND GINELL, WILLIAM. S., 1997, The Role of Clays in the Decay of Ancient Egyptian Limestone Sculptures: Journal of the America Institute for Conservation. **36**, 151 – 163.

RODRIGUEZ-NAVARRO, CARLOS. AND DOEHNE, ERIC., 1999, Salt weathering: Influence of Evaporation Rate, Supersaturation and Crystallization Pattern: Earth Surface Processes and Landforms. **24**, 191 – 209.

RODRIGUEZ-NAVARRO, CARLOS. DOEHNE, ERIC. AND SEBASTIAN, EDUARDO., 2000, How does sodium sulphate crystallize? Implications for the decay and testing of building materials: Cement and Concrete Research. **30**, 1527-1534.

RØGEN, BIRTE. GOMMESEN, LARS. AND FABRICIUS, IDA. L., 2001, Grain size distributions of chalk from image analysis of electron micrographs: Computers and Geoscience. **27**, 1071 – 1080.

ROSS, K. D. HART, D. AND BUTLIN, R. N., 1991, Durability tests for natural building stone: In Baker, J. M. Nixon, P. J. Majumdar, J. And Davies, H. (eds) Durability of Building Materials and Components, Proceedings of the 5th International Conference. Chapman and Hall, London. 97 – 111.

ROSSANA, BELLOPEDE, AND PAOLA, MARINI., 2012, The effect of water on the strength of building stone: American Journal of Environmental Sciences. **8**, **(2)**, 158 – 161.

ROSSI-MANARESI, R. AND TUCCI, A., 1991, Pore Structure and the Disruptive or Cementing Effect of Salt Crystallization in Various Types of Stone: Studies in Conservation. **36**, 53 – 58.

ROTHERT, E. EGGERS, T. CASSAR, J. RUEDRICH, J. FITZNER, B. AND SIEGESMUND, S., 2007, Stone properties and weathering induced by salt crystallization of Maltese Globigerina Limestone: Geological Society, London, Special Publications. **271**, 189 – 198.

ROUSSET-TOURNIER, B. MAZEROLLE, F. GÉRAUD, Y. AND JEANNETTE, D., 2003, Rock drying tests monitored by X-ray computed tomography – the effect of saturation methods on drying behaviour: Geological Society, London, Special Publications. **215**, 117 – 125.

RUEDRICH, JOERG. AND SIEGESMUND, SIEGFRIED., 2006, Salt and ice crystallisation in porous sandstones: Environmental Geology. **52**, **(2)**, 225 – 249.

RUEDRICH, J. SEIDEL, M. ROTHERT, E. AND SIEGESMUND, S., 2007, Length changes of sandstones caused by salt crystallization: Geological Society, London, Special Publications. **271**, 199 – 209.

RUSSELL, S. A., 1927, Stone preservation committee report: Appendix 1. H.M. Stationary Office, London.

RUIZ DE ARGANDOÑA, VICENTE. G. CALLEJA, LOPE. RODRÍGUEZ-REY, ÁNGEL. SUÁREZ DEL RÍO, LUIS. MIGUEL. AND CELORIO, CARMEN., 2009, X-ray Computed Tomography study of the influence of consolidants on the hydric properties of sandstones for stone conservation studies: Engineering Geology. **103**, 69 – 75.

RUIZ-AGUDO, E. PUTNIS, C. V. HÖVELMANN, J. ÁLVAREZ-LLORET, P. IBÁÑEZ-VELASCO, A. AND PUTNIS, A., 2015, Experimental study of the replacement of calcite by calcium sulphates: Geochimica et Cosmochimica Acta. **156**, 75 – 93.

ŞAHIN, REMZI. TAŞDEMIR, MEHMET. ALI. GÜL, RÜSTEM. ÇELIK, CAFER., 2010, Determination of the optimum conditions for de-icing salt scaling resistance of concrete by visual examination and surface scaling: Construction and Building Materials. **24**, 353 – 360.

ŞAHMARAN, MUSTAFA. AND LI, VICTOR. C., 2007, De-icing salt scaling resistance for mechanically loaded engineered cementitious composites: Cement and Concrete Research. **37**, 1035 – 1046.

SAIDOV, TAMERLAN. A. ESPINOSA-MARZAL, ROSA. M. PEL, LEO. AND SCHERER, GEORGE. W., 2012, Nucleation of sodium sulphate heptahydrate on mineral substrates studied by nuclear magnetic resonance: Journal of Crystal Growth. **338**, 166 – 169.

SALT INSTITUTE., 2004, Highway salt and our environment, 1 – 27.

SALT INSTITUTE., 2011, How does road salt work: (www.saltinstitute.org/Uses-benefits/Winter-road-safety/How-does-road-salt-work), Accessed 2011.

SALT UNION., 2012, Facts about Salt and De-icing: (www.saltunion.com/news/quick-facts/), Accessed 2012.

SANCHEZ, J. SANJURJO. ROMANI, J.R.VIDAL. AND ALVES, C., 2011, Deposition of particles on gypsum-rich coatings of historic buildings in urban and rural environments: Construction and Building Materials. **25**, 813-822.

SANZO, DOMENICO. AND HECNAR, STEPHEN. J., 2006, Effects of road de-icing salt (NaCl) on larval wood frogs (*Rana sylvatica*): Environmental Pollution. **140**, 247 – 256.

SASS, O. AND VILES, H.A, 2010, Wetting and drying of masonry walls: 2D-resistivity monitoring of driving rain experiments on historic stonework in Oxford, UK: Journal of Applied Geophysics. **70**, 72 – 83.

SAWDY, ALISON. AND HERITAGE, ADRIAN., 2007, Evaluating the influence of mixture composition on the kinetics of salt damage in wall paintings using time lapse video imaging with direct data annotation: Environmental Geology. **52**, 303 – 315.

SCHERER, GEORGE. W., 1990, Theory of Drying: Journal of the American Ceramic Society. **73**, 3 – 14.

SCHERER, GEORGE. W., 1999, Crystallization in pores: Cement and Concrete Research. **29**, 1347 – 1358.

SCHERER, GEORGE. W., 2002, Factors Affecting Crystallization Pressure: Proceedings of International RILEM TC 186-ISA Workshop on internal Sulfate Attack and Delayed Ettringite Formation, 139 – 154.

SCHERER, GEORGE. W., 2004, Stress from crystallization of salt: Cement and Concrete Research. **34**, 1613 – 1624.

SCHERER, GEORGE. W., 2006, Internal stress and cracking in stone and masonry: Measuring, Monitoring and Modelling Concrete Properties. In M. S. Konsta-Gdoutos. (eds), 633 – 641.

SEBASTIÁN, EDUARDO. CULTRONE, GIUSEPPE. BENAVENTE, DAVID. FERNANDEZ, LUCIA. LINARES. ELERT, KERSTIN. AND RODRIGUEZ-NAVARRO, CARLOS., 2008, Swelling damage in clay-rich sandstones used in the church of San Mateo in Tarifa (Spain): Journal of Cultural Heritage. **9**, 66 – 76.

SGHAIER, NOUR. AND PRAT, MARC., 2009, Effect of Efflorescence Formation on Drying Kinetics of Porous Media: Transport in Porous Media. **80**, 441 – 454.

SHAW., 2007, Environmental Statement, Braidbar Quarry Housing Development, Unpublished, 1-16.

SHERWOOD, T. K., 1930, The drying of solids, Pt III, Mechanism of the drying of pulp and paper: Industrial and Engineering Chemistry Research. **22**, 132 – 136.

SHI, XIANMING. FAY, LAURA. GALLAWAY, CHASE. VOLKENING, KEVIN. PETERSON, MARIJEAN, M. PAN, TONGYAN. CREIGHTON, ANDREW. LAWLOR, COLLINS. MUMMA, STEPHANIE. LIU, YAJUN. AND NGUYEN, TUAN ANH., 2009, Evaluation of alternative anti-icing and deicing compounds using sodium chloride and magnesium chloride as baseline deicers – Phase 1: Colorado Department of Transportation DTD Applied Research and Innovation Branch. Report No. CDOT-**2009-1**, 1 – 270.

SHI, XIANMING. FAY, LAURA. PETERSON, MARIJEAN. M. AND YANG, ZHENGXIAN.M, 2010, Freeze-thaw damage and chemical change of a Portland cement concrete in the presence of diluted deicers: Materials and Structures. **43**, 933 – 946.

SHOKRI, N. LEHMANN, P. AND OR, D., 2010, Liquid-phase continuity and solute concentration dynamics during evaporation from porous meda: Pore-scale processes near vaporization surface: Physical Review E. **81**, 1 – 7.

SHOKRI, N. LEHMANN, P. AND OR, D., 2010, Evaporation from layered porous media: Journal of Geophysical Research. **115**, N/A.

SILVA, Z.S.G. AND SIMÃO, J.A.R., 2009, The role of salt fog on alteration of dimension stone: Construction and Building Materials. **23**, 3321 – 3327.

SIEDEL, HEINER. SIEGESMUND, SIEGFRIED. AND STERFLINGER, KATJA., 2011, Characterisation of Stone Deterioration on Buildings: Institute of Geotechnical Engineering. **4**, 347 – 410.

SILVA, B. PRIETO, B. RIVAS, T. SANCHEZ-BIEZMA, J. PAZ, G. AND CARBALLAL, R., 1997, Rapid Biological Colonization of a Granitic Building by Lichens: International Biodeterioration and Biodegradation. **40**, 263 – 267.

SIMÃO, J. RUIZ-AGUDO, E. AND RODRIGUEZ-NAVARRO, C., 2006, Effects of particulate matter from gasoline and diesel vehicle exhaust emissions on silicate stones sulfation: Atmospheric Environment. **40**, 6905 – 6917.

SINKE, G.C. AND MOSSNER, E.H., 1976, Laboratory Comparison of Calcium Chloride and Rock Salt as Ice Removal Agents: Transportation Research Record. **598**, Maintenance Management.

SMITH, T. E., 1967, A preliminary study of sandstone sedimentation in the Lower Carboniferous of the Tweed Basin: Scottish Journal of Geology. **3**, 282 – 305.

SMITH, B. J. AND MCGREEVY, J. P., 1988, Contour scaling of a sandstone by salt weathering under simulated hot desert conditions: Earth Surface Processes and Landforms. **13**, 697 – 705.

SMITH, B. J. TURKINGTON, A. V. WARKE, P. A. BASHEER, P. A. M. MCALISTER, J. J. MENEELY, J. AND CURRAN, J. M., 2002, Modelling the rapid retreat of building sandstones: a case study from a polluted maritime environment: Geological Society, London, Special Publications. **205**, 347 – 362.

SMITH, B. J. TÖRÖK, A. MCALISTER, J. J. AND MEGARRY, Y., 2003, Observations on the factors influencing stability of building stones

following contour scaing: a case study of oolitic limestones from Budapest, Hungary: Building and Environment. **38**, 1173 – 1183.

SMITH, B. J. WARKE, P. A. MCGREEVY, J. P. AND KANE, H. L., 2005, Salt-weathering simulations under hot desert conditions: agents of enlightenment or perpetuators of preconceptions: Geomorphology. **67**, 211 – 227.

SMITH, B.J. AND PRIKRYL, R., 2007, Diagnosing decay: the value of medical analogy in understanding the weathering of building stones: Geological Society, London, Special Publications. **271**, 1 - 8.

SMITH, B. J. SRINIVASAN, S. GOMEZ-HERAS, M. BASHEER, P. A. M. AND VILES, H. A., 2009, Near-surface temperature cycling of stone and its implications for scales of surface deterioration: Geomorphology. **130**, 76 – 82.

SMITH, B.J. MCCABE, S. MCALLISTER, D. ADAMSON, C. VILES, H.A. AND CURRAN, J.M., 2011, A commentary on climate change, stone decay dynamics and the "greening" of natural stone buildings: new perspectives on "deep wetting": Environmental Earth Science. **63**, 1691 – 1700.

SMITH, B. J. SRINIVASAN, S. GOMEZ-HERAS, M. BASHEER, P. A. M. AND VILES, H. A., 2011, Near-surface temperature cycling of stone and its implications for scales of surface deterioration: Geomorphology. **130**, 76 – 82.

SOUSA, LUÍS. M. O. SUÁREZ DEL RÍO, LUIS, M. CALLEJA, LOPE. RUIZ DE ARGANDOÑA, VICENTE. G. AND REY, ANGEL. RODRÍGUEZ., 2005, Influence of microfractures and porosity on the physic-mechanical properties and weathering of ornamental granites: Engineering Geology. **77**, 153 – 168.

SPRAGG, ROBERT. P. CASTRO, JAVIER. LI, WENTING. POUR-GHAZ, MOHAMMAD. HUANG, PAO-TSUNG. AND WEISS, JASON., 2010, Wetting and drying of concrete using aqueous solutions containing deicing salts: Cement and Concrete Composites. **33**, 535 – 542.

STEIGER, MICHAEL., 2005, Crystal growth in porous materials – I: The crystallization pressure of large crystals: Journal of Crystal Growth. **282**, 455 – 469.

STEIGER, MICHAEL., 2005, Crystal growth in porous materials – II: Influence of crystal size on the crystallization pressure: Journal of Crystal Growth. **282**, 470 – 481.

STEIGER, MICHAEL. AND ASMUSSEN, SÖNKE., 2008, Crystallization of sodium sulphate phases in porous materials: The phase diagram Na_2SO_4-H_2O and the generation of stress: Geochimica et Cosmochimica Acta. **72**, 4291 – 4306.

STEIGER, MICHAEL. KIEKBUSCH, JANA. AND NICOLAI, ANDREAS., 2008, An improved model incorporating Pitzer's equations for calculation of thermodynamic properties of pore solutions implemented into an efficient program code: Construction and Building Materials. **22**, 1841 – 1850.

STEIGER, MICHAEL. AND HERITAGE, ALISON., 2012, Modelling the crystallization behaviour of mixed salt systems: Input data requirements: Proceedings of the International Stone Conference. 2 – 13.

STOKES, DEBBIE. J., 2003, Recent advances in electron imaging, image interpretation and applications: environmental scanning electron microscopy: Philosophical Transactions of the Royal Society A. **361**, 2771 – 2787.

SUMMER, P. D. AND LOUBSTER, M. J., 2008, Experimental sandstone weathering using different wetting and drying moisture amplitudes: Earth Surfaces Processes and Landforms. **33,** 985 – 990.

SUNAGAWA, I., 1981, Characteristics of crystal growth in nature as seen from the morphology of mineral crystal: Bulletin Mineralogie. **104**, 81 – 87.

TAYLOR, SARAH. C. HALL, CHRISTOPHER. HOFF, WILLIAM. D. AND WILSON, MOIRA. A., 200, Partial Wetting in Capillary Liquid Absorption by Limestones: Journal of Colloid and Interface Science. **224**, 351 – 357.

THARP, THOMAS. M., 1987, Conditions for crack propagation by frost wedging: Geological Society of America Bulletin. **1**, 94 – 102.

THEOULAKIS, P. AND MOROPOULOU, A., 1997, Microstructural and mechanical parameters determining the susceptibility of porous buildings to stone decay: Construction and Building Materials. **11**, 65 – 71.

THEOULAKIS, P. AND MOROPOULOU, A., 1999, Salt Crystal Growth as Weathering Mechanism of Porous Stone on Historic Masonry: Journal of Porous materials. **6**, 345 – 358.

THOMACHOT, C. AND JEANNETTE, D., 2002, Evolution of the petrophysical properties of two types of Alsatian sandstone subjected to simulated freeze-thaw conditions: Geological Society, London, Special Publications. **205**, 19 – 32.

THOMAS, IAN. A. AND COOPER, BARRY. J., 2014, Hierarchical Approaches Toward Safeguarding Heritage Building Stone Resources in England and Wales: In G. Lollino et al. (eds), Engineering Geology for Society and Territory – Volume 5. 313 – 318.

TIANO, P. ACCOLLA, P. AND TOMASELLI, L., 1995, Phototrophic Biodeteriogens on Lithoid Surfaces: An Ecological Study: Microbial Ecology. **29**, 299 – 309.

TOMASELLI, LUISA. LAMENTI, GIOIA. BOSCO, MARCO. AND TIANO, PIERO., 2000, Biodiversity of photosynthetic micro-organisms dwelling on stone monuments: International Biodeterioration and Biodegradation. **46**, 251 – 258.

TÖRÖK, ÁKOS., 2003, Surface strength and mineralogy of weathering crusts on limestone buildings in Budapest: Building and Environment. **38**, 1185 – 1192.

TÖRÖK, Á. AND VÁSÁRHELYI, B., 2010, The influence of fabric and water content on selected rock mechanical parameters of travertine, examples from Hungary: Engineering Geology. **115**, 237 – 245.

TOMAŠIČ, IVAN. LUKIĆ, DRAŽEN. PEČEK, NATAŠA. AND KRŠINIČ, ANA., 2010, Dynamics of capillary water absorption in natural stone: Bulletin of Engineering Geology and the Environment. **70**, 673 – 680.

TRANSPORT SCOTLAND., 2010, South West Unit – Winter Service Plan, 04-SWU-F3-001: Amey, Plc. 1 – 162.

TRANSPORT SCOTLAND., 2014, Winter Service Plans: (www.transportscotland.gov.uk/road/winter-service-ready-winter-and-severe-weather). Accessed 2014.

TRIPP, THOMAS, G., 2009, Production of magnesium from Great Salt Lake, Utah USA: Natural Resources and Environmental Issues. **15** (10).

TSUI, NICHOLAS. FLATT, ROBERT. J. AND SCHERER, GEORGE. W., 2003, Crystallization damage by sodium sulphate: Journal of Cultural Heritage. **4**, 109-115.

TUCKER, MAURICE. E. GALLAGHER, JAMES. AND LENG, MELANIE. J., 2009, Are beds in shelf carbonates millennial-scale cycles? An example from the

mid-Carboniferous of northern England: Sedimentary Geology. **214**, 19 – 34.

TURKINGTON, A. V. SMITH, B. J. AND BASHEER, P. A. M., 2002, The effect of block retreat on sub-surface temperature and moisture conditions in sandstone: In Understanding and Managing Stone Decay, Přykryl, R and Viles, H. A. (eds), 113 – 126.

TURKINGTON, A. V. MARTIN, E. VILES, H. A. AND SMITH, B. J., 2003, Surface change and decay of sandstone samples exposed to a polluted urban atmosphere over a six-year period: Belfast, Northern Ireland: Building and Environment. **38**, 1205 – 1216.

TURKINGTON, ALICE. V. PHILLIPS, JONATHAN. D. AND CAMPBELL, SEAN. W., 2005, Weathering and landscape evolution: Geomorphology. **67**, 1 – 6.

ULUSOY, M., 2007, Different igneous masonry blocks and salt crystal weathering rates in the architecture of historical city of Konya: Building and Environment. **42**, 3014 – 3024.

VADLANI, PRAVEEN V. MATHEWS, ALEXANDER P. AND KARR, GREG S., 2007, Low-cost propionate salt as roadm deicer: evaluation of cheese whey and other media constituents: World Journal of Microbiology and Biotechnology. **24**, 825 – 832.

VALDEON, LUIS. DE FREITAS, M. H. AND KING, M. S., 1996, Assessment of the quality of building stones using signal processing procedures: Quarterly Journal of Engineering Geology. **29**, 299 – 308.

VALENZA II, JOHN J. AND SCHERER, GEORGE. W., 2007, Mechanism for salt scaling of a cementitious surface: Materials and Structures. **40**, 259 – 268.

VALENZA II, JOHN. J. AND SCHERER, GEORGE. W., 2007A, A review of salt scaling: I. Phenomenology: Cement and Concrete Research. **37**, 1007 – 1021.

VALENZA II, JOHN. J. AND SCHERER, GEORGE. W., 2007b, A review of salt scaling II: Mechanisms: Cement and Concrete Research. **37**, 1022 – 1034.

VALLET, J. M. GOSSELIN, C. BROMBLET, P. ROLLAND, O. VERGÈS-BELMIN, V. AND KLOPPMANN, W., 2006, Origin of salts in stone monument degradation using sulphur and oxygen isotopes: First results of the Bourges cathedral (France): Journal of Geochemical Exploration. **88**, 358 – 362.

VAN BRAKEL, J., 1980, mass transfer in convective drying: Advanced Drying. **1**, 217 – 267.

VASCONCELOS, G. LOURENÇO, P. B. ALVES, C. A. S. AND PAMPLONA, J., 2008, Ultrasonic evaluation of the physical and mechanical properties of granites: Ultrasonics. **48**, 453 – 466.

VAZQUEZ, P. ALONSO, F. J. MOLINA, E. CULTRONE, G. BLANCO, M. AND ZAMORA, I., 2013, Evaluation of the petrophysical properties of sedimentary building stones in order to establish quality criteria: Construction and Building Materials. **41**, 868 – 878.

VERAN-TISSOIRES, S. MARCOUX, M. AND PRAT, M., 2012, Discrete Salt Crystallization at the Surface of a Porous Medium: Physical Review Letters. **108**, 1 – 4.

VILES, HEATHER. A., 2001, Scale issues in weathering studies: Geomorphology. **41**, 63 – 72.

VILES, HEATHER. A., 2002, Implications of future climate change for stone deterioration: Geological Society, London, Special Publications. **205**, 407 – 418.

VILES, H. A. AND GOUDIE, A. S., 2007, Rapid salt weathering in the coastal Namib desert: Implications for landscape development: Geomorphology. **85**, 49 – 62.

WANG, KEJIN. NELSEN, DANIEL. E. AND NIXON, WILFRID. A., 2006, Damaging effects of deicing chemicals on concrete materials: Cement and Cocnrete Composites. **28**, 173 – 188.

WARKE, P. AND CURRAN, P., 2003, Condition assessment for building stone conservation: A staging system approach: Building and Environment. **38**, 1113 – 1123.

WARKE, P. A. MCKINLEY, J. AND SMITH, B. J., 2006, Variable weathering response in sandstone: factors controlling decay sequences: Earth Surface Processes and Landforms. **31**, 715 – 735.

WARKE, P. AND MCKINLEY, J., 2011, Scale issues in geomorphology, Editorial: Geomorphology. **130**, 1 – 4.

WARKE, P. A. SMITH, B. J. AND LEHANE, E., 2011, Micro-environmental change as a trigger for granite decay in offshore Irish lighthouses: implications for the long-term preservation of operational historic buildings: Environmental Earth Sciences. 63, 1415 - 1431

WASHBURN, EDWARD. W., 1921, The Dynamics of Capillary Flow: Physical Review. **17**, 273.

WATERS, COLIN. N., 2010, Carboniferous Geology of Northern England: British Geological Society, 1 – 20.

WEATHER UNDERGROUND WEBSITE., (www.weatherunderground.com). Accessed 2014.

WELLMAN, H. W. AND WILSON, A. T., 1965, Salt Weathering, a Neglected Geological Erosive Agent in Coastal and Arid Environments: Nature. **205**, 1097 – 1098.

WENTWORTH, C. K., 1922, A scale of grade and class terms for clastic sediments: The Journal of Geology. **30**, 377 – 392.

WEYL, P. K., 1959, Pressure solution and the force of crystallization – A phenomenological theory: Journal of Geophysical Research. **64**, 2001 – 2025.

WILLIAMS, R. B. G. AND ROBINSON, D. A., 1981, Weathering of sandstone by the combined action of frost and salt: Earth Surface Processes and Landforms. **6**, 1 – 9.

WILLIAMS, R. B. G. AND ROBINSON, D. A., 2001, Experimental frost weathering of sandstones by various combinations of salts: Earth Surface Processes and Landforms. **26**, 811 – 818.

WILSON, M. J. WILSON, L. AND PATEY, I., 2014, The influence of individual clay minerals on formation damage of reservoir sandstones: a critical review with some new insights: Clay Minerals. **49**, 147 – 164.

WRAY, R. A. L., 1997, A global review of solutional weathering forms on quartz sandstones: Earth-Science Reviews. **42**, 137 – 160.

XIE, P. AND BEAUDOIN, J. J., 1992, Mechanism of sulphate expansion I. Thermodynamic principle of crystallization pressure: Cement and Concrete Research. **22**, 631 – 641.

YARDLEY, M. J., 1984, Cross-bedding in the Permian Yellow Sands of County Durham: Proceedings of the Yorkshire Geological Society. **45**, 11 – 18.

YAVUZ, H. ALTINDAG, R. SARAC, S. UGUR, I. AND SENGUN, N., 2006, Estimating the index properties of deteriorated carbonate rocks due to freeze-thaw and thermal shock weathering: International Journal of Rock Mechanics and Mining Sciences. **43**, 767 – 775.

YAVUZ, A. B. AND TOPAL, T., 2007, Thermal and salt crystallization effects on marble deterioration: Examples from Western Anatolia, Turkey: Engineering Geology. **90**, 30 – 40.

YOUNG, ANN. R. M., 1987, Salt as an agent in the development of cavernous weathering: Geology. **15**, 962 – 966.

YOUNG, MAUREEN. E. URQUHART, D. C. M. AND LAING, R. A., 2003, Maintenance and repair issues for stone cleaned sandstone and granite building façades: Building and Environment. **38**, 1125 – 1131.

YU, SWE. AND OGUCHI, CHIAKI, T., 2010, Role of pore size distribution in salt uptake, damage, and predicting salt susceptibility of eight types of Japanese building stones: Engineering Geology. **115**, 226 – 236.

ZEDEF, VEYSEL. KOCAK, KERIM. DOYEN, ADNAN. OZSEN, HAKAN. AND KEKEC, BILGEHAN., 2007, Effect of salt crystallization on stones oh historical buildings and monuments, Konya, Central Tuley: Building and Environment. **42**, 1453 – 1457.

ZEHNDER, K. AND ARNOLD, A., 1989, Crystal growth in salt efflorescence: Journal of Crystal Growth. **97**, 513 – 521.

ZEHNDER, KONRAD. AND SCHOCH, ODILO., 2009, Efflorescence of mirabilite, epsomite and gypsum traced by automated monitoring on-site: Journal of Cultural Heritage. **10**, 319 – 330.

ZHANG, X. C. AND NORTON, L. D., 2002, Effect of exchangeable Mg on saturated hydraulic conductivity, disaggregation and clay dispersion of disturbed soils: Journal of Hydrology. **260**, 194 – 205.

ZHANG, YONG. AND ZHANG, MINGZHONG., 2014, Transport properties in unsaturated cement-based materials – A review: Construction and Building Materials. **72**, 367 – 379.

ZURAKOWSKA, MARTA. AND HUGHES, JOHN. J., 2013, Visual assessment of sandstone building façades: condition factors related to cleaning: Quarterly Journal of Engineering Geology and Hydrogeology. **46**, 459 – 467.

9 Appendix A

High speed synchrotron tomography experiments were undertaken on two sandstone types and capture the spatial differences in capillary uptake between each stone type as influenced by their pore network characteristics.

The rationale and motivation for this study was in order to visualise and understand the ‘complete’ salt crystallisation process within sandstone in 4 dimensions. The rationale was that by using this technique, it would be possible to visualise the capillary uptake of salt solution and the drying of the stone; which are two of the main processes governing salt crystallisation. By visualising these processes within the stone, it would be possible to understand the fluid-rock interactions and subsequent damage caused to the stone from the physical forces of salt crystallisation. This would have combined the different scales of visual analysis of salt crystallisation into one study, revealing the fluid and rock interactions of salt crystallisation in detail that is not possible with ‘standard’ analytical techniques, including SEM. It would also have allowed the visualisation of the entire decay process from sound, durable stone to salt-damaged stone using one stone sample, whereby the changes to the pore structure and individual, known grains could be accurately quantified in much greater precision than before.

9.1 4D Synchrotron CT analysis of capillary uptake.

Four scan-sets are discussed in this section. One set from a Blaxter sample (B) and the following three sets from three individual Locharbriggs samples (L1, L2 and L3). Samples B and L1 are scans from cropped cubic samples and samples L2 and L3 from small cores. The samples were placed through capillary uptake tests with 6M CaI_2 and scanned at 3 minute intervals on beamline i12 at the Diamond Light Source synchrotron in order to visualise the capillary transfer of salt solution within sandstone.

9.1.1 Blaxter (B)

A 3-dimensional visualisation of the open pores, 6M CaI_2 solution, grains and a cropped horizontal cross section through the middle of this block are shown in Figure 9-1. This figure shows a high percentage of filled pores with sporadic open pores of different sizes located between larger clusters of solution. Solution within this sample fills a range of pore sizes, likely the most open and accessible pores with only partial ingress into the remaining open pores as highlighted in Figure 9-1 B. Solution does not follow any petrographic structures within the sample and highlights a well distributed range of pore connectivity within the stone. Due to problems associated with the rapid rate of solution uptake, this was the only scan suitable for analysis and therefore does not provide an initial “dry” scan for comparison.

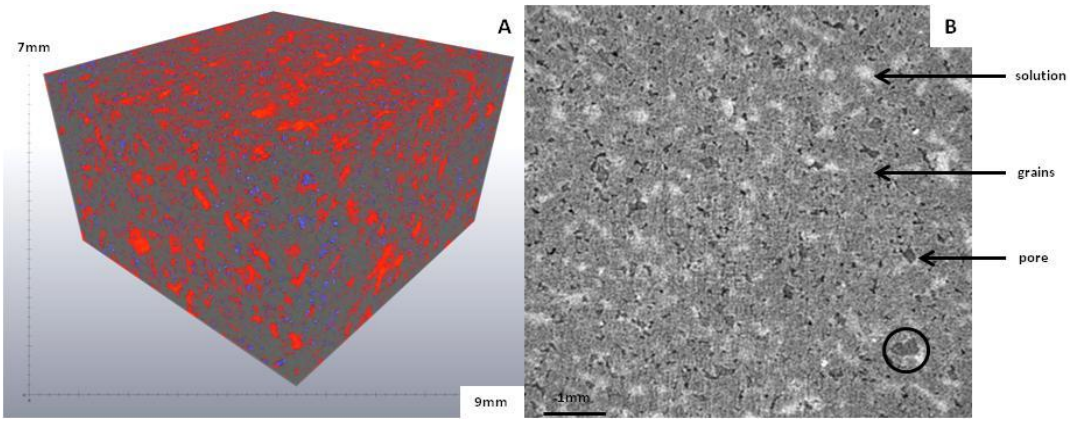

Figure 9-1: Solution distribution within Blaxter sandstone.
(A): 3D visualisation of pores (blue), solution (red) and grains (grey). (B): 2D cropped horizontal cross section showing each distinct phase. Black circle shows partial ingress of solution into an empty pore, with a white halo at the edge of the pore.

9.1.2 Locharbriggs 1 (L1)

Seven scans were acquired and were taken at three minute intervals during capillary uptake experiments. The volumes of salt solution, porosity, quartz/feldspar grains and Fe-oxides are segmented and calculated at each time interval. The initial porosity values throughout the sample are an average of ~ 17%, which varies little throughout the height of the sample. The sample was subject to capillary uptake experiments perpendicular to bedding (Figure 9-2). The data show that solution ingress and subsequent transport through the stone is significantly influenced by the pore structure, specifically in relation to pore size distributions and the internal fabric (i.e. bedding) of the stone. The solution is restricted to one half of the sample, separated by the bedding horizon and a change in rock texture. Porosity in this second layer is significantly lower and less well connected, thus inhibiting solution penetration. It is likely that this solution has hydraulic connectivity throughout the height of the sample. Initial solution ingress is restricted to a small section in the centre of the coarse grained layer.

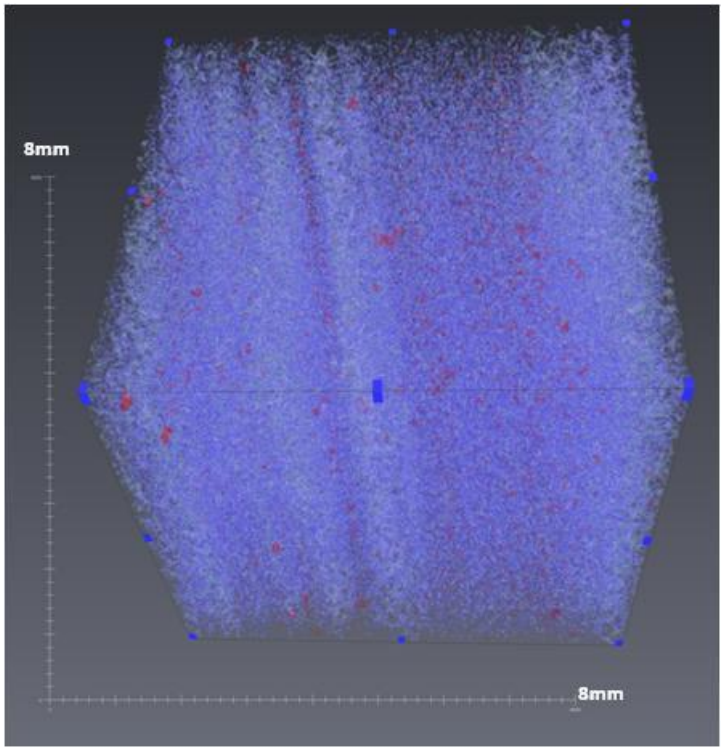

Figure 9-2: Locharbriggs sample L1 showing orientation of bedding planes relative to capillary uptake plane.

Blue represents the porosity within the stone, with light blue areas corresponding to well-connected pores. Red areas represent Fe oxides within the sample.

Figure 9-3 shows the solution volume distribution throughout the sample at each three minute interval. The plot reveals a steady increase of solution volume height and total solution volume. A noticeable peak in the solution volume is at ~ 1.032 mm in height from 12 minutes onwards. Solution volumes below this height appear very similar, with little fluctuation as to suggest that most of the accessible pores below this point were filled by 12 minutes. Open pores below this height in the 9, 12, 15, 18 and 21 minute scans however show that saturation has not been met. Rather than solution moving through the sample by consecutively filling pores, the solution instead ingresses by coating and "wetting" grains. In this process, solution uptake is highly influenced by its viscosity and surface tension. From 12 minutes onwards, vertical solution movement above 1.032 mm is supplied by solution already within the sample at a rate equal to solution ingress into the base of the stone. This rate of capillary uptake would ensure that pores below 1.032 mm would not become filled and solution volume below this height would remain stable. From both the visualisation of solution at each time step within the stone and from Figure 9-3, it is seen that lateral dispersion of solution is more prominent within the first nine minutes of solution uptake. From 12 minutes onwards, vertical intrusion of solution becomes prominent.

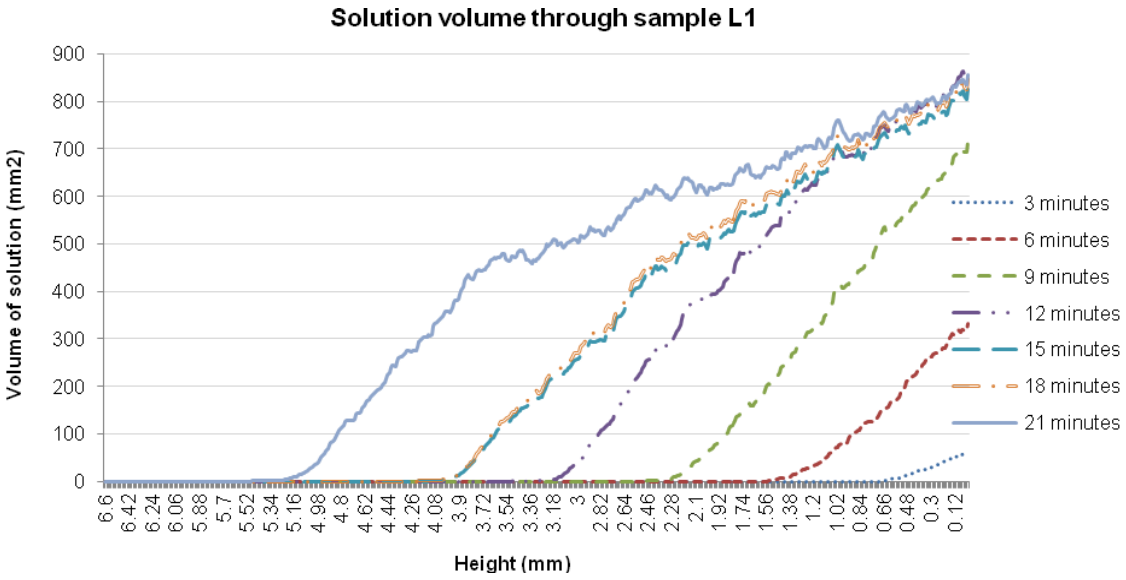

Figure 9-3: Solution volume per slice through Locharbriggs sample L1 at each time step.
Y-axis represents the area of a 2-D slice of stone that is occupied by salt solution.

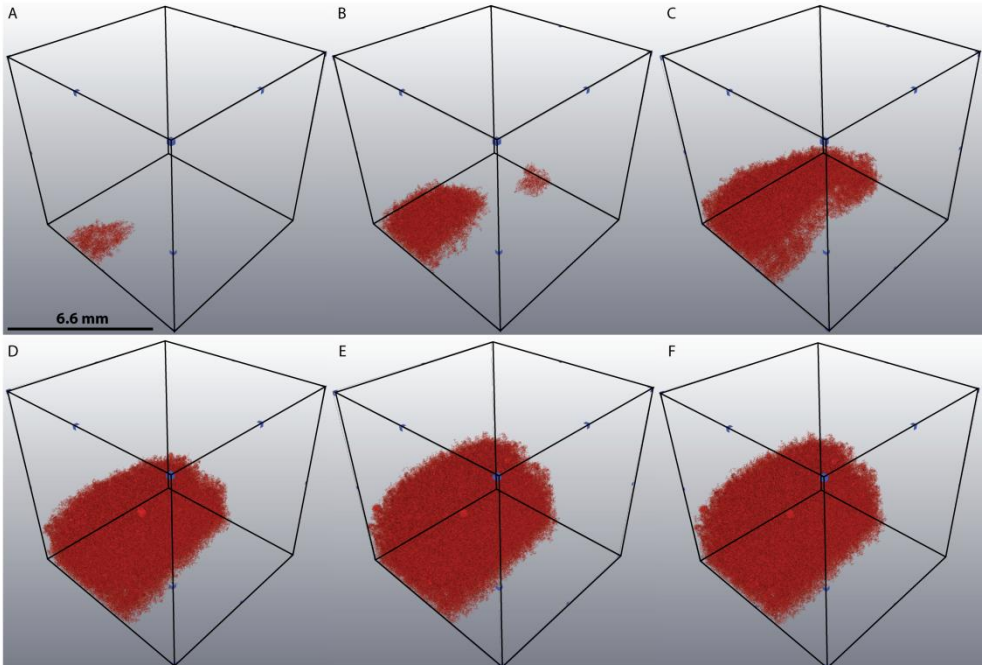

Figure 9-4: Solution movement through Locharbriggs sample L1.
(A): 3 minutes. (B): 6 minutes. (C): 9 minutes. (D): 12 minutes. (E): 15 minutes. (F) 21 minutes.

From solution visualisation at each time step it is obvious that the wetting front is not laterally consistent, with a leading ridge of solution at the centre of the volume (Figure 9-4). This solution movement is in contrast to analysis of B, whereby solution moves through the sample in individual channels as opposed to homogeneous flow with a defined wetting front.

9.1.3 Locharbriggs 2 (L2)

Sample L2 is a scan of the upper seven mm (Figure 9-5 A) of the sample and was necessary due to problems associated with the rapid uptake of solution and therefore does not represent the initial ingress of solution into the stone. Unlike sample L1, Figure 9-5 C shows evidence of complete pore filling in sample L2. The black boxes highlight the infilling of a pore with solution over the full period of scanning. The solution does not neatly “outline” the shape of the pore but instead is imaged within the pore and pore-throats that are undetected at this resolution. The red circles highlight the partial infilling of a smaller pore whereby the solution adheres to the surrounding grain surfaces due to capillary forces. These capillary forces will allow the flow of solution throughout the pore network, in which pores are hydraulically connected through this thin solution layer. Figure 9-6 shows a 3D visualisation of a

cropped section within sample L2 of the same time frames as highlighted in Figure 9-5.

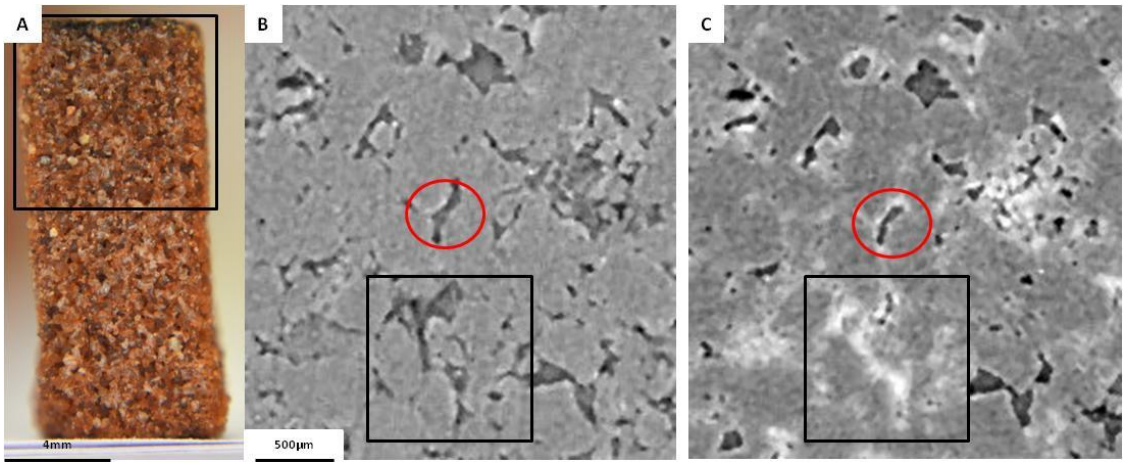

Figure 9-5: Visualisation of salt solution within 2D slices of Locharbriggs sample L2. (A): Black box highlights the scanned area of Locharbriggs sample L2. (B): Cropped area of a 2D slice of sample L2 before solution ingress. (C): The same slice after 15 minutes. Black boxes in B and C highlight the infilling of a pore. Red circles highlight the partial infilling of a pore.

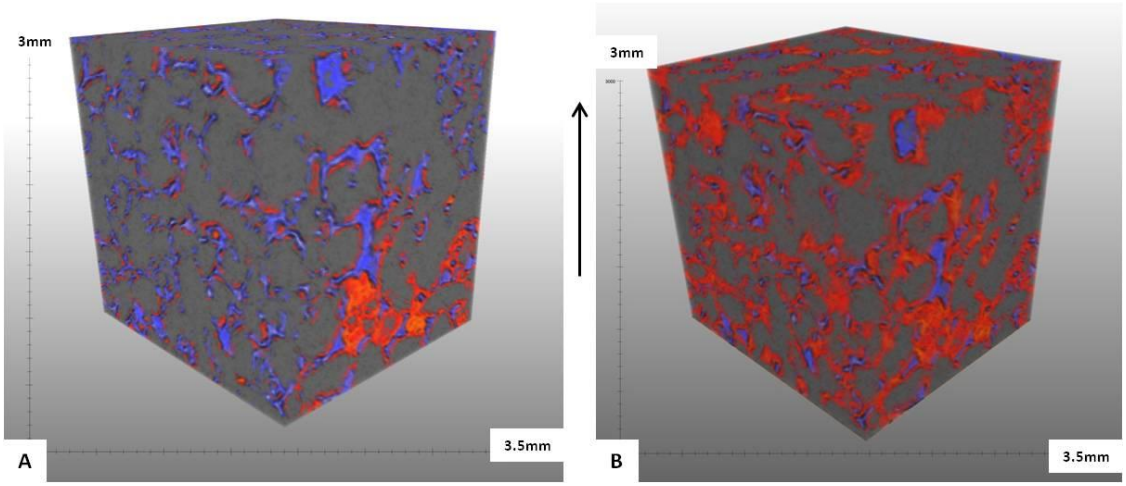

Figure 9-6: Visualisation of grains, pores and solution within Locharbriggs sample L2. Grains: grey, porosity: blue and solution: red. Black arrow shows the direction of fluid movement. (A): Initial scan showing partial infilling of large pore network and grain coating within other pores allowing solution movement through the pore network. (B): Final scan (15 minutes from the initial scan) showing pore infilling and highlighting narrow pore throats that were not initially detected.

It is clearer to see the infilling of the pore network in Figure 9-6. Here the segmentation of solution helps to define smaller pore-throats that are not detected otherwise. Figure 9-6 A shows that solution moves through the rock by capillary action, adhering to the grain surfaces while staying in hydraulic connectivity with the larger solution volume present at lower levels within the sample. Larger pores at this height are incompletely filled with solution over this short scanning period. Figure 9-7 shows the change in porosity

values through the cropped section visualised in Figure 9-6. High porosity peaks at slice numbers 39, 108 and 138 highlights the natural variation of porosity within the Locharbriggs sandstone. Figure 9-7 shows that at the start of scanning some of the porosity of the lower slices were already partially filled. The infilling of porosity is clearly shown, especially over the first six minutes of scanning. From six - nine minutes the change in porosity over each slice is compressed and shows greater evidence of the infilling of pore throats (that are not counted in the porosity values) and the capillary rise of solution, whereby only the partial filling of pores takes place due to greater capillary forces causing the vertical transportation of solution. Figure 9-8 highlights on the macro-scale the influence of bedding on the distribution of fluid movement.

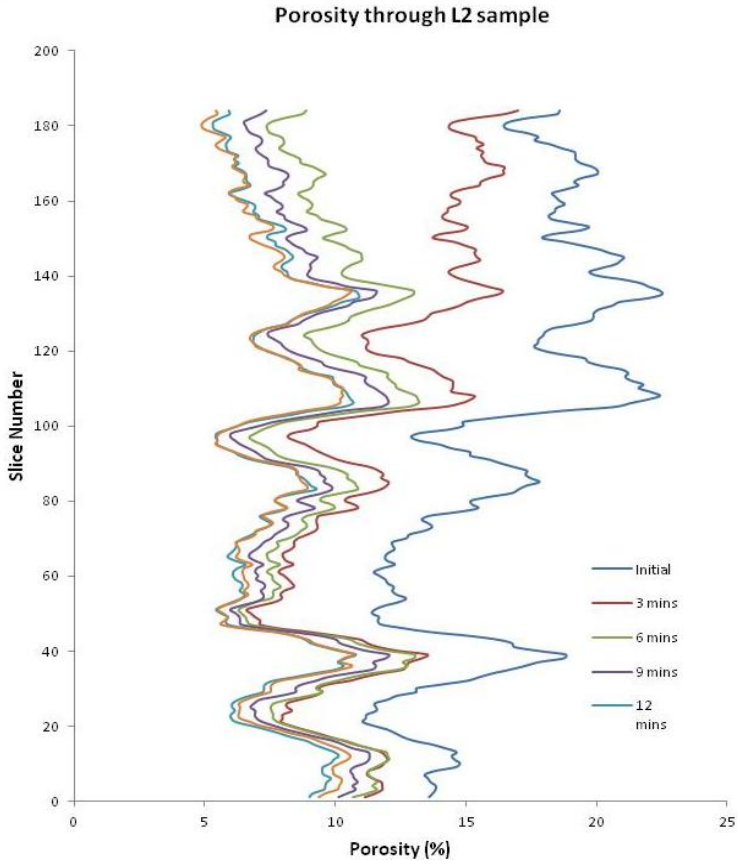

Figure 9-7: Porosity change at each time step through the cropped section of Locharbriggs sample L2 as shown in Figure 3-30.

Y-axis corresponds to the height through the sample. Each slice number = 12µm increase in height.

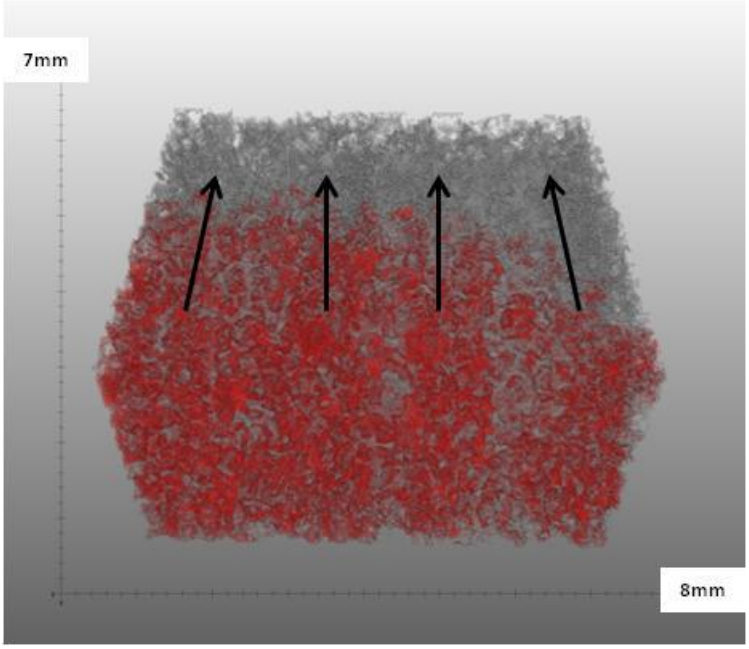

Figure 9-8: Salt solution within Locharbriggs sample L2.

Solution (red) following more porous and permeable bedding planes within the stone. Porosity is shown in grey. Arrow indicates the four distinct packages of solution separated by less permeable layers.

9.1.4 Locharbriggs 3 (L3)

Sample L3 represents the scan of the upper seven mm of the sample. It shows a comparable process of fluid movement to sample L2, whereby the flow is concentrated within more permeable layers of the stone. Preferential solution movement takes place near the edges of the sample. Figure 9-9 A and B are visualisations of the difference between two consecutive scans, showing the change in solution movement over a three minute time period. These images highlight the preferential pathways of fluid movement, indicating a lack of lateral flow. Blue areas represent pores that have lost fluid (i.e. the pores that are feeding the vertical flow) and indicate that the rate of flow is not constant throughout the full section. If the rate of flow was constant throughout the height of the sample then there would be no loss of solution in the feeder pores as they would be continually filled as solution moved through them, penetrating the open pores above.

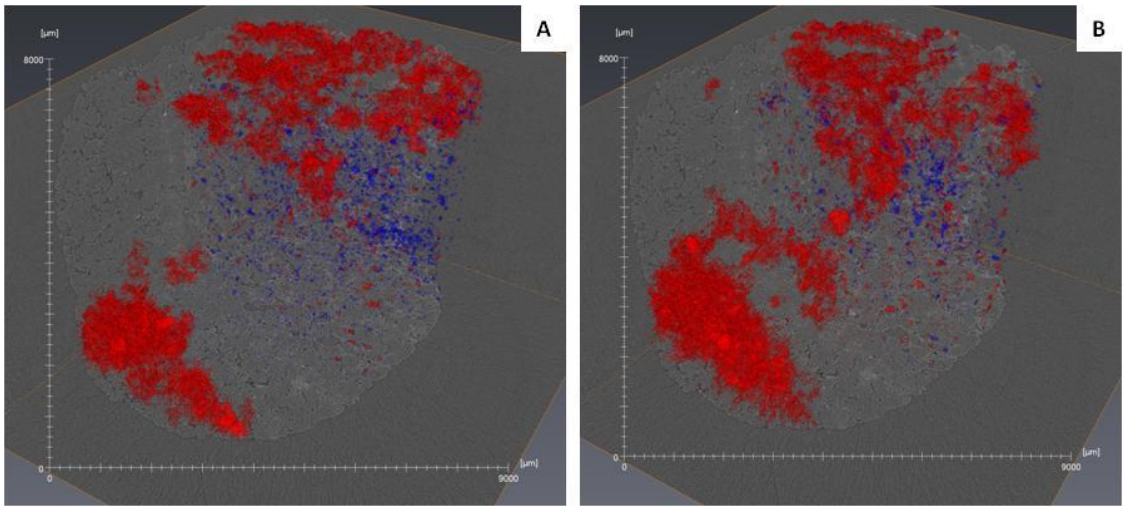

Figure 9-9: Visualisation of the difference field of solution movement between time steps.

(A): Initial scan and scan 1 over a 3 minute period. (B): Scan 1 and scan 2 over a 3 minute period (3 – 6 minutes). Red= gain of solution. Blue: loss of solution.

9.1.5 Implications of synchrotron experiments over traditional methods of measuring capillary flow

Analysis of four samples from two sandstone types shows that the uptake characteristics and flow through each sandstone type differs significantly. Specifically, the mechanisms by which solution is absorbed and transferred through the stone are comparable, however the distribution of solution within the stone is different and is influenced by pore structure. An interesting and important result from all of the Locharbriggs samples is the preferential solution uptake and movement through confined more highly permeable layers, which may be an important determinant of salt crystallisation processes. Graphs of absorbed moisture and remaining porosity indicate a high spatial variability in both the porosity and the distribution of absorbed moisture throughout the height of the samples. Importantly, capillary uptake does not occur as one homogeneous wetting front in Locharbriggs and Blaxter sandstones. Differences in the distribution of moisture between consecutive scans indicate that the rate of capillary uptake is extremely variable throughout the height of the samples and with time. This difference in the rate of capillary uptake is further highlighted in sample L3 (Figure 9-9).

Standard capillary uptake tests can only supply information on the overall volume of moisture absorption. This traditional test remains an extremely useful measurement, but does not provide spatial information relating to the distribution of moisture absorption and what pores sizes are accessed or filled first. Synchrotron analysis shows that during the initial stages of capillary uptake, grain “wetting” occurs, whereby solution is rapidly transported throughout the height of the sample by thin films of solution adhering to the grain surfaces. Furthermore, analysis of Blaxter, and Locharbriggs sample L2, highlights the selective infilling of different sized pores. After 15 minutes of capillary uptake in sample L2, larger pores remained unfilled, while there was the complete infilling of smaller pores and pore throats (< 12 μm diameter as they were not visualised).This is an important observation, because it shows that small pores are preferentially filled during the initial stages of capillary absorption. Therefore, the pores that are expected to induce greater salt crystallisation pressures are filled first, even in the absence of significant moisture volumes and under short time-periods. Additional analysis of sample L3 indicates that most of the flow is vertical, with very little lateral distribution of solution occurring during the first 20 minutes of capillary absorption.

Synchrotron analysis provides important extra insights over traditional methods into the rates and spatial distribution of capillary absorbed moisture. These extra dimensions of insight may signify important implications for the drying regimes and the location of salt crystallisation within the stone. Synchrotron analysis is not fully comparable to capillary uptake tests due to the differences in the availability of free moisture. The changing rates of flow within synchrotron specimens may have been influenced from the limited availability of solution within the saturated filter paper. However, these results remain applicable to real environmental conditions, including the capillary absorption of “road spray” and wind-driven rain, whereby there is a limited availability of free moisture.

The results of this study provide supporting evidence for already known fluid flow characteristics in Locharbriggs sandstone. It reveals that the smallest capillary pores are filled first, which although is an important finding, does

not directly relate to nor explain the behaviour of each sandstone to salt crystallisation tests within this thesis.

This study, although not comprehensive in the range of sandstones tested and does not cover the other important processes in stone weathering research, it does highlight the capabilities of this technique for further research in the field as well as the important advances in scales of research (time resolved three dimensional imaging) over more traditional techniques. The current capabilities of this technique ensure its value as an important technique in this research field, however Synchrotron tomography scanning, like every analytical technique, has several advantages and disadvantages, which must be acknowledged in order to validate the generated results.

The accessibility and cost of synchrotron use can severely limit its usefulness as a common research tool. Academic use of the Diamond Synchrotron is free within the UK subject to a successful peer-reviewed application. Upon successful application, the designated beamtime is limited to a maximum of 9 x 8hour beamline shifts, which can limit the length of experiments and provide issues for the integrity of the experiment if major problems arise (a relatively common occurrence owing to the versatility and complexity of the facility). This was an issue that was encountered during the experiment which significantly altered the final aims and outcome of the work, and subsequently lowered its significance towards the research question within the thesis. Additionally, due to the high resolution capabilities and the subsequent high volume of data acquired from of this technique, sample size, sample number and overall repeatability of experiments can be limited, which may lower its usefulness for certain applications.

10 Appendix B

10.1 Digital Image Analysis (DIA)

Maximum grain size, average grain size, grain shape and total porosity were all determined by DIA. In addition, pore shape and pore size are other important properties that can be measured using the technique. Due to problems in quantifying pore shape and size they were not measured. Table 10-1 shows the average and maximum grain sizes for the stone type analysed. Corsehill and Stanton Moor (Figure 10-1) have the lowest average grain sizes, while Locharbriggs has the highest value. Blaxter and Locharbriggs samples show the largest maximum grain sizes and Corsehill the smallest (Figure 10-2).

Stone Type	Average Grain Size (μm)	Maximum Grain Size (μm)	Standard Deviation	Variance (%)
Blaxter	166	927	93	56
Corsehill	104	442	55	53
Cullalo	140	585	66	48
Doddington	145	627	88	61
Locharbriggs	191	1050/832	109	57
Stanton Moor	107	568	69	64

Table 10-1: Average and maximum grain sizes for each measured sandstone.

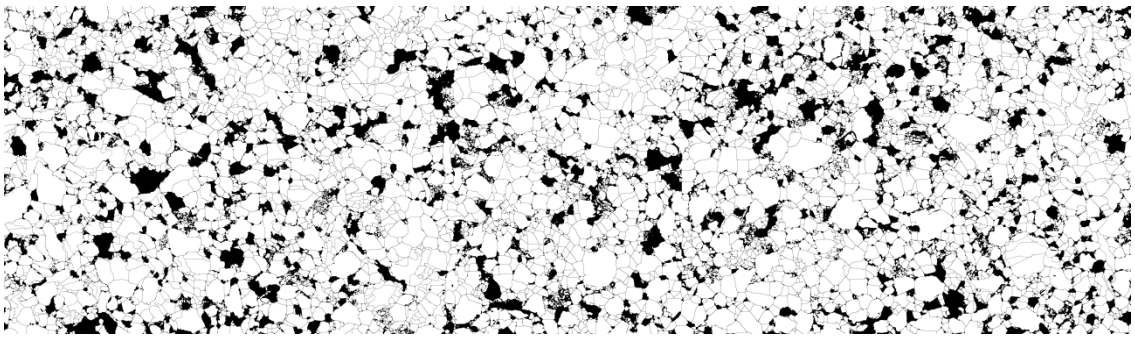

Figure 10-1: Montage of Stanton Moor sandstone pore structure after segmentation and watershed filters. Grains are white, pores are black. Field of view is 12.78mm x 3.62mm.

Using the Wentworth grain size classification (Table 10-2), Locharbriggs, Doddington and Blaxter sandstones are classified as medium grained and Corsehill, Stanton Moor and Cullalo samples described as very fine grained - fine grained sandstones. Corsehill contains 42.3% of all measured grains within the 63 μm – 125 μm range and 27.5% <63 μm. A lower threshold of ~30 μm grain size was used in order to eliminate areas of broken lithic fragments and clays. This lower limit incorporates coarse silt particles and was

determined as satisfactory for the types of sandstones used. Cullalo contains 94.3% of grains <250 μm, with only 10.7% <63 μm, while Locharbriggs contains 27.3% of grains between 250 μm - 500μm. Excluding Corsehill and Stanton Moor, every remaining sandstone has a majority of grains between 125 μm – 250 μm.

Grain Size (μm)	Wentworth Size Class
2000	Very coarse sand
1000	Coarse sand
500	Medium sand
250	Fine sand
125	Very fine sand
63	Coarse silt

Table 10-2: Wentworth grain size classification.

Grain shape was also determined using a circularity index; a scale running between 0.1 (very angular) – 1 (a perfect circle) (Figure 10-3). Cullalo contains the greatest percentage of well rounded grains, with 50.9% of all grains having a circularity >0.7. This is in contrast to Stanton Moor, which contains 46% of grains with a circularity <0.6. This metric is a measure of all segmented grains and will include quartz grains, feldspar grains and micas. It is likely that the most immature sandstones will contain the greatest spread of grain shape, with the inclusion of micas leading to a greater percentage of low circularity values.

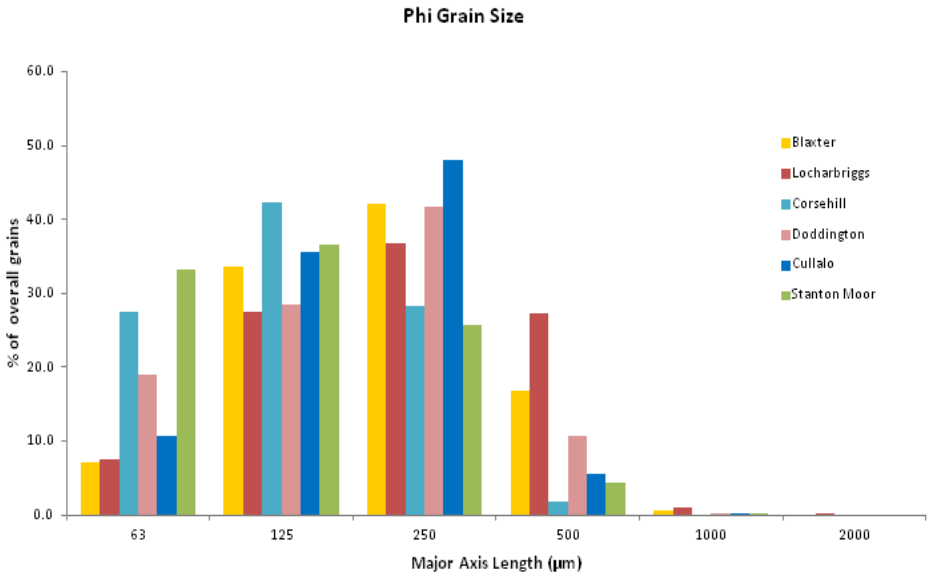

Figure 10-2: Grain size plot of quartz, feldspar and mica for each sandstone.

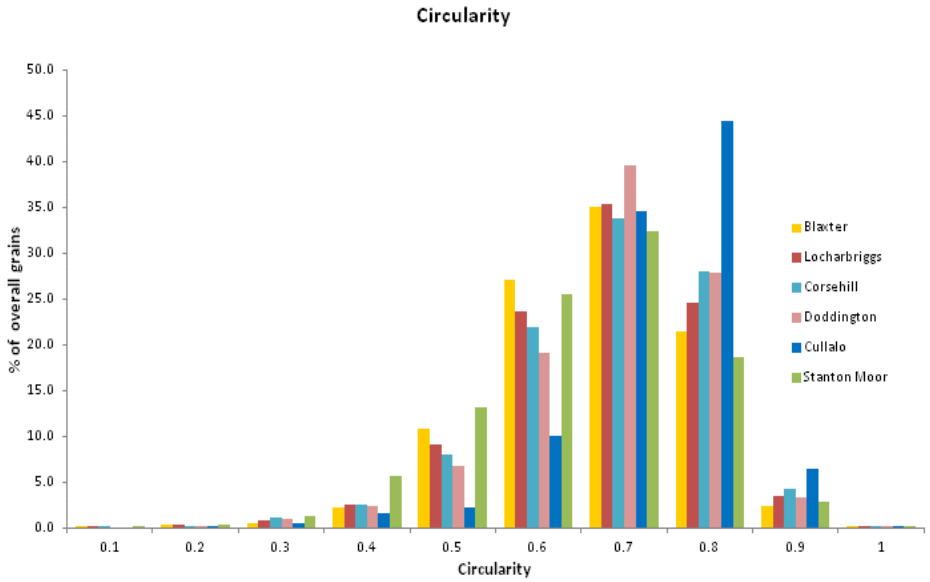

Figure 10-3: Plot of grain circularity of quartz, feldspar and mica for each sandstone.

11 Appendix C

11.1 Salt Crystallisation Test (I) Pilot Study

This test procedure followed the British standard for determination of resistance to salt crystallisation (BS EN12370:1999) as described in Chapter 2. Eight sandstones were tested against the effects of three salts (NaCl, $CaCl_2$ and a chloride blend ($NaCl.MgCl_2.6H_2O$)) over 36 crystallisation cycles. The resistance to salt crystallisation is expressed by the weight change, and damage to the stone surface as recorded by photography after every cycle (as required by the British standard).

11.1.1 Weight change

The change in weight of each sample was monitored after every cycle and reveals a typical evolution of weight change throughout the test, characterised by three distinct stages. An expected increase in weight was registered across every sample between cycle 1 and cycle 10. This initial stage is a result of the continued crystallisation of salts within the free porosity of the stone. Initially, all of the pores that can be accessed by salt solution will be partially filled. During this initial stage, evaporation will take place on the stone surface causing the salt to also crystallise as harmless efflorescence.

Stage two begins at the critical point where pore clogging near the stone surfaces disrupts the pathway for solution movement to the stone exterior. It is at this point, when the evaporation boundary retreats into the stone interior, that vapour diffusion controlled evaporation begins. As pores are continually filled with salt crystals, the space available for further crystallisation is reduced and the initial steep gradient of weight increase flattens out. It is at this point that the “Riecke principle” may start to govern salt crystallisation within the stone (Theoulakis and Moropoulou, 1999). The “Riecke principle” explains that any unconfined crystals within the stone will lower any generated supersaturation ratios and grow at the expense of confined crystals. Weight change during this second stage is a function of the competition between salt uptake and the loss of sandstone material. For

most samples, stage two occurs between cycles 6 and 7, and in the Stanton Moor, Cullalo, Giffnock, Scotch Buff and Clashach samples continues to cycle 36, with the absence of a distinctive third stage of weight loss.

The third stage of weight evolution starts when the gradient of weight change shows a negative trend and weight falls. The amount of weight loss caused by salt crystallisation damage exceeds any further salt uptake and net weight loss is recorded. Locharbriggs, Blaxter, Scotch Buff, Bonhill, Cullalo and Giffnock all experience some loss of weight across every salt, while only Blaxter, Locharbriggs, Bonhill and Cullalo experience net weight loss at any point.

11.1.1.1 ***NaCl***

Stanton Moor, Cullalo and Clashach NaCl samples reached maximum weight gain between 6-12 cycles, with limited weight loss recorded subsequently. Giffnock and Scotch Buff had the greatest salt uptake rates, reaching the second stage plateau after 6 and 7 cycles, respectively. Similar rates of salt uptake were recorded for every other sample, with Stanton Moor having the greatest weight increase. Clashach had the lowest total uptake of NaCl, reflecting its low porosity and water absorption values. The remaining samples all had similar values of weight gain.

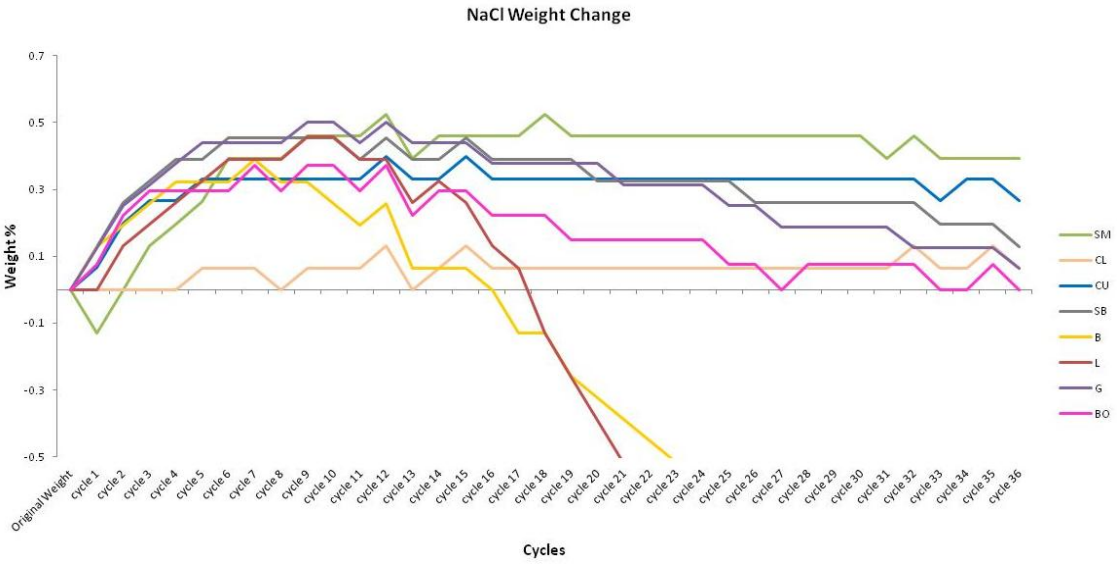

Figure 11-1: Weight percentage evolution of samples treated with NaCl in respect to their original weights. Y axis is stopped at -0.5 in order to highlight the small differences between six samples.

SM: Stanton Moor, CL: Clashach, CU: Cullalo, SB: Scotch Buff, B: Blaxter, L: Locharbriggs, G: Giffnock, BO: Bonhill.

Locharbriggs and Blaxter samples had the greatest material loss, with a maximum accumulated loss of 3.45% and 1.75%, respectively. Giffnock, Bonhill and Scotch Buff samples also experienced weight loss, with Bonhill experiencing no net weight change after the test. Blaxter had the shortest stage two, with weight loss initiated after only 8 cycles. Locharbriggs started to lose weight after 9-10 cycles, while stage three did not occur until after cycle 15 in Scotch Buff. Clashach, Cullalo and Stanton Moor samples had the lowest percentage of weight loss, significantly lower than Blaxter and Locharbriggs samples. The percentage weight change is illustrated in Figure 11-1.

11.1.1.2 *Chloride Blend*

Similar trends of weight change were recorded for the chloride blend samples, with an increase over NaCl treated samples in both the absorption rate and weight gain for most sandstones (minus Giffnock and Cullalo). Blaxter and Giffnock samples show near-identical weight change graphs to their respective NaCl samples. Cullalo and Bonhill show the greatest difference in their weight change, experiencing greater weight loss than their corresponding NaCl samples. Stanton Moor had the greatest weight increase, while Clashach had the lowest. Both of these samples continued to be unaffected by further salt absorption after 23 and 3 cycles, respectively, and experienced negligible weight loss. Maximum weight gain is reached at similar times for all sandstones; with the onset of stage three initiated earlier in Bonhill and later in Locharbriggs (Figure 11-2).

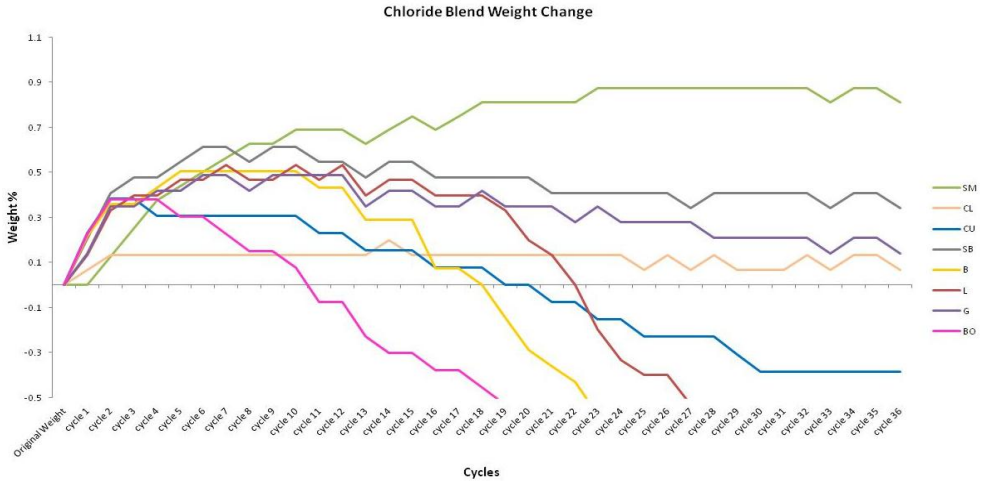

Figure 11-2: Weight percentage evolution of samples treated with chloride blend salt. SM: Stanton Moor, CL: Clashach, CU: Cullalo, SB: Scotch Buff, B: Blaxter, L: Locharbriggs, G: Giffnock, BO: Bonhill.

11.1.1.3 *$CaCl_2$*

Results from $CaCl_2$ samples show a significant contrast to both NaCl and chloride blend salts. $CaCl_2$ caused a significantly greater weight gain across every sandstone, with also faster uptake rates recorded across each sample (Figure 11-3). No significant weight losses are recorded for any stones, with only Blaxter experiencing a stage three weight loss. The remaining samples reach a weight plateau after 8 cycles, with little weight change recorded subsequently. Locharbriggs absorbed the greatest percentage of $CaCl_2$, with Stanton Moor, Scotch Buff and Blaxter also experiencing high absorption values and Clashach again absorbing the lowest percentage.

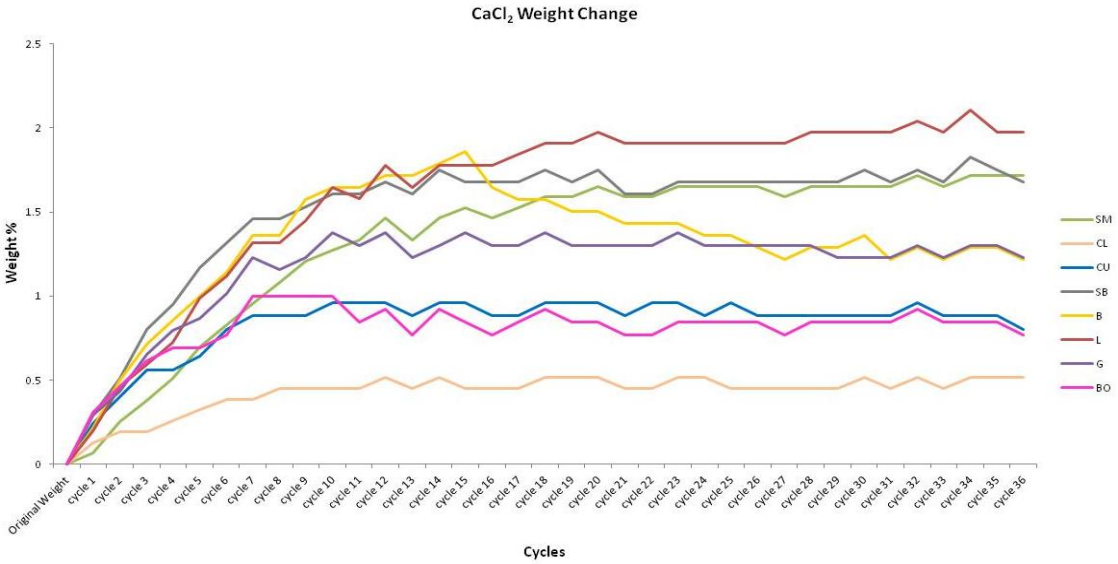

Figure 11-3: Weight percentage evolution of $CaCl_2$.

SM: Stanton Moor, CL: Clashach, CU: Cullalo, SB: Scotch Buff, B: Blaxter, L: Locharbriggs, G: Giffnock, BO: Bonhill.

11.1.1.4 *Weight Change Summary*

Locharbriggs had the greatest weight change with each salt type, experiencing the highest weight loss for NaCl (Figure 11-4) and chloride blend (Figure 11-5), and the greatest salt weight gain with $CaCl_2$ (Figure 11-6). Stanton Moor samples had the greatest NaCl and chloride blend enrichment, and the highest average weight increase across all three salts. Clashach samples showed the lowest percentage of salt uptake across each salt type and experienced no visual decay. The trend in Stanton Moor and Locharbriggs samples is likely controlled by the petrographic properties of the stones, while $CaCl_2$ is the controlling factor in samples immersed in this salt. Physical observations of each sandstone suggest that the low salt absorption in

samples, including Clashach, was not caused by an equilibrium being met between salt enrichment and the physical loss of material. Rather, this low absorption is controlled by pore blocking from salts.

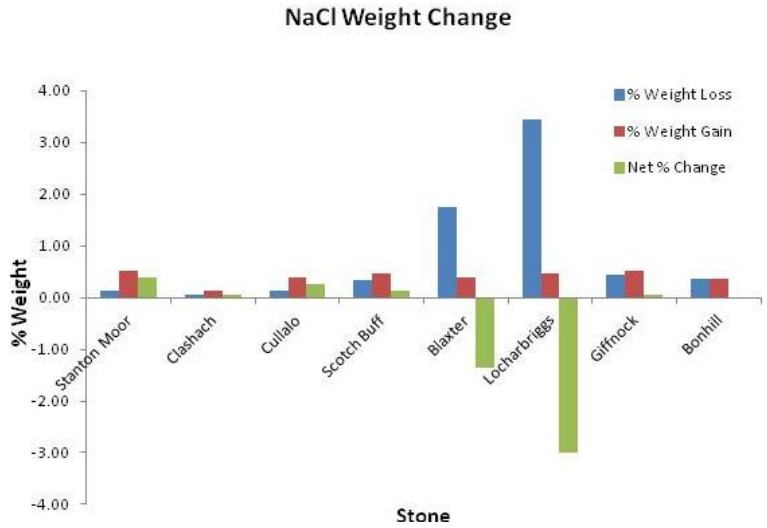

Figure 11-4: NaCl weight change after 36 cycles.

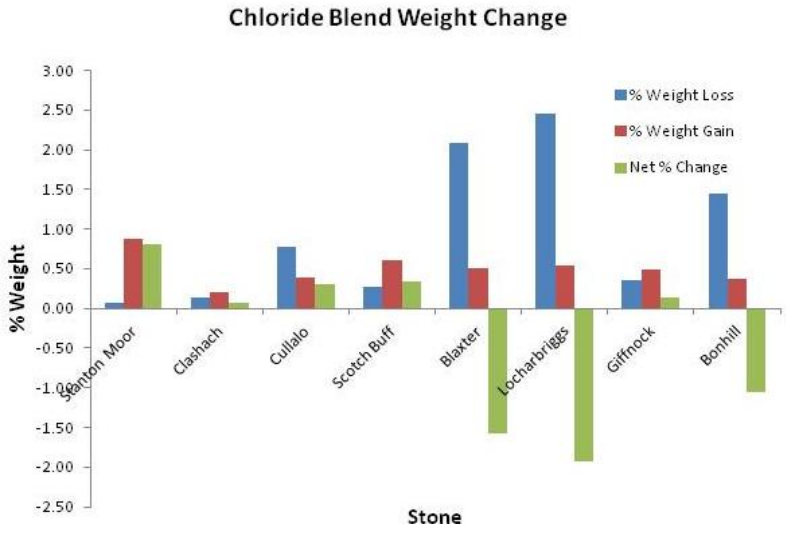

Figure 11-5: Chloride blend weight change after 36 cycles.

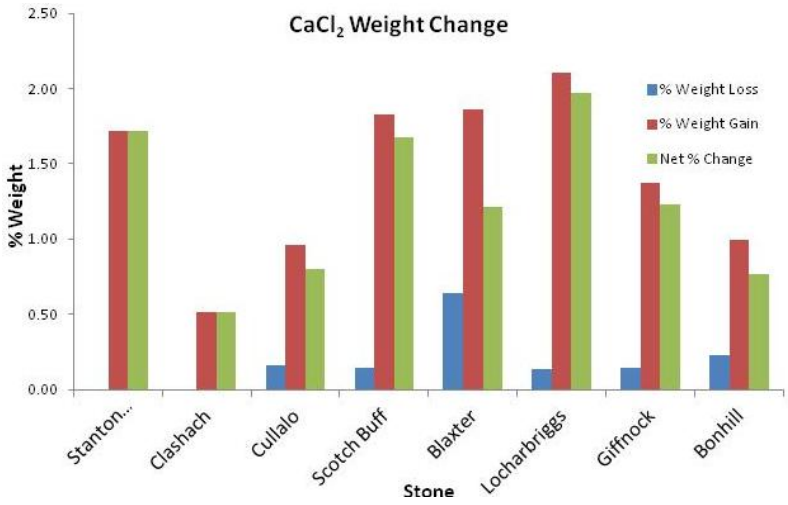

Figure 11-6: $CaCl_2$ weight change after 36 cycles.

11.1.2 Visual change

The physical alteration of each stone sample was documented photographically after every cycle. Throughout the experiment, a progressive discolouration of all chloride blend samples was evident. This discolouration was apparent on all top faces of the samples and was most significant on the Bonhill, Stanton Moor and Locharbriggs samples. Colour measurements were performed at the end of the test. Four colour parameters were measured: lightness (L*), red-green (a*), yellow-blue (b*) and total change (E) in relation to the original (un-weathered) samples.

$CaCl_2$ caused a consistent surface darkening (-L* values) in all but the Stanton Moor sample. As expected, every chloride blend sample showed negative a* values, indicative of movement towards the green value of the red-green spectrum. This change was most significant in Locharbriggs (a*: -6.53, b*: -4.63), Stanton Moor (a*: -7.13, b*: -7.46) (Figure 11-7 and Figure 11-11) and Bonhill (a*: -11.01, b*: -9.01). Every other sample showed lower a* and b* values, with b* values showing little deviation from 0. This green discolouration is caused by the colourant mixed with chloride blend salt forming a thin efflorescence on the surface. Microscope observations of the Bonhill sample suggest that this discolouration penetrates less than a millimetre beneath the surface, with discolouration focussed on layers in the Cullalo and Locharbriggs samples (Figure 11-8). These discoloured layers may correspond to areas of petrographic variation such as the alignment of grains and increased porosity, allowing a greater enrichment of salt in these layers.

Interestingly, every $CaCl_2$ sample bar Stanton Moor showed positive a* and b* values, with positive b* values indicative of movement towards the yellow value of the blue-yellow spectrum. All of these samples (minus Stanton Moor and Bonhill) show very similar a* and b* values, with the Bonhill sample displaying considerably higher a* and b* values (a*: 14.99, b*: 19.69) and the Stanton Moor displaying negative a* and b* values (a*: -0.18, b*: -2.29). $CaCl_2$ also caused a greater total change on average across each stone type, with only the Stanton Moor and Bonhill samples showing greater total change with the chloride blend and NaCl respectively. Although the Stanton Moor sample absorbed the second greatest amount of $CaCl_2$, it experienced the least

colour change. NaCl samples displayed no significant trends across each stone type. However both the red sandstones, Bonhill and Locharbriggs, had the greatest total colour change and showed very similar trends across each colour parameter.

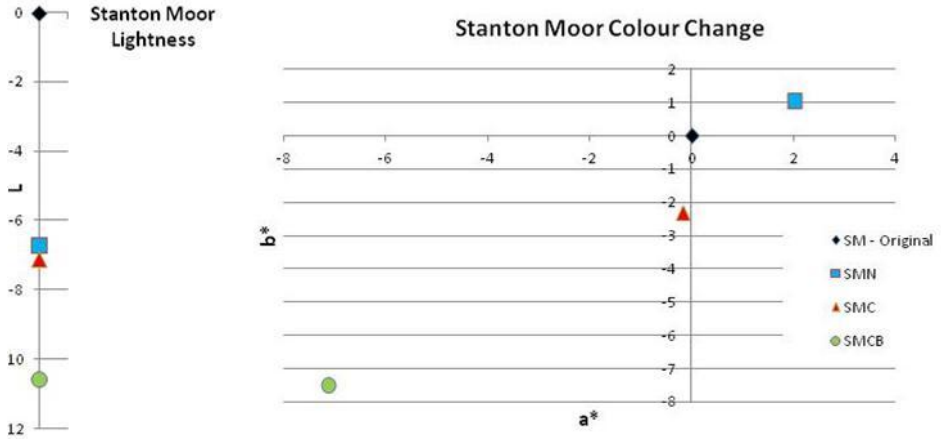

Figure 11-7: Stanton Moor colour change.

L: lightness value. Positive represents a move towards white and negative values represents a move towards black. a*: red-green spectrum. Positive change represents a move towards red and negative values represents a move towards green. b*: yellow-blue spectrum. Positive change represents a move towards yellow and negative change represents a move towards blue. The zero marker represents the original base-line value that each sample is compared against.

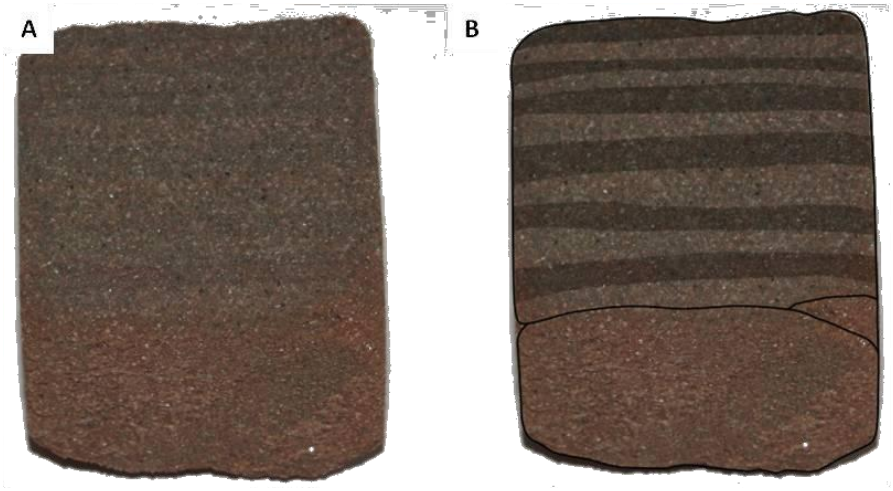

Figure 11-8: Colour change of sample LCB_{1post}.

(A): Sample LCB_{1post} on completion of the test after 36 cycles. (B) Discoloured bands are highlighted. The chloride blend caused a consistent "greening" of all samples, with most discolouration focussed within the bedding planes of the Locharbriggs sandstone. Samples are 40mm cubes.

Various salt efflorescence phenomena were evident across the majority of NaCl samples and were apparent on Bonhill (BON_{1post}), Giffnock (GN_{1post}), Cullalo (CLN_{1post}), Locharbriggs (LN_{1post}), Clashach (CHN_{1post}) and Blaxter (BN1post) samples to varying degrees. Efflorescence is located predominantly on the top faces of the stones, with Bonhill (BON_{1post}) showing efflorescence

on all six faces and Cullalo (CLN_{1post}) displaying only moderate efflorescence located in narrow layers within the stone. Sample LN_1 started to show initial efflorescence on the bottom face after eight cycles and sample LCB_{1post} after only three cycles. No significant trends are observed, although on average stones containing a larger range of pore sizes show slightly more efflorescence, while efflorescence is absent from all $CaCl_2$ samples.

From observation and photography, two main decay patterns are observed. Various stones are characterised by a progressive rounding and smoothing of the corners and edges of the cubes, described as 'homogeneous decay', occurring across every sample that was susceptible to alteration. This process is caused by granular decay and the loss of individual quartz grains as drying takes places across all six faces of the stone; this process is unlikely to take place in stone blocks that are incorporated into a building façade. The BN_1 and $BOCB_1$ samples are shown in Figure 11-9, and show granular decay of the sample corners and edges.

The second decay pattern is differential decay within layers in Cullalo and Locharbriggs samples (Figure 11-9), caused by heterogeneities in the rock. LN_1, LCB_1 and $CLCB_1$ samples show this progressive decay pattern owing to the loss of quartz grains, focussed in dark layers of grain alignment and smaller pore sizes within the stone.

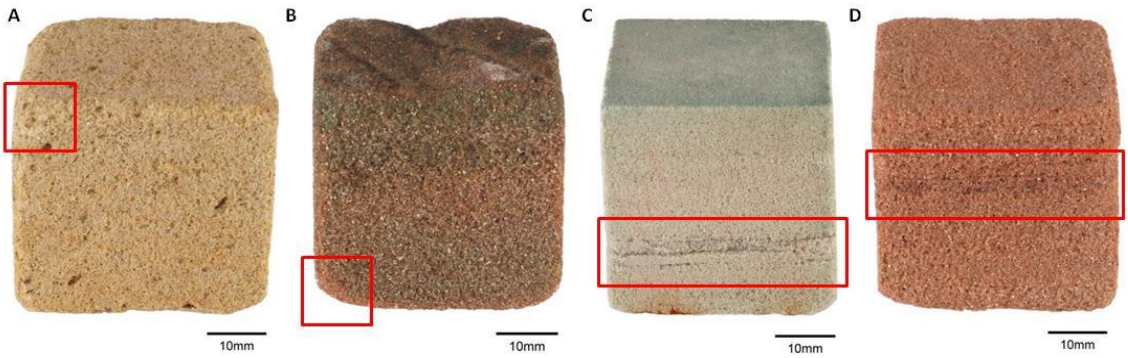

Figure 11-9: Post crystallisation test photographs of samples at the end of the test. (A): BN_{1post}, (B): $BOCB_{1post}$, (C): $CLCB_{1post}$, (D) LN_{1post}. Red boxes highlight main areas of differential decay. (A) and (B) are characterised by the rounding of the corners and edges of the samples, while material loss in (C) and (D) is focussed along bedding planes.

In most samples the detachment of material regularly took place during the process of complete immersion in salt solution. This detachment was caused

by the uptake of salt solution displacing trapped air in the pore spaces. As the air was forced out of the stone, material initially weakened by earlier salt crystallisation was displaced and became detached. It must also be noted that during the immersion stage of each cycle, significant expulsions of air were observed for samples exposed to NaCl and the chloride blend solutions. This was in contrast to $CaCl_2$ samples, where only a small volume of air was visibly displaced from the stone. Additional analysis after two hours immersion during cycle 21 confirmed that all $CaCl_2$ samples showed a smaller percentage of weight increase when compared to NaCl and chloride blend samples, indicating a lower absorption of $CaCl_2$ solution across each stone. A decrease in the absorption of $CaCl_2$ solution is attributed to salt related features of the stone such as increased pore clogging and a reduction in available and effective pore spaces caused by considerable salt crystallisation throughout the full stone.

11.1.3 Salt crystallisation damage to the grain structure

Dry-Cut Samples	Thin Section Samples
BCB_{1post}	BN_{1post}
$SMCB_{1post}$	LN_{1post}
$CLCB_{1post}$	
LN_{1post}	
LC_{1post}	
SBC_{1post}	

Table 11-1: Samples analysed by SEM.
Dry-cut sample analysis reveals information on salt distribution and morphology, while thin section analysis took place following dry-cut analysis in order to better understand changes to the pore network within the two most affected samples.

SEM analysis of several dry-cut samples (stone block sawn without lubricant in order to preserve salt crystals) shows the morphology, crystallisation sites and damage caused by each salt. The studied samples are listed in Table 11-1. In all but one of the investigated NaCl and chloride blend contaminated stones, salt was found as accumulations filling pores and crystallising on the surface of quartz grains. NaCl (as also crystallised in the chloride blend samples) was not evident in large accumulations at depth within these samples, penetrating only to around 500-800µm beneath the surface. Smaller traces of the salt were evident towards the centre of the stones. Fracturing

of quartz grains and quartz overgrowths are evident in the LN_{1post} sample (Figure 11-10), with salt crystals being found within some of these fractures. In the $CLCB_{1post}$ sample, most of the salt accumulation is found near the edges of the sample but is discontinuous throughout. Salt crystallisation is related to a weak microscopic fabric in the stone, with thin bands of high salt accumulation evident along the edges of the sample (Figure 11-10 B). In all studied samples there is a distinct change in microscopic texture between the edges and the centre of the stone. There is a more open pore structure at the edges, as decay is by the loss of individual quartz grains. SEM images of salt distribution in Locharbriggs, Cullalo, Blaxter and Scotch Buff sandstones are in Figure 11-10.

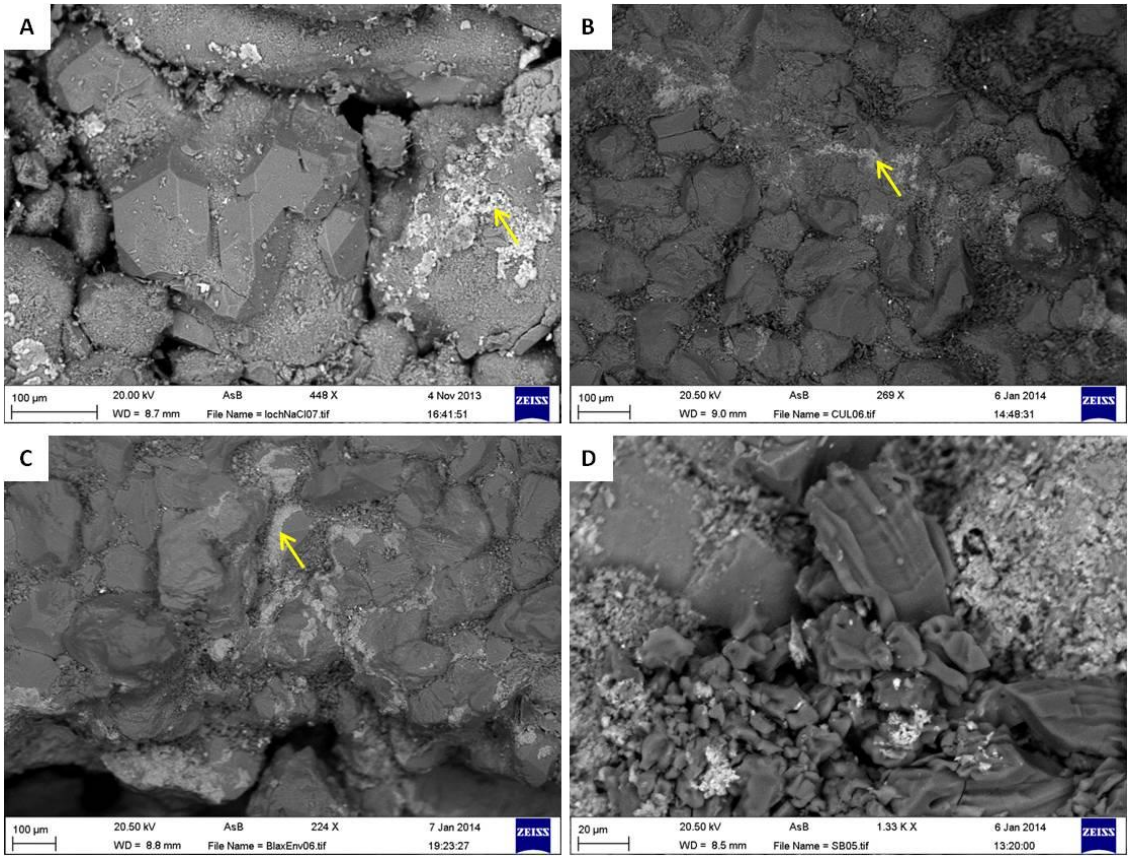

Figure 11-10: Backscatter electron SEM images of dry-cut sandstone samples.

(A): LN_{1post} sample showing a salt crust coating a grain of quartz (yellow arrow) and a broken quartz overgrowth. (B): Yellow arrow indicates the differential crystallisation of halite crystals within a narrow plane in the $CLCB_{1post}$ sample. (C) Salt crust accumulating on the edge of the BCB_{1post} sample, as highlighted by the yellow arrow. (D) $CaCl_2$ crystals (dark crystals) within the SBC_{1post} sample.

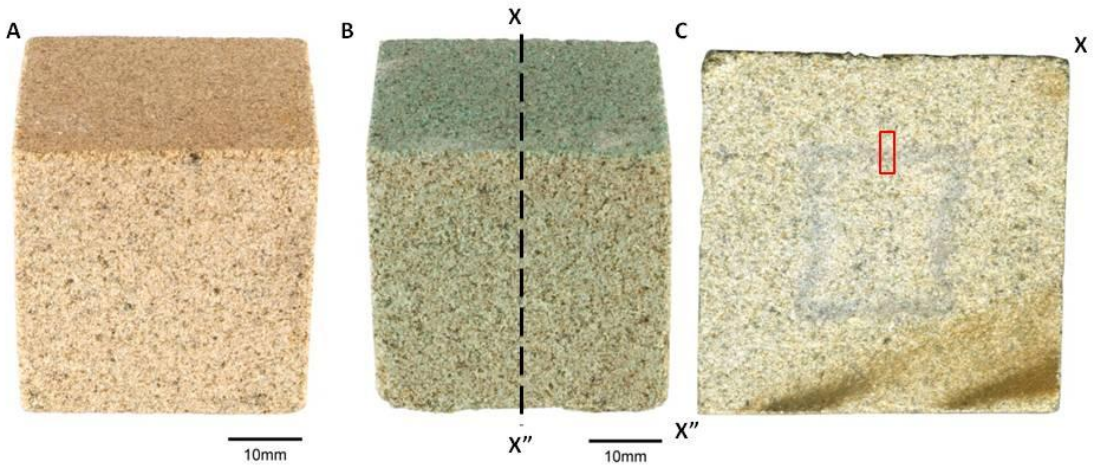

Figure 11-11: Colour changes to $SBCB_{1post}$ and internal cross section from the same sample.
(A) Stanton Moor control sample showing the original colour of the stone. (B) Colour change of $SMCB_{1post}$ sample after 36 cycles. (C) SEM analysed internal cross section of $SMCB_{1post}$ sample showing the dark salt horizon, as described below. X and X” denote the cross section path.

Figure 11-11 shows the colour change experienced by the $SMCB_{1post}$ sample and an interior section of the stone. The stone interior contains an unusual dark pattern that follows the external shape of the sample block and is visible in hand specimen. This same pattern was also found in the SMN_{1post} sample. SEM analysis has shown that this dark layer corresponds to an area of high salt accumulation. In contrast to Cullalo (CLN_{1post}), Locharbriggs (LN_{1post}) and Blaxter (BN_{1post}) samples, salt in Stanton Moor is as small individual crystals. Crystals have an average size of 11 μm^2 and were found in areas of high clay content and in fractures, joints and pores between quartz grains. Salts were found on both sides of the boundary and were widely associated with kaolinite throughout. Due to the small size and distance between each salt crystal, associated damage was absent. A mapped section through the layer and SEM images of halite distribution within the $SMCB_{1post}$ sample are shown in Figure 11-12.

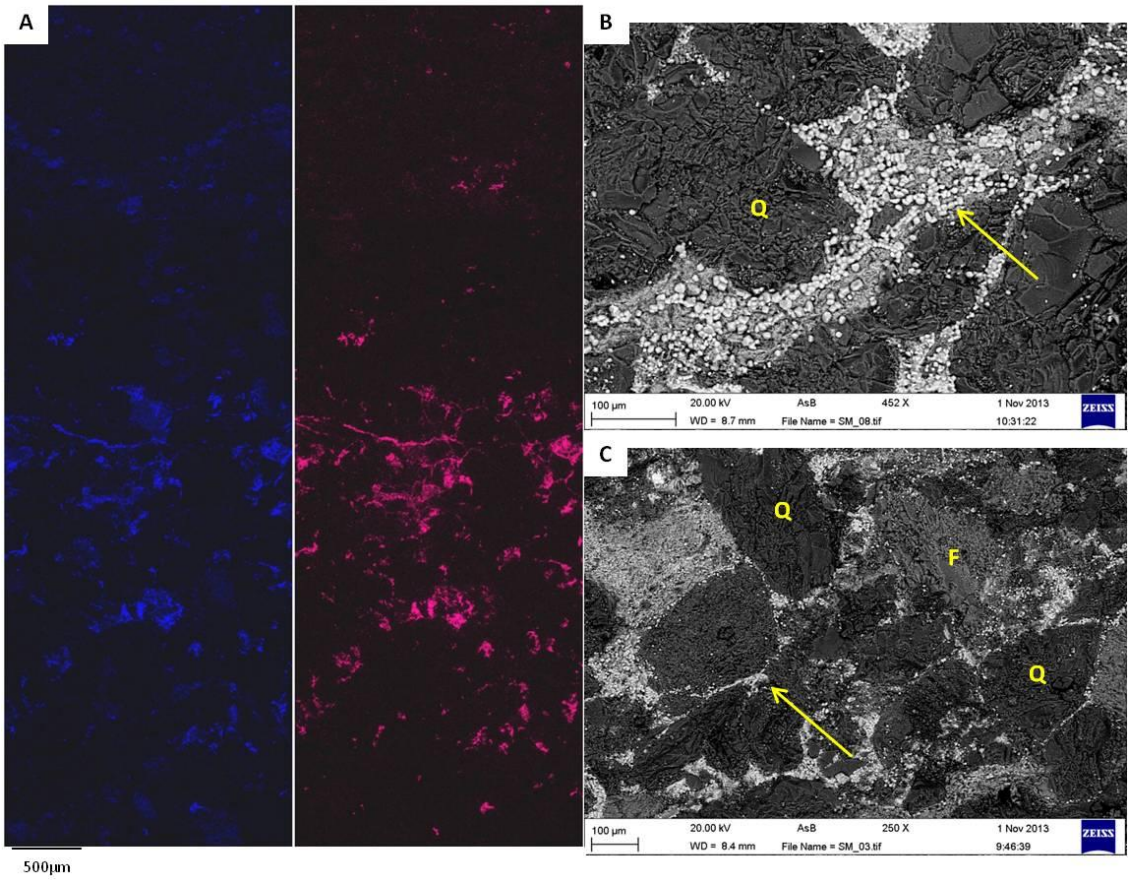

Figure 11-12: Backscatter electron SEM images and X-ray maps of dry-cut $SMCB_{1post}$ sample.

(A): SEM EDS mapping of Na (blue) and Cl (pink) through a section of $SMCB_{1post}$ as highlighted in Figure 11-11 C. (B) Small halite crystals within a clay filled pore. Arrow highlights the location of halite crystals. (C) Distribution of halite crystals (white) within the salt horizon, crystallising in the pore spaces surrounding feldspar and quartz grains. Arrow highlights the halite distribution around a quartz grain. Q: quartz, F: feldspar.

There is no obvious pattern of salt crystal growth in $CaCl_2$ samples. $CaCl_2$ crystals are found as small accumulations filling pores. Individual crystals are generally <30 µm in diameter, showing a ridged texture through repeated crystallisation events. $CaCl_2$ crystals are shown in Figure 11-10, crystallising within Scotch Buff sandstone. EDX analysis shows that Ca and Cl concentrations are evenly spread across each sample, possibly as a thin residue coating grains, as visualised in ESEM experiments (Chapter 6).

Analysis of polished thin sections of LN_{1post} and BN_{1post} samples reveal similar changes in their pore structure from NaCl crystallisation. Both samples show an increase in the amount of large pores, caused by the amalgamation of several smaller pores, creating large pore "chains"; this process is especially noticeable within Locharbriggs (Figure 11-13). Some of these pores are >500 µm in diameter and are larger than the maximum pore sizes that were

measured by MIP in both Locharbriggs and Blaxter. Without repeat MIP measurements, quantified changes in absolute pore size cannot be made, however from comparisons with thin sections of untreated samples, significant changes are evident.

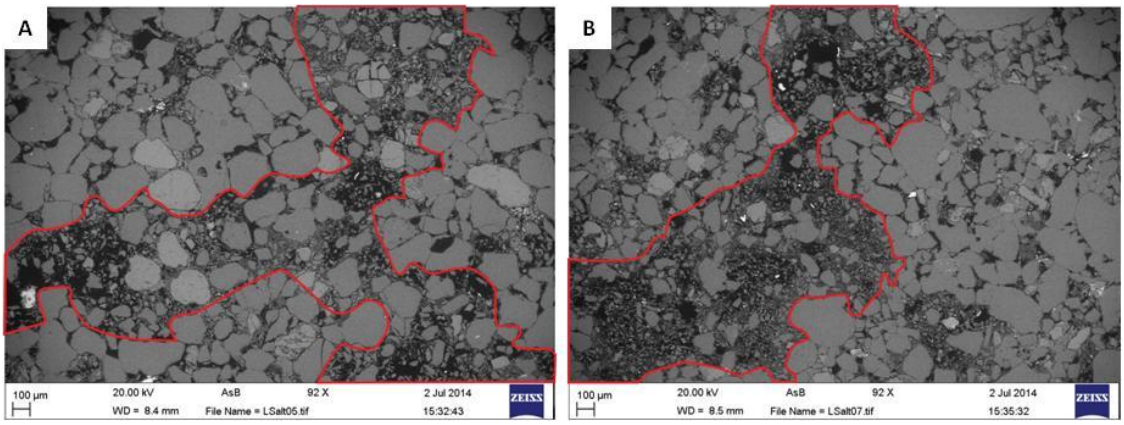

Figure 11-13: Backscatter electron SEM images of a polished thin section of the LN_{1post} sample.
(A) and (B): Red areas highlight "Fracture chains" within the LN_{1post} sample, showing connected areas of enlarged pores in-filled within broken lithic fragments.

These large pores contain a significant infill of broken lithic fragments and displaced debris, which is composed mainly of clay and silt-fine sand fractions. Evidence of infill material is also found in smaller pores that are disconnected (in 2D) from the main pore chains, but may remain connected in 3D. There is no indication of the provenance of the infill material; however small elongate fragments may be the remnants of broken grain overgrowths (Figure 11-14). Figure 11-14 highlights areas where broken fragments can be traced to their original quartz grain, while the remaining infill material is likely more mobile and cannot be traced to its source.

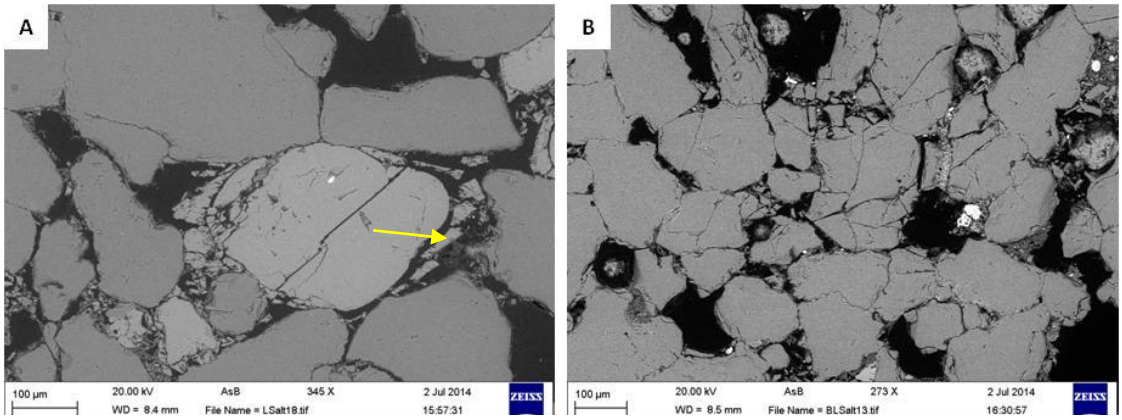

Figure 11-14: Backscatter electron SEM images of polished thin sections of Locharbriggs and Blaxter salt damaged sandstones.

(A): Yellow arrow showing a fractured feldspar grain with broken and disconnected overgrowths within the LN_{1post} sample. (B): Fractured quartz grains within the BCB_{1post} sample.

Large quartz and feldspar grains (≥300 μm) in both Locharbriggs and Blaxter sandstones contain cracks and fractures that traverse the length of the grains and in some instances break them apart. The size and shape of these broken fragments closely resemble larger fragments of the infill material and this is the likely origin of these infill fragments. Damage is only associated with quartz and feldspar grains; Fe-oxides and micas remain unaffected.

The infill material/debris is distinct from authigenic pore filling clays and from diagenetic processes (Figure 11-15) as indicated by further comparisons between fresh and weathered samples (Figure 11-16 and Figure 11-17). Undamaged regions of both sandstones also highlight the contrast in damaged areas, with small, well rounded quartz and feldspar grains surrounding larger grains within the unaltered sections of Locharbriggs sandstone. Undamaged areas within the stone highlight the heterogeneity of the decay process, with salts preferentially crystallising in distinct areas that with time during the experiments develop into fracture chains. This heterogeneity of damage within Locharbriggs sandstone is shown in Figure 11-18.

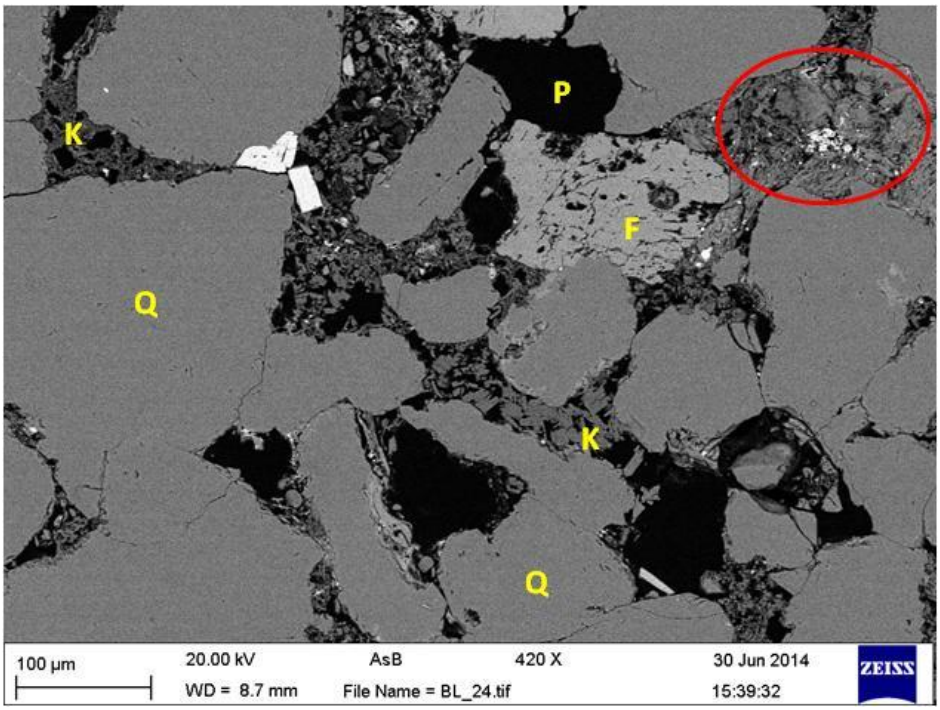

Figure 11-15: Backscatter electron SEM image of a polished thin section of Blaxter sandstone.

Q: quartz, F: feldspar, K: kaolinite, P: pore. Red circle indicates pore filling clays, likely produced from the decomposition of feldspar or mica grains. Pore infill material is generally composed from authigenic clays and is distinctively different from the broken lithic material found within thin sections of salt damaged Locharbriggs and Blaxter sandstone.

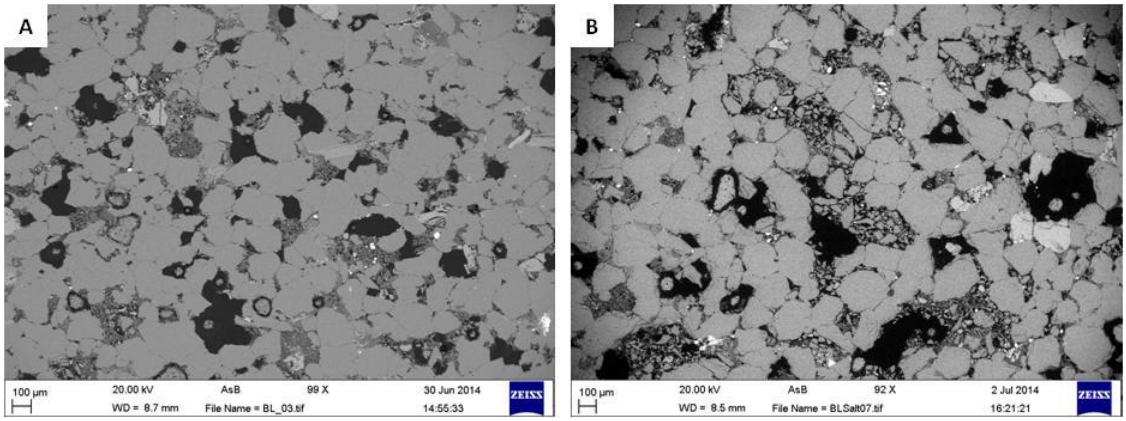

Figure 11-16: Backscatter electron SEM images of polished thin sections of Blaxter sandstone.

(A): Clean, undamaged Blaxter sandstone not used in the experiments. (B): Sample BN_{1post} used in the experiments, after 36 cycles.

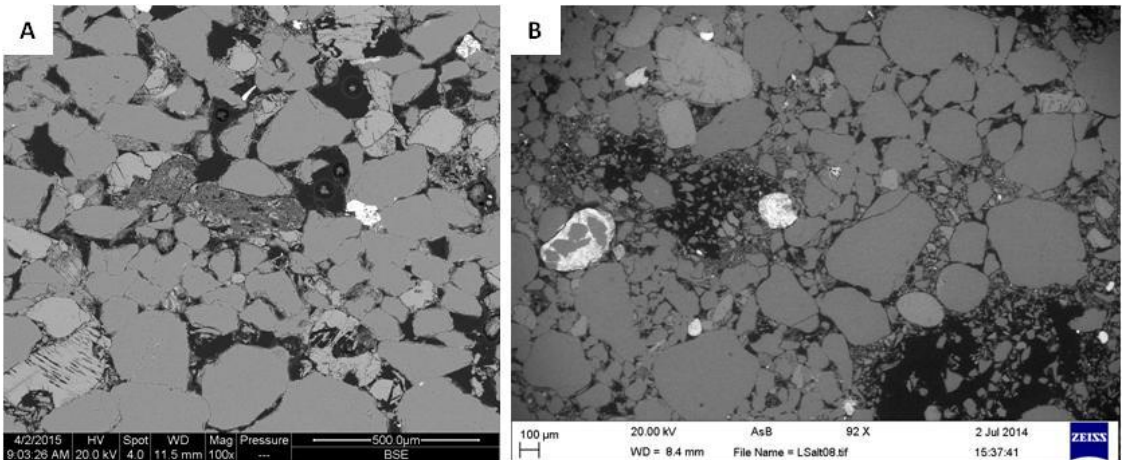

Figure 11-17: Backscatter electron SEM images of polished thin sections of Locharbriggs sandstone.

(A): Clean, undamaged Locharbriggs sandstone not used in the experiments. (B): Sample LN_{1post} used in the experiments, after 36 cycles.

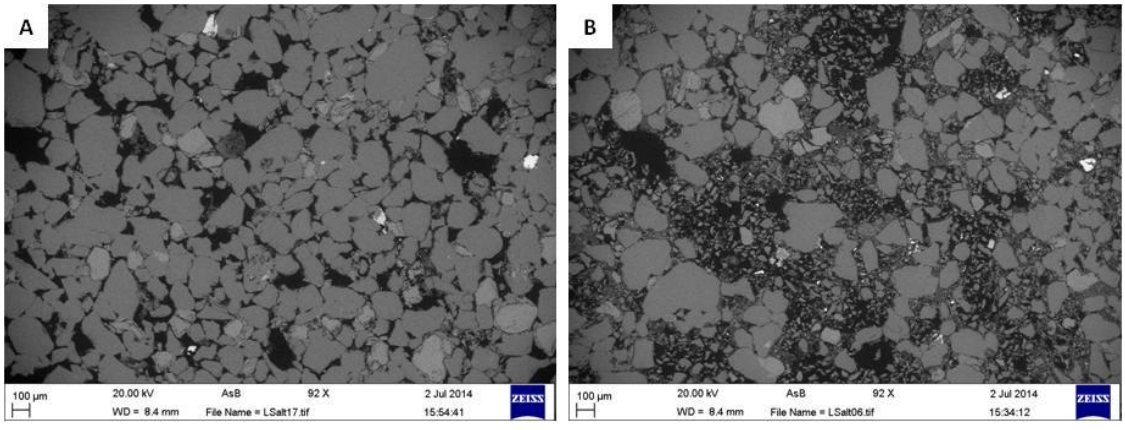

Figure 11-18: Backscatter electron SEM images of a polished thin section of LN_{1post} sample used in the experiments, after 36 cycles.

(A): An undamaged area within the LN_{1post} sample characterised by open pores and undamaged, sub-rounded quartz and feldspar grains showing a high variability in grain size. (B): A damaged section from the same thin section, characterised by large pores, filled with broken lithic fragments.

12 Appendix D

Colour measurements were conducted after 16 cycles in the second crystallisation test and compared to L*, a* and b* measurements of pre-experiment samples. Every measured sample, neglecting Blaxter $CaCl_2$, shows an increase in a* and b* values, with movements towards the yellow and red values of the blue-yellow and green-red spectra, respectively. There was no significant changes in any of the measured L* values, indicating no change in the lightness values of any stone. Cullalo and Blaxter had the lowest average change, while Doddington and Locharbriggs had the greatest number of significant changes in a* and b* values across every salt. Giffnock, Hazeldean and Cullalo had the highest variability in both original and repeat measurements and although the changes in certain values across these salts were large (20-60%) they were still within the variability error associated with either the stones original or post-crystallisation values. Doddington, Corsehill and Locharbriggs, all red sandstones, showed the lowest variations in both original and post-crystallisation measurements, with Doddington and Locharbriggs displaying the largest amount of significant changes. Lastly, there was no trend between salt types, with all three salts equally affecting different sandstones to different extents

12.1 Laser scanning

Six samples comprising four NaCl samples, one $CaCl_2$ and one $MgCl_2$ were chosen to undergo repeat laser scanning analysis using a “next engine” laser scanner in order to quantify the change in surface topography as caused by salt crystallisation. Three steel screws were drilled into each sample as reference points and scanned at the start of the test. After 16 cycles the samples were then repeat scanned and analysed using “cloud compare” software. By referencing each scan together using the screws, a colour coded image representing the difference in surface height is produced. Unfortunately, due to limitations caused by the file type, each resulting image does not differentiate between height gain and loss. In most samples however it is possible to determine by visual inspection what areas gained and lost material. On the images, dark blue represents areas of little or no

change, ranging through green, yellow and eventually red which represents the greatest change.

12.1.1 Blaxter NaCl

The change to Blaxter sandstone corresponds to both material loss and gain. Material loss occurs on the bottom edge and corners of the sample, extending to a height of ~25 mm on the right side of the stone. Material gain is through the growth of efflorescence located in the fracture that extends between the two top screws. Although this is an area of stone decay, the infill of salt crystals represents an increase in surface height. By cropping the small area of efflorescence, a maximum height increase of 2.23 mm and mean height increase of 0.33 mm is recorded (Figure 12-1). The remaining area of stone shows a maximum height decrease of 3.96 mm and mean height decrease of 0.42 mm (Figure 12-2).

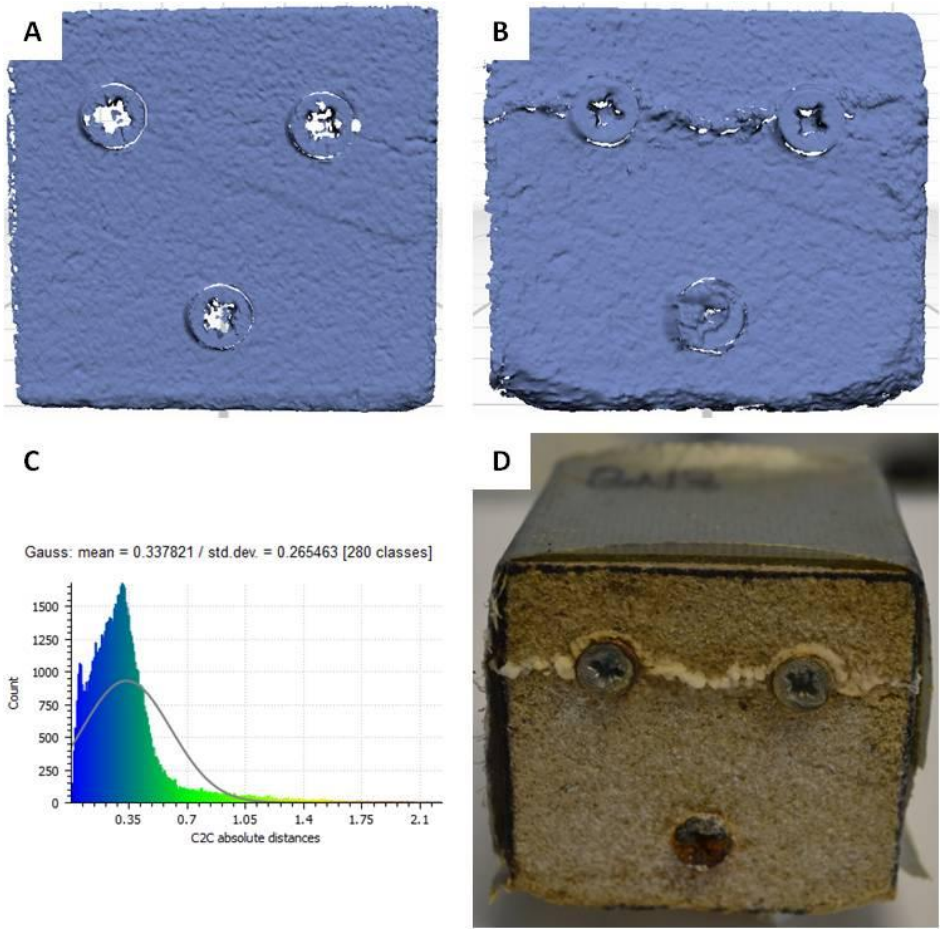

Figure 12-1: 3D scanning data for Blaxter NaCl.

(A): Original 3D scan. (B): Post crystallisation 3D scan. (C) Histogram of absolute change in mm. (D) Photograph of sample after 16 NaCl crystallisation cycles.

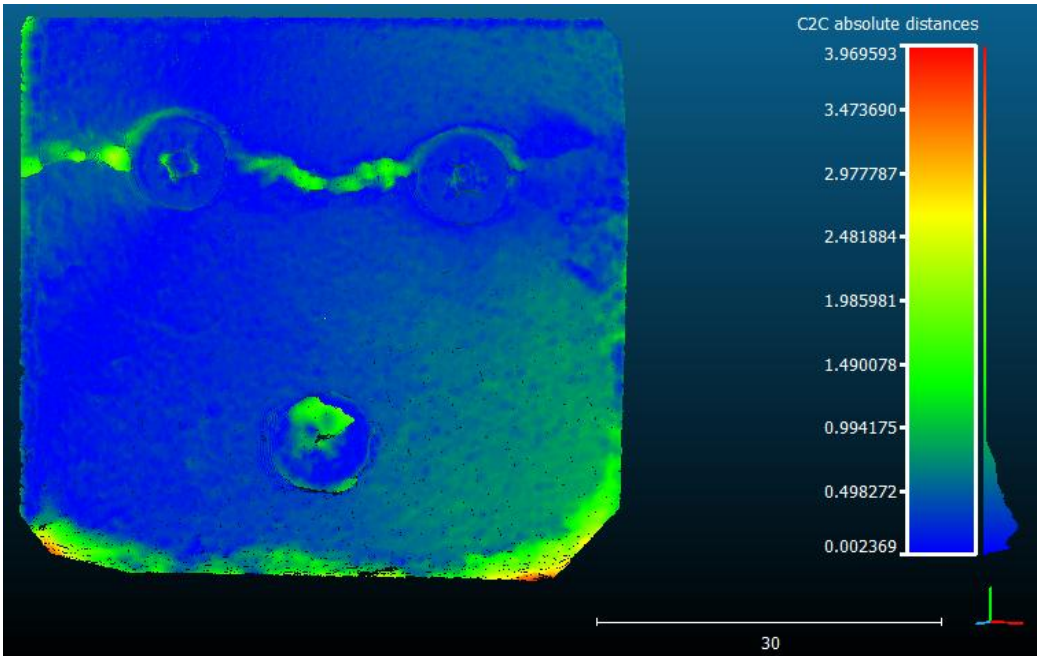

Figure 12-2: Cloud comparison of initial scan and final scan after 16 cycles. Absolute distances and scale are in mm.

12.1.2 Stanton Moor NaCl

Stanton Moor shows a similar trend of height increase and decrease; but is not as clearly defined as the Blaxter sample. The maximum height change is recorded as 2.02 mm (Figure 12-4), and from visual inspection this corresponds to an area of stone decay. The greatest change in height is located in the bottom right of the sample and relates to material loss. On the other hand, dark blue areas in the top left of the sample correspond to salt efflorescence and an increase in height. Stanton Moor has the highest mean change of 0.58 mm (Figure 12-3), representing both height gain and loss and indicates that Stanton Moor underwent a greater overall change over the full face of the stone.

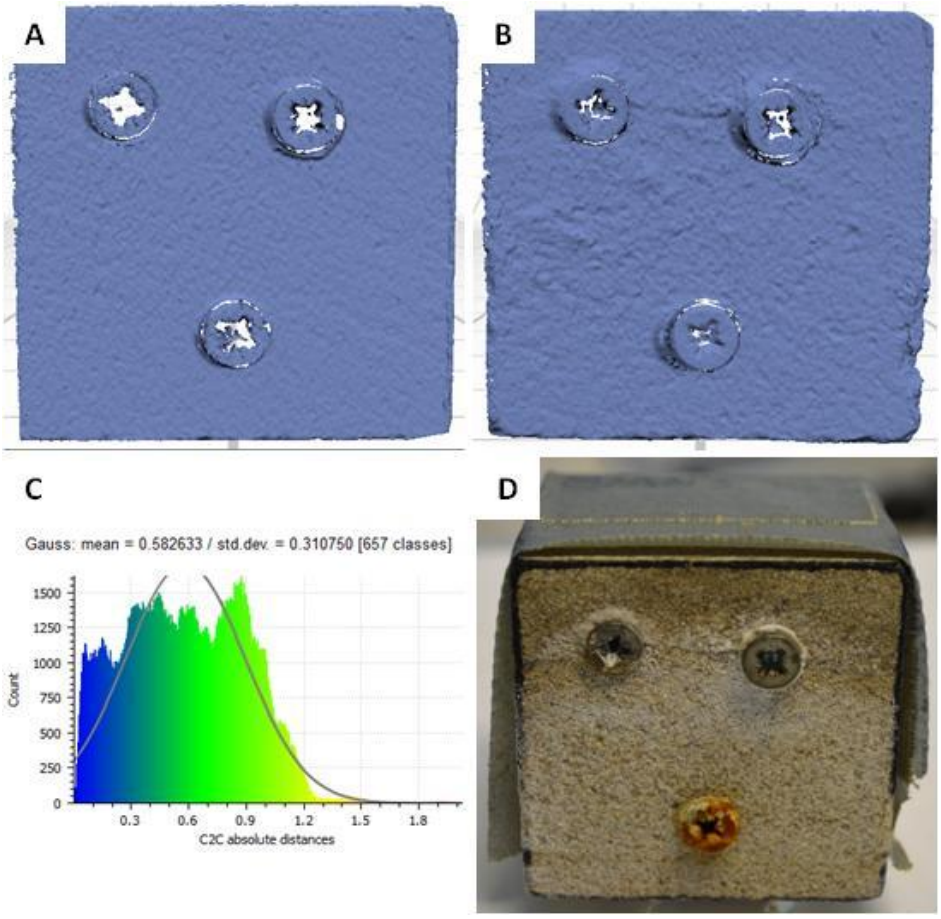

Figure 12-3: 3D scanning data for Stanton Moor NaCl.

(A) Original 3D scan. (B) Post crystallisation 3D scan. (C) Histogram of absolute change in mm. (D) Photograph of sample after 16 NaCl crystallisation cycles.

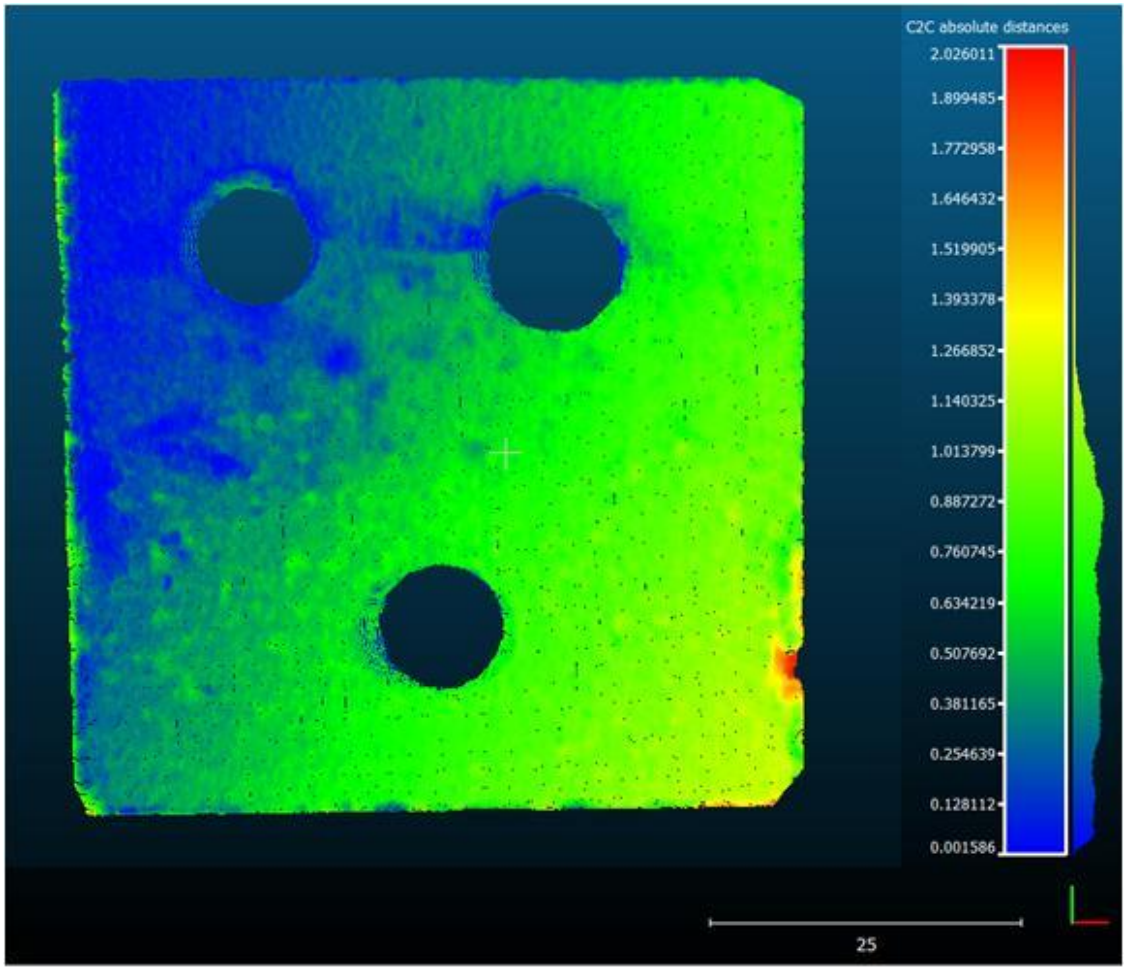

Figure 12-4: Cloud comparison of initial scan and final scan after 16 cycles.

Absolute distances and scale are in mm. Screws were cropped to ensure that measured distance data was composed entirely of changes within the stone.

12.1.3 Corsehill NaCl

Unlike the other NaCl samples, Corsehill experienced no weight loss and no visual decay. Height change in this sample is therefore attributed to an increase through salt efflorescence. A distinct boundary at ~30 mm separates a lower section of minimum change and an upper section of salt efflorescence. A maximum height increase of 1.20 mm (Figure 12-6) and a mean increase of 0.16 mm are recorded (Figure 12-5). By multiplying the mean increase by the analysed area, an average salt volume on the stone surface of 413 mm^2 is calculated (Table 12-1).

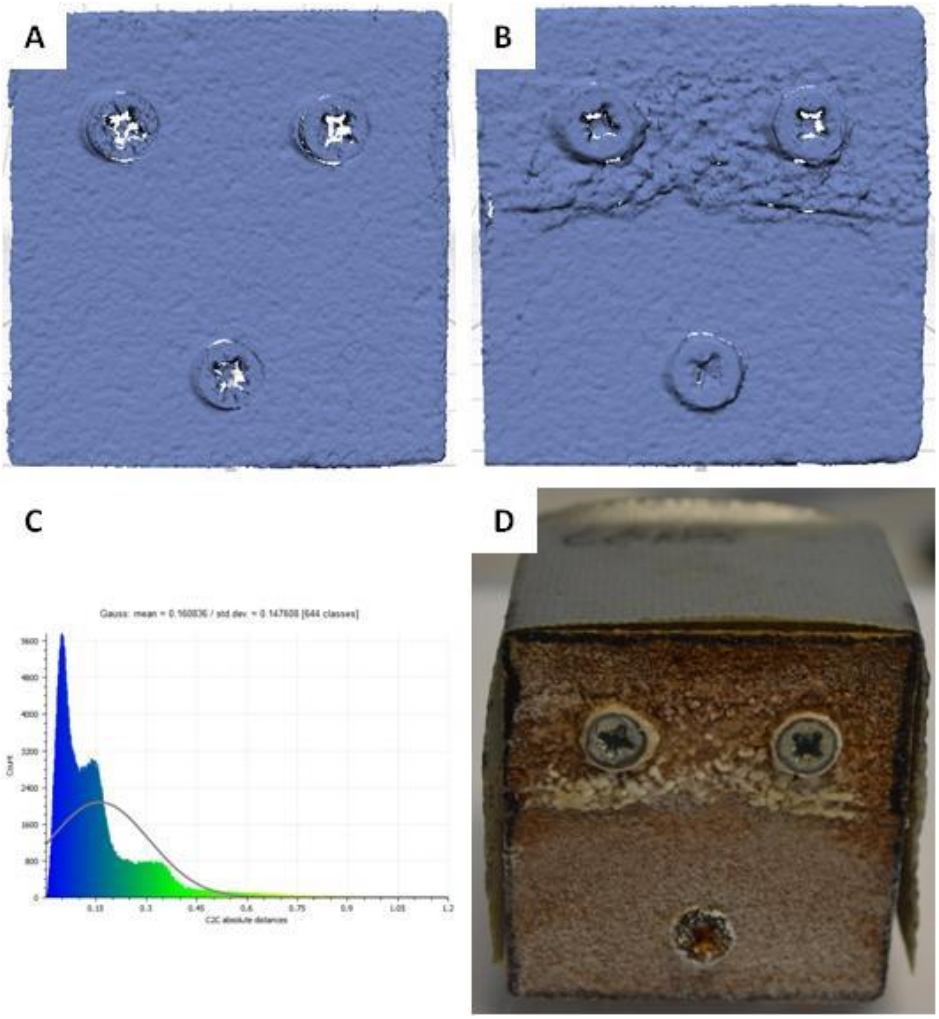

Figure 12-5: 3D scanning data for Corsehill NaCl.
(A): Original 3D scan. (B): Post crystallisation 3D scan. (C): Histogram of absolute change in mm. (D): Photograph of sample after 16 NaCl crystallisation cycles.

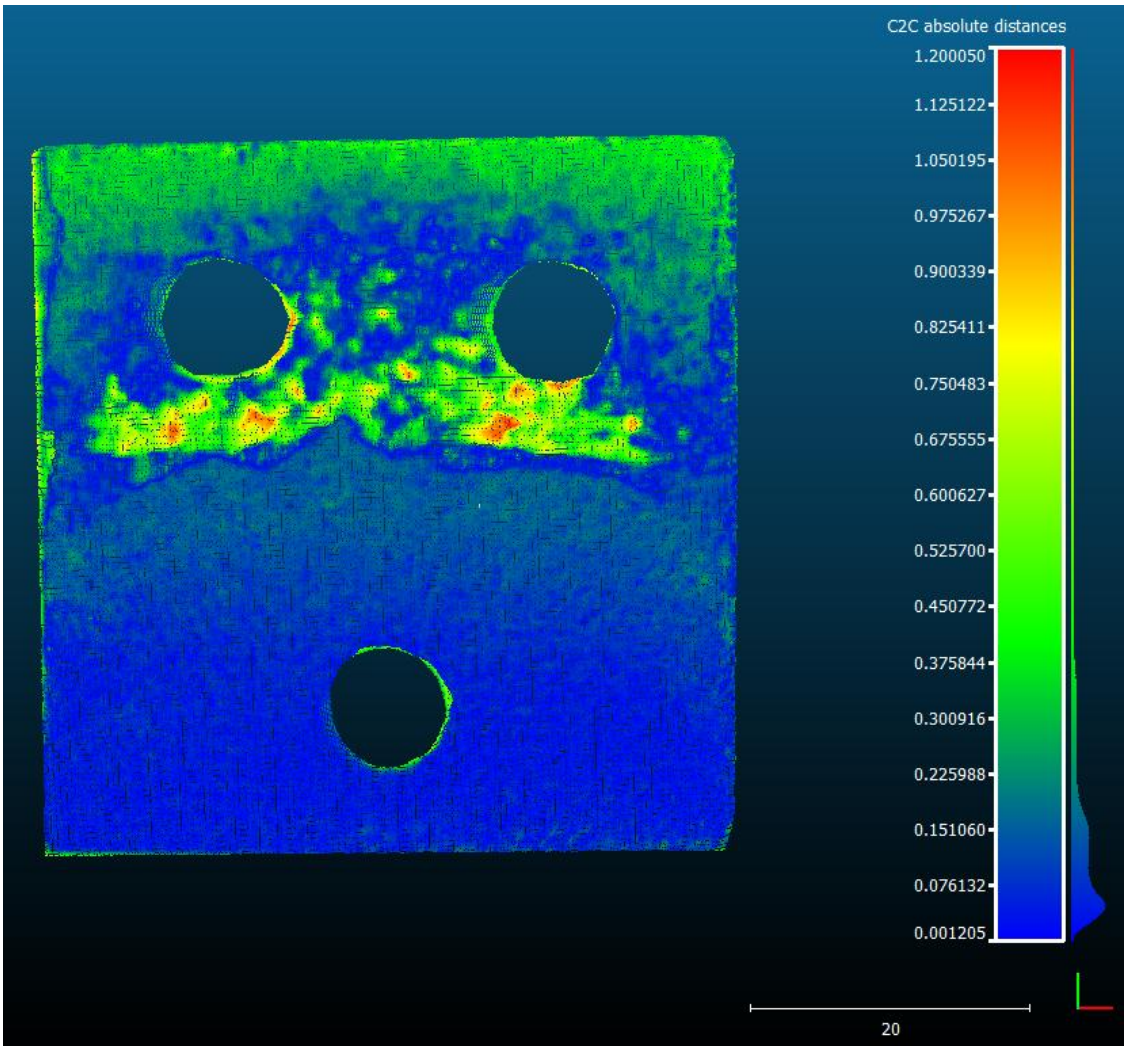

Figure 12-6: Cloud comparison of initial scan and final scan after 16 cycles. Absolute distances and scale are in mm. Screws were digitally removed for greater accuracy.

12.1.4 Locharbriggs NaCl

This sample shows typical NaCl decay, characterised by a lower section of granular loss, with large decreases focussed on the bottom edges and corners of the sample. An efflorescence boundary comparable to that in Corsehill is located in a similar position, separating a bottom area of material loss and a top area of salt efflorescence. A maximum height change of 4.86 mm (Figure 12-8) corresponds to loss associated with granular decay in the bottom left corner. A mean value of 0.23 mm is recorded as loss in the bottom section, while maximum and mean values of 1.5 mm and 0.24 mm (Figure 12-7) respectively show increases in height caused by salt efflorescence.

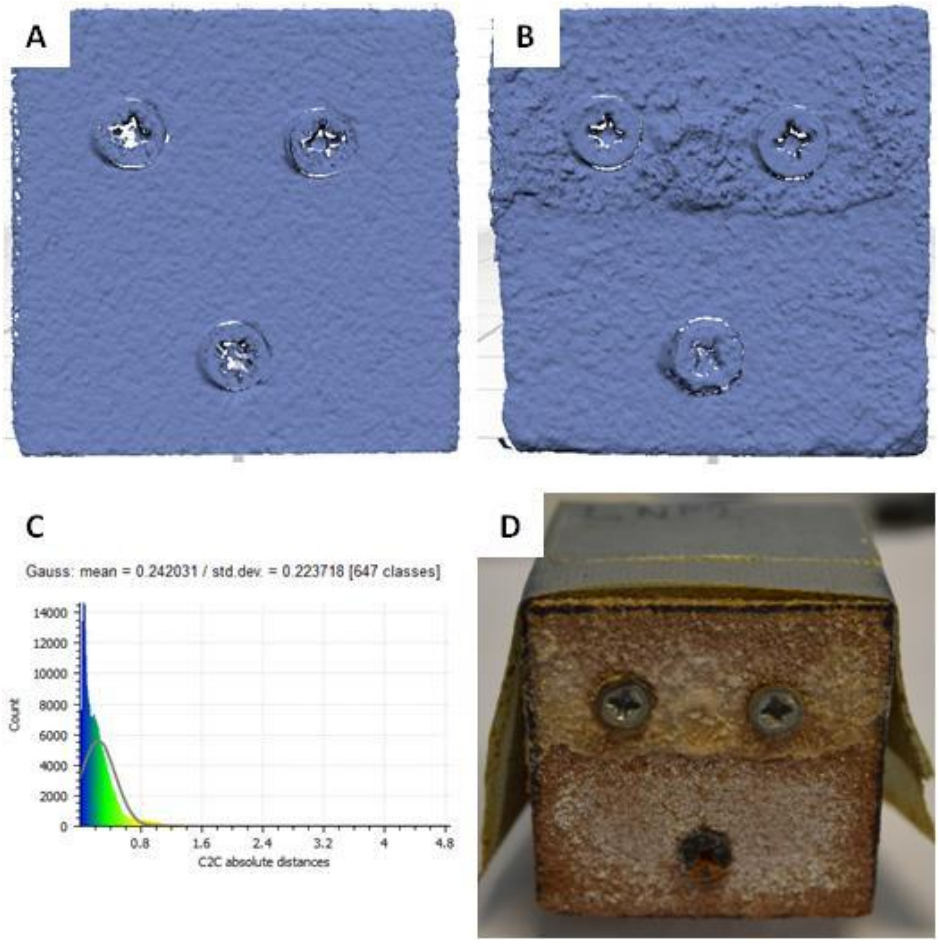

Figure 12-7: 3D scanning data for Locharbriggs NaCl.

(A): Original scan. (B): Post crystallisation 3D scan. (C): Histogram of absolute change in mm. (D): Photograph of sample after 16 NaCl crystallisation cycles.

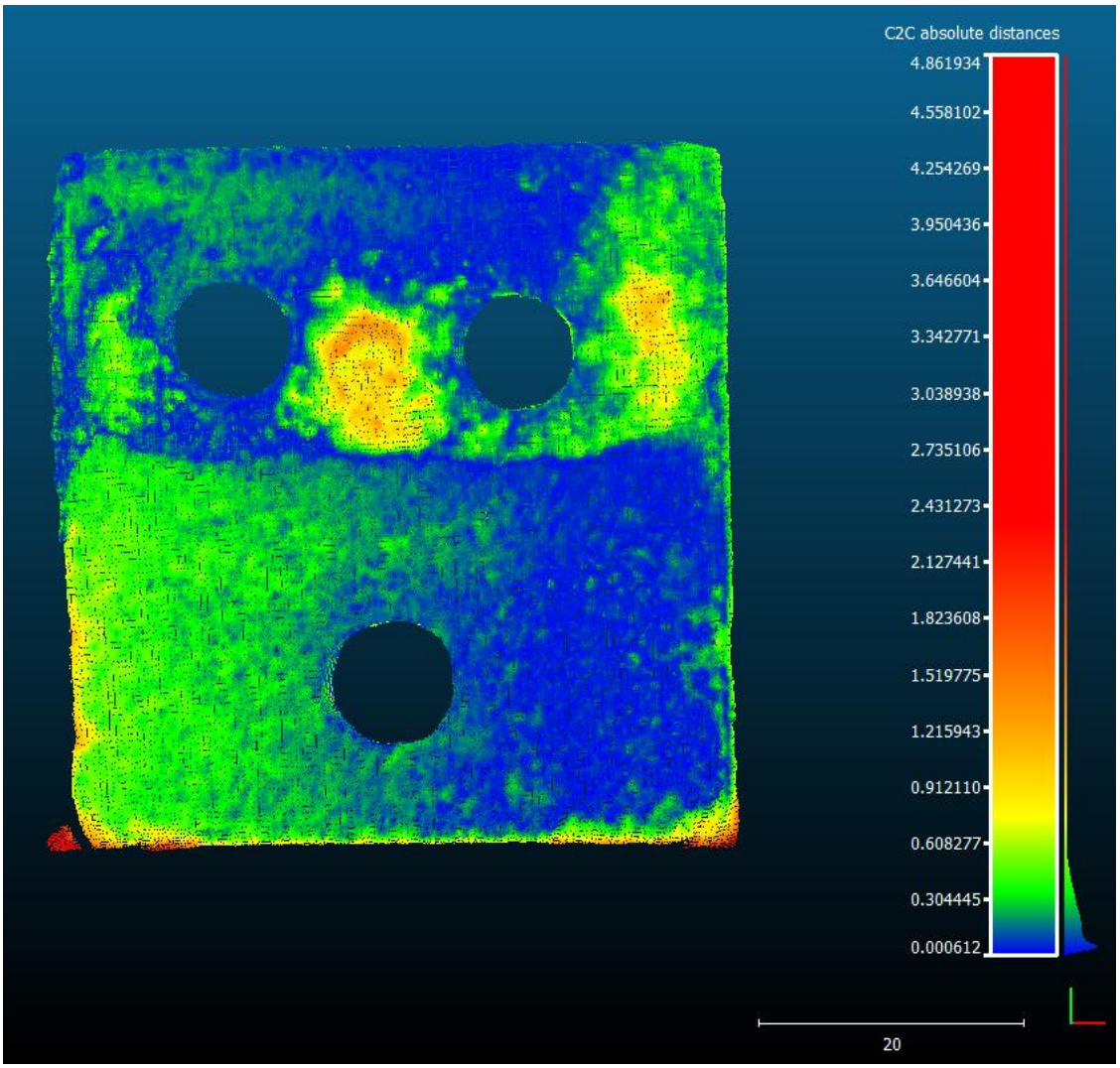

Figure 12-8: Cloud comparison of initial scan and final scan after 16 cycles. Absolute distances and scale are in mm. Screws were digitally removed for greater accuracy.

12.1.5 Locharbriggs $MgCl_2$

Values of topographic change ranging from <0.63 mm to 5.11 mm (Figure 12-10) correspond to a narrow area of material loss from the bottom edge of the sample. A narrow section extending the full height of the sample shows a maximum height decrease of 1.27 mm-1.91 mm (Figure 12-10), while the remaining central area of the sample shows negligible height change. The sample records a mean change of 0.08 mm (Figure 12-9) showing extremely focussed decay that is limited to the bottom and side edges of the sample. From visual inspection, it is inferred that all of the change in this sample is from material loss, with an average total loss of 1215 grains at an average rate of 0.03 grains/mm^2 per cycle (Table 12-1).

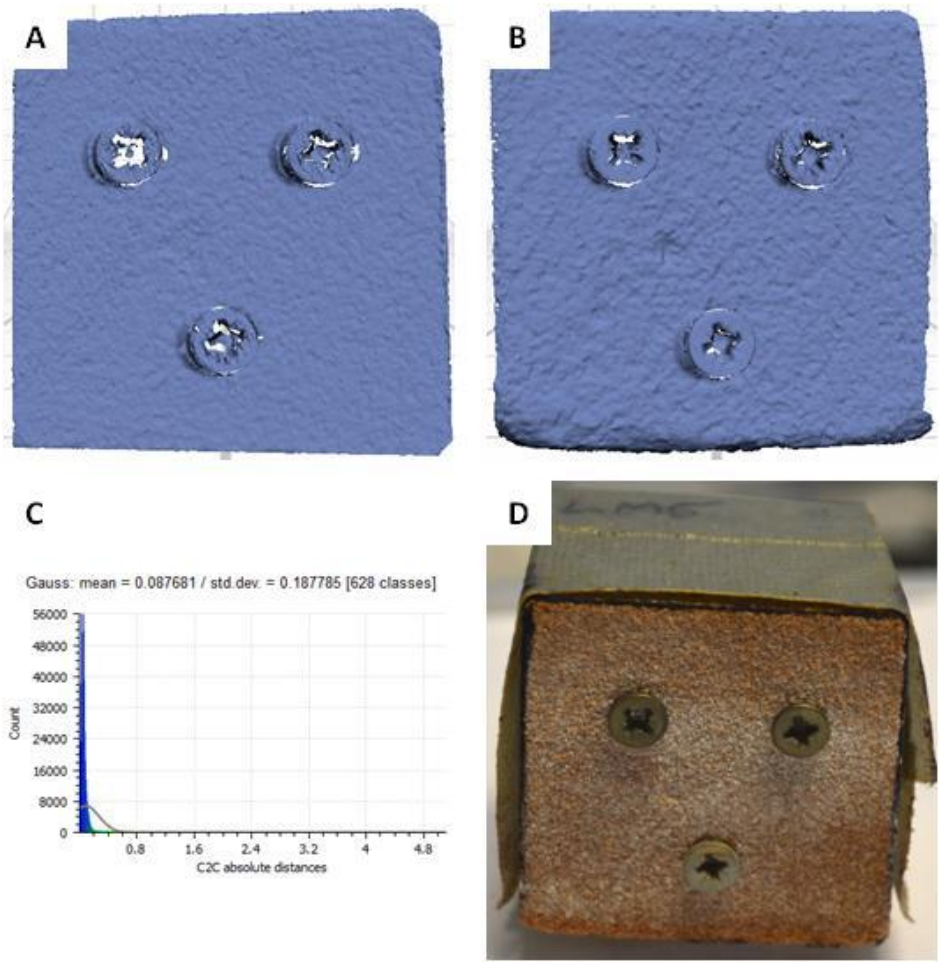

Figure 12-9: 3D scanning data for Locharbriggs $MgCl_2$.

(A): Original scan. (B): Post crystallisation 3D scan. (C): Histogram of absolute change in mm. (D): Photograph of sample after 16 $MgCl_2$ crystallisation cycles.

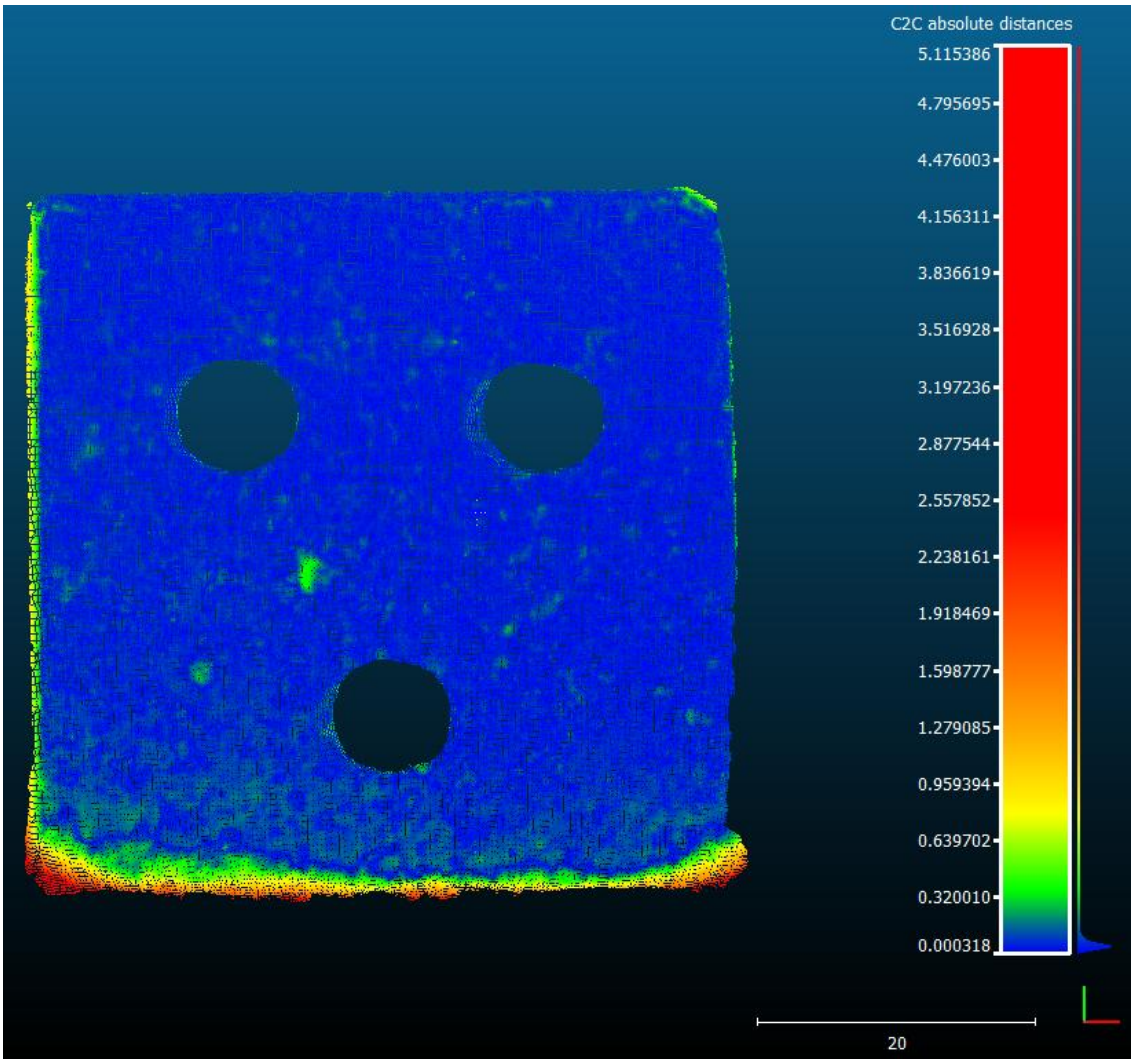

Figure 12-10: Cloud comparison of initial scan and final scan after 16 cycles. Absolute distances and scale are in mm. Screws were digitally removed for greater accuracy.

12.1.6 Locharbriggs $CaCl_2$

Total change here is related to a reduction in height of the stone surface and material loss. The greatest amount of change is concentrated in the lower 25 mm section of the stone (Figure 12-11), with the maximum surface retreat restricted to the bottom edge. The lower left side of the sample shows a large area with an average loss of 0.18 mm – 0.53 mm (Figure 12-12); while a small area to the right of the bottom screw is also affected. Loss in this small area is caused by differential decay taking place in a small indent that was caused during the drilling of the reference screw. The top section on the other hand shows negligible height loss, with all decay associated with the lower capillary section of the stone. Maximum and mean height loss of 2.87 mm (Figure 12-12) and 0.172 mm (Figure 12-11) are recorded, respectively, with the sample experiencing an average loss of 2247 grains at an average rate of 0.1 grains/mm^2 per cycle (Table 12-1).

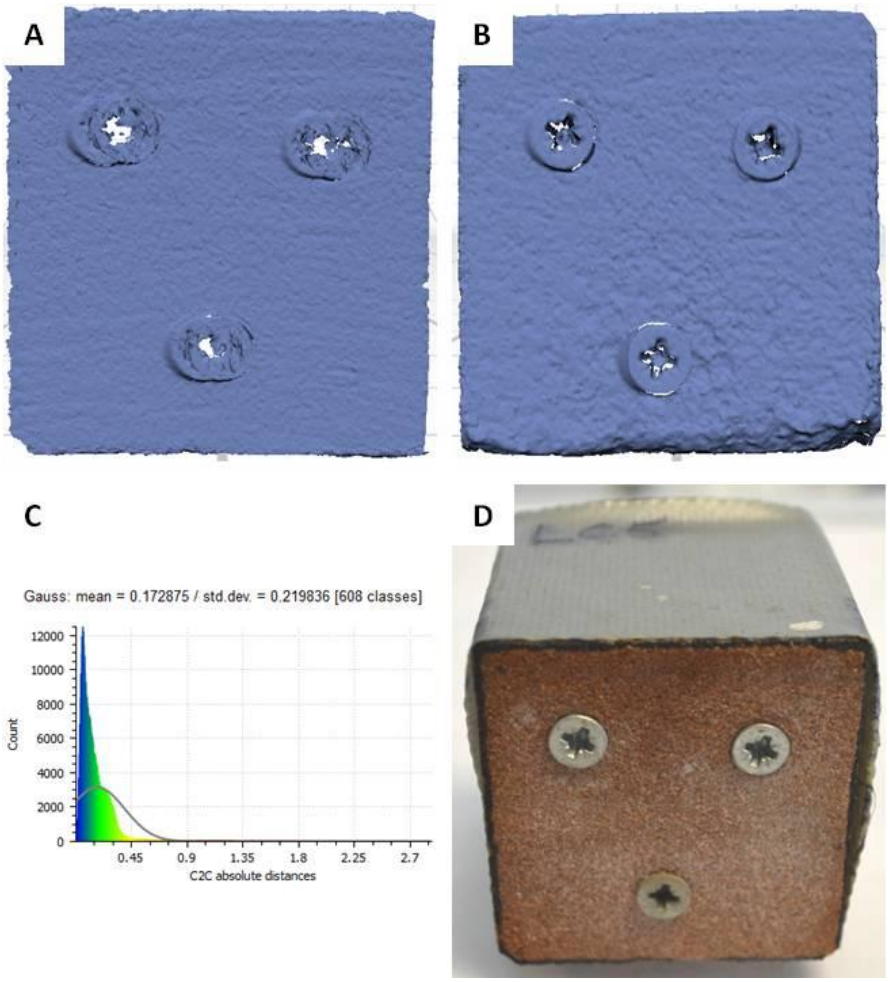

Figure 12-11: 3D scanning data for Locharbriggs $CaCl_2$.

(A): Original scan. (B): Post crystallisation 3D scan. (C): Histogram of absolute change in mm. (D): Photograph of sample after 16 $CaCl_2$ crystallisation cycles.

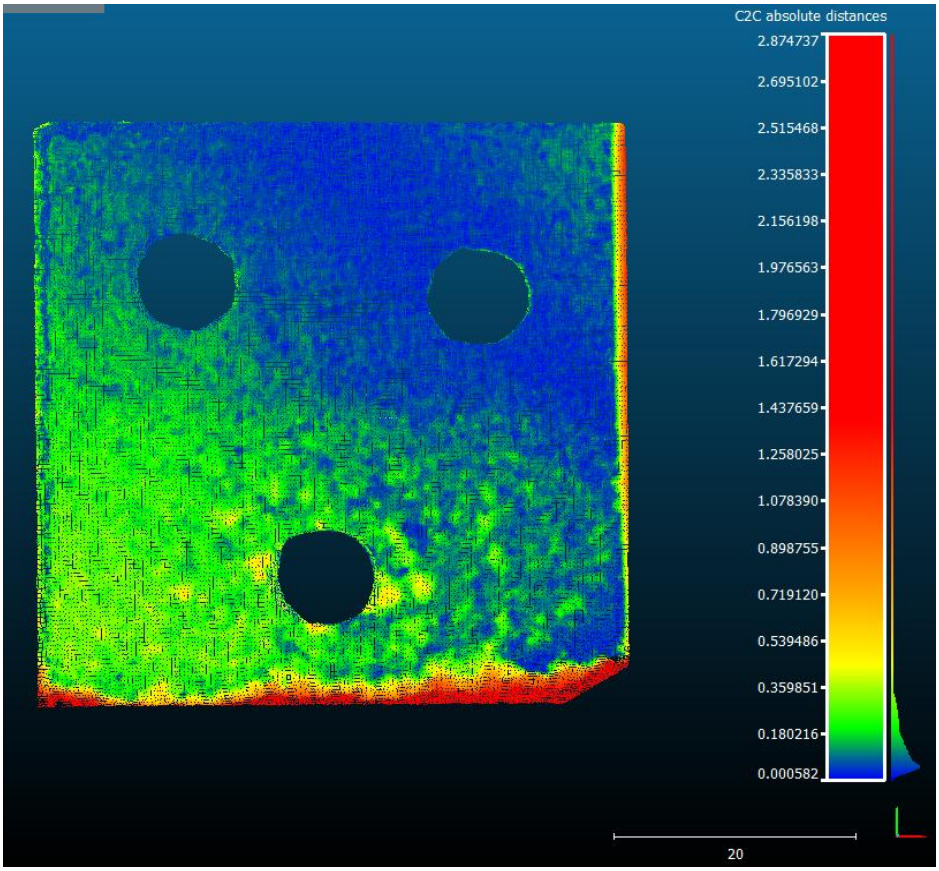

Figure 12-12: Cloud comparison of initial scan and final scan after 16 cycles. Absolute distances and scale are in mm. Screws were digitally removed for greater accuracy.

12.1.6.1 *Visual surface change summary*

Height loss (i.e. surface retreat) across every sample is focussed in the lower 25 mm to 30 mm of the stone. There is a trend of decay evident in Blaxter, Stanton Moor and Locharbriggs NaCl samples whereby efflorescence is restricted to the top section of the stone, with decay located in the lower capillary zone. In this bottom section, decay is focussed in the corners and edges of the samples, with the greatest surface lowering of 4.8 mm measured from Locharbriggs NaCl. Locharbriggs $CaCl_2$ and $MgCl_2$ samples showed no efflorescence, with surface lowering concentrated in the bottom corners and edges of the stone, while central parts of the face were unchanged. Corsehill (CN_{2post}) experienced the greatest gain in height through salt efflorescence located in the upper section of the stone. Stanton Moor (SMN_{2post}) had the greatest mean change associated with both gain and loss, while Locharbriggs $MgCl_2$ had the lowest mean change. The average loss of grains is given in Table 12-1, while the summary of the main visual changes is given in Table 4-2.

Sandstone	Average total loss of grains	Average total loss of grains/mm^2	Average total loss of grains per cycle	Average total loss of grains per mm^2/cycle
Blaxter NaCl	6199	3	388	0.2
Stanton Moor NaCl	9759	4	610	0.2
Locharbriggs NaCl	3480	1	218	0.1
Locharbriggs $CaCl_2$	2247	1	150	0.1
Locharbriggs $MgCl_2$	1215	0.5	141	0.03

Table 12-1: Total average loss of grains and average loss of grains/cycle. Results were calculated using the mean grain size for each sandstone.

13 Appendix E

Repeat colour measurements were made on two repeat samples of each salt contaminated sample following desalination after 50 cycles. Only the front face that was exposed for solution ingress and drying was measured. General trends across the changes to L*, a* and b* values are evident in all sandstones, with NaCl and $CaCl_2$ causing a consistent increase in L* values and all three salts causing a decrease in a* and b* values for every sandstone. $MgCl_2$ caused a lower overall colour change to every sample and in Locharbriggs, Corsehill and Stanton Moor samples, caused a decrease in L* values. NaCl and $CaCl_2$ caused similar changes with every colour value, showing increases with L* and decreases to a* and b* values. Locharbriggs and Corsehill had more statistically significant changes with every salt due to the low variance values of original measurements, while the largest changes were recorded with Stanton Moor NaCl a* (-41%), Doddington $CaCl_2$ b* (-47%) and Cullalo a* (-80%). Each salt caused every sandstone to become generally lighter in colour (positive L* values), with a general movement towards the green (negative a*) and blue (negative b*) values of the green-red and blue-yellow spectra, respectively. This change is in complete contrast to colour measurements of crystallisation test 2 samples, whereby no significant changes in L* values and increases to both a* and b* values were recorded across most sandstones.

13.1 Laser Scanning

Six samples from two of the sandstones were laser scanned after every ten cycles using the same procedure as listed in Section 12.1. Locharbriggs and Corsehill were the only stones that were analysed in this way due to the difficultly in drilling reference screws in Stanton Moor and Cullalo samples.

13.1.1 Locharbriggs NaCl

Surface change corresponds to both an increase in height from surface efflorescence, located in the top left section of the stone, and height loss focussed in the bottom left corner and within fractures extending between reference screws after 37 cycles. There is a mean change of 0.852 mm (Figure 13-1) and a maximum height change of 4.46 mm associated with material loss within the fracture cross-cutting the surface (Figure 13-2). A height increase of ~0.8 mm – 3.34 mm is found in the top left section of the stone, whilst height loss is also located in (i) the bottom left edge of the sample; (ii) a section extending 15 mm from the bottom; (iii) a small area in the top right of the stone (Figure 13-2). The main fracture is the result of salts exploiting a smaller weakness that was produced by the drilling of reference screws, and is similar to the fracture within the Blaxter NaCl sample from the second test.

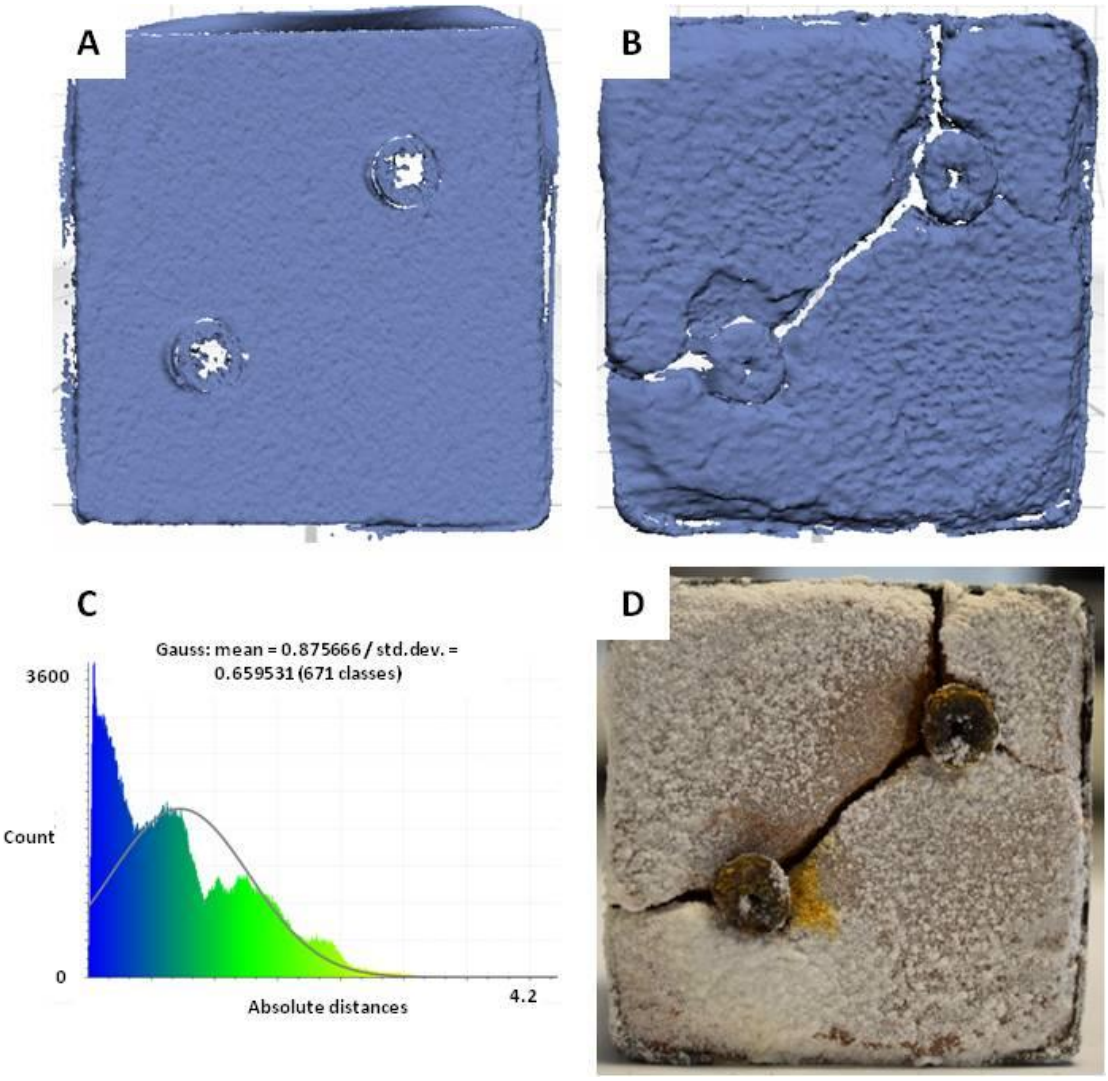

Figure 13-1: 3D scanning data for Locharbriggs NaCl. The decay has been driven by the insertion of reference screws.

(A): Original scan. (B): Post crystallisation 3D scan after 37 cycles. (C): Histogram of absolute change in mm. (D): Photograph of sample after 37 NaCl crystallisation cycles.

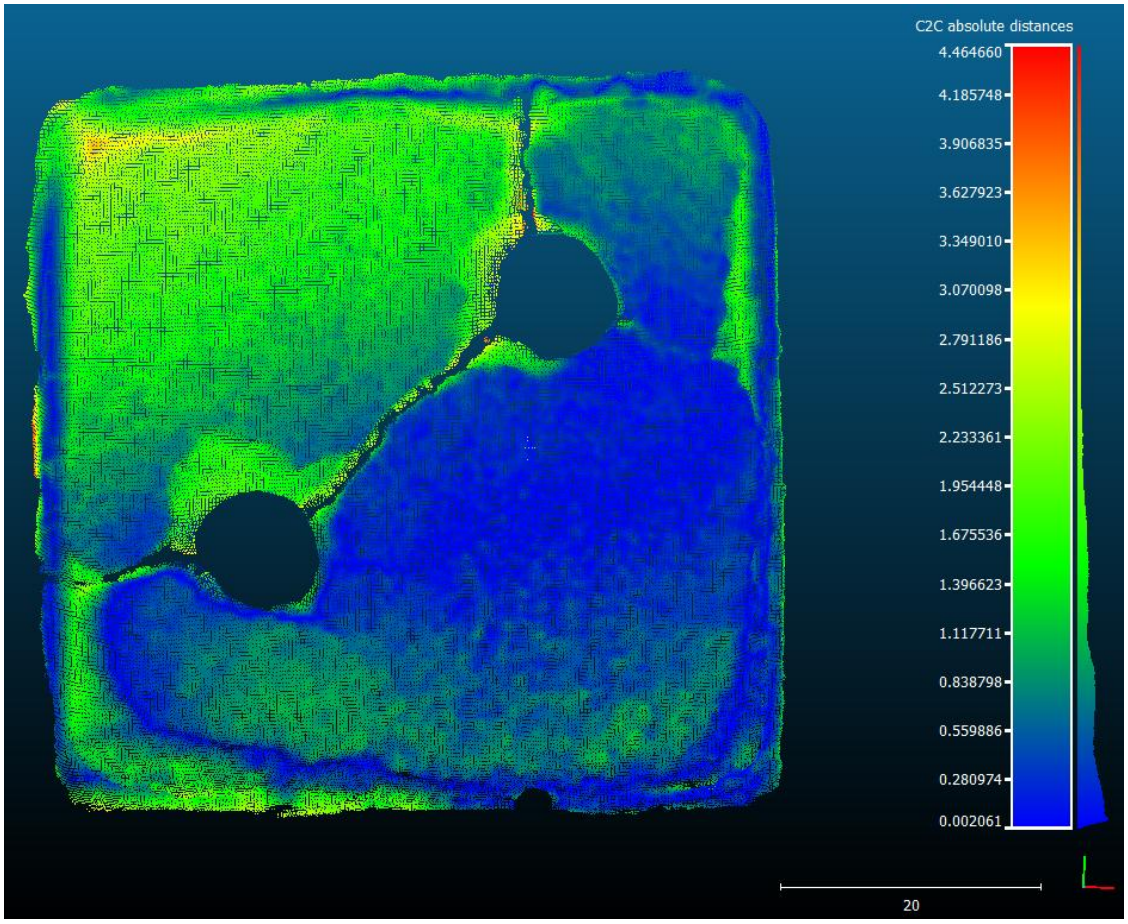

Figure 13-2: Cloud comparison of initial scan and final scan after 37 cycles. Absolute distances and scale are in mm. Screws were digitally removed for greater accuracy in measuring change within the stone.

13.1.2 Corsehill NaCl

The pattern of decay is very similar to the Locharbriggs sample, with the maximum height loss located in narrow fractures extending between the reference screws (Figure 13-3). The mean overall change is related to height loss as inferred from the absence of any visible surface efflorescence. A maximum height loss of 6.38 mm is located within the fracture, whilst a large section in the top left corner corresponds to losses of ~0.8 mm to 2.8 mm (Figure 13-4). Mean change is 1.6 mm, showing a greater overall surface alteration than the Locharbriggs sample, and with most of this change related to surface decay. The average total grain loss was calculated as 15 grains/mm^2 at a rate of 0.3 grains/mm^2 per cycle (Table 13-1).

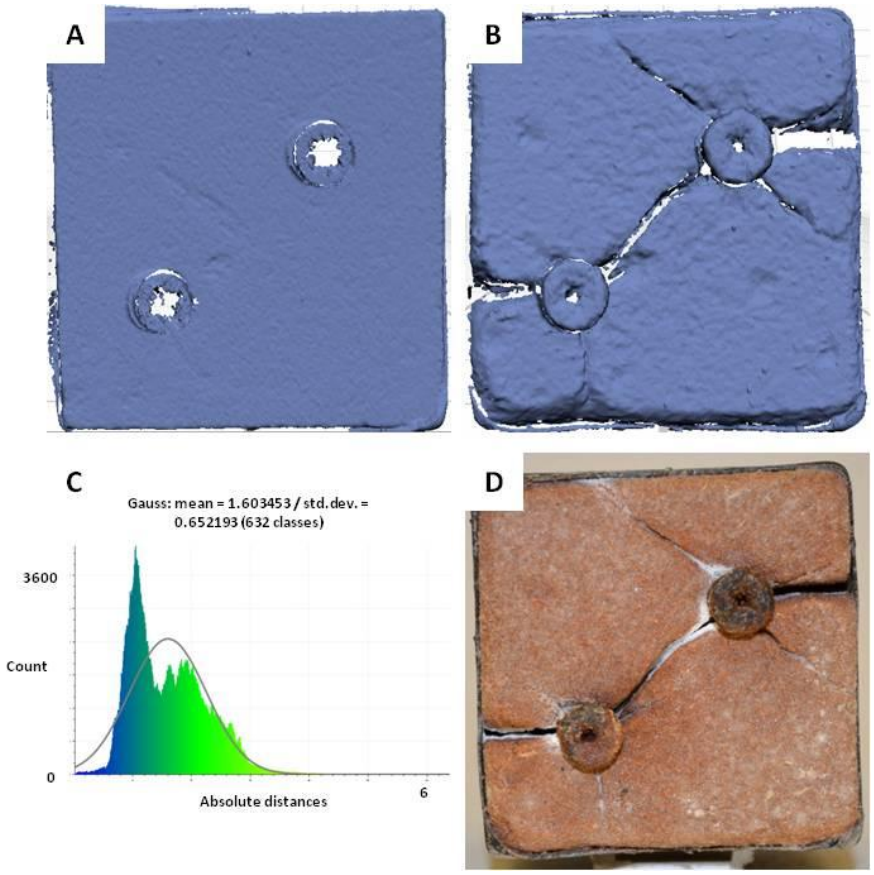

Figure 13-3: 3D Scanning data for Corsehill NaCl.
(A): Original pre-test scan. (B): Post crystallisation 3D scan. (C): Histogram of absolute change in mm. (D): photograph of sample after 50 NaCl crystallisation cycles.

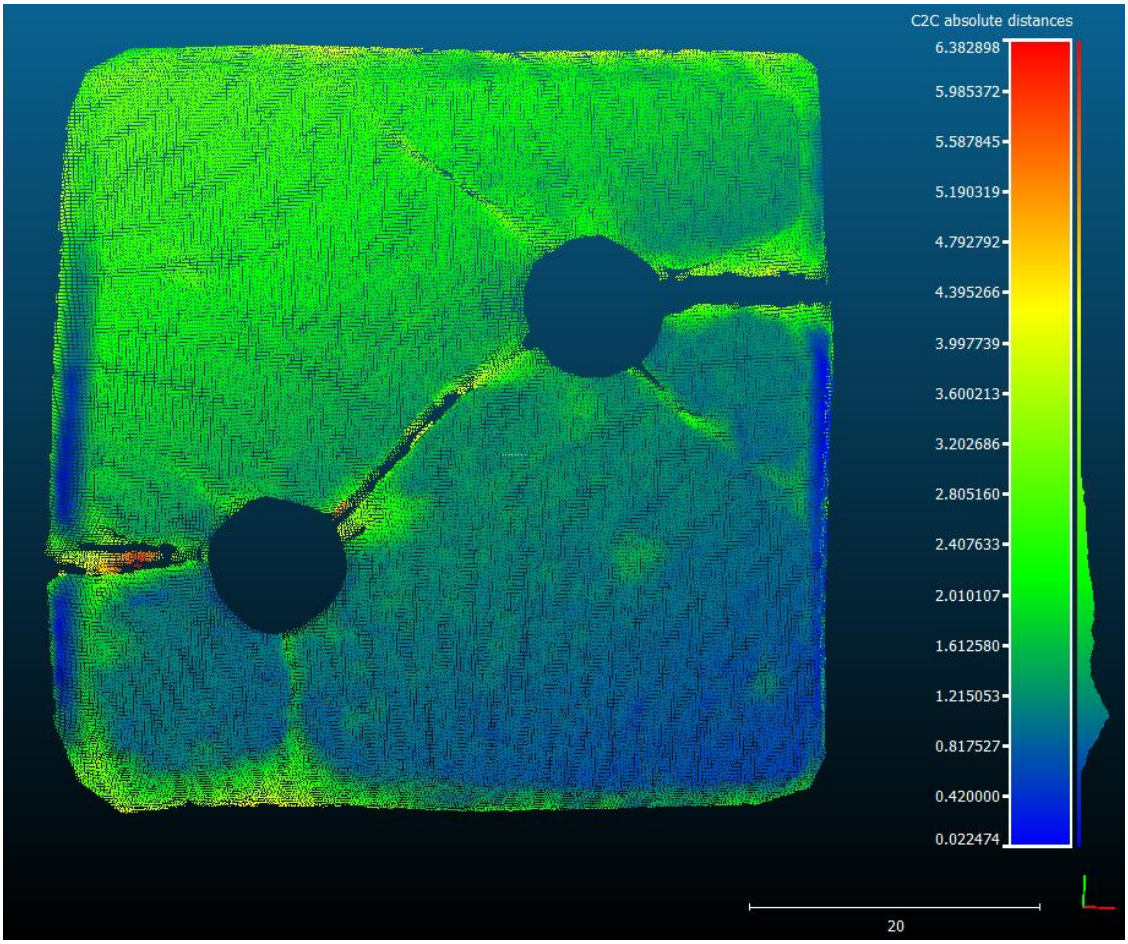

Figure 13-4: Cloud comparison of original scan and final scan after 50 cycles. Absolute distances and scale are in mm. Screws were digitally removed for greater accuracy in measuring change within the stone.

13.1.3 Locharbriggs $MgCl_2$

All of the change in surface topography of this sample is thought to correspond to height gain from surface efflorescence and from swelling of the rock surface due to internal crystallisation pressures. It is not possible to accurately identify the overall effect of each process however. The maximum height gain is 1.17 mm, located in a small patch in the bottom left corner of the sample (Figure 13-6). Mean change is the smallest of all the samples at 0.174 mm (Figure 13-5); it is focussed across the left edge, top left corner and the top edge of the sample. A small area in the bottom right shows an increase of ~0.22 mm – 0.44 mm surrounded by an area of bare stone. The mean change corresponds to an estimated salt efflorescence volume of 501 mm^3 (Table 13-1).

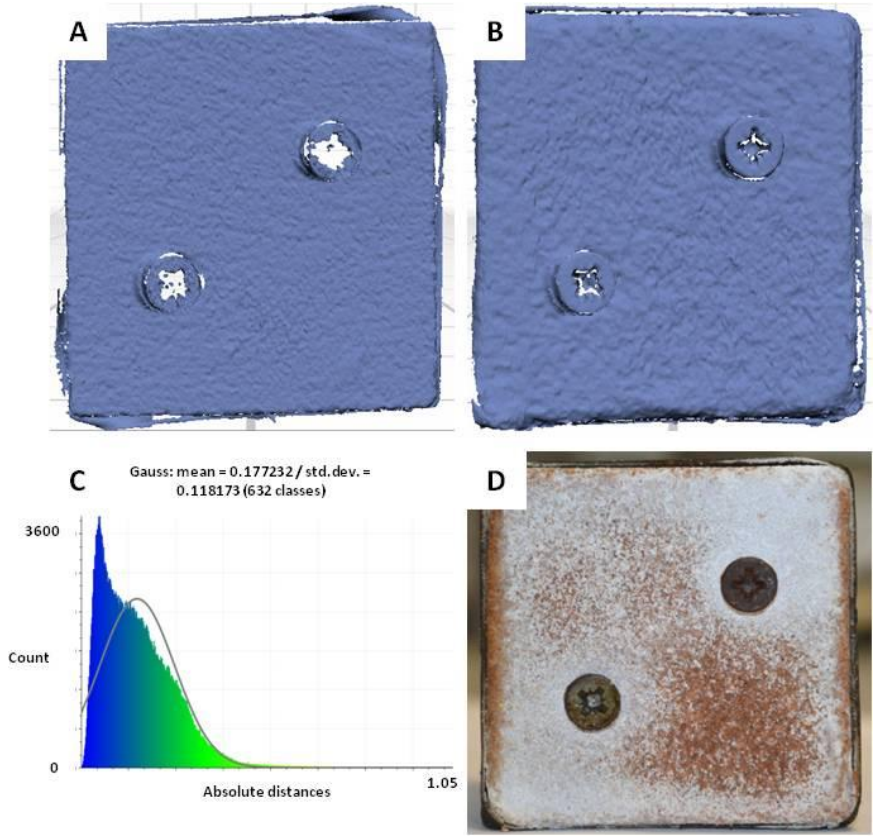

Figure 13-5: 3D scanning data for Locharbriggs $MgCl_2$.

(A): Original pre-test scan. (B): Post crystallisation 3D scan. (C): Histogram of absolute change in mm. (D): Photograph of sample after 36 $MgCl_2$ crystallisation cycles.

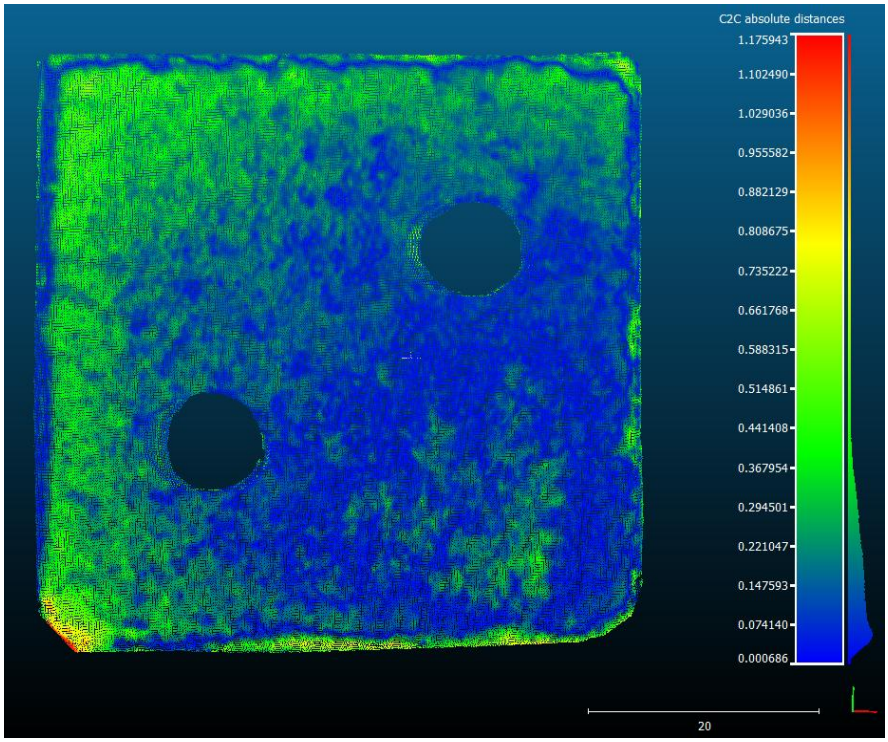

Figure 13-6: Cloud comparison of original scan and scan after 36 cycles.

Absolute distances and scale are in mm. Screws were digitally removed for greater accuracy in measuring change within the stone.

13.1.4 Corsehill $MgCl_2$

This sample has an extremely high maximum height loss of 16.03 mm, which is focussed in the top corners of the sample. A mean change of 1.12 mm (Figure 13-7) shows that the rest of the sample remained relatively unaltered, with the majority of the sample experiencing ≤1 mm of change. The lower right hand side corner shows granular decay with an average height decrease of 3 mm (Figure 13-8). The large values of loss in the top corners are the result of the sudden detachment of large pieces of rock; earlier scans showed minimal surface alteration prior to this damage.

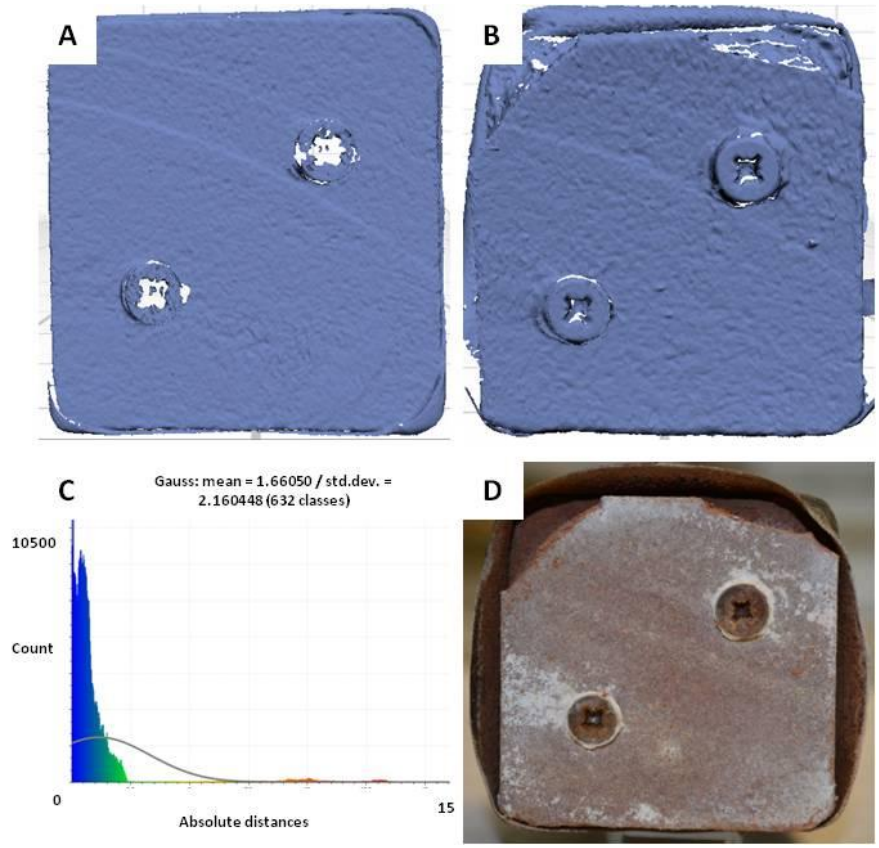

Figure 13-7: 3D scanning data for Corsehill $MgCl_2$.
(A): Original pre-test scan. (B): Post crystallisation 3D scan. (C): Histogram of absolute change in mm. (D): Photograph of sample after 50 $MgCl_2$ crystallisation cycles.

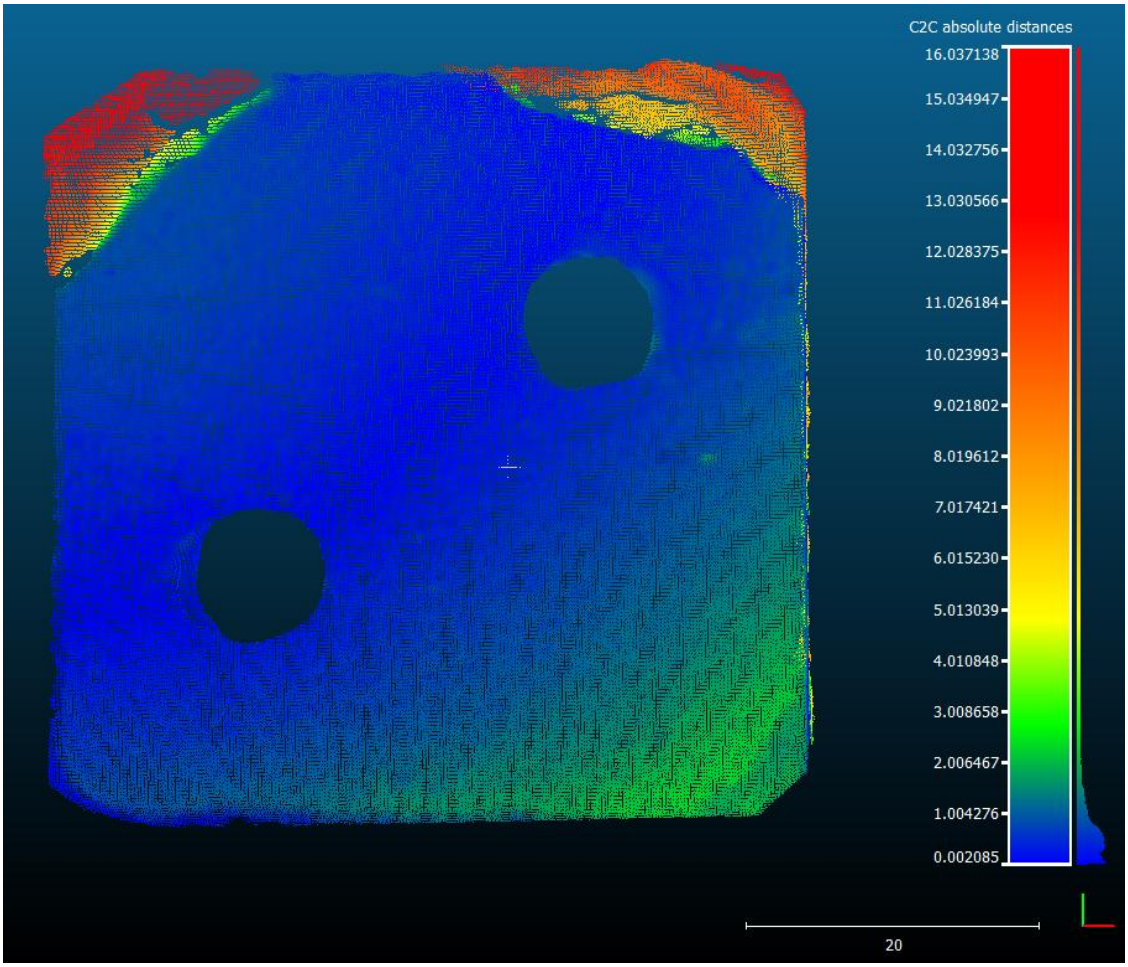

Figure 13-8: Cloud comparison of original scan and scan after 50 cycles. Absolute distances and scale are in mm. Screws were digitally removed for greater accuracy in measuring change within the stone.

13.1.5 Locharbriggs $CaCl_2$

This sample shows the highest average rate of decay, with visually significant decay beginning after 20 cycles (Figure 13-9 and Figure 13-10). A steady lowering in height is recorded after every 10 cycles, with the maximum loss ranging from 1.25 mm after 20 cycles to 15.01 mm after 45 cycles. Decay initially takes place as a thin band on the right edge of the sample, with a larger area experiencing ≤0.6 mm height loss on the top left of the stone. After 30 cycles, the small band on the right has grown and now extends to the top and bottom right corners. The central area of the stone remains unaffected after 30 cycles. Over the next 10 cycles, substantial height loss through granular decay takes place on all edges and corners of the sample, experiencing a mean loss of 2.13 mm. By the end of the test, the central area that experienced less change has now decreased in size considerably with maximum height loss located on the four corners of the sample, extending ≥5

mm into the centre of the sample face (Figure 13-10). The average total grain loss was estimated at 13 grains/mm^2 after 45 cycles (Table 13-1), showing a positive feedback of increased decay rate over time, ranging from 0.1 grains/mm^2 per cycle after 20 cycles to 0.7 grains/mm^2 per cycle after 45 cycles.

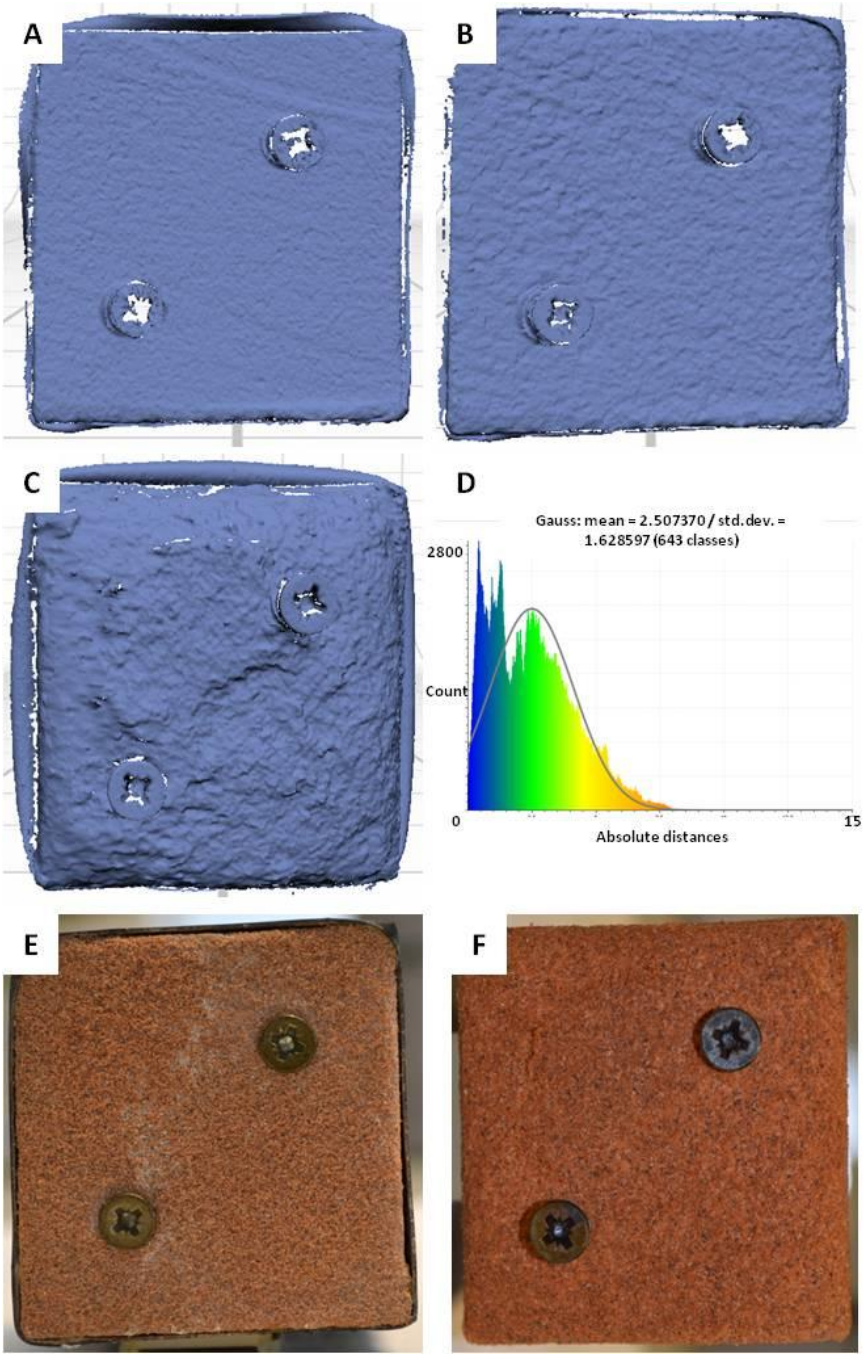

Figure 13-9: 3D scanning data for Locharbriggs $CaCl_2$.
(A) Original pre-test scan. (B) Scan after 20 cycles. (C) Post crystallisation 3D scan after 46 cycles. (D): Histogram of absolute change in mm. (E): Photograph of sample after 20 $CaCl_2$ crystallisation cycles. (F): Photograph of sample after 46 $CaCl_2$ crystallisation cycles. Near-surface crystallisation of $CaCl_2$ must explain the phenomena of granular decay.

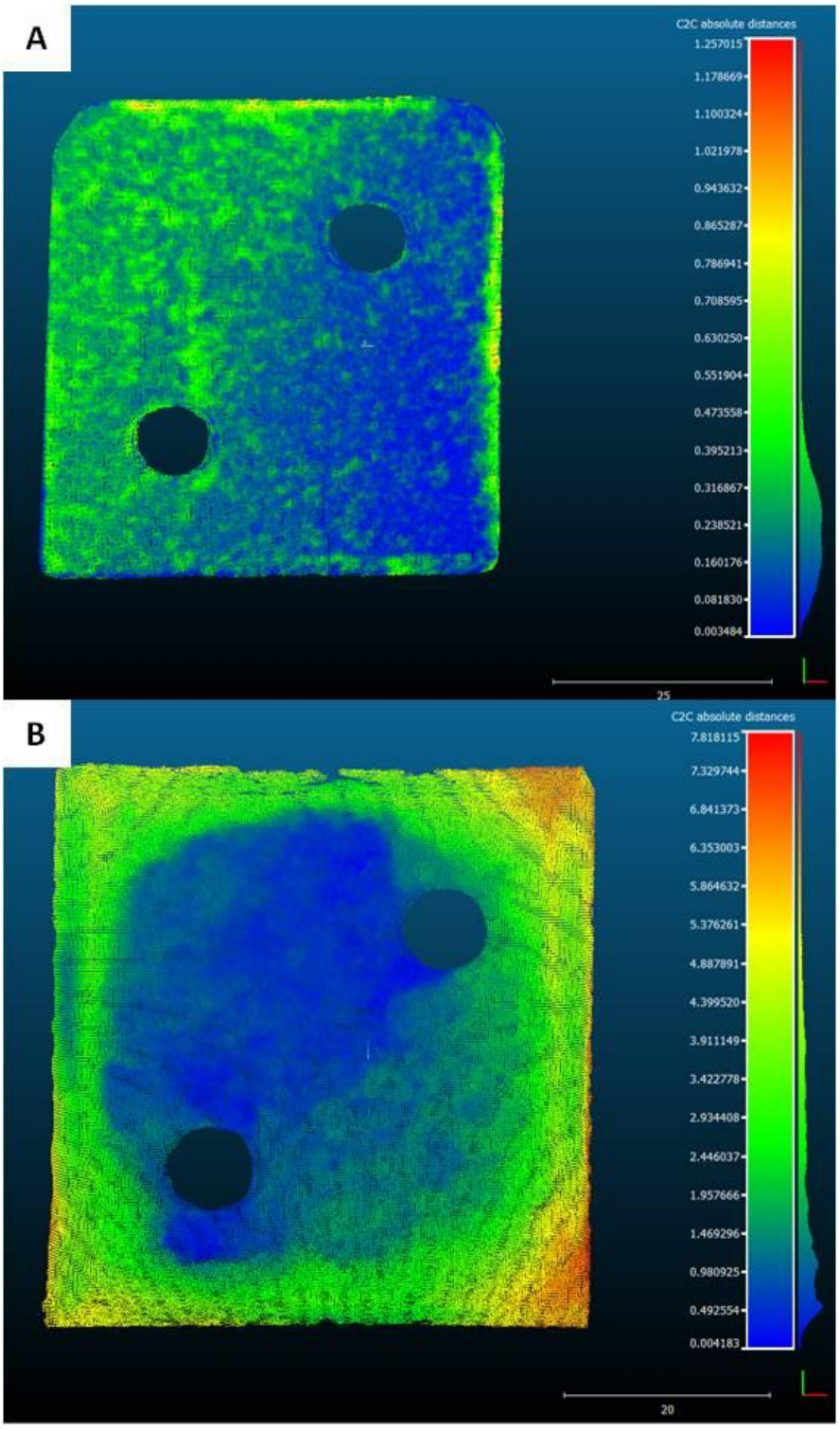

Figure 13-10: Cloud comparison images of Locharbriggs $CaCl_2$.

(A): Cloud comparison of original scan and scan after 20 cycles. (B) Cloud comparison of original scan and scan after 46 cycles. Absolute distances and scale are in mm. Screws were digitally removed for greater accuracy in measuring change within the stone.

13.1.6 Corsehill $CaCl_2$

In contrast to Locharbriggs, Corsehill was relatively unaffected by $CaCl_2$; it experienced a maximum height loss of 1.81 mm and a mean loss of 0.312 mm (Figure 13-11). The maximum height loss is from a small area in the bottom right of the sample, extending 7-8 mm from the sample base (Figure 13-12). The majority of the sample remains relatively unchanged, experiencing no surface efflorescence and height loss values <1 mm. The average total grain loss is calculated as 3 grains/mm^2 at a rate of 0.1 grains/mm^2 per cycle (Table 13-1).

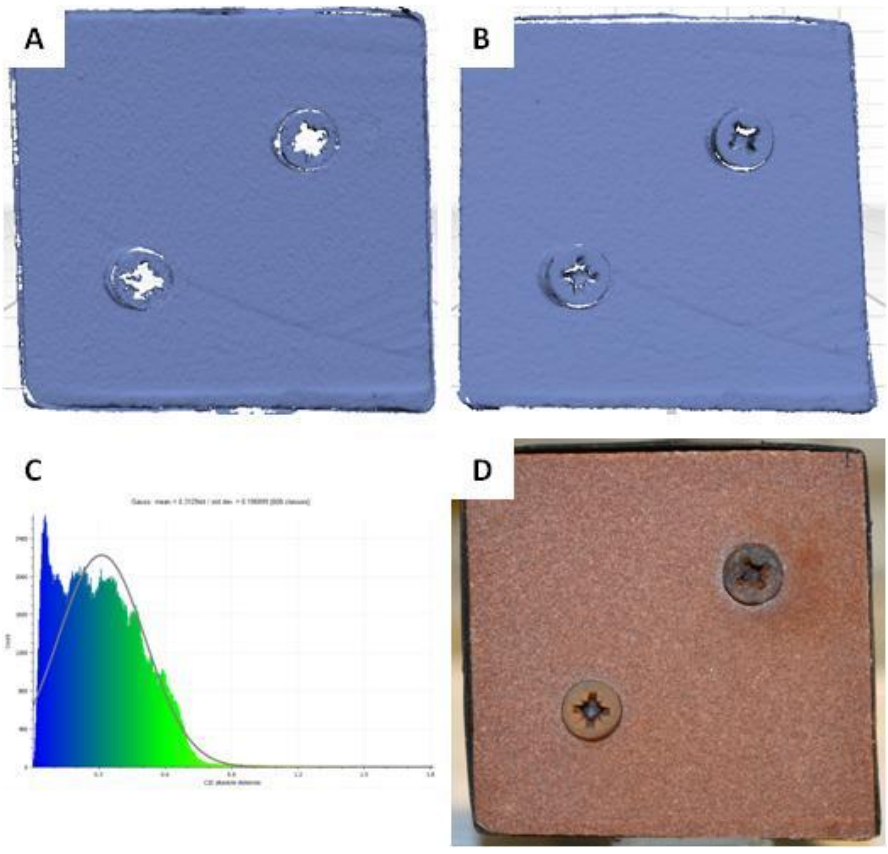

Figure 13-11: 3D scanning data for Corsehill $CaCl_2$.
(A) Original pre-test scan. (B): Post crystallisation 3D scan. (C): Histogram of absolute change in mm. (D): Photograph of sample after 50 $CaCl_2$ crystallisation cycles.

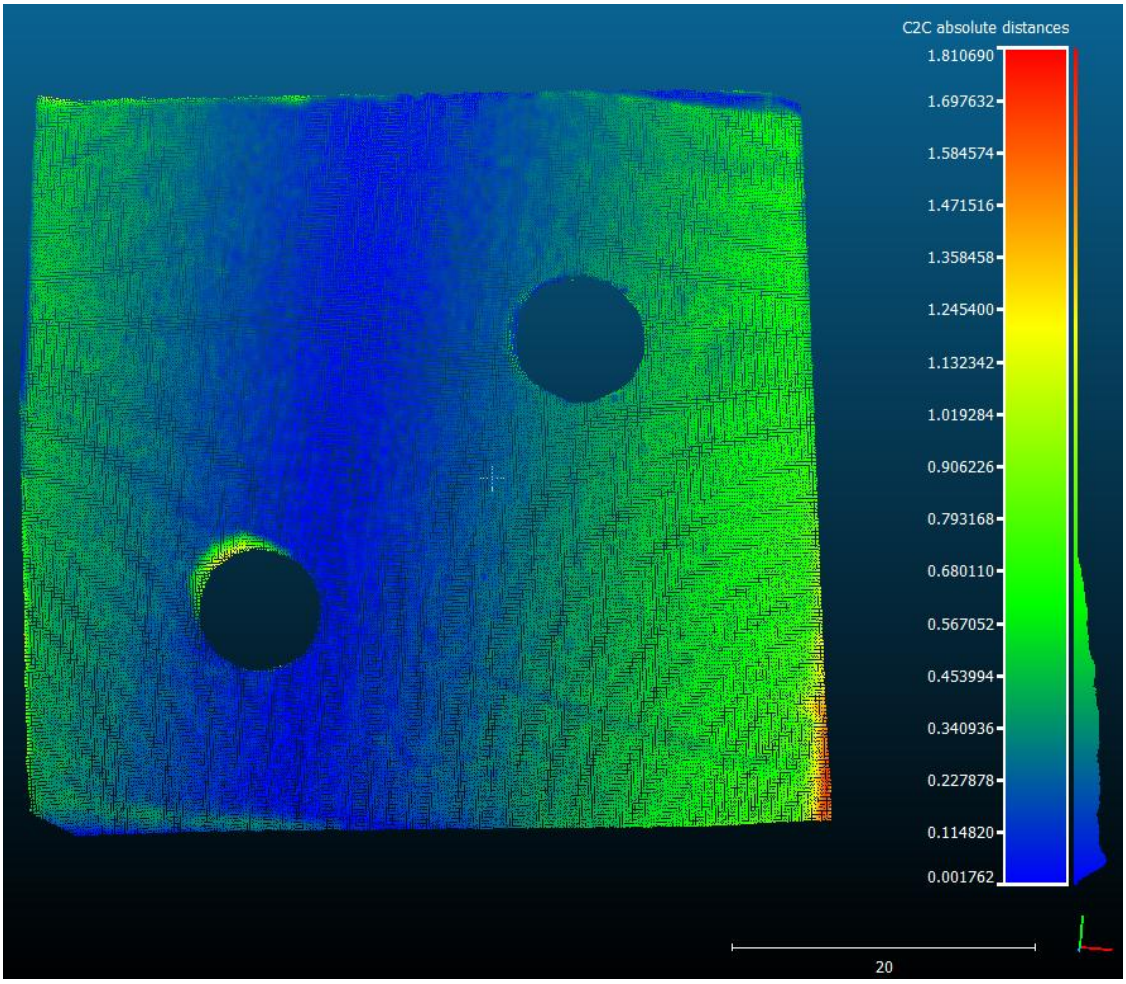

Figure 13-12: Cloud comparison of original scan and scan after 50 cycles. Absolute distances and scale are in mm. Screws were digitally removed for greater accuracy in measure change within the stone.

Sandstone	Average total loss of grains	Average total loss of grains/mm^2	Average total loss of grains/cycle	Average total loss of grains/mm^2/cycle
Locharbriggs NaCl	13336	5	267	0.1
Corsehill NaCl	39332	15	787	0.3
Locharbriggs $CaCl_2$ (20)	3664	1	184	0.1
Locharbriggs $CaCl_2$ (30)	8422	3	422	0.1
Locharbriggs $CaCl_2$ (40)	32816	11	1641	0.6
Locharbriggs $CaCl_2$ (45)	39011	13	1951	0.7
Corsehill $CaCl_2$	8304	3	166.1	0.1
Corsehill $MgCl_2$	31484	11	630	0.2

Table 13-1: Total average loss of grains and average loss of grains/cycle after 50 cycles unless otherwise stated. Stated cycle numbers are given in brackets next to the sample name. Results were calculated using the mean grain size for each sandstone.

14 Appendix F

14.1 Case Study: In-situ salt crystallisation changes

In order to further understand the damaging effects of increased de-icing salt concentrations within masonry sandstone, a theoretical salt crystallisation case study was undertaken. By using measured environmental conditions and salt ion concentrations in masonry sandstone from a busy urban area in Glasgow, a theoretical crystallisation model was run in order to estimate and predict the effect of increased ion levels of common de-icing salts on crystallisation pathways. Building stones contain a complex mixture of salt ions that will behave differently from single salts in stone. Although important in understanding the “isolated” effects of individual salts in stone, the salt crystallisation tests used within this study do not incorporate the complex interactions of mixed salt systems. It is unlikely that the isolated crystallisation of individual salt phases would take place exclusively within a mixed salt system. It is therefore important to consider any change to the salt crystallisation pathways of these mixed salt systems when theoretically increasing the ion concentrations of different de-icing salts in response to a speculative increase in their use. Furthermore, environmental monitoring of these sites from Glasgow, and elsewhere, will help to predict the number of damaging crystallisation cycles that are expected to take place annually. This case-study is presented as a preliminary ‘pilot study’ due to the limited number of environmental and salt ion data from different locations. The analysed temperature and RH data does not account for changes in building height and importantly facade aspect, while salt ion data may not necessarily account for the large range of salt values that are expected in a busy city environment. The reported data is therefore only representative of a spatially constrained part of Glasgow.

14.2 Temperature and Relative Humidity Monitoring

Temperature and RH, along with water, are the most important factors that influence the phase changes of salts within natural stone. In order to understand the complex interactions of salt phase changes, an accurate knowledge of the environmental conditions experienced by the stone is needed. Using data collected by ibutton loggers from locations around The University of Glasgow, temperature and RH conditions on the stone surface and at depth were analysed and the number of salt phase transitions calculated. The locations are shown in Figure 14-1 and Figure 14-2. Site 1 of ibutton collection was located at a height of 1m on a South-facing boundary wall adjacent to University Avenue. Site 2 was located at a height of 0.5m on the East-facing façade of The James Watt Building.

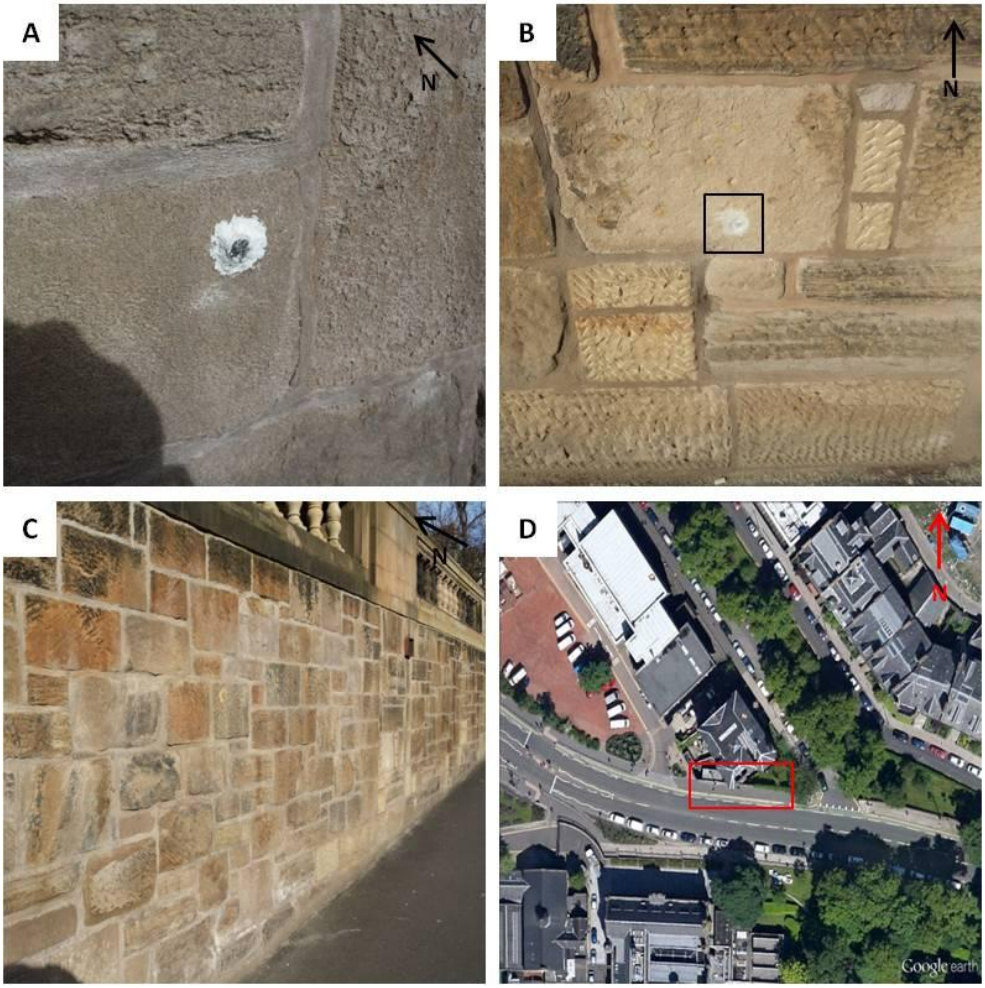

Figure 14-1: Site 1: University Avenue. The location of drilling sites A and B.

(A): Location of the surface ibutton, attached to the wall using exterior polyfill. (B): Black box highlights the locality of the ibutton at depth within the stone. (C): A larger picture of Site 1, showing stone decay near the bottom of the wall and replacement of both stone blocks and columns at the top of the wall. (D): Google map image showing the location of site 1 adjacent University Avenue: a busy road that regularly receives salt deposition.

Figure 14-2: Site 2: James Watt building. The location of drilling site D.

(A): Location of the surface ibutton. (B): Google map image showing the location of site 2. Red box highlights the locality of the surface ibutton and the red circle represents the location of the ibutton at depth and drilling site D.

Data were recorded at two hour intervals between March 2014 and March 2015, with 4201 measurements collected in total. Figure 14-3 shows an initial steady increase in surface temperature between March and August, 2014, followed by a steady decrease between August 2014 and January 2015. Highest temperatures occurred in July 2014 and lowest temperatures in January 2015. This trend is mirrored by data recorded at a depth of 5 cm, but with the temperature differences buffered due to insulation by the stone.

The annual variation in RH at the stone surface shows that the lowest average values occurred between July and August 2014 and the highest values in January 2015 (Figure 14-4). RH at depth follows the same trend, but shows a lower range of values. Thus, internal parts of the wall do not experience high amplitude changes in temperature and RH. RH values from all four locations (both internal and external) did not fall below 50% at any time, with temperature values ranging between a minimum of -1.9^{o}C in February 2015 and a maximum of 42.5^{o}C in July 2014. Throughout 2014, Glasgow experienced a consistently high RH of average 78% - 88%, with mean temperatures of around 13^{o}C; consistent with its maritime temperate climate. The solid red lines on each RH graph represent the deliquescent point of NaCl (75% RH) and the dashed red lines represent a reduced NaCl deliquescent point of 68% RH.

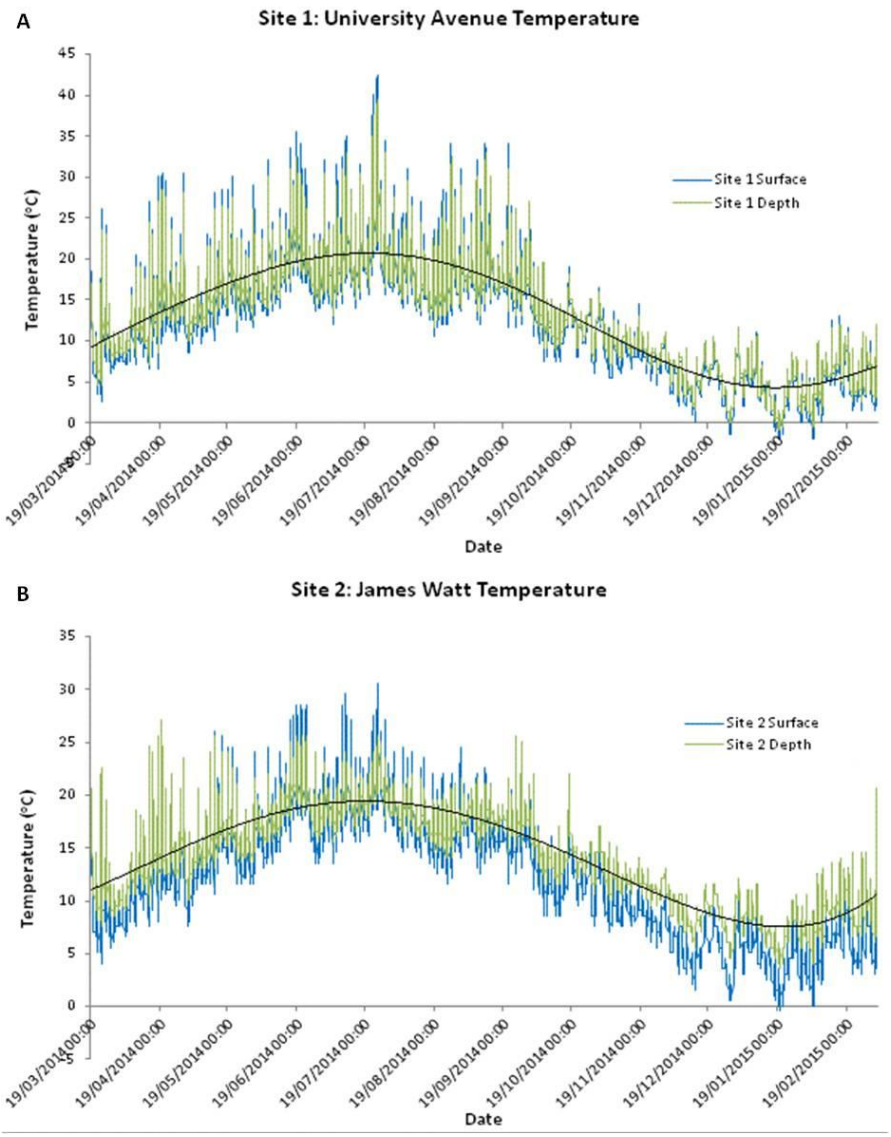

Figure 14-3: Measured temperature for two sites at The University of Glasgow between 19 March, 2014 and 04 March, 2015.

(A): Measured temperature at Site 1. (B) Measured temperature at Site 2. Measurements were made at two hour intervals. Thin black line represents the average trend.

All salts within building stone undergo phase changes that are closely linked to temperature and RH. Most salts are hygroscopic and will readily absorb water vapour from the air. Certain salts such as NaCl have a simple relationship with temperature and RH and will precipitate at a fixed RH value (75%). Other salts such as Na_2SO_4 have a more complex thermo-hygric relationship, which makes them more sensitive to low amplitude changes in temperature and RH. A simple method of evaluating the quantity and frequency of salt crystallisation-dissolution events is by counting the number of times the measured RH crosses the deliquescence point of each salt: halite (75%), $MgCl_2/CaCl_2$ (~33%). One cycle represents each time the RH dropped

below the deliquescence point (crystallisation) and then increased above this value (dissolution).

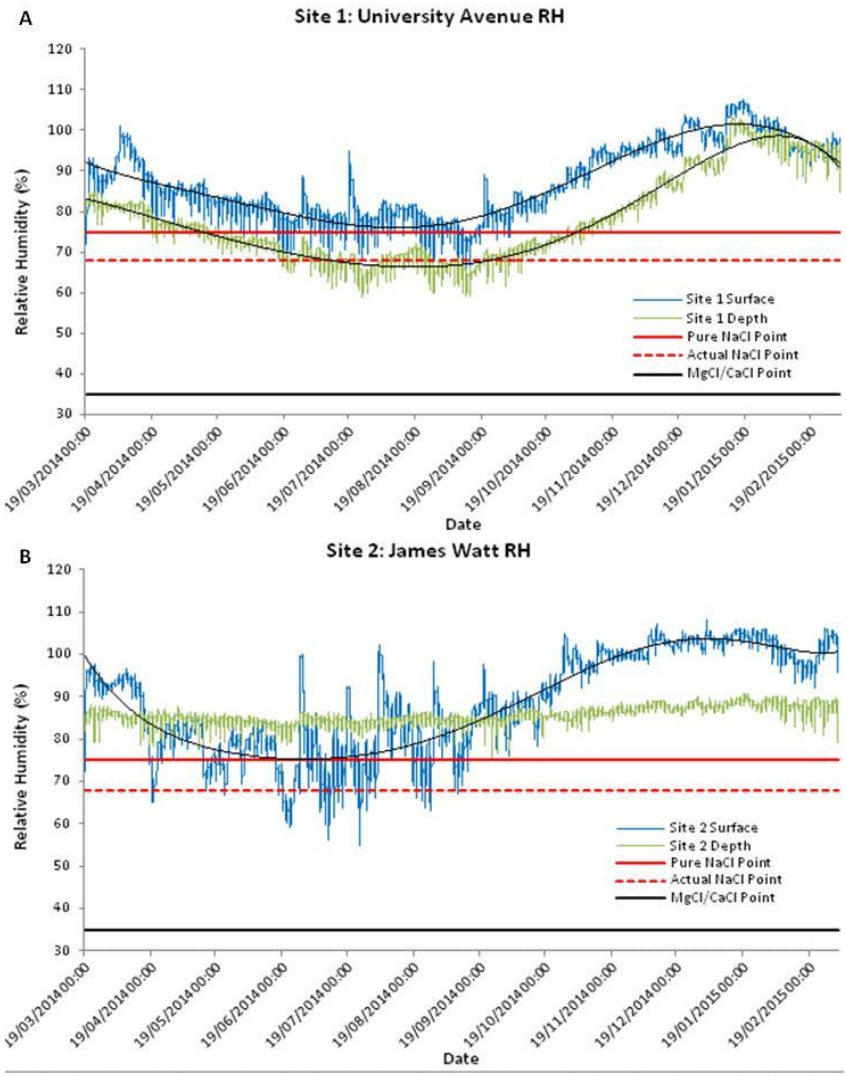

Figure 14-4: Measured relative humidity (RH) for two sites at The University of Glasgow between 19 March, 2014 and 04 March, 2015.
(A): Measured RH at site 1. (B): Measured RH at site 2. Measurements were made at two hour intervals. Thin black line represents the average trend.

Figure 14-4 shows the RH for each site. From the start of monitoring (19th March 2014) until 18th April 2014, and then from mid November 2014 until the end of monitoring (4th March 2015), RH at the surface and at depth, at both sites, remained above 75% RH. Most of the transitions at site 1 take place on the stone surface, with cycles restricted to the summer months (May – October). At depth, the stone RH is above 75% for most of this period. Over the monitoring period there were 67 crystallisation-dissolution cycles recorded on the surface at site 1 and 27 cycles at 5 cm depth.

At site 2 on the other hand, only 45 surface cycles were recorded, with no cycles recorded at depth; RH at depth fell below 80% on only 33 occasions, and never below 75%. It is important to note, however, that due to moisture retention at depth within the stone, there will be a reduction in the frequency of recorded crystallisation cycles. Areas of the graph that lie above and below the red line are assumed stable conditions, whereby NaCl is in either crystalline form (below red line) or in solution (above red line).

An idealised situation is assumed when using the aforementioned theoretical deliquescence values. These are values taken for pure salt solutions, which are unlikely to be found in building stones (De Clercq et al., 2013; Steiger and Heritage, 2012). Within a salt mixture, individual salts will generally crystallise at a lower deliquescence point (Price, 2007). RunSalt analyses of drillings taken from sites across the university reveals that the deliquescence point of NaCl is reduced by 7% when present within these salt mixtures.

A second measurement of salt crystallisation-dissolution cycles using the deliquescence point of 68% RH is highlighted by the dashed red line in Figure 14-4. As expected, this point has fewer cycles in most locations, with only four cycles expected to occur on the surface of site 1 (a reduction of 94% relative to cycles at 75% RH), and 29 cycles on the surface of site 2 (a reduction of 35% relative to cycles at 75% RH). However, there was an increase in the number of cycles expected at depth in site 1, from 27 cycles at 75% RH to 61 cycles at 68% RH.

RH and temperature data for Glasgow were also analysed for crystallisation-dissolution cycles throughout 2013 using maximum and minimum daily values from weather station data (www.weatherunderground.com). Similar trends to ibutton measurements are recorded, reflecting an increase in RH during winter months (peak in December 2013), and lower values during summer months (minima in May 2013). There were theoretically 244 crystallisation-dissolution cycles across the full year. The greatest number of cycles took place between June and August 2013, and the lowest between December and January 2013. By taking into account wet days, where it is thought that stone walls would become surface wet, the total number of cycles fell to 98 throughout the year. High-resolution temporal analysis of 30 minute and 60

minute monitoring intervals over a week in March 2013 and a week in June 2013 highlight that, on average, between 1-2 crystallisation/dissolution cycles can take place through the course of one day, occurring in the early afternoon (Figure 14-5). Therefore, the number of cycles that were measured at the two university sites using ibuttons, and with a two hour frequency, may under-estimate the number of cycles experienced at each locality.

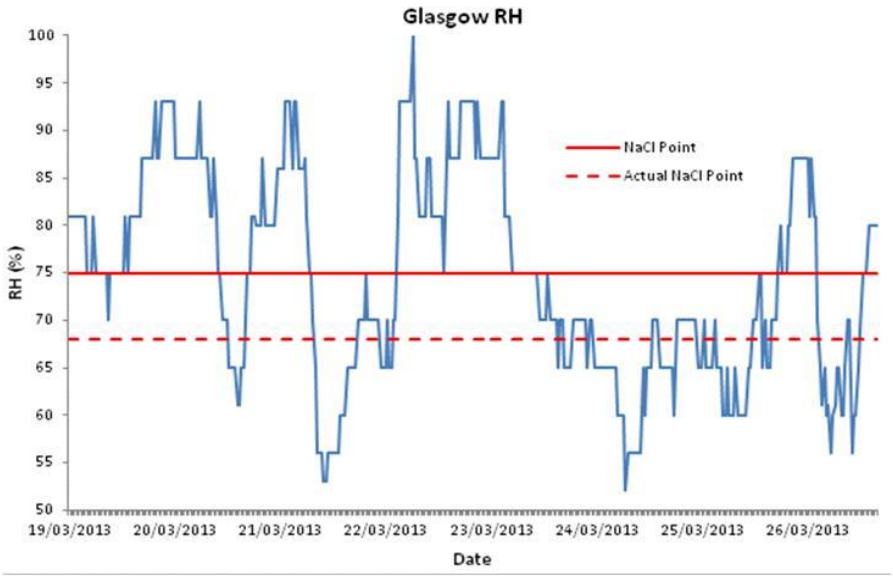

Figure 14-5: RH weather station measurements for Glasgow over a 1 week period. Measurements were recorded over a 1 week period from 19 March, 2013 – 26 March, 2013. (www.weatherunderground.com).

The black line on each RH graph in Figure 14-5 and Figure 14-6 represents the deliquescence point of both $MgCl_2$ and $CaCl_2$. This value (33% RH) is substantially lower than that of NaCl and was not crossed at any point during either the ibutton monitoring period (2014-2015) (Figure 14-4) or in Glasgow throughout 2013 (Figure 14-6). This finding indicates that both $MgCl_2$ and $CaCl_2$ are extremely unlikely to crystallise, at any time, within building stones in Glasgow. Thus there may be a recommendation to use $MgCl_2$ and $CaCl_2$ in Scotland, regarding the vulnerability of building stones to the direct crystallisation of both salts. However, in other climates, the crystallisation and damage potential of both salts could be greater. In order to test this possibility, data from other cities were used to calculate the number of theoretical crystallisation-dissolution cycles throughout 2013. Cities were chosen in order to satisfy the criteria: (i) either $MgCl_2$ or $CaCl_2$ are used as de-icing salts by either the road maintenance authority or are commercially available for private use; (ii) they have buildings constructed from sandstone.

Meteorological data was taken from weatherunderground.com, with maximum and minimum RH values used for each day.

The cities of Denver, Toronto, Stockholm and Salt Lake City use $MgCl_2$ and $CaCl_2$ as de-icing products and have sandstone buildings. For each city, the NaCl and $MgCl_2/CaCl_2$ crystallisation-dissolution cycles were counted to evaluate the crystallisation damage potential for each salt. The number of cycles for each city is given in Table 14-1. Interestingly, Glasgow, Denver and Toronto all experienced 98 NaCl cycles in 2013, assuming there was only one crystallisation event per day. Stockholm on the other hand experienced nearly 60 additional events throughout the year. Significantly, all four overseas cities experienced a high number of potential $MgCl_2/CaCl_2$ cycles. For each city, the greatest number of cycles for each salt was recorded during the summer months, with the exception of Denver that experienced 23, 17 and 22 cycles in November, December and January, respectively. Building stones during these months are likely to be wetter and so it is unlikely that each recorded cycle represents an actual crystallisation event. Rather, this chapter considers the potential of these climates to produce crystallisation events. Deliquescence values of pure salt solutions were used due to the lack of measured ion data for stones in each city. The number of crystallisation cycles for each salt in Glasgow and Denver are compared in Figure 14-6.

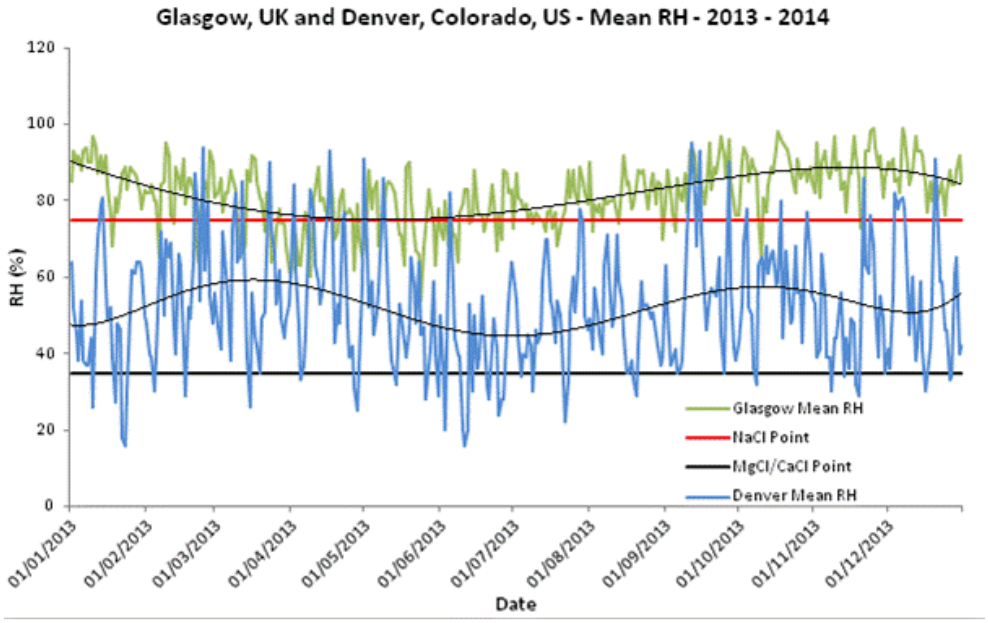

Figure 14-6: RH comparison between Glasgow, UK and Denver, Colorado, US through 2013.

City	75% cycles	75% cycles - wet days	33% cycles	33% cycles - wet days
Glasgow	244	98	0	0
Denver	176	98	264	203
Salt Lake City	140	58	204	161
Toronto	287	98	67	40
Stockholm	297	157	112	84

Table 14-1: Predicted crystallisation-dissolution cycles between 1 January, 2013 and 31 December, 2013.

14.3 Runsalt® Analysis

RunSalt is a vital tool in understanding salt crystallisation pathways under changing temperature and RH conditions. Due to the presence of salt mixtures within most building stones, understanding the aggressiveness of each salt and the conditions under which they are likely to crystallise can be extremely difficult to predict. Furthermore, salt mixtures could be more damaging than single salt solutions due to the potential of recurrent crystallisation episodes of several salts over a short period of time.

Four sites were chosen across The University of Glasgow campus to measure salt concentrations (Figure 14-1 and Figure 14-2). At each site, three depth measurements were taken (1 cm, 3 cm and 5 cm), giving 12 samples in total. As expected, the maximum salt concentrations at each site were in the outer 1 cm of the stone, with a gradual reduction in concentrations to 5 cm depth in sites 2 and 3. Sites 1 and 4 had a greater proportionate reduction in concentration between 1 cm and 3 cm and these were the same sites that gave the greatest salt concentrations at the surface, over double that of sites 2 and 3. Site 1 samples were taken from a section of wall adjacent to a busy road (University Avenue), while site 4 samples were taken from a low, decayed section of a building adjacent to a quieter road (within the main university campus that allowed access to a car park and did not permit through traffic). Site 2 samples were extracted from a higher elevation on the same wall as site 1, and site 3 samples taken from a low elevation section of wall on the North façade of the main University building.

Site 1 contains a greater percentage of $CaSO_4$ than every other site with lower values of NaCl, while site 2, which is from the same location but located at a greater height, has a higher percentage of Cl^-, but with similar amounts of Mg^{2+}, Ca^{2+} and slightly less Na^+. Site 3 has similar cation values to site 2 but with a greater SO_4^{2+} concentration. Site 4 shows high values of Na^+ and Ca^{2+} and is dominated by Cl^-. The measured salt ion values are given in Table 14-2.

Site	Na^+ (wt %)	Ca^{2+} (wt %)	Mg^{2+} (wt %)	K^+ (wt %)	Cl^- (wt %)	$NO3^-$ (wt %)	SO_4^{2-} (wt %)
1A	0.247	0.696	0.006	0.007	0.168	0	1.875
1B	0.013	0.084	0.056	0.008	0.021	0	0.003
1C	0.013	0.066	0.046	0.011	0.021	0	0.005
2A	0.076	0.172	0.197	0.012	0.156	0.021	0.030
2B	0.038	0.135	0.147	0.012	0.076	0.007	0.012
2C	0.037	0.063	0.069	0.019	0.074	0.005	0.007
3A	0.101	0.105	0.036	0.007	0.150	0	0.254
3B	0.109	0.113	0.085	0.007	0.168	0	0.007
3C	0.095	0.110	0.078	0.008	0.147	0	0.007
4A	0.520	0.407	0.134	0.042	0.693	0.001	0.122
4B	0.153	0.037	0.020	0.052	0.342	0.003	0.013
4C	0.200	0.063	0.033	0.059	0.312	0.001	0.009

Table 14-2: Weight percentages of measured cations and anions from each drilling site, measured by ion chromatography and atomic absorption spectroscopy.
A sites = surface - 1 cm. B sites = 1 - 3 cm. C sites = 3 - 5 cm.

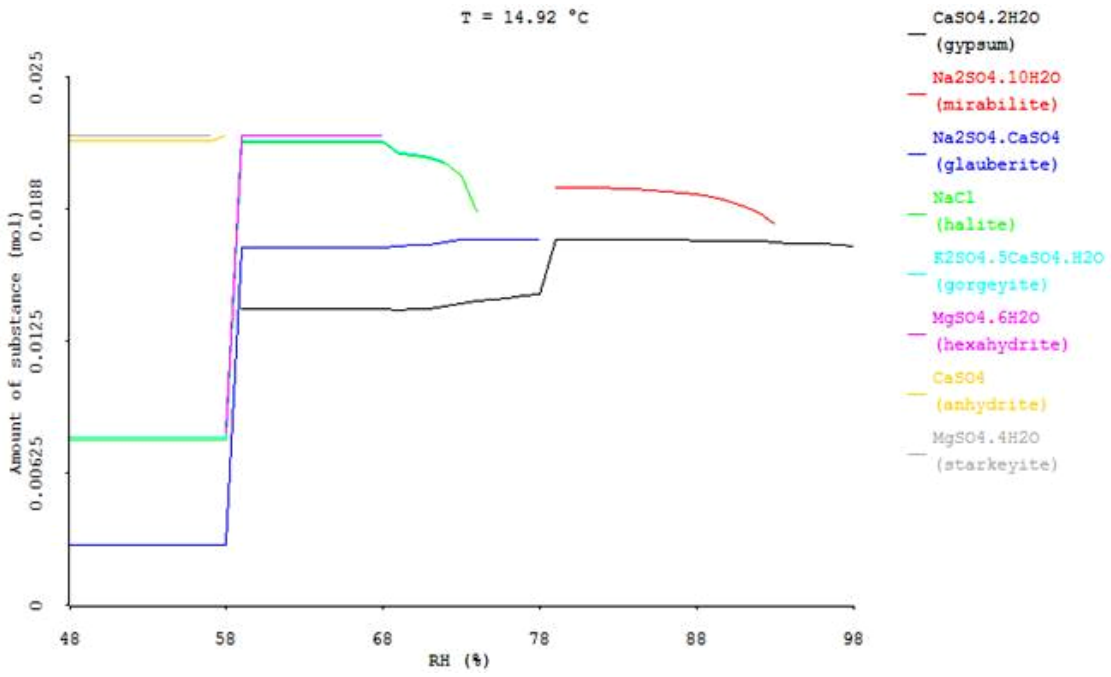

Figure 14-7: RunSalt graph for site 1A.

A RunSalt simulation was undertaken for each analysis using the average annual temperature and the range of RH values as recorded by both ibuttons. As RH has a greater influence on crystallisation-dissolution cycles than temperature, it was decided that RH was the variable parameter. Figure 14-7 shows the RunSalt output from site 1A, using the average temperature of 14.92 ^{o}C, and RH range of 48% - 98%. Results predict that the outer 1 cm of the wall contains gypsum, mirabilite, glauberite, halite, gorgeyite, hexahydrite, anhydrite and starkeyite. Gypsum is expected to be in crystalline form even at extremely high RH values of 98%, while mirabilite is expected to crystallise below 93% RH. Halite will crystallise at 73% RH, which is slightly lower than the expected deliquescent point for pure halite (75% RH). Only anhydrite and starkeyite are expected to crystallise below 60% RH, while mirabilite, gypsum, glauberite and halite are predicted to crystallise regularly throughout the year. The salt phases predicted for below 1 cm are significantly different, whereby only gypsum, anhydrite, carnallite and halite are expected. Although the halite deliquescence point at this depth is significantly lowered (58% RH) relative to a pure NaCl solution, the extra moisture that is expected within the stone below 1 cm depth would ultimately limit the number of crystallisation cycles that would take place.

RunSalt analysis on site 2A shows that higher up the wall there is both a reduction in the quantity of salt ions and the expected salt phase transitions, with only halite and gypsum crystallising in this part of the wall. The removal of gypsum from the RunSalt analysis was required at this site. This is because the model assumes that gypsum under these conditions is insoluble, and therefore omits gypsum from the calculations. Site 3 has a similar sequence to site 1, with a range of salts predicted to crystallise in the outer 1 cm of the wall. Halite will crystallise at 71% RH, followed by gorgeyite at 68% RH and hexahydrite at 69% RH. Analysis of sites 3B and 3C reveal a similar sequence to the same depths at site 1, with only gypsum, halite and anhydrite expected to crystallise. Analysis of site 4 required the removal of gypsum, with no salts expecting to crystallise within the outer 1 cm over the 54 – 97% RH range. At depth at site 4, halite and sylvite (a potassium chloride salt), are predicted to crystallise below 72% and 67% RH respectively.

Halite is predicted to form at all four sites and has the potential to crystallise at depth within the stone at each location. Sites 1 and 3 had the greatest range of salt types, containing a variety of chloride and sulphate salts. The greatest concentration of salt minerals was in the outer 1 cm of the stone, with only gypsum/anhydrite and halite found at depths greater than 1 cm at every site. Due to the presence of salt mixtures, the deliquescence point of each salt, specifically halite, was reduced.

Owing to the temperate climate of Scotland, $MgCl_2$ and $CaCl_2$ are extremely unlikely to crystallise as single salts within building stone. Furthermore, laboratory salt crystallisation tests show that both salts are absorbed by sandstones to the same, if not to a greater extent than NaCl. These points therefore beg the question: What are the effects on salt phase changes in masonry sandstone with Ca^{2+}, Mg^{2+} and Cl^- ions by the increased use of $CaCl_2$ and $MgCl_2$ de-icing salts?

By simulating increased levels of Ca^{2+}, Mg^{2+} and Cl^- into salt concentration profiles, it is possible to predict the effect use of $MgCl_2$ and $CaCl_2$ de-icing salts on salt phase transitions. It was decided that due to the relatively low salt levels measured at each site, doubling the concentrations of Mg^{2+}, Ca^{2+} and Cl^- would still provide realistic levels after the addition of $MgCl_2$ and $CaCl_2$.

Simulations were run and compared to the initial RunSalt sequences for each site. Table 14-3, Table 14-4 and Table 14-5 show the original salt volumes and the simulated changes. An input of $MgCl_2$ is likely to cause a small increase in all of the salt phases in site 1A, but with an expected drop in each salt phase in the remaining sites, with the exception of a slight increase in sylvite at site 4B. There is a similar trend across every site with input of $CaCl_2$. The model predicts an increase in halite, gypsum and anhydrite at site 1A, with a similar increase in halite expected at sites 3A, 4A and 4B but with a reduction in every other salt phase across each site. The addition of extra NaCl results in the increase of halite in all but sites 1C, 2C, 3B and 3C. Generally, NaCl input has a greater enhancement on the crystallisation of each salt phase throughout each site. Only $CaCl_2$ caused a significant reduction in the deliquescence point of halite; from 73% to 67% RH at site 1A,

generally reducing the number of crystallisation-dissolution cycles (Figure 14-4). In contrast, the addition of extra NaCl would raise the deliquescence point of halite, potentially causing increased damage through extra crystallisation-dissolution cycles. Repeat RunSalt simulations were made for increases in each salt (i.e. doubling the Na^+ and Cl^-, Mg^{2+} and Cl^-, and Ca^{2+} and Cl^- ion concentrations relative the measured values at each site) using the same temperature and RH values

Site	Na^+ (wt %)	Ca^{2+} (wt %)	*Mg^{2+} (wt %)*	K^+ (wt %)	*Cl^- (wt %)*	$NO3^-$ (wt %)	SO_4^{2-} (wt %)
1A	0.247	0.696	*0.012*	0.007	*0.180*	0	1.875
1B	0.013	0.084	*0.112*	0.008	*0.133*	0	0.003
1C	0.013	0.066	*0.092*	0.011	*0.113*	0	0.005
2A	0.076	0.172	*0.394*	0.012	*0.550*	0.021	0.030
2B	0.038	0.135	*0.293*	0.012	*0.369*	0.007	0.012
2C	0.037	0.063	*0.137*	0.019	*0.211*	0.005	0.007
3A	0.101	0.105	*0.073*	0.007	*0.223*	0	0.254
3B	0.109	0.113	*0.170*	0.007	*0.338*	0	0.007
3C	0.095	0.110	*0.156*	0.008	*0.303*	0	0.007
4A	0.520	0.407	*0.268*	0.042	*0.961*	0.001	0.122
4B	0.153	0.037	*0.040*	0.052	*0.382*	0.003	0.013
4C	0.200	0.063	*0.067*	0.059	*0.378*	0.001	0.009

Table 14-3: Weight percentages used within RunSalt analyses after doubling Mg^{2+} and Cl^- ion values relative to the measured values for each site. Changed Mg^{2+} and Cl^- values are in italics. Values were initially doubled before RunSalt auto-balanced every ion value.

Site	Na^+ (wt %)	*Ca^{2+} (wt %)*	Mg^{2+} (wt %)	K^+ (wt %)	*Cl^- (wt %)*	$NO3^-$ (wt %)	SO_4^{2-} (wt %)
1A	0.247	*1.391*	0.006	0.007	*1.559*	0	1.875
1B	0.013	*0.167*	0.056	0.008	*0.188*	0	0.003
1C	0.013	*0.132*	0.046	0.011	*0.153*	0	0.005
2A	0.076	*0.344*	0.197	0.012	*0.500*	0.021	0.030
2B	0.038	*0.270*	0.147	0.012	*0.346*	0.007	0.012
2C	0.037	*0.126*	0.069	0.019	*0.200*	0.005	0.007
3A	0.101	*0.211*	0.036	0.007	*0.361*	0	0.254
3B	0.109	*0.227*	0.085	0.007	*0.395*	0	0.007
3C	0.095	*0.219*	0.078	0.008	*0.366*	0	0.007
4A	0.520	*0.814*	0.134	0.042	*1.507*	0.001	0.122
4B	0.153	*0.074*	0.020	0.052	*0.416*	0.003	0.013
4C	0.200	*0.127*	0.033	0.059	*0.438*	0.001	0.009

Table 14-4: Weight percentages used within RunSalt analyses after doubling Ca^{2+} and Cl^- ion values relative to the measured values for each site. Changed Ca^{2+} and Cl^- values are in italics. Values were initially doubled before RunSalt auto-balanced every ion value.

Site	*Na^+ (wt %)*	Ca^{2+} (wt %)	Mg^{2+} (wt %)	K^+ (wt %)	*Cl^- (wt %)*	$NO3^-$ (wt %)	SO_4^{2-} (wt %)
1A	*0.493*	0.696	0.006	0.007	*0.414*	0	1.875
1B	*0.026*	0.084	0.056	0.008	*0.034*	0	0.003
1C	*0.025*	0.066	0.046	0.011	*0.033*	0	0.005
2A	*0.151*	0.172	0.197	0.012	*0.231*	0.021	0.030
2B	*0.076*	0.135	0.147	0.012	*0.114*	0.007	0.012
2C	*0.074*	0.063	0.069	0.019	*0.111*	0.005	0.007
3A	*0.201*	0.105	0.036	0.007	*0.251*	0	0.254
3B	*0.217*	0.113	0.085	0.007	*0.276*	0	0.007
3C	*0.190*	0.110	0.078	0.008	*0.241*	0	0.007
4A	*1.040*	0.407	0.134	0.042	*1.213*	0.001	0.122
4B	*0.307*	0.037	0.020	0.052	*0.495*	0.003	0.013
4C	*0.400*	0.063	0.033	0.059	*0.511*	0.001	0.009

Table 14-5: Weight percentages used within RunSalt analyses after doubling Na^+ and Cl^- ion values relative to the measured values for each site. Changed Na^{2+} and Cl^- values are in italics. Values were initially doubled before RunSalt auto-balanced every ion value.

Based on the original RunSalt data and on theoretical RunSalt simulations with input of $MgCl_2$, $CaCl_2$ and NaCl, the following findings are summarised. Halite is a very common salt and was found at every site, with simulations showing that it has the potential to crystallise at depth within the stone. Most salts accumulate in the outer 1 cm, with concentrations falling sharply below this depth. Increasing the amount of Na^{2+} and Cl^- within the RunSalt simulation enhanced the yields of halite in all but four sites, and increased the deliquescence point of halite in all sites. Conversely, addition of $CaCl_2$ caused a reduction in halite concentration in all but four sites, and with $MgCl_2$, in all but one site. The addition of extra $CaCl_2$ caused the greatest reduction in salt concentrations, especially at lower RH levels. Both salts also lowered the deliquescence point of halite in each site and importantly, did not cause the crystallisation of any new salt phases, while generally having a negative effect on additional salt crystallisation.

There is no specific trend in salt phase changes after the addition of $CaCl_2$ and $MgCl_2$. NaCl on the other hand produced an increase in both the concentration and the deliquescence point of halite at most sites. It is shown that a building containing a salt with a high deliquescence point is likely to experience a greater number of crystallisation-dissolution cycles, which therefore increases the risk of extra damage taking place. The addition of $CaCl_2$ and $MgCl_2$ is expected to decrease the deliquescence point of most

salts. This effect would likely decrease the number of crystallisation-dissolution cycles experienced by the stone, and could be viewed as beneficial for the stone under the RH conditions measured for Glasgow.

A known problem when working with RunSalt is the inability to accurately measure gypsum concentrations. The effects of increased Ca^{2+} levels on gypsum concentrations within the stone are unknown. Extra Ca^{2+} could likely raise the concentration of gypsum, and by using the available SO_4^{2+} ions within the solution, would subsequently decrease the possibility of other sulphate salts forming. There is indeed evidence of this trend, with a decrease in anhydrite estimated at low RH levels at various sites.

To summarise, the effect of increased Ca^{2+}, Mg^{2+}, Na^{+} and Cl^{-} ions on salt phase transitions is dependent on the original ion content of the stone. A moderate similarity between the impacts of increased $CaCl_2$ and $MgCl_2$ suggests that the addition of these solutions may well depress the expected salt concentrations and lower the deliquescence points of several salt phases. By focussing particularly on halite, a known damaging salt, input of $CaCl_2$ and $MgCl_2$ seems to have a positive impact, reducing the number of crystallisation cycles and the amount of halite crystallising.

15 Appendix G

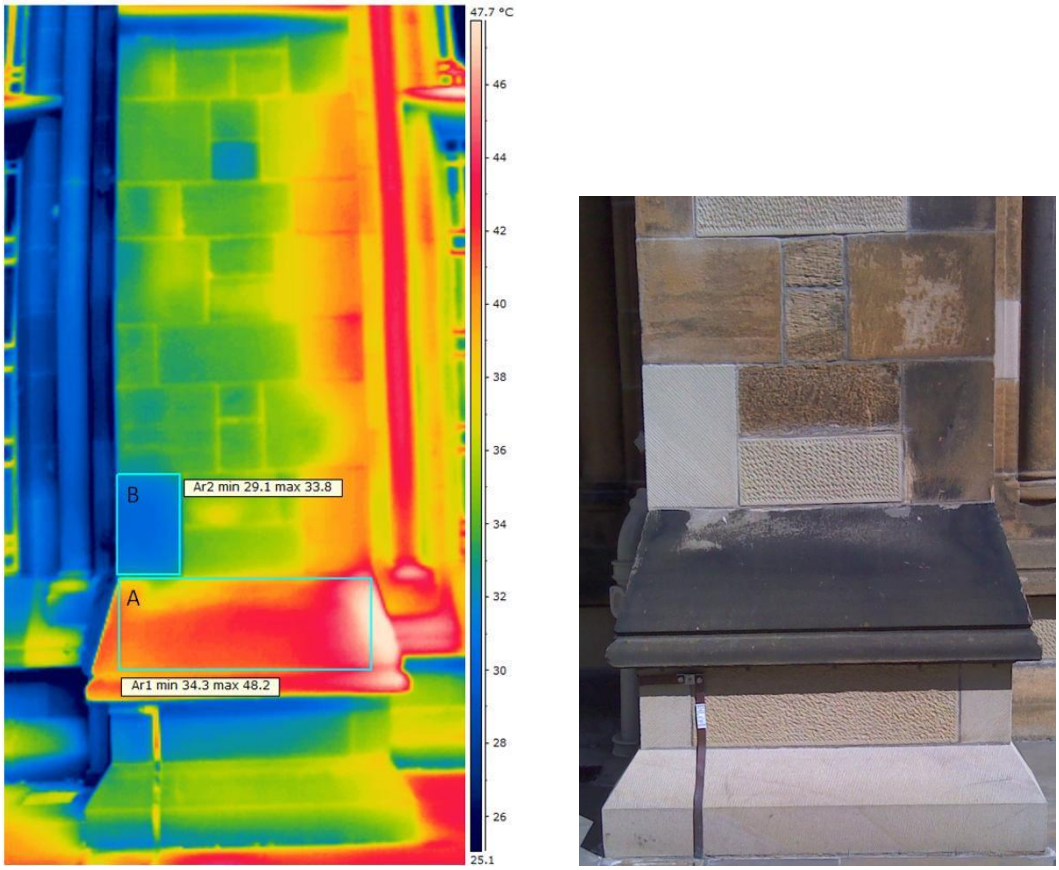

Figure 15-2: Infrared thermography image of a section of the University building.

Left: Infrared thermography image showing the surface temperature of sandstone blocks within a wall in the East quadrangle of The University of Glasgow. Block A corresponds to the large dark crusted sandstone block on the right image, while block B shows the surface temperature of a newly emplaced blonde sandstone block. Minimum and maximum temperatures are given for each block.

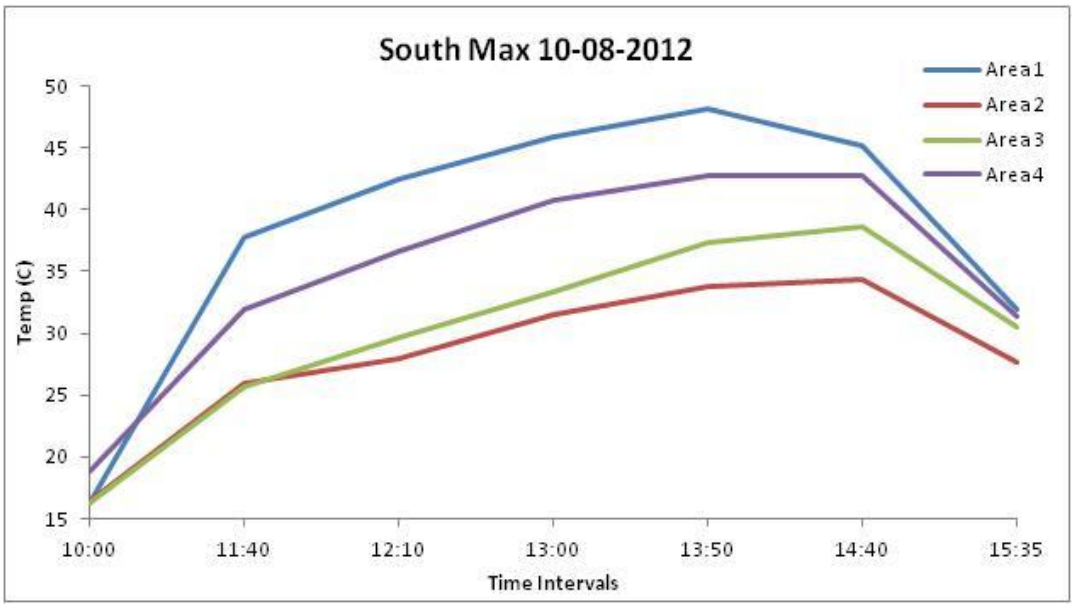

Figure 15-1: Maximum recorded stone surface temperatures across four different areas from the above location.

16 Appendix H

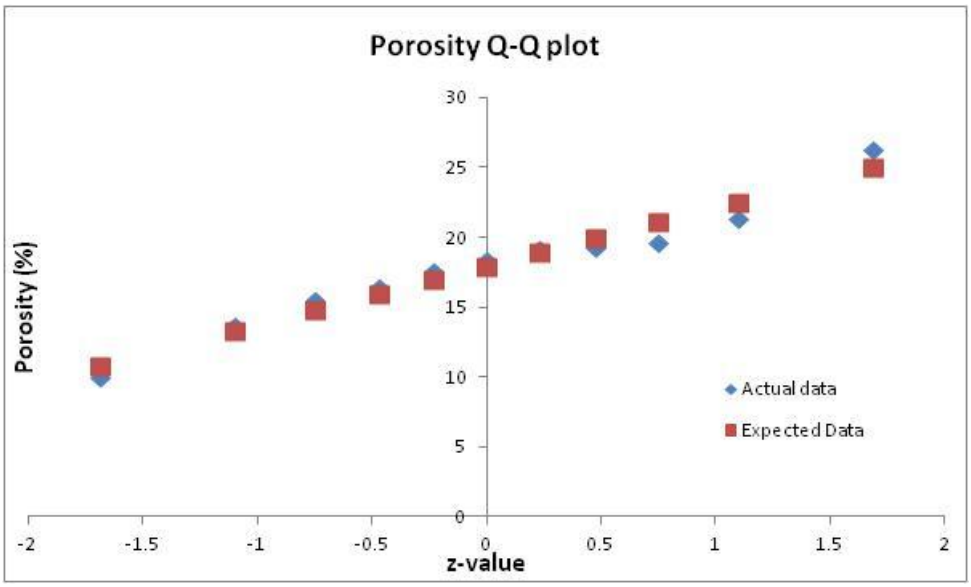

Table 16-1: Porosity Q-Q plot.

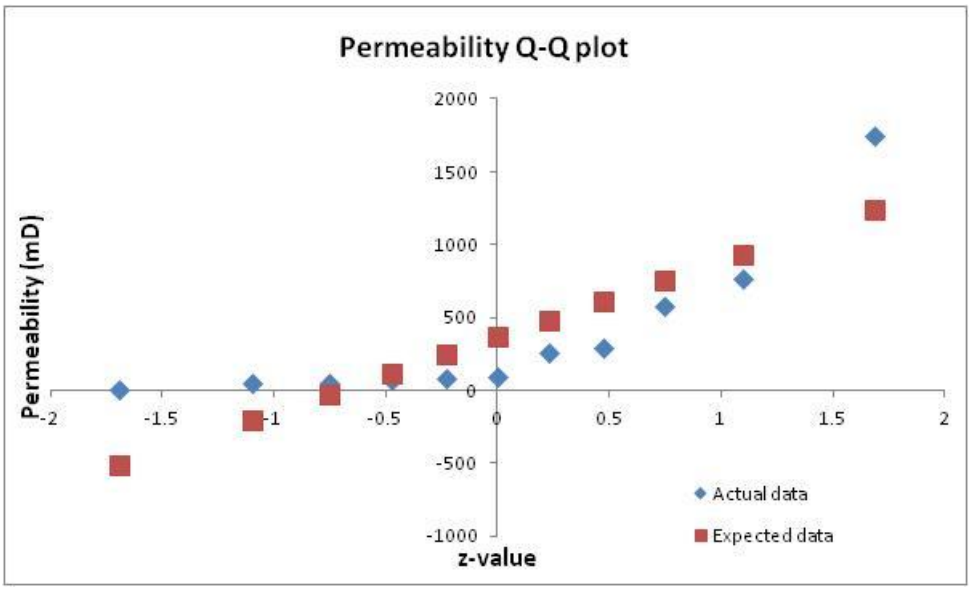

Table 16-2: Permeability Q-Q plot.

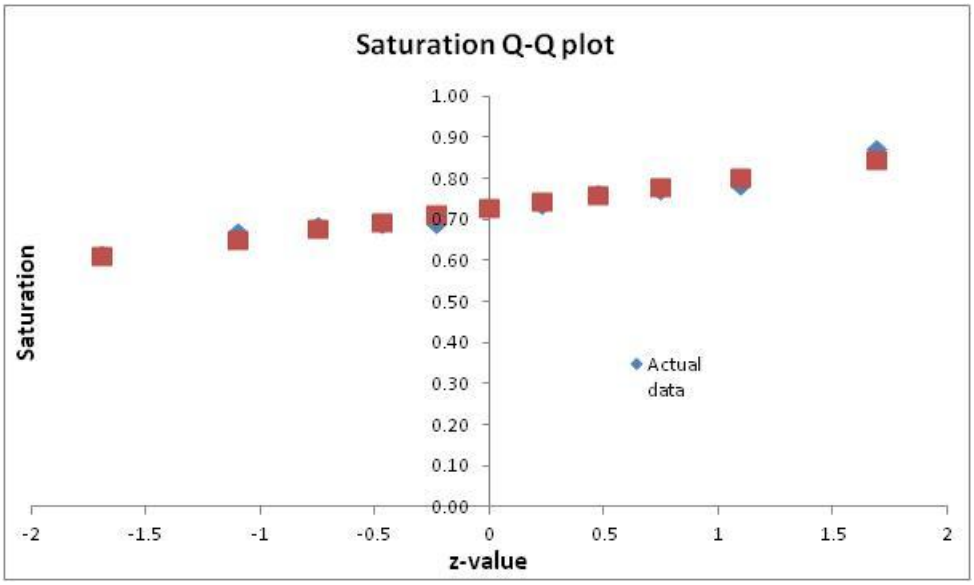

Table 16-3: Saturation Q-Q plot.

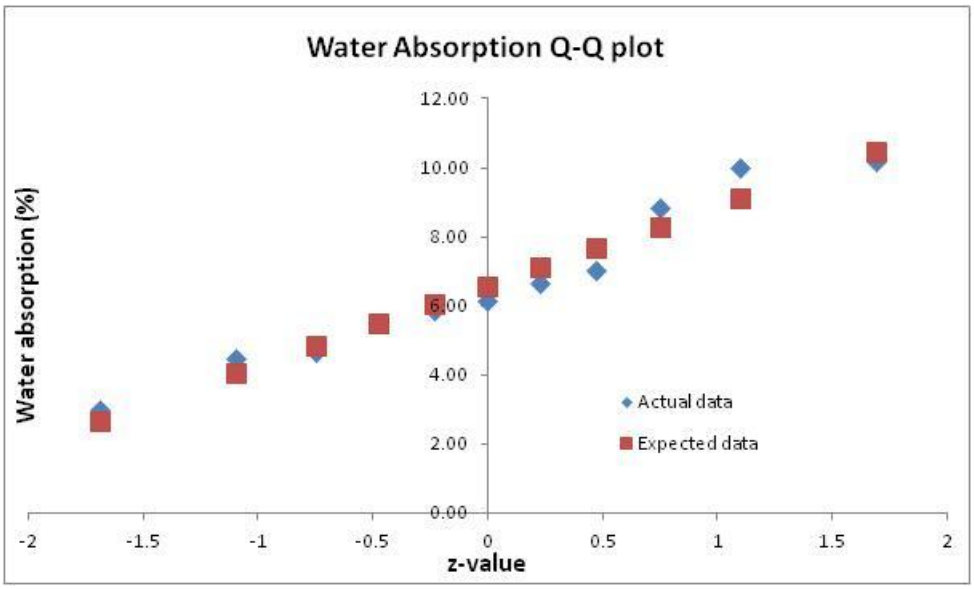

Table 16-4: Water absorption Q-Q plot.

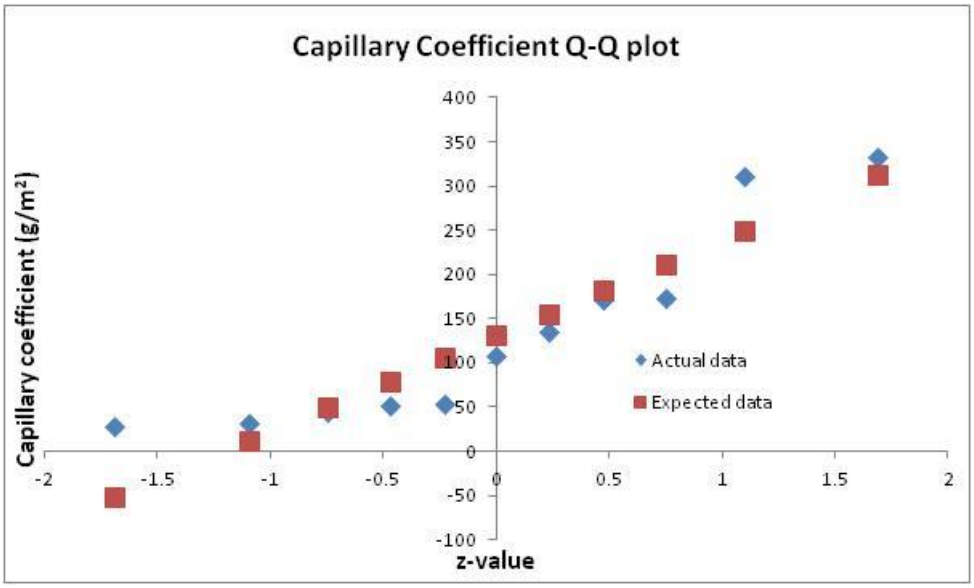

Table 16-5: Capillary coefficient Q-Q plot.

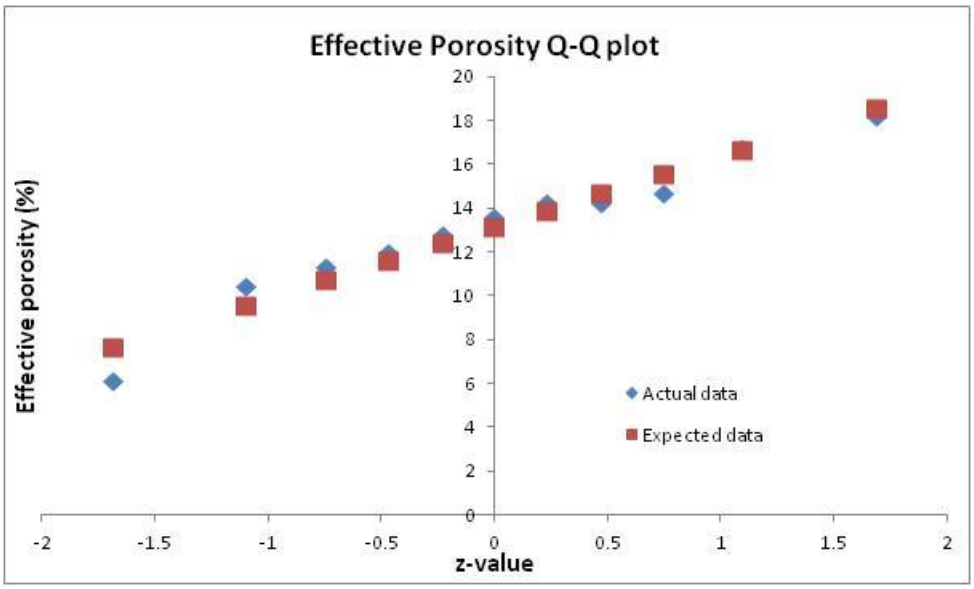

Table 16-6: Effective porosity Q-Q plot.